Towards Understanding the Formation of Water on Interstellar Dust Grains

Victoria Louise Frankland

Submitted for the degree of Doctor of Philosophy

Heriot-Watt University

School of Engineering and Physical Sciences

September 2011

ABSTRACT

Although several research groups have studied the formation of H_2, both experimentally and computationally, few have explored the surface formation of more complex molecules. A small number of these reactions produce molecules that remain on the surface and, over time, lead to the formation of icy mantles coating interstellar dust grains. The most abundant of these species within the ice is H_2O. The first half of this thesis introduces the construction and characterisation of the new dual atomic beam apparatus built to explore the surface formation mechanism of H_2O. The apparatus has been designed to enable singular or dual atomic or molecular oxygen and hydrogen beams to be adsorbed onto a range of astronomically relevant substrates. Analysis of the surface chemistry can be performed using a combination of temperature programmed desorption, molecular beam modulation spectrometry, quartz crystal microgravimetry and reflection-adsorption infrared spectroscopy techniques.

The remainder of this thesis discusses the results obtained by performing temperature programmed desorption experiments. Kinetic analysis was deduced for: H_2O on bare silica; O_2 on bare silica; O_2 on compact amorphous solid water on silica; and O_2 on porous amorphous solid water on silica. The results obtained were used towards constructing a simulation model mimicking the desorption of O_2 from the icy mantles of interstellar dust grains under dense molecular cloud environments. The analysis revealed that sub-monolayer coverages of O_2 followed first order desorption kinetics with a range of desorption activation energies from all of the surfaces studied. Multilayer coverages of O_2 from silica were unexpectedly found to follow fraction order kinetics. Further experiments were performed to explore the origins of this multilayer fractional desorption order. The results obtained revealed that the kinetic order decreased roughly by half as the species change from O_2 to CO to N_2 suggesting the underlying amorphous silica surface appeared to be the cause for this unusual observation.

Preliminary atomic O beam TPD experiments had also been performed from a range of astronomical relevant surfaces. The initial results indicated that O_2, O_3, H_2O_2 and $^{13}CO_2$ were formed on the surface. However, the exact surface formation mechanism could not be concluded from these single experiments.

ACKNOWLEDGEMENTS

The work presented in this thesis could not have been achieved without the support and encouragement of many people. Although my thanks go to everyone involved, it would not be possible to list them all.

Firstly I would like to thank my primary supervisor Prof. Martin McCoustra for his continuous support, encouragement and guidance which were very much appreciated throughout my PhD. I also acknowledge the support of my secondary supervisor Prof. Ken McKendrick. Secondly, to the late Bernard Hanks for designing and organising the manufacture of the new apparatus required for this thesis and for the swift organisation of the additional extra parts and alterations needed. I am also grateful for the support of the rest of the surface astrochemistry research group (Dr. Mark Collings, Simon Green, John Thrower and Ali Abdulgalil) in helping me to construct and modify the apparatus as well as training me in the basics of UHV. Additionally, I would also like to thank Iain Drummond, Alan Barton, Paul Allan and all who helped from the Heriot-Watt University electronics workshop in the continuous construction and modifications to the apparatus.

I am also grateful for the help obtained from all my undergraduate project students. Particular thanks go to Ryan Nish for performing the experiments required for Chapter 5 along with Claire Pommier, Aude Pleuvry and Anais Auriau. Additionally, I would like to thank Frances Chapman for providing me with the opportunity to supervise two Nuffield funded students, Ellen Kendrick and Sandy Watts, whom both enhanced my joy of outreach. Acknowledgements are also given to: the Engineering and Physical Sciences Research Council (EPSRC) for funding this research; BBC Scotland for the outreach work experience gained; Mary for her advice and encouragement; and to Dr June McCombie at the University of Nottingham for all the initial encouragement and support to do this PhD.

A final thank you goes to my parents for their support and encouragement throughout the last five years.

Stuck in this Lab

By Victoria L. Frankland

Stuck in this lab,
Experiment gone bad.
Peak is way too low,
Now the theory out the window.
Better take my supervisor to tea
So he can explain this to me.

But I'm just

Stuck in this lab,
Trying not to go mad.
The thesis incomplete
And there's deadlines to meet.
Alter experiment list,
Repeat results that miss.
With the apparatus dieing
I just keep on trying.

Must keep on trying.

Stuck on a plane
Trying to stay sane.
Got this big presentation to do
And answer dreaded questions too.
Come on, deep breath. "I can".
Yet here I am.

Wishing I was

Stuck in that lab,
Trying not to go mad.
Thesis still incomplete
Even more deadlines to meet.
Alter experiment list,
Repeat results that miss.
With the apparatus dieing
I just keep on trying.

Must keep on trying.

Is it so hard to believe,
Back then I was so naïve.
Three years to do a PhD,
Just how easy can that be?
And now I am waiting,
Few results and no funding.

I'm just

Stuck in this lab,
Trying not to go mad.
Thesis now complete
Just one deadline to meet.
Can't alter the experiment list,
Hid the results that miss.
Just the viva to go
That's all! So,

I'm just

Stuck in this lab.
Yeah, stuck in this lab.
Just stuck in this lab
Trying not to go mad!

DECLARATION STATEMENT

(Research Thesis Submission Form should be placed here)

TABLE OF CONTENTS

GLOSSARY

AC – Alternating Current

AES – Auger Electron Spectroscopy

AFM – Atomic Force Microscopy

ASW – Amorphous Solid Water

cASW – Compact Amorphous Solid Water

CSW – Crystalline Solid Water

DC – Direct Current

E-R – Eley-Rideal

FTIR – Fourier Transform Infrared

FUV – Far Ultraviolet

HAS – Helium Atom Scattering

HV - High Vacuum

IR - Infrared

ISM – Interstellar Medium

LEED – Low Energy Electron Diffraction

L-H – Langmuir-Hinshelwood

MBMS – Molecular Beam Modulation Spectrometry

MW – Microwave

OFHC – Oxygen Free High Conductivity

PAH – Polycyclic Aromatic Hydrocarbons

pASW – Porous Amorphous Solid Water

PDRs – Photodissociation Regions

PTFE - Polytetrafluoroethylene

QCM – Quartz Crystal Microgravimetry

QMS – Quadrupole Mass Spectrometer

RAIRS – Reflection-Adsorption Infrared Spectroscopy

RF – Radio Frequency

TMP – Turbomolecular Pump

TPD – Temperature Programmed Desorption

TSP – Titanium Sublimation Pump

UHV – Ultrahigh Vacuum

UV - Ultraviolet

CHAPTER 1 - Introduction

Contents

1.1 Astrochemistry

Water is the dominant species observed in the icy mantles coating interstellar dust grains under dense molecular cloud environments. Astronomical observations of these dust grains under diffuse cloud conditions reveal that the grain surfaces are mostly bare suggesting that the icy mantles do not form until the cloud has collapsed in on itself resulting in a dense molecular cloud. Although the water molecules can be formed through gaseous reactions and adsorb onto the grain surface, the observed molecular abundance can not be matched through gas phase chemistry alone implying that another more efficient mechanism is required. Therefore the aim of this ongoing research is to experimentally explore the surface formation mechanism of water under interstellar environments.

1.1.1 Interstellar Medium (ISM)

At first thought, the vast gulfs of space lying between the stars, like the Horsehead Nebula pictured in **Figure 1.1** [1], were believed to be empty. Unprotected from cosmic rays and ultraviolet (UV) photons from nearby stars, the majority of molecules

Figure 1.1: The Horsehead Nebula [1]

would easily have been destroyed. Yet by the early 1960s these volumes of space, known as the Interstellar Medium (ISM), were known to contain gaseous molecules of CH (detected in 1937), CN (1940), CH^+ (1941) and OH (1963) [2]. In the following years, further observations were made of several other molecules. By 1972, the molecule list had extended to include: CH_2O, HCN, CH_3COH, C_3HN, $HCONH_2$, CH_3CN, CH_3OH, CS, H_2O, NH_3, CO and H_2 [2-6]. To date over 120 different molecular species have been identified through a combination of radio, microwave (MW), infrared (IR), and ultraviolet (UV) observations (see **Table 1.1**) [7, 8]. The only way these molecules could exist in the ISM was if they were formed through chemical reactions. This lead to the birth of a new discipline; Astrochemistry.

Further analysis of the ISM reveals that it consists of 99% by mass of gas, mostly hydrogen, and 1 % dust [9]. The evidence for dust is discussed in more detail in **Section 1.1.2**. There are several different environments within the ISM which are linked to the cycle of star formation as shown in **Figure 1.2**. The top picture of **Figure 1.2** represents a diffuse cloud. These are formed by gravity populating the ISM with gas and dust from the mass outflow of nearby aging stars and supernovae explosions [10]. Over time, the diffuse cloud collapses in on itself resulting in the formation of a dense molecular cloud (right hand picture). Particular parts of these molecular clouds continue to collapse further triggering star formation and in some cases, like our own Sun, the formation of planetary systems (bottom picture). As the star dies its matter is released back into the ISM to be recycled into the next generation of stars (left hand picture).

Each of these ISM environments is characterised by their physical conditions and chemical composition. Those of the diffuse and dense molecular clouds, which are the environments of most interest in this study, are discussed further below. Both of these environments are of particular interest to the astronomers and astrophysicists researching star formation as when a clump of gas begins to collapse in on itself, the clump begins to heat up. As clump collapse continues, the increasing thermal motion of the gaseous atoms and molecules in the gas cloud comes to resist the gravitational collapse preventing any further reduction of the clump's size. However, the atoms and molecules present inside the clump can radiate some of the thermal energy out into the

2 Atoms	3 Atoms	4 Atoms	5 Atoms	6 Atoms	7 Atoms	8 or More Atoms
H_2	C_3	c-C_3H	C_5	C_5H	C_6H	CH_3C_3N
AlF	C_2H	l-C_3H	C_4H	l-H_2C_4	CH_2CHCN	$HCOOCH_3$
AlCl	C_2O	C_3N	C_4Si	C_2H_4	CH_3C_2H	CH_3COOH
C_2	C_2S	C_3O	l-C_3H_2	CH_3CN	HC_5N	C_7H
CH	CH_2	C_3S	c-C_3H_2	CH_3NC	$HCOCH_3$	H_2C_6
CH^+	HCN	C_2H_2	CH_2CN	CH_3OH	NH_2CH_3	CH_2OHCHO
CN	HCO	CH_2D^+	CH_4	CH_3SH	c-C_2H_4O	CH_2CHCHO
CO	HCO^+	HCCN	HC_3N	HC_3NH^+	CH_2CHOH	CH_3C_4H
CO^+	HCS^+	$HCNH^+$	HC_2NC	HC_2CHO		CH_3CH_2CN
CP	HOC^+	HNCO	HCOOH	NH_2CHO		$(CH_3)_2O$
CSi	H_2O	HNCS	H_2CHN	C_5N		CH_3CH_2OH
HCl	H_2S	$HOCO^+$	H_2C_2O	HC_4N		HC_7N
KCl	HNC	H_2CO	H_2NCN			C_8H
NH	HNO	H_2CN	HNC_3			CH_3C_5N
NO	MgCN	H_2CS	SiH_4			$(CH_3)_2CO$
NS	MgNC	H_3O^+	H_2COH^+			NH_2CH_2COOH
NaCl	N_2H^+	NH_3				CH_3CH_2CHO
OH	N_2O	SiC_3				HC_9N
PN	NaCN	C_4				$CH_3OC_2H_5$
SO	OCS					$HC_{11}N$
SO^+	SO_2					
SiN	c-SiC_2					
SiO	CO_2					
SiS	NH_2					
CS	H_3^+					
HF	SiCN					
SH	AlNC					
FeO	SiNC					
O_2						

Table 1.1: List of Molecules Observed in the ISM [7, 8]

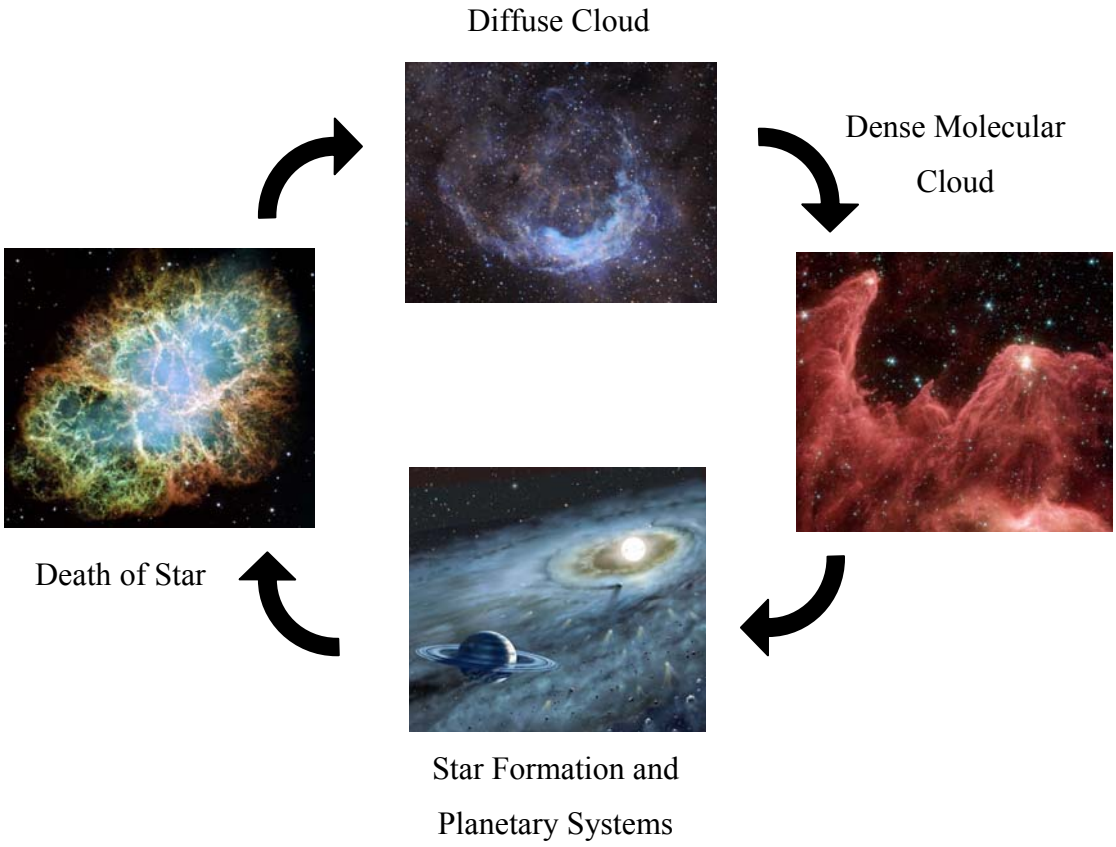

Figure 1.2: The Star Formation Cycle

(Pictures from NASA Picture of the Day Archive [1])

ISM on vibrational, rotational and ro-vibrational spectroscopic transitions. These species are also known as coolant species and result in the clump to collapse further in on itself triggering the formation of a new star or cluster of new stars. This phenomenon relies on the chemical composition of the gas clump. The first gas clumps were composed of H and H_2 coolant species resulting in large, hot, short lived stars. Thermonuclear reactions inside these first generation stars formed heavier elements which led to a larger range of element and molecular species in the sequent gas clumps. This in turn resulted in an increased range of coolant species allowing the clump to further collapse in on itself to form smaller, cooler, longer lived stars. Knowledge of the chemical species in the gas clump inside dense molecular clouds and their chemistry is required to fully understand this process. Before the chemistry in these environments is explored (see **Section 1.2**), the physical conditions in the diffuse and dense molecular clouds are first introduced.

In diffuse clouds, the density is less than 300 H atoms cm^{-3} with the dominant species being atomic H [11]. The temperatures of the gas and dust grain surfaces are 50 - 100 K and approximately 15 K respectively. The main source of heating in the diffuse clouds is from the photoelectric effect caused by dust grains absorbing far ultraviolet (FUV) photons from nearby stars [12]. This process creates electrons with energies of the region of 200 to 250 eV (roughly 3.2×10^{-17} to 4.0×10^{-17} J). These electrons heat the surrounding gas to a few hundred degrees through collisions. An additional heating process occurring in the diffuse clouds is from cosmic rays. These have energies typically between 1 – 10 MeV (approximately 2×10^{-12} to 2×10^{-13} J) and are efficient at ionizing and heating the gas. The primary electrons created from the ionization of the gas have an average kinetic energy of 35 eV (5.6×10^{-18} J) which is transferred through collisions leading to excitation or further ionization of the surrounding gaseous atoms and molecules [12]. The effects of FUV photons and cosmic rays continue to ensure the destruction of chemically complex species resulting in only a relatively few, small molecules surviving to be observed.

In a dense molecular cloud, the density is over 300 molecules cm^{-3} [11]. The presence of molecular species at densities of over 300 cm^{-3} results in the FUV photons being absorbed in the outer regions of the cloud; the so-called photodissociation regions (PDRs). As with diffuse clouds, the PDRs of the molecular cloud exhibit large temperature ranges for the gas (100 – 1000 K) and dust grains (10 – 100 K) due to the photoelectric effect, which is the dominant heating source, and cosmic rays heating [12]. In the inner regions of the molecular cloud, where the FUV photons cannot penetrate, the temperatures of the gas and grain surfaces reduce to 10 - 20 K and 5 - 10 K respectively. The lack of FUV photons allows the larger, more complex molecular species in **Table 1.1** to be formed as destructive processes are minimized.

The physical conditions of these environments, along with the interstellar dust (see **Section 1.1.2**), play a key role in the chemistry occurring in the ISM. This chemistry will be explored in detailed in **Section 1.2**.

1.1.2 Evidence for Interstellar Dust

Advances in telescope design and astronomical observation techniques have revealed much about the ISM. The original visible observations of the night sky, like that of the Flame Nebula in **Figure 1.3** (left) [1], revealed dark regions surrounded by stars. It was

not until observations were made with other parts of the electromagnetic spectrum, particularly with infrared (IR) radiation, did this theory change. IR observations of these dark regions revealed that there were stars and star clusters present (see right hand picture in **Figure 1.3** [1]). These observations have created many theories for the observable lack of their visible light. Today, these dark regions are known to be clouds of gas and dust; and the seats of star formation.

Figure 1.3: The Flame Nebula in Visible Light (left) and in Infrared (IR) [1]

(Please note that the right hand picture is rotated slightly anticlockwise to that of the left)

As starlight passes through the ISM, the dust grains reduce the amount of blue and ultraviolet light passing through causing the remaining light to appear more red in colour. This process is known as *interstellar reddening* and was first observed by Trumpler in 1930 [13]. However it is important to note that this interstellar reddening is not related to the Doppler shift of receding objects. This reddening can be described through the *interstellar extinction curves*. The average extinction curve was first determined in 1948 by Whitford [14] for the UV to near IR region and was updated in 1958 [15] to give the total extinction curve across the IR to the FUV range (red line in **Figure 1.4**). This is the main source of evidence for interstellar dust grains. For comparison, the plot also displays the visual extinction curve (purple dash line).

To determine the extinction curve, the apparent magnitude, m, of a star at a distance, d, from an observer (see **Equation 1.1**) needs to be calculated first. Here M is the absolute magnitude and $A(\lambda)$ is the extinction due to dust [11]. The extinction of a star in the ISM is commonly expressed in comparison to a reference wavelength usually in the

visual part of the spectrum, *A(V)*, using a common colour difference. The B-V colour in the Johnson colour system is shown as an example in **Equation 1.2**.

$$m(\lambda) = M(\lambda) + 5\log_{10}[d] + A(\lambda) \tag{1.1}$$

$$\frac{E(\lambda - V)}{E(B - V)} = \frac{A_\lambda - A_V}{A_B - A_V} \tag{1.2}$$

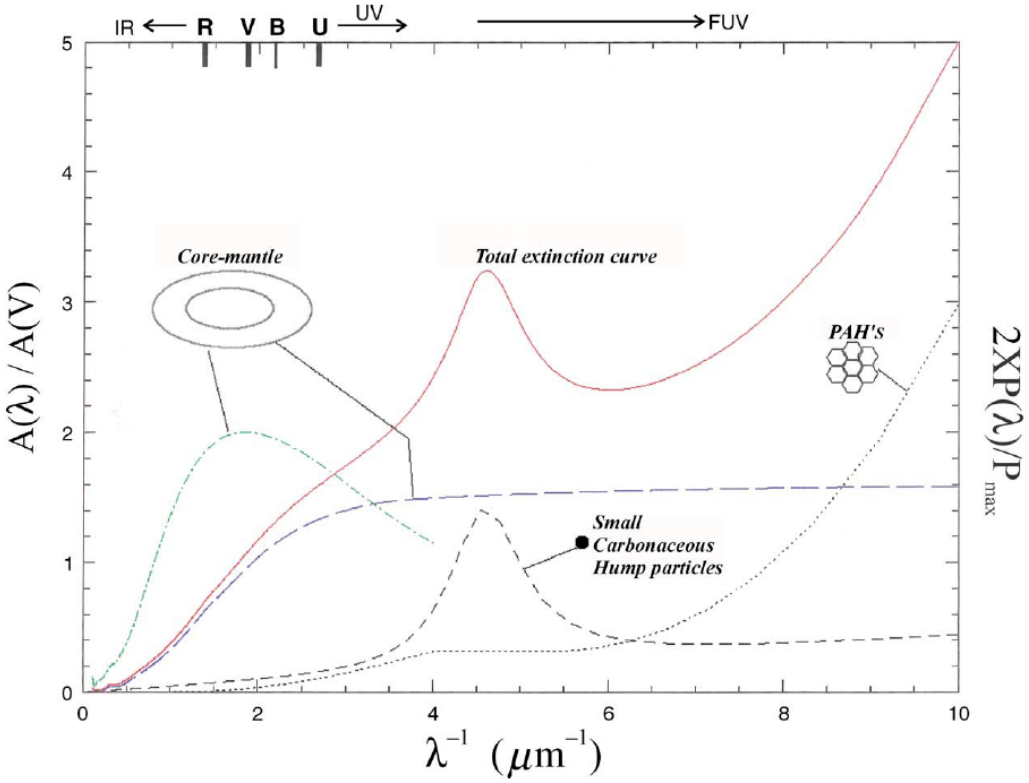

Figure 1.4: Interstellar Extinction Curve for a Diffuse Cloud [11]

In **Figure 1.4**, the curve is expressed in terms of a normalized extinction ratio A_λ / A_V (**Equation 1.3**) where R_V is the total-to-selective ratio (**Equation 1.4**). λ^{-1} is the inverse wavelength of the starlight. This variable can also be expressed in units of wavenumbers (where 1 μm^{-1} is equivalent to 10,000 cm^{-1}) or in terms of the different parts of the electromagnet spectrum where *IR* is infrared, *R* red, *V* visual, *B* blue, *U* the start of the ultraviolet range (UV) and far ultraviolet *FUV*. It is this large spectral range that provides more detailed information about the size range of interstellar dust grains.

$$\frac{A_\lambda}{A_V} = \frac{1}{R_V}\frac{E(\lambda - V)}{E(B - V)} + 1 \tag{1.3}$$

$$R_V = \frac{A_V}{E(B - V)} \tag{1.4}$$

The total extinction curve can be deconvolved to reveal three main groups of particles: core-mantle grains (mean radius of 0.1 μm); very small particles (mean radius of 0.003 μm); and PAH (polycyclic aromatic hydrocarbons) molecules [11]. The extinction curves for the latter two particle groups are displayed in **Figure 1.4** as a brown short dash line and dotted line respectively. For the core-mantle grains, the mean polarization curve (green dot-dash line) is shown where *P(λ)* is the polarization value at λ and P_{max} is the maximum polarization. This curve was determined from the polarization results of radiation passing through the ISM where the dust grains are aligned causing them to act like a polarizer. From basic electromagnetic scattering properties of particles, the grain size of the responsible particles can be calculated. It is the surfaces of these core-mantle particles (known from here as dust grains) that will be the focus of this study.

Although the interstellar extinction curves reveal the presence and size of dust grains, they tell us little about the *chemical composition* other than the 217 nm (46,100 cm^{-1}) bump. This is generally taken to be consistent with small carbonaceous particles rich in graphite-like material produced from nearby carbon rich stars. Further information on dust composition can be obtained from *metal depletion* data. **Table 1.2** displays the stellar abundance of a range of elements with respect to hydrogen and the fraction of those elements in the gas-phase in a gas cloud towards the bright star Zeta Ophiuchi [16]. The depletion fractions generally reveal that the light elements remain mostly in the gas-phase whilst the heavier ones are depleted and must therefore contribute to the chemical composition of interstellar dust grains.

Astronomical IR observations give us further composition information. The W33A IR spectrum in **Figure 1.5** shows the dust embedded in front of the high mass star obtained by the ISO (IR Space Observatory) [17]. The strong, broad features at 9.7 (Si-O stetch) and 18 μm (O-Si-O bend) [18] are consistent with solid silicate materials, produced in

Element	Stellar Abundance with Respect to H	Depletion Fraction
C	2.1×10^{-4}	0.63
O	4.6×10^{-4}	0.72
Mg	2.5×10^{-5}	0.23
Si	1.9×10^{-5}	0.09
Cr	3.2×10^{-7}	1.1×10^{-2}
Fe	2.7×10^{-5}	7.1×10^{-3}
Ti	6.5×10^{-8}	4.2×10^{-3}
Ca	1.6×10^{-6}	3.2×10^{-4}

Table 1.2: Elemental Stellar Abundance and Depletion Fractions from the Gas Cloud Towards Zeta Ophiuchi [16]

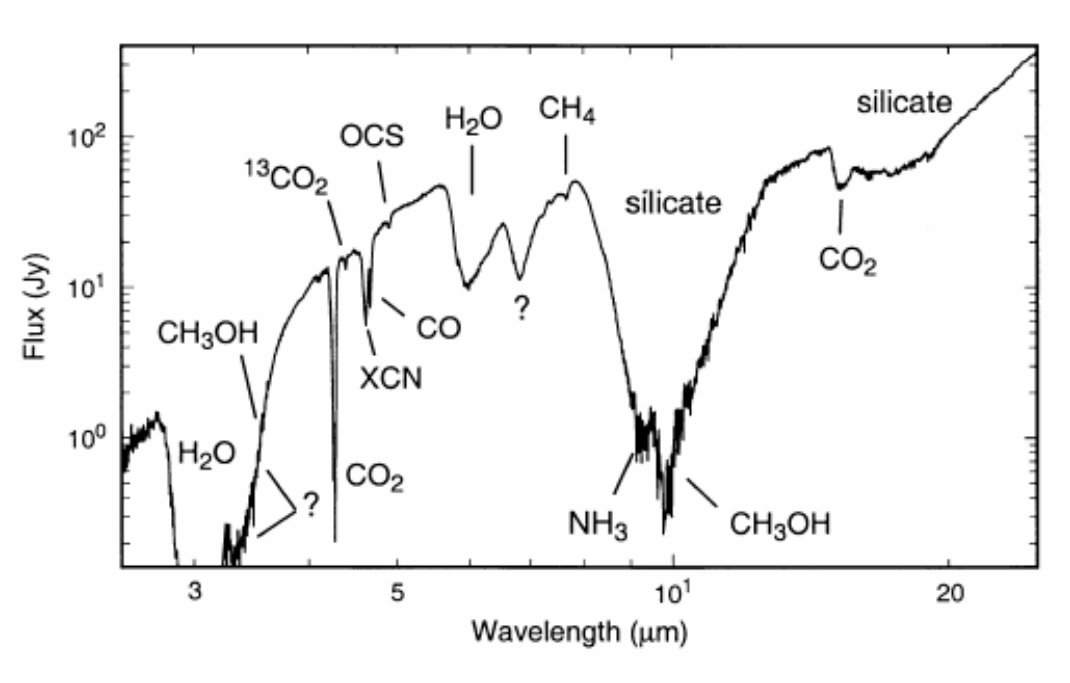

Figure 1.5: IR Spectrum of the Gas in front of the High Mass Star W33A [17]

oxygen rich stars. Whether each cloud contains one or a mixture of grains with amorphous silicate or carbonaceous core materials is still unclear. Other information that can be obtained from such IR observations is the chemical composition of the icy mantles coating the dust grains. This is especially true if the spectrum was taken from a very cold dusty object, like the cloud where the high mass star W33A is found, as the

spectrum would not show any gas-phase species. The broad feature around 3 μm and the smaller feature at 6 μm in **Figure 1.5** were respectively assigned as the O-H stretch mode and H-O-H bending mode in water. This molecule was first observed in the icy mantles by Gillett and Forest in 1973 [19] and accounts between 60 and 70 % of the species found in these icy mantles in dense molecular clouds, not just in the IR spectrum shown in **Figure 1.5**, [20]. H_2O is therefore the dominant species in these icy mantles. The icy mantles also contain smaller concentrations of species like carbon monoxide, carbon dioxide, ammonia and methanol and this is considered typical for molecular clouds environments. However, not all the features in **Figure 1.5** have been identified.

IR spectra have also been taken from diffuse clouds (**Figure 1.6** for an example). The observations reveal that these silicate dust grains (9.7 μm feature) are mostly bare as there is no or little observation of the H_2O feature at 3 μm [11, 21-23]. This implies that the icy mantles grow when the gas cloud becomes a dense molecular cloud.

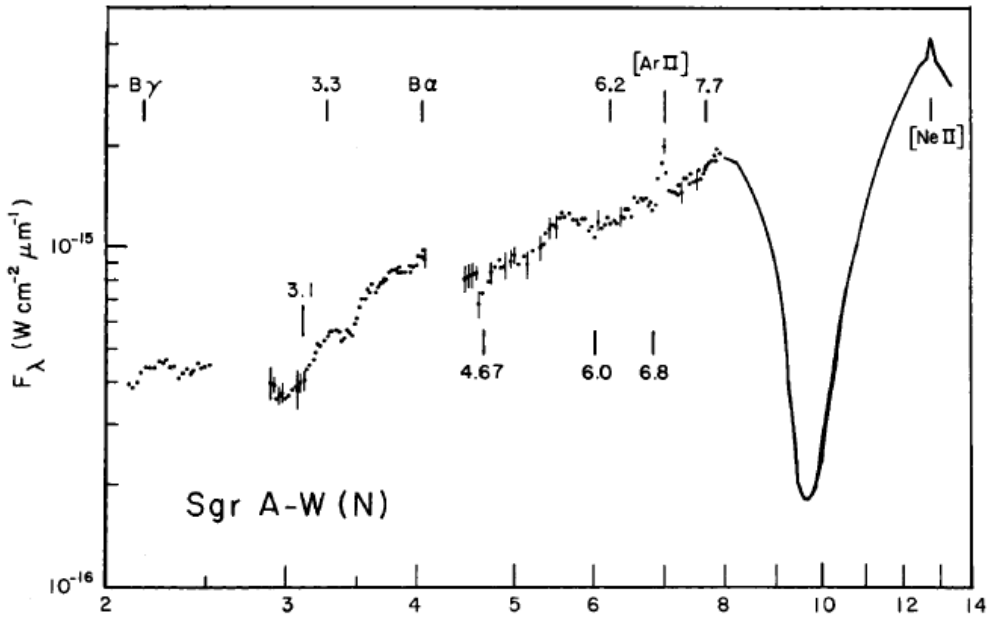

Figure 1.6: Example IR Spectrum from Diffuse Cloud [11]

Little more is known about their physical and chemical composition. The only other comparable source of evidence was believed to be dust particles ejected from comets. The most widely accepted view was that comets were a mixture of ice and interstellar

(core mantle) dust grains [24]. Predictions were also made on the morphology of comet's dust particles hypothesising them to be fluffy and high porous materials [25]. On the 2nd January 2004 these theories were tested when the *Stardust Mission* collected over 10,000 dust particles in silica aerogel at a distance of 234 km from the surface of the Wild 2 comet and return them to Earth [26]. A high-angle annular darkfield (HAADF) image of one of these collected dust particles is displayed in **Figure 1.7**. Initial research into the collected dust particles and their deceleration tracks in aerogel revealed the particles size to be between 1 and 300 μm [26]; an order of magnitude larger than interstellar core mantle dust grains (0.1 μm). The densities of these particles ranged from approximately 0.3 for the large, non-porous silicates objects to 3 g cm^{-3} in the fine, highly porous aggregates [27]. The cartoon on the right hand side of the HAADF image in **Figure 1.7** reveals that the comet dust particles were composed of three main components: the iron sulfide mineral pyrrhotite (left); the silicate mineral enstatite (upper middle); and fine grain porous aggregate material containing elements of magnesium, aluminium, silicon, sulfur, calcium, chromium, manganese, iron and nickel (right). Chemically, the main difference between the comet and interstellar grains is that the comet particles were composed of crystalline silicates, mostly olivine and pyroxene, and iron sulfides [27] instead of amorphous silica or carbonaceous materials. Amorphous silicates can be annealed to form crystalline silicates at temperatures of 800 K. However, further analysis of the comet material indicated that

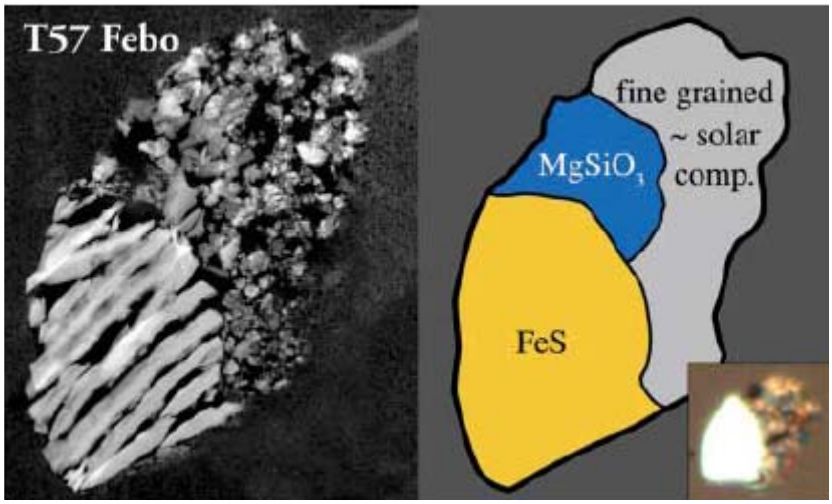

Figure 1.7: HAADF Image of Captured Wild 2 Comet Dust Particles (left), Cartoon of the Chemical Composition of the Dust Particle (right) and a Reflected Light Image (insert) [26]

the isotopic composition, minor element composition and the range of ratios of iron to silicon in the silicates would not have been the result of annealing of radiation damaged amorphous silicates [26]. Instead, the material for the Wild 2 comet is now considered to be formed in the early inner Solar System.

Despite this, the current morphology of interstellar dust grains are believed to have a high surface area in proportion to the grain diameter which adsorbed gaseous species can use as a substrate to react with other adsorbed species. The following section will explore the modelling of chemistry in the ISM, both with and without these dust grains.

1.2 Modelling Astronomical Environments

1.2.1 Introduction

To understand how the observed molecular species in **Table 1.1** were formed, chemical models are constructed. The simplest models discussed in this study are the gas-phase chemistry models (see **Section 1.2.2**). However, these do not include any effects from the interstellar dust grains which become important when considering the observed abundance of some key molecules (**Section 1.2.3**). To ultimately be able to understand the full chemistry occurring in these ISM environments and to develop a greater knowledge of star formation, both of these models will need to be integrated.

1.2.2 Gas-Phase Chemistry

Astronomical observations of the ISM have identified over 120 different molecular species (as seen in **Section 1.1.1**). The basic models explore the gas-phase chemistry of a small network of species connected together in a reaction mechanism under a defined set of interstellar conditions. As the total number of formation, reaction and destruction steps increases, the more complex the model becomes. Advanced versions of these models also include the dynamical changes of the ISM environment or environments. These models are of particular interest to astronomers as they are being used to explain how clumps of gas can continue to collapse in on themselves triggering star formation without leading to the clumps thermally expanding (as previously discussed in **Section 1.1.2**).

The allowed gas-phase chemistry is limited by the interstellar conditions of the chosen environment or environments. The first restriction is the low pressure (10^{-13} to 10^{-16} mbar) which prevents any three-bodied reactions from occurring. Under normal laboratory conditions, the presence of the third body in a reactive collision removes energy from the newly formed molecule preventing dissociation. In the ISM, the energy is loss through the emission of radiation either as a visible photon or as a cascade of IR and MW photons until the molecule reaches its ground state. However, this limits the gas-phase formation reaction steps to those that have an allowed transition for any emission to take place [17]. Another restriction to this model is the gas-phase temperature (10 to 100 K) which is low enough to only allow two-bodied reactions with zero or negligible activation energy barriers to have sufficient rates of reactions. Additional complications to the reaction mechanism result when processes involving UV radiation from nearby stars (for diffuse and PDRs regions) and cosmic rays are included. A selection of allowed gas-phase reactions are displayed in **Figure 1.8** [28].

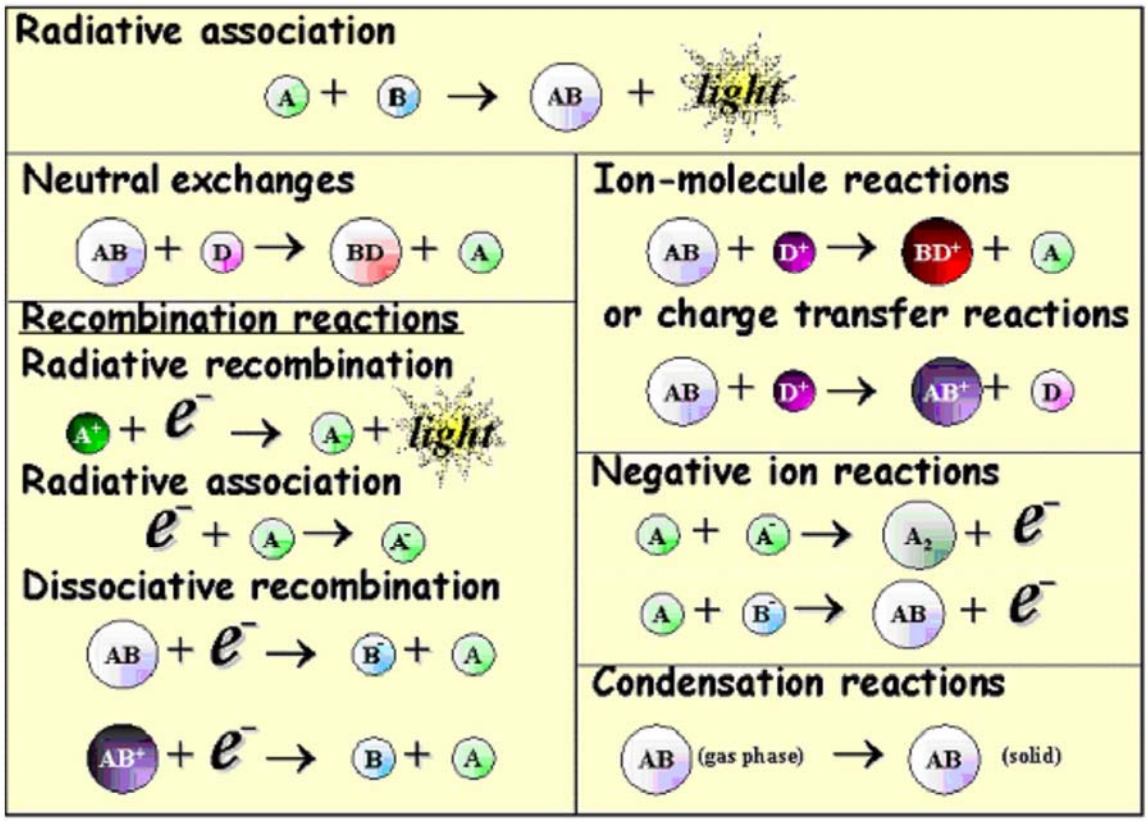

Figure 1.8: Typical ISM Gas-Phase Reactions [28]

In dense molecular clouds, the dominant gas-phase reactions are ion-molecule reactions. These reactions occur with a higher probability than neutral-neutral reactions or neutral-neutral exchanges due to the difference in charge attracting the ion to the molecule. The positive ions are usually formed by cosmic ray bombardment but can be formed by photoionization in diffuse regions and PDRs [29]. The most common ion produced is the H_2^+ ion which can react with H_2 to forms H_3^+ through the ion-molecular reaction shown in **Figure 1.9**. The resultant H_3^+ ion acts as H^+ donor to the majority of other gaseous species. This is achieved through charge transfer reactions of which a selection is displayed in **Figure 1.10**. Additional multiple ion-molecule reactions of these formed ions with H_2 results in the formation of larger ions. For example, reactions of OH^+ with H_2 would lead to the formation of H_2O^+ and H_3O^+ [30] (this mechanism is described in more detail later in this sub-section).

$$H_2^+ + H_2 \rightarrow H_3^+ + H$$

Figure 1.9: Dominant Ion-Molecular Reaction in Molecular Clouds [29]

$$H_3^+ + O \rightarrow OH^+ + H_2$$
$$H_3^+ + C \rightarrow CH^+ + H_2$$
$$H_3^+ + N \rightarrow NH^+ + H_2$$
$$H_3^+ + HD \rightarrow H_2D^+ + H_2$$
$$H_3^+ + CO \rightarrow HCO^+ + H_2$$
$$H_3^+ + CS \rightarrow HCS^+ H_2$$

Figure 1.10: Examples of H_3^+ Charge Transfer Reactions

Another family of gas-phase reactions are radical reactions (sometimes referred as neutral-neutral reactions). These reactions occur less frequent than the ion-molecule reactions described above as there is no charge attraction between the species. However, most of these reactions have either no or a weakly inverse temperature dependence [29] allowing these to occur under ISM conditions. **Figure 1.11** displays the radical formation reactions of O_2 [29, 31] and CO [32].

$$O + OH \rightarrow O_2 + H$$

$$C + O \rightarrow CO$$

Figure 1.11: Examples of Radical Reactions [29, 31, 32]

Despite these limitations to the gas-phase chemistry the concentrations of most species, like CO, agree well with the observed molecular abundances. First detected in 1970 [2], CO has only been observed in dense molecular clouds. **Figure 1.12** displays the direct and indirect formation mechanisms of CO. The dominant route is through the ion-molecule reactions of C^+ with O and O^- with C (top four reaction steps in the direct mechanism). The probability of CO forming in the gas-phase is increased with the knowledge that C is the fourth most abundant element in diffuse clouds after H, He and O [32]. However, very few neutral C atoms are observed in the ISM as the atoms react rapidly with other species. This includes the radical recombination with O [32] discussed previously and is re-shown in the bottom reaction step in the direct mechanism. Another CO formation mechanism is shown in the indirect mechanism (**Figure 1.12**). This mechanism contains a mixture of: radiative association (first); ion-molecule (second and fourth); charge transfer (third) and dissociative recombination (fifth) reaction types. The CO molecule can be photodissociated back into its atomic species by UV irradiation when λ is less than 111 nm [6] (top reaction step in **Figure 1.13**Figure 1.13) but the triple bond within the molecule has a high dissociation energy (1076 kJ mol^{-1} at 298 K [33]) which greatly limits this reverse step [2]. Both of these

$$C \xrightarrow{h\upsilon} C^+ + e^-$$
$$C^+ + O \rightarrow CO$$
$$O + e^- \rightarrow O^- + h\nu$$
$$C + O^- \rightarrow CO + e^-$$
$$C + O \rightarrow CO$$

$$O + e^- \rightarrow O^- + h\nu$$
$$O^- + H \rightarrow OH + e^-$$
$$C \xrightarrow{h\upsilon} C^+ + e^-$$
$$C^+ + OH \rightarrow CO^+ + H$$
$$CO^+ + H_2 \rightarrow HCO^+ + H$$
$$HCO^+ + e^- \rightarrow H + CO$$

Figure 1.12: CO Direct (left) and Indirect (right) Formation Mechanisms

$$CO \xrightarrow{h\upsilon} C + O$$

$$H_3^+ + CO \rightarrow HCO^+ + H_2$$

Figure 1.13: Examples of CO Destruction Mechanisms

factors contribute to the observed molecular abundance of CO in dense molecular clouds including the PDRs where most species would ready be photodissociated. However, CO can react with other species, like H_3^+ (see **Figure 1.13**), reducing the molecular abundance.

Although the gas-phase chemistry model works well for most species, this type of model is unable to explain the formation of several essential molecules. These include the species of interest in this study which are H_2, H_2O, O_2 and O_3.

H_2 is the simplest and most dominant molecule in dense molecular clouds and was first observed in 1970 [2]. Not only do the vast majority of the observed molecules contain H atoms but H_2 is also the dominant collision partner in these clouds, regulating the excitation and cooling of regions of warms gas in the ISM. H_2 has also been detected in a wide variety of other interstellar objects including reflection nebulae, planetary nebulae, regions of low-mass and high-mass star formation, supernova remnants and galactic nuclei. However, this molecule can not be formed by the reaction of two H atoms as the resulting H_2 molecules have no dipole. This results in the radiative relaxation of the H_2 molecule being a forbidden spin transition causing the nascent molecule to dissociate back to H atoms.

In the early universe, H_2 was formed from the reaction of protons and electrons left over from the Big Bang (see **Figure 1.14**) [34, 35]. The first reaction step is the formation of H atoms which subsequently react in one of two catalytic cycles: electron or proton. The electron catalytic cycle is displayed in the second and third reactions steps of **Figure 1.14** and occurred more dominantly than the proton catalytic cycle (fourth and fifth reaction steps). The formation of H and H_2 in the early universe was important as these species became coolants in the first gas clumps (as previously introduced in **Section 1.1.1**). As the first gas clumps began to collapse under gravity the thermal motion of the H atoms and H_2 molecules increased. Collisions between the gaseous

species can result in the ionization of H atoms and the excitation of H_2. The recombination and relaxation of these species respectively radiated some of the thermal energy out of the clump. This cooled the clump allowing further collapse of the gas clump triggering the formation of the first generation of stars. As the universe developed, the concentrations of these charged species decreased eventually terminating this H_2 formation mechanism. The formation of the stars resulted in the emission of UV light photodissociating the H_2 molecules. Therefore another formation route is required that is more efficient than the rate of destruction to account for the present observed molecular abundance.

$$e^- + H^+ \rightarrow H$$
$$H + e^- \rightarrow H^- + h\nu$$
$$H^- + H \rightarrow H_2 + e^-$$
$$H + H^+ \rightarrow H_2^+ + h\nu$$
$$H_2^+ + H \rightarrow H_2 + H^+$$

Figure 1.14: Formation Mechanism of H_2 in the Early Universe [34, 35]

Another molecule of interest in this research is H_2O which was first observed in 1968 [2]. Unlike H_2, H_2O can be formed in the gas-phase. **Figure 1.15** shows the gas-phase formation mechanisms as described by Taylor and Williams [30] for different types of gas clouds due to the difference in radiation. The dominant reaction type occurring in the gas phase dense molecular clouds H_2O mechanism is the ion-molecule reactions. These make up all of the steps along the top line except for the first one which is formed by cosmic ray bombardment (as previously discussed in this sub-section). The final stage to create the H_2O molecule is by dissociative recombination. Unfortunately, the dissociative recombination of H_3O^+ ions can also form H, H_2 and the dominant product OH [29] (not shown in **Figure 1.15**) which greatly limits the formation of H_2O molecules.

The diffuse cloud formation mechanism is similar to that of the molecular cloud as the reaction steps along the top line (excluding the first one) are all ion-molecule reactions which are known to be relatively efficient. Again, the H_2O molecule is formed from

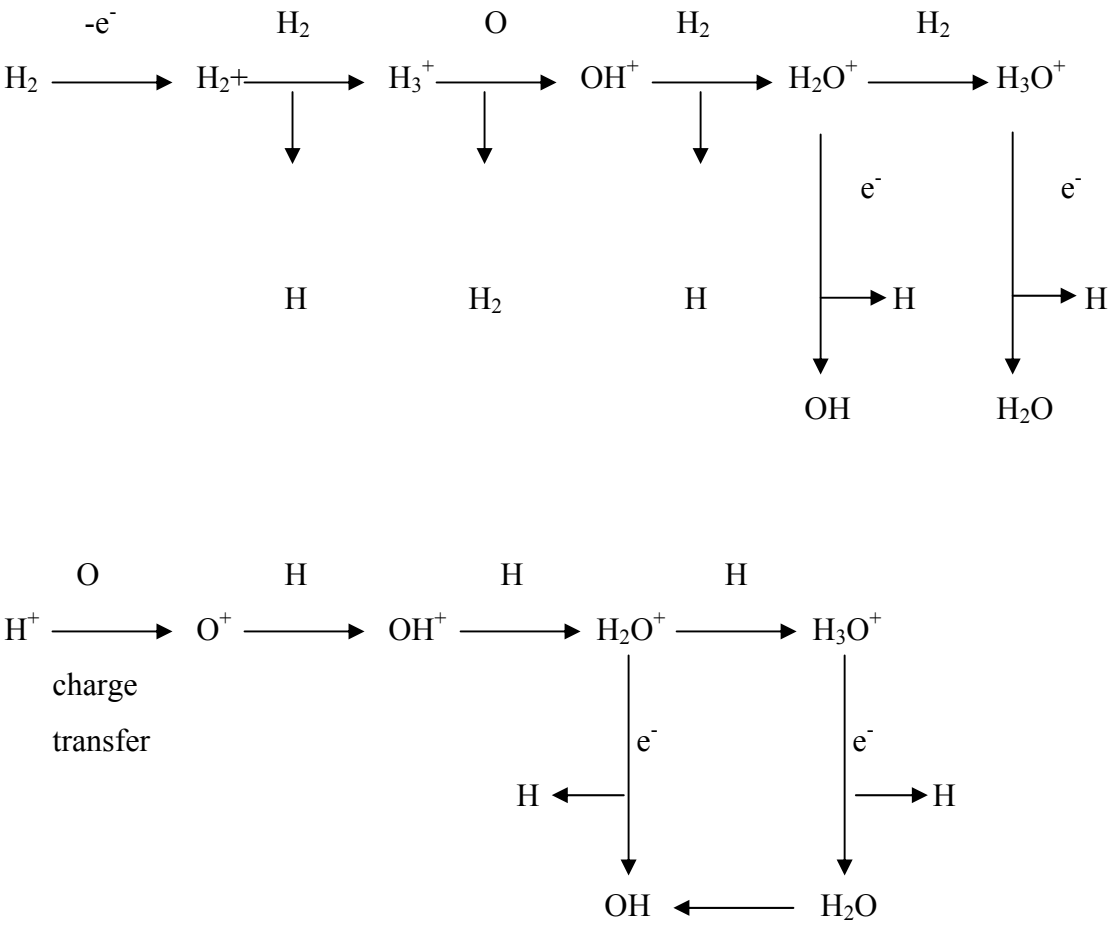

Figure 1.15: Gas-Phase Production Routes of H_2O in a Dense Molecular Cloud (top) and Diffuse Cloud (bottom) [30]

H_3O^+ ions through dissociative recombination which results in the same problem as described for the molecular cloud case. The abundance of H_2O molecules formed in the diffuse cloud is even lower than in the molecular cloud due to the additional UV photodissociation reaction step. This would also be the case for PDRs. However, the observed molecular abundance of H_2O is much greater than can be explained through this gas-phase chemistry model alone. Therefore an additional, more efficient formation mechanism is required.

The last group of species to be discussed with respect to the gas-phase chemistry model are O, O_2 and O_3. In the atomic form, O is the third most abundant element in the ISM after H and He with an abundance of 3×10^{-4} (or 319 ± 14 O atoms for every 10^6 H atoms) in diffuse clouds [36]. Although the concentration of O atoms is much less than H, a range of O bearing species have been observed (see **Table 1.1** in **Section 1.1.1**),

suggesting that O_2 molecules should also be present in the ISM. Like H_2O, O_2 can be formed in the gas-phase. The radical reaction for this is displayed in **Figure 1.16** and occurs rapidly at temperatures below 50 K [29] which is low enough to occur in diffuse clouds and PDRs. However, like the H_2O molecules in these ISM environments, O_2 can be photodissociated (**Figure 1.17**) [12] limiting the molecular abundance. The production of O_2 through the radical reaction shown in **Figure 1.16** has been explored by theoretical calculations and compared with experimental results [31]. The results revealed that the exothermic reaction of $O(^3P)$ with the $OH(^2\Pi)$ radical proceeds through the deep O_2H well where the O_2 product can be form in either the $(a^1\Delta_g)$ state or the $(X^3\Sigma^-_g)$ state if a non-adiabatic electronic relaxation of the O_2H complex occurs.

$$O + OH \rightarrow O_2 + H$$

Figure 1.16: O_2 Radical Formation Reaction [29 31]

$$O_2 \xrightarrow{h\upsilon} 2O(^3P)$$
$$O_2 \xrightarrow{h\upsilon} O(^3P) + O(^1D)$$

Figure 1.17: Photodissociation of O_2 [12]

In recent years there have been two satellites, ODIN and SWAS, and two balloon missions, PRONAOS-SMH and PIROG 8, launched to detect different gas-phase O_2 rotational lines in the ISM [37]. The Swedish ODIN satellite searched for the (N,J): (1,1) → (1,0) and the (3,3) → (1,2) lines at 119 and 487 GHz respectively. The US satellite SWAS also searched for the (3,3) → (1,2) line at 487 GHz. The CNES (Centre Nationak d'Etudes Spatiales) stratospheric balloon-borne observatory PRONAOS-SMH was designed to search for the (3,2) → (1,1) line at 368 GHz and the Swedish-French balloon PIROG (point infrared observatory gondola) 8 the (3,2) → (1,2) 425 GHz line.

The first set of results from these missions was from PIROG 8 observing the giant molecular cloud NGC7538 where they observed the O_2 425 GHz line. Their findings concluded a low interstellar abundance [38] but little theoretical work has been performed on their findings. The results from ODIN and SWAS satellite missions were

more successful and placed an upper limit on the O_2 abundance in molecular clouds as 3×10^{-6} to 1×10^{-7} [7, 39, 40]. This is approximately 1000 times lower than predicted from the gas-phase chemistry models [41] implying that the additional predicted reaction to form O_3 is unlikely to occur. Like O_2, O_3 can photodissociate through the reaction given in **Figure 1.18** when λ is less than 1180 nm resulting in a decrease in the molecular abundance. This may also be the reason why O_3 has yet to be observed in the ISM.

$$O_3 \xrightarrow{h\upsilon} O_2 + O$$

Figure 1.18: Photodissociation of O_3

Another observation is that the O_2 abundance in a dense molecular cloud is also considerably lower than the observed atomic O abundance in a diffuse cloud. As a dense molecular cloud form from the gravitational collapse of a diffuse cloud (**Figure 1.2**) then this apparent reduction in the total oxygen abundance is unclear. A range of suggestions have been hypothesis about the missing oxygen. The main theory related to the gas-phase chemistry model is the formation of CO which has been previously discussed above. O atoms can also react to form other molecules in the gas-phase, like OH, but the observed abundance of all the O bearing species does not match that of the original atomic O abundance [42]. Another suggestion for the missing oxygen is that the atoms are located in the reactions that occur on the interstellar dust grains. This, along with the answers to the formation of H_2 and H_2O, is explored in the following sub-section using the dust grain model.

1.2.3 Dust Grain Chemistry

In 1963, Gould and Salpeter [43] suggested that the interstellar dust grains themselves provided a surface which acts as a third body. This provided a greater number of reactions to occur in the ISM environments than with just the gas-phase chemistry model alone. Unlike the vast majority of molecules released into the ISM from nearby dieing stars, the dust grains survive the harsh radiation conditions. The grains make up approximately 1% of the mass in the ISM [9] and range from 5 to 250 nm [10] in radius with a mean radius of 100 nm [11]. The main source of evidence for the presence of these dust grains, along with two smaller groups of particles, was found from interstellar

extinction curves (as discussed in **Section 1.1.2**). Other evidence for dust grains includes: polarization of starlight; interstellar depletion; and IR observations (as discussed in **Section 1.1.2**).

For most reactions to occur, a third body is required to remove the excess energy produced from creating a bond to form a new molecule. This was one of the main limitations for allowed gas-phase reactions in the above sub-section but this is overcome by the interstellar dust grains providing a substrate for species to adsorb and react. These processes can be described using either the Langmuir-Hinshelwood; Eley-Rideal; or Hot Atom surface reaction mechanisms [44]. The cartoon in **Figure 1.19** displays the formation of H_2 and H_2O using the Langmuir-Hinshelwood mechanism. The cartoon describes the reactants adsorbing onto the surface, thermally diffusing, bonding with another atom and then (if possible) being ejected from the surface. The ejection step is based on the product's chemical characteristics. Some species, like H_2, are volatile and desorb from the surface upon formation. Others, like H_2O, remain on the surface. This mechanism is typical of those dust grain reactions occurring in diffuse clouds.

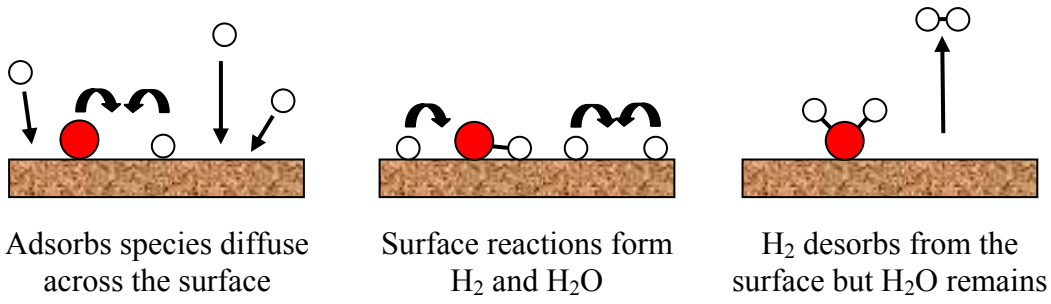

Figure 1.19: Cartoon of the Langmuir-Hinshelwood Mechanism Describing the Formation of H_2 and H_2O

The Eley-Rideal mechanism describes an incoming atom reacting directly with a partner on the surface without prior accommodation (**Figure 1.20**). For this mechanism to occur there must already be at least a sub-monolayer coverage on the surface. Although this is unlikely to be the case in diffuse clouds, IR observations of dense molecular clouds reveal that the dust grains are covered in an icy mantle (as previously seen in **Figure 1.5**). The cartoon in **Figure 1.20** illustrates this mechanism with the formation of H_2 on H_2O ice.

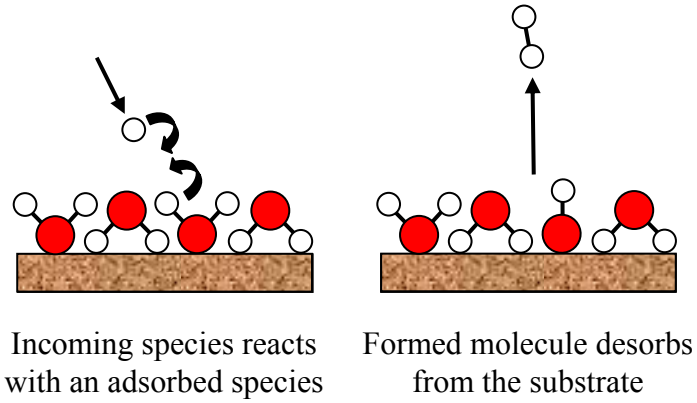

Figure 1.20: Cartoon Example of the Eley-Rideal Mechanism

The last possible formation process is the Hot Atom mechanism which is a combination of the two above (see cartoon in **Figure 1.21**). In this case the incoming atom retains part of its original kinetic energy on the surface (or gains some energy from the surface) in order to move at superthermal speeds whilst undergoing several collisions with the surface. Each of these collisions has a non-zero probability of reacting with another adsorbed species. Atoms generated by photochemical process, for example; those reactions involving UV photons with the icy mantle can undergo Hot Atom reactions.

The diffusion process in these mechanisms could be further complicated by quantum tunnelling [45]. However, subsequent work by Biham and Lipshtat [46] has confirmed that the main diffusion process is through thermal activity.

As with the gas-phase chemistry model, the dust grain model can be made more complex by including the characteristic changes in the environment as the gas cloud collapses from a diffuse to a dense molecular cloud. A summary of this is shown in **Figure 1.22**. The top cartoon describes those processes involved in a diffuse cloud. Atoms and ions adsorb onto the bare grain surface, diffuse (or "hop") and finally react through the Langmuir-Hinshelwood mechanism (labelled L-H on diagram). The more volatile species, like H_2, desorb from the surface on formation whilst others, like H_2O, remain. Over time, these latter molecules form multilayer islands on the grain surface which continue to grow through a mixture of Langmuir-Hinshelwood and Eley-Rideal (labelled E-R on diagram) surface formation mechanisms (middle cartoon in summary).

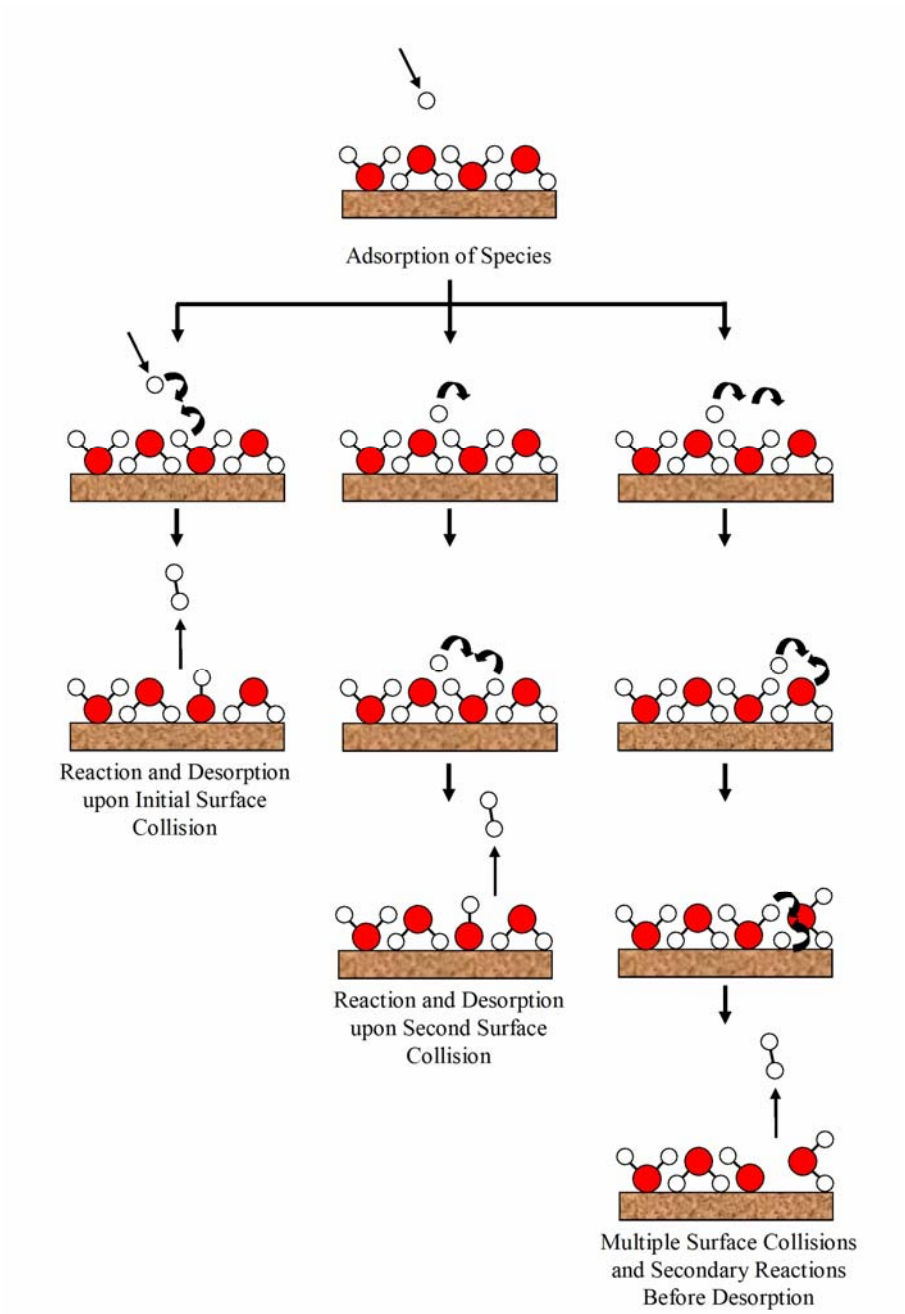

Figure 1.21: Cartoon Example of the Hot Atom Mechanism

This continues until a complete icy mantle is created. At this stage, the dust grain is in a dense molecular cloud environment (bottom cartoon of **Figure 1.22**). Here additional surface reactions occur on the icy mantle for adsorbed species, like CO (the second dominant molecule in the icy mantles after H_2O) to form CO_2; charged particles created by cosmic rays (for more details see **Section 1.1.1**); and, if the grain is in a PDR (photodissociation region), UV photons from nearby stars.

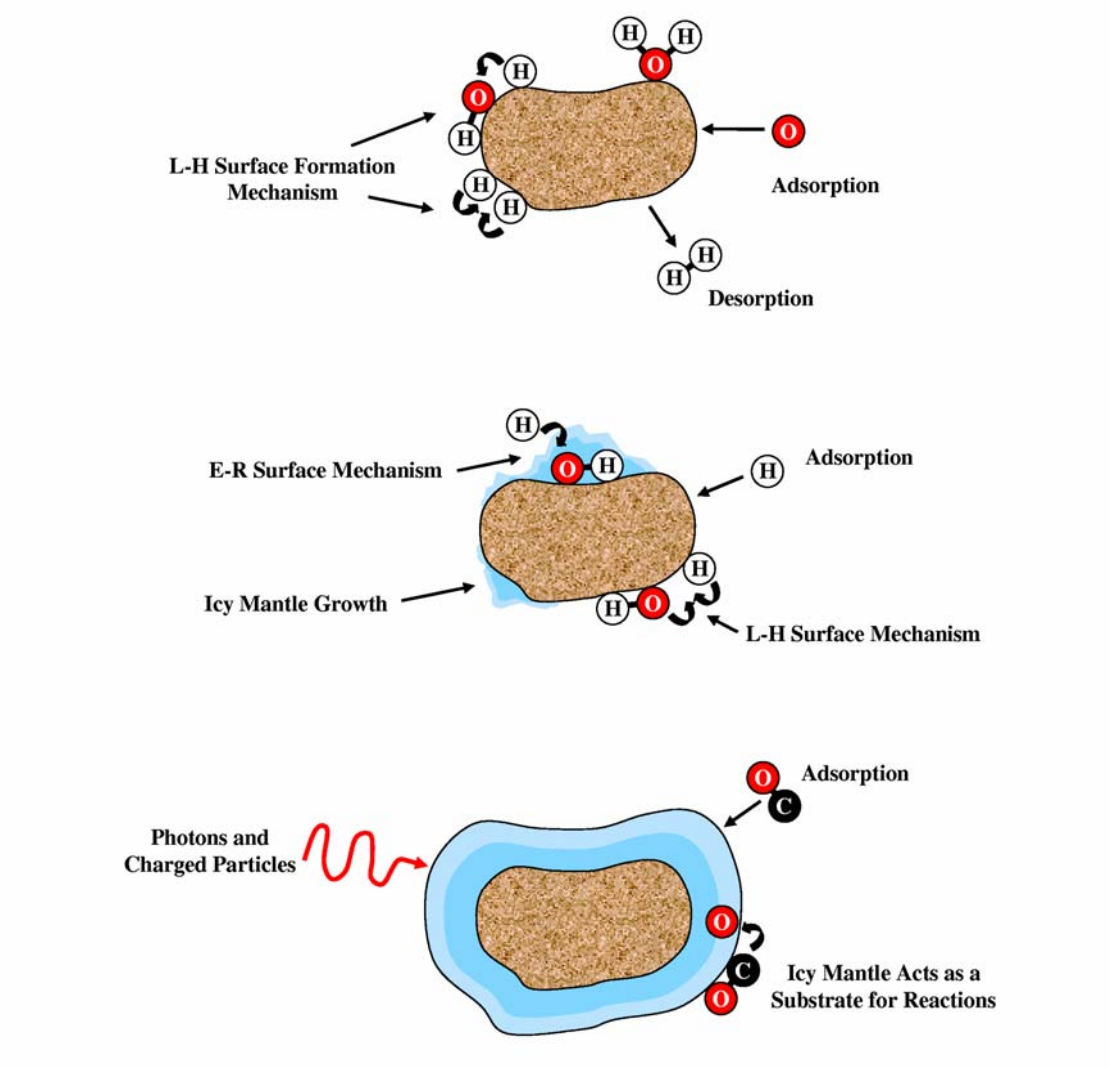

Figure 1.22: Cartoon Summary of the Dust Grain Model

In the past decade, the dust grain chemistry model has been demonstrated to lead to the efficient formation of H_2, both from bare dust grain and water ice substrates by several research groups using both experimental [47-53] and computational [46, 54-59] techniques.

The dust grain chemistry model is also being applied to H_2O formation (for more details see **Section 1.3.2**). However, initial experiments performed to explore the behaviour of H_2O films under ISM conditions revealed that the structure of these films was strongly dependent on surface temperature. When water vapour is background deposited onto a cold surface below 145 K an amorphous solid water (ASW) film is formed [60]. Above 145 K, the H_2O film is crystalline solid water (CSW). ASW films have a higher free

energy than those of CSW and, as a consequence, have a higher desorption rate and vapour pressure [60]. In 1987, Hallbrucker *et al*. reported that ASW films have a reversible glass-liquid transition at 136 ± 1 K with a heat capacity change at this temperature of 1.6 ± 0.1 J K^{-1} mol^{-1} [61]. The exact transformation from ASW to CSW through this glass-liquid transition is not completely understood. Spectroscopic studies by Fisher and Devlin [62] concluded that the very weak glass transition was due to the onset of molecular rotation and ASW freezes directly into CSW without passing through an intermediate liquid state. In comparison, Smith *et al*. molecular beam temperature programmed desorption (TPD) experiments indicated that their ASW films exhibited liquid-like translational diffusion prior to crystallisation at temperatures near 155 K [60]. At even higher temperatures (typically 200 K) the CSW films form hexagonal crystalline ice.

The structure of the ASW and CSW films were explored by Kimmel *et al*. through N_2 dosing on water substrates with TPD analysis [63]. The N_2 TPD curves are displayed in **Figure 1.23** from: Pt (111) (top); 50 bilayers of CSW (deposited at 145 K) on Pt (111) (middle); and N_2 on 50 bilayers of ASW (deposited at 22 K and annealed to 70 K) on Pt (111) (bottom). Monolayer coverages of N_2 desorb from each of the surfaces at roughly 43, 36 and 32 K respectively indicating that the underlying substrate has an affect on the N_2 desorption. Desorption from the Pt crystal results in peaks that are similarly shaped which is typical of monolayer desorption (for more details see **Section 2.3.4**). N_2 desorption from CSW and ASW substrates display TPD curves with coincident falling edges which is normally observed when the species recombines on the surface before desorption. This is not the case in these experiments implying that the ASW and CSW substrates contain a range of binding energies to which the adsorbed N_2 molecules were bound to the strongest unoccupied sites first before filling the weaker bound sites with increasing coverage. This range of binding sites suggested that the ASW and CSW films were heterogeneous. The sources of heterogeneous surfaces are molecular disorder and proton disorder. In CSW films, the oxygen atoms sit in well defined lattice sites but the protons are disordered. This results in a variety of proton configurations at the film surface which causes a range of binding energy sites for the N_2 molecules. The heterogeneity of ASW films is greater as proton disorder occurs in addition to molecular disorder as the H_2O molecules no longer sit in well defined latticed sites.

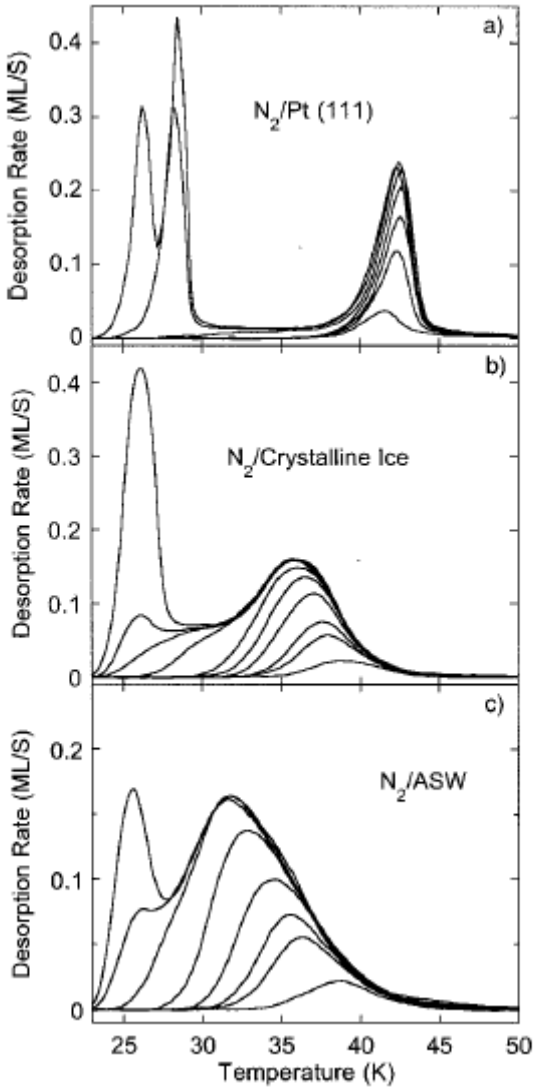

Figure 1.23: Kimmel *et al* [63] TPD Curves of N_2 on Pt (111) Crystal (top); N_2 on CSW on Pt (111) Substrate (middle); and N_2 on ASW on Pt (111) Substrate (bottom)

Additional experiments were performed by this research group to determine the density of multilayer ASW films [64]. The results displayed in **Figure 1.24** (along with the refractive index of the film) reveal that the density of an ASW film (non-annealed) is highly dependent on the surface temperature. If the film was annealed then the ASW substrate would remain at the density corresponding to the annealing temperature unless the surface temperature was raised further. As a consequence, the possibility of certain

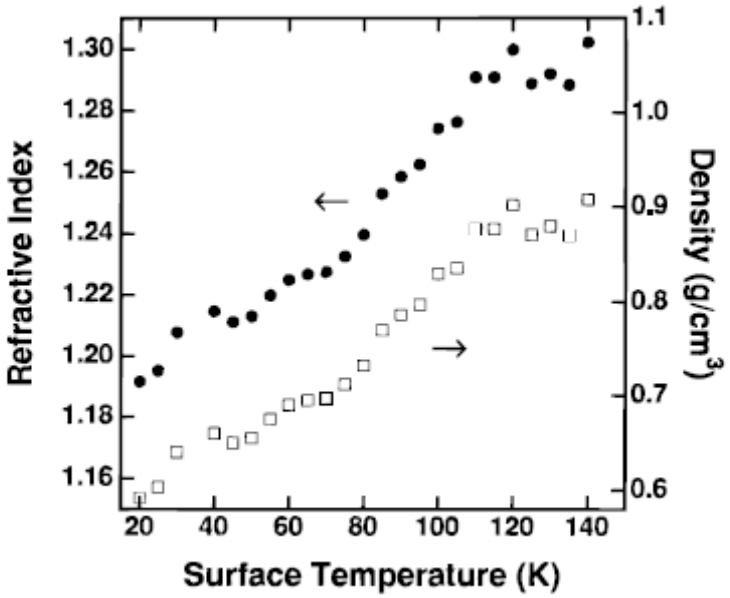

Figure 1.24: Relationship of Density (open squares) and Refractive Index (filled squares) with Respect to the ASW Film Surface Temperature (non annealed) [64]

species becoming trapped in the ASW film is also dependent on the maximum temperature the surface is exposed to. Due to this, ASW films can be further split into two separate groups: pASW (porous amorphous solid water); and cASW (compact amorphous solid water). pASW films are generally formed when water vapour is deposited onto a surface held below 40 K (without any annealing) and so have a density of less than 0.7 g cm^{-3}. cASW films are formed when the surface is between 100 and 120 K leading to these films having a higher density typically of 0.9 g cm^{-3}.

In 1985, Bar-Nun *et al*. explored the trapping and desorption of H_2, CO, CO_2 CH_4, Ar, Ne and N_2 on pASW substrates [65]. Their results revealed CO, CH_4, Ar and N_2 desorbed from the substrate at three distinct temperature ranges: 30 – 55 K; 135 - 155 K; and 165 - 190 K. Desorption between 30 and 55 K was assigned to species desorbing from on top of the ASW film whilst the 135 -155 K was the desorption of species during the ASW to CSW phase change. The final temperature range (165 -190 K) was assigned to the desorption of the species with the desorption of the CSW film. This is also known as co-desorption. Similar experiments have been performed by Collings *et al*. for a range of astronomical relevant species desorbing from pASW films (see **Figure 1.25**) [66]. Their results concluded that all the species

explored followed one of three desorption mechanism. The first category described was *CO-like species*. This group included the most volatile species, like N_2, O_2, and CO, which desorb following the three peak desorption mechanism observed by Bar-Nun *et al.* described above. The TPD curve for O_2 is of interest for this study as

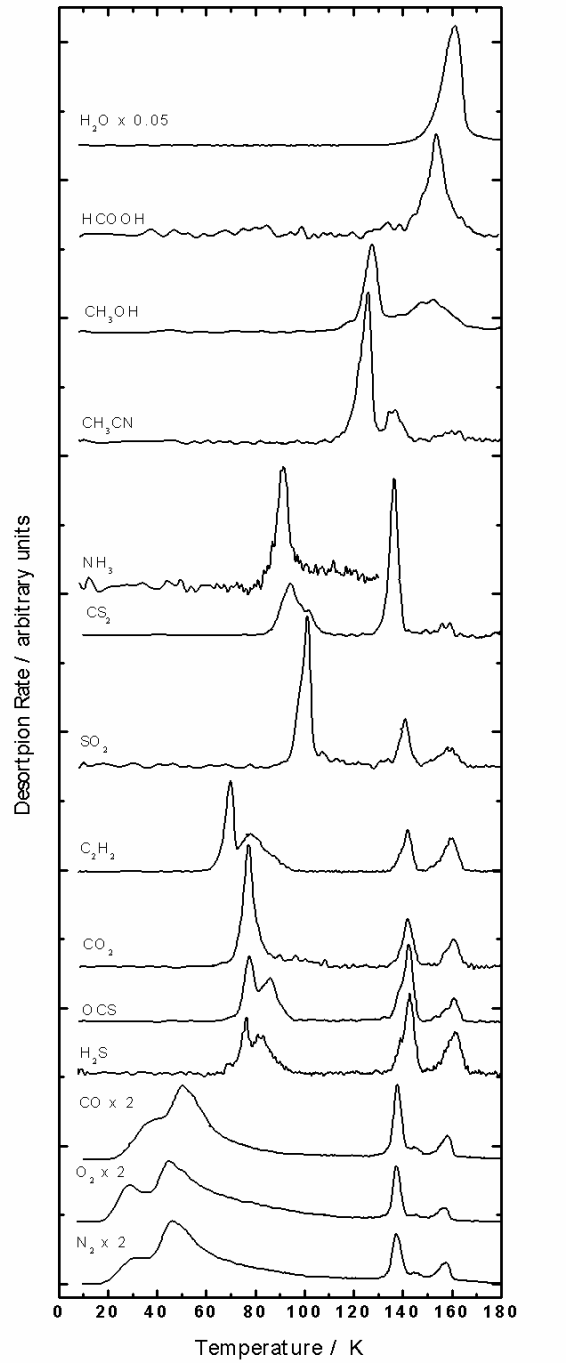

Figure 1.25: TPD Curves of a Range of Astronomical Relevant Species on ASW Films [66]

this result implied that small concentrations of O_2 molecules may be trapped in the icy mantles coating interstellar dust grains, like CO, instead of entering the gas-phase. This would also indicate why ODIN and SWAS detected a small gaseous O_2 abundance in the ISM. The second category was for *H_2O-like species* which desorbed from the surface at two temperatures. Unlike the CO-like species, H_2O-like species (which include: NH_3; CH_3OH; and HCOOH) are unable to diffuse into the porous ASW film and so sit on top of the film. At the first desorption peak, not all these molecules desorb. This is because these species interact more strongly with the underlying H_2O substrate than with each other. As a consequence, the remaining molecules require a higher surface temperature before desorbing. The last category is for *intermediate species* which follow a desorption mechanism between that of CO-like and H_2O-like species. This group includes SO_2; CS_2; OCS; and CO_2.

More detailed experiments exploring the trapping and desorption mechanism of CO on a range of ASW substrates was performed by Collings *et al.* [67]. The ^{13}CO TPD results are displayed in **Figure 1.26** from: a gold surface (a); cASW substrate formed at 120 K (b); ASW substrate formed at 70 K (c); pASW substrate formed at 8 K (d); and deposited simultaneously with H_2O on the gold at 8 K (e). All of these TPD curves reveal that ^{13}CO desorbs between 20 and 60 K. Additional desorption peaks for ^{13}CO were observed from the pASW and simulataneously deposited substrates (bottom two TPD curves) at 140 and 160 K (corresponds to the ASW to CSW phase change and co-desorption peaks respectively). These findings indicating that the higher density cASW substrates do not trap ^{13}CO molecules unlike the lower density pASW films. The results from all of these ^{13}CO TPD experiments were applied to explain the trapping behaviour of ^{13}CO in ASW (see **Figure 1.27**) [68]. After the double vapour deposited of CO on pASW (labelled I_{hda}) on gold held at 10 K, the substrate was slowly heated linearly (top image in cartoon). Between 10 and 25 K, the CO molecules diffuse into the porous ASW film (second image). Multilayer desorption of CO from on top of the pASW surface starts at 30 K. As the surface temperature continues to increase, the entrances to the pores in the pASW film begin to close. By 70 K, the pore entrances become fully closed trapping the remaining CO inside the ASW film and increases the density of the ASW film to that of cASW (labelled I_{lda} in cartoon). No further desorption is observed until the ASW to CSW (I_c) phase change at 140 K where the

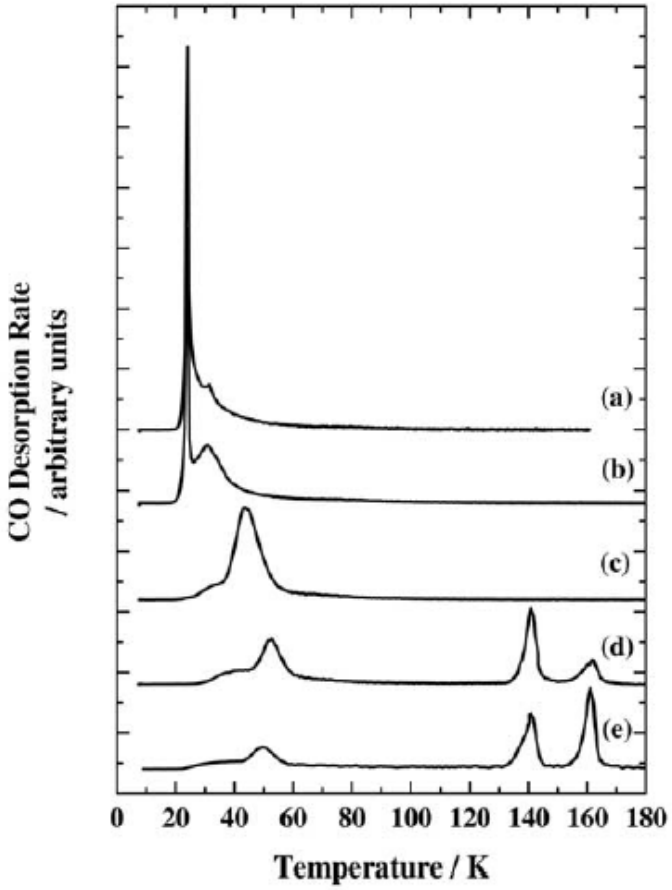

Figure 1.26: TPD Curves of ^{13}CO from: a Gold Substrate (a); cASW Substrate Formed at 120 K (b); ASW Substrate Formed at 70 K (c); pASW Substrate Formed at 8 K (d) and Deposited Simultaneously with H_2O on the Gold Surface at 8 K (e). Traces offset for clarity [67]

once trapped CO molecules can desorb. At 160 K, any remaining CO molecules co-desorbs with the H_2O film. The knowledge obtained from this trapping mechanism has been used to construct simulation models predicting the behaviour of CO molecules in the icy mantles coating interstellar dust grains [67]. As O_2 has been shown to follow a similar trapping behaviour to that of CO (see **Figure 1.25**) then it is expected that similar simulation models could be constructed for O_2 on H_2O substrates. The results of these O_2 TPD experiments and simulation models will be discussed in **Chapter 4**.

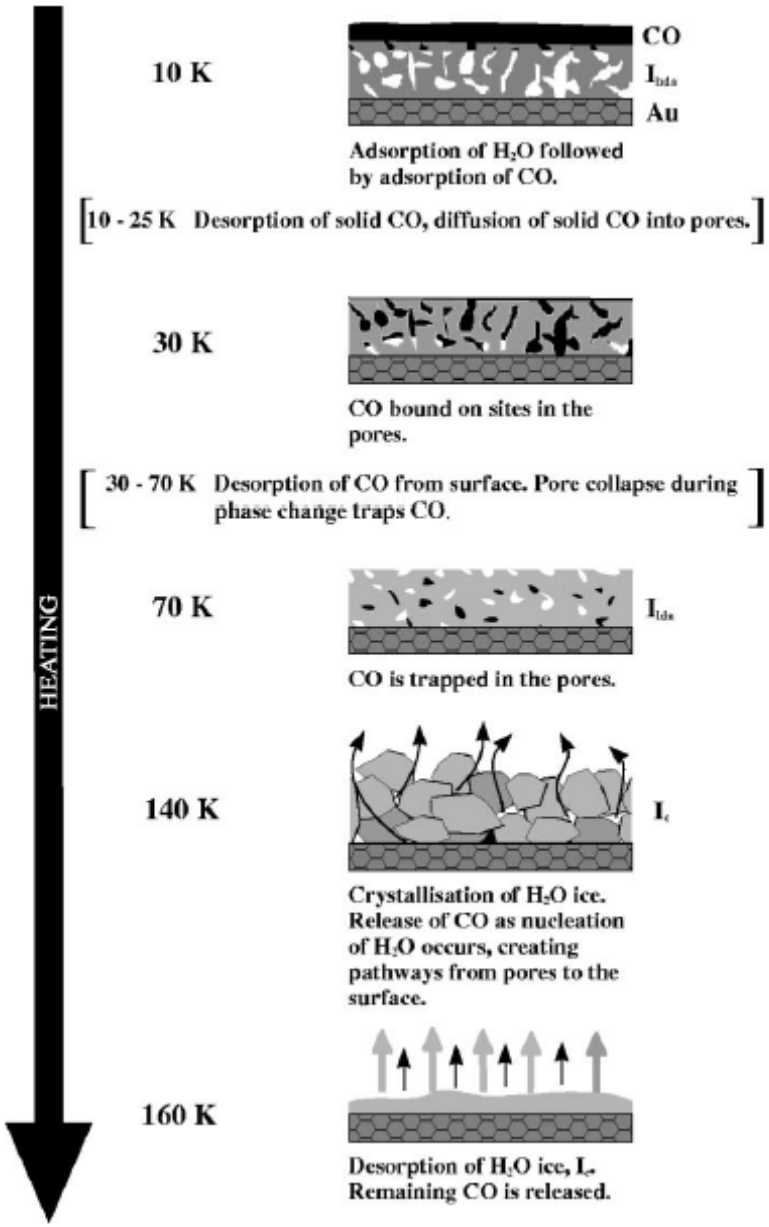

Figure 1.27: Cartoon Describing the Trapping Behaviour of ASW with CO [68]

Research carried out by Ehrenfreund *et al*. [69] explored the trapping behaviour of O_2 in different ice mixtures using IR studies. The IR vibrational stretching mode of homonuclear diatomic molecules, like O_2, are forbidden and should not be detected. This was the case in pure O_2 ice but in mixed ice the other molecular species, like H_2O and CO¸ interact with the O_2 molecules. As a consequence of the broken symmetry, the O_2 vibrational stretching mode was detected at 6.45 μm (1550 cm^{-1}) (see **Figure 1.28**). However, this O=O stretching model has so far not been observed in interstellar icy mantles [70] and further analysis of O_2 on H_2O substrates is required.

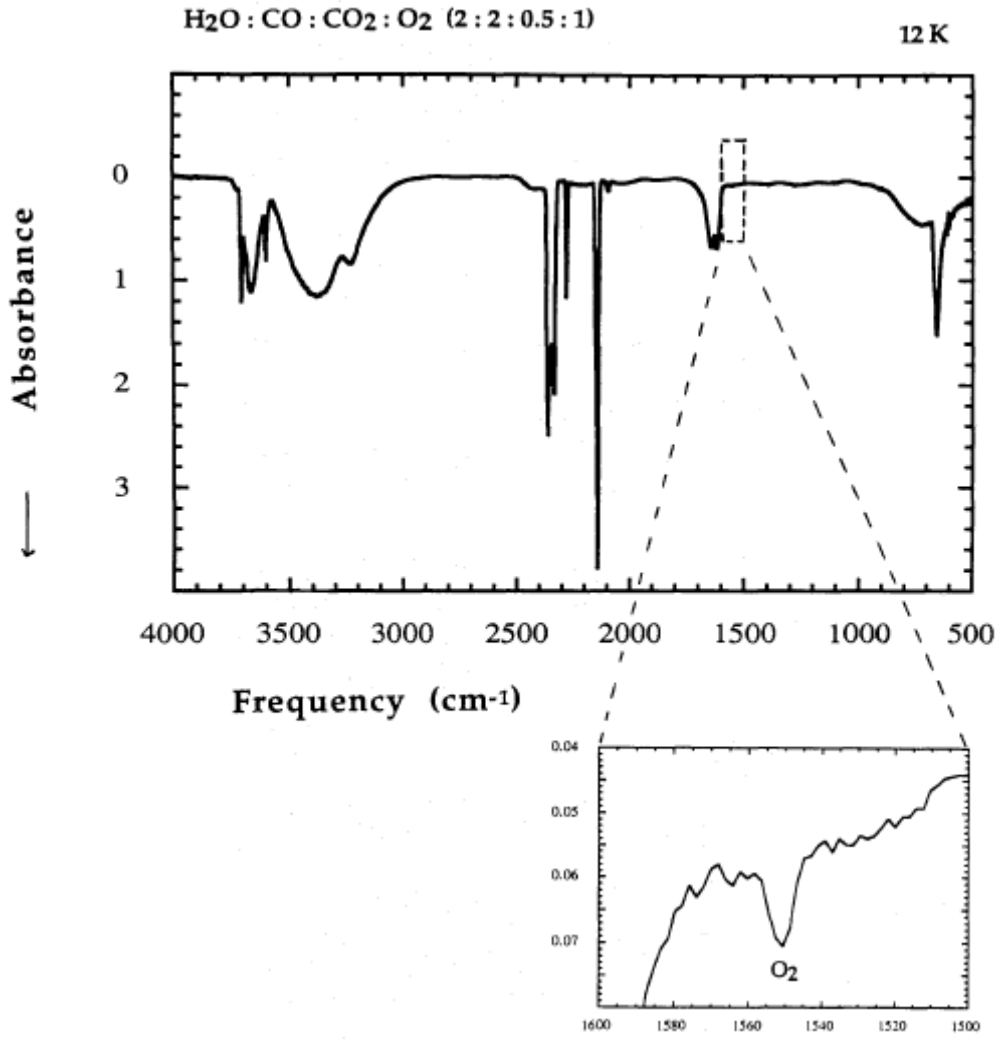

Figure 1.28: Laboratory Figure Displaying O=O Broken Symmetry mode [69]

TPD experiments have also been performed to explore O_2 on polycrystalline gold, CO on polycrystalline gold and CO/O_2 mixed and layered ices on polycrystalline gold [71]. The TPD curves are displayed in **Figure 1.29** and all show coincident leading edges (within experimental error) indicating desorption from the bulk ice. O_2 desorbs at a slightly higher temperature than CO by approximately 2 K. The TPD plots also display a slight difference in the desorption peak temperature (typically 0.5 K) between $^{16}O_2$ and $^{18}O_2$. This difference is more clearly revealed by the vertical line indicating the desorption peak maximum for the 40 L dose of $^{18}O_2$ on the $^{16}O_2$ TPD plot. Interestingly, there is minimal isotopic difference in desorption peak temperature for

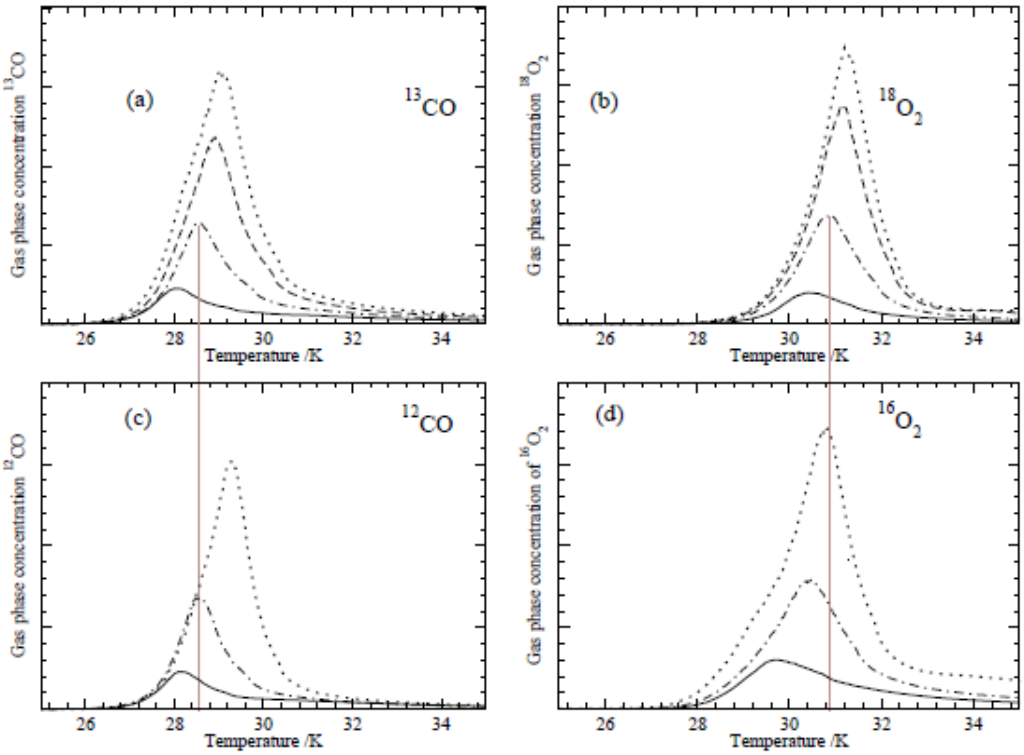

Figure 1.29: TPD curves of ^{13}CO (top left); ^{12}CO (bottom left); $^{18}O_2$ (top right); and $^{16}O_2$ (bottom right) from polycrystalline gold for 20 (solid line); 40 (dot-dashed); 60 (dashed – displayed only for ^{13}CO and $^{18}O_2$); and 80 L (dotted) [71]

CO. Although the underlying surface is not an interstellar dust grain mimic, these results do indicate that multilayers of O_2 follows similar multilayer desorption behaviour to CO. However, further analysis of O_2 from interstellar dust grain mimic is required to fully understand the desorption behaviour of this molecule.

Recently some surface-chemistry experiments have been performed using bare dust grain mimics concluding that a more complex modelling technique was required for sub-monolayer coverages [72]. Experiments have also been conducted investigating the desorption of simple mixed and layered thick ices on metallic surfaces [69, 71, 73]. However, more research is required to understand these simple ice systems before exploring more complex ice mantles (like those observed in the ISM, see **Figure 1.5**) and those icy mantles on dust grain mimics.

Other surface formation mechanisms using the dust grain chemistry model have been performed to explore the affect of UV, proton and electron irradiation. These experiments mimic the affect of UV photons (from nearby stars) and cosmic rays on the icy mantles. The recent electron irradiated experiments of $H_2{}^{18}O/N_2$ ice mixtures performed by Zheng *et al*. revealed the $H_2{}^{18}O$ molecules decomposed to form $N^{18}O$, $N_2{}^{18}O$, $H_2{}^{18}O_2$ and N_2H_4 [74]. The formation of $N^{18}O$ and $N_2{}^{18}O$ could only occur in this experiment through the reaction of N and N_2 with free O atoms (see **Figure 1.30**). However, the reaction of ground state $O(^3P)$ with N_2 has a high energy barrier [75] implying that the free O atoms were either in the $O(^1D)$ excited state or in a superthermal $O(^3P)$ ground state. As a consequence, the findings suggest that the O atoms maybe present in the icy mantles coating interstellar dust grains.

$$H_2{}^{18}O \rightarrow {}^{18}OH + H$$
$$H_2{}^{18}O \rightarrow H_2 + {}^{18}O$$
$$N + {}^{18}O \rightarrow N^{18}O$$
$$N_2 + {}^{18}O \rightarrow N_2{}^{18}O$$

Figure 1.30: $N^{18}O$ and $N_2{}^{18}O$ Formation Mechanism from Decomposed $H_2{}^{18}O$

The formation of O_3 has been experimentally studied using similar techniques to those mentioned above combined with low energy electron (90 eV [76] and 5 keV [77]) irradiation of O_2 ice. Thick layers of ices were used so that the underlying metal surface would have negligible affect on the irradiated systems. In all the cases referenced, O_3 was observed by the 1038 cm^{-1} (9.634 μm) absorption line using RAIRS (**Figure 1.31**). The formation reactions of O_3 for both irradiation procedures are shown in **Figure 1.32** [69, 77].

Another set of pure ice irradiation experiments to form O_3 were performed by Loeffler *et al.* [78]. In these experiments, a thick layer of H_2O_2 ice was irradiated with 50 keV protons. Their results revealed that O_2, O_3 and H_2O molecules and the OH radical were formed. Their results indicated that the O_3 molecules produced were mostly destroyed above 90 K by reacting with the formed OH radicals (as shown in **Figure 1.33**)

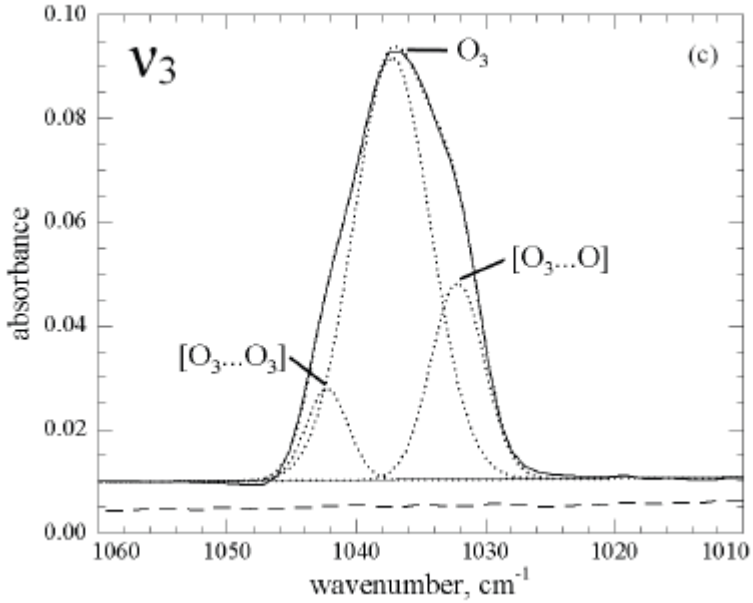

Figure 1.31: RAIRS Results for O_3 Absorption Line [76]

$$O_2 (X\ ^3\Sigma^-_g) + e^- \rightarrow O (^3P) + O (^3P) + e^-$$

$$O_2 (X\ ^3\Sigma^-_g) + e^- \rightarrow O (^3P) + O (^1D) + e^- \text{ (dominantes when } e^- \text{ energy > 100 eV [76])}$$

$$O (^1D) \rightarrow O (^3P) + \lambda\upsilon$$

$$O(^1D) + M \rightarrow O (^3P) + M$$

$$O_2 (X\ ^3\Sigma^-_g) + O (^3P) \rightarrow O_3 (X\ ^1A_1)$$

Figure 1.32: O_3 Formation Mechanisms by Low Energy Electrons

$$OH + O_3 \rightarrow HO_2 + O_2$$

$$OH + HO_2 \rightarrow H_2O + O_2$$

Figure 1.33: O_3 Destruction Mechanism by OH Radicals [78]

Irradiation experiments have also been performed on H_2O films to explore the formation of O_2. Zheng *et al.* explored this surface formation mechanism by irradiating a thick CSW film on a silver substrate with 5 keV electrons for 180 minutes [79]. Their IR and mass spectra observations indicate that the irradiated H_2O molecules decomposed as shown by the top two reaction steps in **Figure 1.34**. The formed H and H_2 species

desorbed from the surface but the other two species reacted with neighbouring molecules leading to the formation of H_2O_2 (third, fourth and fifth reaction steps) and O_2 (seventh to tenth reaction steps). H_2O_2 can also decompose to form the reaction intermediate HO_2 (sixth reaction step) which further reacts with H to form O_2. However, HO_2 was not detected indicating that HO_2 is short lived. These experiments also did not observe any O_3 molecules.

$$H_2O(X^1A_1) \rightarrow H(^2S_{1/2}) + OH(X^2\Pi_\Omega)$$
$$H_2O(X^1A_1) \rightarrow O(^1D) + H_2(X^1\Sigma_g^+)$$
$$2OH(X^2\Pi_\Omega) \rightarrow H_2O_2(X^1A)$$
$$O(^1D) + H_2O(X^1A_1) \rightarrow H_2O_2(X^1A)$$
$$O(^1D) + H_2O(X^1A_1) \rightarrow OOH_2(X^1A) \rightarrow H_2O_2(X^1A)$$
$$H_2O_2(X^1A) \rightarrow HO_2(X^2A'') + H(^2S)$$
$$OH(X^2\Pi) + O(^3P) \rightarrow HO_2(X^2A'')$$
$$HO_2(X^2A'') \rightarrow H(^2S) + O_2(X^3\Sigma_g^-)$$
$$O(^3P) + O(^3P) \rightarrow O_2(X^3\Sigma_g^-)$$
$$H_2OO(X^1A) \rightarrow O_2(a^1\Delta_g) + H_2(X^1\Sigma_g^+)$$

Figure 1.34: Surface Formation Mechanism of e^- Bombardment of CSW [79]

Irradiation of H_2O films using UV photons has also been studied. Experiments performed by Hama *et al*. irradiated vapour deposited ASW at 90 K with UV photons (λ = 157 nm) for 30 minutes [80, 81]. Their time-of flight spectra observations revealed that the H_2O molecules were photodissociated on the surface (top two reaction steps in **Figure 1.35**). Additional reactions of the photodissociated formed OH radicals led to the formation of H_2O_2 and O atoms (third and fourth reaction step). The H_2O_2 molecules were also photodissociated by the UV photons producing hot OH radicals which can form O atoms in the first excited state (bottom two reaction steps in **Figure 1.35**). Unlike in the above H_2O electron irradiation experiment, no O_2 molecules were detected suggesting that the reaction intermediate species OOH was not formed or the probability of two O atoms reacting together was considerably lower than an O atom reacting with another species.

$$H_2O \xrightarrow{h\upsilon} H_2 + O(^1D)$$

$$H_2O \xrightarrow{h\upsilon} H + OH$$

$$2OH \rightarrow H_2O_2$$

$$2OH \rightarrow H_2O + O(^3P)$$

$$H_2O_2 \xrightarrow{h\upsilon} 2OH \text{ (hot)}$$

$$2OH \text{ (hot)} \rightarrow H_2O + O(^1D)$$

Figure 1.35: UV Irradiation of ASW Films [80 81]

Irradiation experiments of ice mixtures have also been performed. The ice mixture used by Ehrenfreund and co-workers [69] contained H_2O, CO and O_2 in a 1:1:1 ratio and was irradiated with an UV discharge lamp. Their observations revealed not just the formation of O_3 but also CO_3 and H_2CO and an enhanced formation of CO_2. Their results concluded that O_3 was formed through the same mechanism as described in **Figure 1.36**.

$$O_2 \xrightarrow{h\upsilon} O + O$$

$$O + O_2 \longrightarrow O_3$$

$$O_3 \xrightarrow{h\upsilon} O_2 + O$$

UV Irradiation Mechanism

Figure 1.36: Formation and Destruction Mechanism of O_3 by UV Irradiation

Despite all the different O_3 formation mechanisms discussed above, there are a few limitation problems when transferring the laboratory case to the ISM. The first one is that the O atoms formed can not diffuse in an ice matrix [76] so O_3 could only be formed if there was an adjacent O_2 molecule. Combining this with the observation that O_2 has not been observed in the icy mantles coating interstellar dust grains greatly limits the probability of O_3 forming. Another limitation problem is that H atoms can diffuse in an ice matrix so any O atoms formed from UV photons or electrons would have a higher probability of reacting with H to form OH and, in addition, H_2O. This would

also lead to O_3 destruction reactions like those shown in **Figure 1.33**. These reasons could explain why O_3 has so far not been detected in the ISM [76].

1.3 Laboratory Astrochemistry Questions

1.3.1 Introduction

The main focus of interest for this ongoing research is to explore the formation of H_2O on interstellar dust grains. **Section 1.3.2** introduces the H_2O formation mechanism and reviews the research performed on different parts of this mechanism by other groups and their conclusions. The current sets of single and dual atomic beam apparatus and the analytical techniques used to explore the H_2O formation mechanism are described in **Section 1.3.3** along with the astronomical case for the new dual atomic beam system built in this study. The main focus of this thesis was the construction, testing and calibrating of the dual atomic beam system. The planned procedure for on-going experiments using this apparatus is discussed in **Section 1.3.4**.

1.3.2 The H_2O Formation Mechanism on Dust Grains

The simplest reaction mechanism describing the formation of H_2O on the surfaces of interstellar dust grains was proposed by Tielens and Hagen [82] (see **Figure 1.37**). The dominant formation route of H_2O is from the surface reaction of H and O atoms which

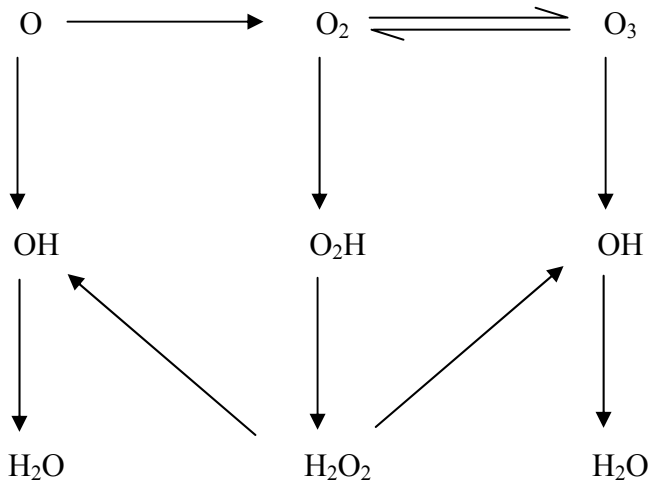

Figure 1.37: Formation Mechanism of H_2O [82]

is shown on the left hand side of the reaction mechanism in **Figure 1.37**. Although the interstellar abundance of H is considerably greater than that of O, the surface reaction of two O atoms to form O_2 could occur. From O_2, H_2O can be formed by H atom addition through the intermediate of H_2O_2 (middle reaction route of mechanism in **Figure 1.37**). Similarly O_3 could be formed resulting in another formation route to H_2O (right hand reaction route). Further analysis of this formation mechanism using a Monte Carlo approach was performed by Cuppen and Herbst [83]. Their results predict that O_2 and O_3 are formed when the grains are in a dense molecular cloud implying that knowledge of the full H_2O formation mechanism is required.

Observationally there are three problems with the H_2O formation mechanism displayed in **Figure 1.37**. Firstly, (as discussed in **Section 1.2.2**) the recent satellite missions of ODIN and SWAS places an upper limit of gaseous O_2 (3×10^{-6} to 1×10^{-7}) in dense molecular clouds [7, 39, 40]. Although some O_2 was expected to be found within the icy mantle coating the dense molecular cloud dust grains none has so far been observed [70] through the O=O vibrational stretching mode of 6.45 μm which becomes detectable in ice mixtures (see **Figure 1.28**) [69]. The second is that O_3 has never been detected in the ISM [78], either in the gas-phase or in the icy mantles. All of these observations imply that very little if any O_2 and O_3 could be formed on the grain surfaces making the formation routes of H_2O for these species highly unlikely. This is emphasised by the probability of an O atom meeting a H atom on a bare dust grain surface greatly exceeds that of the O atom meeting another O atom due to the sufficiently large interstellar abundance of H atoms in both the diffuse clouds, PDRs and dense molecular clouds. This limitation increases sufficiently when the grains are in the inner regions of a dense molecular cloud as the grains are coated in an icy mantle. This ice prevents O atoms from diffusing in the ice matrix unlike H atoms [76]. However, unlike O_3, H_2O_2 has recently been observed in the ISM [84].

To explore the formation of H_2O in the laboratory, the full reaction mechanism is required. Unlike in the ISM, the timescale to perform an experiment in the laboratory is a few hours. Under ultrahigh vacuum (UHV) conditions (10^{-10} to 10^{-12} mbar), as used in this study, the sample surface remains relatively clean for a few hours whereas a dust grain in the ISM would remain relatively clean for the lifetime of a diffuse cloud. Because of this, the amount of each species used in each experiment is much larger which greatly increases the probably of the formation of O_2 and O_3 molecules.

Additionally the current techniques used to produce atomic O and H beams cannot produce 100 % dissociation of O_2 or H_2 molecules (for more details see **Section 2.3.2**). Therefore there will always be some O_2 or H_2 in the system which can adsorb onto the sample surface.

To be able to apply the experimental results in the laboratory case to the ISM case, the kinetic rates for all the reaction, adsorption, desorption and diffusion steps in the H_2O formation mechanism need to be determined first. Once this has been achieved, only those selected reaction steps required for the ISM case can be applied to improve the computational models describing the formation of water-ice and, in the future, the formation of the icy mantles.

Several research groups have begun exploring different parts of the H_2O formation mechanism in **Figure 1.37**. Dulieu *et al.* have recently explored the formation of D_2O and HDO from D and O atoms on a layered substrate [85]. H_2O was vapour deposited onto a copper surface held at 120 K to form a thick layer of cASW before applying a further thinner film of H_2O at 10 K (pASW). The reason for a double layer ice system was to isolate the pASW layer (where the reactions of D and O would occur) from the copper surface. Before the start of each irradiation experiment, the substrate was annealed to 90 K (to mimic the amorphous ice (cASW) in the ISM that has been process by UV and cosmic rays [86]) and then cooled back to 10 K.

Initial experiments revealed that the D atoms do not react with the H_2O substrate at 10 K (bottom trace in **Figure 1.38**) or with the O atoms and O_2 molecules [85]. TPD curves of HDO and D_2O formed after 30 minutes of irradiation of D and O atoms are displayed in **Figure 1.38**. Although more D_2O was expected to be observed, the amount observed is lower due to H and D exchange process being thermal active during the ASW to CSW phase change. This results in most of the formed D_2O molecules exchanging one of the D atoms with a H atom from the underlying H_2O substrate to form two HDO species [60]. Further experiments using a pulsed ^{18}O atomic beam (20 s of irradiation every 2 minutes) and a continuous D atomic beam were irradiated for 10 minutes onto the same substrate used above. The TPD results in **Figure 1.39** revealed the same conclusions as those using dual continuous beams of D and O atoms.

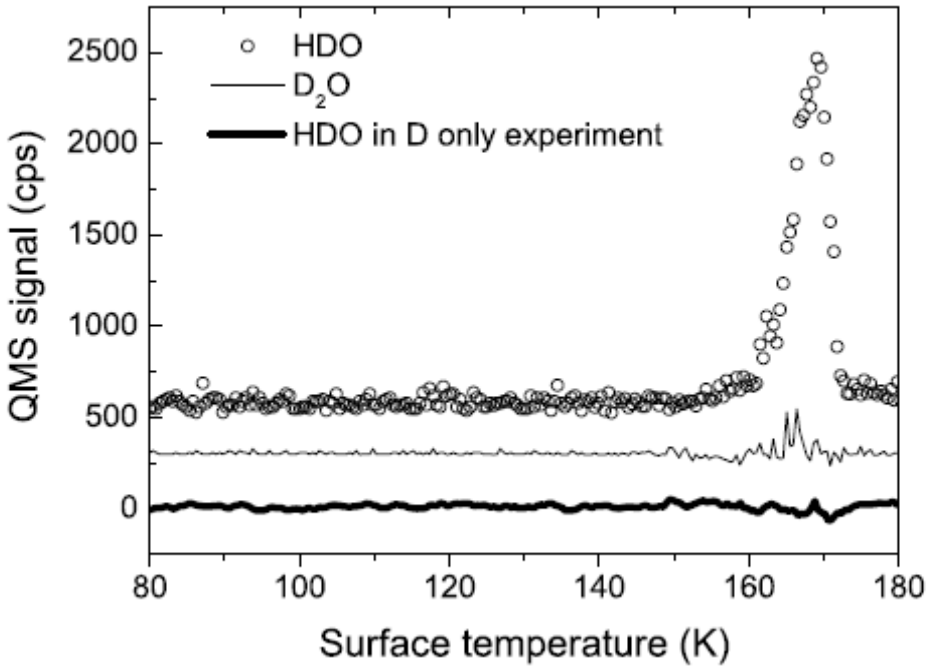

Figure 1.38: D_2O and HDO TPD Curves [85]

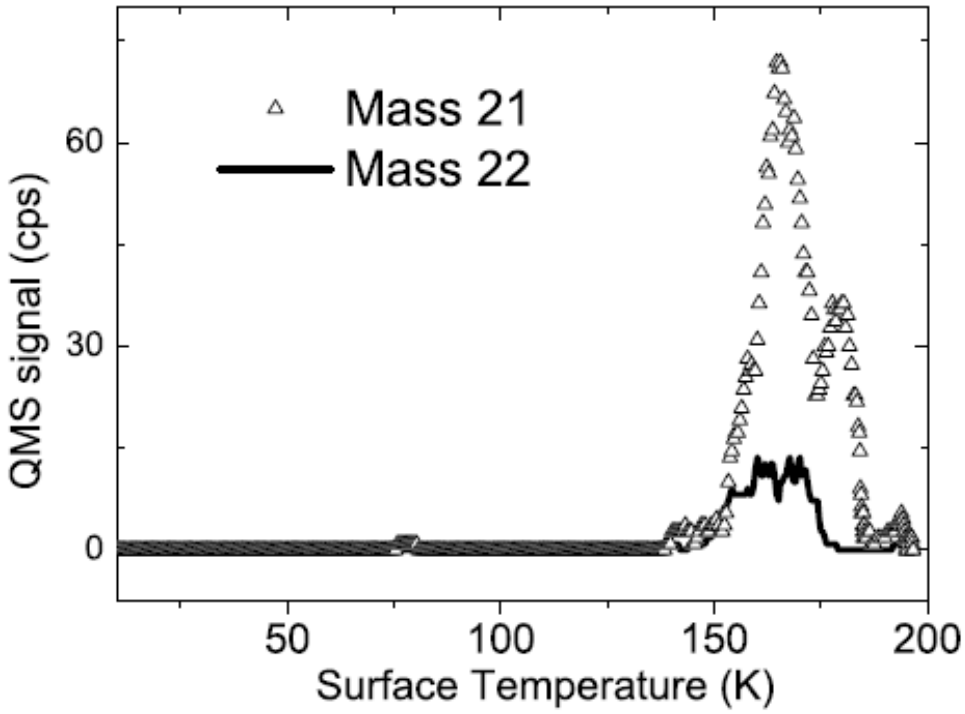

Figure 1.39: $HD^{18}O$ (open triangle) and $D_2{}^{18}O$ (solid line) TPD Traces [85]

Miyauchi *et al*. [87]; Ioppolo, Cuppen and co-workers [88-90]; and Oba *et al*. [91] have explored the formation of H_2O by the hydrogenation of O_2 (middle reaction route of the H_2O formation mechanism in **Figure 1.37**). The experiments performed by Miyauchi *et al.* [87] and Ioppolo, Cuppen and co-workers [88-90] involved irradiating a vapour deposited thick layer of O_2 with H atoms on an aluminium surface at a H flux of 2×10^{14} atoms cm^{-2} s^{-1} (Miyauchi *et al.*) or on a gold coated copper substrate with a H flux of 5×10^{13} atoms cm^{-2} s^{-1} (Ioppole and co-workers). Using reflection-absorption infrared spectroscopy (RAIRS) taken over time, both sets of results revealed the immediate observation of H_2O_2 (3250, 2830 and 1405 cm^{-1} absorbance bands) followed by H_2O (3432, 1650 and 820 cm^{-1}) (see **Figure 1.40** (top)). No absorbance bands of O_2H (1142 cm^{-1}) [92] were observed implying that the formation of O_2H occurs at a slower rate than the formation of H_2O_2 from O_2H. Comparison experiments were performed using a D atomic beam (**Figure 1.40** bottom) concluding that the H_2O_2 (D_2O_2) and H_2O (D_2O) species observed were formed by the irradiation experiments. The overall conclusions of these experiments are that the formation rate of H_2O_2 and H_2O occur rapidly on the O_2 surface at 10 K. Further calculations by Miyauchi *et al.* [87] determined the rate of formation of H_2O_2 (from O_2 + H reaction) and H_2O (from H_2O_2 + H reaction) as 0.21 and 0.065 s^{-1}.

The more recent experiments performed by Ioppolo *et al*. exploring the formation of H_2O by hydrogenation of O_2 films combined TPD and RAIRS analysis to obtain a more detailed analysis of the chemical processes involved [89]. Their results concluded that the formation rates of H_2O and H_2O_2 were temperature and thickness dependent with the final yield of these species restricted by the competing H diffusion and reaction steps. Further experiments were performed exploring the penetration depth of the diffusing H atoms into the O_2 film. Although there were a range of values for the penetration depth of the H atoms, the results revealed that the hydrogenation of the O_2 film mainly occurred from the bottom upwards. Interestingly, the results obtained also revealed the presence of O_3 molecules indicating that other reactions were occurring than those shown in the middle step of **Figure 1.37**. Additional experiments were performed by Cuppen *et al*. (using the same apparatus) where the temperature of the O_2 film and the H/O_2 ratio were varied [90]. The most intense signal for O_3 was obtained either at low temperatures (15 and 20 K) for low H/O_2 ratios or at a high temperature

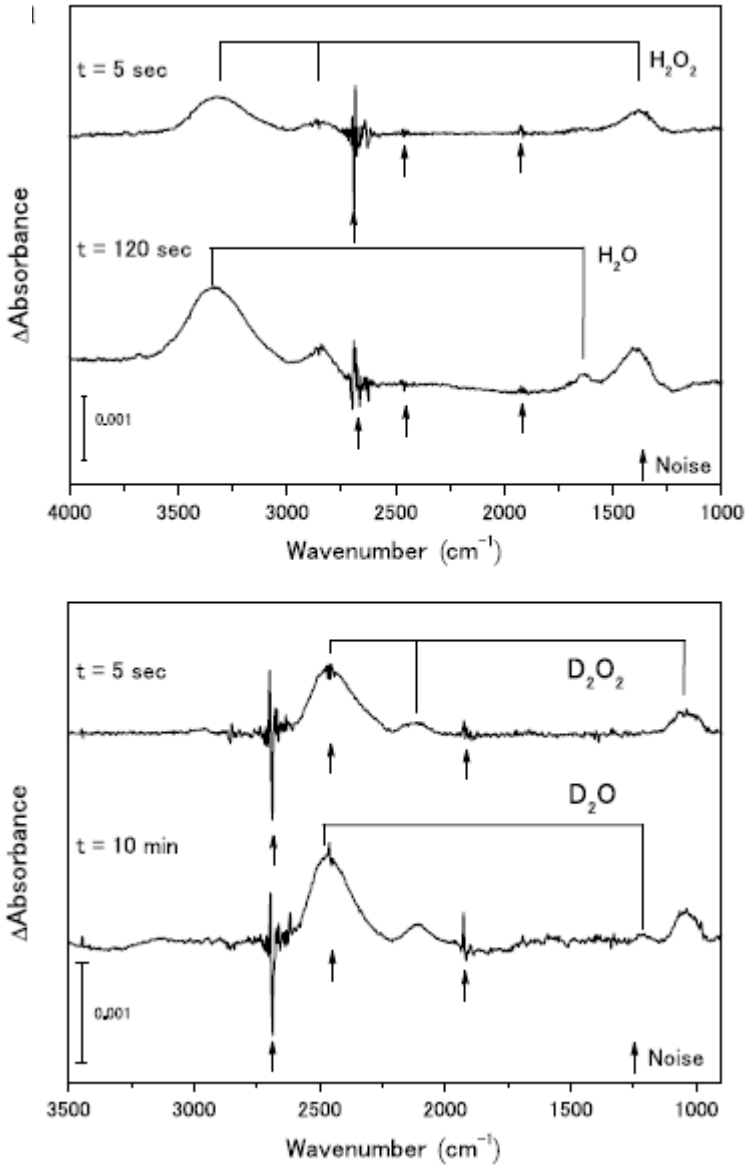

Figure 1.40: RAIRS Results for the Formation of H_2O_2 and H_2O (top) and D_2O_2 and D_2O (bottom) from Hydrogenation of O_2

(25 K) with a high H/O_2 ratio. Overall the results concluded that the O_3 molecules were formed through the top reaction of **Figure 1.37** in the O_2 film where the O atoms were formed through the proposed reactions shown in **Figure 1.41**. As a consequence, the results obtained from these experiments suggest that the overall H_2O formation mechanism on interstellar dust grains is more complicated than the mechanism proposed by Tielens and Hagen (**Figure 1.37**).

$$H(ads) + HO_2(ads) \rightarrow H_2O(ads) + O(ads)$$
$$OH(ads) + O_2(ads) \rightarrow HO_2(ads) + O(ads)$$

Figure 1.41: Proposed O Formation Reactions Involved in the Hydrogenation of O_2

The experiments performed by Oba *et al.* explored the structure of the H_2O ice formed from the hydrogenation of O_2 in comparison to pASW [93]. The IR spectrum of vapour deposition H_2O at 20 K (pASW) is displayed in the top plot of **Figure 1.42** [91]. Due to the relatively high heterogeneity in pASW films (see **Section 1.2.3**), two small peaks are observed at 3721 and 3698 cm^{-1} in pASW ices [94]. These peaks are assigned to the two OH dangling bonds from two- and three-coordinated H_2O molecules at the surface.

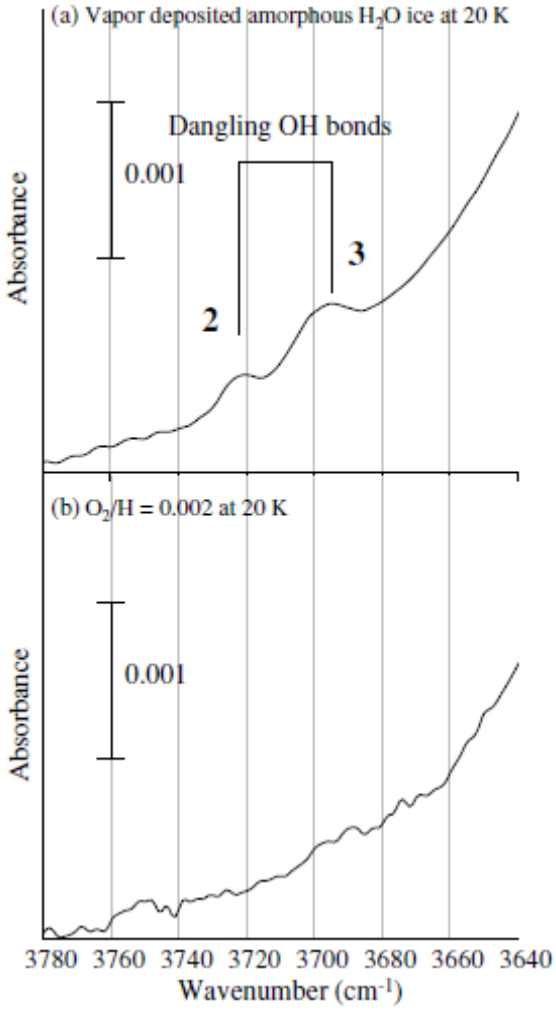

Figure 1.42: IR Spectra of Vapour Deposited H_2O Ice (top) and H_2O Formed Through Hydrogenation of O_2 Ice (bottom) [91]

Neither of these two OH dangling bonds were observed in the H_2O ice formed by the hydrogenation of O_2 (see bottom plot in **Figure 1.42**) [91] indicating that the H_2O molecules arrange themselves in a cASW structure. The lack of OH dangling bonds may also be a consequence of small concentrations of H_2O_2 formed in the H_2O formation mechanism (see **Figure 1.37**) found in the ice mixture. The disappearance of the OH dangling bonds in the formed H_2O is consistent with the IR features of H_2O observed in the icy mantles covering dust grains in dense molecular clouds [95].

The formation of H_2O from O_3 (right hand mechanism in **Figure 1.37**) has been explored by Mokrane *et al.* [96]. Their experiments used a thick vapour deposited O_3 substrate (dosed at 50 K) on top of a thick compact amorphous solid water (cASW) ice film (also vapour deposited) on a copper surface. This layered ice system was cooled to 10 K and irradiated with a D atomic beam. For comparison, two initial calibration experiments were performed. The first consisted of D irradiated cASW ice on copper and concluded that no HDO or D_2O species were observed implying that the D_2O observed in the above experiment was formed from O_3 and not H_2O. The second involved irradiating the cASW surface with the D beam before vapour depositing the O_3 layer. The TPD results revealed that the O_3 molecules desorbed from the surface without reacting implying that O_3 does not react with D_2. In turn, this second experiment revealed that the reactions of O_3 with D to form D_2O occur around 10 K and not higher temperatures as the D atoms react to form D_2 which desorbs above 13 K [97].

The surface formation of D_2O from O_3 is displayed in **Figure 1.43**. TPD analysis revealed that the first reaction step occurs rapidly on the surface below 10 K [96]. D_2O can be formed by additional reactions with either of the products formed from the first reaction step (reaction step two from OD and reaction steps three to four from O_2). The final reaction step in **Figure 1.43** is the H and D exchange with the underlying H_2O substrate which occurs during the ASW to CSW phase change (as previously discussed) [96]. This process occurs readily in this set of experiments as very few D_2O molecules were observed. Additional experiments were performed using a low exposure of D atom to the system so that not all the O_3 molecules would react leaving a thin layer separating the underlying water film from those O_3 molecules reacting with D atoms. In this experiment, O_2 was detected as well as D_2O implying that not all the formed O_2 molecules (first reaction step in **Figure 1.43**) reacted with D atoms.

$$O_3 + D \rightarrow OD + O_2$$
$$OD + D \rightarrow D_2O$$
$$O_2 + D \rightarrow DO_2$$
$$DO_2 + D \rightarrow D_2O_2$$
$$D_2O_2 + D \rightarrow D_2O + D$$
$$D_2O + H_2O \rightarrow 2HDO \text{ (above 140 K)}$$

Figure 1.43: D_2O Formation Mechanism from O_3 [96]

In conclusion, each of the three downward mechanisms in **Figure 1.37** to form H_2O have been explored using either TPD (D + O [85]; D + ^{18}O [85]; and D + O_3 [96]) or RAIRS (D + O_2 [87, 88, 91]) techniques. For a greater understanding of the chemical processes occurring in each mechanism, both RAIRS and TPD analysis need to be performed together. This has only been performed for the middle H_2O formation mechanism in **Figure 1.37** by Ioppolo *et al*. [89] and Cuppen *et al*. [90]. Overall, the results from these experiments indicate that the H_2O formation mechanism proposed by Tielens and Hagen [82] was too simple. A more complex surface formation mechanism derived by Cuppen *et al*. is shown in **Figure 1.44** [90].

Currently, all of the research performed explore thick layers of vapour deposited O_2 and O_3 on either metal or H_2O film on a metal surface. Sub-monolayer coverages of O_2 and O_3 on either pASW, cASW or dust grain mimics (like amorphous silica; olivine; or graphite) have yet to be investigated. O and H (or D) atomic beam irradiation on these surfaces would also be required to study the H_2O formation mechanism.

Other research required to understand the full H_2O formation mechanism is the ratio of O, O_2 and O_3 situated on either bare dust grains or their icy mantles at different stages during the diffuse and dense molecular cloud lifetime (top reaction line in **Figure 1.37**). This would determine the proportion of H_2O formed in the ISM from O, O_2 and O_3. However, to perform all the experiments required to understand the complete H_2O formation mechanism on interstellar dust grains, a new dual atomic beam system is required. The following sub-section reviews the single and dual atomic beam systems

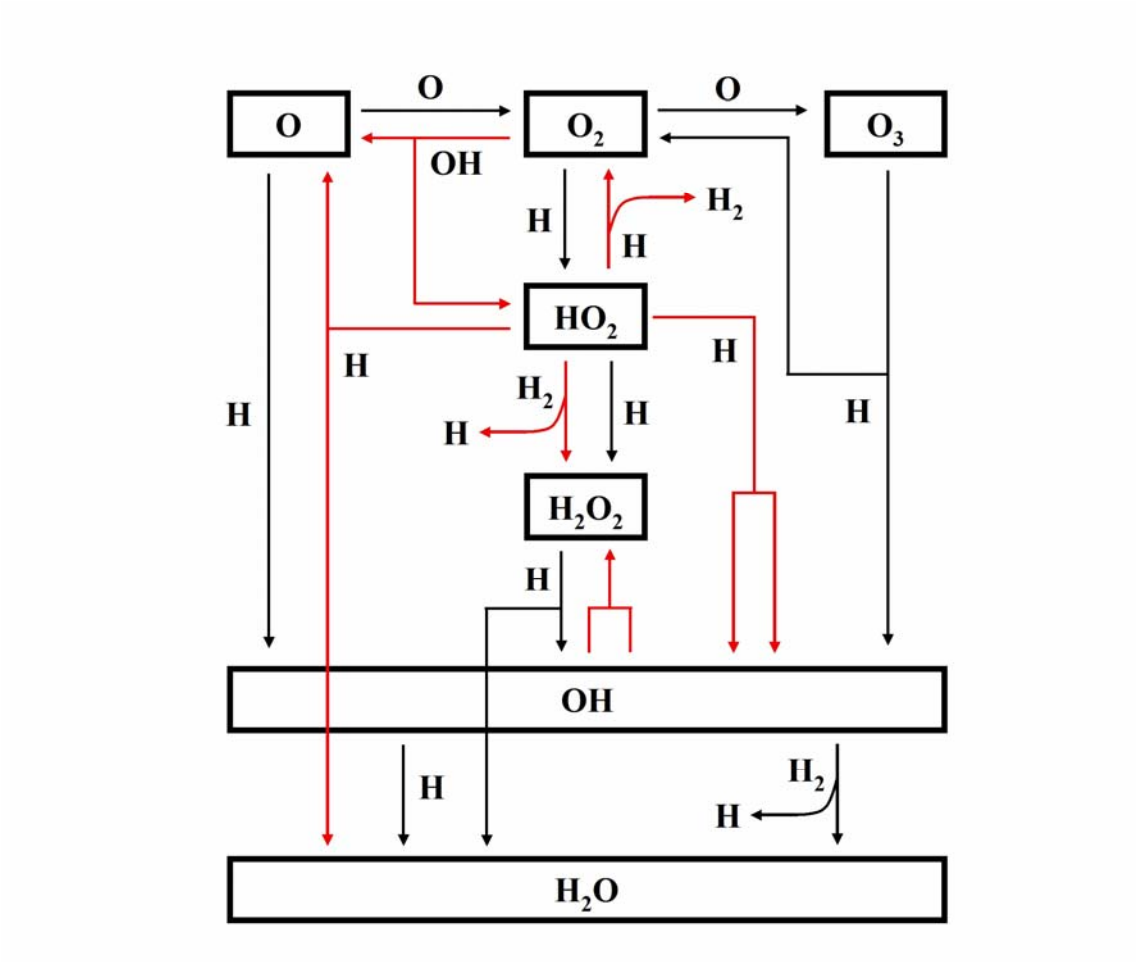

Figure 1.44: Full H_2O Surface Formation Mechanism [90] where the Black Arrows Represent the Reactions Occurring in the Original Formation Mechanism (see **Figure 1.37**)

currently being used to explore surface formation mechanisms on interstellar dust grains and the advantages and disadvantages of each system. **Section 1.3.3** concludes with the astronomical case for the new piece of apparatus built in this study. The planned procedure for the apparatus for this ongoing research is discussed in **Section 1.3.4**.

1.3.3 Current Single and Dual Atomic Beam Apparatus

As mention in the above section, there are several research groups working on the H_2O formation mechanism on interstellar dust grains. At present, these groups are Linnartz (Leiden, Netherlands); Kouchi (Hokkaido, Japan); and Lemaire (Paris, France). Each of these groups has their own set of apparatus from which a range of analytical techniques can be applied. The single atomic beam systems in Leiden and Hokkaido will be discussed first in this study and then the dual atomic beam system in Paris. Another dual

atomic beam system is used by the Vidali research group (Syracuse, NY) to explore the formation of H_2 on a range of astronomical surfaces. This set of apparatus will also be reviewed in this sub-section.

The apparatus used by Linnartz's research group in Leiden is a single H atomic beam arrangement (see **Figure 1.45**) [98]. The main chamber regularly reaches a base pressure lower than 3×10^{-10} mbar. Situated in the centre of this chamber is a gold coated copper substrate which is mounted on the end of a cold finger connected to a helium cryostat and is typically cooled to 10 K. The main chamber is equipped with a quadrupole mass spectrometer (QMS) for TPD experiments; apparatus for RAIRS; and a dosing line for vapour deposition experiments. The atomic H beam is formed by thermal dissociation of H_2 molecules in a tungsten thermal cracking source (for more details on this technique, see **Section 2.3.2**). However, this technique produces H atoms with temperatures of approximately 2000 K which is hot enough to affect the vapour deposited ice on the gold substrate. To prevent this from happening, the H atoms are cooled to room temperature through surface collisions in a nose shaped quartz pipe situated between the thermal cracking source and the main chamber. The flux of the atomic H beam formed was calibrated as $10^{12} - 10^{14}$ atoms cm^{-2} s^{-1}.

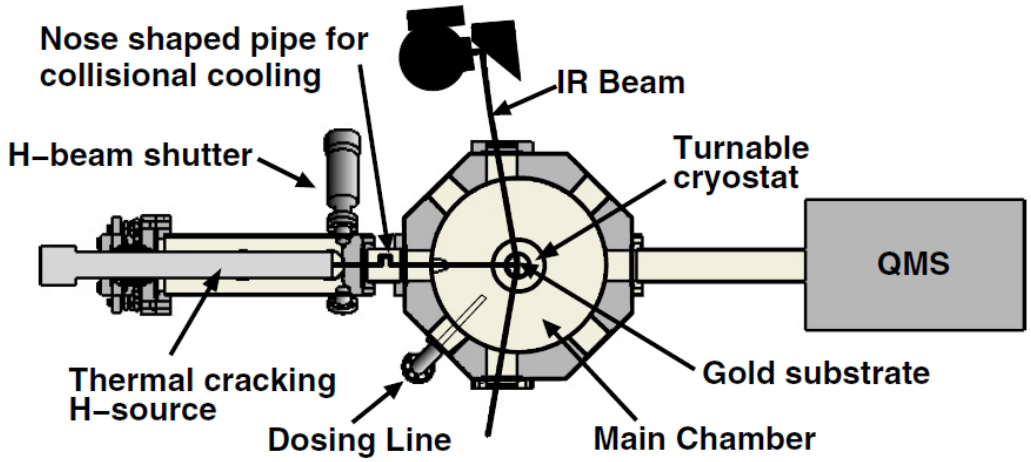

Figure 1.45: Apparatus Used at Leiden University [98]

Hydrogenation of background deposited ice experiments performed using this apparatus include: O_2 (to form H_2O_2 and H_2O as discussed in **Section 1.3.2**) [88-90]; and CO,

CO_2, HCOOH and CH_3CHO (as described by the hydrogenation mechanism shown in **Figure 1.46**) [98, 99].

$$H + CO \rightarrow HCO$$
$$H + HCO \rightarrow H_2CO$$
$$H + H_2CO \rightarrow CH_3O$$
$$H + CH_3O \rightarrow CH_3OH$$

Figure 1.46: CH_3OH Formation Mechanism on Interstellar Dust Grains [98]

Although the apparatus in Leiden was designed to use RAIRS and TPD analytical techniques, the apparatus is restricted to the range of astronomical relevant hydrogenation experiments that can be performed. Firstly, the gold coated copper substrate limits these experiments to only those with thick pre-adsorbed substrates otherwise the underlying metal surface would greatly affect the results. Secondly, the fixed position of their QMS behind the sample prevents any analytical techniques, like molecular beam modulation spectrometer (MBMS) (see **Section 2.3.3**), being performed to detect the range and intensity of desorbing species from the surface during the beam irradiation part of the experiment. Thirdly, like with all single atomic beam apparatus, only one species in the atomic form can be studied at any one time. Also, the type of atomic beam apparatus used limits the species range of atomic beams that can be created (for more information on this subject, see **Section 2.3.2**).

Another set of apparatus is the single atomic H (or D) beam system called ASURA (apparatus for surface reactions in astrophysics) used by Kouchi and co-workers in Japan. The design of this piece of apparatus was based on the research group's earlier system known as LASSIE (Laboratory Setup for the Surface Reactions in Interstellar Environments) [100, 101]. ASURA consists of an atomic source chamber and a main chamber as shown in **Figure 1.47** [102]. The main chamber is pumped using a turbomolecular pump (TMP) backed by a foreline trapped rotary pump. The base pressure of the main chamber typically reaches 5×10^{-10} Torr (approximately 7×10^{-10} mbar). A 30 mm diameter aluminium sample was mounted on the end of a He refrigerator cold finger which can be cooled to a base temperature of 8 K. This in turn

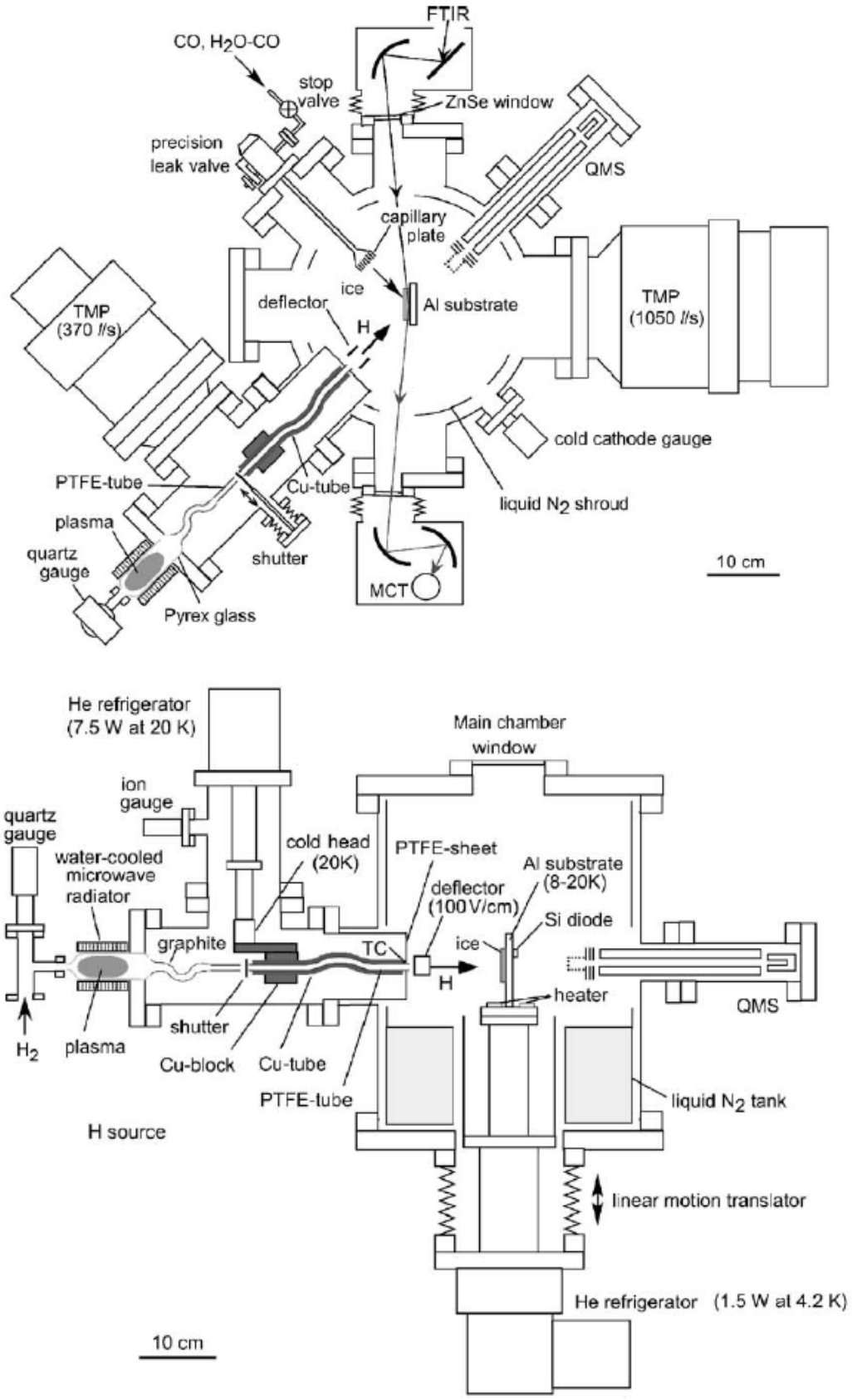

Figure 1.47: Schematic Diagram Plan (top) and Cut-Through (bottom) of the ASURA [102]

is mounted on a linear motion translator, enabling the sample to be raised for the H beam flux and dissociation fraction calibrations to be performed. The main chamber is equipped with a QMS; a Fourier transform infrared (FTIR) spectrometer for RAIRS; and vapour deposition apparatus.

Adjoining the main chamber is the atomic source chamber. Like the main chamber, the atomic source chamber is pumped by a TMP backed by a foreline trap rotary pump. The base pressure in this chamber is typically 10^{-8} Torr (approximately 10^{-8} mbar) but reaches 10^{-5} Torr (approximately 10^{-5} mbar) when the beam is in operation. H_2 is leaked into a Pyrex tube and the H atoms are formed using a water cooled MW plasma source (2.45 GHz frequency setting). A graphite coated nozzle, 4 cm in length and 1 mm in diameter, is situated on the end of the Pyrex tube to create the atomic beam. The atomic beam is directed into the main chamber through a polytetrafluoroethylene (PTFE) tube surrounded by a copper tube which is connected to a separate He refrigerator allowing the beam to be cooled to a base temperature of 20 K. At the end of the PTFE tube is a deflector which is designed to eliminate charged particles and 2S-metastable H atom contaminants. A shutter is situated between the graphite coated nozzle and the PTFE tubing to control the release of the atomic beam into the main chamber. The atomic beam system can also be used to form D beams. The flux and dissociation fractions of the H and D atomic beam were calibrated by Hidaka *et al.* [103]. Both beams typically operate with a flux of 2×10^{14} cm^{-2} s^{-1} and at least a 20 % dissociation fraction [87].

Early work performed on ASURA also explored the hydrogenation of CO [102, 104, 105]. More recently, Kouchi *et al.* have used their single beam system to investigate the hydrogenation of O_2 to form H_2O *via* the reaction intermediate H_2O_2 [87] (see middle reaction route in **Figure 1.37**). The results of these experiments have previously been discussed in the previous sub-section.

The disadvantages with ASURA are the same as those discussed for the Leiden apparatus making a single atomic beam system with a metal substrate sample unsuitable for exploring the full formation mechanism of H_2O. One advantage of ASURA over Leiden is that their MW plasma source can also be used to form OH radicals as well as H and D atoms [106].

The apparatus used by the research group in Paris is a dual atomic beam system called FORMOLISM (FORMation of MOLecules in the ISM) [107]. The apparatus consists of a central chamber (base pressure typically 10^{-10} mbar) with two adjoining triply differentially pumped beam lines (see **Figure 1.48**). Inside the central chamber, an oxygen free high conductivity (OFHC) copper cylinder block sample is mounted on the end of a cold finger of a closed-cycle He cryostat. The sample holder is equipped with an 800 K heating interface. The base sample temperature is monitored using a Silicon diode and KP-type (chromel/gold-iron) thermocouple and can be typically cooled to 8 K. This chamber is also equipped with a QMS. The atomic beams are formed by dissociating D_2 and O_2 in MW discharges at 2.45 GHz. The temperature of the D beam can be controlled between 30 and 350 K by passing the gas through an aluminium nozzle connected to a He closed-cycle cryostat [108]. The flux of the D beam was calibrated at approximately 5×10^{15} atoms cm^{-2} s^{-1} with a dissociation fraction of typically 60% [96]. For the O beam, the dissociation fraction is lower at approximately 40% with a flux of 10^{12} atoms cm^{-2} s^{-1} [85].

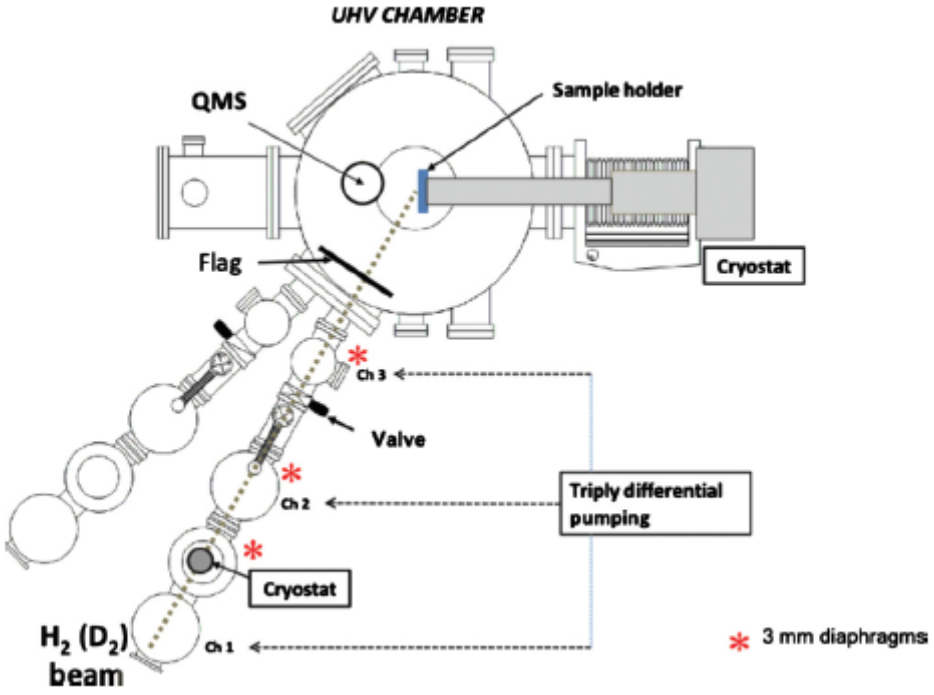

Figure 1.48: Schematic Diagram Plan of the FORMOLISM Apparatus [108]

Experiments performed using this apparatus include: exploring the reactions of O and D atoms on a pASW substrate (as previously discussed in **Section 1.3.2**) [85]; hydrogenation of O_3 (see **Section 1.3.2**) [96]; and D_2 TPD from pASW on copper and from cASW on copper [93, 107].

The main advantage of the FORMOLISM apparatus in comparison to the two single atomic beam systems discussed above is that both atomic beams can be used simultaneously and the D beam species can be cooled. However, this apparatus is not equipped with RAIRS which restricts the analysis to TPD only. Another disadvantage with FORMOLISM is the metal surface limits the range of experiments to those with thick pre-adsorbed substrates (like those performed on the single atomic beam systems).

Another research group that uses a dual atomic beam system is Vidali *et al.* in Syracuse (NY, US). In the past, this apparatus has been used to study the formation of HD on an olivine surface [49, 109]; amorphous silicate surface [35]; amorphous carbon [50]; and water ice substrates [110, 111]. The schematic drawing for the Syracuse apparatus is displayed in **Figure 1.49** [110]. The main chamber is pumped with a cryopump (labelled C in **Figure 1.49**) and TMPs (T1, T2 and T3) and reaches a base pressure of around 5×10^{-10} Torr (approximately 7×10^{-10} mbar). The main chamber is equipped with a QMS; titanium sublimation pump (TSP) (labelled Ti); a leak valve (LV) for vapour depositing thin films on the surface; and a magnesium fluoride view port (VW) for admitting UV radiation (where λ is below 350 nm) from a short arc xenon flash lamp into the main chamber. The UV flux was calculated as approximately 6×10^{15} photons s^{-1} cm^{-2} [110]. A copper sample holder is mounted on the end of a cold finger cooled by a closed cycle liquid helium cryostat and is designed so that the sample can be replaced or swapped for one of a different material (for example, olivine or copper). The surface temperature is monitored using two KP-type thermocouples and the base temperature of 4.5 K is regularly reached [112]. The sample can be heated for TPD analysis using a constantan wire heater located in a small cavity behind the sample. However, in most of the TPD experiments the sample is heated by shutting off the liquid helium supply in the cryostat.

Adjoining the main chamber are two beam lines which are split into three separate chambers. In the first stage chamber, the required gas (either H_2 or D_2) is leaked into a

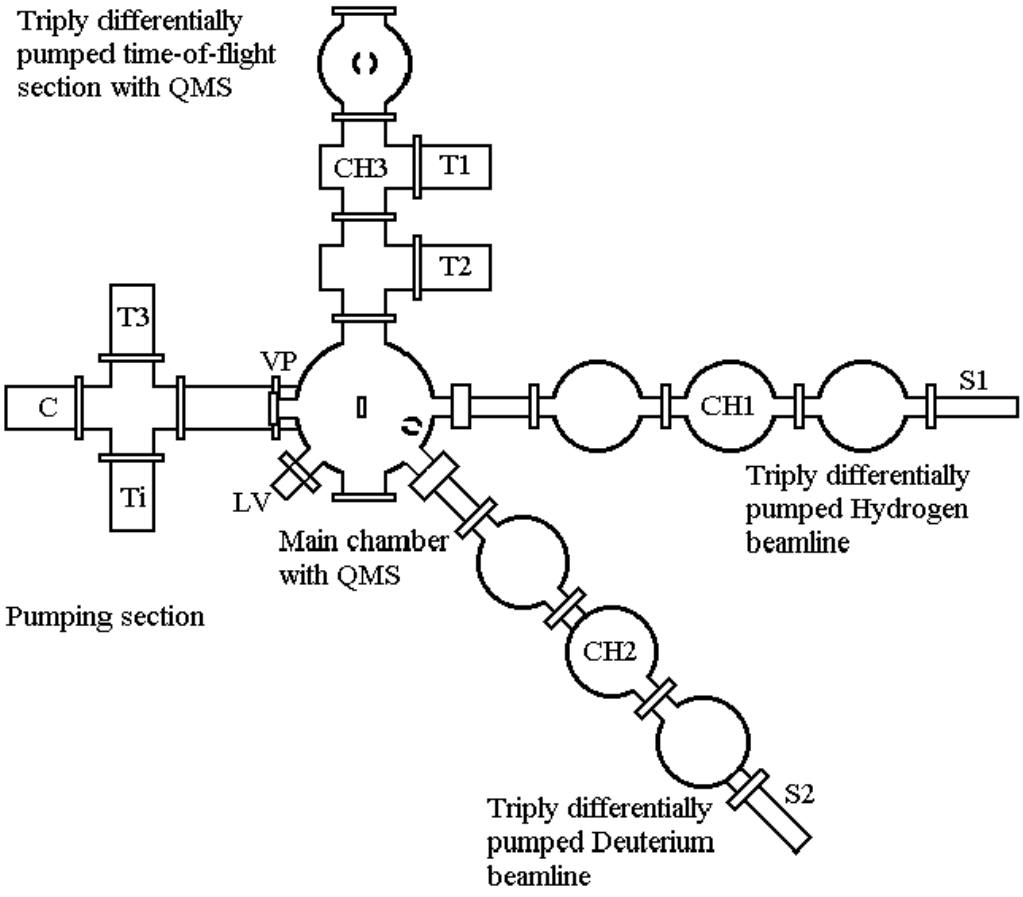

Figure 1.49: Schematic Diagram of the Dual Atomic Beam Apparatus Used in Syracuse (NY, US) [110]

water cooled Pyrex tube. The gas is dissociated using a RF discharge (S1 and S2) and the beam is formed as the atomic gas enters the second chamber through a liquid nitrogen cooled aluminium capillary of 1 mm in diameter. The second stage chamber is also fitted with chopper apparatus (labelled CH1 and CH2 in the H and D beam lines respectively). The beam width is refined by a 3 mm collimator between the second and third stage. Calibrations using the QMS in the main chamber revealed that the dissociation fractions are typically 80% and 90% for D_2 and H_2 respectively [110] and the beam flux for each beam is approximately 10^{12} atoms cm^{-2} s^{-1} [49]. The H atomic beam source has also been used to produce an atomic oxygen beam with a dissociation fraction between 30 and 40 % [47].

Although this set of apparatus allows flexibility in the range of astrophysically relevant surfaces, unlike the previously apparatus systems mentioned, the analysis of the

experiments is limited to TPD techniques. Additionally, the Pyrex tubing inside the beam source restricts the range of other atomic beam species from being formed. One advantage of this apparatus from the others discussed in this section is that the QMS is situated in a suitable position to allow the detection of desorbing species from the surface during the beam irradiation part of the experiment. This would allow techniques like MBMS to be performed.

In reviewing the current single and dual atomic beam systems used to explore the formation of species on interstellar dust grains, a new dual atomic beam system is required to explore the H_2O formation mechanism (**Figure 1.37**) in detail. A full description of this apparatus can be found in **Chapter 2**. The main features of this apparatus includes: two RF powered plasma sources (with a boron nitride plasma tube for hydrogen and quartz tube for oxygen); QMS which can be used to monitor gaseous species desorbing from the surface during both the beam irradiation experiments (MBMS) and TPD analysis; RAIRS apparatus; and a dosing line for vapour deposited ices. The astronomically relevant surface was chosen to be amorphous silica which is deposited on a copper plate mounted into a sample mount. This allows the sample to be change when necessary like in the apparatus used by Vidali's research group. The sample is cooled using a closed cycle compressed helium gas cryostat to a base temperature cool enough for atomic oxygen to stick. A heater is situated behind the sample for greater control of the heating ramp for TPD experiments. Another analytical technique that is included on this apparatus is a quartz crystal microgravimetry (QCM) (see **Section 2.3.5** for more details) which will be used as an additional method to determine the beam fluxes.

1.3.4 Planned Procedure

The main aim of this study was to build a new dual atomic beam system that contained the apparatus required for TPD, RAIRS, MBMS and QCM analytical techniques. A full description of the new apparatus and the calibrations performed can be found in **Chapters 2** and **3** respectively. This apparatus would be used to explore the whole H_2O formation mechanism on interstellar dust grains (see **Figure 1.44**).

The first collection of ongoing experiments is designed to explore the kinetic behaviour of O, O_2 and O_3 from a range of astronomically relevant surfaces (top line of the H_2O formation mechanism in **Figure 1.44**). **Chapter 4** discusses the results of TPD

experiments of O_2 from: bare silica; pASW on silica; and cASW on silica. For comparison, the results of pASW on silica TPD experiments were included. The kinetic parameters obtained from these TPD experiments were used in a simulation model to mimic the desorption of O_2 in these experiments. These results were then applied to describe the desorption of O_2 from icy mantles coating interstellar dust grains found in dense molecular clouds. Additional TPD experiments investigating the multilayer kinetic desorption of CO and N_2 are discussed in **Chapter 5**.

A collection of preliminary TPD results exploring the desorption of O atoms from a range of astronomically relevant surfaces are discussed in **Chapter 6**. The results to determine the oxygen beam flux and O plasma analysis are discussed in **Chapter 3**. Additional O TPD experiments from pASW on silica are required before the full kinetic desorption analysis can be applied. Other future O atom TPD experiments include those from bare silica and cASW on silica substrates which will be performed with RAIRS and MBMS analysis. The kinetic parameters obtained from all these experiments, including those in **Chapter 4**, will be used to construct a model mimicking the desorption of O and formation of O_2 in the laboratory and in interstellar icy mantles.

The remaining set of initial experiments to be performed explore the desorption of O_3 from bare silica; pASW on silica; and cASW on silica. The chosen synthesis and apparatus design to form O_3 are described in **Chapter 2** (**Section 2.5**). O_3 TPD experiments with RAIRS and MBMS analysis are planned from bare silica; pASW on silica; cASW on silica; and O_2 on silica substrates. The kinetic parameters obtained from these experiments will be used to evaluate the desorption kinetics of O_3 and the rate of decomposition of O_3 on these surfaces. These results, along with those of O_2 from **Chapter 4**, will be used to construct a simulation model mimicking the O_3 desorption and decomposition in the laboratory before being applied to the dust grains in the dense molecular clouds.

The results from each of these simulation models will be used to construct an overall simulation model mimicking the behaviour of O, O_2 and O_3 on interstellar dust grains. This model will include the diffusion, trapping and desorption of O, O_2 and O_3 from icy mantles; the formation of O_2 and O_3; and the decomposition of O_3. The results from this model may be able to explain why the observed abundance of O_2 is approximately 1000 times lower than predicted from gas-phase chemistry models (see

Section 1.2.2) [41] and why O_2 has not been detected in the icy mantles [70] or why O_3 has yet to be observed in the ISM [76] (**Section 1.2.3**). Additionally, if this model was combined with the gas-phase model for oxygen then this new model would provide the $O:O_2:O_3$ ratio throughout the lifetime of diffuse and dense molecular cloud environments. These ratios could then be used to estimate the proportion of H_2O formed from O, O_2 and O_3 during the cloud's lifetime (both as a diffuse and dense molecular cloud). This would complete the analysis of the top line of the H_2O formation mechanism in **Figure 1.44**.

The next collection of experiments to explore in the H_2O formation mechanism in **Figure 1.44** are the hydrogenation of O, O_2 and O_3 using the atomic hydrogen beam. The hydrogen plasma analysis is discussed in **Chapter 3**. Additional calibration work would be required to determine the atomic beam flux and, along with the new design method for the O_2 beam, the dissociation fraction (see **Section 3.4.3**). Although the hydrogenation of O_2 and O_3 has been previously explored by other research groups (as discussed in **Section 1.3.2**), these experiments only analysis their results using one technique. A wider range of experimental techniques (MBMS, TPD, RAIRS and QCM) are available on this new apparatus allowing for a more detailed understanding of these H_2O formation routes. Also, these previous experiments were performed with thick layers of O_2 and O_3 on metal surfaces which would not be the case in the ISM. Therefore these reactions will be reproduced using the dual atomic beam system built in this study and will explore both multilayer and sub-monolayer coverages of O_2 and O_3 on bare silica. Along with the results obtained from the dual atomic beam experiments of O and H on bare silica (using MBMS, RAIRS and TPD analysis), the kinetic parameters deuced will be used to construct simulation models describing the formation of H_2O and desorption of those species involved in each of the three systems (O + H; O_2 + H; O_3 + H). These models will then be applies to the diffuse and dense molecular cloud environments using the predicted ratios obtained from the combined gas-phase and dust grain model for O, O_2 and O_3 (top line reaction mechanism in **Figure 1.44**) to obtain one model describing the full H_2O formation mechanism on interstellar dust grains.

The conclusions and astronomical implications of the work covered in this study, along with suggested future work and modifications to the apparatus, are discussed in **Chapter 7**. Once the H_2O formation mechanism on interstellar dust grains has been

explored, the dual atomic beam system can be used to explore other interstellar systems. Current plans included exploring the desorption and reactions of a H and C (fourth most abundant element in the ISM) system; and a H and N (fifth most abundant element in the ISM) system. Both of these systems will be explored on a range of astronomically relevant surfaces like: bare silica; pASW on silica; and cASW on silica.

1.4 References

[1] NASA, *Astronomy Picture of the Day Archive*, Accessed 23 April 2010.

[2] D. Buhl, *Nature*, 1971, **234**, 332.

[3] L. E. Snyder, D. Buhl, B. Zuckerman and P. Palmer, *Phys. Rev. Lett.*, 1969, **22**, 679.

[4] L. Snyder and D. Buhl, *Ap. J.*, 1971, **163**, L47.

[5] *Nature Physical Science*, 1971, **229**, 36.

[6] C. Sagan, *Nature*, 1972, **238**, 77.

[7] R. Liseau and O. Team, *Astrochemistry: Recent Successes and Current Challenges*, Cambridge University Press, Cambridge, 2006.

[8] *129 reported interstellar and circumstellar molecules*, Accessed 23 April 2010.

[9] E. Gibbs, D. Whittet, W. Schutte, A. Boogert, J. Chiar, P. Ehrenfreund, P. Gerakines, J. Keane, A. Tielens, E. van Dishoeck and O. Kerkhof, *Ap. J.*, 2000, **536**, 347.

[10] E. Herbst and H. Cuppen, *Proceedings National Academy Sci.*, 2006, **103**, 12257.

[11] J. M. Greenberg, *Surface Science*, 2002, **500**, 793.

[12] A. G. G. M. Tielens, *The Physics and Chemistry of the Interstellar Medium*, Cambridge University Press, Cambridge, 2006.

[13] R. J. Trumpler, *Lick Obs. Bull.*, 1930, **14**, 154.

[14] A. E. Whitford, *Ap. J.*, 1948, **107**, 102.

[15] A. E. Whitford, *Astron. J.*, 1958, **63**, 201.

[16] D. A. Williams and E. Herbst, *Surf. Sci.*, 2002, **500**, 823.

[17] A. Shaw, *Astrochemistry: From Astronomy to Astrobiology*, Wiley, 2006.

[18] E. L. Gibb, D. C. B. Whittet, A. C. A. Boogert and A. G. G. M. Tielens, *Ap. J. Supplement Series*, 2004, **151**, 35.

[19] F. C. Gillett and W. J. Forrest, *Ap. J.*, 1973, **179**, 483.

[20] D. C. B. Whittet, *Dust in the Galactic Environment*, IOP Publ. Ltd., Bristol, 2003.

[21] A. Li and J. M. Greenberg, *Astron, Astrophys.*, 1997, **323**, 566.

[22] I. Butchart, A. D. McFadzean, D. C. B. Whittet, T. R. Geballe and J. M. Greenberg, *Astron. Astrophys.*, 1986, **154**, L5.

[23] S. P. Willner, R. W. Russell, R. C. Puetter, B. T. Soifer and P. M. Harvey, 1979, **229**.

[24] J. M. Greenberg, *Astron. Astrophys.*, 1998, **330**, 375.

[25] J. M. Greenberg and A. Lin, *Space Sci. Rev.*, 1999, **90**, 149.

[26] D. Brownlee, P. Tsou, J. Aleon, C. M. O. D. Alexander, T. Araki, S. Bajt, G. A. Baratta, R. Bastien, P. Bland, P. Bleuet, J. Borg, J. P. Bradley, A. Brearley, F. Brenker, S. Brennan, J. C. Bridges, N. D. Browning, J. R. Brucato, E. Bullock, M. J. Burchell, H. Busemann, A. Butterworth, M. Chaussidon, A. Cheuvront, M. Chi, M. J. Cintala, B. C. Clark, S. J. Clemett, G. Cody, L. Colangeli, G. Cooper, P. Cordier, C. Daghlian, Z. Dai, L. D'Hendecourt, Z. Djouadi, G. Dominguez, T. Duxbury, J. P. Dworkin, D. S. Ebel, T. E. Economou, S. Fakra, S. A. J. Fairey, S. Fallon, G. Ferrini, T. Ferroir, H. Fleckenstein, C. Floss, G. Flynn, I. A. Franchi, M. Fries, Z. Gainsforth, J. P. Gallien, M. Genge, M. K. Gilles, P. Gillet, J. Gilmour, D. P. Glavin, M. Gounelle, M. M. Grady, G. A. Graham, P. G. Grant, S. F. Green, F. Grossemy, L. Grossman, J. N. Grossman, Y. Guan, K. Hagiya, R. Harvey, P. Heck, G. F. Herzog, P. Hoppe, F. Horz, J. Huth, I. D. Hutcheon, K. Ignatyev, H. Ishii, M. Ito, D. Jacab, C. Jabonsen, S. Jaconsen, S. Jones, D. Joswiak, A. Jurewicz, A. T. Kearsley, L. P. Keller, H. Khodja, A. L. D. Kilcoyne, J. Kissel, A. Krot, F. Langenhorst, A. Lanzirotti, L. Le, L. A. Leshin, J. Leitner, L. Lemelle, H. Leroux, M. C. Liu, K. Luening, I. Lyon, G. MaxPherson, M. A. Marcus, K. Marhas, B. Marty, G. Matrajt, K. McKeegan, A. Meibom, V. Mennella, K. Messenger, S. Messenger, T. Mikouchi, S. Mostefaoui, T. Nakamura, T. Nakano, M. Newville, L. R. Nitter, I. Ohnishi, K. Ohsumi, K. Okudaira, D. A. Papanastassiou, R. Palma, M. E. Palumbo, R. O. Pepin, D. Perkins, M. Perronnet, P. Pianetta, W. Rao, F. J. M. Rietmeijer, F. Robert, D. Rost, A. Rotundi, R. Ryan, S. A. Sandford, C. S. Schwandt, T. H. See, D. Schlutter, J. Sheffield-Parker, A. Simionvici, S. Simon, I. Sitnitsky, C. J. Snead, M. K. Spencer, F. J. Stadermann, A. Steele, T. Stephen, R. Stroud, J. Susini, S. R. Sutton, Y. Suzuki, M. Taheri, S. Taylor, N. Teslich, K. Tomeoka, N. Tomioka, A. Toppani, J. M. Trigo-Rodriguez, D. Troadec, A. Tsuchiyama,

A. J. Tuzzolino, T. Tyliszczak, K. Uesugi, M. Velbel, J. Vellenga, E. Vicenzi, L. Vincze, J. Warren, I. Weber, M. Weisberg, A. J. Westphal, S. Wirick, D. Wooden, B. Wopenka, P. Woziakiewicz, I. Wright, H. Yabuta, H. Yano, E. D. Young, R. N. Zare, T. Zega, K. Ziegler, L. Zimmerman, E. Zinner and M. Zolensky, *Science*, 2006, **314**, 1711.

[27] F. Horz, R. Bastien, J. Borg, J. P. Bradley, J. C. Bridges, D. E. Brownlee, M. J. Burchell, M. Chi, M. J. Cintala, Z. R. Dai, Z. Dkouadi, G. Dominguez, T. E. Economou, S. A. Fairey, C. Floss, I. A. Franchi, G. A. Graham, S. F. Green, P. Heck, P. Hoppe, J. Huth, H. Ishii, A. T. Kearsley, J. Kissel, J. Leitner, H. Leroux, K. Marhas, K. Messenger, C. S. Schwandt, T. H. See, C. Snead, F. J. Stadermann, T. Stephen, R. Stroud, N. Teslich, J. M. Trigo-Rodriguez, A. J. Tuzzolino, D. Troadec, P. Tsou, J. Warren, A. Westphal, P. Wozniakiewicz, I. Wright and E. Zinner, *Science*, 2006, **314**, 1716.

[28] H. J. Fraser, M. R. S. McCoustra and D. A. Williams, *Astro. Geophys.*, 2002, **43**, 210.

[29] E. Herbst, ESA SP-577, Paris, Editon edn., 2004.

[30] S. Taylor and D. Williams, *Chemistry in Britain*, 1993, 680.

[31] F. Lique, M. Jorfi, P. Honvault, P. Halvick, S. Y. Lin, H. Guo, D. Q. Xie, P. J. Dagdigian, J. Klos and M. H. Alexander, *J. Chem. Phys.*, 2009, **131**, 221104.

[32] G. J. White and R. Padman, *Nature*, 1991, **354**, 511.

[33] P. Atkins and J. de Paula, *Atkins' Physical Chemistry*, 7 edn., Oxford University Press, Oxford, 2002.

[34] W. C. Saslaw and D. Zipoy, *Nature*, 1967, **216**, 976.

[35] G. Vidali, V. Pirronello, L. Li, J. E. Roser, G. Manico, E. Congiu, H. Mehl, A. Lederhendler, H. B. Perets, J. R. Brucato and O. Biham, *J. Phys. Chem. A*, 2007, **111**, 12611.

[36] D. M. Meyer, M. Jura and J. A. Cardelli, *Ap. J.*, 1998, **493**, 222.

[37] P. Marechal, Y. P. Viala and J. J. Benayoun, *Astron. Astrophys.*, 1997, **324**, 221.

[38] G. Olofsson, L. Pagani, J. Tauber, P. Febvre, A. Deschamps, P. Encrenaz, H. G. Floren, S. George, B. Lecomte, B. Ljung, L. Nordh, J. R. Pardo, I. Peron, M. Sjokvist, K. Stegner, L. Stenmark and C. Ullberg, *Astron. Astrophys.*, 1998, **339**, L81.

[39] P. F. Goldsmith, G. J. Melnick, E. A. Bergin, J. E. Howe, R. L. Snell, D. A. Neufeld, M. Harwit, M. L. N. Ashby, B. M. Patten, S. C. Kleiner, R. Plume, J.

R. Stauffer, V. Tolls, Z. Wang, Y. F. Zhang, N. R. Erickson, D. G. Koch, R. Schieder, G. Winnewisser and G. Chin, *Ap. J.*, 2000, **539**, L123.

[40] L. Pagani, A. O. H. Olofsson and P. Mergman, *Astron. Astrophys.*, 2003, **402**, L77.

[41] D. Carty, A. Goddard, S. P. K. Kohler, I. R. Sims and I. W. M. Smith, *J. Phys. Chem.*, 2006, **110**, 3101.

[42] D. C. B. Whittet, *Ap. J.*, 2010, **710**, 1009.

[43] R. Gould and E. Salpeter, *Ap. J.*, 1963, **138**, 393.

[44] K. Kolasinski, *Surface Science: Foundations of Catalysis and Nanoscience*, Wiley, 2002.

[45] D. Hollenbach, M. Werner and E. Salpeter, *Ap. J.*, 1971, **163**, 165.

[46] O. Biham and A. Lipshtat, *Phys. Rev. E*, 2002, **66**, 56103.

[47] G. Vidali, J. Roser, G. Manico and V. Pirronello, *Adv. Spa. Res.*, 2004, **33**, 6.

[48] G. Vidali, J. Roser, G. Manico, V. Pirronello, H. Perets and O. Biham, *J. Phys. Conference Series*, 2005, **6**, 36.

[49] V. Pirronello, C. Liu, L. Shen and G. Vidali, *Ap. J.*, 1997, **475**, L69.

[50] V. Pirronello, C. Liu, J. Roser and G. Vidali, *Astron. Astrophys.*, 1999, **344**, 681.

[51] L. Hornekaer, A. Baurichter, V. Petrunin, A. Luntz, B. Kay and A. Al-Halabi, *J. Chem. Phys.*, 2005, **122**, 124701.

[52] F. Dulieu, L. Amiaud, S. Baouche, A. Momeni, J. Fillion and J. Lemaire, *Chem. Phys. Lett.*, 2005, **404**, 187.

[53] J. Perry, J. Gingell, K. Newson, J. To, J. Watanabe and S. Price, *Meas. Sci. Technol.*, 2002, **13**, 1414.

[54] N. Katz, I. Furman, O. Biham, V. Pirronello and G. Vidali, *Ap. J.*, 1999, **522**, 305.

[55] S. Cazaux and A. Tielens, *Ap. J.*, 2004, **604**, 222.

[56] O. Biham, A. Lipshtat and H. Perets, *Astrochemistry: Recent Successes and Current Challanges*, Cambridge University Press, Cambridge, 2006.

[57] T. Stantcheva, V. Shematovich and E. Herbst, *Astron. Astrophys.*, 2002, **391**, 1069.

[58] S. Charnley, *Ap. J.*, 2001, **562**, L99.

[59] T. Stantcheva, P. Caselli and E. Herbst, *Astron. Astrophys.*, 2001, **375**, 673.

[60] R. S. Smith, C. Huang and B. D. Kay, *J. Phys. Chem. B*, 1997, **101**, 6123.

[61] A. Hallbrucker, E. Mayer and G. P. Johari, *J. Phys. Chem.*, 1989, **93**, 4986.

[62] M. Fisher and J. P. Devlin, *J. Phys. Chem.*, 1995, **99**, 11584.

[63] G. A. Kimmel, K. P. Stevenson, Z. Dohnalek, R. S. Smith and B. D. Kay, *J. Chem. Phys.*, 2001, **114**, 5284.

[64] D. E. Brown, S. M. George, C. Huang, E. K. L. Wong, K. B. Rider, R. S. Smith and B. D. Kay, *J. Phys. Chem.*, 1996, **100**, 4988.

[65] A. Bar-Nun, G. Herman, D. Laufer and M. L. Rappaport, *Icarus*, 1985, **63**, 317.

[66] M. P. Collings, M. A. Anderson, R. Chen, J. W. Dever, S. Viti, D. A. Williams and M. R. S. McCoustra, *Mon. Not. R. Astron. Soc.*, 2004, **354**, 1133.

[67] M. P. Collings, J. W. Dever, H. J. Fraser and M. R. S. McCoustra, *Astrophys. Space Sci.*, 2003, **285**, 633.

[68] M. P. Collings, J. W. Dever, H. J. Fraser, M. R. S. McCoustra and D. A. Williams, *Ap. J.*, 2003, **583**, 1058.

[69] P. Ehrenfreund, R. Breukers, L. d'Hendecourt and J. M. Greenberg, *Astron. Astrophys.*, 1992, **260**, 431.

[70] B. Vandenbussche, P. Ehrenfreund, A. C. A. Boogert, E. F. van Dishoeck, W. A. Schutte, P. A. Gerakines, J. Chiar, A. G. G. M. Tielens, J. Keane, D. C. B. Breitfellner and M. Burgdorf, *Astron. Astrophys.*, 1999, **346**, L57.

[71] K. Acharyya, G. W. Fuchs, H. J. Fraser, E. F. van Dishoeck and H. Linnartz, *Astron. Astrophys.*, 2007, **466**, 1005.

[72] J. D. Thrower, Heriot-Watt University, 2009.

[73] R. Breukers, University of Leiden, 1991.

[74] W. Zheng, Y. S. Kim and R. I. Kaiser, *Phys. Chem. Chem. Phys.*, 2011, **13** 15749.

[75] A. H. H. Chang and D. R. Yarkony, *J. Chem. Phys.*, 1993, **99**, 6824.

[76] C. J. Bennett and R. I. Kaiser, *Ap. J.*, 2005, **635**, 1362.

[77] B. Sivaraman, C. S. Jamieson, N. J. Mason and R. I. Kaiser, *Ap. J.*, 2007, **669**, 1414.

[78] M. J. Loeffler, B. D. Teolis and R. A. Baragiola, *Ap. J.*, 2006, **639**, L103.

[79] W. Zheng, D. Jewitt and R. I. Kaiser, *Ap. J.*, 2006, **639**, 534.

[80] T. Hama, A. Yabushita, M. Yokoyama, M. Kawasaki and N. Watanabe, *J. Chem. Phys.*, 2009, **131**, 114511.

[81] T. Hama, A. Yabushits, M. Yokoyama, M. Kawasaki and N. Watanabe, *J. Chem. Phys.*, 2009, **131**, 114510.

[82] A. G. G. M. Tielens and W. Hagen, *Astron. Astrophys.*, 1982, **114**, 245.

[83] H. Cuppen and E. Herbst, *Ap. J.*, 2007, **668**, 294.

[84] P. Bergman, B. Parise, R. Liseau, B. Larsson, H. Olofsson, K. M. Menten and R. Gusten, *Astron. Astrophys.*, 2011, **531**, L8.

[85] F. Dulieu, L. Amiaud, E. Congiu, J. H. Fillion, E. Matar, A. Momeni, V. Pirronello and J. L. Lemaire, *Astron. Astrophys.*, 2010, **512**, A30.

[86] M. E. Palumbo, *Astron. Astrophys.*, 2006, **453**, 903.

[87] N. Miyauchi, H. Hidaka, T. Chigai, A. Nagoka, N. Watanabe and A. Kouchi, *Chem. Phys. Lett.*, 2008, **456**, 27.

[88] S. Ioppolo, H. M. Cuppen, C. Romanzin, E. F. van Dishoeck and H. Linnartz, *Ap. J.*, 2008, **686**, 1474.

[89] S. Ioppolo, H. M. Cuppen, C. Romanzin, E. F. van Dishoeck and H. Linnartz, *Phys. Chem. Chem. Phys.*, 2010, **12**, 12065.

[90] H. M. Cuppen, S. Ioppolo, C. Romanzin and H. Linnartz, *Phys. Chem. Chem. Phys.*, 2010, **12**, 12077.

[91] Y. Oba, N. Miyauchi, H. Hidaka, T. Chigai and N. K. Watanabe, A., *Ap. J.*, 2009, **701**, 464.

[92] P. D. Cooper, M. H. Moore and R. L. Hudson, *J. Phys. Chem.*, 2006, **110**, 7985.

[93] L. Amiaud, J. H. Fillion, S. Baouche, F. Dulieu, A. Momeni and J. L. Lemaire, *J. Chem. Phys.*, 2006, **124**, 094702.

[94] V. Buch and J. P. Devlin, *J. Chem. Phys.*, 1991, **94**, 4091.

[95] J. V. Keans, A. C. A. Boogert, A. G. G. M. Tielens, P. Ehrenfreund and W. A. Schutte, *Astron. Astrophys.*, 2001, **375**, L43.

[96] H. Mokrane, H. Chaabouni, M. Accolla, E. Congiu, F. Dulieu, M. Chehrouri and J. L. Lemaire, *Ap. J.*, 2009, **705**, L195.

[97] L. Amiaud, F. Dulieu, J. H. Fillion, A. Momeni and J. L. Lemaire, *J. Chem. Phys.*, 2007, **127**, 144709.

[98] G. W. Fuchs, H. M. Cuppen, S. Ioppolo, C. Romanzin, S. E. Bisschop, S. Anderson, E. F. van Dishoeck and H. Linnartz, *Astron. Astrophys.*, 2009, **505**, 629.

[99] S. E. Bisschop, G. W. Fuchs, E. F. van Dishoeck and H. Linnartz, *Astron. Astrophys.*, 2007, **474**, 1061.

[100] N. Watanabe and A. Kouchi, *Ap. J.*, 2002, **571**, L173.

[101] H. Hidaka, N. Watanabe, T. Shiraki, A. Nagaoaka and A. Kouchi, *Ap. J.*, 2004, **614**, 1124.

[102] N. Watanabe, A. Nagaoka, H. Hidaka, T. Shiraki, T. Chigai and A. Kouchi, *Planet. Space Sci.*, 2006, **54**, 1107.

[103] H. Hidaka, A. Kouchi and N. Watanabe, *J. Chem. Phys.*, 2007, **126**, 204707.

[104] N. Watanabe, A. Nagaoka, T. Shiraki and A. Kouhi, *Ap. J.*, 2004, **616**, 638.

[105] H. Hidaka, N. Miyaucji, A. Kouchi and N. Watanabe, *Chem. Phys. Lett*, 2008, **456**, 36.

[106] O. Yasuhiro, N. Watanabe, A. Kouchi, T. Hama and V. Pirronello, *Ap. J.*, 2010, **712**, L174.

[107] J. H. Fillion, L. Amiaud, E. Congiu, F. Dulieu, A. Momeni and J. L. Lemaire, *Phys. Chem. Chem. Phys.*, 2009, **11**, 4396.

[108] E. Matar, H. Bergeron, F. Dulieu, H. Chaabouni, M. Accolla and J. L. Lemaire, *J. Chem. Phys.*, 2010, **133**, 104507.

[109] V. Pirronello, O. Biham, C. Liu, L. Shen and G. Vidali, *Ap. J.*, 1997, **483**, L131.

[110] J. E. Roser, G. Manico, V. Pirronello and G. Vidali, *Ap. J.*, 2002, **581**, 276.

[111] G. Manico, G. Raguni, V. Pirronello, J. E. Roser and G. Vidali, *Ap. J.*, 2001, **548**, L253.

[112] G. Vidali, J. E. Roser, L. Ling, E. Congiu, G. Manico and V. Pirronello, *Faraday Discuss.*, 2006, **133**, 125.

Chapter 2 - Experimental Techniques and Procedures

Contents

2.1 Introduction

This chapter discusses the new dual atomic beam apparatus built in this study for the ongoing research to explore the full surface formation mechanism of H_2O on interstellar dust grains (as previously discussed in **Section 1.3**). The dual atomic beam chambers were attached in January 2007 to a pre-existing UHV chamber which was constructed in 1998. The original apparatus, previously called the ICE RIG (see **Figure 2.1**), was used to explore the desorption of ^{12}CO and ^{13}CO from pre-deposited H_2O films on a gold surface through temperature programmed desorption (TPD) [1, 2] and reflection-absorption infrared spectroscopy analysis (RAIRS) [2]. Both of these analytical techniques were required for the new dual atomic beam system. The ICE RIG was also fitted with quartz crystal microgravimetry (QCM) equipment and a quadrupole mass spectrometer (QMS) that could be positioned in-line with the sample during a beam irradiation experiment for molecular beam modulation spectrometry (MBMS). A photograph of the complete dual atomic system is displayed in **Figure 2.2**.

Figure 2.1: Photograph of the Original Ultrahigh Vacuum Apparatus at the University of Nottingham

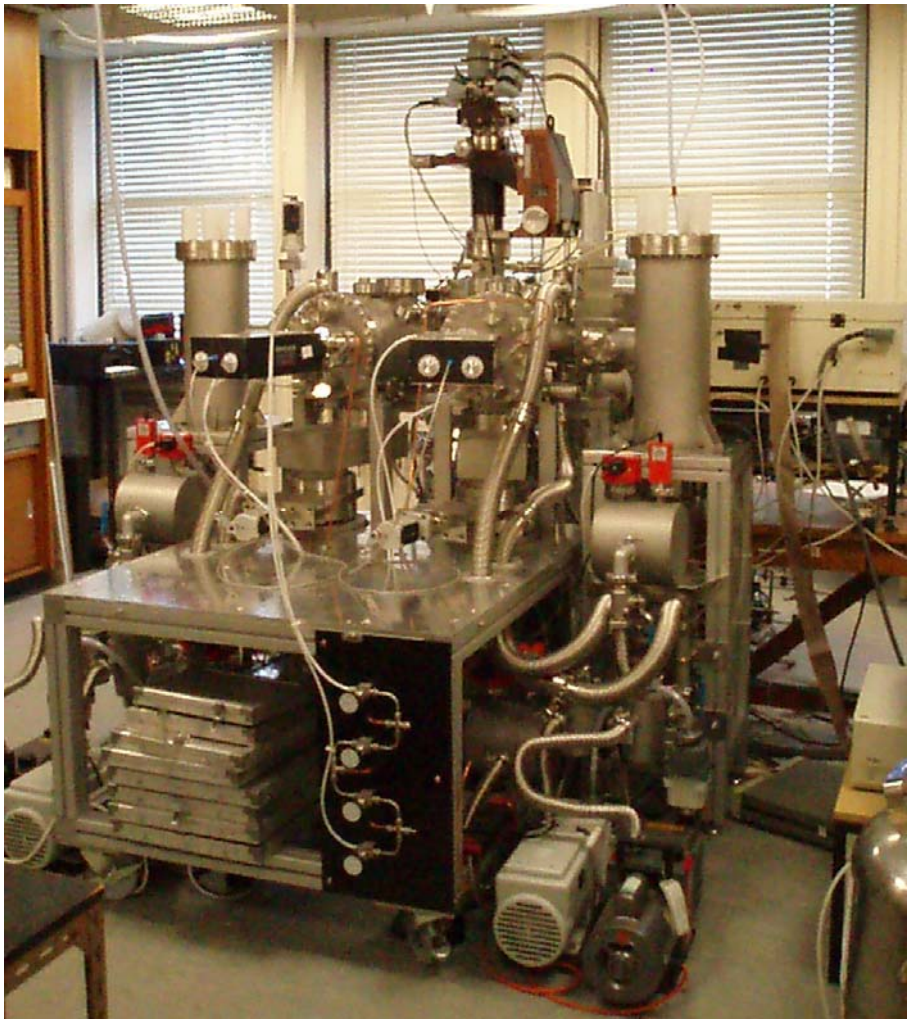

Figure 2.2: Photograph of the New Dual Atomic Beam Apparatus

The dual atomic beam system is described in detail in **Section 2.2** whilst **Section 2.3** introduces each of the experimental techniques available. A general procedure for each experiment type is provided in **Section 2.4**. For future experiments using O_3, a range of synthesis procedures are reviewed in **Section 2.5** before concluding with the synthesis procedure chosen for this ongoing study and the apparatus required.

2.2 Apparatus

2.2.1 The Ultrahigh Vacuum (UHV) System

The experiments were performed in a central 30 cm diameter, stainless steel ultrahigh vacuum (UHV) chamber (Instrument Technology Ltd.) with two 25 cm diameter,

doubly differentially pumped stainless steel atomic beam chambers (Instrument Technology Ltd.) attached (see **Figure 2.2** and **Figure 2.3**). The central chamber (originally from the ICE RIG) is pumped by a liquid nitrogen trapped 6" diffusion pump (Edwards, E06) which is backed by a mechanical rotary pump (Edwards, E2M18) as shown in **Figure 2.4**. These pumps can be isolated from the central chamber by a gate valve. Additional pumping from a liquid nitrogen trapped titanium sublimation pump (TSP) (AML, TSP2) reduces the amount of residual gases. The pressure in the central chamber is measured using a nude Hot Cathode Ionization gauge with Thoria coated filaments (Instrument Technology Ltd.). UHV pressures (10^{-10} to 10^{-12} mbar) are regularly obtained to a base pressure of less than 2×10^{-10} mbar after baking the apparatus at 120˚C for 48 to 72 hours. The baking procedure is required following exposure of the chamber to atmosphere. Baking accelerates the desorption rate of molecules such as H_2O from the chamber walls which would otherwise desorb slowly keeping the chamber pressure at high vacuum (10^{-6} to 10^{-9} mbar). The pressure between the liquid nitrogen 6" diffusion pump and rotary pump is monitored in two places using active pirani gauges (Edwards, APG-L).

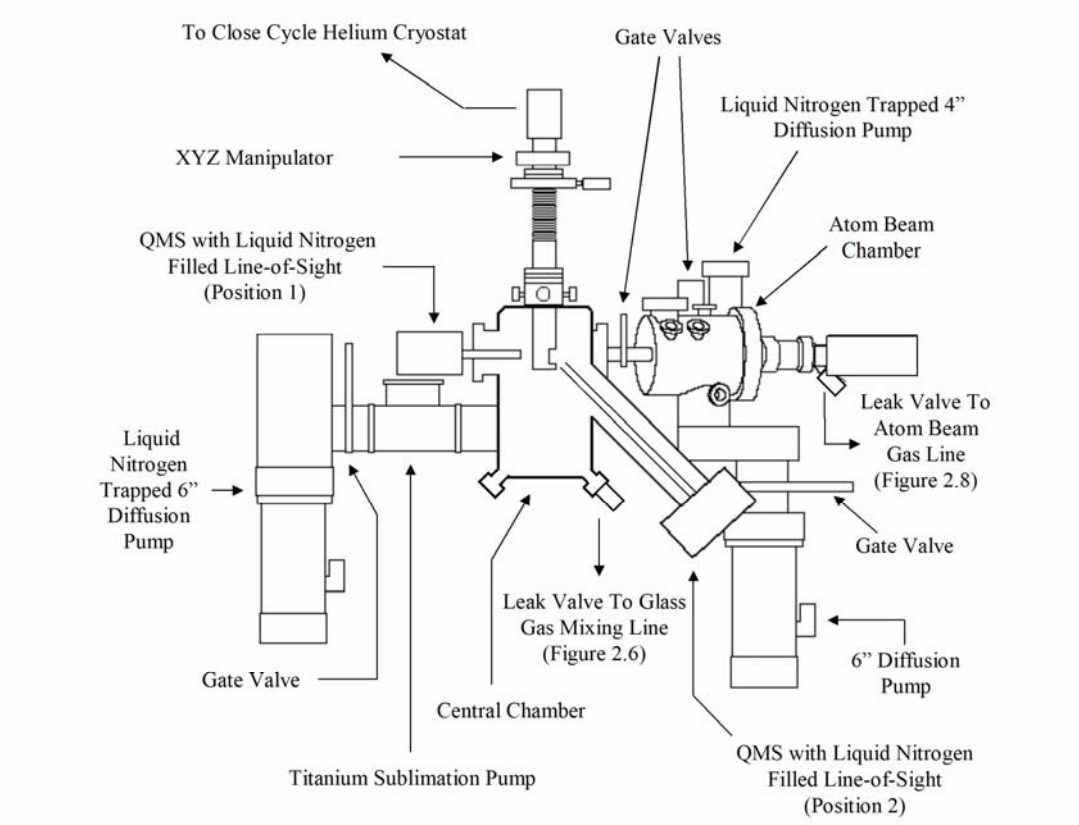

Figure 2.3: Cut Through Schematic Drawing of the Apparatus and Dual Atomic Beams

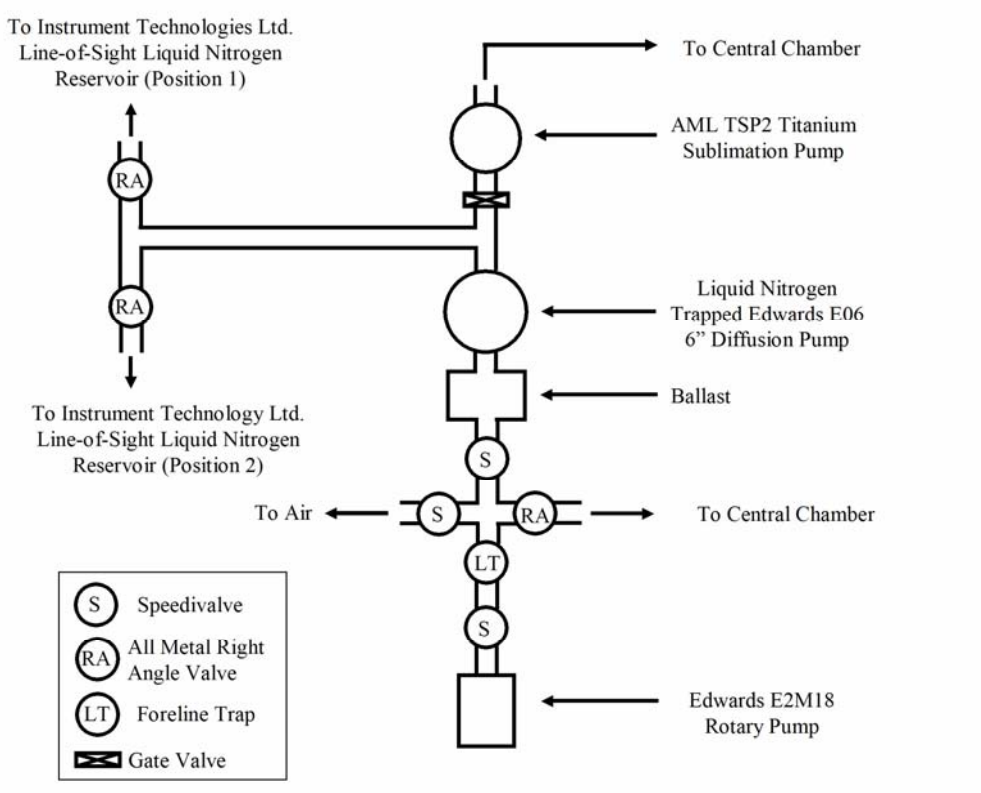

Figure 2.4: Schematic Drawing of the Pumping Arrangement for the Central Chamber

The central chamber is equipped with a line-of-sight (Instrument Technology Ltd, custom build) QMS (Hiden Analytical Ltd, HAL301) based on the design of Jones and Turton [3, 4] which can be attached in two locations as shown in **Figure 2.3** and **Figure 2.5.** The addition of the liquid nitrogen reservoir reduces the amount of background contamination of species desorbing from other surfaces inside the chamber. However, this capability will not be used in this study as the oxygen species desorb below liquid nitrogen temperatures. This chamber is also fitted with RAIRS apparatus; QCM (Oxford Applied Research); and differentially pumped glass gas handling lines for direct vapour deposition experiments (see **Figure 2.6** and **Figure 2.7**).

Adjoining the central chamber are two new stainless steel atomic beam chambers. These can be separated from the central chamber by gate valves (**Figure 2.3**; **Figure 2.5** and **Figure 2.8**) allowing either one of the atomic beam chambers or the main central chamber to be vented for alterations whilst the other chambers are still under UHV pressures. Each of the atomic beam chambers are split into plasma and beam chambers

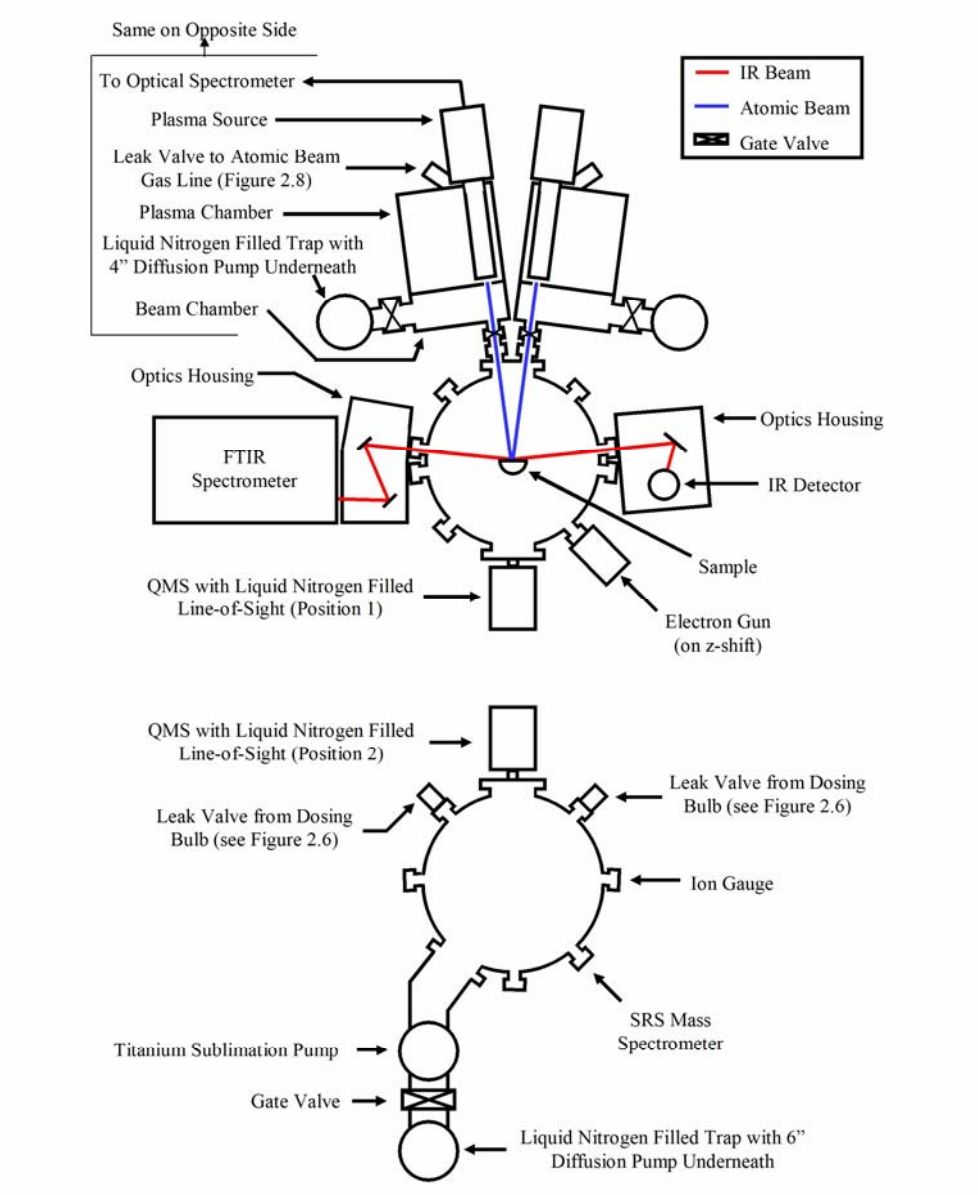

Figure 2.5: Schematic Diagrams of the First Experimental Level (top) and Second Experimental Level (bottom)

internally by a stainless steel wall fitted with a 5 mm collimator flange. The plasma chambers are separately pumped by their own dedicated pumping system, which consists of a 6" diffusion pump (Edwards, E06) backed by a rotary pump (Edwards, E2M18) fitted with a foreline molecular sieve trap and an oil mist filter (see **Figure 2.8**). These foreline molecular sieve traps decrease the amount of pump oil contamination reaching the atomic beam chambers however it also significantly reduces the rotary pumping speed. This only becomes a problem when the atomic or molecular

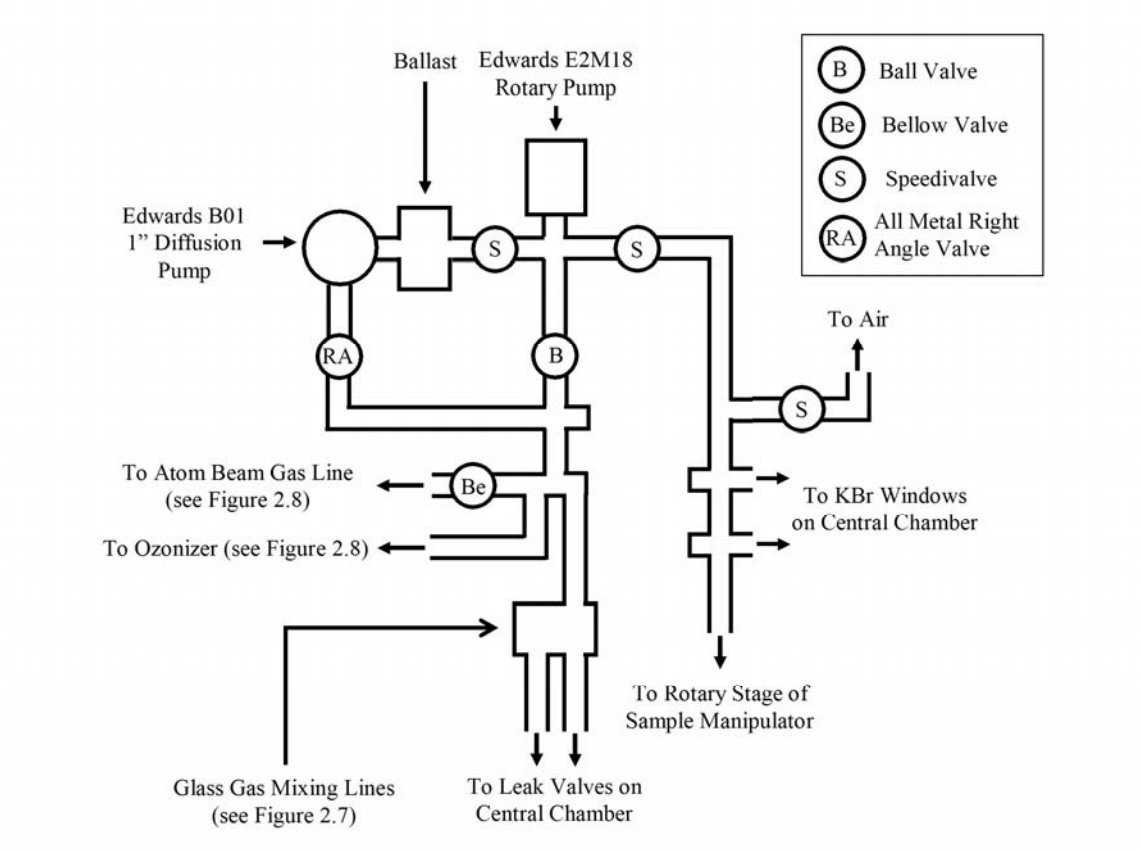

Figure 2.6: Schematic Diagram of the Differential Pumping for the Central Chamber and the Gas Lines for the Central and Atom Beam Chambers.

beam is in operation as the reduced pumping speed leads to an increased backing pressure behind the diffusion pump. In some cases, this resulted in the diffusion pump stalling. The solution was to remove these foreline molecular sieve traps only when an atomic or molecular beam was required and then reinstall them after the experiment was completed.

The beam chambers are each pumped by a 4" diffusion pump (Edwards, E04) also backed by a rotary pump (Edwards, RV8) fitted with a foreline molecular sieve trap and an oil mist filter (**Figure 2.8**). These pumps can be isolated from the atomic beam chambers using gate valves. The pressure in the plasma and beam chambers are measured using a nude Hot Cathode Ionization gauge with Thoria coated filaments. The base pressure in the plasma chambers regularly reaches below 2×10^{-9} mbar when the atomic beams are not in use. The pressure between the diffusion and rotary pumps is monitored using active pirani gauges.

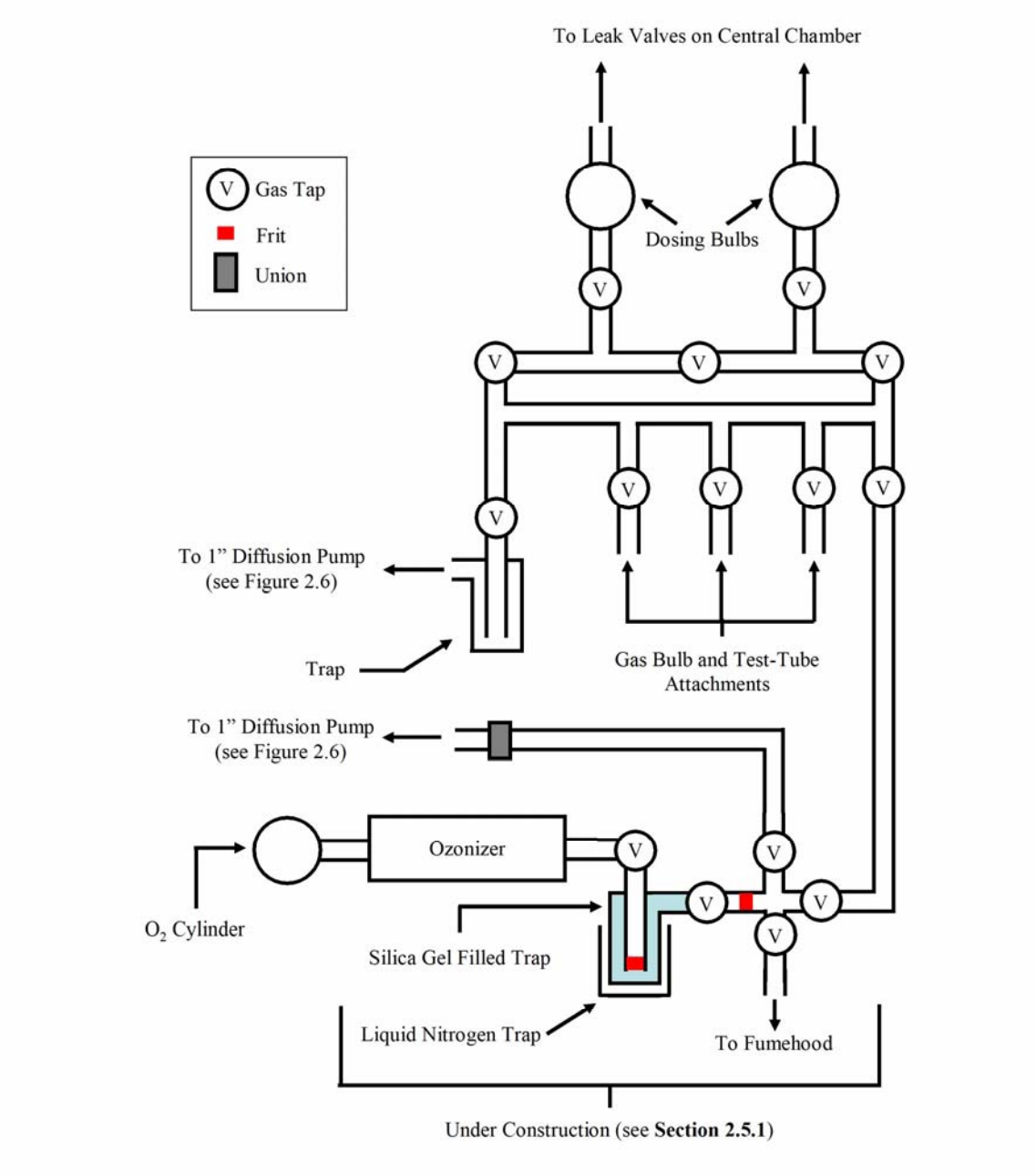

Figure 2.7: Schematic Diagram of the Glass Gas Handling Lines

Each plasma chamber is equipped with a radio frequency (RF) powered plasma source (Oxford Scientific, RF OSPREY plasma sources) and a USB 2.0 fibre optic spectrometer (Ocean Optics, USB4000) (see **Figure 2.5**). The gases are supplied to the plasma sources by the atomic beam gas line (**Figure 2.9**) *via* the differentially pumped glass gas line (Edwards, B01), backed by a rotary pump (Edwards, E2M18) (**Figure 2.6**).

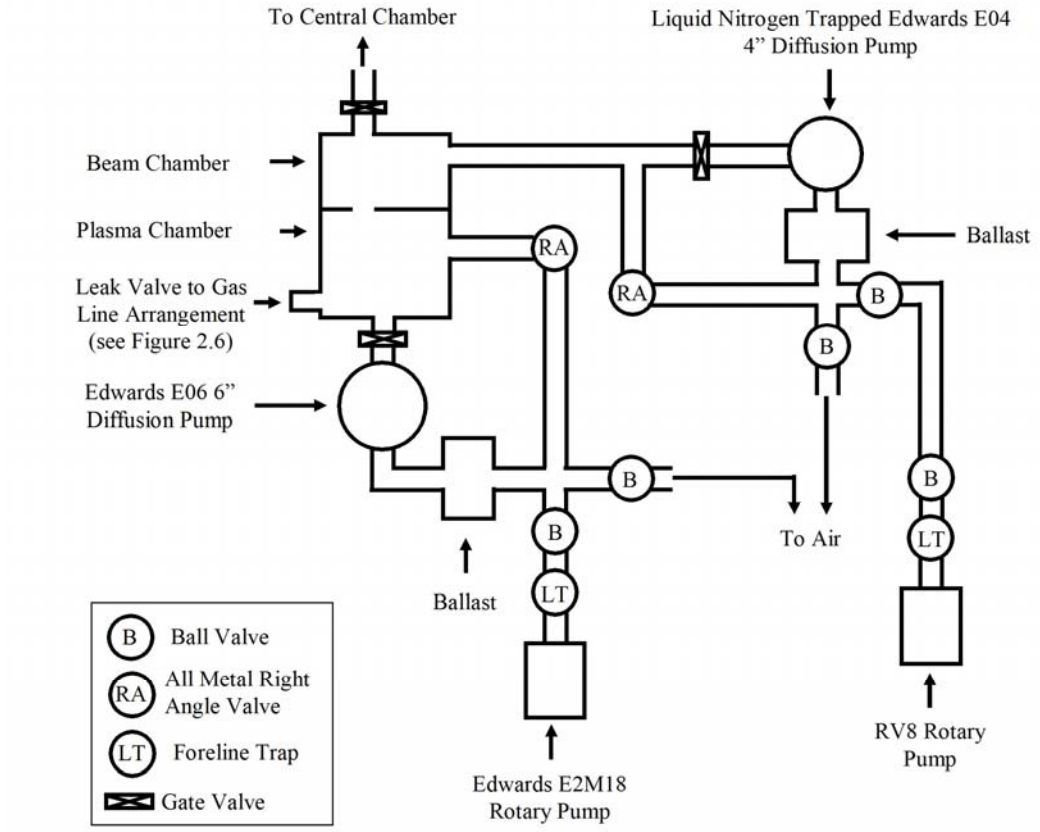

Figure 2.8: Schematic Drawing of the Pumping Arrangement for the Atom Beam Chamber

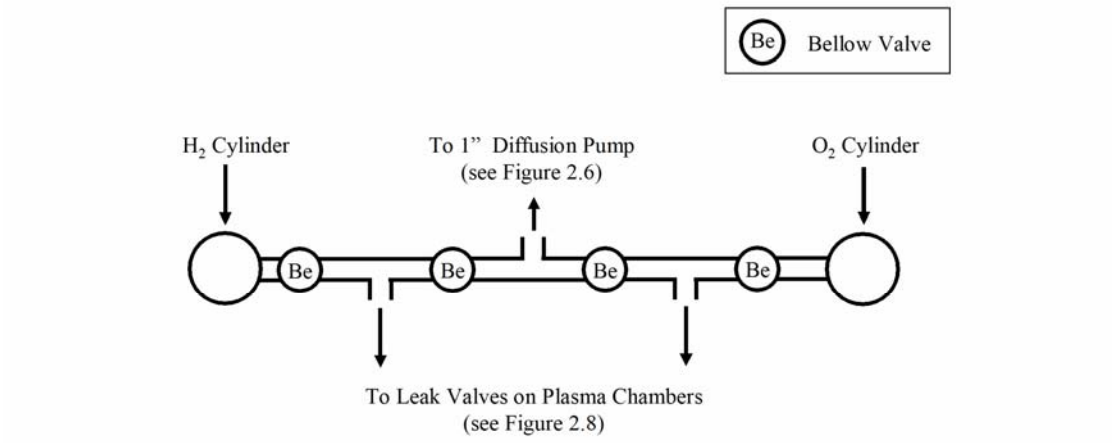

Figure 2.9: Schematic Diagram of the Gas Line Arrangement for the RF Plasma Sources

2.2.2 Dual Atomic Beam System

The main advantage with the dual atomic beam system is that one or both of the beams (either as atomic or molecular) can be directed onto the sample simultaneously. This provides a flexible arrangement for exploring the surface formation mechanism for a range of species. The atomic beams are formed using RF powered plasma sources (see **Figure 2.10** and **Figure 2.11**). The RF energy is produced using a power supply (Dressler, Cesar 136) at a frequency of 13.56 MHz. This was supplied to the reactor along the RF feedthrough (coloured grey in **Figure 2.10**) to the inductively coupled, water-cooled RF coil. The forward and reflected forms of the RF energy were controlled using the capacitors in the manual tuning unit. The gas was suppied to the plasma tube from the gas line arrangement in **Figure 2.9**. The material of the plasma tube was chosen to produce the highest dissociation fraction for the gaseous species used to create the beam (for more details see **Section 2.3.2**). In this study, a boron nitride plasma tube and reactor were used for the atomic hydrogen beam whilst quartz was used for the atomic oxygen beam. Only the gas inside the reactor (coloured green) absorbs the RF energy and becomes excited and ionized creating a glow discharge plasma in the low brightness mode (see the left diagram in **Figure 2.12**). Under these conditions, the molecules in the gas are excited into the low molecular excited states before returning back to the ground state by fluorescence. The atomic plasma was obtained by reducing the gas flow into the plasma tube which resulted in the concentration of free electrons (made available from the excitation and ionization of the gas) increasing with respect to the gaseous species. At this stage, each molecule can absorb more RF photons to reach the higher molecular excited states or the atomic orbital energy levels allowing the molecule to dissociate (right hand diagram in **Figure 2.12**). This results in a greater amount of fluorescence being observed indicating that the plasma has reached the high brightness mode. A more detailed discussion about the low and high brightness modes in glow discharge plasmas can be found in **Section 2.3.2**.

Analysis of the plasma was conducted using an USB fibre optic spectrometer located at the back of the radio frequency power unit. The plasma analysis results for the oxygen and hydrogen atomic plasmas are discussed in **Section 3.2**. An atomic beam was obtained as the neutral species inside the reactor effuse out through the 5×0.2 mm diameter holes in the aperture plate into the plasma chamber. The beam is further aligned using a 5 mm collimator flange situated on the internal wall separating the

plasma and beam chambers. If a molecular beam was required then these were produced using the same procedure as above but with the RF power supply turned off.

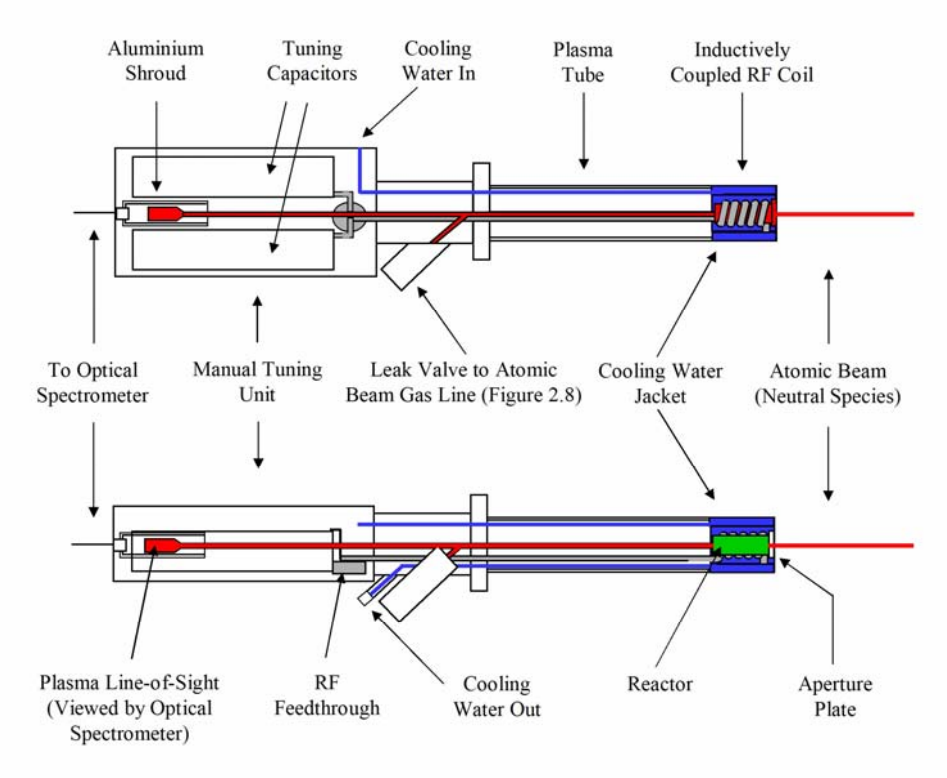

Figure 2.10: Plan and Side Cut-Through View of RF Plasma Sources

Figure 2.11: Photograph of the RF Plasma Source

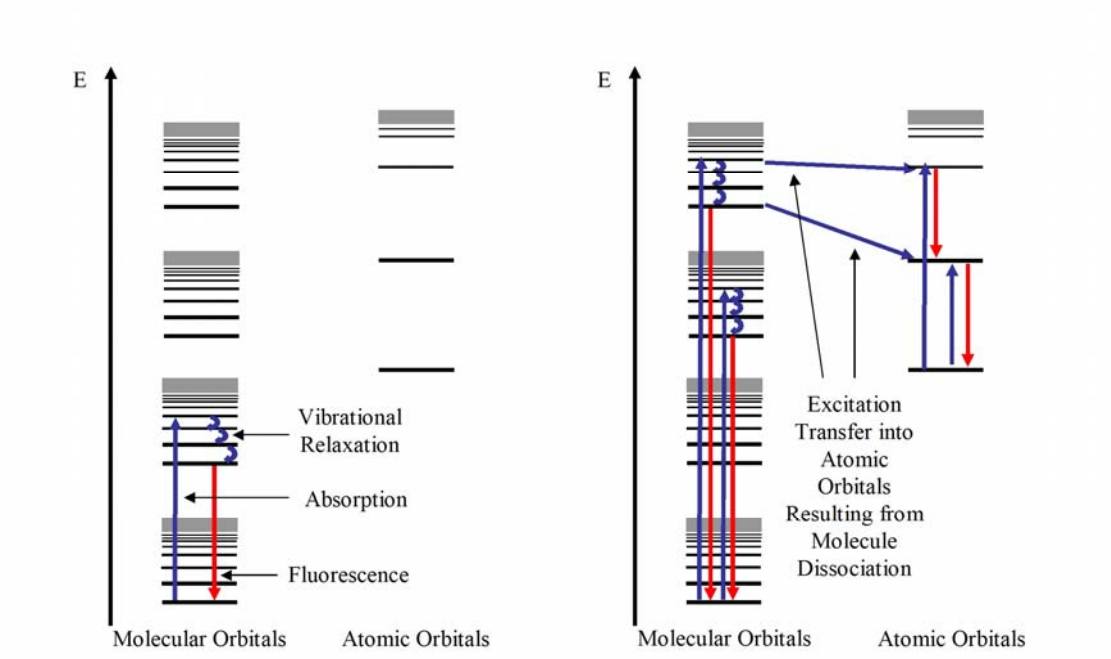

Figure 2.12: Cartoon of Low (left) and High (right) Brightness Modes

When the beam was required to enter the central chamber, the gate valve between the central and atomic beam chambers was opened (**Figure 2.5**). In the future, this procedure will be replaced by constructing a flag on the end of a wobble stick inside the beam chamber to intercept the beam. The beam chambers will also be fitted with chopper apparatus allowing for future experiments using a mixture of continuous, pulsed and relative phase (0 to 180˚) beams. This apparatus consists of a thin stainless steel blade mounted in a clamp (see **Figure 2.13** and **Figure 2.14** respectively) which is attached to a motor spindle by a grub screw. The whole assembly is mounted in a chopper motor clamp (see **Figure 2.15**). The blade has been designed to achieve a minimum of 10 μs pulses at a maximum speed of 20,000 rpm. Therefore, the width of the blade must be thin enough to reach this speed without overheating the motor but thick enough so that the blade does not lose its rigidity. The chopper motor clamp will be attached to the end of a z-shift. Therefore, when a pulse beam is required, the blade can be lowered into the beam and the speed of the blade adjusted to give a range of pulse lengths. Although this apparatus has been built, it has yet to be tested.

The atomic beams were first tested in November 2007 when it was discovered that there were problems with obtaining a stable hydrogen plasma. Despite several attempts to

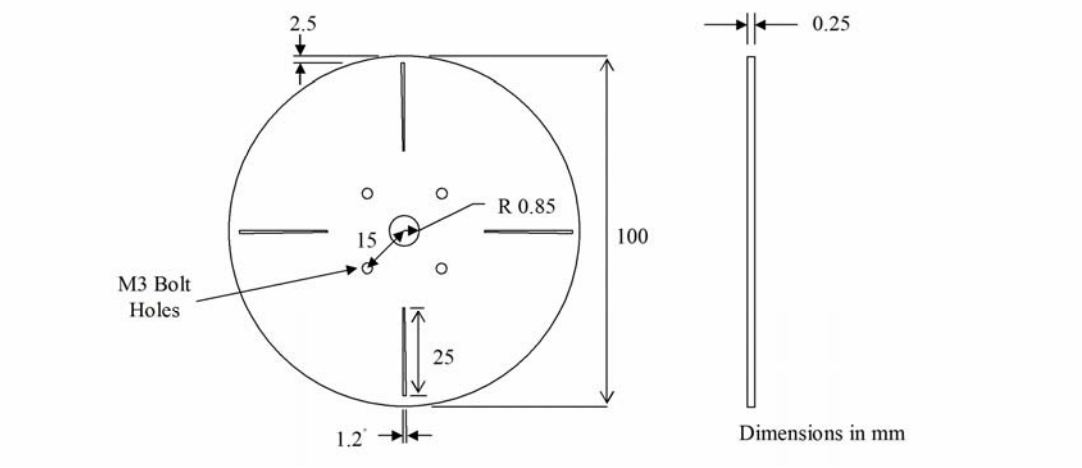

Figure 2.13: Schematic Drawings of Chopper Blade

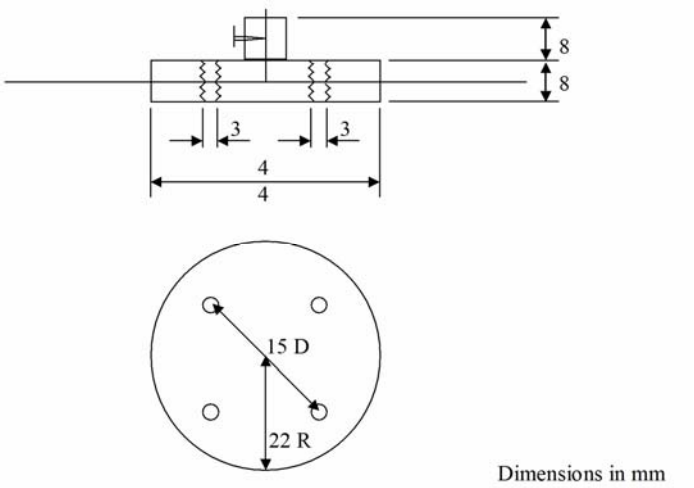

Figure 2.14: Schematic Drawings of Chopper Blade Mount

improve the system the plasma failed to strike. Initial observations of the tuning unit revealed no evidence of overheating. If overheating occurred then this would imply that there was a source of resistance in the circuit (also known as resistant displacement) which would reduce the amount of RF power reaching the reactor. The formation of a hydrogen plasma using a second gas was then attempted. This method is known as the secondary gas technique. An atomic plasma is first generated with the secondary gas that is easier to excite, ionize and dissociate, providing a supply of free electrons for the plasma (in this case nitrogen). Once the atomic plasma is stable, the desired gas (hydrogen) is slowly leaked into the plasma source. The higher concentration of free electrons from the secondary plasma enables the desired gas to strike, resulting in a

mixed atomic plasma. When the mixed plasma has stabilised, the secondary gas is slowly closed off, leaving a strong atomic plasma from the desired species.

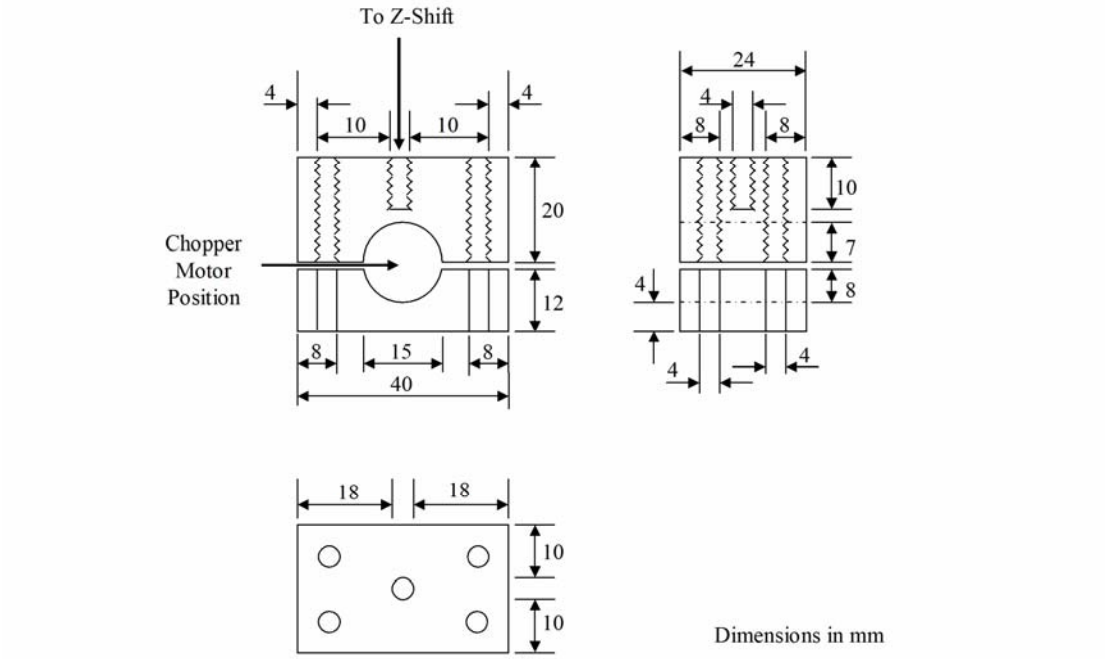

Figure 2.15: Chopper Motor Clamp Design

Initial attempts to generate a hydrogen plasma using air as the secondary gas suffered further difficulties with resistance displacement and overheating of the water cooled RF coils. When these problems had been overcome, further attempts were made to obtain a plasma from hydrogen, oxygen and then air but all failed. In April 2009 after all local knowledge of remotely fixing the plasma source had been exhausted; the RF hydrogen plasma source was sent to the company for repairs and did not return until the end of June 2009.

The initial tests with the newly repaired source did provide a hydrogen plasma but it appeared to be very weakly contaminated with the secondary gas nitrogen (upper diagram in **Figure 2.16**). A pure hydrogen plasma was obtained but the H emission peaks were several orders of magnitude weaker than the contaminated version (lower diagram). Currently, the gas line arrangement for the atomic beams is not equipped for any additional gases (see **Figure 2.9**). The apparatus could either be modified to include a secondary gas supply (see **Figure 2.17** for a possible arrangement) or the hydrogen plasma could be created using gas from a pre-blended cylinder of hydrogen

and an inert secondary gas such as argon. Initial attempts to analyze the H plasma are described in **Section 3.2.3**.

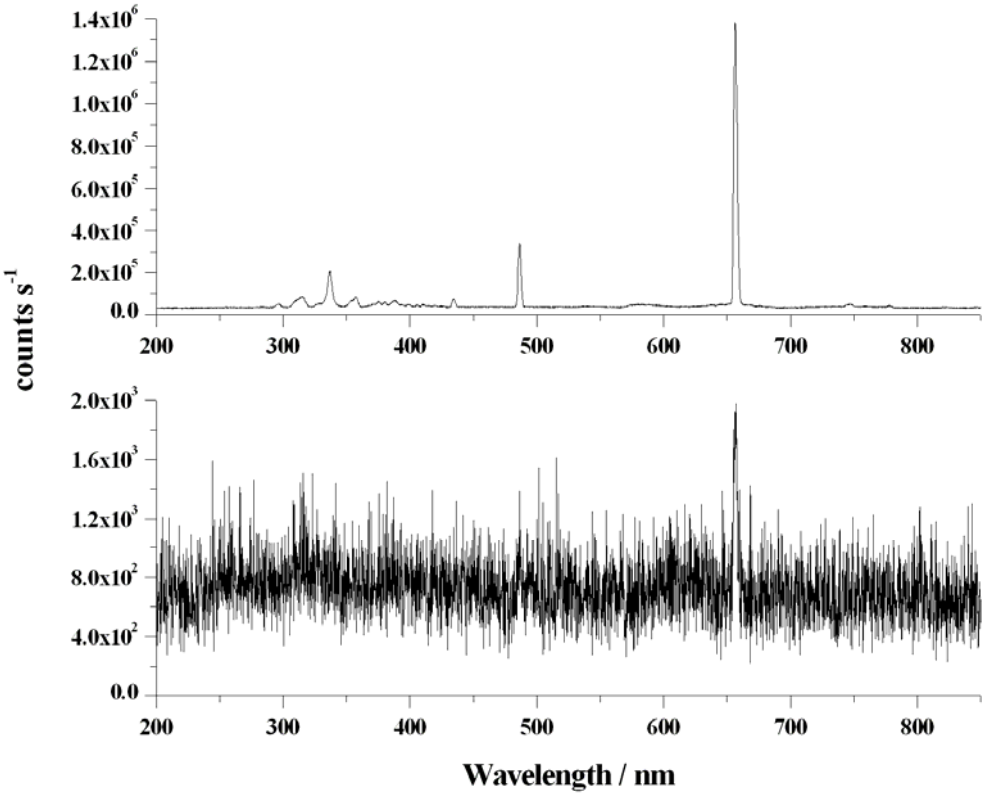

Figure 2.16: Visible Spectra of the Hydrogen Atomic Plasma with (top) and without (bottom) the Second Gas Technique

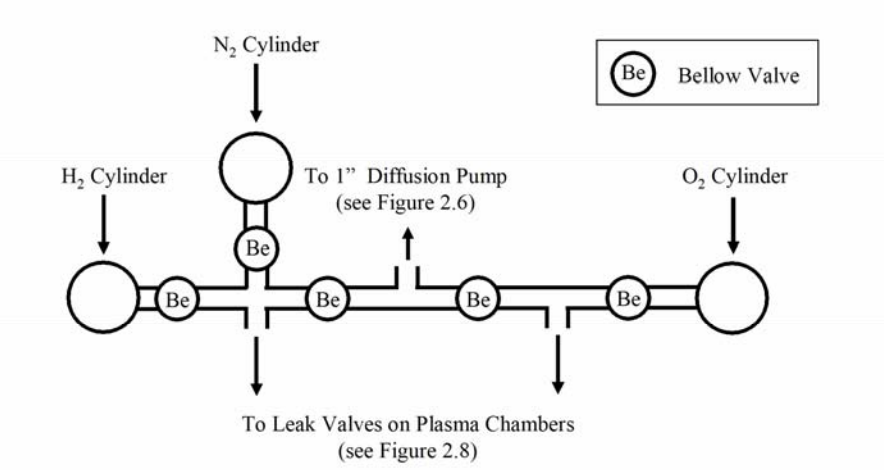

Figure 2.17: Possible Future Arrangement of the Atomic Beam Gas Line

2.2.3 Sample Mounting and Temperature Control

To mimic surface formation mechanisms on interstellar dust grains a suitable substrate is required. This is particularly important for those experiments that need to consider adsorbed species - grain surface interactions which cannot be studied using most other apparatus systems (as previously discussed in **Section 1.3.3**). As mentioned in **Chapter 1**, dust grains consist of either silicate or amorphous carbonate materials. The exact physical and chemical characteristics of these grains has yet to be fully understood although it was believed to be similar to the interplanetary dust particles collected from the *Stardust Mission* [5]. In this study, a previously made amorphous SiO_2 substrate was chosen as a representation of silicate dust grains.

The amorphous silicate film was deposited onto a copper sample plate using electron beam evaporation [6, 7] in a purpose built high vacuum chamber in the Microsystems Engineering Centre at Heriot-Watt University. This chamber was fitted with QCM apparatus (for more details see **Section 2.3.5**) and a carousel which can position the sample in and out of alignment with the bulk silica source overhead. The chamber is currently unequipped with any apparatus to cool or heat the sample so the deposition was performed at room temperatures.

With the sample mount out of alignment with the silica source, the silica was evaporated using the electron gun held at 7 keV. Once the deposition rate had stabilized, the sample was moved in-line with the source and the QCM, used to monitor the film thickness, started. When the desired film thickness had been obtained (100 to 200 nm), the sample was moved back out of alignment with the source. The coated sample was removed from the vacuum chamber once the electron gun and source had cooled back to base temperatures.

A silica film thickness of 100 to 200 nm was sufficient to ensure that the underlying metal surface has no effect on the adsorbed species-silica surface interactions. Atomic force microscopy (AFM) images revealed that this technique provided a uniform coverage of silica across the sample [6, 7]. On a smaller scale, the surface displayed a high degree of roughness which is ultimately likely to contain a range of desorption energy sites for the adsorbed species.

The silica coated copper sample plate was mounted at the end of a 1 m long gold-coated oxygen free high conductivity (OFHC) copper cold finger (**Figure 2.18** and **Figure 2.19**) just above the QCM. The cold finger is cooled by a closed cycle compressed helium gas cryostat (APD Cryogenics, HC-2), which in turn is mounted on a x,y,z manipulator allowing the sample (or QCM) to be accurately positioned in line with the atomic or molecular beams and line-of-sight QMS.

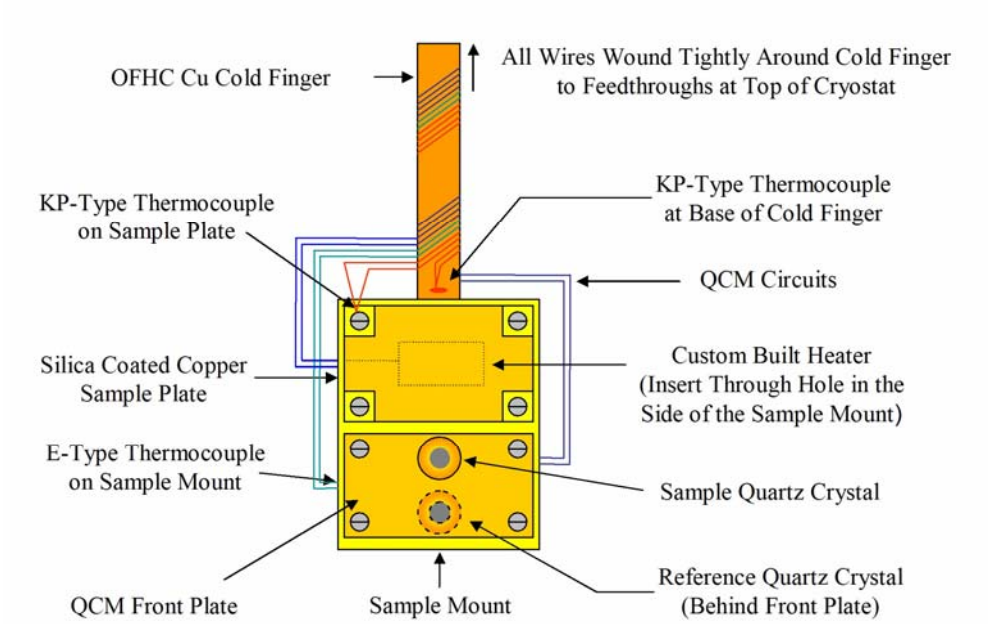

Figure 2.18: Schematic diagram of the Sample Assembly

Before the addition of the dual atomic beam apparatus to the ICE RIG; the surface temperature was controlled using a 2 mm diameter cartridge heater (Heatwave Labs Inc., TB-175) situated inside the sample plate (see **Figure 2.19**). When a replacement heater was required, the decision was made to design and produce a new heater in the laboratory to reduce costs. To fit inside the sample plate, these heaters had to be no larger than 6 mm in diameter by 20 mm in length.

The filament was constructed by cutting a piece of 0.15 mm diameter, temper annealed tungsten wire (Advent Research Materials Ltd.,) to a resistance of approximately 1.0 Ω and tightly coiling it. The wire was then folded into four sections and the coils coated with ceramic glue (Aremco Products Inc., Cerambond 552) so that none of the wire

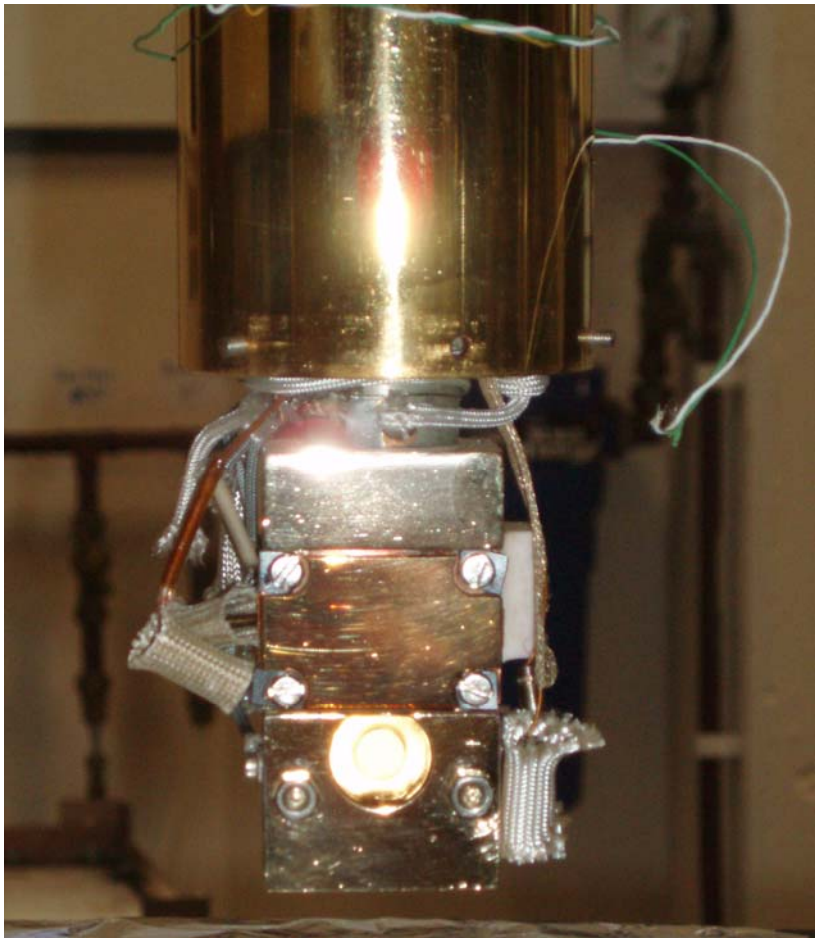

Figure 2.19: Photograph of the Sample Assembly.

touched itself (see top diagram in **Figure 2.20)**. When the glue was almost dry, a small amount more was added to fold the wire into place (**Figure 2.20** bottom). The end of the tungsten wire was wrapped tightly around a support wire from a standard 60 W light bulb and spot-welded into place. More ceramic glue was applied (shaded light blue in **Figure 2.20**) to coat the remaining tungsten wire with care taken to ensure that the heater could still fit inside the sample plate. Once the heater had dried overnight at room temperature, it was placed in an oven at approximately 95˚C for 2 hours. The heater was then left in the oven to slowly cool down for 1 hour and then heated at approximately 205˚C for another 2 hours. A photograph of one of these heaters used throughout this study is shown in **Figure 2.21**. Finally, the heater was fitted into place through the side of the sample mount into the sample plate and spot welded to the heater control wires (blue lines on **Figure 2.18**).

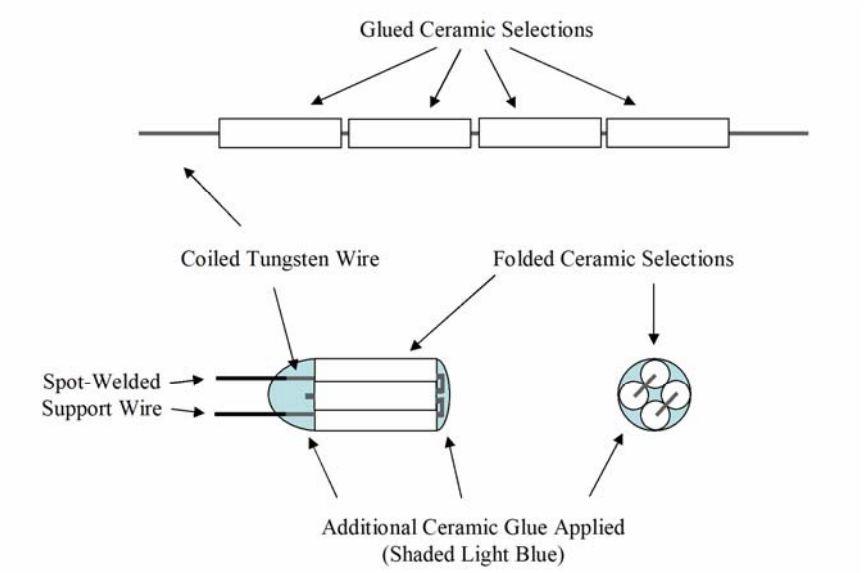

Figure 2.20: Schematic Assembly Drawings of the Sample Heater

Figure 2.21: Photograph of the Constructed Sample Heater Used in this Study

The surface temperature is monitored using a KP-type (chromel–gold/iron) thermocouple situated on the sample plate (see **Figure 2.18**). Although the KP-type response is not linear, the response has been previously calibrated to provide sensitive readings to approximately 250 K. The sample thermocouple reading is compared with another KP-type thermocouple located at the base of the coldfinger. This is necessary as although the heater is locally efficient; the surface temperature of the rest of the mount, for example: the coldfinger and QCM front plate, begins to warm up allowing species deposited on these surfaces to desorb as well. This can result in some experiments, like TPD (**Section 2.3.4**), showing additional desorption peaks that are not related to the species on the sample. An example of this is shown in **Figure 2.22**.

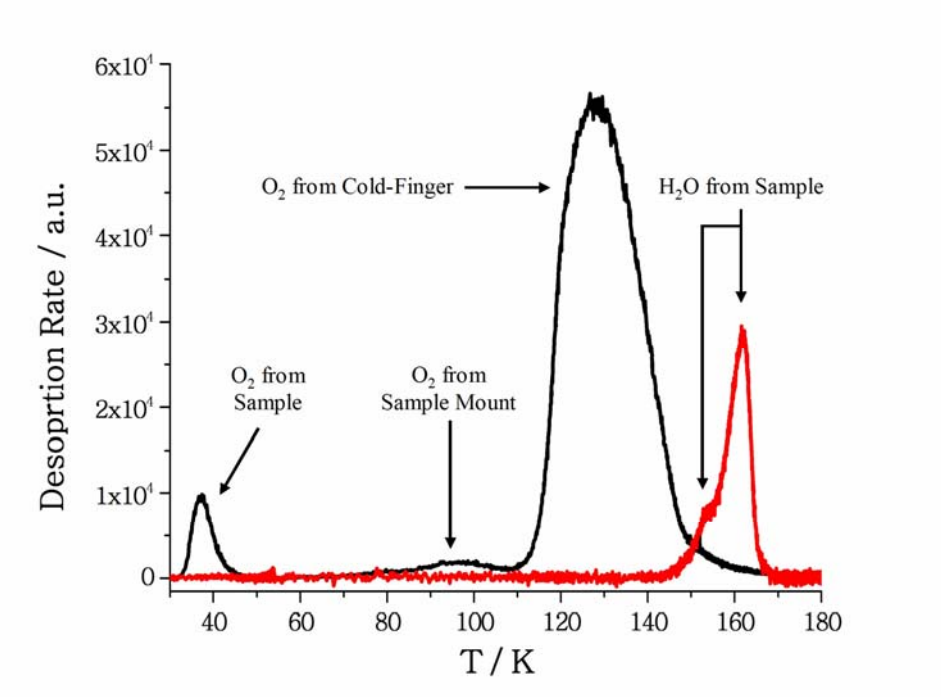

Figure 2.22: Example of a TPD Experiment Containing Additional Desorption Peaks

To determine which desorption peaks correspond to desorption from the sample or the surface mount, the KP-type thermocouple voltages, *V*, were converted into temperatures using a predetermine calibration equation [1]. These are displayed in **Equations 2.1** and **2.2** for the sample and sample mount respectively. The sample mount is also fitted with an E-type thermocouple but, as this is not sensitive to the base temperatures required in this study, this thermocouple was not used.

$$T_{sample} = 0.0321V^6 - 0.24725V^5 - 0.83986V^4 + 13.04568V^3 - 46.57462V^2 + 122.80208V - 23.97914 \quad (2.1)$$

$$T_{mount} = -0.0455V^6 + 0.85661V^5 - 6.5387V^4 + 25.2385V^3 - 52.92676V^2 + 110.8450V - 11.68421 \quad (2.2)$$

When a new heater was required, the additional desorption peaks were reassigned due to the different heating efficiencies. In some cases, the relocation of these additional desorption peaks would occur at the same sample temperatures as desorption for the sample resulting in the new heater having to be replaced. Therefore the process of designing and constructing sample heaters with similar heating efficiencies is ongoing.

2.3 Experimental Techniques

2.3.1 Ultrahigh Vacuum (UHV)

The experiments were performed at UHV pressures (10^{-9} to 10^{-12} mbar) in order to keep the surface relatively clean to conduct astrophysically relevant experiments [8]. This assumption was based on the rate of surface bombardment equation (**Equation 2.3**) where Z_w is the rate of surface bombardment, P the pressure, m the molecular mass, T the temperature of the gaseous species and k_B as Boltzmann constant. At UHV pressures, Z_w is low enough for the sample surface to remain relatively clean for a few hours which is long enough to perform both the dosing and analytical part of the experiment. If high vacuum (HV) pressures were used instead, then the sample would have become contaminated within a few seconds. To determine the exact value of Z_w, the sticking coefficient, S, would also be required in this equation as not all the molecules that collide with the surface will adsorb. The value of S is between 0 (no species sticking to the surface upon collision) and 1 (all species sticking). However, the values of S are experimentally difficult to determine as they are dependent on both the molecule of interest and the temperature of the surface it is colliding with. This is complicated further by there being a range of available surfaces for gaseous species to adsorb onto inside the chamber. For this reason, S was not deduced in this study.

$$Z_w = \frac{PS}{\left(2\pi m k_B T\right)^{\frac{1}{2}}} \tag{2.3}$$

UHV pressures cannot be obtained in the central chamber without baking the chamber after each vent. The mass spectra shown in black in **Figure 2.23** reveals that the two dominant species preventing the pressure from falling below 10^{-8} mbar are H_2 (2 amu) and H_2O (18 amu). To remove H_2O the apparatus was baked at 120 ˚C for 48 to 72 hours. The filling of the liquid nitrogen trap situated above the 6" diffusion pump (see **Figure 2.3** and **Figure 2.5**) decreased the gas phase concentrations of several species including H_2. The advantage of applying these processes can be seen in the mass spectrum shown in red in **Figure 2.23** resulting in the central chamber pressure reducing to roughly 10^{-9} mbar. The remaining mass spectrum shown in **Figure 2.23** displays the gas phase concentrations when the sample is held at base temperatures. Further reductions in the gas phase concentration of H_2 were obtained by filling the titanium sublimation pump with liquid nitrogen (see **Figure 2.3** and **Figure 2.5**) which

increases the rate of adsorption of H_2 onto the titanium filaments resulting in the apparatus obtaining base pressures of typically less than 2×10^{-10} mbar.

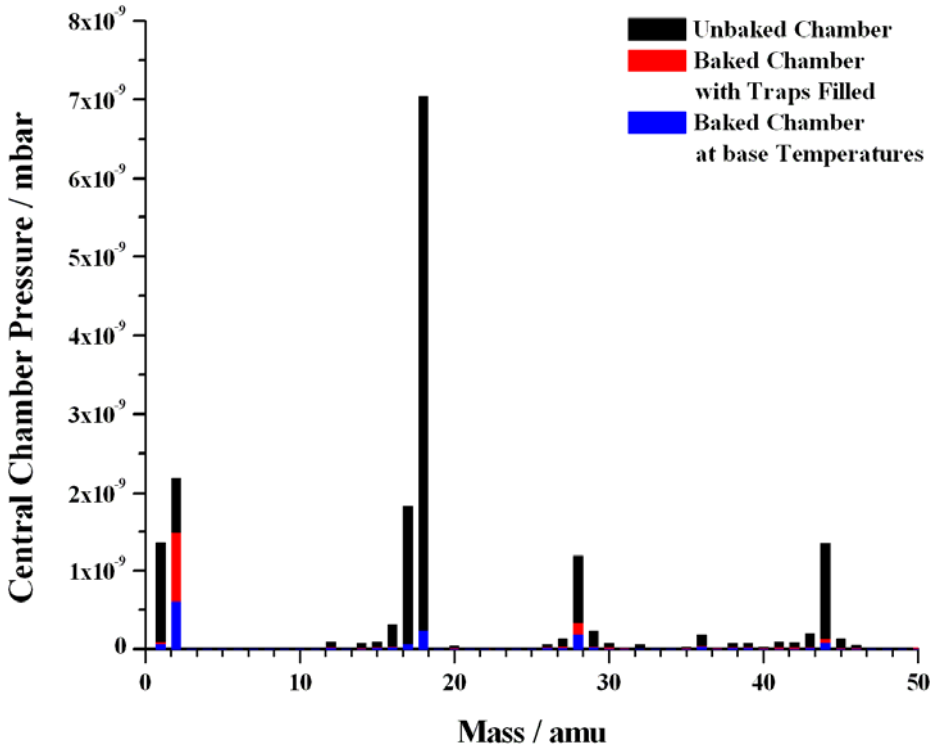

Figure 2.23: Mass Spectra of the Central Chamber Before Baking (black) and After Baking with the Traps Filled (red) and with the Apparatus at Base Temperatures (blue)

2.3.2 Atomic Beams

Often atomic and molecular beams are used in scattering experiments to evaluate surface information for a vast array of different solids [9]. The gaseous atoms or molecules have a low kinetic energy (<0.1 eV) allowing these species to act as a very soft surface probe preventing surface destruction. This is exemplified by Helium Atom Scattering (HAS). As the gaseous atoms or molecules are physically unable to penetrate the solid, the obtained information exhibits an extreme sensitivity that surpasses other surface techniques like LEED (Low Energy Electron Diffraction) or AES (Auger Electron Spectroscopy). However, this increased sensitivity does present a problem as surfaces that would normally show no impurities in AES and display sharp,

well-defined LEED patterns are often not clean enough for atomic and molecular beam research.

In this study, the atomic beams were used to adsorb gaseous atoms and molecules of oxygen and hydrogen onto the silica sample. The low kinetic energy of these species allowed the deposition to occur without chemically altering the surface providing a suitable mimic of the adsorption processes occurring on interstellar dust grains. Once the gaseous species had been adsorbed onto the surface, one of three possible reaction mechanisms could occur (as previously discussed in **Section 1.2.3**). The conclusion was that the Langmuir-Hinshelwood mechanism [10] best described the grain surface reactions in cold diffuse interstellar environments whereas in the laboratory case, a mixture of all three mechanisms will occur depending on the surface concentrations of species adsorbed. Another possibility is that some of the gaseous atoms will not adsorb onto the surface. The identity and intensity of these species will be determined using Molecular Beam Modulation Spectroscopy (MBMS) (see **Section 2.3.3**) [11].

The simplest way of creating an atomic beam is by applying heat to crack molecules. These are known as thermal beams and they have been previously used to determine: absolute total cross scattering ratios in D-He [12] and H-He [13]; hyperfine structure separation [14]; and cross beam reactions like that of O with CS_2 [15]. The beams are created by heating the molecular species of interest inside an oven. If the required temperature is below 2800 K (approximately 2500 ˚C); then the oven is generally heated directly by passing a current through the oven walls. At temperatures above 2800 K, the source material is typically heated through electron bombardment. In both cases the choice of material for the apparatus is critical as it must retain its material properties at these temperatures without changing or reacting with the beam species. Often this limits the use of the thermal beam apparatus to one species. For example, H_2 and D thermal beams use a tungsten oven which is heated by electron bombardment up to 3000 K (approximately 2700 ˚C) [12, 13]. If an attempt was made to create an O beam using this apparatus then the tungsten would oxidise and evaporate. Instead, O thermal beams are created using an iridium oven [15]. Another important part of the thermal beam apparatus is the surrounding shield. This minimises the amount of heat loss from the source which would otherwise lead to the source chamber walls heating and outgassing.

The main disadvantage of using thermal beams in this study is that this technique forms hot atoms which would result in additional reactions, like oxidation, occurring inside the chamber. There are techniques that can be used to cool the hot atoms, like surface collision cooling (used by Linnartz and co-workers to cool H atoms from approximately 2000 K to room temperature as previously mentioned in **Section 1.3.3** [16]) but this would require additional equipment which would have to be continuously monitored for damage. Therefore, thermal beam techniques are not preferred for this study.

Atomic and molecular beams can also be created using plasmas. A plasma is generally defined as a electrically neutral system composed of charged gaseous species [17]. The arrangement of these charged species is such that they shield externally and internally generated electrostatic fields. As a consequence, the plasmas are strongly influenced by both electric and magnetic fields. There are several different types of plasma based on their physical characteristics. For example: cold plasmas (also known as low electron-energy plasmas) include those found in interstellar and interplanetary space; and arc discharge plasmas have electron temperatures similar to those of the gas and can be used to describe plasma jets. The glow discharge plasma of interest in this study can be created using two techniques. The first method applies direct current (DC) or low frequency alternating current (AC) across two electrodes situated inside the reactor. These plasmas generally operate at 10 to 100 V cm^{-1} with pressures of 0.1 to 1 Torr (approximately 0.1 to 1 mbar) and powers up to 50 W [17] which would not be suitable for this study. Another disadvantage with this method is that the gas comes into contact with the electrodes leading to an additional source of contamination preventing the production of high purity atomic beams. The alternative method of producing a glow discharge plasma, and the one used in this study, uses high frequency energy (between 1 and 200 MHz). This is usually in the form of radio frequency (RF) or microwave (MW) energy which is transferred directly to the reactor through a section of wave guides in the case of MW generation, or by capacitive or inductive coupling with RF generation (see **Figure 2.24)**. Not only does this remove the risk of electrode contamination but this also improves the reliability and reproducibility of the plasma and increases the lifetime of the plasma reactor.

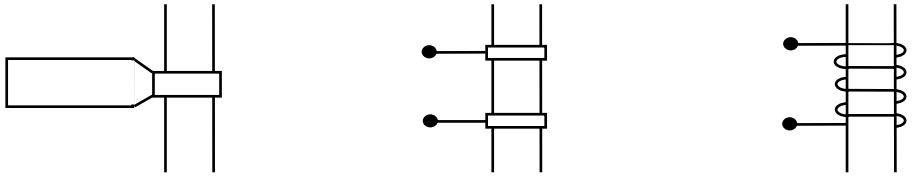

Wave Guide (MW) | Capacitive Coupling (RF) | Inductive Coupling (RF)

Figure 2.24: Coupling Arrangements in RF and MW Plasma Sources

MW plasma sources typically have a frequency of 2.45 GHz and the discharge can be magnetized. The operating gas pressure for an unmagnetized discharge is approximately between 1×10^{-2} to 1×10^{3} mbar but this can be lowered from 10 mTorr (roughly 1×10^{-2} mbar) to a few μTorr (low 1×10^{-9}) for magnetized discharges. MW plasmas characteristically produce a higher fraction of ionized and dissociated species than RF plasma sources due to their higher electron kinetic temperature (5 to15 eV compared to 1 to 2 eV) and lower operating pressures [18].

Both types of RF plasma source produce a lower beam temperature than thermal beams, reducing the extent of recombination [19] and have greater stability and higher electron efficiency than DC or AC plasmas [17]. Capacitively coupled RF plasma sources use a frequency range of 10 kHz to 30 MHz and a higher pressure range of a few to a few hundred mbar [18]. In comparison inductive RF plasma sources tend to operate with a frequency range between 1 – 100 MHz (typically set to 13.56 MHz) with a power range of 50 – 500 W and gas pressure of between 4×10^{-3} to 7 mbar. The lower pressure range and the variable RF power range of the inductive RF plasma source make this more suitable in this study.

To determine whether to use MW or RF powered plasma sources in this study, comparisons were made with current atomic beam systems. The ASURA (Hokkaido, Japan) and FORMOLISM (Paris, France) (both reviewed in **Section 1.3.3**) use MW plasma sources. Calibrations of the ASURA atomic H (or D) beam concluded a dissociation fraction of at least 20 % with a flux of 2×10^{14} cm^{-2} s^{-1} [20]. The MW atomic D beam used on FORMOLISM has a higher dissociation fraction (typically 60 %) and flux (5×10^{15} atoms cm^{-2} s^{-1}) than ASURA [21]. However, the RF plasma sources used in Syracuse (NY, US) produced considerably higher dissociation fractions

of 80 and 90 % for their D and H beams respectively [22] with lower beam fluxes of approximately 10^{12} atoms cm^{-2} s^{-1} [23] (see **Section 1.3.3**). For this reason, an inductive RF plasma source was chosen to form the atomic H beam in this study.

Although the dissociation fraction should be as high as possible to produce the best atomic beams, this depends on the bond dissociation enthalpy of the species of interest. H_2 has a bond dissociation enthalpy of 436 kJ mol^{-1} at 298 K which is lower than O_2 (497 kJ mol^{-1} at 298 K) [24] so the dissociation fraction of H_2 using the same dissociation method will always be higher than O_2. This was true when similar comparison were made with known atomic beam systems using oxygen. The FORMOLISM apparatus uses a MW powered plasma source to form their atomic O beam. Their calibrations revealed that the dissociation fraction was typically 40 % with a flux of 10^{12} atoms cm^{-2} s^{-1} [25]. For one set of experiments, Vidali *et al.* produced an atomic oxygen beam [26] with a dissociation fraction between 30 and 40 %. However, this beam was created using their RF hydrogen plasma source which contains a Pyrex tube. This material is more suitable for producing an atomic hydrogen or deuterium than oxygen which would reduce the oxygen dissociation fraction. Therefore a second inductive RF powered plasma source (with a more suitable material for the plasma tube and reactor) was chosen to produce the atomic oxygen beam in this study.

As previously described in **Section 2.2.2**, the low frequency energy (either RF or MW) is absorbed by the gas in the reactor leading to the molecules becoming excited and ionized producing free electrons. These free electrons continue to transfer the RF or MW energy to the gaseous species within the reactor through elastic and inelastic electron-molecule collisions. The elastic collisions lead to an increase of kinetic energy within the collision molecule producing molecular or molecular-ion plasmas. Inelastic collisions are required in producing atomic plasmas as these result in the collision molecules becoming excited, ionized or fragmented. Once the plasma has been created, either atomic or molecular, the excited species return to their ground state by radiating energy. Most of this radiation is often in the ultraviolet part of the electromagnetic spectrum [17]. However, a small part of this radiation is released in the visible part of the spectrum allowing the products within the plasma to be determined. The exact colour of the glow discharge depends on the intensity of all the energy state transitions occurring within the plasma. For example, the atomic hydrogen spectrum in the upper

diagram of **Figure 2.16** is pink-red in colour. Most of this colour is due to the large 656 nm peak which is in the red part of the visible spectrum.

The intensity of the visible light is an indication of whether the plasma obtained is molecular or atomic. For molecular and molecular-ion plasmas, the intensity of the visible light emitted is low as the proportion of elastic to inelastic electron-molecular collisions are high. This stage is often referred to as the low brightness mode (as previously shown in the left hand diagram of **Figure 2.12**). This brightness is characteristic of molecules absorbing energy into the low molecular excited states and fluorescing back to the ground state. The atomic plasmas are produced by reducing the gas pressure resulting in a decrease in the elastic to inelastic electron-molecule collisions. This process increases the rate of excitation and allows the gaseous species to reach the higher excited molecular states and the atomic orbitals causing dissociation (as shown in the right hand diagram of **Figure 2.12**). This diagram also indicates that atomic plasmas are a mixture of atomic and molecular species. The increased rate of excitation increases the overall amount of fluorescence producing a plasma in the high brightness mode.

The ease of producing an atomic plasma depends on the ability to ionize the molecule. Molecules like oxygen and nitrogen are relatively easy to form atomic plasmas despite containing a double and triple bond respectively as their electrons in the outer shell are partially shielded from the nuclei. Hydrogen is notably the most difficult molecule to ionize. Unlike oxygen and nitrogen, hydrogen only has two available electrons per molecule which require higher quantities of RF or MW energy for ionization to occur as the electrons are unshielded. The lower number of electrons per hydrogen molecule results in a lower free electron concentration in the plasma which in turn may mean that the molecular plasma will not convert into the atomic form or will only form a poor quality atomic plasma. Another problem with hydrogen is the pumping speed is considerably higher than that of oxygen or nitrogen. The higher pumping speed of hydrogen (2000 l s^{-1} in an Edwards 6" diffusion pump compared to1350 l s^{-1} for air [27]) may also result in neutral species effusing from the reactor before dissociation can take place. To overcome this, the secondary gas technique is used to produce sufficient free electrons by creating a plasma with another gas (in this study, nitrogen). The atomic or molecular beam is created by the effusion of neutral species from the reactor. The plasma itself remains confined to the reactor.

The RF inductively coupled plasma sources used in this study were situated in a doubly differentially pumped atomic beam chambers (separately labelled as plasma and beam chamber in **Figure 2.5**). This allows the plasma chamber pressure to be adjusted giving a Knudsen number (the ratio of the gas mean-free path to the orifice of the source diameter) greater than unity and, therefore, provides free molecular flow through the plasma source [9]. A pressure gradient between the plasma chamber (held at approximately $1x10^{-4}$ mbar when the beam is in use) and the central chamber (typically less than $2x10^{-10}$ mbar) is necessary to induce a significant mass transport in the direction of the beam.

The velocity distribution of the atoms within the beam, v, is Maxwellian (as shown in **Equation 2.4**) and is directly dependent on the gas temperature. As this system has no method of cooling the atomic or molecular beam, then the temperature of the gaseous species in the beam is assumed to be about 300 K. The atomic (or molecular) beam flux, F, is determined using **Equation 2.5** where P is the beam pressure, A_s the area of the source aperture and l the distance between the source to the surface. However, there is currently no direct method of monitoring the beam pressure with the dual atomic beam system as there is no pressure gauge in-line with the beam. Instead the atomic and molecular beam fluxes used in this study were determined using pump-down experiments. This calibration technique is discussed in more detail in **Section 3.4.2** for the oxygen beam.

$$v \propto \left(\frac{v^3 m^2}{(2k_B T)^2} \right) \exp\left(\frac{v^2 m^2}{(2k_B T)^2} \right) \tag{2.4}$$

$$F = \frac{1.118 \times 10^{22} P A_s}{l^2 (mT)^{1/2}} \tag{2.5}$$

As previously discussed, the species in the atomic beams are not fully dissociated (see **Section 3.4.3** for the initial attempts to determine the dissociation fraction of the atomic O beam) which can lead to problems with contamination in surface experiments. In the dual atomic beam system, the surfaces inside the UHV central chamber are too warm for H_2 to adsorb so no surface contamination is observed. However, the sample, sample mount and cold finger are typically cool enough for O_2 to adsorb. This can cause

problems with interpreting experimental data; for example: how much of the observed O_2 is formed by recombination on the surface or by adsorption during the atomic beam irradiation experiment. To determine whether the results are from processes involving O_2 or O, two sets of beam experiments, analyzed using MBMS, TPD, QCM, RAIRS or a combination of these techniques, are required. The first experiment uses no RF power forming a molecular beam giving details of those surface processes using O_2. These results are then compared to the atomic beam version of the experiment to give information on O atom surface processes.

2.3.3 Molecular Beam Modulation Spectrometry (MBMS)

During an atomic or molecular beam irradiation experiment, the identity and intensity of the gaseous species is required. In most systems, the gaseous species monitored is part of the atomic or molecular beam, either as the major species or a background (contaminant) species. However, some species are formed through surface reactions. These processes are surface temperature dependent as the thermal energy available from the surface becomes sufficient to allow some of the adsorbed species to break the physisorption surface bonds and desorb.

MBMS works by monitoring the species of interest during a beam irradiation experiment. **Figure 2.25** displays the two experimental setups of the MBMS technique. The top diagram is a *reflection arrangement* where the mass spectrometer is situated in-line with the specular reflection direction of the incident molecular beam. This setup is used to explore the short time events that do not significantly perturb the outgoing beam from the specular. In this case, the short time scale events are single collisions typically observed in simple scattering or Eley-Rideal (see **Section 1.2.3**) type reactions. Simple applications of MBMS using this arrangement can be used to analyze fluxes of majority species beamed on to and desorbing from a substrate in order to obtain surface residence times and hence binding energies. More complex analysis can reveal those desorbed species formed through single step surface formation reactions allowing for a more detailed analysis of the surface mechanism occurring on the substrate with respect to surface temperature [28-30].

The MBMS experimental setup in the bottom diagram of **Figure 2.25** positions the mass spectrometer behind the sample, but could equally well be positioned at any angle

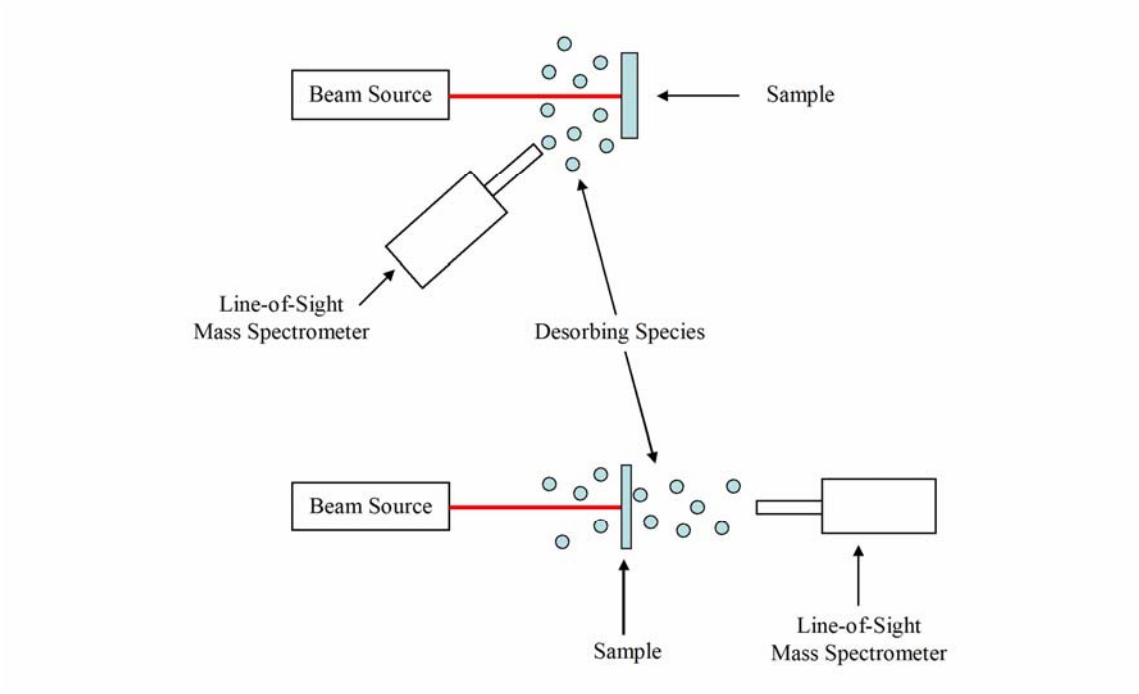

Figure 2.25: Experimental Layouts of MBMS for Sample Substrates (top) and Thin Film Samples (bottom)

other than the specular, and is used to analyze long time scale events on the surface where the desorbing species shows a thermalised spatial distribution. Of course, with the mass spectrometer behind the sample such experiments must rely on collisions reflecting species from the walls of the chamber into the direction of the mass spectrometer. Although the QMS can be positioned both behind (position 1) and in front off the sample (position 2) (see **Figure 2.3**), the sample mount design would greatly restrict the concentration of desorbed species from being detected by the QMS in position 1. The line-of-sight capability using liquid nitrogen cooling to reduce background signal is not applied since most of the species of interest will not adsorb onto a surface held at liquid nitrogen temperatures. The QMS data is recorded using the MASsoft software package[1] whilst the pressure and thermocouple voltages are monitored using a separate data acquisition program. The results will be used to identify those desorbed species formed through chemical reactions on the substrate and their intensities. As MBMS alone can not determine more complex multiple reaction step mechanisms then the results obtained will be compared and applied with other

[1]MASsoft version 3.5.3, Hiden Analytical Limited, 1997. Further information maybe obtained from http://www.hidenanalytical.com/reference/software/index.html.

analytical techniques, such as TPD (see **Section 2.3.4**) and RAIRS (**Section 2.3.6**), to provided a more detailed surface chemistry mechanism.

For the majority of experiments discussed in this thesis, the QMS was situated in position 1 so no MBMS experiments were performed. An example set of MBMS results by Foord *et al*. are shown in **Figure 2.26** [28] and were used to analyze the growth of semiconductor films. The plot displays the intensities of Ga (gallium), mTBG (monotertiarybutylgallium) and dTBG (ditertiarybutylgallium) with respect to surface temperatures for constant incident fluxes of arsenic molecules (As_2) and TTBG (tritertiarybutylgallium). The results indicate that the signals of mTBG and dTBG

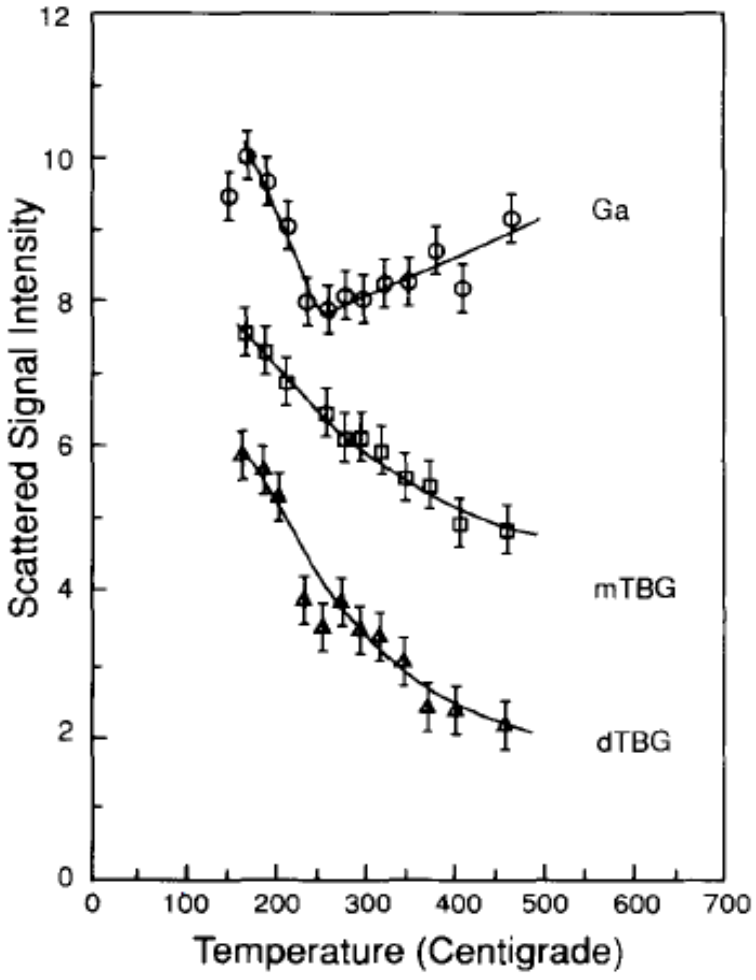

Figure 2.26: Example set of MBMS Experiments Used to Explore the Film Growth of GaAs from TTBG and As_2 in Semiconductors [28]

gradually decrease with temperature whilst Ga first decreases before increasing at surface temperatures above 250 ˚C. The conclusions for these results hypothesize that the increase in the Ga signal was suggested to be because of a new species (like gallium hydride) was formed on the surface or during the time-of-flight to the mass spectrometer; or there was a temperature dependence with the cracking pattern of the desorbing gallium alkyl species. It is expected that the MBMS results obtained in the future will reveal a surface temperature dependence for the desorbing species. In some cases, the intensity of a desorbing species may influence the signal intensity of another. More detailed analysis of the surface processes occurring in these experiments will be made by comparing the MBMS results with those from TPD and RAIRS.

2.3.4 Temperature Programmed Desorption (TPD)

To determine the species adsorbed on a surface, TPD is used. This technique measures the desorption temperature of the adsorbed species [8], from which, the binding energy of these species to the surface can be evaluated. As the temperature rises, the thermal energy available becomes sufficient to allow the species to break the bonds with the surface and desorb. The desorbed species were detected using the same line-of-sight QMS as for the MBMS experiments but the QMS can be situated in either position 1 or 2 (see **Figure 2.3**). A slow linear temperature ramp is applied to the sample using the custom built heater (see **Section 2.2.3**) which allows for a more accurate analysis of the desorption temperature for each species.

The desorption rate coefficient, k_{des}, is described using the Arrhenius equation (**Equation 2.6**) where ν is the pre-exponential factor and E_{des} the activation energy for desorption. The rate of desorption, r_{des}, is displayed in **Equation 2.7**, where N is the number of absorbed molecules, n the kinetic order of the reaction and β the heating rate (dT/dt).

$$k_{des} = \nu \exp\left(\frac{E_{des}}{kT}\right) \tag{2.6}$$

$$r_{des} = -\frac{dN}{dT} = \frac{k_{des}}{\beta} N^n \tag{2.7}$$

When TPD experiments are performed in a continuously pumped vacuum chamber (as in this study), the temperature at which the maximum desorption peak occurs, T_p, corresponds to the maximum desorption rate. Therefore, by differentiating **Equation 2.7** with respect to T and equating it to zero (substituting **Equation 2.6**), the Polanyi-Wigner equation is obtained (**Equation 2.8**).

$$-\frac{dN}{dt} = v_{des} N^n \exp\left(\frac{-E_{des}}{k_B T}\right) \tag{2.8}$$

In 1962 Redhead proved that for T_p / β in the range of 10^8 to 10^{13} s the relationship between T_p and E_{des} was, to a good approximation, linear [9]. By taking this assumption and v as a standard constant (10^{13} s^{-1}) **Equation 2.8** was simplified to give the Redhead Equation (**Equation 2.9**).

$$\frac{E_{des}}{RT_p^2} = \frac{A}{\beta} n N^{n-1} \exp\left(\frac{E_{des}}{RT_p}\right) \tag{2.9}$$

The Redhead equation revealed that the kinetic order of the desorbing species from the surface affected the overall shape of the TPD peaks providing information on the different bonding sites available on the surface. **Figure 2.27** portrays some typical TPD curves for zeroth, first and second order (n = 0, 1 and 2 respectively). For first order kinetics (middle plot in **Figure 2.27**), the desorption peak maximum is independent of adsorbate coverage, N. Therefore as the surface coverage increases, the asymmetric peak increases with intensity but at the same temperature. These type of TPD curves are typical of sub-monolayer desorption. Second order TPD curves are usually associated with recombination desorption (see bottom plot in **Figure 2.27**). Here the desorption peaks become dependent on adsorbate coverage. Hence, as N increases, T_p decreases for a fixed value of E_{des}. This results in the symmetric TPD peaks having common falling edges with T_p shifting to lower temperatures with increasing N. For zeroth order kinetics (top plot in **Figure 2.27**), the Redhead Equation no longer holds so the TPD curves have to be described using the original Polanyi-Wigner Equation (**Equation 2.8**). As the desorption peaks are all independent of N the curves have coincident leading edges with T_p shifting to higher temperatures for increased surface coverage. This is typical of species desorbing from the bulk ice.

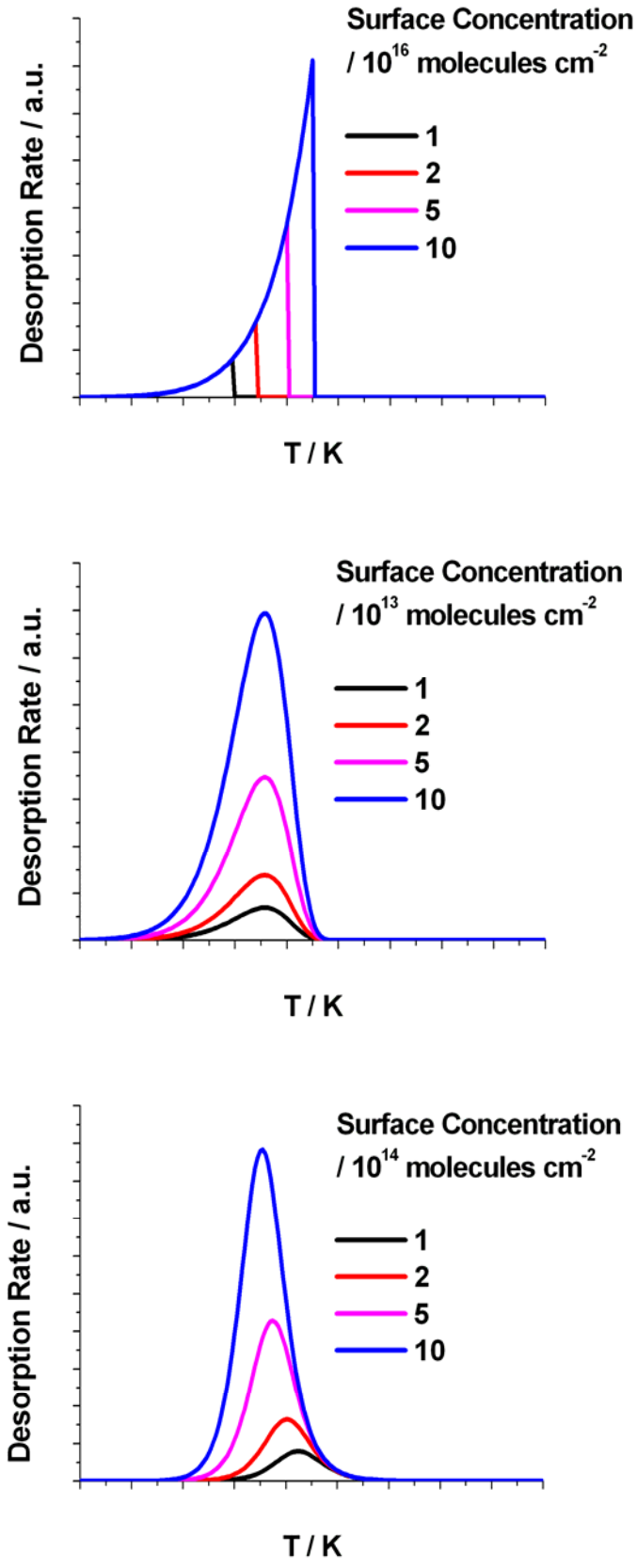

Figure 2.27: Kinetic Order Effects of Desorption Process on the TPD Curves for Zeroth (top), First (middle) and Second Order (bottom).

For the TPD experiments performed in this study, the curves are expected to follow either first or zeroth order kinetics for sub-monolayer and multilayer coverages respectively. However, the rough silica sample is expected to provide a range of binding sites for the adsorbed species (as previously discussed in **Section 2.2.3**). As E_{des} would no longer be constant, this would alter the shape of the sub-monolayer TPD curves to ones with coincident falling edges [31].

2.3.5 Quartz Crystal Microgravimetry (QCM)

QCM is often used to monitor desorption rates and the mass deposited on a surface. This technique can also be used as an estimate of the mass deposited on an adjacent surface (as described in **Section 2.2.3** for applying the thin film of silica to the sample plate). In this study, the QCM apparatus was situated underneath the silica sample (see **Figure 2.18**) and was used to determine the ultimate position of the silica sample with respect to the atomic and molecular oxygen beams (see **Section 3.2**). Ideally this procedure would be repeated for the hydrogen beam. However, due to the continuous problems with the RF hydrogen plasma source, this was not attempted. Also the limitations of the closed cycle helium gas cryostat may prevent the crystal surface from cooling enough to allow hydrogen to adsorb. Therefore when the ultimate position of the silica sample is determined with respect to the atomic and molecular hydrogen beam in the future, the beam will be formed using nitrogen (which can adsorb onto the crystal at these surface temperatures) instead of hydrogen. Further work using this apparatus will include calculating the mass deposited per unit time by the oxygen beam as this will provide an alternative method to determine the atomic and molecular beam flux.

The QCM technique works by monitoring the mass on a surface *via* a sample to reference comparison of oscillating crystals. The tiny changes in the mass on the crystal surface, Δm, lead to a pronounced shift, Δf, in the crystal's resonant frequency f_0 (approximately 15 MHz). This is indicated by the Sauerbry equation (**Equation 2.10**) [32], where h is the harmonic index of f_0, A_s the exposed sample surface area of the crystal, χ the sheer modulus of quartz (2.947×10^{11} g cm^{-1} s^{-2}) and d the density of the quartz (2.648 g cm^{-3}) [1]. However, in practice f_0 is not precisely known so when the system was calibrated the Sauerbry equation reduces to **Equation 2.11** where F is the calibration factor.

$$\Delta f = \frac{2 f_0^2 h}{A\sqrt{\chi d}} \Delta m \tag{2.10}$$

$$\Delta m = F \Delta f \tag{2.11}$$

2.3.6 Reflection-Adsorption Infrared Spectroscopy (RAIRS)

The advantage of using RAIRS is its ability to detect reaction intermediate species [8] which are often missed using other analytical techniques. This knowledge can be used to construct more detailed molecular reaction mechanisms. Ideally, RAIRS would be performed at the same time as a TPD experiment providing additional information on the temperature dependent parts of the surface mechanism.

The techniques works by focusing an IR beam onto the sample surface. The chosen angle of incidence of the beam needs to be considered carefully [33]. If the beam is directed with an angle of incidence near perpendicular to a surface, then the incident and reflective waves combine to form a standing wave but the amplitude would be zero. In this situation, the wave would not interact with the adsorbed molecules on the surface and the required information would not be obtained. If the beam is directed at a grazing angle (angle close to 90˚ from the surface normal) then the phase change of the IR beam (red line) becomes dependent on the incident angle and the polarization of the light as shown by the electric vector diagram in **Figure 2.28**.

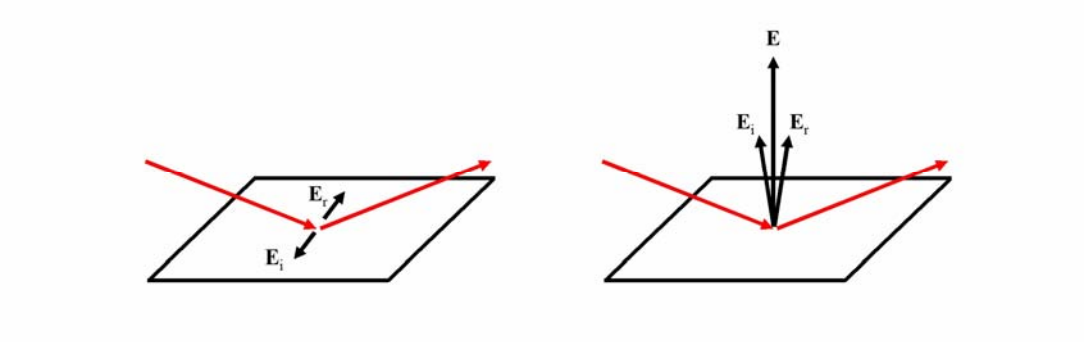

Figure 2.28: Electric Vector Diagram for the Phase Shifts Components of Perpendicular (left) and Parallel (right) Polarized Light

The left hand diagram in **Figure 2.28** displays the perpendicular polarized component. Here the phase shift is close to 180˚ for all angles of incidence so the incident, $\boldsymbol{E}_i$, and

reflection, $\boldsymbol{E}_r$, vectors almost cancel each other out resulting in little absorption being observed. The parallel polarized component is shown in the right hand diagram of **Figure 2.28**. Here the phase shift changes rapidly at high incident angles resulting with the $\boldsymbol{E}_i$ and $\boldsymbol{E}_r$ vectors leading to an elliptical standing wave with a sizeable electric vector, $\boldsymbol{E}$, directed perpendicular to the surface. The maximum enhancement is when the angle of incidence is at 88˚. The result of this leads to the Metal Surface IR Selection Rule [8] which is summarized in the cartoon shown in **Figure 2.29**. When a molecule is parallel to the surface (left diagram in **Figure 2.29**), the oscillating molecular dipole, μ_M, cancels out with the oscillating image molecular dipole, μ_I, in the surface preventing IR absorption and therefore the molecule cannot be detected. This is equivalent to the perpendicular polarized component. When the molecule lies perpendicular to the surface, the two dipoles reinforce each other (mimicking the addition of the incident and reflection vectors for the parallel polarized component) allowing the species to be IR active.

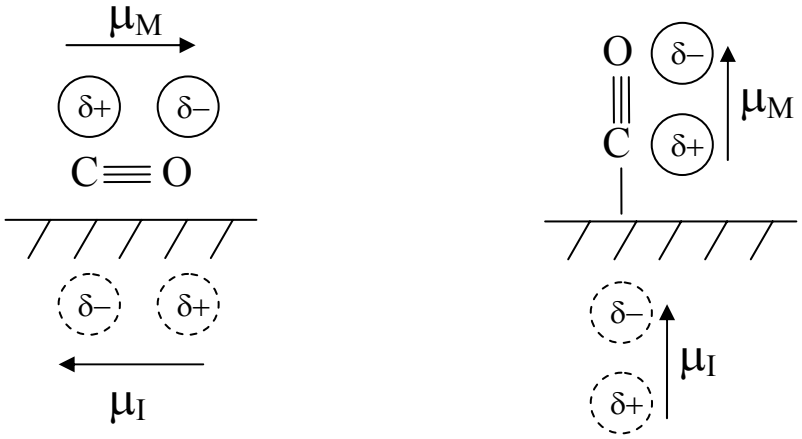

Bonds lying parallel to the surface have molecular and image dipoles cancelling each other out. IR inactive

Bonds lying perpendicular to the surface have molecular and image dipoles re-enforce. IR active.

Figure 2.29: Cartoon of IR Metal-Surface Selection Rule [8]

For experiments that use a metal surface, the RAIRS signal of the metal surface is removed by performing a background scan. In this study, the substrate is a porous silica surface and this causes several complications to the simple IR Metal-Surface Selection Rule [34, 35]. The main difference observed on the RAIRS spectra in these systems is

the adsorbed layer changes the optics of the underlying silica. As the coverage of the adsorbate layer increases the height of the silica peak also increases. An additional complication observed is that some of the peaks shift with increased coverage. This is particularly true for systems exploring mixed or layered ice systems that include H_2O. The peak shifts are a result of H-bonding, mostly between the H atoms in the species in the adsorbed layer (like H_2O) and O atoms in the silica surface (SiO_2) or O, F, or N bearing species within the ice, stretching and weakening the internal bonds of the molecules involved. Both of these effects were predicted to be observed in any RAIRS experiments performed in this study.

A schematic diagram of the RAIRS set up for the apparatus used in this study is shown in **Figure 2.5**. The IR beam is directed through a KBr window on one side of the chamber onto the sample surface at an incident angle of 75˚. The beam is reflected through another KBr window on the opposite side of the chamber where it is detected by an IR spectrometer. However, due to continuing problems with the IR spectrometer (BIORAD, FTS-40A), these RAIRS experiments were unable to be performed.

2.4 Experimental Procedures

2.4.1 Atomic and Molecular Beam Dose Experiments

Once the central chamber has reached UHV conditions, atomic or molecular beam dosing experiments can be performed. For the atomic beam dosing, the gate values between the atomic beam chambers and the central chamber were closed and the plasma for the required beams was created and adjusted to the desired RF power. The plasma chamber pressure was monitored using an ion gauge in order to maintain a relatively constant beam flux. The sample was positioned in-line with the beams (see **Figure 2.5**) and the data acquisition program set to monitor the central chamber pressure and all the thermocouple voltages on the sample mount (see **Figure 2.18** in **Section 2.2.3**). The intensity of the species of interest were monitored using MASsoft along with the KP-type thermocouples on the sample and cold finger. Once the intensity of the monitored species had reached base levels on the MASsoft program, then the gate valves between the atomic beam chamber or chambers and the central chamber were opened for the required dosing time.

When the dose was complete the gate valves were closed and the two programs left running until the pressure in the central chamber had returned to base levels. The RF powered plasma sources were turned off and any additional dosing or analytical surface experiments were performed. For the molecular beam dosing experiments, the same procedure for the atomic beam dosing was applied except that the RF power for the plasma sources remained turned off.

2.4.2 Background Dose Deposition

Before any background dose deposition experiments began, the vapour of the required species needed to be obtained in one of the two dosing bulbs on the glass gas lines (see **Figure 2.7**). For liquids, a test tube containing approximately 1 ml^3 of the substance was attached to the glass line. With the gas taps to the dosing bulbs closed the substance was purified using several freeze-pumped-thaw cycles. This procedure was used to pump away the air above the liquid by submerging the liquid containing part of the test tube in liquid nitrogen. Any contaminants at the air-liquid interface were removed when the substances began to melt as the interface layer evaporated first. Once this process has been repeated several times, the gas taps to the required dosing bulb were opened and the bulb flushed and filled with the liquid vapour. The pressure inside the dosing bulbs was monitored using Edwards Barocel pressure sensors. For gases, a gas bulb of the required substance was attached onto the glass gas line. The dosing bulb was flushed with small quantities of the gas to clean the bulb and then filled.

The background dose deposition was performed with the sample situated in-line with the QMS either in position 1 or 2 (see **Figure 2.3**). The data acquisition and MASsoft programs were started (as in the atomic and molecular beam dose experiments). Once the intensity of the monitored species had reached base levels on the MASsoft program, the gas was dosed into the central chamber *via* a leak valve (**Figure 2.3** and **Figure 2.5**). The pressure, P, and time, t, values for each dose were approximated using **Equation 2.12**. Once the pressure had returned to base levels, additional dosing or analytical experiments could be performed.

$$dose / L = \frac{Pt}{10^{-6}} \tag{2.12}$$

2.4.3 Molecular Beam Modulation Spectrometry (MBMS)

At the same time as an atomic or molecular beam experiment (see **Section 2.4.1**), MBMS can be performed if the QMS was situated in position 2 (see **Figure 2.3**). The MASsoft and data acquisition program were set to run as before but with MASsoft also monitoring those species that may have been produced through surface formation reactions. Once the intensity of all the species monitored by MASsoft have reached base levels then the gate valve between the central chamber and the atomic beam chamber (or chambers if both beams were in use) was opened for a set dose time.

When the atomic beam dose has been completed, the gate valve between the chambers was closed. The two programs were left running until the pressure inside the central chamber returned to base levels. Further analytical experiments, like TPD and RAIRS, could then be performed.

2.4.4 Temperature Programmed Desorption (TPD)

This experiment was performed after a dose experiment (or experiments) (see **Section 2.4.1** and **2.4.2**) and the central chamber pressure had fallen back to base levels. The sample was positioned in front of the QMS (in either position 1 or 2) and the MASsoft and data acquisition program set as in **Section 2.4.1**. Once the species had reached base levels, a linear heating ramp between 0.01 and 0.20 K s^{-1} was applied to the sample using the custom built heater (see **Figure 2.18** in **Section 2.2.3**). The sample was heated until either a set temperature has been reached or until there was no further desorption observed from the sample.

2.4.5 Quartz Crystal Microgravimetry (QCM)

Before a QCM experiment could begin, the apparatus first needed to be checked for mass sensitivity. This was achieved by performing a short background dose deposition experiment of the species of interest (as in **Section 2.4.2**) but with the data acquisition program set to monitor the central chamber pressure and sample crystal frequency. If the QCM apparatus was mass sensitive then the sample crystal frequency would linearly decrease over time (**Section 2.3.5**).

The QCM was moved to a position in-line with the atomic beams and the atomic (or molecular) beam created (as in **Section 2.4.1**). The data acquisition (monitoring central

chamber pressure and sample crystal frequency) and the MASsoft program were set as in **Section 2.4.1** and started. Once the monitored species had reached base levels, the gate valve between the atomic beam chamber and the central chamber was opened for a set dose time. Once completed, the gate valve was closed and the programs left running until the pressure in the central chamber had returned to base. If no further QCM or analytical experiments were required, the crystal was heated clean using the custom built heater (see **Figure 2.18**).

The above procedure describes isothermal QCM experiments. Temperature-programmed QCM experiments can also be performed with this apparatus but were not used in this study. The procedure for this second technique is similar to that of the first except that a linear heating ramp (similar to those used in TPD experiments, see **Section 2.4.4**) would be applied using the custom built heater. This technique is expected to give similar temperature-dependent results to those obtained from TPD experiments. The disadvantage of temperature-programmed QCM experiments is the linear heating ramp increases the signal to noise ratio resulting in poorer quality results.

2.4.6 Reflection-Adsorption Infrared Spectroscopy (RAIRS)

Once the pressure has returned to base levels after a dosing experiment (or experiments), either isothermal or temperature-programmed RAIRS techniques can be performed. In isothermal RAIRS experiments, the sample is first heated to the required temperature using the custom built heater (see **Figure 2.18**) before the IR spectra were recorded. The procedure for the temperature-programmed RAIRS experiments is similar to the Isothermal RAIRS experiment except that the surface was continuously heated with a slow, constant temperature gradient (provided by the custom built heater) with IR spectra taken at set time intervals. Often the temperature-programmed RAIRS experiments would be performed at the same time as TPD experiments. This technique was expected to give similar temperature dependent results to those obtained through TPD experiments as well as more detailed information concerning surface reaction mechanism, different bonding sites and reaction intermediate species. However, due to continuing problems with the IR spectrometer, no RAIRS experiments were performed in this study.

2.5 Synthetic Procedures

2.5.1 Introduction

Most of the species required for the experiments were supplied in either gas bottles or cylinders; or were formed using the RF powered plasma sources. The only species for which laboratory synthesis is required is O_3. The following sub-section explores the different O_3 synthesis techniques available before drawing a conclusion as to the preferred method. A description of the required apparatus and calibration procedure is also given. However, due to the late delivery of the equipment, none of the planned O_3 TPD experiments discussed in **Section 1.3.4** were performed in this study but will be performed at a later date for this ongoing research.

2.5.2 Ozone Synthesis

There are several different procedures that can be used to form ozone both *ex situ* and *in situ* of the apparatus. The *ex situ* techniques include ozonizers; RF electric discharges; UV lamp; polmer-electroyte membrane (PEM) cell; and high voltage corona discharge.

Ozonizers use dielectric barrier discharges to generate O_3 either from O_2 or air [36]. The first reports of O_3 being produced from O_2 using dielectric barrier discharge was made by Siemens [37] in 1857. Since then, there have been several improvements to the apparatus design and now one of three designs are generally used (**Figure 2.30**). The material for the dielectric barrier is usually glass or silica glass although other materials like ceramic and thin enamel are sometimes used. Liquid cooling techniques are applied to at least one of the electrodes to prevent overheating.

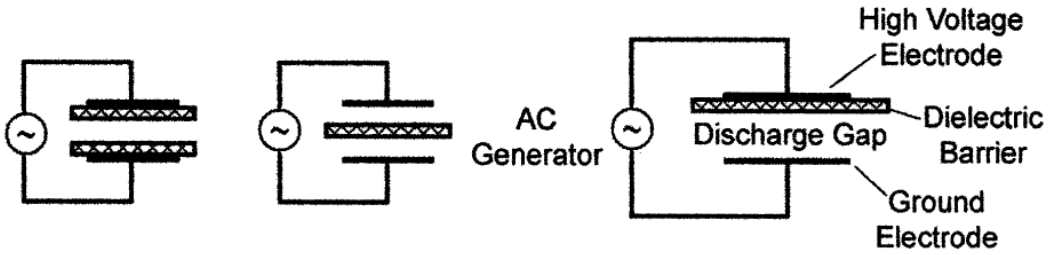

Figure 2.30: Schematic Drawings of the Three Main Designs of a Dielectric Barrier Discharges [36]

O_3 is produced by flowing O_2 gas at pressures of the order 10^5 Pa (1×10^5 Pa is equivalent to 1×10^3 mbar) through the dielectric barrier whilst applying an alternating current (AC). Direct current (DC) can not be used as the dielectric barrier, which acts as an insulator, and can not pass DC. When the electric field in the discharge gap is high enough, a large number of microdischarges are observed (see **Figure 2.31**). This results in an electric conductivity that is restricted by the microdischarges. The gas in the discharge gap serves as a background reservoir where the species absorb the energy dissipated by the microdischarges. This causes the gaseous species to become excited rather than ionized. Absorption of the energy produced by the microdischarges leads to the gaseous species dissociating.

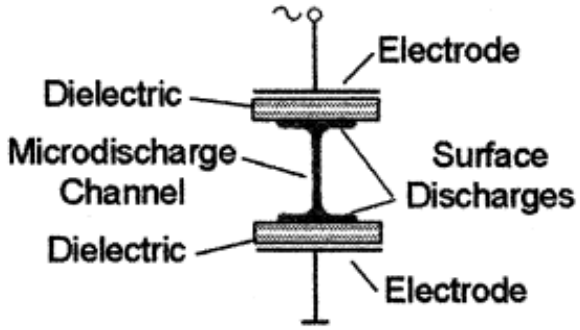

Figure 2.31: Schematic Drawing of a Microdischarge in a Dielectric Barrier Discharge Apparatus [36]

Although the formation of O_3 from O_2 (rather than air) is of interest in this study, this technique can be applied for the formation of excimers or the destruction of pollutants such as volatile organic compounds, ammonia, hydrogen sulfide, nitrogen oxides and sulfur dioxide [36]. Depending on the application, the dominant reaction type follows one of two paths: charged particle; or free-radical reactions. Charge particle reactions are generally observed in lower pressure discharges where a plasma is produced. In most dielectric barrier discharge applications, including ozonolysis, the dominant reaction type is free-radical. For the formation of O_3 from O_2, the dominant reaction pathway is the latter as shown in the reaction mechanism in **Figure 2.32**.

The initial major fraction of the energy gained by the electrons in the electric filed is used to excite the gaseous species (first two reaction steps) before the dissociation of the

$$O_2(X\ ^3\Sigma_g^-) + e^- \rightarrow O_2(A^3\Sigma^+_u) + e^- \qquad (\sim 6\ eV)$$

$$O_2(X\ ^3\Sigma_g^-) + e^- \rightarrow O_2(B^3\ \Sigma^-_u) + e^- \qquad (\text{starting at } 8.4\ eV))$$

$$O_2(X\ ^3\Sigma_g^-) \rightarrow O(^3P) + O(^3P)$$

$$O_2(X\ ^3\Sigma_g^-) \rightarrow O(^3P) + O(^1D)$$

$$O + O + M \rightarrow O_2 + M$$

$$O + O_2 + M \rightarrow O_3^* + M \rightarrow O_3 + M$$

$$O + O_3 + M \rightarrow 2O_2 + M$$

$$O + O_3^* + M \rightarrow 2O_2 + M$$

Figure 2.32: O_3 Formation Mechanism in an Ozonizer using O_2

O_2 molecules occurs (third and fourth reaction steps). Recombination of the O_2 molecule can occur through the fifth reaction step where *M* represents the third body which, if pure O_2 is used, is O, O_2 or O_3. From these species, O_3 is formed by the three-body reaction in the sixth step *via* the transient excited state species O_3^* and dissociates in the seventh and eight reaction steps.

Air can also be used to create O_3 but the quantity produced is limited by additional reactions between N_2 and O to form NO, N_2O, NO_2, NO_3 and N_2O_5. About half the O_3 formed from air is through indirect reactions so the O_3 formation process takes longer (approximately 100 μs) than with O_2 (approximately10 μs) [36]. In addition, if the air flow is reduced or the voltage set too high then O_3 or N_2O_5 is no longer formed. This process is known as discharge poisoning [36]. Under these conditions, the rapid formation of NO, N_2O and NO_2 consume the O atoms terminating the O_3 formation step. Any O_3 molecules already formed are removed from the system by reactions with NO and NO_2.

The optimum amount of O_3 formed is dependent on the microdischarge properties. If the microdischarges are too weak then energy is lost by ions whereas if the microcharges are too strong then the amount of dissociation of the O_2 molecule is too large limiting the O_3 formation reaction step. In an ozonizer, the amount of O_3 is controlled by the maximum applied voltage, V_{Max}. This relationship is described by the *dielectric barrier discharge power formula* in **Equation 2.13** [38] where *P* is the total

power, f the operating frequency, C_D and C_G the capacitances of the dielectric and discharge gap respectively, and V_{Min} the minimum external voltage at which microdischarges are observed in the discharge gap.

$$P = 4fC_D^2 + \frac{V_{Min}\left(V_{Max} - V_{Min}\right)}{C_D C_G} \tag{2.13}$$

Although V_{max} is the main variable influencing the rate of O_3 formation, other parameters that can be adjusted are distance of the discharge gap, the gas concentration and the gas flow. Due to this flexibility, ozonizers are the most commonly used technique to produce O_3 from small laboratory systems to large industrial scales [36]. However, other techniques are required to extract O_3 from the gas mixture. The simplest procedure to achieve this is by collecting the gas mixture in a glass tube or bulb and submerging it in liquid nitrogen. At this temperature, O_3 condenses onto the wall whilst O_2 remains in the gas-phase allowing this species to be pumped away. The glass tube or bulb containing the synthesis O_3 gas, once slowly warmed back to room temperatures, could be transferred to the glass gas handling lines on the apparatus used in this study. However, O_3 would decompose back to O_2 on the glass surfaces. This problem will need to be addressed if this technique was to be applied in this study.

A more complex technique using surface barrier discharges was developed by Alemskaya *et al.* [39]. Here they replaced the metal corona-free electrode with a low pressure discharge plasma. **Figure 2.33** displays the schematic drawing of the apparatus used. The design consists of two glass tubes one inside the other (numbered 2 and 3 on diagram) surrounded by a water-cooled tubular jacket (1). The cooling water acts as a corona-free electrode as well as preventing overheating of the system. Inserted inside the inner glass tube (3) is a leak tight tubular metal electrode (4). A nichrome coil corona electrode (5) surrounds the inner glass tube. Dried oxygen is released between the glass tubes through the inlet valve (6) and the O_3:O_2 gas mixture is collected through the outlet value (7). The inlet and outlet pipes to the water cooled tubular jacket are labelled (8) and (9) respectively. The advantage of using running water is that it acts as a grounded electrode preventing the outer sides of the apparatus becoming charged. This apparatus works by applying an AC voltage to the Nichrome coil corona electrode until a volume barrier discharge is created inside the inner glass

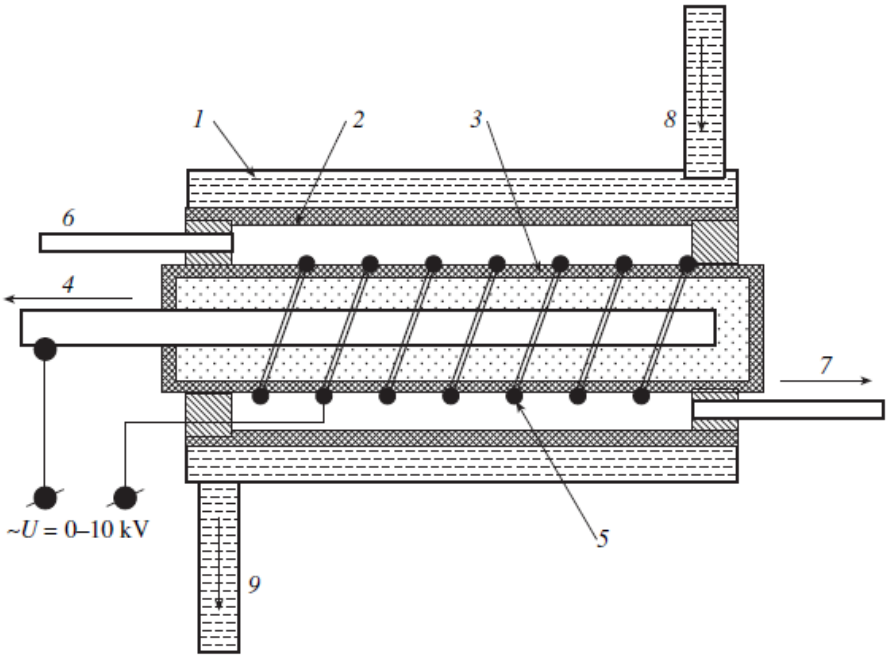

Figure 2.33: Schematic Diagram of the Surface Barrier Discharge Apparatus [39]

tube. As the voltage is increased further, a surface barrier discharge is formed between the Nichrome coils. This second barrier discharge leads to the formation of O_3 from the O_2 gas located between the outer and inner glass tubes. The most efficient O_3 synthesis was with an O_2 gas pressure of 6.65 kPa (equivalent to66.5 mbar) at an AC voltage between 2 to 10 kV. The highest O_3 concentration produced using this technique is approximately 200 g m^{-3} at a typical minimum energy consumption of 15 kW h kg^{-1} [39].

As with the ozonizer, the requirement to separate the O_2/O_3 mixture is a disadvantage. Furthermore, the surface barrier discharge is difficult to control in this apparatus and it has high utility requirements, both of power and cooling water. Although this could easy be plumbed into the existing system, the current water flow is already close to the minimum necessary so a second water supply and outlet pipe would need to be installed. Another disadvantage is that the characteristics of the surface barrier discharge are difficult to control and the apparatus would require a large amount of electrical energy to synthesize O_3.

Another *ex situ* O_3 synthesis technique uses RF irradiation of O_2. This method was applied in a recent astrophysically relevant laboratory study by Mokrane *et al*. [21].

The synthesis apparatus consisted of a copper coil surrounding a gas bottle containing approximately 30 mbar of O_2. The gas was excited by passing a RF electric discharge (approximately 2 MHz) through the copper coil and the blue gas of O_3 was formed by the recombination of O_2 and O species during the discharge. The O_3 gas was separated with liquid nitrogen cooling and the gas bottle mounted onto their apparatus system. Analysis of the synthesis gas revealed that some dissociation of O_3 on the inlet metallic surfaces had reduced the O_3 purity to 70%. Although there are RF sources already fitted on the dual atomic beam system, these are tuned to a frequency of 13.56 MHz for production of atomic O rather than O_3 synthesis. Installation of an additional RF source may cause interference in the exciting sources.

O_3 can also be formed through UV irradiation. This technique is widely used for a range of applications. In the formation of single walled carbon nanotubes, *UV-Ozone treatment* is used to suppress metal migration of a metal catalyst, such as Fe-Mo [40] whilst *UV cleaning* monitors the intensity of O_3 formed in comparison to CO, CO_2 and H_2O to remove hydrocarbon residues by the reaction of O atoms from semiconductor substrates [36]. The O_3 molecules are formed by irradiating O_2 gas with a UV lamp through the reaction mechanism shown in **Figure 2.34**. The main disadvantage with this technique is the amount of O_3 synthesised is restricted by the photodissociation step (bottom reaction in **Figure 2.34**). One method of resolving this problem is to combine the UV radiation with a dielectric-barrier discharge (or ozonizer) system [36]. In this case the UV radiation increases the amount of O_3 produced but the amount of photodissociation is reduced due to the gas flow. However, these systems require more power and water cooling.

$$O_2 \xrightarrow{h\upsilon} O + O$$
$$O + O_2 \longrightarrow O_3$$
$$O_3 \xrightarrow{h\upsilon} O_2 + O$$

Figure 2.34: O_3 Synthesis Mechanism using UV

O_3 can also be synthesized using a variety of set-ups based on a polmer electroyte membrane (PEM) cell. The apparatus used by Wang and co-workers [41] uses a PEM cell with an air cathode and nickel-antimony doped tin oxide anode (see **Figure 2.35**). O_2 was diffused from the air into the porous gas diffusion cathode before reacting with

electrons (from the external circuit) and protons to form H_2O. Oxidation of these H_2O molecules occurs at the anode to form O_3, electrons (to complete the external circuit) and protons (which diffuse back through the membrane to the cathode). Approximately 20 mg L^{-1} of the synthesized O_3 remains dissolved in the water. The remainder enters the gas-phase where the O_3 molecules are collected. In comparison to the other synthesis techniques, the concentration of O_3 formed is lower at typically 15%. Furthermore, other impurities in the gas mixture may necessitate additional purification steps and, therefore, the PEM cell technique is not suitable for this study.

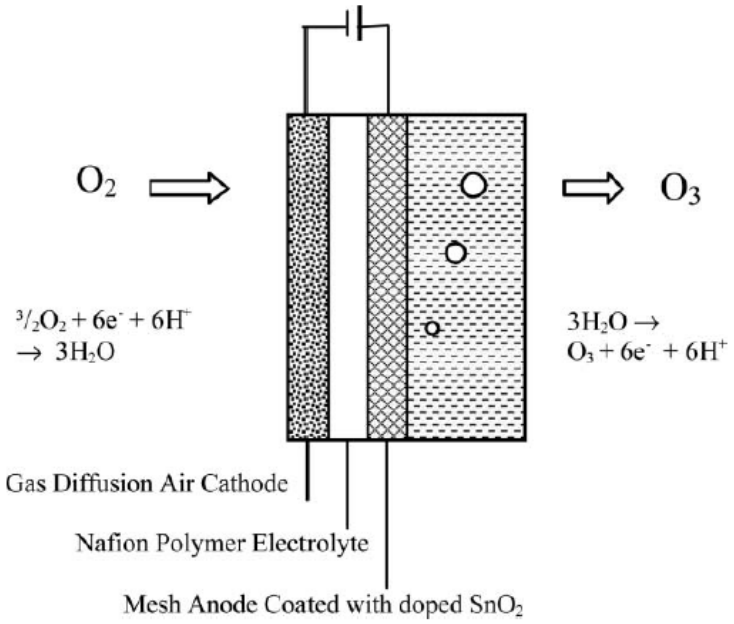

Figure 2.35: O_3 Synthesis using a PEM Cell [41]

Another technique used to form O_3 is through high voltage corona discharges. The apparatus required is similar to that of the dielectric barrier discharge used in ozonizers except that the discharge is applied between bare metal electrodes without the dielectric [36]. The main disadvantages with this technique are that the apparatus requires large amounts of energy and synthesizes very small amounts of O_3.

The main limitation with all the O_3 synthesis techniques described above is that they are formed outside the apparatus system. Not only would O_3 gas decompose inside the container but there would be an increased amount of decomposition when transferring the gas into the apparatus system, especially in the presence of metal surfaces. To reduce this rate, the synthesised gas would have to be formed fresh for each experiment.

Another problem with *ex situ* methods is the increased risk of contamination in the transfer process as this would ultimately lead to further decomposition of the O_3 gas.

Alternatively, O_3 can be formed *in situ* through recombination layer and irradiation techniques. These procedures typically have reduced amount of O_3 decomposition due to the limited number of surfaces the gas is exposed to and the risk of contamination in the transfer process is removed. The simplest synthesis procedure for forming O_3 *in situ* is by surface recombination and was proposed as a possible method by Mokrane *et al.* [21]. The technique works by dosing a layer of O atoms on top of pre-adsorbed layer of O_2 on a surface held below 25 K and waiting a set time for the adsorbed species to recombine to form O_3. The O and O_2 impurities could be desorbed from the surface by slowly heating the sample to 50 K. However, the amount of O_3 produced from this procedure would have to be calculated for each experiment which would lead to problems with reproducibility. Another problem with this technique is that the best synthesis results would only be obtained on relatively smooth surfaces. All the astronomically relevant surfaces are porous resulting in a proportion of the O_2 and O species diffusing into the porous network instead of recombining to form O_3. This problem would be complicated further if the substrate was coated with a thin water film, to represent the icy mantles on the interstellar dust grains, as a fair proportion of O_2 and O (predicted) would remain trapped in the water ice at 50 K [42]. O_3 could be synthesised in an adjacent chamber and vapour dosed into the main chamber but not only would this be difficult to control through a gate valve, there would also be a large amount of decomposition of O_3 on the UHV chamber walls making this process unsuitable. Overall, this technique would limit the choice of layered ice systems that could be explored in this study to those with O_3 as the bottom layer on top of the silica surface.

Another way of forming O_3 *in situ* is by low energy electron or UV irradiation of a deposited layer of O_2 or H_2O. These synthesis procedures have been used to explore the formation of O_3 in astronomically relevant ices (for more details see **Section 1.3.2**). Although O_3 can be synthesized from H_2O, there is no process that can remove the remaining H_2O layer without losing the synthesised O_3 molecules as well making the irradiation of H_2O unsuitable for this study. The removal of O_2 and O from the synthesised O_3 can be removed using the same temperature procedure as that for the recombination layer technique. However, the same technique problems would be

experienced for this as for those discussed for the formation of O_3 through recombination layer procedure.

Having considered the various methods of O_3 synthesis, the ozonizer was chosen as the most suitable for this research.. However, there would be problems with contamination from transferring the gas from the collection bottle to the UHV chamber and with the amount of decomposition of the O_3 molecules due to the increased exposure to a range of surfaces. To reduce the problems of transferring the O_3 gas, the ozonizer apparatus used in this study was designed to connect to the UHV system as shown in **Figure 2.7** (re-shown in more detail in **Figure 2.36**). The apparatus consists of an O_2 cylinder (standard purity of 99.999%), ozonizer (Pennwalt, BA.023012) and custom built glass to collect and separate the O_3 from the O_2 gas. Polytetrafluoroethylene (PTFE) tubing (blue line) was used to join these pieces together. The tubing was connected to the 1" diffusion pumping line, using a Swagelok stainless steel union with graphite ferrals, and to the glass gas handling line with a custom built glass connection join.

O_3 would be produced by leaking O_2 gas through the ozonizer at a set voltage and the gas mixture collected in the glass tube. With the glass tube held in the liquid nitrogen, the O_3 would condense in the silica gel, which causes less decomposition than the glass [43], whilst O_2 was pumped away using the 1" diffusion pumping line. When enough O_3 had been formed, the valve joining the glass tube to the ozonizer would be closed and the liquid nitrogen trap removed. The slow evaporation of O_3 from the silica gel would result in a blue gas being observed. This gas would be collected into one of the glass dosing bulbs on the glass gas handling line where O_3 could be background deposition into the central chamber. However, the quantity of O_3 synthesis would need to be calibrated by varying the O_2 gas flow from the cylinder and adjusting the ozonizer voltage setting.

The initial calibrations planned involve visually observing the presence and intensity of the blue O_3 gas synthesised in the glass tube after the liquid nitrogen cooling is removed. Further analysis of the best settings would be performed by analyzing the O_3 purity in the central chamber using the SRS mass spectrometer (**Figure 2.5**). This can be best achieved with cryogenic cooling switched off to prevent O_3 adsorption on cold surfaces.

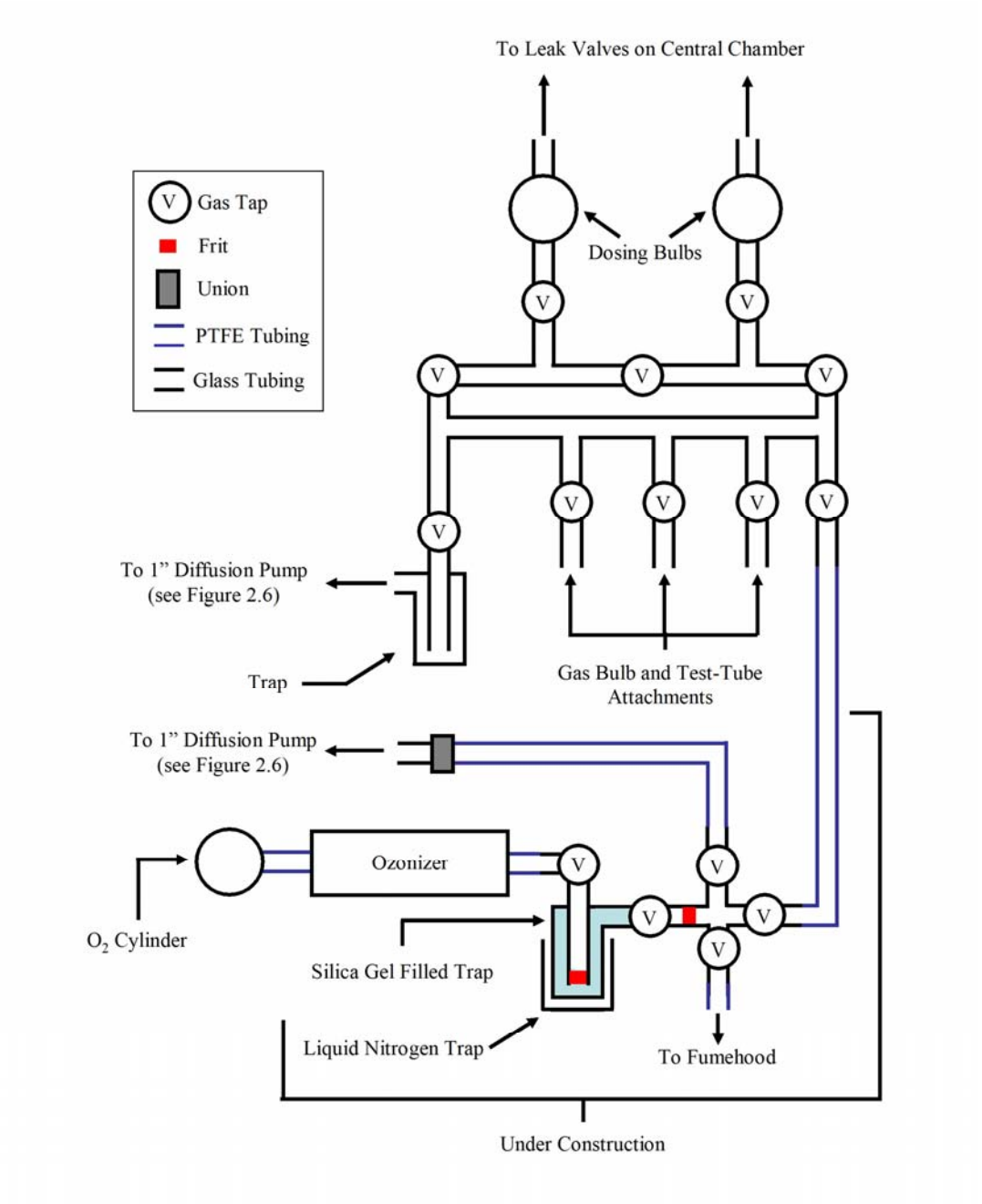

Figure 2.36: Schematic Drawing of the *In situ* Ozonizer Apparatus
(Previously Displayed as **Figure 2.7**)

The best synthesis settings will be used to form O_3 for the required range of TPD experiments. Currently these include: O_3 from bare silica; O_3 from porous amorphous solid water (pASW) (adsorbed onto the surface held at base temperatures) on silica; O_3 from compact amorphous solid water (cASW) (adsorbed onto the surface held at 100 K) on silica; and O_3 from O_2 on silica. However, due to the late arrival of the equipment, the apparatus for the O_3 system is under construction.

2.6 References

[1] H. J. Fraser, M. P. Collings and M. R. S. McCoustra, *Rev. Sci. Instr.*, 2002, **73**, 2161.

[2] M. P. Collings, J. W. Dever, H. J. Fraser, M. R. S. McCoustra and D. A. Williams, *Astrophysics Journal*, 2003, **583**, 1058.

[3] R. Jones and S. Turton, *Surface Science*, 1997, **377-379**, 719.

[4] R. Jones, *Surface Science*, 1999, **424**, 127.

[5] D. Brownlee, P. Tsou, J. Aleon, C. M. O. D. Alexander, T. Araki, S. Bajt, G. A. Baratta, R. Bastien, P. Bland, P. Bleuet, J. Borg, J. P. Bradley, A. Brearley, F. Brenker, S. Brennan, J. C. Bridges, N. D. Browning, J. R. Brucato, E. Bullock, M. J. Burchell, H. Busemann, A. Butterworth, M. Chaussidon, A. Cheuvront, M. Chi, M. J. Cintala, B. C. Clark, S. J. Clemett, G. Cody, L. Colangeli, G. Cooper, P. Cordier, C. Daghlian, Z. Dai, L. D'Hendecourt, Z. Djouadi, G. Dominguez, T. Duxbury, J. P. Dworkin, D. S. Ebel, T. E. Economou, S. Fakra, S. A. J. Fairey, S. Fallon, G. Ferrini, T. Ferroir, H. Fleckenstein, C. Floss, G. Flynn, I. A. Franchi, M. Fries, Z. Gainsforth, J. P. Gallien, M. Genge, M. K. Gilles, P. Gillet, J. Gilmour, D. P. Glavin, M. Gounelle, M. M. Grady, G. A. Graham, P. G. Grant, S. F. Green, F. Grossemy, L. Grossman, J. N. Grossman, Y. Guan, K. Hagiya, R. Harvey, P. Heck, G. F. Herzog, P. Hoppe, F. Horz, J. Huth, I. D. Hutcheon, K. Ignatyev, H. Ishii, M. Ito, D. Jacab, C. Jabonsen, S. Jaconsen, S. Jones, D. Joswiak, A. Jurewicz, A. T. Kearsley, L. P. Keller, H. Khodja, A. L. D. Kilcoyne, J. Kissel, A. Krot, F. Langenhorst, A. Lanzirotti, L. Le, L. A. Leshin, J. Leitner, L. Lemelle, H. Leroux, M. C. Liu, K. Luening, I. Lyon, G. MaxPherson, M. A. Marcus, K. Marhas, B. Marty, G. Matrajt, K. McKeegan, A. Meibom, V. Mennella, K. Messenger, S. Messenger, T. Mikouchi, S. Mostefaoui, T. Nakamura, T. Nakano, M. Newville, L. R. Nitter, I. Ohnishi, K. Ohsumi, K. Okudaira, D. A. Papanastassiou, R. Palma, M. E. Palumbo, R. O. Pepin, D. Perkins, M. Perronnet, P. Pianetta, W. Rao, F. J. M. Rietmeijer, F. Robert, D. Rost, A. Rotundi, R. Ryan, S. A. Sandford, C. S. Schwandt, T. H. See, D. Schlutter, J. Sheffield-Parker, A. Simionvici, S. Simon, I. Sitnitsky, C. J. Snead, M. K. Spencer, F. J. Stadermann, A. Steele, T. Stephen, R. Stroud, J. Susini, S. R. Sutton, Y. Suzuki, M. Taheri, S. Taylor, N. Teslich, K. Tomeoka, N. Tomioka, A. Toppani, J. M. Trigo-Rodriguez, D. Troadec, A. Tsuchiyama, A. J. Tuzzolino, T. Tyliszczak, K. Uesugi, M. Velbel, J. Vellenga, E. Vicenzi, L.

Vincze, J. Warren, I. Weber, M. Weisberg, A. J. Westphal, S. Wirick, D. Wooden, B. Wopenka, P. Woziakiewicz, I. Wright, H. Yabuta, H. Yano, E. D. Young, R. N. Zare, T. Zega, K. Ziegler, L. Zimmerman, E. Zinner and M. Zolensky, *Science*, 2006, **314**, 1711.

[6] J. D. Thrower, Heriot-Watt University, 2009.

[7] J. D. Thrower, M. P. Collings, F. J. M. Rutten and M. R. S. McCoustra, *Monthly Notices of the Royal Astronomical Society*, 2009.

[8] G. Attard and C. Barnes, *Surfaces*, Oxford University Press, Oxford, 2004.

[9] D. Woodruff and T. Delchar, *Modern Techniques of Surface Science*, 2nd edn., Cambridge University Press, Cambridge, 1994.

[10] K. Kolasinski, *Surface Science: Foundations of Catalysis and Nanoscience*, Wiley, 2002.

[11] A. Herring, T. McKinnon, D. Petrick, K. Gneshin, J. Filey and B. McCloskey, *J. Anal. Appl. Pyrol*, 2003, **66**, 165.

[12] R. Gengenbach, C. Hahn and J. P. Toennies, *Phys. Rev. A*, 1973, **7**, 98.

[13] R. Gengenbach, J. Strunck and J. P. Toennies, *J. Chem. Phys.*, 1971, **54**, 1830.

[14] G. Wolber, H. Figger, R. A. Haberstoh and S. Penselin, *Phys. Lett.*, 1969, **29A**, 461.

[15] J. Geddes, P. N. Clough and P. L. Moore, *J. Chem. Phys.*, 1974, **64**, 2145.

[16] G. W. Fuchs, H. M. Cuppen, S. Ioppolo, C. Romanzin, S. E. Bisschop, S. Anderson, E. F. van Dishoeck and H. Linnartz, *Astron. Astrophys.*, 2009, **505**, 629.

[17] H. Boenig, *Plasma Science and Technology*, Cornell University Press, London, 1982.

[18] J. R. Roth, *Industrial Plasma Engineering*, IOP Publishing Ltd., London, 1995.

[19] G. Scoles, D. Bassi, U. Buck and D. Laine, *Atomic and Molecular Beam Techniques*, Oxford University Press, Oxford, 1988.

[20] N. Watanabe, A. Nagaoka, H. Hidaka, T. Shiraki, T. Chigai and A. Kouchi, *Planet. Space Sci.*, 2006, **54**, 1107.

[21] H. Mokrane, H. Chaabouni, M. Accolla, E. Congiu, F. Dulieu, M. Chehrouri and J. L. Lemaire, *Ap. J.*, 2009, **705**, L195.

[22] J. E. Roser, G. Manico, V. Pirronello and G. Vidali, *Ap. J.*, 2002, **581**, 276.

[23] V. Pirronello, C. Liu, L. Shen and G. Vidali, *Ap. J.*, 1997, **475**, L69.

[24] P. Atkins and J. de Paula, *Atkins' Physical Chemistry*, 7 edn., Oxford University Press, Oxford, 2002.

[25] F. Dulieu, L. Amiaud, E. Congiu, J. H. Fillion, E. Matar, A. Momeni, V. Pirronello and J. L. Lemaire, *Astron. Astrophys.*, 2010, **512**, A30.

[26] G. Vidali, J. Roser, G. Manico and V. Pirronello, *Adv. Spa. Res.*, 2004, **33**, 6.

[27] Edwards, *Instruction Manual: E02K, E04K, E06K and E09K Diffusion Pumps*, Issue D edn., Edwards High Vacuum International, Sussex.

[28] J. S. Foord, N. K. Singh, E. T. FitzGerald, G. J. Davies and A. C. Jones, *J. Cryst. Growth*, 1992, **120**, 103.

[29] C. L. Levoguer, J. S. Foord, G. J. Davies and P. J. Skevington, *J. Cryst. Growth*, 1994, **136**, 109.

[30] M. L. Yu and L. A. DeLouise, *Surf. Sci. Rep.*, 1994, **19**, 285.

[31] J. D. Thrower, Heriot-Watt University, 2009.

[32] G. Sauerbrey, *Z. Phys.*, 1959, **155**, 206.

[33] R. G. Greenler, *J. Chem. Phys.*, 1966, **44**, 310.

[34] M. E. Palumbo, G. A. Baratta, M. P. Collings and M. R. S. McCoustra, *Phys. Chem. Chem. Phys.*, 2006, **8**, 279.

[35] M. E. Palumbo, *Astron. Astrophys.*, 2006, **453**, 903.

[36] U. Kogelschatz, *Plasma Chem. Plasma Processing*, 2003, **23**, 1.

[37] W. Siemems, *Poggendorff's Ann. Phys. Chem.*, 1857, **102**, 66.

[38] T. C. Manley, *Trans. Electrochem. Soc.*, 1943, **84**, 83.

[39] O. P. Alemskaya, V. M. Lelevkin, A. V. Tokarev and V. A. Yudanov, *High Energy Chemistry*, 2005, **39**, 307.

[40] T. J. Lee and H. Lee, *Carbon*, 2008, **46**, 1443.

[41] Y. Wang, S. Cheng and K. Chan, *Green Chemistry*, 2006, **8**, 568.

[42] M. P. Collings, M. A. Anderson, R. Chen, J. W. Dever, S. Viti, D. A. Williams and M. R. S. McCoustra, *Mon. Not. R. Astron. Soc.*, 2004, **354**, 1133.

[43] J. T. Yates, *Experimental Innovations in Surface Science: a Guide to Practical Laboratory Methods and Instruments* Verlag Inc., New York, 1998.

CHAPTER 3 - Atomic Beam System Characterisation

Contents

3.1 Introduction

This chapter focuses on the experiments performed to characterise the atomic and molecular oxygen beams in the new dual atomic beam system. **Section 3.2** analyzes the atomic oxygen and hydrogen plasmas (**Section 3.2.2** and **3.2.3** respectively). **Section 3.3** discusses the experiments to determine the position of the O atomic beam in the central UHV chamber using the quartz crystal microgravimetry (QCM) apparatus and the mass deposited onto the crystal over time. The final set of calibration experiments discussed in this chapter calculates the O_2 beam flux through pump-down experiments (**Section 3.4.2**) and the $O:O_2$ dissociation fraction by cracking fraction calibrations (**Section 3.4.3**). Similar experiments were planned for the hydrogen atomic and molecular beams but due to continuous problems with the RF powered plasma source (see **Section 2.2.2**) this was not achieved in this study. The summary and conclusions to this chapter are discussed in **Section 3.5**.

3.2 Plasma Analysis

3.2.1 Introduction

This section explores the analysis of the RF powered atomic O and H plasmas (**Sections 3.2.2** and **3.2.3** respectively). Each sub-section reviews the ease of producing the atomic plasma. The dissociation mechanism and the emission peak wavelengths, λ, are discussed and compared against example plasma spectra obtained from this study. Additional emission peaks are identified along with suggestions for the chemical reactions that produced them. Further analysis of the O plasma in **Section 3.2.2** explores the relationship of the plasma chamber pressure, P, against intensity for a selection of emission peaks over a range of different RF powers. The information obtained was used to determine the best settings for the plasma source used for the atomic O beam experiments performed in **Chapter 6** and in the future. The summary and conclusions are discussed in **Section 3.2.4**.

3.2.2 O Plasma Analysis

As discussed in **Section 2.3.2**, the ease of producing an atomic plasma depends on the ability to ionize the precursor molecule and its bond dissociation enthalpy. In the case of O_2, the atomic plasma was relatively easy to form. This is due to partial shielding of

the outer electrons from the nucleus of the O_2 molecule which allows easier ionization. This process provided the necessary free electrons required to change the plasma from the low brightness molecular mode to the high brightness atomic mode. However, the O_2 molecule contains a double bond causing the molecule to have a higher bond dissociation enthalpy (497 kJ mol^{-1} at 298 K [1]) compared with a molecule containing a single bond. This prevents the atomic plasma from having a high dissociation fraction. Additionally, the efficiency of O_2 dissociation was reduced by the molecule's electronegative nature. The presence of a noble gas (like helium or argon) applied through the secondary gas technique can increase the O_2 dissociation fraction [2] but this was not attempted in this study. The RF and MW atomic O beams reviewed in **Section 1.3.3** do not use the secondary gas technique and typically contain dissociation fractions of 30 to 40 % [3, 4].

Before dissociation can occur, the molecules require enough internal energy for the atoms to separate. In this case, the RF energy was supplied to the O_2 gas in the reactor of the plasma source leading to the molecules becoming excited and ionizing to produce the free electrons. The free electrons continued to transfer the RF energy through elastic and inelastic electron-molecule collisions. The ratio of elastic to inelastic collisions determines whether a molecular (low brightness mode) or atomic (high brightness mode) plasma is formed. A more detailed explanation of the plasma physics and chemistry has previously been given in **Chapter 2** so a brief description is given here specifically for the O plasma.

In the low brightness mode, the free electrons with energies around 4.53 eV (equivalent to 437 kJ mol^{-1}) [1] [5] excite the ground state molecules into the lower excited molecular states (as described by the reaction mechanism displayed in **Figure 3.1**). Excitation into the dissociation region does not occur with significant probability in a vertical transition from these excited states [6]. Instead the O_2 molecule is electronically excited upon electron impact. To return to the ground state, the molecules emit radiation through fluorescence. From the lowest molecular excited state ($a^1\Delta_g$), the emission peak wavelength, λ, occurs at 1.27 μm [7] whilst the fluorescence transition from the second lowest molecular state ($b^1\Sigma_g^+$) has an emission peak at 761.8 nm [8]. Although the first emission peak occurs in the IR region of the electromagnetic spectrum, the latter lies in

[1] 1 eV equals 96.485 kJ mol^{-1} [1]

the visible range allowing this peak to be observed with the optical spectrometer used in this study.

$$O_2(X^3\Sigma_g^-) + e^- \rightarrow O_2(a^1\Delta_g) + e^-$$

$$O_2(X^3\Sigma_g^-) + e^- \rightarrow O_2(b^1\Sigma_g^+) + e^-$$

Figure 3.1: Low Brightness Mode Excitation Reactions in O_2 Plasma

In the high brightness mode, the concentration of free electrons in the plasma has increased in comparison to the low brightness mode. This allows the O_2 molecules to reach higher molecular excited states which can result in dissociation. The potential energy curve displayed in **Figure 3.2** reveals that the O atoms can be formed in different excited states depending on the electron energy of the vertical transition (shaded area) [6]. Dissociation can occur directly from the ground state, $O_2(X^3\Sigma_g^-)$, to form two O atoms in the ground state, (^{3}P), but this process is spin forbidden and requires electron energies of 5.16 eV (498 kJ mol^{-1}) [9]. Alternatively, dissociation occurs readily through the O_2 molecular excited states. The two lowest molecular excited states ($a^1\Delta_g$ and $b^1\Sigma_g^+$) have similar potential energy curves to that of $O_2(X^3\Sigma_g^-)$ and so are not shown in **Figure 3.2** but these cannot be excited into the dissociation region (as previously discussed). The first dissociation region (labelled *I* on **Figure 3.2**) includes dissociation from the $c^1\Sigma_u^-$, $A'^3\Delta_u$ and $A^3\Sigma_u^+$ excited states, which are produced following excitation at electron energies around 6 eV (roughly 580 kJ mol^{-1}), to form two O(^{3}P) atoms. The potential energy curves for the $A'^3\Delta_u$ and $A^3\Sigma_u^+$ excited states are similar in shape and energy to that of the $c^1\Sigma_u^-$ so only the latter potential energy curve is displayed.

Excitation into the higher excited molecular states with electron energies of around 8 eV (roughly 770 kJ mol^{-1}), like $O_2(B^3\Sigma_u^-)$, leads to the formation of O atoms in the second dissociation region (labelled II in **Figure 3.2**). Here one O atom is formed in the ground state O(^{3}P) and the second in the first atomic excited state O(^{1}D). The amount of O(^{1}D) formed in proportion to O(^{3}P) is of interest in this study as the vast majority of

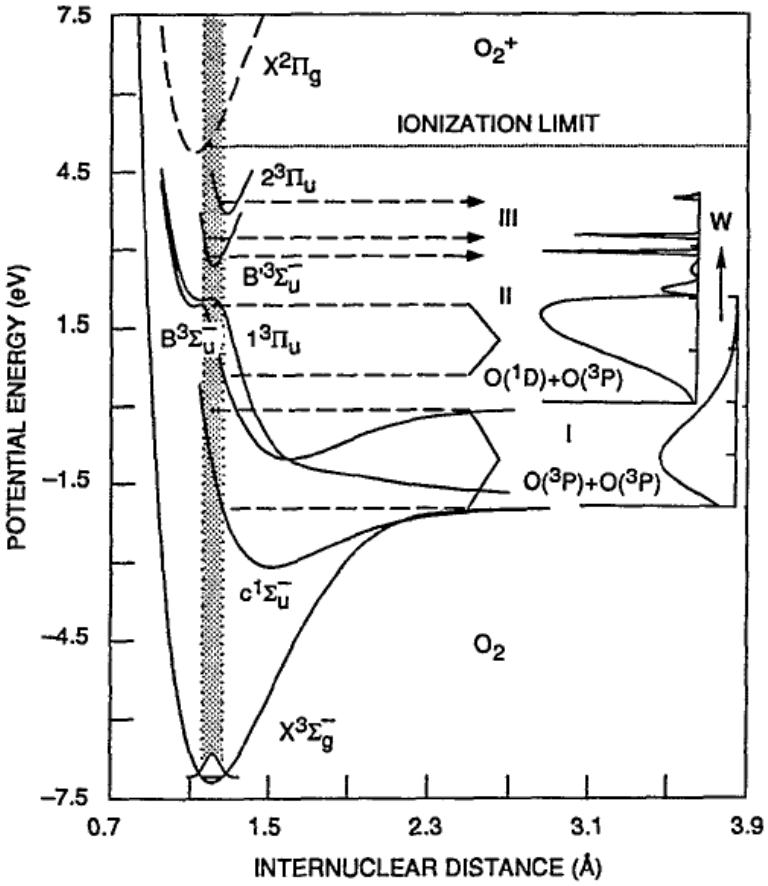

Figure 3.2: Potential Energy Curves for the Dissociation of O_2 Through Electron Impact. Shaded Area Indicates the Vertical Excited Region from $O_2(X^3\Sigma_g^-)$ (v=0) [6]

the O atoms in the ISM are believed to be in the ground state. As a consequence, the proportion of O(^{1}D) to O(^{3}P) produced in the plasma ideally needs to be relatively small to reliably mimic the conditions of the ISM. The exact proportion of O(^{1}D) is difficult to determine as the excited atom can be deactivated through radiation or collision (bottom two reaction steps in **Figure 3.3** where *M* represents an additional body). However, electric dipole transitions occurring between singlet and triplet states are forbidden which would usually prevent a radiation deactivation route from occurring. Instead the species can decay through the emission on a magnetic dipole or electric quadrupole transition. In this case, O(^{1}D) decayed to the O(^{3}P) state by magnetic dipole transitions at 630.0 and 636.4 nm (top reaction step in **Figure 3.3**) [10, 11]. The radiative lifetime of O(^{1}D) in the gas-phase is 148 s [6] and the solid state collisional deactivation is rapid resulting in the O(^{1}D) to O(^{3}P) transition being difficult to observe [8].

$$O\,(^1D) \rightarrow O\,(^3P) + h\upsilon$$

$$O(^1D) + M \rightarrow O\,(^3P) + M$$

$$O(^1D) + O_2(X\,^3\Sigma_g^-) \rightarrow O_2(b^1\Sigma) + O(^3P)$$

Figure 3.3: Deactivation of $O(^1D)$

Dissociation of O_2 with higher electron energies results in the formation of O atoms in the second lowest excited state, $O(^1S)$. Radiative transitions from this excited state to the lower atomic states are electric dipole forbidden but, like the $O(^1D) \rightarrow O(^3P)$ transition, radiative deactivation still occurs. The decay of the $O(^1S)$ to $O(^1D)$ occurs through an electric quadrupole transition with an emission peak at 557.7 nm [10]. $O(^1S)$ can also decay to the atomic ground state by emitting radiation through a magnetic dipole transition at 297.2 nm [10]. At even higher electron energies, the O_2 molecule can dissociate to form an O atom and an O^+ ion of which two examples are displayed in **Figure 3.4** [12]. The first reaction occurs with electron energies around 28 eV (2700 kJ mol^{-1}) and forms the O^+ ion in the ground state. The $O(^3S)$ excited state lies above the $O(^1S)$ and $O(^5S)$ atomic states and decays to the ground state with emission peaks at 130.2, 130.5 and 130.6 nm [10]. The second reaction requires a larger amount of electron energy and forms the O atom in the ground state and the O^+ ion in the second lowest excited state. Radiative decay of the $O^+(^2P)$ ion to the ground state occurs in a two step process. The first step is the $O^+(^2P) \rightarrow O^+(^2D)$ electric quadrupole transition which forms emission peaks at 731.9 and 733.0 nm [10]. Radiative decay from the O^+ lowest excited state to the ground state ($O^+(^2D) \rightarrow O^+(^4S)$) can occur either through a magnetic dipole transition at 372.6 nm or by the electric quadrupole transition at 372.9 nm [10].

$$O_2(X\,^3\Sigma_g^-) + e^- \rightarrow O(^3S) + O^+(^4S) + 2e^-$$

$$O_2(X\,^3\Sigma_g^-) + e^- \rightarrow O(^3P) + O^+(^2P) + 2e^-$$

Figure 3.4: Example Dissociation Reactions to Form O^+ Ions

Excitation into O_2 excited molecular states above the ionization limit results in the formation of the O_2^+ ion. As with O atoms, the O_2^+ ion can be formed in its ground or excited states from which fluorescence transitions can occur. An example is the $O_2^+(A^2\pi_u) \rightarrow O_2^+(X^2\pi_g)$ first excited state to ground state fluorescence transition which occurs as a broad emission band with peaks at 383.0, 385.9, 408.2, 411.6, 433.9 and 549.8 nm [13]. As with the $O(^1D)$ species, the ratio of $O(^1S)$ atoms, and O^+ and O_2^+ ions to $O(^3P)$ in this study should be negligible so that the atomic beam irradiation experiments performed in the laboratory can be accurately transferred into the conditions found in the ISM. By knowing the wavelengths of these undesirable transitions, the RF powered plasma source settings were adjusted to minimise the intensity of these emission peaks in order to reduce the abundance of these species.

Another collection of emission peaks that occurs in the high brightness mode is the fluorescence transitions from O_2 molecular excited states. These transitions are present as not all the gas in the reactor of the RF powered plasma source dissociates or ionizes. An example transition is the $O_2(B^3\Sigma_u^-) \rightarrow O_2(X^3\Sigma_g^-)$ resulting in the Schumann-Runge band between 175 and 205 nm [14] which is just outside the visible range.

Optical emission analysis of the atomic O plasma cannot determine the $O{:}O_2$ dissociation fraction as only the fluorescence transitions from excited species are observed. These fluorescence transitions are further limited in this study to those in the visible range of the electromagnetic spectrum. Attempts to measure the dissociation fraction of the atomic O beam were made in **Section 3.4.3** but this will have to be repeated in the future once the modifications to the apparatus have been completed.

The general reaction mechanism describing the excitation, ionization and dissociation processes occurring in the atomic O plasma discussed above is displayed in the top and middle section of **Figure 3.5**. The dominant reactions in the mechanism required to produce a stable atomic O plasma are shown in bold. If the electron energies were increased by increasing the RF power, the ionization and dissociation reactions to form O_2^+, O_2^-, O^+ and O^- would become dominant and an ion-molecule plasma would be obtained which is not desired in this research. The final group of reactions displayed in **Figure 3.5** describe the O_2 recombination processes. The dominance of these reactions

must be low in comparison to the excitation and dissociation reaction steps otherwise the atomic plasma would fail.

$$\mathbf{O_2 + e^- \rightarrow O_2^* + e^-}$$
$$O_2 + e^- \rightarrow O_2^+ + 2e^-$$
$$O_2 + e^- \rightarrow O_2^-$$
$$2O_2 + e^- \rightarrow O_2 + O_2^-$$
$$O_2^* + e^- \rightarrow O_2^+ + 2e^-$$

$$\mathbf{O_2 + e^- \rightarrow 2O + e^-}$$
$$\mathbf{O_2^* + e^- \rightarrow 2O + e^-}$$
$$O_2 + e^- \rightarrow O + O^-$$
$$O_2^* + e^- \rightarrow O + O^-$$
$$O_2^+ + e^- \rightarrow 2O$$
$$O_2^- \rightarrow O + O^-$$

$$2O + O_2 \rightarrow 2O_2$$
$$O^- + O \rightarrow O_2 + e^-$$
$$O_2^- + O_2^* \rightarrow 2O_2 + e^-$$
$$O_2^+ + e^- + M \rightarrow O_2 + M$$

Figure 3.5: Processes Occurring in O_2 Glow Discharge Plasmas

The emission peaks for the O bound-bound transitions are displayed in a *Grotrian* diagram (**Figure 3.6**) [15]. Additional O bound-free transitions connect all the atomic energy levels with the O_2 ground state (labelled O II on diagram) but these were not shown for clarity. The forbidden $O(^1D) \rightarrow O(^3P)$ transition is represented by the red line labelled [OI] whilst the other red line (labelled OI IR3) indicates the dominant O transition which has an emission peak at 777 nm. By using the Grotrian diagram, the atomic O transitions that are of interest in this study were determined. These transitions along with their emission peaks are displayed in **Table 3.1**.

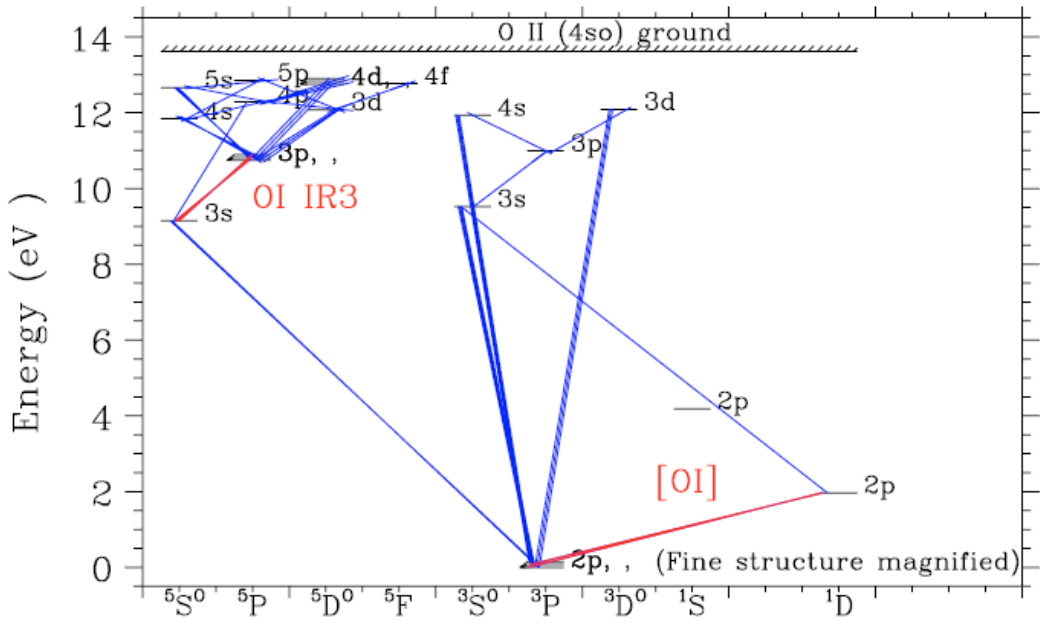

Figure 3.6: Grotrian Diagram for O [15]

O Transition	Emission Peak / nm
$(3p\ ^5P) \rightarrow (3s\ ^5S)$	777.7
$(3p\ ^3P) \rightarrow (3s\ ^3S)$	844.6
$(5s\ ^5S) \rightarrow (3p\ ^5P)$	645.6
$(4d\ ^5D) \rightarrow (3p\ ^5P)$	615.7
$(5d\ ^5D) \rightarrow (3p\ ^5P)$	533.0
$(4p\ ^3P) \rightarrow (3s\ ^3S)$	436.8
$(4p\ ^5P) \rightarrow (3s\ ^5S)$	394.8

Table 3.1: O Transitions and Emission Peaks [2, 11]

An example spectrum of an atomic O plasma (formed at 150 W with a plasma chamber pressure of 1.0×10^{-4} mbar) obtained from the RF powered plasma source used in this study is displayed in **Figure 3.7**. The most intense peak occurred at 777 nm corresponding to the $O(3p\ ^5P) \rightarrow O(3s\ ^5S)$ but other weaker O emission peaks were detected at 848, 645, 616, 533, 437 and 395 nm. Radiative deactivation of O atoms and

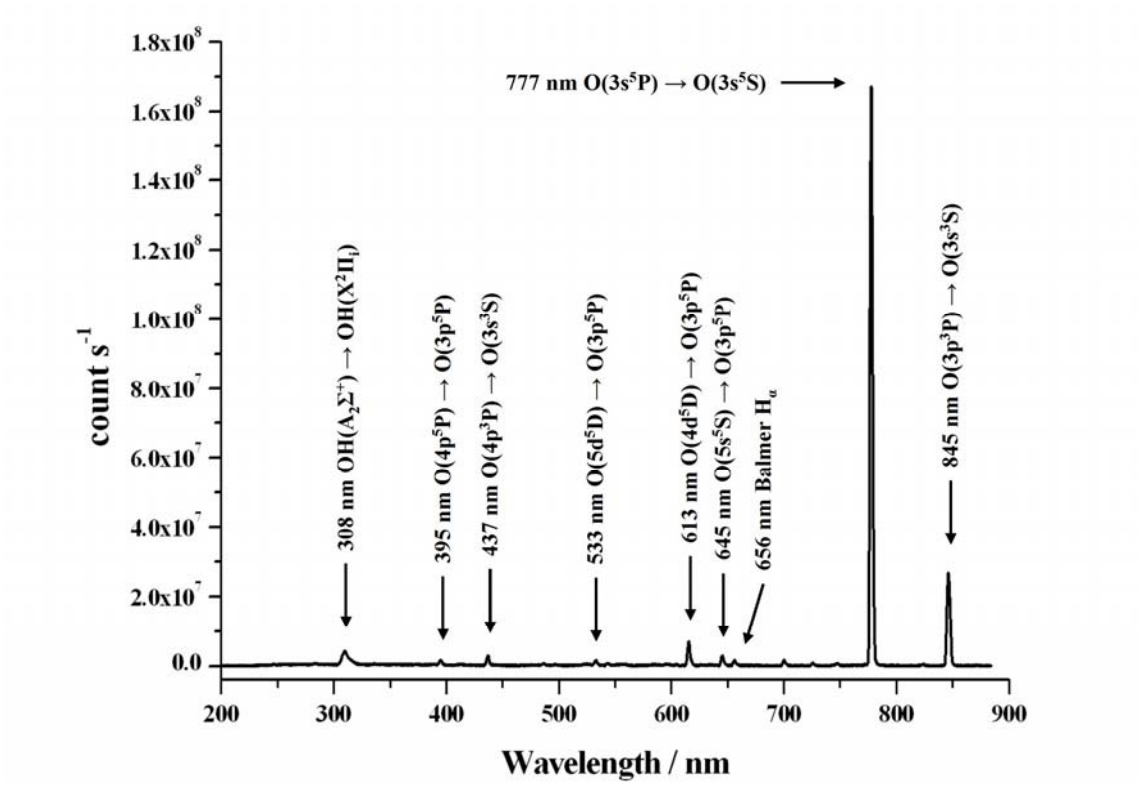

Figure 3.7: Example Spectrum of an Atomic O Plasma

O^+ ions from the excited states discussed above was not observed. The $O_2^+(A^2\pi_u) \rightarrow O_2^+(X^2\pi_g)$ transition emission band peaks were also not observed suggesting that the vast majority of the O_2 molecules were dissociating from those molecular states below the $O_2(B^3\Sigma_u^-)$ molecular excited state. However, the $O(^1D) \rightarrow O(^3P)$ transition is very weak and could possibly be occuring below the detection limit of the spectrometer. If this was the case, emission peaks relating to the collisional deactivation of $O(^1D)$ atoms would be observed. An example would be the $O_2(b^1\Sigma) \rightarrow O_2(X^3\Sigma^-_g)$ transition (see **Figure 3.3**) at 761.8 nm but this was not detected in this RF plasma spectrum. Other peaks assigned in the atomic O plasma spectra included the Balmer H_α (656 nm) (see **Section 3.2.3** for more details) and the $OH(A^2\Sigma^+) \rightarrow OH(X^2\Pi_i)$ transition (308 nm) suggesting that other chemical reactions were occurring in the plasma.

The dominant collision routes in a glow discharge plasma are between ion-neutral and neutral-neutral species as the gas in the plasma source reactor is only weakly ionized [5]. The dominant species in the plasma chamber, when the beam was not in

operation, was H_2 which is known to react rapidly with $O(^1D)$ atoms (as shown in **Figure 3.8**) but not with $O(^3P)$ [16]. Collisional deactivation of $O(^1D)$ could result in the formation of OH (which was observed at 308 nm) reducing the possibility of detecting the very weak $O(^1D)$ radiative decay transitions at 630.0 and 634.4 nm [17]. Further collision reactions of the produced OH radical with H_2 could result in the formation of H_2O.

$$O(^1D) + H_2 \rightarrow H_2 + O(^3P)$$
$$O(^1D) + H_2 \rightarrow H + OH$$
$$O(^1D) + H_2 + M \rightarrow H_2O + M$$

Figure 3.8: $O(^1D)$ Deactivation Reactions with H_2 [17]

An alternative OH formation mechanism is from the reactions of H atoms with O or O_2 (see **Figure 3.9**). The strongest Balmer H atom emission peak (H_α) was weakly observed in the atomic O plasma spectra (**Figure 3.7**) indicating the presence of H atoms. These atoms could be formed through the dissociation of H_2 molecules which occurs at electron energies of 9 eV (roughly 870 kJ mol^{-1}) or greater [5]. As a consequence, electrons with this amount of energy would also result in the formation of $O(^1D)$ atoms (which requires around 770 kJ mol^{-1}) despite the lack of evidence for the very weak magnetic dipole transitions. This suggests that if OH radicals were formed with reactions of O and O_2 through dissociated H_2 molecules, then the $O(^1D)$ atoms also formed at these electron energies must be reacting rapidly to form either OH or H_2O.

$$H_2 + e^- \rightarrow 2H + e^-$$
$$H + O \rightarrow OH$$
$$H + O_2 + M \rightarrow HO_2 + M$$
$$H + HO_2 \rightarrow H_2 + O_2$$
$$H + HO_2 \rightarrow 2OH$$
$$H + HO_2 \rightarrow H_2O + O$$

Figure 3.9: H Reactions Occurring in the Atomic O Plasma [5]

A third possible formation route of the OH radial is through the dissociation of H_2O. The bond dissociation enthalpy of the H-O bond in H_2O is 492 kJ mol^{-1} (at 298 K) [1] which is lower than the bond dissociation enthalpy for the O=O bond. Unlike most other species, H_2O cannot be raised into the excited molecular states without directly resulting in ionization or dissociation through the ionized species [18]. As a consequence, the neutral H_2O molecule has no electronic emission and therefore cannot be detected by the spectrometer alone. Ionization through electron impact in the plasma results in the formation of H_2O^- ions. A hypothetical energy level diagram used by Schulz to describe the dissociation of H_2O through the H_2O^- ion is displayed in **Figure 3.10** [19] and reveals that the H and OH dissociated species formed were both in the excited states. The emission peaks from the H atoms formed with lower electron energies were found in the Lyman range (see **Section 3.2.3**), which occurs in the UV region of the electromagnetic spectrum. This is outside of the detection range of the spectrometers used in this study. Excitation of the H_2O^- ion into higher excited states results in the emission of radiation in the measurable Balmer range (visible region) by

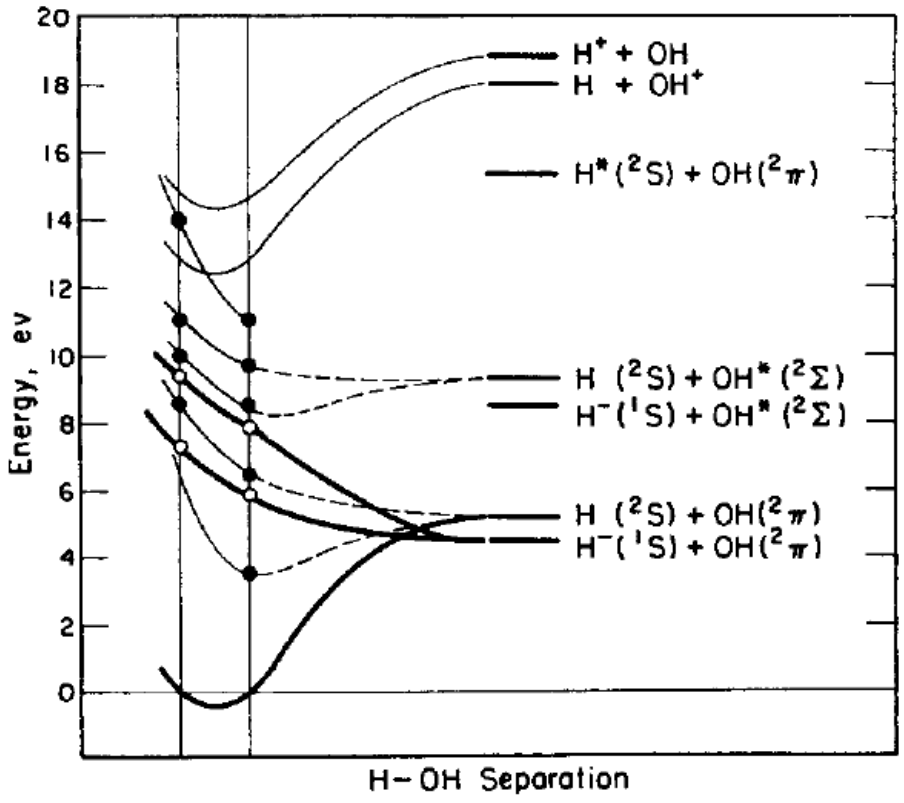

Figure 3.10: Hypothetical Energy Level Diagram of H_2O^- Ion [19]

the dissociation of H atom products. This could account for the Balmer H_α peak at 656 nm which is the most intense of the Balmer emission peaks. However, the minimum electron energy required to dissociate H_2O through H_2O^- is 15.2 eV (1470 kJ mol^{-1}) [20] resulting in the electron energy required to form the H atoms emitting Balmer emission peaks to be considerably higher. If the atomic plasma contained electrons with these energies, then the plasma spectra would also contain emission peaks relating to the radiative deactivation of species such as $O(^1D)$ and $O(^1S)$. However, although these peaks were not observed in the example spectrum in **Figure 3.7** these species could still be present as the radiative decay transitions are weak and may be below the detection limit of the spectrometer. If this was the case, then the dissociation of H_2O could explain the observation of both the OH and H emission peaks.

A fourth formation route to form the OH radical in the $(A^2\Sigma^+)$ excited state is through the reaction of $O(^3P)$ atoms with H_2O. As the plasma source settings were varied to maximise the proportion of O atoms formed in the ground state then this reaction is limited by the background concentration of H_2O. Relaxation of the OH radical into the ground state results in the detection of the $OH(A^2\Sigma^+) \rightarrow (X^2\Pi)$ transition at 308 nm in the atomic O plasma spectrum as seen in **Figure 3.7**. Overall, this fourth formation route is likely to be the dominant formation route of the OH radical. Once OH is formed, the radical can be re-excited through electron collisions into the first excited state before decaying back to the ground state.

The concentration of OH radicals in the atomic O plasma is restricted by the destruction reactions displayed in **Figure 3.11**. The first reaction describes the dissociation of the radical. This process can occur directly from the H_2O^- ion but requires electrons with energy of roughly 24 eV (2300 kJ mol^{-1}) [20] which would results in the formation of other species such as $O(^1D)$ and $O(^1S)$. As these atomic O species are undesirable and the plasma has been tuned to limit the formation of these species, then the destruction of OH through dissociation is unlikely to be occurring in the atomic O plasma used in this study. An alternate, and more likely, destruction reaction for the OH radical can occur through the reaction of O to form the starting plasma gas O_2 (second reaction). The OH radical could also be removed by reacting with another OH radical to form H_2O (third reaction) but, due to the small concentration of OH in the O plasma, this would be a minor reaction.

$$OH + e^- \rightarrow O + H + e^-$$

$$OH + O \rightarrow O_2 + H$$

$$2OH \rightarrow H_2O + O$$

Figure 3.11: OH Destruction Reactions

To determine the ideal settings for the RF plasma source, further analysis of the atomic O plasma was performed to explore the intensity of selected emission peaks (with the signal-to-noise ratio removed) with respect to the plasma chamber pressure, *P*, (plotted on a logarithm scale) and RF power. The schematic diagram in **Figure 3.12** shows that *P* was taken as the pressure inside the plasma chamber. A more accurate analysis of the peak intensities would be to take *P* as the beam pressure but currently there is no method of monitoring this. In the future the apparatus will be modified so that the beam pressure can be monitored instead of *P* (for more details see **Section 3.5**).

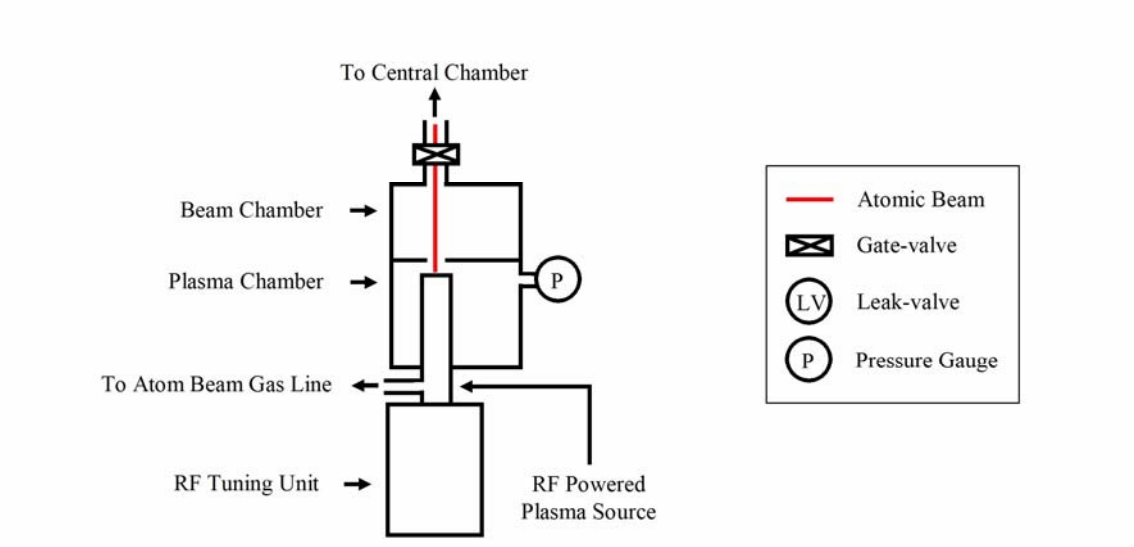

Figure 3.12: Schematic Diagram Illustrating the Position of the Pressure Gauge Used to Monitor *P*

The results displayed in **Figure 3.13** are for the peak transitions: $O(^1S) \rightarrow O(^3P)$ at 297 nm (top left); $OH(X^2\Pi) \rightarrow OH(A^2\Sigma^+)$ at 308 nm (top right); $O(^1S) \rightarrow O(^1D)$ at 557 nm (second from top left); $O(^1D) \rightarrow O(^3P)$ at 630 (second from top right) and 636 nm (second from bottom left); Balmer H_α at 656 nm (second from bottom right);

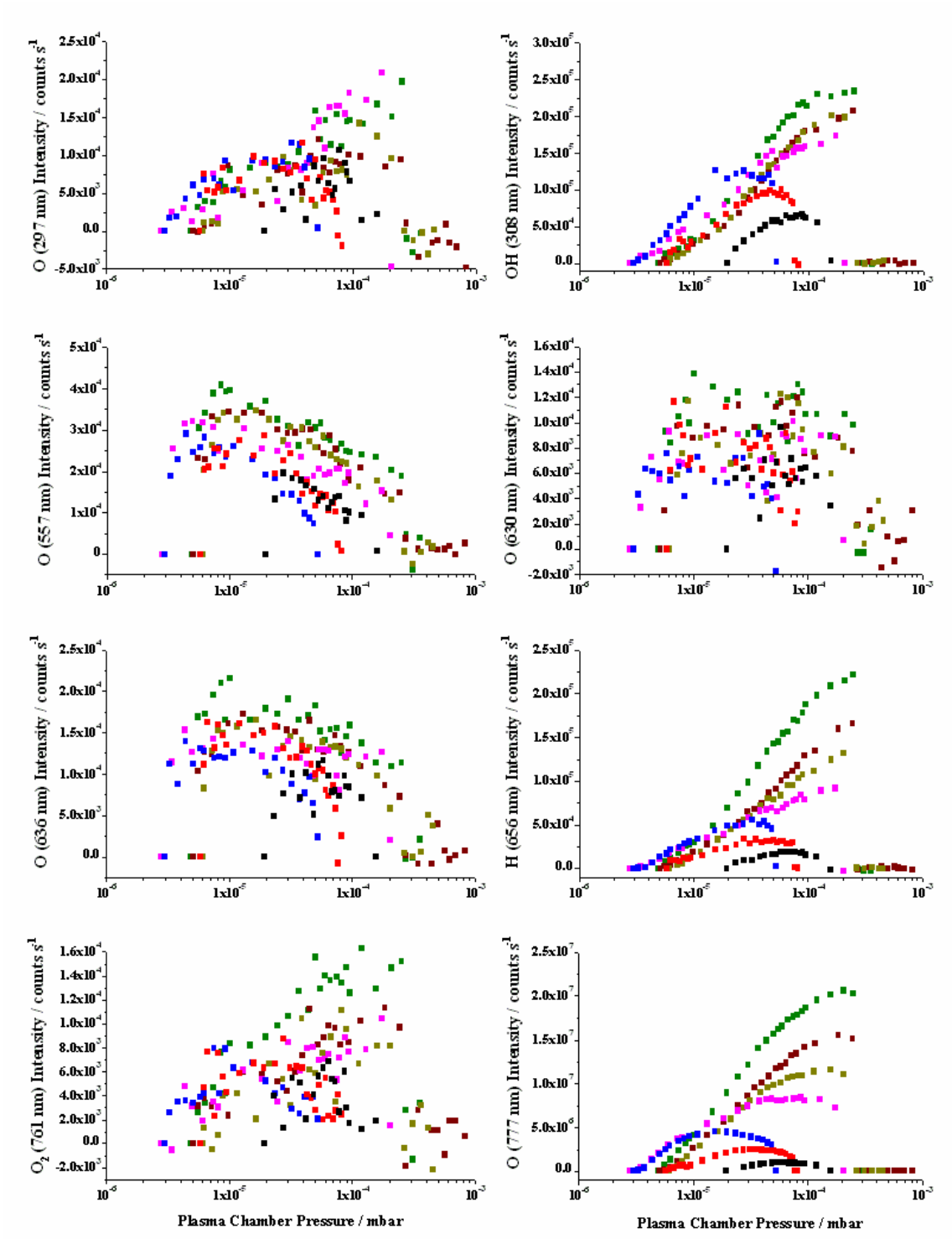

Figure 3.13: Plots of Peak Intensity against Plasma Chamber Pressure at RF Power of: 80 (black); 100 (red); 120 (blue); 150 (magenta); 170 (gold); 190 (dark red); and 210 W (green)

$O_2(b^1\Sigma) \rightarrow O_2(X^3\Sigma^-_g)$ at 761 nm (bottom left); and the $O(3p\ ^5P) \rightarrow O(3s\ ^5S)$ at 777 nm (bottom right). The intensity of the three transitions that were the most affect by the RF power were the OH, H and O peaks at 308, 656 and 777 nm respectively. The O (777 nm) transition had the largest peak intensity in the visible spectrum indicating that this was the dominant radiative decay species in the atomic O plasma. The shape of the 100 to 210 W peaks had coincident leading edges (within experimental error) with the peak maximum generally shifting to higher pressures. The pressure range for this emission lay between 5×10^{-6} and 2×10^{-4} mbar (in this RF region). Most of the peaks had a peak maximum close to 1×10^{-4} mbar which initial experiments revealed produces a stable atomic plasma. As a consequence, the atomic O plasma was always formed at *P* of 1.0×10^{-4} mbar. However, as the plasma failed at this pressure for 100 and 120 W then the ideal RF power setting must be above 120 W.

Although the O (777 nm) plot reveals that the highest RF power used produced the highest emission peak intensity, the OH (308 nm) and H (656 nm) plots also indicate that these conditions produce the highest intensity for these species. As these are contaminant species, these emission peaks need to be minimised with respect to the O (777 nm) peak. This is particularly critical for the H (656 nm) transition as the difference between the 150 and 170; 170 and 190; and the 190 and 210 W peaks increased non-linearly with respect to the RF power. As a consequence, the RF power setting needs to be high enough to form a large O (777 nm) emission peak whilst the OH and H emission peaks remain small.

The RF power setting choice was further complicated when the remaining emission peaks in **Figure 3.13** were taken into consideration. The emission plots relating to the presence of $O(^1S)$ at 297 and 557 nm were very similar in shape and intensity at 120 W and below, indicating that in this RF power region, the emission peaks are minimal. However, when the RF power is increased above 120 W, this relationship breaks down. The pattern of the O (297 nm) emissions changed to show a higher maximum with a peak at around $1.0 - 1.1\times10^{-4}$ mbar which coincides with the pressure for the maximum O (777 nm) emission for similar RF power. The O (557 nm) transition produce curves with coincident leading edges with a peak maximum situated at around 6×10^{-6} and 1×10^{-5} mbar with the falling edge shifting to higher pressures. At 1×10^{-4} mbar, the difference between the O(557 nm) peaks above 150 W becomes more pronounced. Although these emission are weak, the transitions from which they originate are electric

dipole forbidden indicating a significant concentration of the $O(^1S)$ atoms in the plasma. This revealed that the concentration of $O(^1S)$ species formed in the plasma was higher than the emission peaks suggested. In addition, the presence of $O(^1S)$ atoms also suggests the presence of $O(^1D)$ atoms as these are formed with lower electron energies and through the $O(^1S) \rightarrow O(^1D)$ radiative decay transition at 557 nm. The effect of the RF power on the $O(^1D) \rightarrow O(^3P)$ transition at 630 nm is small and forms with the second weakest intensity of all the selected emission peaks explored. The O (636 nm) plot revealed that the curves increased slightly with increasing RF power with the peak maximum situated around 8×10^{-6} and 2×10^{-5} mbar (with the exception of the lowest RF power setting). As with the $O(^1S)$ emission peaks, the $O(^1D)$ transitions are electric dipole forbidden which again implied that the concentration of $O(^1D)$ species was higher than the emission peaks suggested. The emission peaks from both the $O(^1S)$ and $O(^1D)$ atoms are undesirable for the surface science experiments performed in this ongoing research, as there are few energy sources in the ISM that would excite or form O atoms in the excited states. To keep these emission peaks to a minimum, the RF power had to be set below 150 W.

Further supporting evidence for the upper limit on the RF power is displayed in the O_2 (761 nm) plot (bottom left in **Figure 3.13**). At 120 W and below, these peaks had the lowest emission intensities of all those transitions selected with the peak maximum shifting to lower pressures as the RF power increased. Above 120 W, the peaks had coincident leading and falling edges (within experimental error) with the peak maximum roughly centred at the same pressure as the peak intensity of the O (777 nm) transition. The intensity of the O_2(761 nm) peaks increased with increasing RF power. As O_2 molecules in the $O_2(b^1\Sigma)$ excited state can be formed by the collisional deactivation of $O(^1D)$ atoms then this result suggested that concentration of $O(^1D)$ atoms started to increase at 150 W. The findings from all the emission peaks explored concluded that the RF power setting required would lie between 120 and 150 W.

Further analysis of the atomic O plasma revealed that the O (777 nm) intensity varied considerably more by other factors than those explored above. The major factor was how long and how frequent the plasma source had been used prior to the experiment. The solution to this was to run the atomic beams continuously for a few weeks prior to the experiments. However, the RF power would have to be terminated for every experiment that required thermocouple readings due to interference. For the present, the

RF setting for the all the atomic O beam was varied until the O 777 nm peak reached a coincident intensity at a set P of 1.0×10^{-4} mbar. Overall, the results obtained in this sub-section have enabled the atomic O plasma to be analyzed.

3.2.3 H Plasma Analysis

The atomic H plasma is the most difficult of the atomic plasmas to form. As previously mentioned in **Section 2.3.2**, higher quantities of energy were required to ionize the molecule as the outer electrons in H_2 are not shielded from the atom's nucleus. This results in the concentration of free electrons formed often being too small to excite, ionize and dissociate the majority of the molecules preventing the plasma from striking. An additional problem with the H_2 molecule was that the pumping speed was considerably higher than that of other species. As a consequence, H_2 readily effuses from the plasma source before dissociation could occur. To overcome this problem, the secondary gas technique will be used in this study to first create an atomic N plasma which is then mixed by leaking H_2 into the plasma chamber. The larger concentration of free electrons formed from the N plasma allowed the hydrogen plasma to strike in the high brightness mode. Once the H plasma was stable, the N_2 gas supply was terminated. The advantage of using this technique under the same conditions (150 W and P at 1.0×10^{-4} mbar) has been previously shown in **Section 2.2.2** but is shown again in **Figure 3.14**. On the current apparatus, the atom beam gas line was not designed to include a second gas. For the hydrogen plasmas formed in this study, the O_2 cylinder was replaced with a N_2 cylinder and the gas directed into the hydrogen RF plasma source (see **Figure 3.15**). However, this procedure prevents both the beams from being formed at the same time as the apparatus system was designed too. In the future, the apparatus will be modified to include the required secondary gas (see **Section 3.5** for more details).

The H:H_2 dissociation fraction is typically higher in comparison to O:O_2. This is due to the H_2 molecule not being electronegative in nature and having a single bond as this results in a lower bond dissociation enthalpy of 436 kJ mol^{-1} (at 298 K) [1]). The RF powered plasma source used by the Vidali research group in Syracuse (NY, US) obtained a 90 % dissociation fraction for their atomic H beam [21]. However, electrons with energies of 436 kJ mol^{-1} will not cause the H_2 to dissociate [5] as the molecule-electron collisions are elastic. Dissociation occurs through the H_2 repulsive

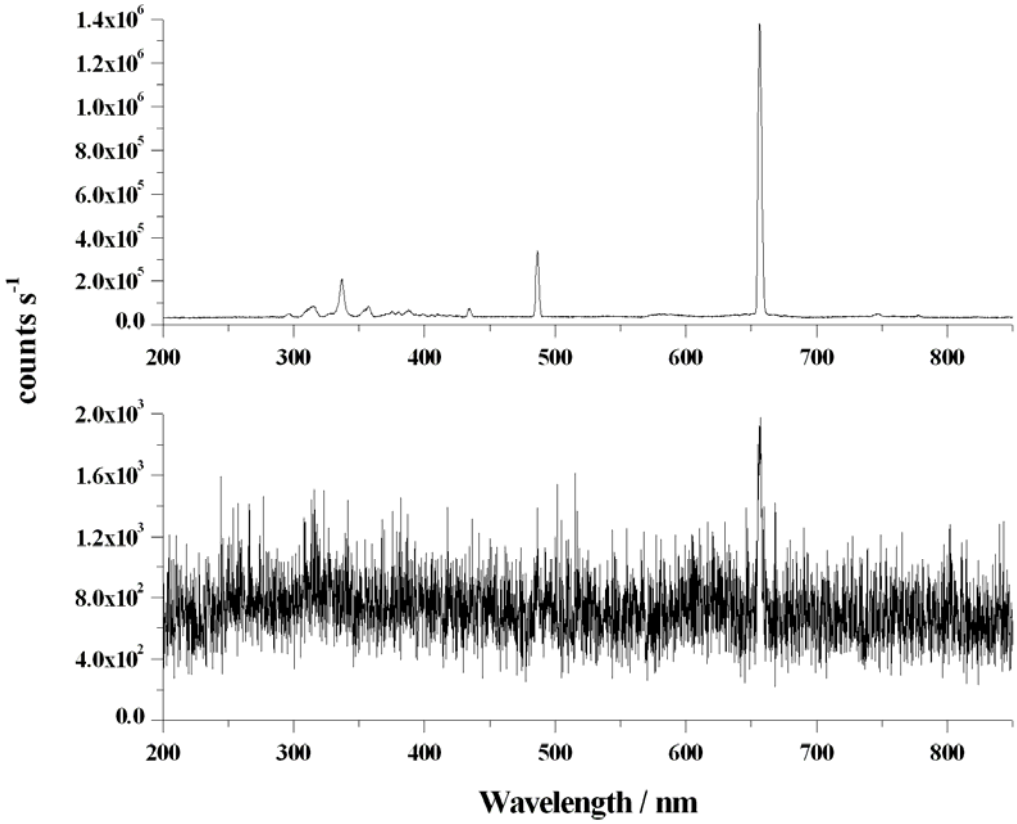

Figure 3.14: Spectra of the Atomic H Plasma Formed With (top) and Without (bottom) the Secondary Gas Technique

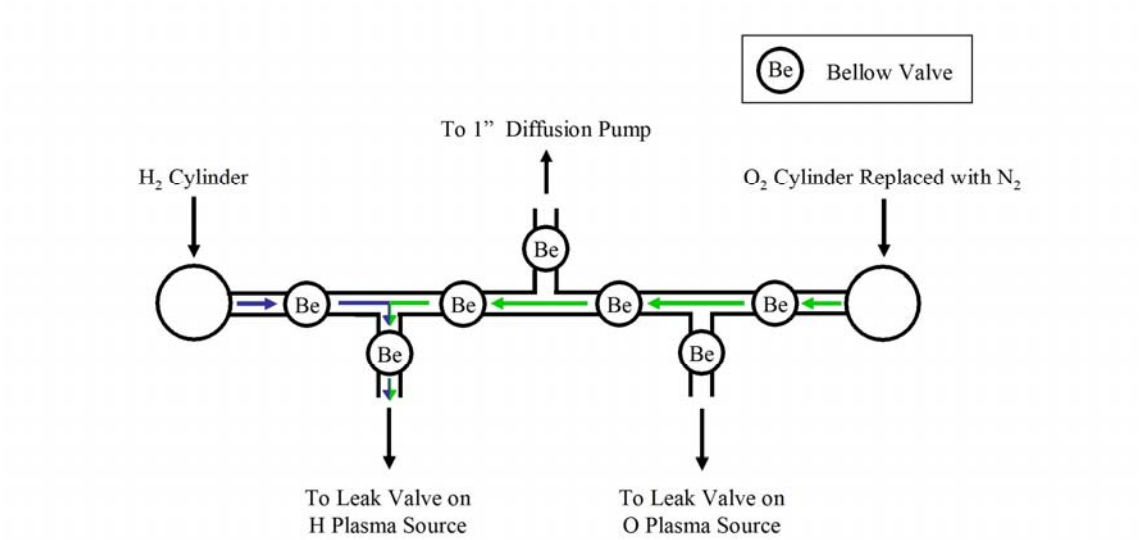

Figure 3.15: Temporary Modification to the Atom Beam Gas Line to Include the Secondary Gas Technique (coloured arrows represent the H_2 and N_2 gas flow).

triplet state (first reaction step in **Figure 3.16**) when the electron energy was increased to approximately 9 eV (roughly 870 kJ mol^{-1}) to produce two H atoms in the ground state. At electron energies of 15.4 eV (roughly 1490 kJ mol^{-1}), the stable H_2^+ ion was formed (second reaction step). Recombination of the H_2 molecule without a third-body does not occur as the transition is spin forbidden.

$$H_2(X^1\Sigma_g^+) + e^- \rightarrow H_2(b^3\Sigma_u^+) + e^- \rightarrow 2H(1^2S_{1/2}) + e^- \qquad (e^- \geq 870 \text{ kJ mol}^{-1})$$

$$H_2(X^1\Sigma_g^+) + e^- \rightarrow H_2^+ + 2e^- \qquad (e^- > 1490 \text{ kJ mol}^{-1})$$

Figure 3.16: H_2 Dissociation Mechanism in Glow-Discharge Plasmas

The fluorescence transitions of H atoms are displayed in the *Grotrain* diagram in **Figure 3.17** with the most intense transitions represented by the thicker arrows. The transitions are split into three series: Lyman; Balmer; and Paschen. The Lyman and Paschen transitions occur in the UV and IR region of the electromagnetic spectrum. Only the Balmer transitions (visible) were observed with the spectrometer used in this study. The wavenumber, $\tilde{\nu}$, for each of these transitions were calculated using **Equation 3.1** where R_H is the Rhyberg constant (109677 cm^{-1}); n_1 equals 1 for the

$$\tilde{\nu} = R_H\left(\frac{1}{n_1^2} - \frac{1}{n_2^2}\right) \tag{3.1}$$

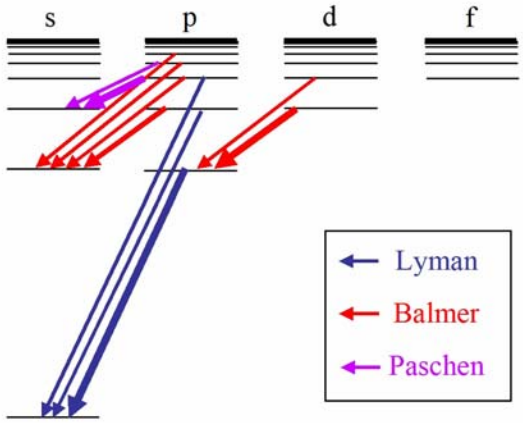

Figure 3.17: Grotrian Diagram for H

Lyman series, 2 for the Balmer series or 3 for the Paschen series; and n_2 equals n_1+1, n_1+2, and so on [1]. To convert $\tilde{\nu}$ into λ (in units of nm), **Equation 3.2** was used. The values of $\tilde{\nu}$ and λ for the first five transitions in each of the three series are displayed in **Table 3.2**.

$$\lambda(nm) = \frac{1}{\tilde{\nu} \times 10^{-7}} \tag{3.2}$$

Transitions	**Lyman**		**Balmer**		**Paschen**	
	$\tilde{\nu}$ / cm^{-1}	λ / nm	$\tilde{\nu}$ / cm^{-1}	λ /nm	$\tilde{\nu}$ / cm^{-1}	λ / nm
H_α	82257	121.57	15238	656.25	5331.5	1875.6
H_β	97491	102.57	20571	486.12	7799.3	1282.2
H_γ	102820	97.256	23039	434.05	9139.8	1094.1
H_δ	105290	94.976	24380	410.17	9948.0	1005.2
H_ε	106630	93.782	25181	397.12	10473	954.87

Table 3.2: $\tilde{\nu}$ and λ for the First Five Fluorescence Transitions for the Lyman, Balmer and Paschen Series

The upper spectrum previously shown in **Figure 3.14** is redisplayed in **Figure 3.18** with the emission peaks assigned. The tallest peak detected was the Balmer H_α emission at 656 nm. Other Balmer H peaks were observed at 486 and 434 nm (in order of decreasing intensity). A weak broad H_2 peak was detected at 580 nm suggesting that the vast majority of the H_2 molecules had dissociated into atoms. Exact calculations of the H:H_2 dissociation fractions have yet to be obtained due to problems with the H RF powered plasma source (as discussed in **Section 2.2.2**) and with aligning the QMS with the beams (see **Section 3.4.3**). Remnants of the secondary gas used to form the H plasma was observed by the $N_2(C^3\pi_u) \rightarrow N_2(B^3\pi_g)$ at 337 nm peak [1]. The other peaks in the spectrum in **Figure 3.18** were assigned to the $OH(A^2\Sigma^+) \rightarrow OH(X^2\Pi_i)$ and the $O(3p^5P) \rightarrow O(3s^5S)$ transitions at 308 and 777 nm respectively.

The formation of the OH radical implied that other reactions were occurring in the atomic H plasma. In the previously discussed atomic O plasma the dominant formation

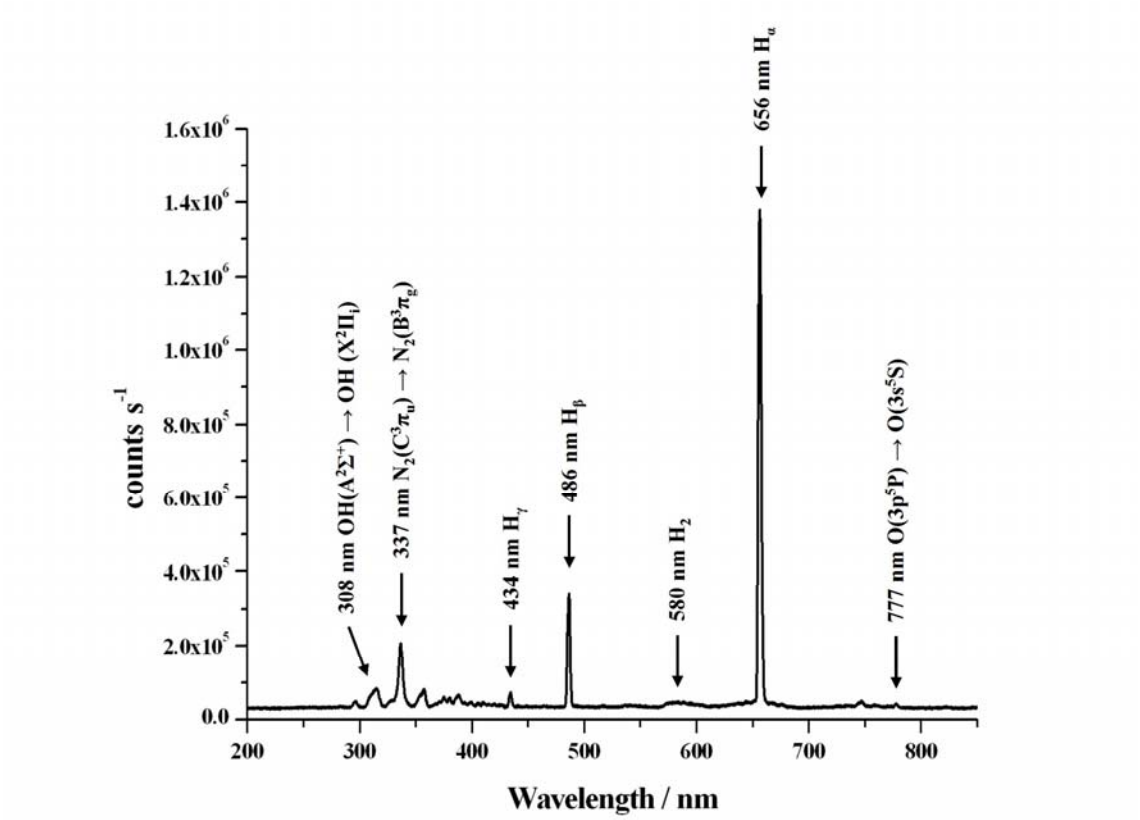

Figure 3.18: Assigned Spectrum of the Atomic H Plasma

route was concluded to be through the reaction of O(^{3}P) atoms with residual H_2O. Although the O 777 nm peak was very weakly observed, the background concentration of O_2 in the plasma chamber was typically 10^{-12} mbar which was too low to produce the observed intensity of the OH emission peak. This also indicated that the OH radical would not be dominantly formed through the reactions of O_2 with H or through collisional deactivation of O(^{1}D). The removal of these OH formation mechanisms resulted in the reduced intensity of this OH emission peak in comparison to the one formed in the atomic O plasma under the same conditions.

The remaining OH formation route discussed for the atomic O plasma was from the dissociation of H_2O. Although this required considerably higher electron energies (approximately 1470 kJ mol^{-1}), this process was occurring as a minor mechanism due to the RF power setting limits applied to reduce the formation of O atoms in the O(^{1}D) and O(^{1}S) excited states. However, the minimum electron energy required to dissociate H_2 was higher than that for O_2 molecules suggesting that this mechanism was responsible for the presence of the OH emission peaks. Further dissociation of the OH radical was

unlikely to result in the observation of the O emission peak at 777 nm due to the much larger electron energy required (around 2300 kJ mol^{-1}). The small concentration of O atoms forming the emission peak was more likely to be formed by the reaction of OH with H atoms.

Further analysis to explore the affects of RF power and *P* on the intensity of the H_α emission peak and other selected emission peaks like OH and O were planned. However, due to continuous problems with the H RF powered plasma source, this was not achieved during this study. Overall the results obtained have enabled the H atomic plasma to be initially analyzed.

3.2.4 Conclusions

The calibration experiments performed in this sub-section were used to analyze the atomic O and H plasmas in **Sections 3.2.2** and **3.2.3** respectively. The visible spectrum obtained for the atomic O plasma formed at 150 W and 1.0×10^{-4} mbar (see **Figure 3.7**) revealed the most intense peak as the $O(3p^5P) \rightarrow O(3s^5S)$ transition at 777.7 nm. Other weaker atomic O transitions were assigned to the peaks at 844.6, 645.6, 615.7, 533.0, 436.8 and 394.8 nm (in order of decreasing intensity). No peaks were observed relating to the radiative decay of $O(^1S)$ and $O(^1D)$ (at 297.2, 557.7, 630.0 and 636.4 nm) or the O_2 collisional deactivation of $O(^1D)$ (at 761.8 nm). However, the fluorescence transitions from these species are weak and were likely to be occurring in the plasma below the spectrometer detection limit. The two remaining peaks were assigned to the $OH(A^2\Sigma^+) \rightarrow OH(X^2\Pi_i)$ transition around 308 nm and the Balmer H_α line at 656.3 nm. The presence of these two peaks implied that other chemical reactions between the O and O_2 species with the background gas were occurring in the plasma.

The formation of the OH peak was described through four mechanisms: $O(^1D)$ collisional deactivation with H_2; atomic H reactions with O and O_2; dissociation of H_2O; and reactions of $O(^3P)$ with H_2O. The dominant formation mechanism was concluded as being the last of the four listed with the other three forming smaller concentrations of OH and H_2O. Once formed, the OH radical could be re-excited through electron collisions before decaying back to the ground state. Consideration was also given to the destruction reactions of OH. The dominant reaction for this was concluded to be through reactions of OH with O atoms to form O_2 and H although some of the

destruction of OH could have been occurring through the minor reaction of two OH radical to form H_2O and O.

Further analysis of the atomic O plasma explored the affects of peak intensity of selected transitions with respect to the *P* and RF power. The results concluded that the higher the RF power, the larger the O emission peak at 777 nm became with the peak maximum situated around 1×10^{-4} mbar when the RF power was above 120 W. This provided an operation *P* of 1.0×10^{-4} mbar and a lower limit for the RF power. However, by increasing the RF power also increased the relative intensities of the emission peaks relating to OH, H, O(^{1}S) and O(^{1}D) including the radiative decay of $O_2(b^1\Sigma)$ formed by the collisional deactivation of O(^{1}D) with $O_2(X^3\Sigma_g^-)$. To minimise the formation of these species, an upper limit on the RF power was set at 150 W.

Further observations of the atomic O plasma revealed that other factors were causing the peak intensities to vary considerably. The dominant factor was how long and how frequent the plasma source had been used previously. The solution for this was to run the atomic beams for a few weeks prior to the experiments. However, the RF power would have to be terminated for every experiment that required thermocouple readings due to interference and, for safety reasons, the beam could not be run overnight. For the present, the RF power setting for all the atomic O beam experiments was varied until the O(777 nm) peak reached a coincident intensity at a set *P* of 1.0×10^{-4} mbar. The accuracy of obtaining stable emission peak intensities could have been improved if the beam pressure was used instead of the plasma chamber pressure, *P*, (see **Figure 3.12**). A suggestion for the modification required to directly measure the beam pressure is discussed in **Section 3.5** and will be applied to both the hydrogen and oxygen beams.

The visible spectrum obtained for the atomic H plasma was formed at 150 W and 1.0×10^{-4} mbar (see **Figure 3.18**). The most intense peak was assigned to the Balmer H_α at 656.3 nm. Other Balmer H peaks were assigned at 486.1 and 434.1 nm (in order of decreasing intensity). A H_2 molecular transition was assigned to the broad weak peak at 580 nm. As this plasma was formed using the secondary gas technique, remnants of this gas was observed through the $N_2(C^3\pi_u) \rightarrow N_2(B^3\pi_g)$ transition at 337 nm. The remaining two peaks were assigned to the: $OH(A^2\Sigma^+) \rightarrow OH(X^2\Pi_i)$ transition around 308 nm; and $O(3p^5P) \rightarrow O(3s^5S)$ at 777 nm. As in the atomic O plasma, the presence of

these peaks in the atomic H plasma revealed that other chemical reactions were occurring. The results concluded that these peaks were caused by the dissociation of H_2O molecules in the background gas.

Further analysis of the atomic H plasma to explore the affect of peak intensity (for selected peaks) with respect to *P* and RF power was planned. However, due to continuous problems with the hydrogen RF powered plasma source, this work was not achieved during this study and will be performed in the future.

3.3 O_2 Beam Position by Quartz Crystal Microgravimetry

3.3.1 Introduction

This section explores the characterisation of the O_2 molecular beam; in particular the experiments to determine the position of the beam in the UHV chamber using the quartz crystal microgravimetry (QCM). The experimental procedure and the results are discussed in **Section 3.3.2**. This section also explores the results to determine the mass deposited onto the crystal over time, Δm, with respect to the plasma chamber pressure, *P* (see **Figure 3.12**). The final sub-section (**Section 3.3.3**) reviews the summary and conclusions. The results obtained will be used to position the silica sample in-line with the atomic and molecular oxygen beam for beam irradiation experiments both in this thesis (see **Chapters 4** and **6**) and in future oxygen beam dose experiments.

3.3.2 O_2 Beam Position Quartz Crystal Microgravimetry Calibration

Once UHV conditions had been achieved, the sample was raised until the quartz crystal was judged to be in-line of the O_2 beam and the sample position noted. The gate valves between the central chamber and the atomic beam chambers were closed and the central chamber pressure recorded. To check for mass sensitivity in the QCM apparatus, O_2 was background deposited at a steady pressure of approximately 5×10^{-8} mbar whilst the data acquisition program monitored the sample crystal frequency and the central chamber pressure. If the QCM was mass sensitive, than the frequency of the crystal decreased linearly over time (for a more detailed explanation of this process see **Section 2.3.5**). Once this had been achieved, the dosing was stopped and the data acquisition program terminated. The molecular beam was created by leaking O_2 into the plasma source chamber until the chamber reached a steady pressure of 1.0×10^{-4}

mbar. The data acquisition program, using the same settings as for the mass sensitivity test, was re-started and the test repeated using the O_2 molecular beam.

Once mass sensitivity had been established, the quartz crystal was positioned with *y* (forwards and backwards) and θ (rotational angle of the sample) held constant at 0 mm and -0.5˚ respectively. The *x* (side to side) and *z* (up and down) positions were recorded (see **Figure 3.19**). Using the same settings for the mass sensitivity test, the data acquisition program was started. After a delay of a few minutes, the gate valve between the central chamber and oxygen atomic beam chamber was opened for a dose of 5 minutes and then closed. The data acquisition program was stopped a few minutes later and the data saved. The experiments were repeated for a range of *x* and *z* positions.

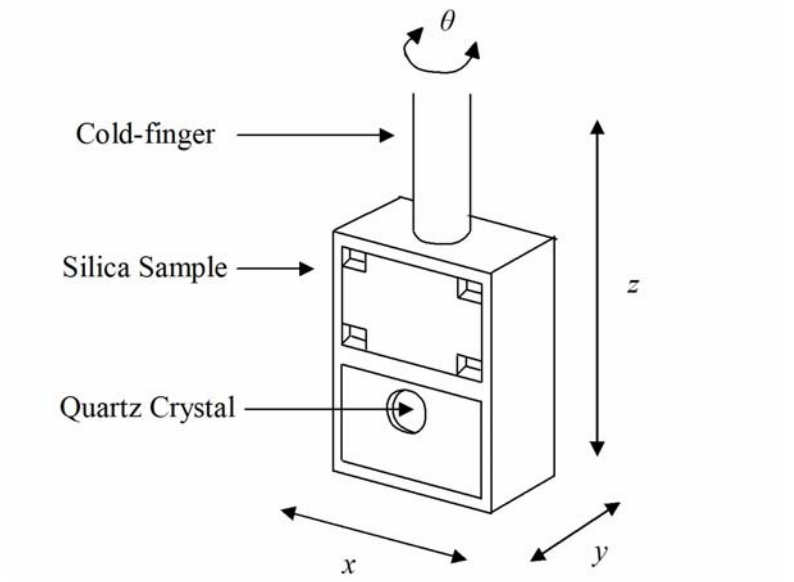

Figure 3.19: Schematic Diagram of O_2 Beam Position Calibration using the QCM

The data was imported into Origin[2] and plots of crystal frequency against time for each crystal position were constructed (see **Figure 3.20**). The change in frequency, Δf, was obtained from the total difference in the frequency for the dose. This was then plotted against the corresponding crystal position (**Figure 3.21**). The data in **Figure 3.21** revealed a maximum curve relationship for both the *x* and *z* positions indicating that as

[2] Microcal Origin: version 6.0, Microcal Software Inc., 1999. Further information maybe obtained from http://www.originlab.com

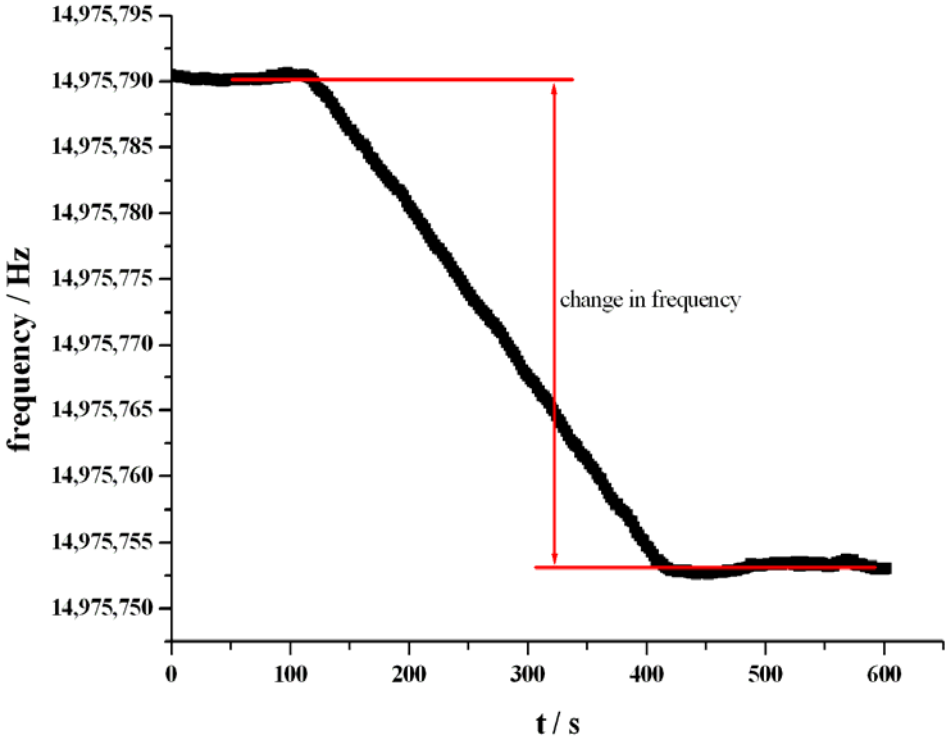

Figure 3.20: Example Plot of *f* Versus *t*

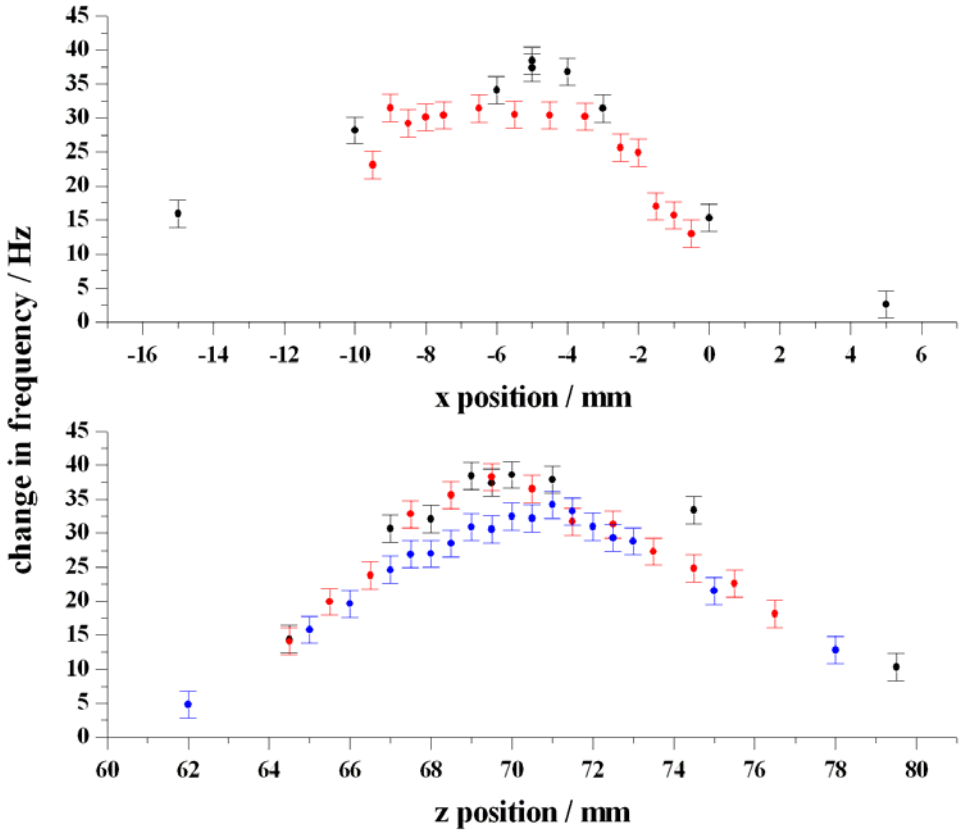

Figure 3.21: Plots of Frequency Change, Δf, Against Crystal *x* and *z* Positions

more of the molecular beam cross section irradiated the crystal, the greater the mass deposited onto the crystal. The slight variation between the different data sets was a result of the small changes in the beam flux, F_{beam}. The ultimate x and z positions for the O_2 beam were taken at the highest point on the curves. Hence the ultimate QCM position for the O_2 beam was taken as x = -5.0 mm, y = 0.0 mm, z = 70.0 mm and θ = -0.5°.

Situated above the quartz crystal is the silica sample (see **Figure 2.18** in **Chapter 2**) which will be used for all the dosing experiments. By knowing the vertical distance between the crystal and the sample, the ultimate position for the silica sample in respect to the oxygen beam was calculated as x = -0.5 mm, y = 0.0 mm, z = 50.0 mm and θ = -0.5°. This position will be used for all the atomic and molecular oxygen beam irradiation experiments performed in this ongoing research.

As mentioned earlier, the slight difference in Δf for the data sets used to determine the ultimate crystal position was due to small changes in the F_{beam}. The amount of mass deposited onto the crystal for a set dose, Δm, is related to Δf by the Sauerbry equation as shown in **Equation 3.3** [22] where A is the area of the crystal, χ the sheer modulus of the quartz (2.947×10^{11} g cm^{-1} s^{-2}), d the density of the quartz (2.648 g cm^{-3}) and f_0 the crystal's resonant frequency. Δm is also dependent on the pressure settings of the beam, P, (which was measured in terms of the pressure in the plasma chamber and not the actual beam pressure as previously shown in **Figure 3.12**) and the temperature of the beam species, T_{beam}, (assumed to be 300 K). This relationship is described through the time-dependent version of the *rate of bombardment equation* (see **Equation 3.4**) where Z_w is the rate of bombardment, S the sticking coefficient; m the mass of the beam species, and k_B Boltzmann's constant. As the small variations in P would affect the value obtained for Δf, an additional experiment was performed to explore this relationship. Ideally, the affect of T_{beam} on Δf should also be explored. However, the current apparatus has no method to measure and monitor T_{beam}.

$$\Delta m = \frac{\Delta f A \sqrt{\chi d}}{2 f_0^{\,2} h} \tag{3.3}$$

$$\Delta m = Z_w t = \frac{PSt}{\sqrt{2\pi m k_B T_{beam}}} \tag{3.4}$$

When the apparatus was under UHV conditions, the quartz crystal was positioned in the calculated ultimate position with the gate valve closed between the central UHV chamber and the oxygen atomic beam chamber. As before, the QCM was checked for mass sensitivity using the data acquisition program. Once this had been established, O_2 gas was leaked into the plasma chamber through the RF powered plasma source (RF power turned off) at a pressure, *P*, of 5×10^{-6} mbar. After a short delay, the gate valve was opened for a dose of 5 minutes and then closed. The data acquisition program was stopped a few minutes later and the data saved. The experiment was repeated for a range of *P* between 5×10^{-6} and 5×10^{-3} mbar.

The plot of Δf against *P* displayed in **Figure 3.22** reveals that there were three *P* dependent stages. The first stage occurred at pressures below 7×10^{-5} mbar where there was little change in Δf with respect to *P*. This indicated that the flux was roughly constant and was a result of the background flux leaking from the plasma chamber. The

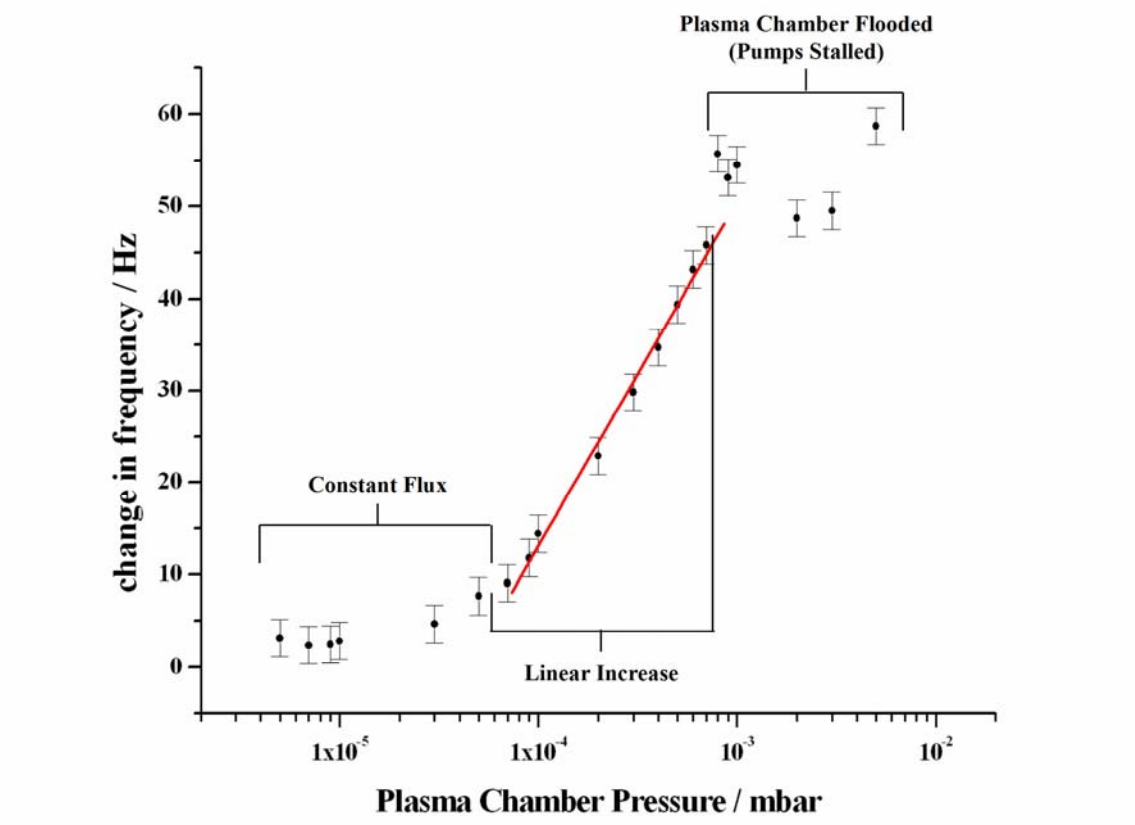

Figure 3.22: Plot of Frequency Change Against O_2 Gas *P* for a Five Minute Dose

second *P* dependent stage occurred between approximately 7×10^{-5} and 7×10^{-4} mbar and formed a linear relationship which was consistent with the increasing flux due to the O_2 molecular beam. In this pressure range, the ideal *P* setting to form the atomic O beam (concluded in **Section 3.2** as 1.0×10^{-4} mbar) occurs. By applying a line-of-best fit (see **Equation 3.5**) the average value of Δf at this pressure for a five minute dose was calculated as 13±2 Hz.

$$\left(\Delta f / Hz\right) = \left(3.7 \times \log_{10}\left[\left(P_{O_2} / mbar\right)\right]_{7\times10^{-5}}^{7\times10^{-4}}\right) \pm 2 \tag{3.5}$$

The final stage in **Figure 3.22** revealed that the linear relationship in the second stage breaks down as the pumping system on the plasma chamber begins to stall. As a consequence, the plasma chamber became flooded with O_2 providing a near constant background to leak out of the plasma chamber.

From the data obtained in the second *P* dependent stage, the mass deposited onto the crystal, Δm, was determined using the Sauerbry equation (see **Equation 3.3**). As mentioned in **Section 2.3.5**, f_0 is not precisely known so Δm was calculated using **Equation 3.6** which was obtained when the original UHV system was calibrated. The value of the calibration fractor, *F*, was calculated as $3.0\pm0.3\times10^{-10}$ g Hz^{-1} (corrected from the work performed by Thrower [23]). The units of Δm were converted into molecules cm^{-2} by dividing by the mass of 1 molecule (5.3×10^{-23} g for O_2) and *A* (0.5 cm^2).

$$\left(\Delta m / g\right) = F \times \Delta f \tag{3.6}$$

The plot of the mass deposited, Δm, for the five minute dose against *P* is displayed in **Figure 3.23** and reveals a linear relationship. The errors in Δm were determined by calculating through the error obtained for Δf and *F* and varied from 4×10^{13} to 8×10^{13} molecules cm^{-2} (see **Table 3.3**). By knowing the pressure in the plasma chamber, Δm could be estimated using the line-of-best fit displayed in **Equation 3.7**. Initial attempts to form an atomic oxygen plasma revealed the ideal plasma chamber pressure was around 1.0×10^{-4} mbar. At this pressure, Δm was calculated as $1.6\pm0.5\times10^{14}$ molecules cm^{-2}. However, the error analysis applied to Δm does not take

$$\Delta m \text{ / molecules cm}^{-2} = 4.1\times10^{14}\left[\log_{10}\left(P_{O_2}\text{ / mbar}\right)\right]_{7\times10^{-5}}^{7\times10^{-4}} + 1.8\times10^{15} \qquad (3.7)$$

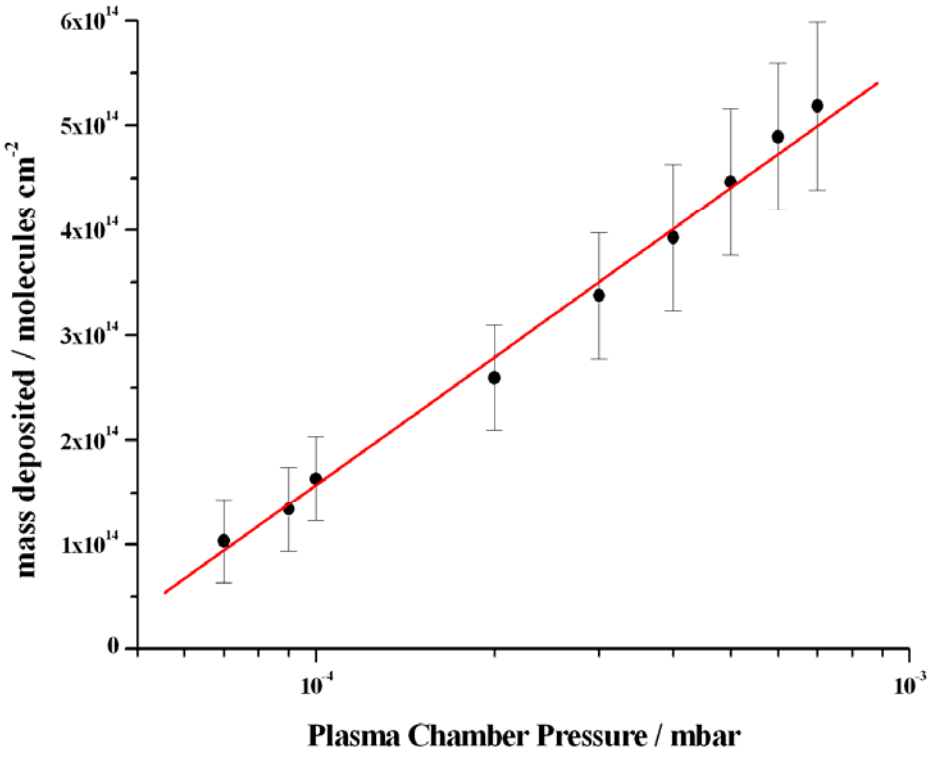

Figure 3.23: Plot of the Mass Deposited Against *P*

***P* / mbar**	***Δm / molecules cm*$^{-2}$**	***F*$_{beam}$ / *molecules cm*$^{-2}$ *s*$^{-1}$**
7.0×10^{-5}	$1.0\pm0.4\times10^{14}$	$3.4\pm0.4\times10^{11}$
9.0×10^{-5}	$1.3\pm0.4\times10^{14}$	$4.5\pm0.4\times10^{11}$
1.0×10^{-4}	$1.6\pm0.4\times10^{14}$	$5.4\pm0.4\times10^{11}$
2.0×10^{-4}	$2.6\pm0.5\times10^{14}$	$8.6\pm0.5\times10^{11}$
3.0×10^{-4}	$3.4\pm0.6\times10^{14}$	$1.1\pm0.6\times10^{12}$
4.0×10^{-4}	$3.9\pm0.7\times10^{14}$	$1.3\pm0.7\times10^{12}$
5.0×10^{-4}	$4.5\pm0.7\times10^{14}$	$1.5\pm0.7\times10^{12}$
6.0×10^{-4}	$4.9\pm0.7\times10^{14}$	$1.6\pm0.7\times10^{12}$
7.0×10^{-4}	$5.2\pm0.8\times10^{14}$	$1.7\pm0.8\times10^{12}$

Table 3.3: Calculated Values of Δm for a Five Minute Dose and F_{beam}

into account the larger experimental errors obtained from the UHV system. With these errors included, the value of Δm for a five minute dose at P of 1.0×10^{-4} mbar becomes $2\times10^{14\pm1}$ molecules cm^{-2}.

The O_2 molecular beam flux, F_{beam}, was determined using **Equation 3.8** where t is the dose time in units of seconds. The results are displayed in **Table 3.3** with the analytical error deduced from the analytical error of Δm. However, as with Δm, the experimental error associated with the UHV apparatus needed to be applied to the values of F_{beam}. Hence, at the ideal pressure setting deduced to form the atomic O beam (1.0×10^{-4} mbar), F_{beam} becomes $5\times10^{11\pm1}$ molecules cm^{-2} s^{-1}.

$$F_{beam} = \frac{\Delta m}{t} \tag{3.8}$$

For an effusive beam system (as in this study) the values of F_{beam} were expected to in the range of 10^{13} to 10^{15} molecules cm^{-2} s^{-1}. The results obtained are just outside the lower limit suggesting that the calculations of F_{beam} using the QCM may be inaccurate. The two most likely causes for this were the assumption made on S (from **Equation 3.4**) and the surface temperature of the quartz crystal.

The exact value of S lies between 0 (where no species stick to the surface upon collision) and 1 (all species sticking). This is represented by the flux diagram displayed in **Figure 3.24** where J_{in} is the incoming flux (which is equivalent to F_{beam}); J_{ref} the flux of species reflected from the surface on impact; and J_{ads} the adsorbed flux. In the case where S equals 1, J_{ads} becomes equal to J_{in} whilst the value of J_{ref} remains zero. However, the value of S is difficult to determine experimentally as S depends on the molecule of interest and the temperature of the surface it is colliding with. As O_2 is relatively large and heavy and multilayers of O_2 were expected to be adsorbing onto the surface, S was assumed to be 1. If the value of S was less than 1 then the values of Δm were underestimated as J_{ref} would be non-zero resulting in the actual F_{beam} being larger than predicted.

Additionally, the surface temperature of the crystal was unknown as the E-type thermocouple was not sensitive at base temperatures and therefore was not used (see **Section 2.2.3** for more details). As a consequence, the stability of the surface

temperature was unknown suggesting that the value of S may also not have been constant. The surface temperature of the silica sample situated above the QCM apparatus was held at a base temperature of approximately 20 K suggesting that the surface temperature of the crystal was roughly 23 to 28 K. Temperature programmed desorption (TPD) experiments performed previously on the ICE RIG from porous amorphous solid water (pASW) ice [24] and from other astronomically relevant surfaces (see **Chapter 4**) indicate that O_2 molecules start to desorb just above this temperature at around 30 K. Although this implied that the vast majority of the O_2 molecules would remain adsorbed on the crystal, a relatively few molecules may have had enough energy to desorb during the dose, particularly if the sample was at the higher end of the estimated surface temperature. This flux of molecules desorbing from the surface is labelled as J_{des} in **Figure 3.24**. This would result in both J_{ref} and J_{des} being non-zero and the values of Δm and F_{beam} being underestimated. Overall, a more accurate method of determining the actual F_{beam} was required. This was achieved using pump-down experiments which are discussed in **Section 3.4.2**.

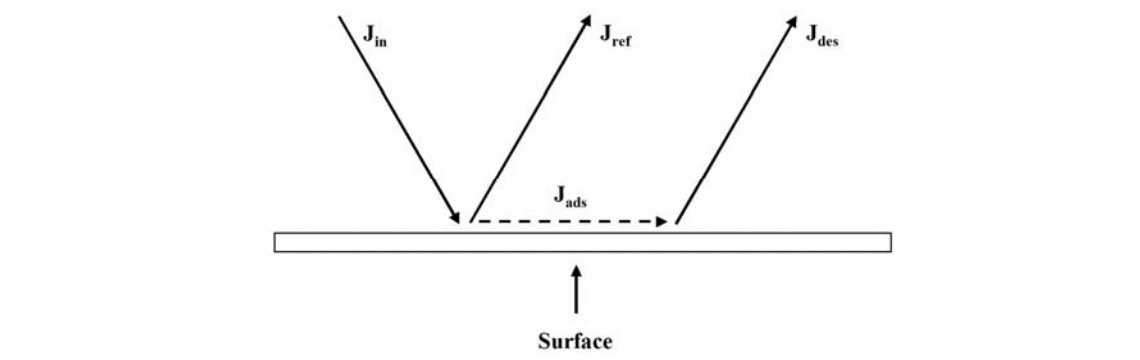

Figure 3.24: Flux Diagram Describing the Sticking and Accommodation Coefficients

Despite the low values of F_{beam}, the QCM experiments have provided the ultimate position to place the crystal or the silica sample in-line with the oxygen molecular or atomic beam. Ideally, the ultimate position of the crystal and silica sample with respect to the H_2 molecular beam is required too. However, due to the hydrogen RF powered plasma source being returned to the company for repairs (as discussed in **Chapter 2**) these experiments were unable to be performed in time. When this is achieved in the future, these experiments will be performed using a molecular beam of N_2 instead of H_2 as the surface temperature of the quartz crystal can not be cooled to temperatures low

enough for H_2 to remain adsorbed on the surface. The value obtained for Δf will be lower than those for O_2 as N_2 molecules desorb at a slightly lower surface temperature but this should have no affect on determining the overall ultimate position.

Another set of experiments that will be performed in the future would be to determine the value of S on the quartz crystal over a range of surface temperatures for both molecular O_2 and atomic O beams. As mentioned earlier, the value of S is difficult to measure experimental. A more reliable method of calculating S is to experimentally determine the accommodation coefficient, α. This would be achieved by using the beam reflectivity technique known as the *King and Wells method* [25] which works by monitoring the intensity of the species that are scattered from the surface. The intensity of the scattered species is equivalent to the total flux of species leaving the surface, J_{out}, in comparison to J_{in} (see **Equation 3.9**) where J_{out} is the sum of J_{des} and J_{ref} (**Equation 3.10**). The higher the signal intensity of the beam species reflected from the surface, the fewer species that are sticking to the surface which results in the value of α decreasing.

$$\alpha(T) = \frac{J_{in} - J_{out}}{J_{in}} \tag{3.9}$$

$$J_{out} = J_{ref} + J_{des} \tag{3.10}$$

The experiments will be performed under UHV conditions with the apparatus arranged as shown in **Figure 3.25**. The apparatus diagram includes an additional KP-type thermocouple attached to the QCM and linked to the computer system so that the surface temperature of the quartz crystal will be monitored by the MASsoft software. Another addition to the apparatus is a flag which can be lower to intercept the beam. The crystal will be cooled to the desired temperature and positioned in the ultimate position calculated earlier. Once the surface temperature is stable and with the gate valve between the central chamber and plasma chamber closed, the beam will be created at P of 1.0×10^{-4} mbar. The MASsoft program will be set to monitor the intensity of O_2, O and CO/N_2 (both have the same mass) and CH_3 (contaminant) species and the KP-type thermocouple voltages of the silica sample, QCM and cold-finger monitored over time.

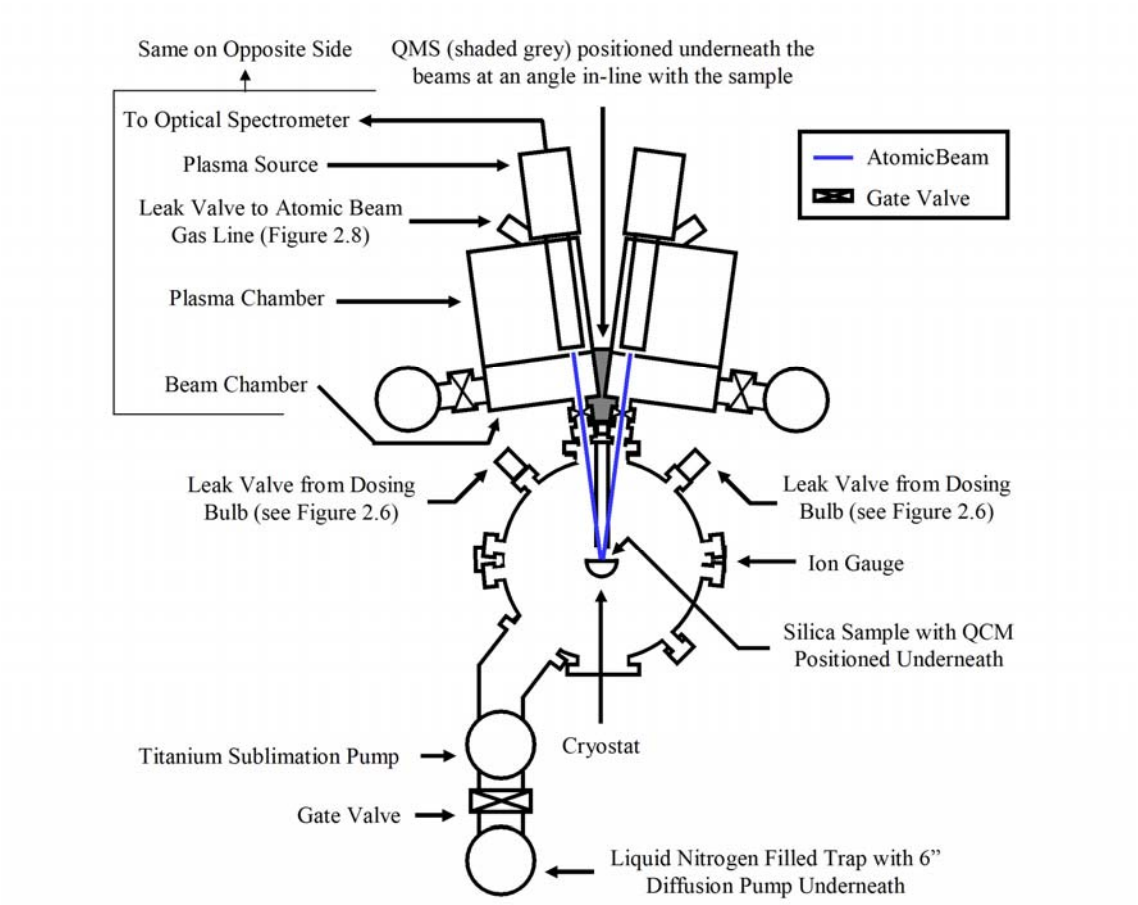

Figure 3.25: Apparatus Diagram for the Proposed King and Wells Experiments

The first stage of the experiment (denoted as A on **Figure 3.26**) will be to start the MASsoft program but with the gate valve closed. This will provide a background reading. After a short time delay, the gate valve between the central chamber and plasma chamber will be opened slightly (B). Once the signal intensity of the reflected beam species has stabilized, the gate valve is full opened but with the flag intercepting the beam (stage C). This will allow a full indirect flux of the beam to be obtained but without any beam dosing occurring. Presently, the plasma chambers do not include a flag but this will be added into each of the beam chambers in the future (for more details see **Section 2.2.2** in **Chapter 2**). The final stage of the experiment (D) occurs after another short delay when the gate valve will be completely open and the flag positioned out-of-alignment with the beam allowing the beam species to reach the surface. This should result in an initial decrease in the intensity of the beam species detected by the QMS where the O_2 molecules are sticking to the surface (D1). Over time, the signal will start to rapidly increase (D2) as the species start to desorb from the surface before stabilizing (D3) to a steady state where the number of molecules sticking to the surface

is equal to the number of molecules desorbing. Once this has been achieved, the gate valve will be closed. The MASsoft program will be stopped a few minutes after and the data saved. An example result performed by Matar *et al.* to determine the sticking coefficient of D_2 on amorphous solid water (AMS) is shown in **Figure 3.26** [26]. The whole experiment will be repeated for a range of quartz crystal surface temperatures.

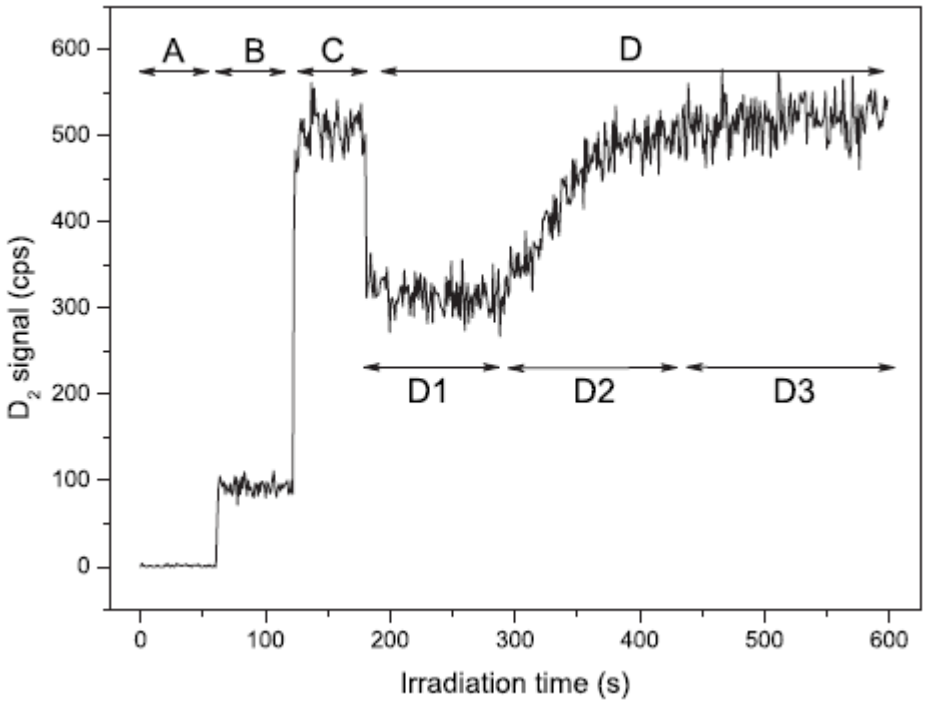

Figure 3.26: Example Result Using the King and Wells Method [26]

The value of α will be determined using the data obtained in stage D3 using **Equation 3.9** when J_{out} is converted from units of mass spectrometer counts to molecules cm^{-2} s^{-1}. S can then be calculated using **Equation 3.11** where k_{des} is the rate coefficient for the desorbing species. The value of k_{des} for the species of interested will be derived from background deposited TPD experiments. The experimental, analytical and modelling procedures required to determine k_{des} for O_2 from bare silica is described in **Chapter 4**. Using the same set of procedures, the value of k_{des} for O_2 could be obtained by repeating the experiment on the quartz crystal.

$$S(T) = \alpha(T) + \frac{k_{des}(T)}{J_{in}} \tag{3.11}$$

As the results are believed to give a value less than 1 for S for the quartz crystal at base temperature, then it is likely that the value of S on the silica sample (used in the beam dosed experiments) will also be less than 1. As a consequence, this will result in the dosed surface concentration, N_{tot}, being considerably less than calculated using F_{beam} (obtained from the pump-down experiments in **Section 3.4.2**) alone. For this reason, these proposed experiments will also be performed using the silica sample to provide a more accurate measurement of N_{tot}. The whole experiment will be repeated using the molecular H_2 and atomic H beams. The surface temperature range will be smaller using the hydrogen beams as both H_2 and H desorb from the surface at lower temperatures than O or O_2. For this reason, the experiments will only be performed on the silica surface as the QCM cannot currently be cooled to temperatures low enough for these species to adsorb.

Another variable that affect S is the beam temperature [26]. If the value of S results in a small range of N_{tot} over a large range of beam irradiation times than the apparatus could be modified to cool the species in the beam. This could be achieved by directing the beam through either a tube surround by a copper tube (like the ASURA apparatus [27]) or aluminium nozzle (FORMOLISM [26]) (for more details see **Section 1.3.3** in **Chapter 1**). This would result in more of the beam species sticking to the surface which would increase α, S and N_{tot}.

3.3.3 Conclusions

The ultimate position of the quartz crystal and the silica sample with respect to the molecular oxygen beam are x = -5.0 mm, y = 0.0 mm, z = 70.0 mm and θ = -0.5˚; and x = -5.0 mm, y = 0.0 mm, z = 50.0 mm and θ = -0.5˚ respectively. The results indicated that Δf was linearly dependent on P between 7×10^{-5} and 7×10^{-4} mbar as a consequence of the increasing F_{beam}. Below this pressure range, Δf was roughly constant due to the background flux from the plasma chamber. Above 7×10^{-4} mbar, the pumping system for the plasma chamber stalled resulting in the chamber being flooded. Further calculations from the data enabled Δm and F_{beam} to be determined. Using the ideal P setting to form a stable atomic beam (1.0×10^{-4} mbar, see **Section 3.2.2**), Δm was estimated as $2\times10^{14\pm1}$ molecules cm^{-2} for a five minute dose and F_{beam} as $5\times10^{11\pm1}$ molecules cm^{-2} s^{-1}. The value of F_{beam} was lower than expected for an effusive beam suggesting that the surface temperature of the quartz crystal was preventing the vast majority of the beam species to stick to the surface. This implied that the values of

J_{ref} and J_{des} were non-zero resulting in S being less than 1. In the future, additional experiments are planned to measure S for the O_2 and O beams at different quartz and silica surface temperatures using the King and Wells method and TPD experiments.

A more accurate technique to determine the actual value of F_{beam} for the O_2 molecular beam was from pump-down experiments which will be discussed in the next section. The results obtained will be compared to F_{beam} obtained from the QCM apparatus allowing an estimate of S on the quartz crystal at base temperature to be obtained.

Ideally the experiments to determine the ultimate position of the quartz crystal and silica sample would be repeated with the H_2 molecular beam but, due to the hydrogen RF powered plasma source being returned for repairs, these experiments were unable to be performed in time. When this experiment is performed in the future, the position would have to be determined using N_2 instead of H_2 as the QCM cannot be cooled to temperatures low enough for H_2 to remain adsorbed onto the surface. Additional, the King and Wells and the TPD experiments to determine α and k_{des} using the H_2 and H beams will be performed on the silica surface to obtain the corresponding value of S if the apparatus can be successfully modified to reduce the base surface temperature low enough for H and H_2 to adsorb.

3.4 O_2 Beam Flux and Beam Cracking Fraction

3.4.1 Introduction

This section explores the calibrations of F_{beam} and the O:O_2 dissociation fractions for the oxygen beam. In **Section 3.4.2** F_{beam} was calculated through pump-down experiments performed with P between 2.1×10^{-5} and 9.7×10^{-4} mbar. The calculated value of F_{beam} formed at 1.0×10^{-4} mbar was compared to the value obtained for Δm using the QCM apparatus obtained in the previous sub-section. **Section 3.4.3** discusses the attempt to determine the cracking fractions of the atomic and molecular beam from which the O:O_2 dissociation fraction could be obtained. The summary and conclusion of both these calibration experiments are discussed in **Section 3.4.4**.

3.4.2 Pump-Down Beam Flux Calibration

The O_2 F_{beam} was determined by performing O_2 pump-down curve experiments. The theory and experimental procedure was based on the calibration experiments performed by Oakes [28]. The calculation works on the assumption that the flux of molecules entering the UHV system by the beam, $|F_{in}|$, was equivalent to the flux of molecules leaving, $|F_{out}|$, (see **Equation 3.12**). $|F_{out}|$ was derived from a time dependent version of the ideal gas equation (**Equation 3.13**) given in **Equation 3.14** where P is the pressure, V_{system} the volume of the system, n the number of moles, k_B Boltzmann's constant and T the temperature. The change in pressure of the gas over time, $|dP/dt|$, was obtained from the pump-down curve.

$$\left|F_{in}\right| = \left|F_{out}\right| \tag{3.12}$$

$$PV = nk_BT \tag{3.13}$$

$$\left|F_{out}\right| = \left|\frac{dn}{dt}\right| = \frac{V_{system}}{k_BT}\left|\frac{dP}{dt}\right| \tag{3.14}$$

An example of a pump-down curve is displayed in **Figure 3.27**. The exponential decay of the gaseous species is described using **Equation 3.15** where P_0 is the initial pressure (before the pump down) and C_m the pumping coefficient for the gaseous species of mass, m. By differentiating **Equation 3.15** at the initial time, t_0, provided the initial change in pressure (see **Equation 3.16**). This value was substituted into **Equation 3.14** to give $|F_{out}|$. As $|F_{out}|$ was assumed to be equal to $|F_{in}|$, then F_{beam}, was calculated using a beam dependent version of **Equation 3.14** (see **Equation 3.17**) where A_{beam} is the cross-sectional area of the beam.

$$P = P_0e^{-C_mt} \tag{3.15}$$

$$\left|\frac{dP}{dt}\right|_{t_0} = C_mP_0e^{-C_mt_0} = C_mP_0e^0 = C_mP_0 \tag{3.16}$$

$$F_{beam} = \frac{V_{system}}{k_BT}\left|\frac{dP}{dt}\right|_{t_0}\frac{1}{A_{beam}} = \frac{V_{system}C_mP_0}{k_BTA_{beam}} \tag{3.17}$$

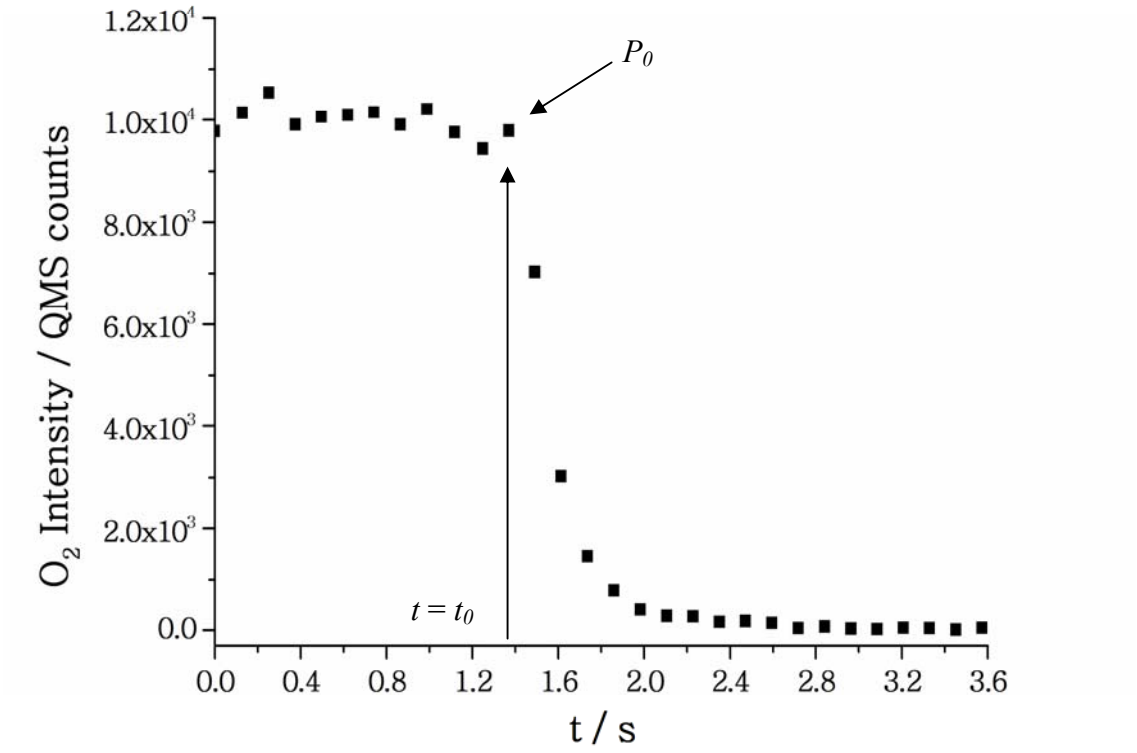

Figure 3.27: Example of a Pump-Down Curve

The pump-down experiments were performed once the apparatus had reached UHV conditions. The gate valves between the central chamber and the atomic beam chambers were closed and the gate valve between the central chamber and the 6" diffusion pump was throttled to reduce the pumping speed (see **Figures 2.3** and **2.5** in **Section 2.2.1**). The sample and QCM were positioned out of line of the beam (using the results obtained in **Section 3.3.2**) and the pressure of the central chamber noted. The molecular beam was created by leaking O_2 into the plasma source (with the RF power turn off) until the plasma chamber had reached a steady pressure of 2×10^{-5} mbar. MASsoft was set to monitor the intensity of O_2, O, CO/N_2 (both have the same mass) and CH_3 (contaminant) species and the KP-type thermocouple voltages of the silica sample and cold finger over time. After a short delay the gate valve between the central chamber and the oxygen atomic beam chamber was opened for approximately 20 seconds and then closed. This procedure was repeated four to six times with a delay between 20 and 40 seconds between each set (see **Figure 3.28** for an example set of

results). Once this had been completed, the MASsoft program was terminated and the data saved. Additional pump-down experiments were performed using this procedure for P of 5×10^{-5}, 8×10^{-5}, 9×10^{-5}, 3×10^{-4}, 5×10^{-4} and 1×10^{-3} mbar.

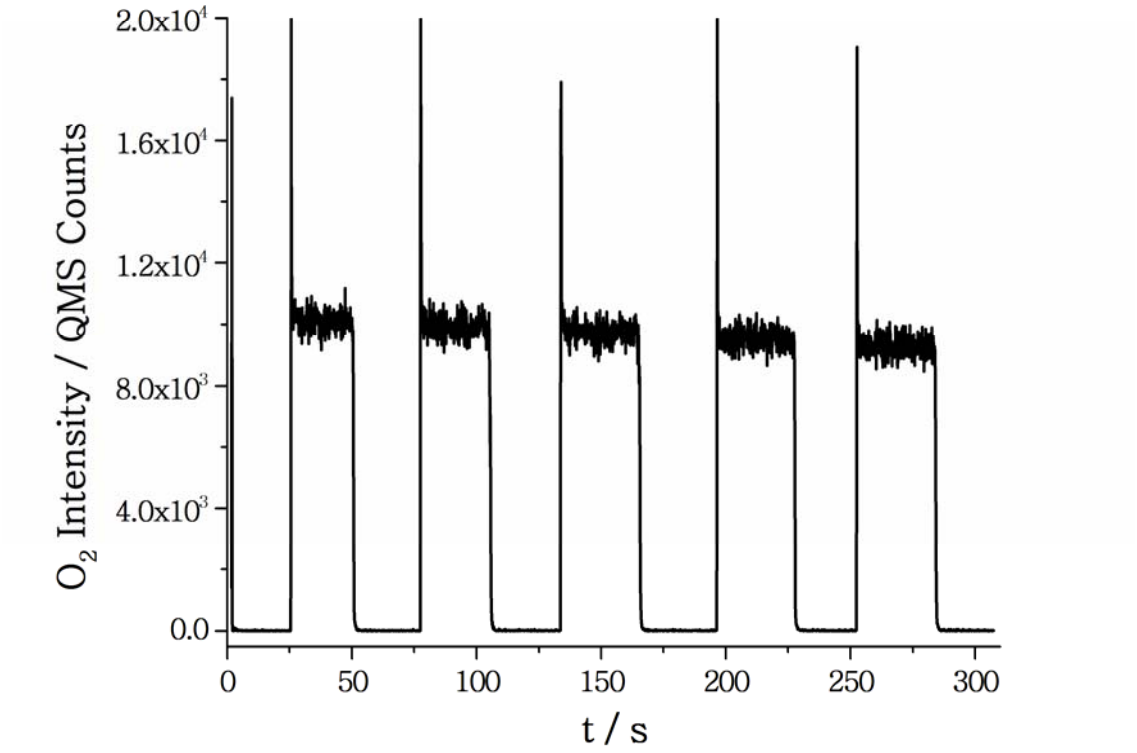

Figure 3.28: Example Experiment of Pump-Down Curves

To apply the values obtained from the data to calculate F_{beam}, a calibration equation was required to convert the units from QMS counts to Pascals. This was achieved by background dosing O_2 into the central chamber and monitoring the QMS counts through MASsoft over a range of pressures (in mbar). **Figure 3.29** displays a plot of the collected data with a line of best to convert the values in QMS counts into mbar. The final conversion to Pascals was achieved by multiplying by one hundred (see **Equation 3.18** for full conversion).

$$\left(O_2 / Pa\right) = \left(O_2 / counts\right) \times 7.08 \times 10^{-13} \times 100 \tag{3.18}$$

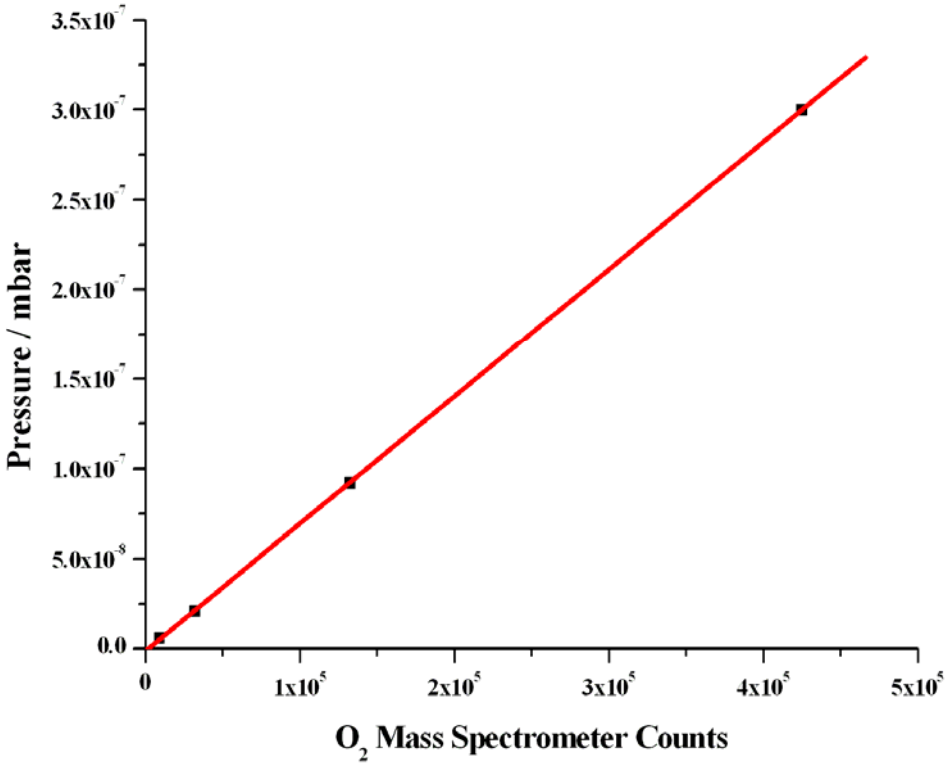

Figure 3.29: Calibration Graph Converting Units of QMS Counts to mbar

The data was imported into Origin and the pump-down data in each experiment separated. Plots of $\ln(P_{O_2})$ (P_{O_2} in units of Pa) against t were constructed and a line of best fit applied (see **Figure 3.30**). This line of best fit equation (**Equation 3.19**) is the logarithm version of **Equation 3.15** allowing P_0 and C_m to be calculated. The average values of P_0 and C_m for each pressure are displayed in **Table 3.4**. Errors for P_0 and C_m were obtained by taking the standard deviation from the range of values collected at each pressure.

$$\ln(P) = -C_m t + \ln(P_0) \tag{3.19}$$

The results indicated that the value of P_0 increased with increasing P as expected. However, when the error analysis was applied, the difference between the average value with the minimum and maximum values varied considerably as a result of converting the intercept from logarithm terms. As a consequence, the values of P_0 (with analytical

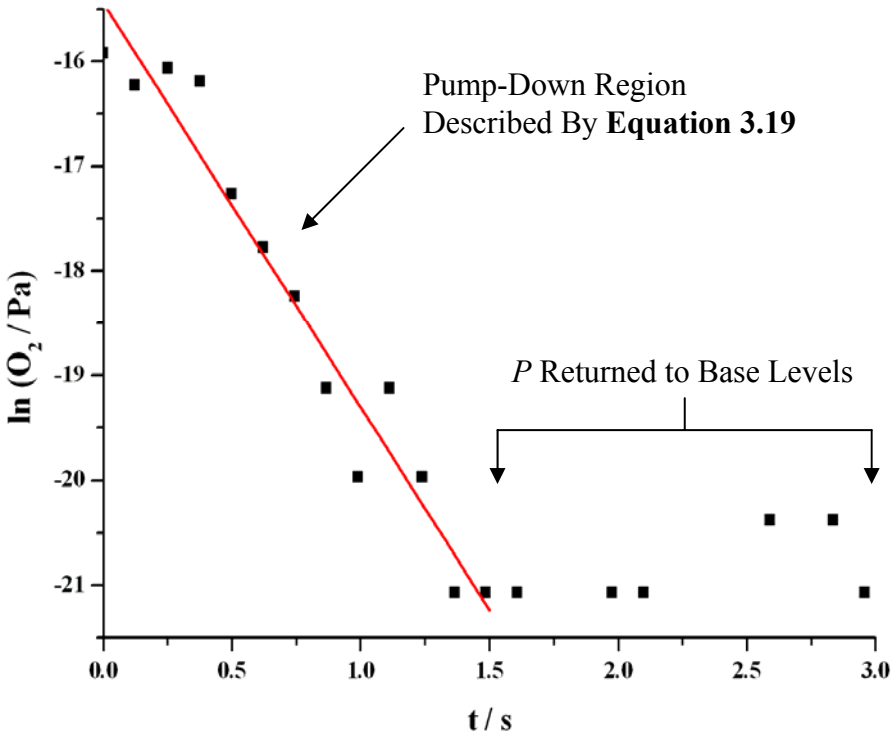

Figure 3.30: Example of Natural Logarithm Plot of Pump-Down Curve

Plasma Chamber Pressure / mbar	**P_0 / Pa**	**C_m / s**	**F_{beam} / molecules cm^{-2} s^{-1}**
2.1×10^{-5}	7.85×10^{-8} ($10^{-8.89\pm0.79}$)	3.68±0.79	$5.56\pm0.47\times10^{13}$
5.2×10^{-5}	1.78×10^{-7} ($10^{-7.25\pm0.02}$)	4.50±0.46	$1.26\pm0.11\times10^{14}$
8.1×10^{-5}	1.93×10^{-7} ($10^{-7.29\pm0.19}$)	4.50±0.46	$1.37\pm0.12\times10^{14}$
8.4×10^{-5}	3.85×10^{-7} ($10^{-7.59\pm0.16}$)	4.76±0.30	$2.73\pm0.23\times10^{14}$
2.9×10^{-4}	1.03×10^{-6} ($10^{-6.01\pm1.94}$)	4.64±0.47	$7.29\pm0.61\times10^{14}$
2.9×10^{-4}	1.06×10^{-6} ($10^{-6.03\pm1.52}$)	4.52±0.62	$7.51\pm0.63\times10^{14}$
5.1×10^{-4}	1.80×10^{-6} ($10^{-6.26\pm1.71}$)	4.95±0.50	$1.27\pm0.11\times10^{15}$
9.7×10^{-4}	2.99×10^{-6} ($10^{-6.48\pm0.23}$)	4.53±0.34	$2.12\pm0.18\times10^{15}$
Average	-	4.51±0.38	-

Table 3.4: Pump-Down Values of P_0, C_m and F_{beam}

errors) are also quoted in the form of powers (shown in brackets in **Table 3.4**). The experimental error in P_0 was expected to be larger than the analytical value quoted due to the UHV apparatus. However, as the exact experiment errors are difficult to determine separately then the analytical error only was used in this calculation and the experimental error for the whole apparatus was applied to the values of F_{beam}.

The values of C_m were expected to be similar throughout as the mass of the species in the beam remained constant. The results indicated that C_m varied from 3.68 to 4.95 s with an average and standard deviation of 4.51±0.38 s.

F_{beam} was calculated at each P using **Equation 3.17** (with the average value of C_m taken). V_{system} and A_{beam} were estimated as 0.13 m^3 and 2×10^{-5} m^2 respectively and T assumed as 300 K. The results are displayed in **Table 3.4** along with their errors which were calculated by multiplying through the errors obtained for P_0 (analytical error) and the standard deviation of the average value of C_m. However, as with P_0 the experimental error was expected to be an order of magnitude in size which is larger than the errors quoted.

A plot of F_{beam} against plasma chamber pressure, P, was constructed (see **Figure 3.31**) and revealed the relationship was approximately linear. The equation for the line of best fit (including analytical errors) is displayed in **Equation 3.20**. By knowing the pressure in the plasma chamber, the flux of the beam can be approximated using this equation. Ideally, this equation should be related to the beam pressure and not the pressure inside the plasma chamber. However, there is currently no method of determining or monitoring the beam pressure for either the hydrogen or oxygen beam on the apparatus. In the future, the apparatus will be modified and **Equation 3.20** adjusted. This is discussed in more detail in **Section 3.5**.

$$(\mathrm{F_{beam}} / \text{ molecules cm}^{-2}\ \text{s}^{-1}) = 2.3(\pm 0.2)\times10^{18}(P/mbar) + 4.4(\pm 13.1)\times10^{12} \quad (3.20)$$

Initial attempts to form an atomic oxygen plasma revealed the ideal value of P was around 1.0×10^{-4} mbar. At this pressure, F_{beam} was calculated to be $2.3\pm0.4\times10^{14}$ molecules cm^{-2} s^{-1}. The maximum atomic O F_{beam} value is twice that of the O_2 molecular F_{beam} (as one molecule of O_2 splits into two O atoms), providing a

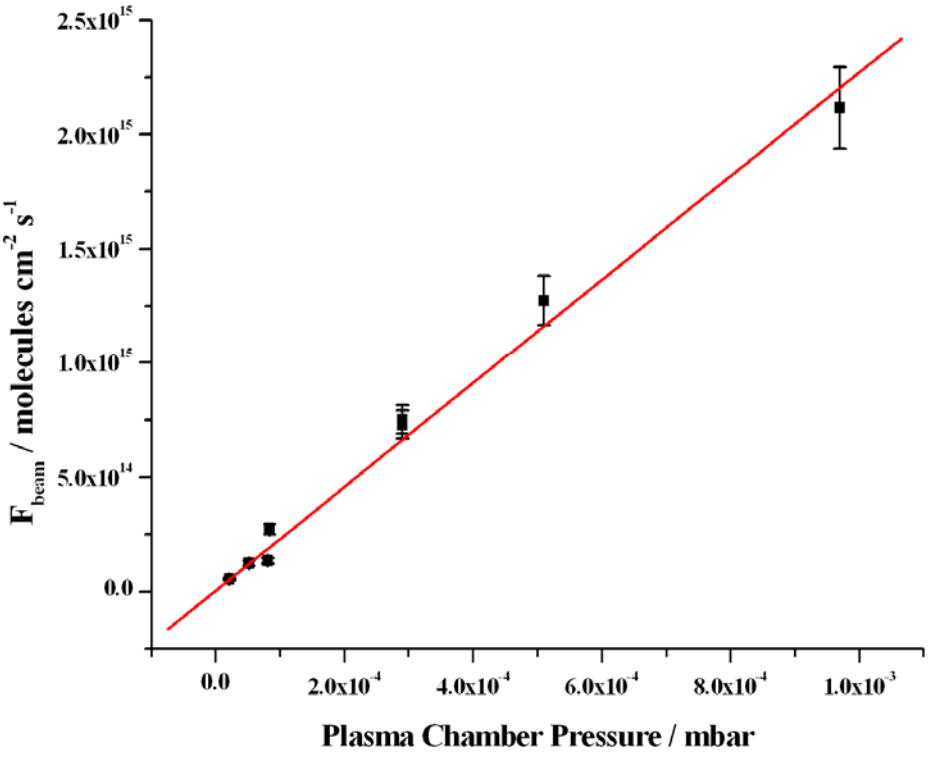

Figure 3.31: Plot of F_{beam} Against Plasma Chamber Pressure

value of $4.6\pm0.4\times10^{14}$ atoms cm^{-2} s^{-1}. However, due to the larger experimental errors on the system, the value of F_{beam} for the molecular and atomic beams was predicted to be $2\times10^{14\pm1}$ molecules cm^{-2} s^{-1} and $5\times10^{14\pm1}$ atoms cm^{-2} s^{-1} respectively. This value lies in the middle of the expect F_{beam} range for effusive beams. Although the units of F_{beam} for the atomic beam are quoted in units of atoms cm^{-2} s^{-1} not all of the species in the beam would have dissociated into the atomic form. The proportion of atomic to molecular species in the beam (also known as the dissociation fraction) is required and is described in the following sub-section.

In **Section 3.3**, F_{beam} was calculated from the mass deposited onto the QCM apparatus. This value, along with the corresponding value deduced from the pump-down experiments performed in this section, are displayed in **Table 3.5** at the ideal pressure setting used to form an atomic O beam (1.0×10^{-4} mbar). The results clearly indicate that the difference between the two values of F_{beam} is larger than the errors implied. The conclusions made in **Section 3.3** suggested that the difference in the results was the unknown temperature of the quartz crystal resulting in a relatively few molecules desorbing from the surface during the dose leading to an underestimated value of F_{beam}

using the QCM apparatus. As a consequence, the value of F_{beam} deduced from the pump-down experiments will be used towards calculating the surface concentration of O and O_2 on the silica sample for the TPD experiments performed in this ongoing research.

***P* / mbar**	**F_{beam} from QCM Experiments / molecules cm^{-2} s^{-1}**	**F_{beam} from Pump-Down Experiments / molecules cm^{-2} s^{-1}**
1.0×10^{-4}	$5\times10^{11\pm1}$	$2\times10^{14\pm1}$

Table 3.5: Comparison of F_{beam} Derived from QCM (middle) and Pump-Down Experiments (right) at the Ideal Pressure Setting Used to Form an Atomic O Beam

Another suggestion for the difference between the two values for F_{beam} was the assumed value for the sticking coefficient, *S*. However, this suggestion was previously seemed as unlikely as multilayers of O_2 were dosed onto the QCM in the experiments implying that the value of *S* should lie close to 1. Using the results displayed in **Table 3.5**, the value of *S* for the O_2 beam on quartz was estimated using **Equation 3.21** as approximately $3\times10^{-3\pm2}$ (at the silica sample base temperature and O_2 beam pressure of 1.0×10^{-4} mbar) which is considerably lower than the original assumption. This indicates that the temperature of the quartz crystal is considerably warmer than the base temperature of the silica sample resulting in relatively fewer molecules remaining adsorbed on the quartz surface. In the future, experiments based on the King and Wells method and TPD experiments will be performed to determine the value of *S* over a range of different quartz crystal temperatures (as previously discussed in **Section 3.3.2**) for the O_2 and O beams. In addition, these experiments will also be performed using the silica sample (used for the beam dosed experiments). The results will provide a more accurate measurement of the surface concentration dosed onto the sample, N_{tot}, then from just F_{beam} (from the pump-down experiments) alone.

$$S = \frac{F_{beam}(QCM)}{F_{beam}(Pump-Down)} \tag{3.21}$$

Ideally the experiment to determine F_{beam} would be repeated using the H_2 molecular beam but, due to the hydrogen RF powered plasma source being returned for repairs (as

discussed in **Chapter 2**), these experiments were unable to be performed in time. When the experiment is performed in the future, the pressure range may have to be reduced as the pump-down curves produced may be difficult to distinguish from the background gas when the H_2 molecular beam is formed at low values of *P*. Additional experiments will also be performed to determine the value of *S* over a range of silica surface temperatures if the base surface temperature can be lowered to allow H_2 and H to adsorb.

3.4.3 Beam Cracking Fraction Calibrations

To date there are no techniques that can produce 100% dissociation in molecular species. When gaseous molecules in a glow discharge plasma absorb energy (in this case, RF) in the high brightness mode, the molecules are excited into molecular excited states (see **Figure 2.12** in **Chapter 2**). Only those molecules that absorb enough energy to reach the dissociative energy levels produce atoms resulting in the atomic beam containing a mixture of atoms and molecules. As previously discussed in **Section 2.3.2**, the dissociation fraction is dependent on the bond dissociation enthalpy of the species of interest. For H_2 and O_2 the bond dissociation enthalpies are 436 and 497 kJ mol^{-1} at 298 K respectively [1]. Along with additional factors, like the electronegative behaviour of the species, this results in atomic H beams exhibiting a higher dissociation fraction than O beams using the same source (as previously discussed in **Section 3.2**). This has been proven using a RF powered plasma source with a Pyrex plasma tube where the dissociation fractions were measured as typically 90 % for H_2 [21] and 30–40% for O_2 [4]. In this study, the material for the plasma tube and reactor were chosen to produce the highest dissociation fraction for the required beam species. In the hydrogen plasma sources, boron nitride was used whilst the plasma tube and reactor in the oxygen plasma source were constructed from quartz.

The dissociation fraction of an atomic beam was determined using beam cracking fraction calibration experiments. This was achieved by positioning the QMS in line with the beam and monitoring the molecular and atomic species for a set irradiation time. On the current dual atomic beam system, there was no position were the QMS could be situated to achieve this (see **Figure 2.5** in **Section 2.2.1**). To reposition the QMS, a new adaptor flange was designed (see **Figure 3.32**) so that the QMS's detector would sit at the position where the two beams would cross in the middle of the central chamber (**Figure 3.33**). This would allow the cracking fraction experiments to be

performed on both the oxygen and hydrogen beams without having to change the apparatus set up.

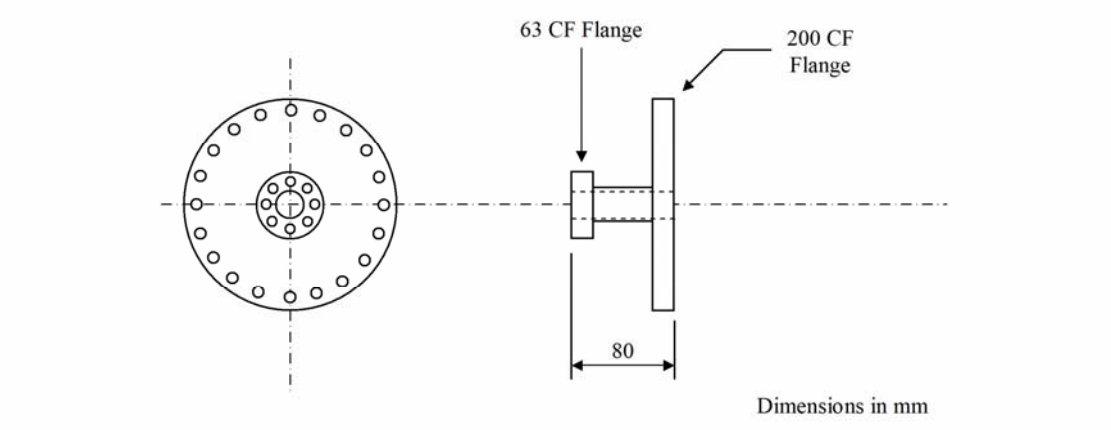

Figure 3.32: Schematic Drawing of the New Adaptor Flange

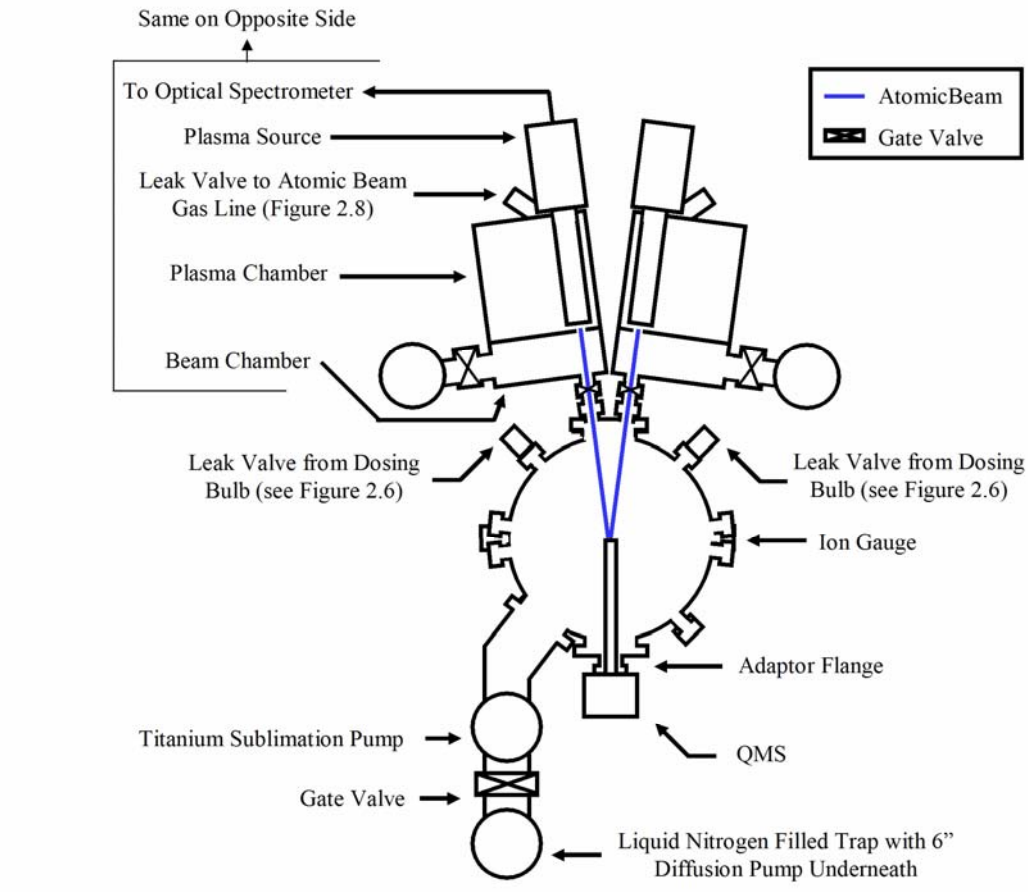

Figure 3.33: Apparatus Diagram for the Cracking Fraction Experiments

The experiments were performed under high vacuum (HV) pressures with the sample mount and cold finger removed. This was to prevent any accidental lowering of the sample assembly onto the QMS detector positioned directly below. With the gate valves closed between the atomic beam chambers and the central chamber, O_2 was leaked into the plasma source and an atomic beam created with P at 7.5×10^{-5} mbar. The RF power was adjusted to produce a stable atomic plasma and maximum intensity of the O emission peak at 777 nm. MASsoft was programmed to monitor the intensity of O_2, O, H_2O and CH_3 (contaminate) species and started. After a short delay, the gate valve between the oxygen atomic beam chamber and the central chamber was opened for a set time and then closed. This was repeated several times with a delay gap of 20 to 40 seconds between each beam irradiation dose. The whole experiment was repeated with P held at 1.0×10^{-4}, 2.5×10^{-4}, 5.0×10^{-4} and 7.5×10^{-4} mbar. The whole experiment was repeated again at each pressure using the O_2 molecular beam so that any dissociated species detected by the QMS that were not formed from the RF plasma source were removed from the final calculation. Ideally, these experiments should be performed by varying the beam pressure instead of P (plasma chamber pressure). However, there is currently no method available to determine and monitor the beam pressure for either the hydrogen or oxygen beams. In the future, the apparatus will be altered to provide an accurate method of monitoring the beam pressure which should increase the accuracy of the results (for more details see **Section 3.5**)

The data was imported into Origin and plots were constructed of O_2 and O QMS intensity (in units of counts) against time, t. An example plot for the molecular beam cracking fraction is displayed in **Figure 3.34**. A small proportion of O atoms were detected using the O_2 molecular beam as some of the O_2 molecules were dissociated in the QMS source. This proportion was between 5 to 11 % of the intensity of the O_2 signal. By taking the average signal intensity of O to O_2 the cracking fraction was calculated for both beams at each pressure. The dissociation fraction was obtained by subtracting the cracking fraction of the O_2 beam from the O beam and multiplied into a percentage. This procedure removed the dissociation of O_2 by the QMS source from the final dissociation fraction.

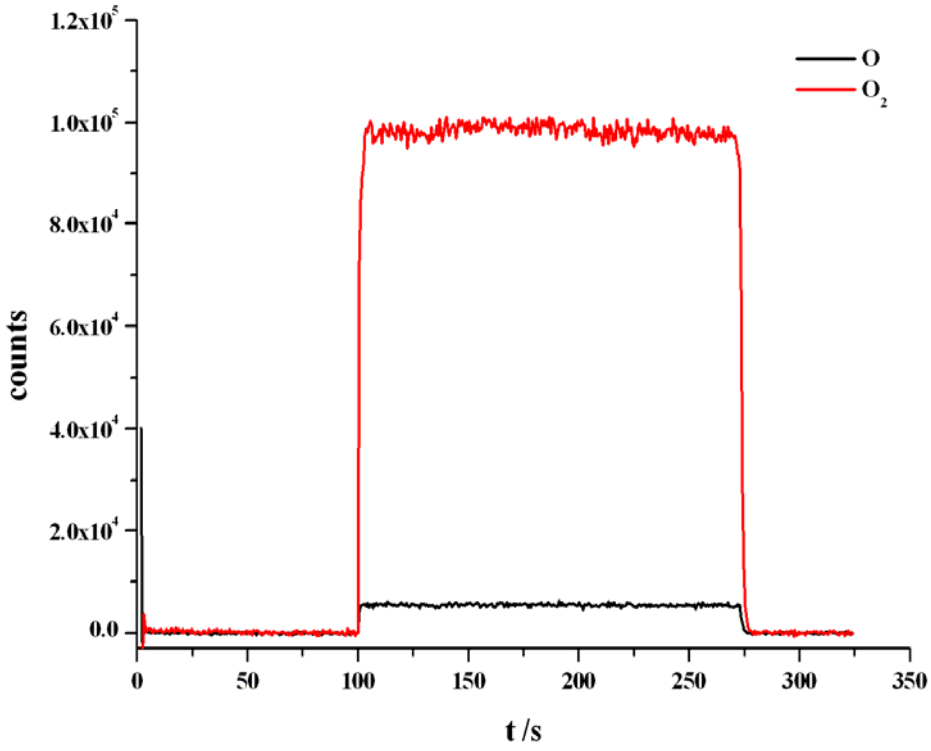

Figure 3.34: Example Plot of O_2 and O QMS Counts against *t*

The results are displayed in **Table 3.6** and revealed that the cracking fraction was typically the same for both the atomic and molecular beams resulting in the dissociation fraction being approximately zero. This implied that the only O species observed were from the dissociation of O_2 molecules in the QMS source and not from the RF powered plasma source. The caused of this was concluded to be that the QMS detector was out-of-alignment with the beams even though the design of the adaptor flange took into account the ultimate position of the O_2 molecular beam with respect to the quartz crystal. In the future, the adaptor flange will be replaced with either a xyz manipulator or a port alignment flange. This will provide greater flexibility in positioning the QMS detector in-line with both the oxygen and hydrogen beams. The cracking fraction experiments will be repeated using the same procedure described above (with the new manipulator or flange) to determine the $O:O_2$ and $H:H_2$ dissociation fractions.

Plasma Chamber Pressure / mbar	O_2 Beam Cracking Fraction	O Beam Cracking Fraction	Atomic Beam Dissociation Fraction
5.0×10^{-5}	0.11	0.11	0 %
7.5×10^{-5}	0.08	0.09	1 %
1.0×10^{-4}	0.07	0.08	1 %
2.5×10^{-4}	0.06	0.07	1 %
5.0×10^{-4}	0.6	0.06	0 %
7.5×10^{-4}	0.5	0.06	1 %

Table 3.6: Cracking Fractions and Dissociation Fraction Results

3.4.4 Conclusions

The experiments performed in this section were used to determine F_{beam} and the dissociation fraction of the atomic oxygen beam formed at P of 1.0×10^{-4} mbar. Pump-down experiments were used to determine F_{beam} over a range of P. Analysis of these results predicted F_{beam} for the O_2 molecular beam as $2\times10^{14\pm1}$ molecules cm^{-2} s^{-1}. This value is considerably larger than the value of F_{beam} determined from the analysis using the QCM apparatus in **Section 3.3** (see **Table 3.5**) indicating that the calculations of F_{beam} using the QCM apparatus were greatly affected by the value of S. The initial assumption was that S lay close to a value of 1 as multilayers of O_2 were dosed onto the quartz crystal. However, further analysis estimated S to be approximately $3\times10^{-3\pm2}$ at this O_2 beam pressure and quartz surface temperature implying that relatively fewer molecules remained adsorbed on the quartz crystal. In the future, experiments based on the King and Wells method and TPD experiments (see **Section 3.3.2** for details) will be performed to determine the values of α and k_{des} to calculate S on quartz and silica over a range of surface temperatures for the O_2 and O beams. This will enable a more accurate measurement to be made of the surface concentration beam dosed onto the surface, N_{tot}.

The results from the pump-down experiments predicted the maximum value of F_{beam} for the atomic O beam as $5\times10^{14\pm1}$ atoms cm^{-2} s^{-1} at P of 1.0×10^{-4} mbar. Similar experiments were planned to calculate F_{beam} for the H_2 molecular and H atomic beams but this was not achieved in this study due to the continuous problems with the hydrogen RF plasma source. Additionally, the King and Wells method and TPD experiments will also be performed using the H_2 and H beams but only on silica once

the apparatus has been adjusted to reduce the base surface temperature low enough to allow H_2 and H to adsorb. The quartz crystal can not be cooled to temperatures low enough to allow H and H_2 to adsorb using the current apparatus system.

The results obtained from the cracking fraction experiments revealed that the only O atoms observed were formed by O_2 molecules dissociating in the QMS source. The cause of this was concluded to be that the QMS detector was not in line with the oxygen beam as planned. In the future, the adaptor flange built for these experiments will be replaced with either a xyz manipulator or a port alignment flange allowing greater flexibility in aligning the QMS with the beams. Once this has been achieved, the cracking fraction experiments will be repeated to determine the $O:O_2$ and $H:H_2$ dissociation fraction.

3.5 Summary and Conclusions

This chapter focused on the calibration experiments performed on the oxygen atomic and molecular beams in the new dual atomic beam system. The calibration experiments performed in **Section 3.2.2** and **3.2.3** analyzed the atomic O and H plasmas respectively. Example atomic O and H plasma spectra taken at 150 W and 1×10^{-4} mbar were displayed in **Figure 3.7** and **Figure 3.18** respectively. In the atomic O plasma spectrum, the most intense transition observed was the $O(3p^5P) \rightarrow O(3s^5S)$ at 777 nm. Other O transitions were assigned at 844.6, 645.6, 615.7, 533.0, 436.8 and 394.8 nm (in order of decreasing intensity). In the atomic H plasma, the Balmer H_α peak at 656 nm was the most intense. This spectra also contained other weaker Balmer transitions at 486.1 and 434.1 nm (in order of decreasing intensity) and a N_2 transition at 337 nm remnant from the secondary gas technique. Both spectra contained the $OH(A^2\Sigma^+) \rightarrow OH(X^2\Pi_i)$ (around 308 nm), Balmer H_α and the $O(3p^5P) \rightarrow O(3s^5S)$ transitions implying that other chemical reactions were occurring in the plasmas. The source of the OH transition was concluded to be from the dissociation of H_2O and through the decay of collisional excited OH radicals. In the O plasma, the three additional mechanisms: collisional deactivation of $O(^1D)$; reactions of dissociated H_2 molecules with O and O_2; and the dominant reaction of $O(^3P)$ atoms with H_2O, increased the formation of OH. Destruction reactions of OH resulted in the formation of O, O_2, H, H_2 and H_2O.

Further analysis was applied to the atomic O plasma to explore the affect of *P* and RF power with the intensity of selected peaks. The results revealed that the intensity of all the peaks generally increased with increasing RF power. As a consequence, an upper limit for the RF power was concluded as 150 W to ensure the emissions from other transitions, like H_2, OH, O(^{1}D) and O(^{1}S), remained as small as possible with respect to the intensity of the O peak at 777 nm. This was especially critical for the undesired O(^{1}S) and O(^{1}D) species which radiative decay through weak electric dipole forbidden transitions indicating that the concentration of these species was higher than the intensity of the emission peaks implied. The shape of the intensity curve for the O(777 nm) peak revealed that at RF powers greater than 120 W, the curve displayed a peak maximum around 1×10^{-4} mbar. In conclusion, all atomic O beam experiments performed in this ongoing research are set at *P* of 1.0×10^{-4} mbar and at a RF power between 120 and 150 W.

Further analysis observations to determine the ideal RF power setting revealed that other larger factors were affecting the intensity of the emission peaks in both the oxygen and hydrogen plasmas. The dominant factor was identified as how long and how frequent the source was used previously. The solution to this factor was to run the atomic beams continuously for a few weeks prior to the experiment. This would remove any traces of out-gassing species and increases the stability of the plasma. However, the beams could not be run continuous as the RF power would have to be terminated for every experiment that required thermocouple readings due to interference. Considerations are being made to shield the thermocouples from the RF power but, due to the delicate arrangement of the sample mount and possible problems with electrical shorts, a suitable modification to the apparatus has yet to be made. Additionally, the atomic beams cannot be run overnight for safety reasons. For the present, the solution was to run the beams as often as possible before the atomic beam experiment and to continuously adjust the RF power to obtain consecutive peak intensities at a plasma chamber pressure of 1.0×10^{-4} mbar. Alternatively, more accurate results may have obtained if the beam pressure was used rather than the plasma chamber pressure. Presently there is no technique available on the current apparatus to determine and monitor the beam pressure. A possible modification to both the atomic beam chambers to achieve this is displayed in **Figure 3.35** and involves adding a pressure gauge between the leak-valve and the plasma source. This alteration would also have

improved the accuracy of the results obtained for all the calibration experiments performed in this chapter.

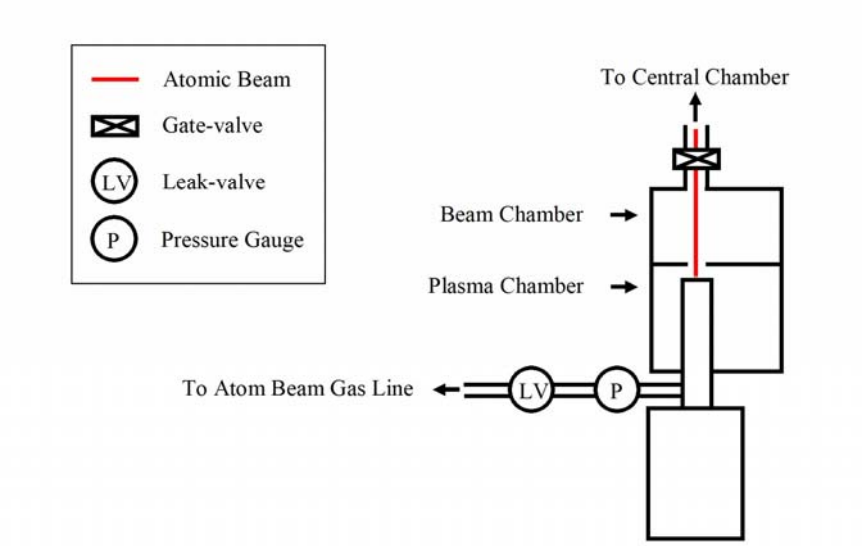

Figure 3.35: Modification to Apparatus to Monitor Beam Pressure

Another modification required to the present UHV system is to control the gas flow of N_2 into the plasma source when using the secondary gas technique. Previously this was achieved by replacing the O_2 cylinder with N_2 and closing off the valves to the oxygen plasma source and the pumping line (see **Figure 3.15** in **Section 3.2.3**). However, this prevented both the hydrogen and oxygen beams from being formed at the same time as the apparatus was designed too. An alternative arrangement would be to either modify the atom beam gas line (see **Figure 3.36** for a suggestion previously shown in **Chapter 2**) or by replacing the H_2 cylinder with a mixed gas one where the H_2:N_2 ratio is high. Although the latter solution would provide a constant error on the purity of the atomic H plasma, the nitrogen species would cause additional surface reactions to occur in the H and H_2 beam dosed experiments which would greatly complicate the experiment. As a consequence, the solution shown in **Figure 3.36** will be used.

The experiments performed in **Section 3.3** used the QCM apparatus to successfully determine the ultimate position of the O_2 molecular beam in respect to the quartz crystal (which is displayed in **Table 3.7**). From this, the ultimate position of the silica sample in respect to the beam was calculated. The results also indicated that Δf (and hence Δm)

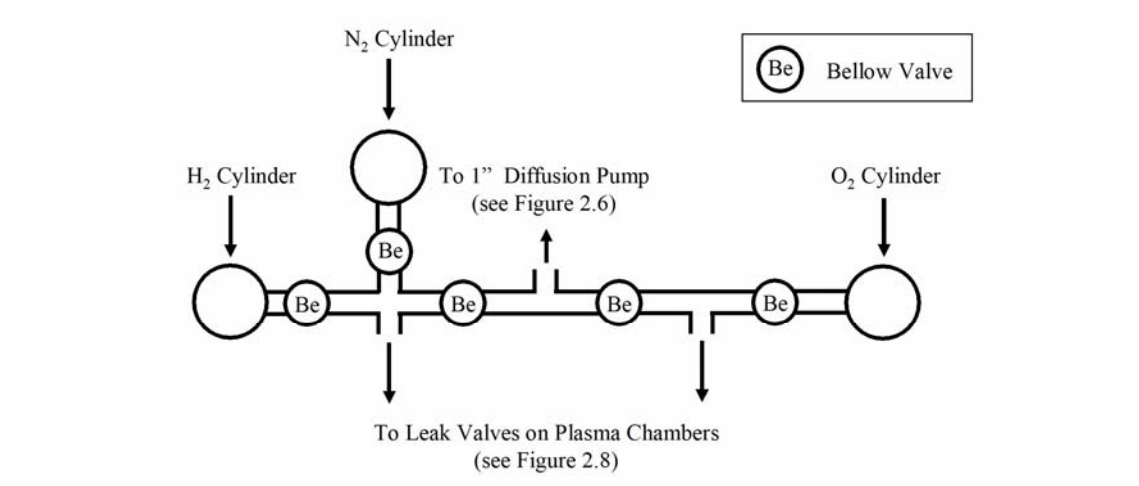

Figure 3.36: Modification to the Atom Beam Gas Line to Include the Gas Required for the Secondary Gas Technique.

Surface	Ultimate Position
Quartz Crystal	x = -5.0 mm, y = 0.0 mm, z = 70.0 mm, θ = -0.5°
Silica Sample	x = -5.0 mm, y = 0.0 mm, z = 50.0 mm, θ = -0.5°

Table 3.7: The Ultimate Position of the Quartz Crystal and the Silica Sample in Respect to the O_2 Molecular Beam

varied slightly from the different sets of measurements due to small changes in the beam flux. Additional experiments using the QCM apparatus were performed with the crystal held in the ultimate position and P varied. The results indicated that Δf was linearly dependent on P between 7×10^{-5} and 7×10^{-4} mbar as a consequence of increasing F_{beam}. Below this pressure range, Δf was roughly constant and consisted of the background flux from the plasma chamber. Above 7×10^{-4} mbar, the pumping system for the plasma chamber stalled resulting in the chamber being flooded.

Values of Δm and F_{beam} were determined from the QCM experiments in the linear dependent region of Δf with P. At the pressure setting determined in **Section 3.2.2** to form an atomic O beam, the values of Δm and F_{beam} were $2\times10^{14\pm1}$ molecules cm^{-2} and $5\times10^{11\pm1}$ molecules cm^{-2} s^{-1} respectively. However, the value of F_{beam} was just outside the expected range for an effusive beam system (10^{13} and 10^{15} molecules cm^{-2} s^{-1}) suggesting that there were other sources of error involved in the experiment. The most

likely cause for this was concluded to be the unknown and possibly variable temperature of the crystal. The surface temperature of the crystal was unable to be monitored during the experiment as the E-type thermocouple was not sensitive at base temperatures but was estimate as being between 23 and 28 K. However, the upper limit of this temperature region is close to that were O_2 is known to start desorbing resulting in a relatively few molecules desorbing from the crystal during the dose. As a consequence, the calculated value of F_{beam} would have been underestimated.

A more accurate calibration of F_{beam} was obtained by performing pump-down experiments (**Section 3.4.2**). The results obtained enabled F_{beam} to be determined over a selected range of P. **Table 3.8** displays the value of F_{beam} for the molecular O_2 beam at 1×10^{-4} mbar and reveals that the value lay in the middle of the expected range of F_{beam} for effusive beams. The table also displays the corresponding value of F_{beam} derived from the QCM experiments and clearly reveals a difference of three orders of magnitude which is larger than the errors suggest. This implies that the conclusion made in **Section 3.3** indicating that F_{beam} using the QCM apparatus was greatly affected by S. Previously, the value of S was assumed to lie close to 1 as multilayers of O_2 were sticking to the crystal. However, further analysis estimated that S was considerably smaller (**Table 3.8**) implying that relatively fewer molecules remained adsorbed on the quartz crystal under the experimental conditions used. In the future, experiments based on the King and Wells method and TPD experiments will be performed using both the molecular O_2 and atomic O beams on quartz over a range of surface temperatures (see **Section 3.3.2** for details).

P / mbar	F_{beam} (QCM) / molecules cm^{-2} s^{-1}	F_{beam} (Pump-Down) / molecules cm^{-2} s^{-1}	S
1.0×10^{-4}	$5\times10^{11\pm1}$	$2\times10^{14\pm1}$	$3\times10^{-3\pm2}$

Table 3.8: Values of F_{beam} Derived from the QCM and Pump-Down Experiments and S at the Ideal Pressure Setting Use to Form an Atomic O Beam

Overall, the value of F_{beam} at 1.0×10^{-4} mbar from the pump-down experiments was concluded to be more accurate representation of the beam flux. The pump-down experiments were also used to obtain a maximum atomic O F_{beam} of

$5\times10^{14\pm1}$ atoms cm^{-2} s^{-1}. Both of these values will be used towards determining the surface concentration of O and O_2 dosed from the atomic or molecular beam in this thesis and in the future. However, as the estimated value of *S* on quartz was considerably smaller than assumed, the King and Wells method and the TPD experiments will also be performed on the silica sample used for the beam dosed experiments. This will provide a more accurate measurement of the surface concentration, N_{tot}, beam dosed onto the surface.

Another variable that affects the value of *S* is the beam temperature. This has recently been explored with an atomic D beam on amorphous solid water (ASW) by Matar *et al*. [26] and revealed that *S* reduced considerably as the beam temperature increased between 30 and 350 K. If the range of N_{tot} is too small over a large range of beam irradiation dose times, then the apparatus could be modified to cool the beam species using a similar technique as used by Matar *et al*. where the gas is passed through an aluminium nozzle connected to a closed-cycle He cryostat. Another method would be to direct the beam through a tube surrounded by a copper tube connected to a closed-cycle He cryostat as used by the research group using the ASURA apparatus [27] (see **Section 1.3.3** in **Chapter 1**). This would result in more of the beam species sticking to the surface which would increase the value of *S* and the range of N_{tot}.

The calibration experiments performed in **Section 3.4.3** were designed to determine the atomic O beam dissociation fraction from the atomic and molecular beam cracking fractions. The results obtained revealed that the cracking fractions were the same for both beams resulting in a dissociation fraction of approximately zero. This implied that the only source of O atoms detected was the dissociation of O_2 in the QMS source indicating that the new adaptor flange was not positioning the QMS detector in-line with the beam. Modifications to the apparatus setup would result in the exchange of the adaptor flange with either a xyz manipulator or a port flange to allow greater flexibility in aligning the QMS with the oxygen atomic and molecular beams. However, this was not achieved in time for this thesis. In the future, this calibration experiment will be repeated with this change included to determine the $O:O_2$ dissociation fraction.

The QCM ultimate position, F_{beam} from pump-down experiments, and the dissociation fraction calibrations are planned to be performed using the hydrogen atomic and molecular beam. However, due to continuous problems and repairs experienced with

the hydrogen RF powered plasma source, this was not achieved during this study and will be performed in the future.

3.6 References

[1] P. Atkins and J. de Paula, *Atkins' Physical Chemistry*, 7 edn., Oxford University Press, Oxford, 2002.

[2] A. M. Al-Jalal and M. A. Khan, *Plasma Chem. Plasma Process.*, 2010, **30**, 173.

[3] F. Dulieu, L. Amiaud, E. Congiu, J. H. Fillion, E. Matar, A. Momeni, V. Pirronello and J. L. Lemaire, *Astron. Astrophys.*, 2010, **512**, A30.

[4] G. Vidali, J. Roser, G. Manico and V. Pirronello, *Adv. Spa. Res.*, 2004, **33**, 6.

[5] H. Boenig, *Plasma Science and Technology*, Cornell University Press, London, 1982.

[6] P. C. Cosby, *J. Chem. Phys.*, 1993, **98**, 9560.

[7] J. C. Gerard, L. Soret, A. Saglam, G. Piccioni and P. Drossart, *Adv. Space Res.*, 2010, **45**, 1268.

[8] R. A. Young, G. Black and T. G. Slanger, *J. Chem. Phys.*, 1968, **49**, 4758.

[9] C. J. Bennett and R. I. Kaiser, *Ap. J.*, 2005, **635**, 1362.

[10] A. Corney, *Nuc. Instrum. Meth.*, 1973, **110**, 151.

[11] A. Sasso, M. I. Schisano, G. M. Tino and M. Inguscio, *J. Chem. Phys.*, 1990, **93**, 7774.

[12] M. J. Mumma and E. C. Zipf, *J. Chem. Phys.*, 1971, **55**, 1661.

[13] D. G. Kuehn and L. M. Chanin, *J. Chem. Phys.*, 1982, **76**, 349.

[14] P. M. Dooley, B. R. Lewis, S. T. Gibson, K. G. H. Baldwin, P. C. Cosby, J. L. Price, R. A. Copeland, T. G. Slanger, A. P. Thorne, J. E. Murray and K. Yoshino, *J. Chem. Phys.*, 1998, **109**, 3856.

[15] M. Asplund, N. Grevesse, A. J. Sauval, C. Allende Prieto and D. Kiselman, *Astron. Astronphys.*, 2004, **417**, 751.

[16] H. Yamazaki and R. J. Cvetanovic, *J. Chem. Phys.*, 1963, **39**, 1902.

[17] W. B. DeMore, *J. Chem. Phys.*, 1967, **47**, 2777.

[18] B. Das and J. W. Farley, *J. Chem. Phys.*, 1991, **95**, 8809.

[19] G. J. Schulz, *J. Chem. Phys.*, 1960, **33**, 1661.

[20] H. D. Morgan and J. E. Mentall, *J. Chem. Phys.*, 1974, **60**, 4734.

[21] J. E. Roser, G. Manico, V. Pirronello and G. Vidali, *Ap. J.*, 2002, **581**, 276.

[22] G. Sauerbrey, *Z. Phys.*, 1959, **155**, 206.

[23] J. D. Thrower, *Atoms and Molecules on Very Cold Surfaces*, The University of Nottingham, Nottingham, 2005.

[24] M. P. Collings, M. A. Anderson, R. Chen, J. W. Dever, S. Viti, D. A. Williams and M. R. S. McCoustra, *Mon. Not. R. Astron. Soc.*, 2004, **354**, 1133.

[25] D. A. King and M. G. Wells, *Surf. Sci.*, 1972, **29**, 454.

[26] E. Matar, H. Bergeron, F. Dulieu, H. Chaabouni, M. Accolla and J. L. Lemaire, *J. Chem. Phys.*, 2010, **133**, 104507.

[27] N. Watanabe and A. Kouchi, *Ap. J.*, 2002, **571**, L173.

[28] D. J. Oakes, University of East Anglia, 1994.

Chapter 4 - H_2O and O_2 Temperature Programmed Desorption

Contents

4.1 Introduction

This chapter focuses on the desorption kinetics of H_2O and O_2 from a range of astrophysically relevant surfaces using temperature programmed desorption (TPD). The data collected was used to build a kinetic simulation model to describe the desorption of O_2 from the icy mantles coating interstellar dust grains in dense molecular cloud environments.

The first set of experiments explore the desorption behaviour of H_2O (in the form of porous amorphous solid (pASW) ice) from a bare silica surface using background dosing TPD (**Section 4.2**). The kinetic parameters were obtained using leading edge analysis [1]. The data was initially fitted by a two population model using Chemical Kinetic Simulator (CKS)[1] package before applying an additional phase change reaction step. In **Section 4.3**, background dosed TPD and molecular beam dosed TPD experiments were performed to investigate the desorption kinetics of O_2 from a bare silica surface. The kinetic parameters obtained from these experiments were obtained by two different analytical methods depending on the O_2 film thickness. For multilayer coverages, leading edge analysis was applied (as in **Section 4.2**) and the data fitted with CKS. Sub-monolayer coverages were analyzed using direct inversion of the Polyani-Wigner equation [2] and were fitted using a more complex multiple activation energy of desorption, E_{des}, simulation model.

The third and fourth set of experiments discussed in this chapter explore the desorption kinetics of O_2 from compact amorphous solid water (cASW) ice (see **Section 4.4**) and porous amorphous solid water (pASW) ice (**Section 4.5**). Both sets of results were analyzed using direct inversion of the Polyani-Wigner equation and fitted with the multiple E_{des} simulation model used to analyze the O_2 sub-monolayer coverages in **Section 4.3**.

The kinetic parameters obtained from each of the four experiments were used to construct a simulation model under dense molecular cloud conditions in the ISM (see **Section 4.6**). This was based on a similar model used to describe the desorption of CO

[1] Chemical Kinetics Simulator, Version 1.0, IBM, IBM Almaden Research Centre, 1995. Further information may be obtained from http://www.almaden.ibm.com/st/msim/ckspage.html.

from the icy mantle under the same interstellar conditions [3]. The overall summary and conclusions for this chapter are discussed in **Section 4.7** along with the astronomical implications.

4.2 H_2O on Bare Silica Surface

4.2.1 Introduction

In this section the results of the H_2O background dosing TPD experiments on bare silica are discussed. **Section 4.2.2** discusses the experimental procedures and **Section 4.2.3** the TPD results. The double peak desorption structure indicated that part of the H_2O ice changes during the TPD experiment from cASW to crystalline solid water (CSW). Leading edge analysis was applied to both peaks to obtain their kinetic parameters. The results obtained were used to fit the TPD curves using two different CKS models (**Section 4.2.4**). The first model fitted the data with separate populations for cASW and CSW to obtain the kinetics of the two desorption steps. The second more complex model used the findings from the first CKS model to obtain the crystallisation rate for the phase change. The conclusions to these experiments are discussed in **Section 4.2.5**. The results obtained were used towards constructing the simulation models discussed in **Sections 4.5** and **4.6**.

4.2.2 Experimental Procedure

After UHV conditions had been achieved, the sample was heated clean at 180 K and cooled back to base temperature. The sample was positioned in line with the atomic beams, with the gate valves between the central chamber and the atomic beam chambers closed, and the central chamber pressure noted.

A dosing bulb was flushed and filled with H_2O vapour previously purified using the freeze-pump-thaw technique (for more details see **Section 2.4.2**). This additional process reduced the amount of contaminant species found in H_2O and removed the air above the liquid. The data acquisition program was set to monitor the central chamber pressure and the thermocouple voltages. MASsoft was programmed to monitor the intensity of H_2O, CO/N_2, O_2 and CH_3 (contaminant) species and the KP-type thermocouple voltages of the silica sample and cold-finger over time. The gas was leaked into the central chamber *via* a leak valve from the gas lines for a set dose of 10,

20, 30, 40, 50, 70, 80, 100, 200, 300, 500 and 1000 L. The pressures, *P*, and times, *t*, values for each dose were determined using **Equation 4.1** (the exact dose was calculated in the results section). Once the dose was complete and the pressure had returned to base levels, the MASsoft and data acquisition programs were stopped.

$$Dose / L = \frac{Pt}{10^{-6}} \tag{4.1}$$

Once the dose stage had been completed, the sample was positioned in front of the QMS (located in position 1). The central chamber pressure was noted and the two programs, using the same settings as in the dosing stage, were started. After a few minutes delay, a linear heating ramp was applied to the sample heater from base temperatures up to 180 K. After the sample had reached this temperature, the two programs were stopped and the heating ramp terminated.

Once the sample had returned to base temperatures, a second dose TPD experiment could be performed. A duplicate set of experiments for each dose was obtained.

4.2.3 Results

The raw data from the MASsoft and data acquisition programs was imported into Origin and the thermocouple voltages converted into temperature units using the method and equations previously described in **Section 2.2.3**. For each dose, the H_2O TPD curves were plotted against temperature (see **Figure 4.1**). The exact background dose was calculated by integrating the pressure dose curve against time from the data acquisition program and converting into units of Langmuir (**Equation 4.1**).

The TPD results in **Figure 4.1** revealed that all the doses exhibited coincident leading edges (within experimental error) indicating that the desorption followed zeroth order kinetics. This implied that the H_2O molecules were desorbing from the bulk ice (or multilayer) and that the dominant interaction was H_2O – H_2O. The 10 to 80 L doses contain a single desorption peak whilst the higher background deposition doses contain two. The desorption peak at the lower temperature (starting at approximately 140 K) represents the desorption of cASW ice. As the surface temperature increased, the cASW ice underwent a phase change to form crystalline solid water (CSW) ice which

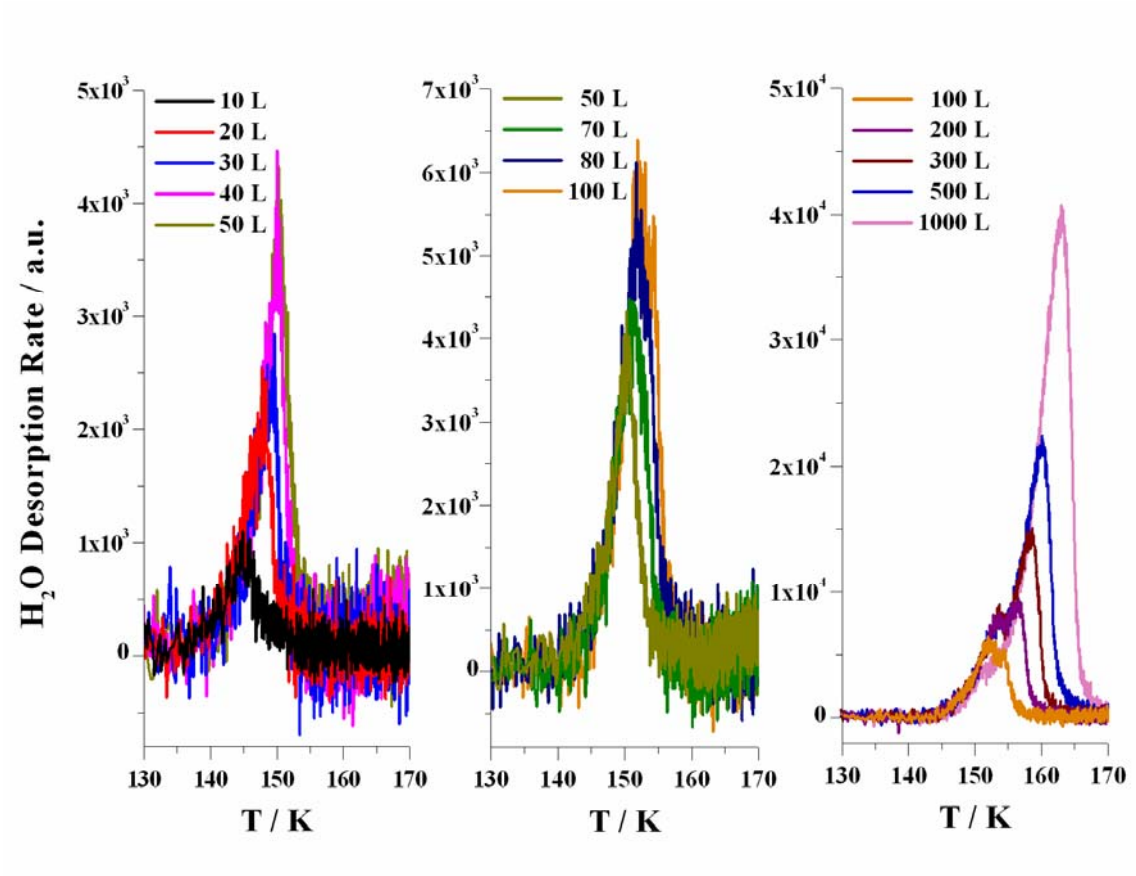

Figure 4.1: H_2O TPD from Bare Silica

desorbs at a higher temperature. This second desorption peak only appeared at higher doses (100 to 1000 L) when the cASW ice layer was thick enough for the phase change step rate to compete with the cASW desorption step rate. By 300 L, the height of the cASW peak was saturated indicating the phase change had become the dominant process. The double peak desorption structure of H_2O TPD curves had been previously observed by several other research groups as discussed in **Section 1.2.3** of **Chapter 1**. At even higher doses, the ASW desorption peak appeared as a shoulder on the larger CSW desorption peak. However, larger doses of H_2O could not be performed using the current apparatus without the risk of the pumping system failing to return the central chamber back to base levels.

The surface concentration, N_{tot}, was calculated for each background dose. This was achieved by approximating N_{tot} to the rate of surface bombardment, Z_w, (where P is the pressure in Pascals, S is the sticking coefficient, k_B is the Boltzmann constant, m is the mass of the molecule, and T is the gas temperature) multiplied by time, t, (see **Equation 4.2**). As previously discussed in **Chapter 3**, the value of S ranges from 0 for

no molecules sticking to 1 where all the molecules stick upon collision. At low surface temperatures (like those used in this study), the flux of species leaving the surface either directly upon collision, J_{ref}, or desorbing at base temperatures, J_{des}, is relatively small allowing S to be approximately equal to 1.

$$N_{tot} = Z_w t = \frac{PSt}{\sqrt{2\pi m k_B T}} \tag{4.2}$$

For each dose, a plot of P against t (obtained from the data acquisition program for the dose stage of the experiment) was constructed. By integrating each plot and converting the units from mbar s to Pa s, the values of Pt required for **Equation 4.2** were obtained. The calculated values of N_{tot} are displayed in **Table 4.1** and reveal that the experiments cover the sub-monolayer to multilayer range (with a monolayer corresponding to approximately 10^{15} molecules cm^{-2}). For most species, desorption of sub-monolayer coverages would follow first order kinetics; for example: HD from olivine [4]; CH_3OH from highly oriented pyrolitic graphite (HOPG) and silica [5]; and C_6H_6 from silica [6, 7]. However, all the TPD curves shown in **Figure 4.1** contained coincident leading edges typical of multilayer desorption which follows zeroth order kinetics. Previous studies by Kaya *et al*. and Wendt *et al*. exploring the desorption of H_2O from

Dose / L	**N_{tot} / molecules cm^{-2}**
10	3.7×10^{15}
20	7.2×10^{15}
30	1.1×10^{16}
40	1.4×10^{16}
50	1.7×10^{16}
70	2.5×10^{16}
80	2.8×10^{16}
100	3.6×10^{16}
200	7.1×10^{16}
300	1.1×10^{17}
500	1.8×10^{17}
1000	3.6×10^{17}

Table 4.1: Corresponding N_{tot} Values for Each Dose

silica also observed zeroth order kinetic desorption with no transition between the sub-monolayer and multilayer observed [8, 9]. The conclusion was that the interaction between the H_2O molecules was greater than between the H_2O molecules and the silica surface resulting in the formation of three-dimensional H_2O clusters or islands. As a consequence, the desorption from these multilayer islands followed zeroth order kinetics, even at low coverages. Further studies made by Wendt *et al*. [9] observed that the desorption followed this trend both on low defect (smooth) and high defect (rough as in this thesis) silica surfaces. The TPD curves produced in this study (**Figure 4.1**) appear to agree with these conclusions. Additionally, this form of desorption behaviour for H_2O has also been observed from Ag [10, 11], Cu [12]; HOPG [13]; and Pt(111) [14, 15] surfaces.

The TPD results in **Figure 4.1** were analyzed using the leading edge technique. This is based on the Polyani-Wigner equation (displayed in **Equation 4.3**) where r_{des} is the desorption rate; dN/dt the change in surface concentration; υ the pre-exponential factor; $N(t)$ the surface concentration at each time interval; R the gas constant; and n the kinetic order of the desorbing species. The negative sign in front of dN/dt indicates that the concentration of the species on the surface is decreasing. As the analysis was applied to desorption, this negative sign was removed as the concentration of the desorbing species entering the gas-phase increased.

$$r_{des} = -\frac{dN}{dt} = \nu N(t)^n \exp\left[\frac{-E_{des}}{RT}\right] \tag{4.3}$$

To determine the kinetic parameters υ and E_{des}, **Equation 4.3** was first divided through by $N(t)^n$ and natural logarithms taken (**Equation 4.4**). This enables plots of $ln[(dN/dt)/(N(t)^n]$ against $1/T$ to be constructed from which the values of v and E_{des} can be determined from the intercept and gradient, respectively, for each dose. Before this could be achieved, dN/dt and $N(t)^n$ were required. dN/dt was calculated by converting the MASsoft data from units of counts into molecules cm^{-2} s^{-1}. The conversion factor was obtained by integrating the TPD peak, with respect to t, and dividing through by N_{tot}. $N(t)$ was obtained using **Equation 4.5** as $N(t)$ equalled the total gas-phase concentration, N_{gas}, for the previous t step substracted from N_{tot}. This was achieved by integrating the desorption peak of H_2O (in units of MASsoft counts) against t and extracting each integration t stage to obtain N_{gas}. However, as the H_2O TPD data

followed zeroth order kinetics (n=0) then $N(t)^n$ equaled 1. In this case, **Equation 4.4** was simplified to give **Equation 4.6** and plots of *ln[dN/dt]* against *1/T* were constructed. An example is displayed in **Figure 4.2** with illustrated lines of best fit for the cASW and CSW desorption peaks (both shown in red) applied to the leading edge of the desorption peak (which is the falling edge in this graph as the data are plotted in units of reciprocal temperature).

$$\ln\left[\frac{dN/dt}{N(t)^n}\right] = \ln\nu - \frac{E_{des}}{RT} \tag{4.4}$$

$$N(t) = N_{tot} - N_{gas} \tag{4.5}$$

$$\ln\left[\frac{dN}{dt}\right] = \ln\nu - \frac{E_{des}}{RT} \tag{4.6}$$

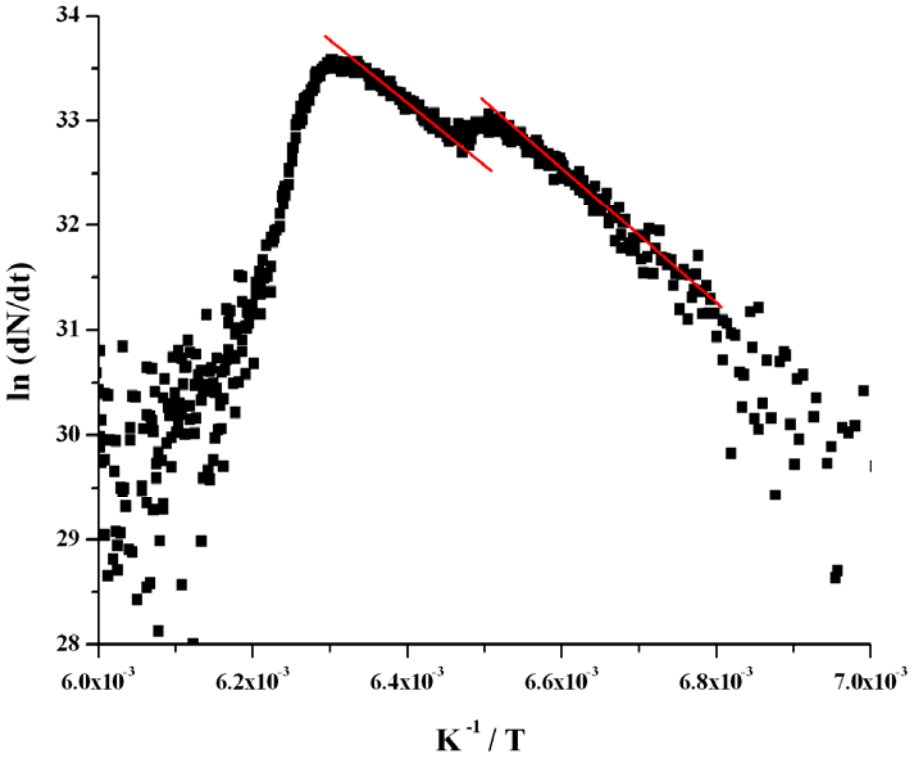

Figure 4.2: Analysis of the Desorption of 300 L of H_2O from the Amorphous Silica Substrate

This technique was applied to both the desorption peaks of cASW and CSW with the average values for the kinetic parameters obtained shown in brackets in **Table 4.2**. The results for υ produced an upper error larger than the average value when the intercept was converted from the logarithm format. As a consequence, the values of υ are quoted in the form of powers. However, the results shown in brackets do not include the much larger experimental errors obtained from the apparatus. With these taken into account, the quoted values of υ and E_{des} are displayed in **Table 4.2** (without brackets).

Desorption Peak	**υ / molecules cm^{-2} s^{-1}**	**E_{des} / kJ mol^{-1}**
cASW	$10^{31\pm2}$ ($10^{31.3\pm1.1}$)	50±3 (49.8±3.0)
CSW	$10^{31\pm2}$ ($10^{30.8\pm1.2}$)	50±3 (49.6±3.0)

Table 4.2: υ and E_{des} from the Leading Edge Analysis for H_2O TPD from the Model Silica Substrate

The kinetic results obtained for the two H_2O desorption peaks are very similar indicating that the desorption of cASW and the crystallisation from cASW to CSW compete with each other. Desorption of H_2O from other non-astronomically relevant surfaces has been explored by other research groups [5, 13, 16-18] and their results are displayed in **Table 4.3**. The values of ν are within experimental error of the value

Surface	**cASW**		**CSW**	
	υ / molecules cm^{-2} s^{-1}	**E_{des} / kJ mol^{-1}**	**υ / molecules cm^{-2} s^{-1}**	**E_{des} / kJ mol^{-1}**
Au [16]	1×10^{30}	47	1×10^{30}	48±1
Ru (001)/ Au (111) [17]	3.75×10^{30}	47±1	4.58×10^{30}	48±1
Sapphire [18]			2.8×10^{30}	50
HOPG [5, 13]			9×10^{21} to 1×10^{23} *	39.9±0.8

Table 4.3: Comparison Kinetic Parameters of H_2O Desorption

*Fractional Order Units are molecules$^{0.76}$ cm$^{-1.52}$ s$^{-0.76}$

obtained in this study, with the exception from the highly oriented pyroltic graphite (HOPG) surface [5, 13]. This difference from the HOPG surface was a result of the CSW film following non-zeroth order desorption kinetics. The values of E_{des} for cASW and CSW were also found to be within experimental error of those in the literature for multilayer coverages. This observation supports the theory that the underlying surface had no affect on the desorption of H_2O from bare silica both as multilayer and sub-monolayer coverages. However, it is important to note that the desorption of sub-monolayer coverages of H_2O from other surfaces to which it is more strongly bound would usually follow first order kinetics.

To further explore the desorption kinetics of cASW and CSW from bare silica, simulation models were constructed based on the kinetic parameters obtained in this sub-section. The procedure and results of these CKS models are discussed in the following sub-section.

4.2.4 Modelling TPD Data

The kinetic values obtained through the TPD analysis in the above sub-section were used to fit simulated models to the data. CKS is a stochastic integration program which works by integrating a rate law equation for each step in a mechanism. The rate law equations are based on the Arrhenius equation (shown in **Equation 4.7**) where k_i is the rate coefficient for each reaction step, i; ν_i the pre-exponential for each step, i; E_{a_i} the activation energy for each reaction step; R the ideal gas constant and T the temperature. The other parameters required for a CKS model were the initial concentration for each species, the kinetic order of the reaction step, n, and the heating rate.

$$k_i = \nu_i \exp\left[\frac{-E_{a_i}}{RT}\right] \tag{4.7}$$

The full mechanism describing the processes occurring in the H_2O TPD experiments is displayed in **Figure 4.3**. The first two steps describe the pASW to cASW phase change through the formation of nucleation centres and the autocatalyic process required for the phase change respectively [3]. The actual phase change is more complex but these two steps were designed by Collings *et al*. to provide a mathematical fit of this process. The fourth step describes the crystallisation of cASW to form CSW whilst the third and fifth

$$H_2O(pASW) \rightarrow H_2O(cASW)$$
$$H_2O(pASW) + H_2O(cASW) \rightarrow 2H_2O(cASW)$$
$$H_2O(cASW) \rightarrow H_2O(g)$$
$$H_2O(cASW) \rightarrow H_2O(CSW)$$
$$H_2O(CSW) \rightarrow H_2O(g)$$
$$H_2O(g) \rightarrow H_2O(pump)$$

Figure 4.3: The Full H_2O TPD Mechanism

steps described the desorption processes. The final reaction step describes the removal of gaseous H_2O from the apparatus. Initially fitting the H_2O TPD data with a model this complex would result in too many variables. Instead, the reaction mechanism was simplified so that the phase change and crystallisation steps were removed (see **Figure 4.4**). This assumption took the two ASW ice structures (pASW and cASW) as the same and treated the two ice structures (ASW and CSW) as two separate populations.

$$H_2O(ASW) \rightarrow H_2O(g)$$
$$H_2O(CSW) \rightarrow H_2O(g)$$
$$H_2O(g) \rightarrow H_2O(pump)$$

Figure 4.4: Two Population CKS Reaction Mechanism for H_2O Desorbing From Bare Silica

The first two steps in this simplified mechanism were both temperature dependent. The initial values of υ and E_{des} were taken from **Table 4.2** and n taken as zero. As E_{des} was more accurately known, then this value was held fixed whilst υ was varied for each of the temperature dependent reaction steps. Only once the general shape of the simulation matched the data was the value of E_{des} adjusted. The final step in **Figure 4.4** was temperature independent. The value of k for this step was obtained by comparing the trailing edge of the simulation model with that of the experimental data for each dose. The heating rate was taken as a function of the sample temperature over time so the heating rate in the simulation was the same as that in the experiment.

The initial surface concentration of H_2O, N_{tot}, was determined as part of the leading edge analysis described above and gave the total populations of ASW and CSW. For doses of 80 L and below, the CSW peak was not observed (see **Figure 4.1**) so the value of N_{tot} for H_2O was taken as the initial surface concentration of ASW, $[ASW]_i$. At 100 L, the CSW peak appeared as a small shoulder on the ASW desorption peak. To a first approximation for the 100 L dose and higher, $[ASW]_i$ was held fixed at the value taken for the 80 L dose and the initial surface concentration of CSW, $[CSW]_i$, taken as the difference between N_{tot} and $[ASW]_i$. However, early fits for the 100, 200 and 300 L doses failed to obtain the double peak structure with the correct peak heights. This implied that the CSW peak was present in the lower doses but the peak was hidden underneath the ASW peak. As a consequence, the value of $[ASW]_i$ was overestimated. By slightly adjusting the values of $[ASW]_i$ and $[CSW]_i$ (but keeping the sum equal to N_{tot}), more accurate fits were obtained for the 100, 200, 300, 500 and 1000 L. To determine the value of $[CSW]_i$ for the lower doses (where the peak was hidden behind the ASW peak), a plot of $[CSW]_i$ against N_{tot} (for the higher doses) was constructed. From the line of best fit, the positive values of $[CSW]_i$ were obtained and the corresponding value of $[ASW]_i$ re-calculated. The final values of $[ASW]_i$ and $[CSW]_i$ used in the CKS models, along with N_{tot}, is displayed in **Table 4.4**.

Dose / L	N_{tot} / **molecules cm^{-2}**	$[ASW]_i$ / **molecules cm^{-2}**	$[CSW]_i$ / **molecules cm^{-2}**
10	3.7×10^{15}	3.7×10^{15}	0
20	7.2×10^{15}	7.2×10^{15}	0
30	1.1×10^{16}	1.1×10^{16}	0
40	1.4×10^{16}	1.4×10^{16}	0
50	1.7×10^{16}	1.7×10^{16}	0
70	2.5×10^{16}	2.3×10^{16}	0.2×10^{16}
80	2.8×10^{16}	$2.3\ 10^{16}$	0.5×10^{16}
100	3.6×10^{16}	2.3×10^{16}	1.3×10^{16}
200	7.1×10^{16}	2.3×10^{16}	4.8×10^{16}
300	1.1×10^{17}	2.3×10^{16}	8.9×10^{16}
500	1.8×10^{17}	2.3×10^{16}	1.6×10^{17}
1000	3.6×10^{17}	2.3×10^{16}	3.4×10^{17}

Table 4.4: Initial Surface Concentration Values of ASW and CSW

The CKS fits are displayed in **Figure 4.5** and reveal the model fits the leading edges of both peaks well and provide an estimated minimum of N_{tot} for when the water crystallisation step starts to occur. At the top of the desorption peak, the fit falls away more sharply resulting in the falling edge running parallel to the experimental data. This observation occurred from a mixture of processes in the experiment including the slight variation of surface temperature over the whole sample. As a consequence, the underlying silica surface broadens the curve at the top of the desorption peak. However, this process was too complex to be modelled. The kinetic parameters used to fit each of the desorption peaks are shown in **Table 4.5** with errors obtained from the second standard deviation. The value of k for the $H_2O(g) \rightarrow H_2O(pump)$ reaction step remained the same for all of the doses so the corresponding error was taken as 0.1 molecules cm^{-2} s^{-1}. The kinetic parameters for the CSW desorption reaction step are not shown below 70 L as the simulation revealed that that no CSW species were present on the surface at these doses. The kinetic parameters for both the desorption steps are within experimental error to those obtained using leading edge analysis (**Table 4.2**) and

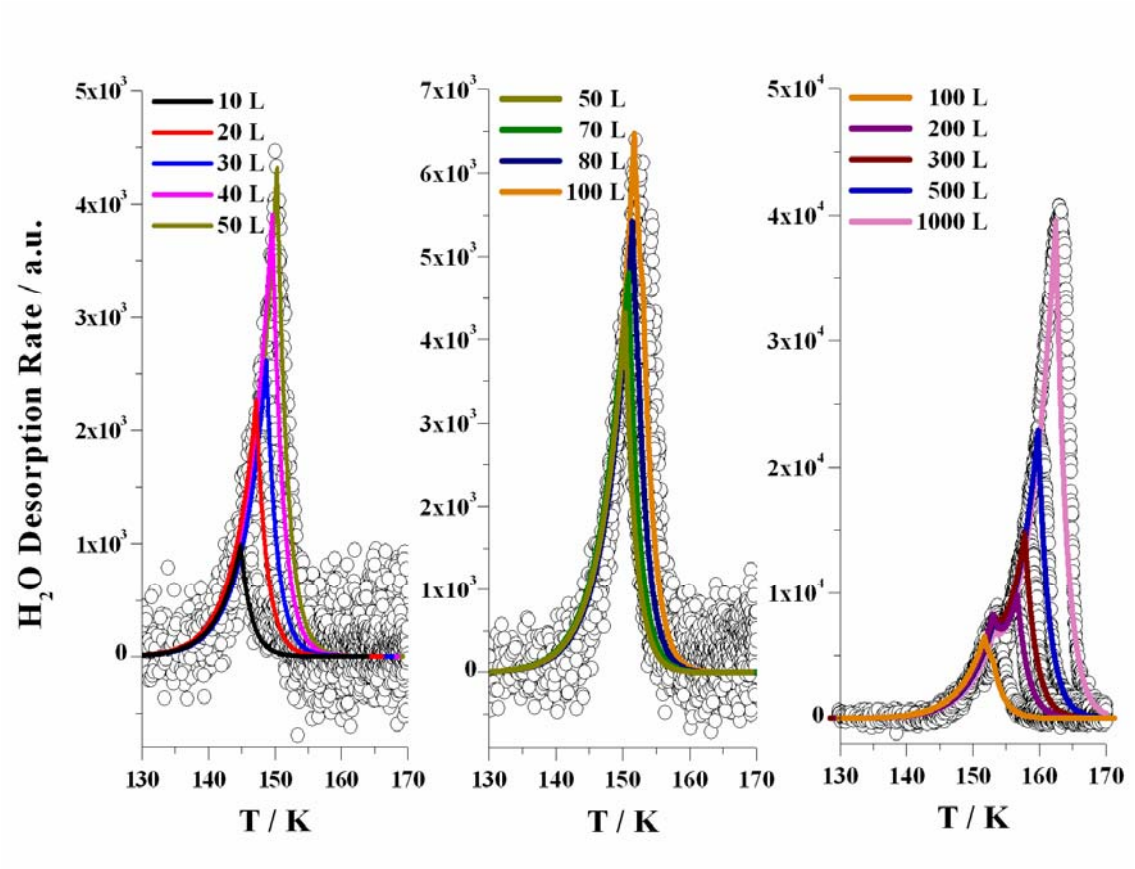

Figure 4.5: Two Population CKS Model Fits of the H_2O TPD Experiment

Dose / L	H_2O(ASW) → H_2O(g)		H_2O(CSW) → H_2O(g)		H_2O(g) → H_2O(pump)
	E_{des} / kJ mol^{-1}	v / molecules cm^{-2} s^{-1}	E_{des} / kJ mol^{-1}	v / molecules cm^{-2} s^{-1}	k / molecules cm^{-2} s^{-1}
10	48.2	2.0×10^{31}	-	-	0.05
20	48.2	2.0×10^{31}	-	-	0.05
30	48.2	2.0×10^{31}	-	-	0.05
40	48.2	2.0×10^{31}	-	-	0.05
50	48.2	2.0×10^{31}	-	-	0.05
70	48.8	2.2×10^{31}	50.6	2.0×10^{31}	0.05
80	48.2	2.0×10^{31}	50.4	2.0×10^{31}	0.05
100	48.4	2.2×10^{31}	49.6	2.3×10^{31}	0.05
200	48.7	2.0×10^{31}	49.4	2.8×10^{31}	0.05
300	48.2	1.3×10^{31}	49.7	5.0×10^{31}	0.05
500	48.2	1.3×10^{31}	49.6	5.0×10^{31}	0.05
1000	48.2	1.3×10^{31}	49.7	6.0×10^{31}	0.05
Average	48.2±0.3	$1.9\pm0.6\times10^{31}$	49.9±0.9	$3.6\pm3.4\times10^{31}$	0.05±0.01

Table 4.5: Kinetic Parameters Used in the Two Population CKS Model

with those in the literature (**Table 4.3**). This implies that the CKS model used describes the two desorption processes well as two separate populations.

To improve the accuracy of the CKS model, the ASW to CSW crystallisation step was reinserted into the mechanism (see **Figure 4.6**). This model still treated the pASW and cASW ice species as the same (ASW) as the kinetic parameters for the pASW and cASW phase change step could not be obtained from this experiment. The results determined from the first CKS model were applied to the three original steps except for the $[ASW]_i$ (now taken as N_{tot}) and $[CSW]_i$ (taken as 0 molecules cm^{-2}). Only during the last stages of fine tuning the simulation fit to the experimental data were any of these values adjusted if the fit could not be improved by altering the crystallisation step.

$$H_2O(ASW) \rightarrow H_2O(g)$$
$$H_2O(ASW) \rightarrow H_2O(CSW)$$
$$H_2O(CSW) \rightarrow H_2O(g)$$
$$H_2O(g) \rightarrow H_2O(pump)$$

Figure 4.6: Phase Change CKS Reaction Mechanism for H_2O Desorbing From Bare Silica

The kinetic parameters for the crystallisation step: n; E_a (denoted as E_{cryst}); and v could not be determined from the data. The TPD results in **Figure 4.1** revealed that the phase change step increased in dominance in comparison to the ASW desorption step with increasing dose coverage. This implied that the phase change step was coverage dependent so n was assumed to be first order. The value of E_{cryst} was taken as 70 kJ mol^{-1} [19] and the value of v was varied until the model fitted the data.

The second CKS model fits of the H_2O TPD data are displayed in **Figure 4.7** with the kinetic parameters for each dose shown in **Table 4.6**. Overall, the results obtained from the phase change model fit the experimental data well with only slight adjustments required to the kinetic parameters for the desorption steps obtained from the two population model. The value of k remained the same. Error analysis was reapplied to the desorption steps and the average values, with an error of two standard deviations, are displayed at the bottom of **Table 4.5**. The kinetic parameters for the crystallisation step are also displayed in the table. As the initial values were not calculated from the data, the errors applied were considerably larger. The values of v are considerably outside the expected range for first order kinetics (typically 10^{12} to 10^{14} s^{-1}) suggesting that either the crystallisation does not follow first order kinetics or that the crystallisation process is too complex to model accurately using only one reaction step. In the future this mechanism could be further developed to improve the kinetic results for the crystallisation step. However, this could only be achieved based on the results obtained from other research groups as the current apparatus is not designed to perform the required experiments.

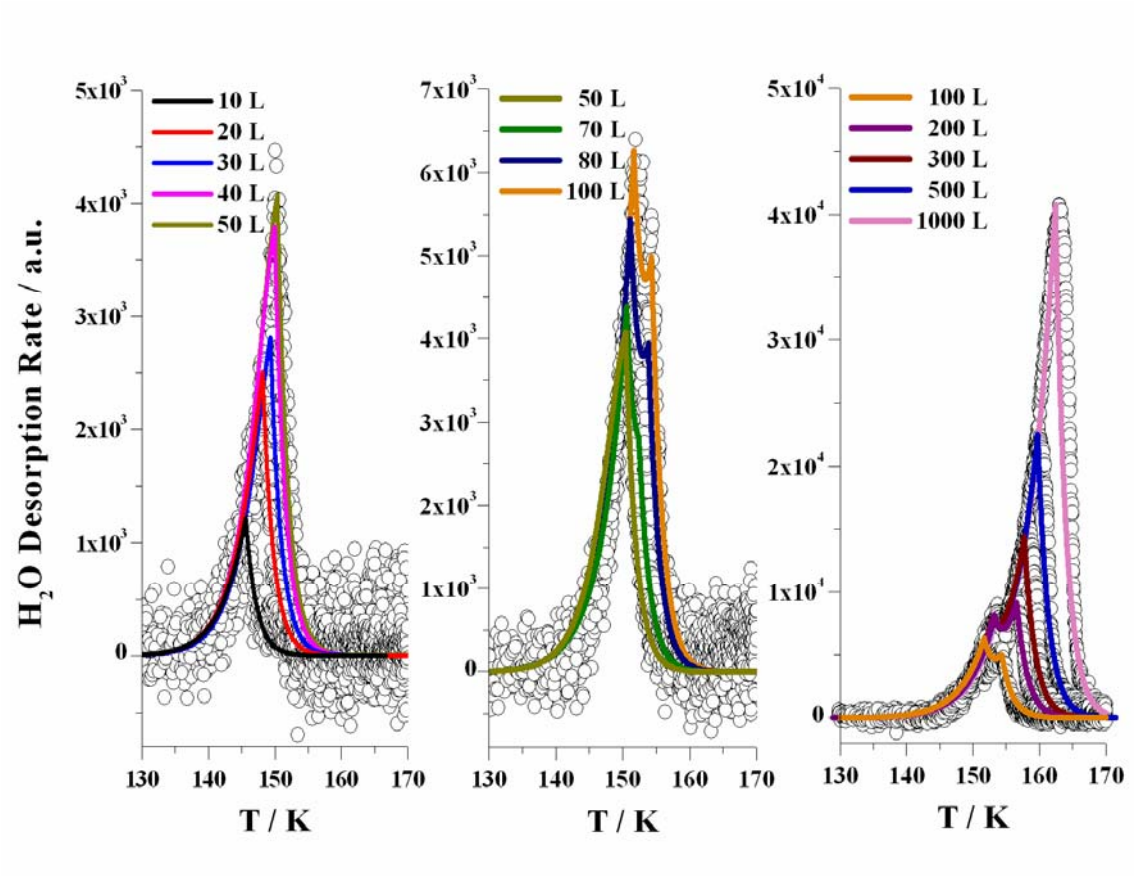

Figure 4.7: Phase Change CKS Model Fits of the H_2O TPD Experiment

Dose / L	H_2O(ASW) → H_2O(g)		H_2O(ASW) → H_2O(CSW)		H_2O(CSW) → H_2O(g)	
	E_{des} / kJ mol^{-1}	v / molecules cm^{-2} s^{-1}	E_{cryst} / kJ mol^{-1}	v / s^{-1}	E_{des} / kJ mol^{-1}	v / molecules cm^{-2} s^{-1}
10	48.4	1.8×10^{31}	70.0	5.5×10^{22}	49.6	3.6×10^{31}
20	48.6	1.8×10^{31}	70.0	5.5×10^{22}	49.6	3.6×10^{31}
30	48.6	1.8×10^{31}	70.0	5.5×10^{22}	49.6	3.6×10^{31}
40	48.6	1.8×10^{31}	70.0	5.5×10^{22}	49.6	3.6×10^{31}
50	48.6	1.8×10^{31}	70.0	5.5×10^{22}	49.6	3.6×10^{31}
70	48.2	1.8×10^{31}	70.0	5.5×10^{22}	49.7	2.0×10^{31}
80	48.6	2.0×10^{31}	70.0	6.5×10^{22}	49.7	2.0×10^{31}
100	48.7	2.2×10^{31}	70.0	5.5×10^{22}	49.6	2.3×10^{31}
200	48.7	2.0×10^{31}	70.0	4.0×10^{22}	49.4	2.8×10^{31}
300	48.2	1.3×10^{31}	70.0	6.0×10^{22}	49.7	5.0×10^{31}
500	48.2	1.3×10^{31}	70.0	8.0×10^{22}	49.6	5.0×10^{31}
1000	48.2	1.3×10^{31}	70.0	9.0×10^{22}	49.7	6.0×10^{31}
Average	48.5±0.4	$1.7\pm0.6\times10^{31}$	70.0±2	$6.0\pm2.6\times10^{22}$	49.6±0.2	$3.6\pm3.4\times10^{31}$

Table 4.6: Kinetic Parameters Used for Phase Change Step

4.2.5 Conclusions

The experiments performed in this section explored the kinetic behaviour in H_2O TPD experiments from bare silica. Overall the desorption of H_2O was observed to follow zeroth order kinetics for both sub-monolayer and multilayer coverages. This implies that the interaction between the H_2O molecules was greater than between the H_2O molecules and the silica surface resulting in the formation of three-dimensional (multilayer) H_2O clusters or islands.

At surface coverages below 70 L (approximately 2×10^{16} molecules cm^{-2}), the H_2O film underwent a phase change from pASW to cASW and desorbed at surface temperatures starting at approximately 140 K. As N_{tot} increased, a second phase change step competed with the cASW desorption step resulting in the observation of a second desorption peak (CSW) at a slightly higher temperature (desorption peak maximum starting at around 155 K). Leading edge analysis was applied to the cASW and CSW

desorption peaks and the results are displayed in the top value lines for the first and third reaction steps in **Table 4.7**. The kinetic parameters for both the desorption steps agreed well with those in the literature for multilayer coverages of H_2O.

Reaction Step	***v* / molecules cm^{-2} s^{-1}**	***E* / kJ mol^{-1}**	***k* / molecules cm^{-2} s^{-1}**
$H_2O(ASW) \rightarrow H_2O(g)$	$10^{31\pm2}$ $1.9\pm0.6\times10^{31}$ $1.7\pm0.6\times10^{31}$	50±3 48.2±0.3 48.5±0.4	-
$H_2O(ASW) \rightarrow H_2O(CSW)$	- - $6.0\pm2.6\times10^{22}$ *	- - 70±2	
$H_2O(CSW) \rightarrow H_2O(g)$	$10^{31\pm2}$ $3.6\pm3.4\times10^{31}$ $3.6\pm3.4\times10^{31}$	50±2 49.9±0.9 49.6±0.2	-
$H_2O(g) \rightarrow H_2O(pump)$	-	-	- 0.05±0.01 0.05±0.01

Table 4.7: Kinetic Parameters Obtained from Leading Edge Analysis (top value), Two Population CKS Model (middle) and the Phase Change CKS model (bottom). (* First order kinetic units are s^{-1})

The first simpler kinetic model was the two population CKS model which described the desorption with no phase change reaction step resulting in separate populations for the ASW and CSW species. Although this was an inaccurate description of the process occurring on the surface, this model enabled the two desorption peaks to be fitted. The results are shown in the first, third and fourth reaction steps in **Table 4.7** with errors obtained from the second standard deviation. From these results, a second model was created based on the first which included the cASW to CSW crystallisation step in the reaction mechanism. The model fits described the TPD data well with only slight changes to the kinetic parameters from the two population model (shown in the third line for all the reaction steps in **Table 4.7**). However, the value of *v* for the phase change step was significantly outside the expected range for first order kinetic processes. This implied that either the crystallisation kinetics did not follow first order

as assumed or the crystallisation process could not accurately be modelled using only one reaction step. In the future, this mechanism could be further developed to improve the kinetic results for the crystallisation step or to provide a mathematical fit of this process.

4.3 O_2 on Bare Silica Surface

4.3.1 Introduction

This section explores the results of O_2 TPD experiments on bare silica using two different dosing methods: background and molecular beam dosing. The experimental procedures are described in **Section 4.3.2**. The TPD results are discussed in **Section 4.3.3** and the doses split into sub-monolayer and multilayer coverages. Initial analysis of the multilayer desorption peaks was performed using leading edge analysis (**Section 4.3.4**) to obtain the kinetic parameters. These were used to construct CKS fits of the experimental data.

Before the beam dose sub-monolayer TPD data could be analyzed the sticking and accommodation coefficients, S and α, of O_2 on bare silica needed to be interpreted (see **Section 4.3.5**). The exact values for S and α will be determined in the future using the procedure previously described in **Chapter 3**. The sub-monolayer desorption peaks required a more complex analytical technique to obtain the kinetic parameters. This was achieved using direct inversion of the Polyani-Wigner equation (**Section 4.3.6**). The results were used to fit simulations to the experimental data using a multiple E_{des} model.

The conclusions for the O_2 TPD experiments on bare silica are summarized in **Section 4.3.7**. The kinetic parameters obtained from this data were used towards modelling the desorption of O_2 from cASW (see **Section 4.4**); O_2 from pASW (**Section 4.5**); and towards constructing a larger simulation model to describe the desorption of O_2 from ice mantles under ISM conditions (**Section 4.6**).

4.3.2 Experimental Procedure

Overall, the experimental procedure for the O_2 TPD experiments from bare silica was similar to those described in **Section 4.2.2** for H_2O. This section will first describe the

basic set up for the experiment and then the two different dosing techniques (background and molecular beam dosing). The final part describes the TPD stage of the experiment.

Once the UHV chamber had reached UHV conditions, the sample was heated clean to 180 K and cooled back to base temperatures. The sample was positioned in line with the atomic beams, with the gate valves between the central chamber and the atomic beam chambers closed, and the central chamber pressure noted. For the background dose experiments, a dosing bulb was first flushed and filled with O_2 (sourced from the cylinder used in the beam experiments). The MASsoft program was set to monitor the intensity of O_2, O, CO/N_2 and CH_3 species and the KP-type thermocouple voltages of the silica sample and cold finger over time. The data acquisition was programmed to monitor the central chamber pressure and KP thermocouple voltages of the sample and cold-finger. The gas was leaked into the central chamber *via* a leak-valve from the glass gaslines for a set dose of 0.3, 1, 4, 6, 10, 20, 30, 40, 50, 100, 200 or 300 L. Once the pressure had returned to base levels, the MASsoft and data acquisition programs were stopped.

For the molecular beam dose experiments, O_2 was leaked into the plasma source chamber at a steady pressure of $1.00\pm0.05\times10^{-4}$ mbar. The same settings for the background dose experiments were applied to the MASsoft and data acquisition programs. When the O_2 beam was required, the gate valve between the atomic beam chamber and the central chamber was opened for a set dose of 5, 10, 15, 30, 45, 60, 90 or 120 minutes. Once the dose was completed, the gate valve was closed and the pressure allowed to recover to base levels before stopping the MASsoft and data acquisition programs.

After the dose stage had been completed, the sample was positioned in front of the QMS (located in position 1). The central chamber pressure was noted and the two programs, using the same settings as in the dosing stage, were started. After a few minutes delay, a linear heating ramp was applied to the sample heater up to 70 K. At this temperature, the two programs were stopped and the heating ramp terminated. Once the sample had returned to base temperatures, a second dose TPD experiment could be performed.

Duplicate sets of O_2 background dose and O_2 molecular beam dose TPD experiments were obtained.

4.3.3 TPD Results – Multilayers and Sub-Monolayer

The background and molecular beam dose TPD graphs were constructed using the same method described in **Section 4.2.3** and are displayed in **Figure 4.8** and **Figure 4.9** respectively. The exact background dose was calculated by integrating the pressure against time curve from the data acquisition program and converting into units of Langmuir (as for the H_2O TPD experiments).

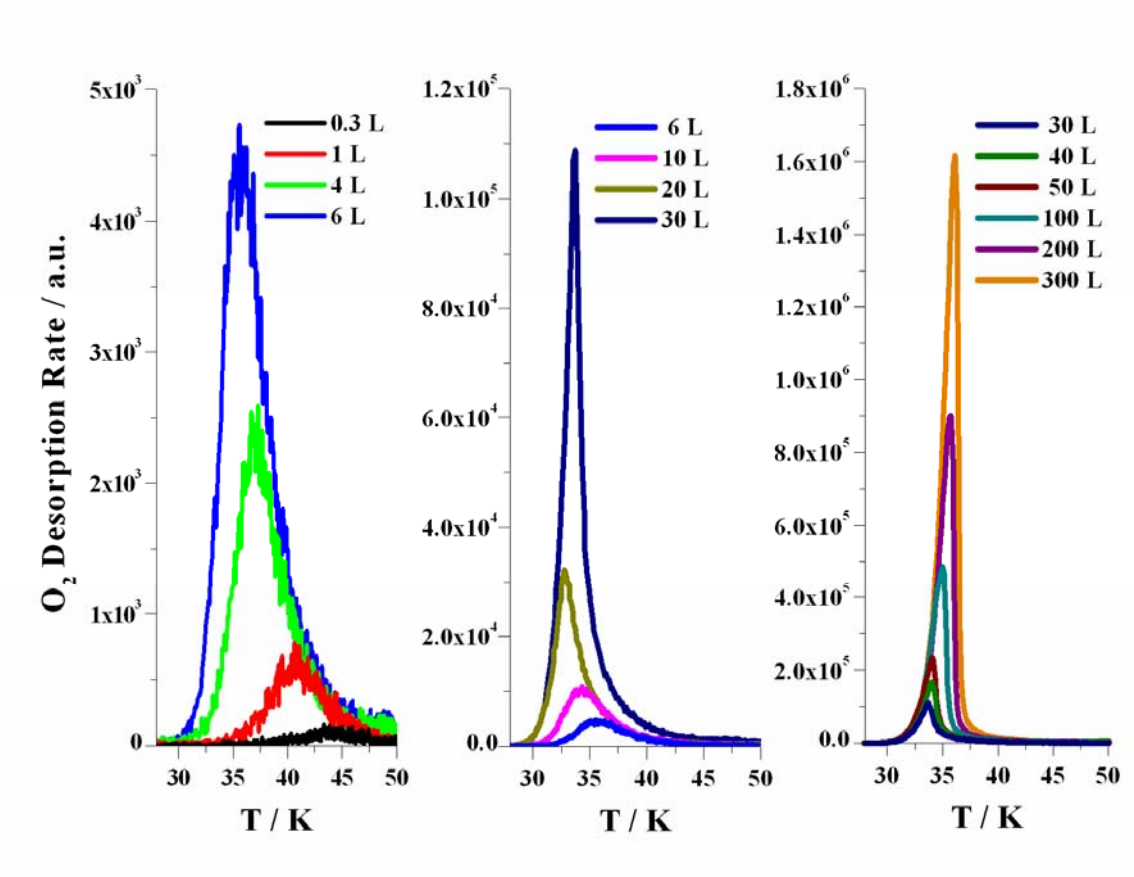

Figure 4.8: O_2 Background Deposition TPD Results from Bare Silica

The 30 to 300 L dose TPD curves shown in **Figure 4.8** all have coincident leading edges, within experimental error, which is typical of zeroth order kinetics. This implied that the O_2 molecules were desorbing from bulk O_2 ice (or O_2 multilayers) and the dominant interaction was $O_2 - O_2$. Analysis of these multilayer desorption peaks was achieved by performing leading edge analysis and the data was fitted using CKS simulations. The results of this analysis will be discussed in the **Section 4.3.4**.

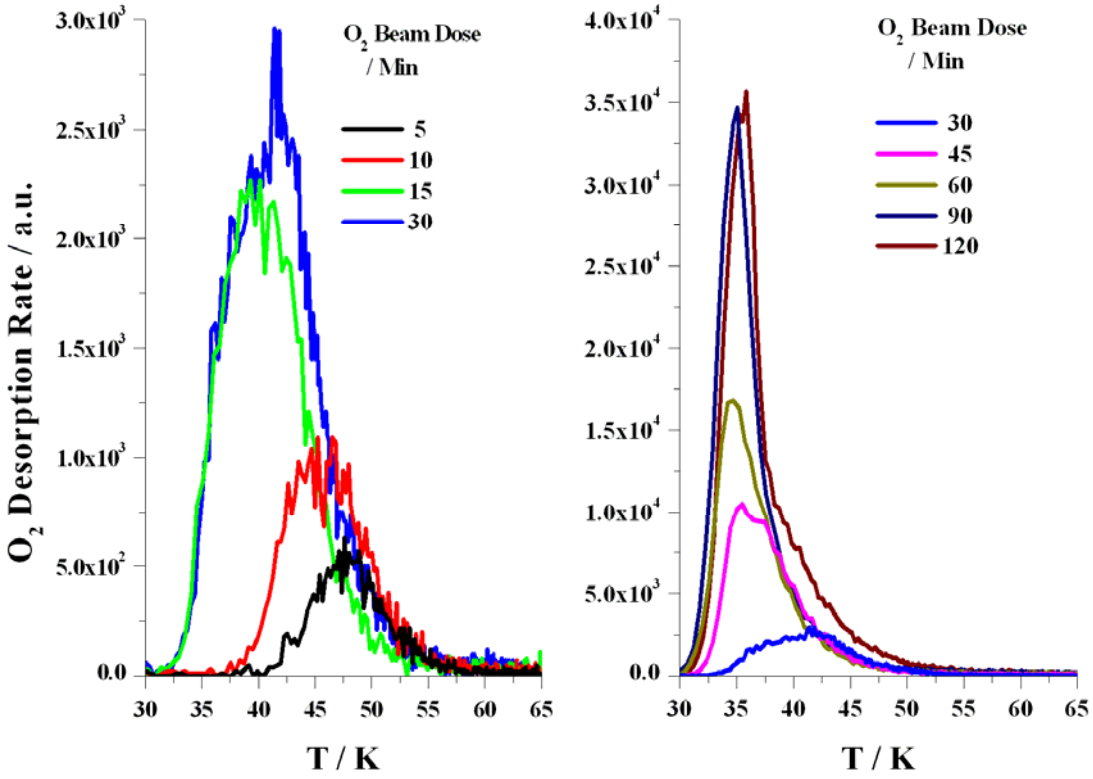

Figure 4.9: O_2 Molecular Beam TPD Curves from Bare Silica

The 0.3 to 10 L background deposition doses were sub-monolayer coverages and should exhibit first order kinetic shaped peaks (see **Figure 2.27** in **Section 2.3.4** for more details). However the O_2 sub-monolayer TPD curves in this study had coincident trailing edges which are typically seen with second order recombinative desorption processes. This type of desorption would not be occurring in these experiments. Instead, the previously known porous and amorphous nature of the silica [20] suggests a range of binding sites for the O_2 molecules to adsorb onto with the stronger binding energy sites being occupied before the weaker ones. When the surface temperature was increased during the TPD stage of the experiment, those molecules located in the weaker binding sites would desorb first. This resulted in the desorption peak broadening to cover the range of E_{des} values provided from the underlying silica surface. This multiple E_{des} sub-monolayer desorption pattern was also observed for the 5 to 60 minute O_2 molecular beam dose TPD curves (see **Figure 4.9**). To compare the molecular beam dose TPD results with those from the background dose ones, the values of S and α had to be interpreted before N_{tot} could be obtained. The procedure and

results for the interpretation of S and α will be discussed in **Section 4.3.5**. Using these results, both the sub-monolayer background and molecular beam dose O_2 TPD data were analyzed to obtain the E_{des} range using direct inversion of the Polyani-Wigner equation and the experimental data fitted with a multiple E_{des} simulation model. The procedure and results for this will be discussed in **Section 4.3.6**.

The remaining 20 L background and the 90 and 120 minute molecular beam dose desorption peaks displayed both a coincident leading edge (multilayer desorption) and falling edge (sub-monolayer desorption). This observation was a consequence of the porous characteristics of the underlying silica surface as the O_2 molecules were desorbing from multilayer islands before a complete monolayer was formed. As a result, the O_2 desorption kinetics followed fractional order between 10 and 30 L (for the background dose data) and above a 60 minute dose (molecular beam). An upper limit for the fractional desorption order for the beam dose would have been obtained if longer beam irradiation times had been used. Fractional order desorption between the sub-monolayer and multilayer regions has been observed before with other small molecules desorbing from similar porous surfaces [5, 20-22]. However, this type of desorption was too complex to analyse and model and, therefore, was not attempted in this study.

4.3.4 Modelling the TPD Data - Multilayers

This sub-section focuses on obtaining the desorption kinetic data for the O_2 multilayers using leading edge analysis and fitting the experimental data with a CKS model. The TPD results discussed in the above sub-section revealed that the desorption peaks which exhibited multilayer desorption behaviour were the 30 to 300 L background dose desorption peaks. The values of N_{tot} were obtained using the same procedure as for the H_2O TPD experiments (**Section 4.2**) and are displayed in **Table 4.8**.

The analytical procedure for leading edge analysis has been previously described in **Section 4.2.3**. As with the H_2O TPD data, the kinetic parameters for the O_2 multilayer data were obtained from similar plots of *ln[dN/dt]* against *1/T*. The values of v and E_{des} for each dose were calculated from the intercept and gradient respectively and are displayed in **Table 4.9**. Little variation is evident in either parameter over the 30 to 300 L range, indicating that the underlying surface was not affecting the desorption kinetics and that the O_2 molecules were desorbing from the bulk ice. The average

Dose / L	N_{tot} / molecules cm^{-2} s^{-1}
30	$8.65\times10^{15\pm1}$
40	$1.06\times10^{16\pm1}$
50	$1.35\times10^{16\pm1}$
100	$2.72\times10^{16\pm1}$
200	$5.20\times10^{16\pm1}$
300	$8.00\times10^{16\pm1}$

Table 4.8: Calculated Values of N_{tot} for Background Deposition Experiments

values for v and E_{des} are also displayed in **Table 4.9** with their experimental errors included. As for the H_2O TPD leading edge analysis, v is quoted in a power format and lies within the expected range typical of zeroth order kinetics. The multilayer value of E_{des} obtained in this study was approximately 3 kJ mol^{-1} higher than the multilayer desorption value of O_2 obtained by Acharyya *et al*. from a polycrystalline gold surface [23] which is just outside the experimental error. To improve the accuracy of the kinetic parameters obtained in this study, the experimental data was then fitted using a CKS model.

Dose / L	v / molecules cm^{-2} s^{-1}	E_{des} / kJ mol^{-1}
30	$10^{31.7\pm0.2}$	10.7±0.2
40	$10^{31.8\pm0.2}$	10.7±0.2
50	$10^{31.6\pm0.2}$	10.5±0.1
100	$10^{32.6\pm0.1}$	11.2±0.1
200	$10^{31.7\pm0.1}$	10.7±0.1
300	$10^{31.8\pm0.2}$	10.7±0.1
Average	$10^{32\pm2}$	10.7±0.4

Table 4.9: Leading Edge Analysis Results for Multilayer Coverages of O_2 Desorbing from Bare Silica

The reaction mechanism used to describe the multilayer desorption of O_2 from bare silica in the CKS model is described in **Figure 4.10** where *ads* represents those molecules adsorbed on the surface; *g* in the gas phase; and *pump* those removed from

$$O_2(ads) \rightarrow O_2(g)$$
$$O_2(g) \rightarrow O_2(pump)$$

Figure 4.10: Reaction Steps Used in CKS Model

the system by pumping. As before, the desorption step (first reaction) was temperature dependent. N_{tot}, v and E_{des} were obtained from the results of the leading edge analysis performed above. The last reaction step was temperature independent and the corresponding value of k was obtained by comparing the trailing edge of the simulation model with that of the experimental data for each dose.

Attempts to fit the experimental data with the CKS model resulted in poorly matched fits (see **Figure 4.11**). The first fit matched the start of the experimental leading edge but was too steep at the top whilst the third simulation fitted the data better at the peak but not in middle of the curve. The initial conclusion for this observation was that the CKS model was designed to model surface processes occurring from a smooth ideal

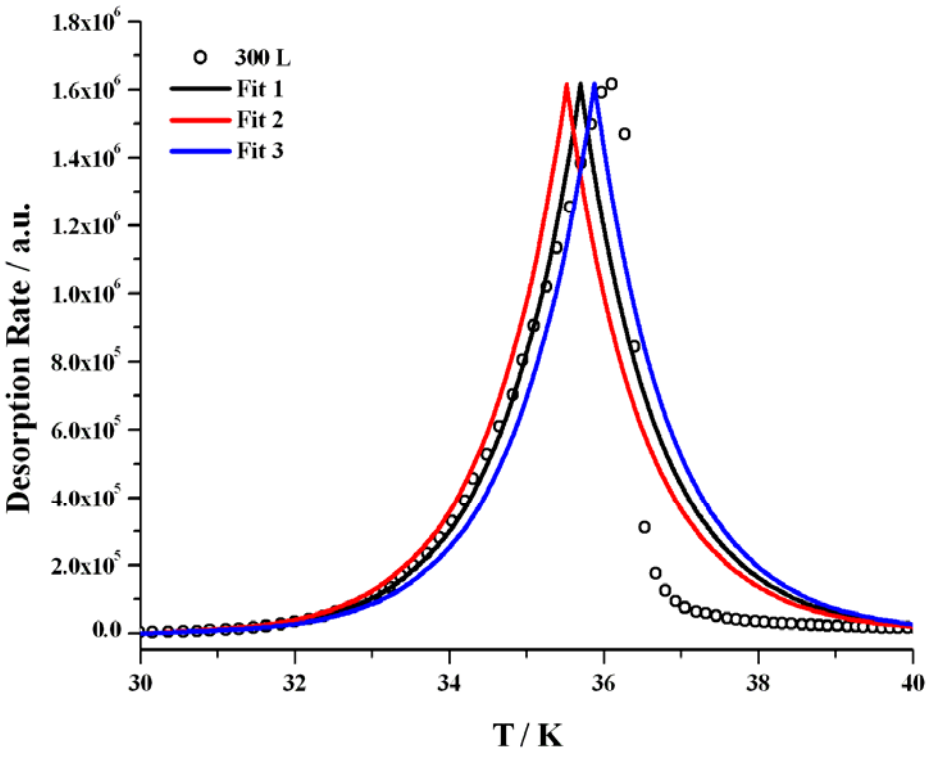

Figure 4.11: Initial Attempts to Fit the CKS Model to the O_2 TPD Data

surface whereas the silica surface used in this study was previously known to be porous. The surface was previously also known to affect the desorption of several different sub-monolayer species (for example: CH_3OH [5]; and C_6H_6 [6, 7]) but had rarely been seen to effect the desorption kinetics of multilayer ices. Additionally, as the CKS model reproduced the experimental data well for H_2O data, the poor CKS fits obtained here suggested that this was unlikely to be due to other experimental artefacts (for example, the heating rate not being uniform across the surface).

To deduce whether the surface might be affecting the desorption of multilayer coverages of O_2, the kinetic order, *n*, was calculated. The procedure to calculate *n* was the same as that discussed by Green *et al.* [5]. Briefly, the natural logarithm was applied to the Polyani-Wigner equation (**Equation 4.3**) to give **Equation 4.9**. Values of r_{des} were taken from the 40 to 300 L desorption peaks at a series of fixed *T*. A plot of $ln(r_{des})$ against *ln(N)* for each *T* was constructed (**Figure 4.12**) and provided a linear

$$\ln\left(r_{des}\right) = \ln\left(\upsilon N^{n}\right) - \frac{E_{des}}{k_B T} \tag{4.9}$$

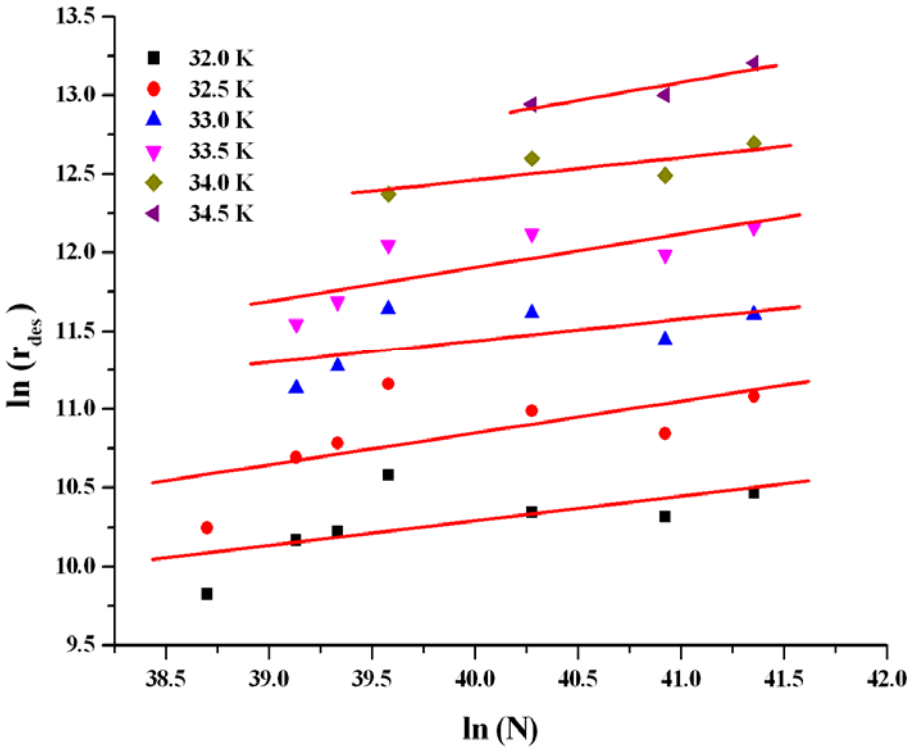

Figure 4.12: Kinetic Order Determination Plot of $\ln(r_{des})$ against ln(N)

relationship where the gradient equalled *n*. The results for *n* are displayed in **Table 4.10** with the average mean values calculated as 0.18±0.04. This indicated that the multilayer O_2 coverages did not truly follow zeroth order desorption kinetics and that the desorption kinetics were weakly affected by the underlying silica surface.

***T* / K**	***n***
32.0	0.16±0.09
32.5	0.20±0.11
33.0	0.14±0.09
33.5	0.21±0.09
34.0	0.14±0.08
34.5	0.23±0.10
Average	0.18±0.04

Table 4.10: Kinetic Order values from **Figure 4.12**

To determine whether *n* was the cause for the poor CKS fits, leading edge analysis was reapplied. The new kinetic parameters are shown in **Table 4.11** and were initially used to construct new CKS fits. The non-zeroth order CKS fit for the 300 L dose is displayed in **Figure 4.13** along with the zeroth order Fit 2 from **Figure 4.11**. The results clearly indicated that the fractional order simulation matched the majority of the TPD curve better than the zeroth order fit. As observed in the H_2O simulated fits, the non-zeroth order fit differed slightly from the experimental data near the top of the CKS peak where a mixture of processes resulted in the broadening of the experimental curve at the top of the desorption peak.

n	***v***	E_{des} **/ kJ mol^{-1}**
0	$10^{32\pm2}$ molecules cm^{-2} s^{-1}	10.6±2.0
0.18	$10^{29\pm2}$ molecules$^{0.82}$ cm$^{-1.64}$ s$^{-0.82}$	10.6±2.0

Table 4.11: Zeroth Order (top) and Fractional Order Kinetic Parameters for the Fractional Order CKS Model

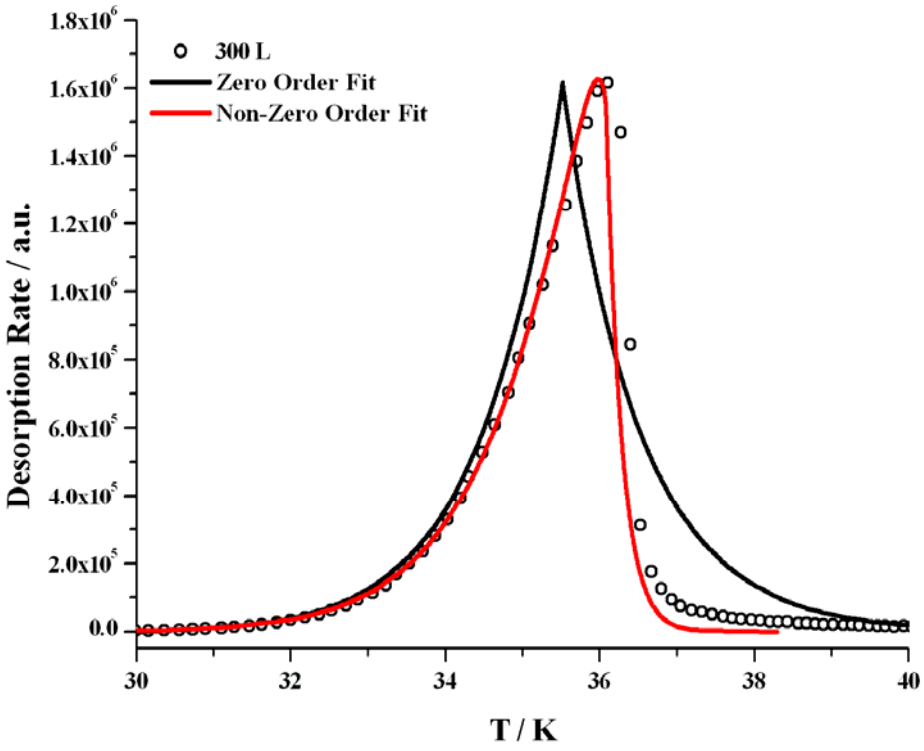

Figure 4.13: Comparison CKS Fits of Zeroth Order and Fractional Order on the 300 L Dose O_2 TPD Curve

The CKS fits for all the O_2 multilayer background deposition doses are displayed in **Figure 4.14**. As with the 300 L dose described above, the other CKS fits describe the experimental data well. The average values for the kinetic parameters obtained from the CKS analysis are shown in brackets in **Table 4.12**. However, the accuracy of these results is lower than the analytical errors alone imply. With the experimental errors from the apparatus system included, the average values of v, E_{des} and k become $10^{27.2\pm2.0}$ molecules$^{0.82}$ cm$^{-1.64}$ s$^{-0.82}$, 9.8±2.0 kJ mol^{-1} and 0.4±0.1 molecules cm^{-2} s^{-1} respectively (see **Table 4.12**). The kinetic parameters for the desorption kinetics were both lower than those derived through the non-zeroth order leading edge analysis but were still within experimental error.

The multilayer O_2 desorption kinetic parameters obtained in this study were again compared to those obtained by Acharyya *et al*. from a polycrystalline gold surface **Table 4.13** [23]. With the addition of the CKS model fits, both the kinetics parameters

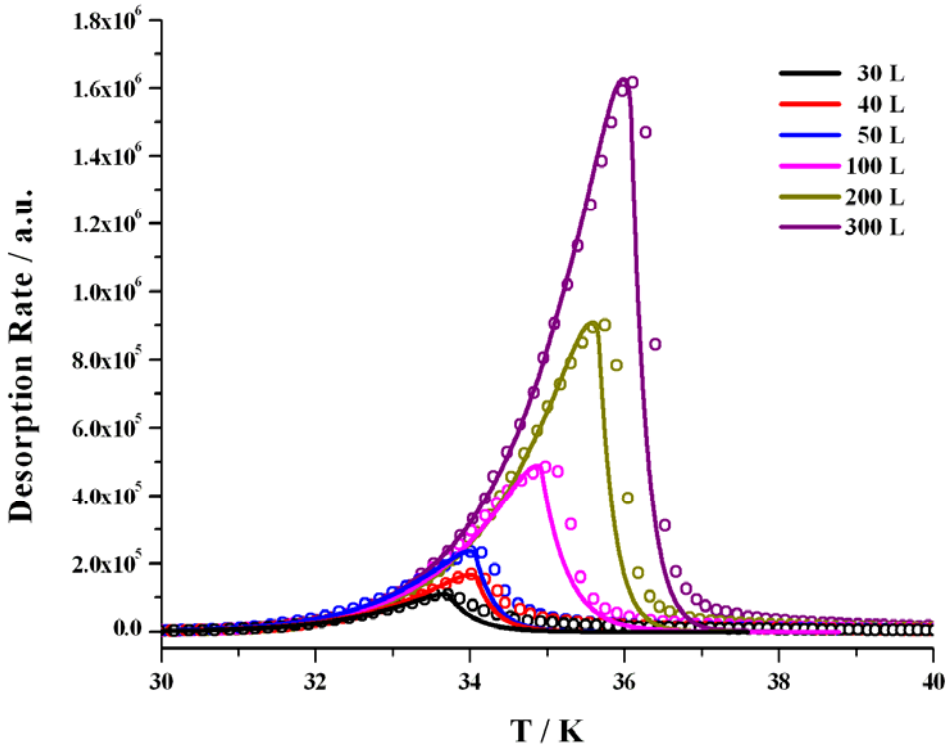

Figure 4.14: Fractional Order CKS Fits of Multilayer O_2 TPD from Silica

Reaction Step	**v / molecules$^{0.82}$ cm$^{-1.64}$ s$^{-0.82}$**	**E_{des} / kJ mol^{-1}**	**k / molecules cm^{-2} s^{-1}**
$O_2(ads) \rightarrow O_2(g)$	$(1.6\pm0.3\times10^{27})$ $10^{27.2\pm2.0}$	(9.8 ± 0.1) 9.8 ± 2.0	-
$O_2(g) \rightarrow O_2(pump)$	-	-	(0.4 ± 0.1) 0.4 ± 0.1

Table 4.12: Kinetic Parameters Required to Fit the CKS Model

Surface	**υ /molecules cm^{-2} s^{-1}**	**E_{des} / kJ mol^{-1}**
Bare Silica (this study)	$1.6\times10^{27\pm2}$ *	9.8±2.0
Polycrystalline Gold [23]	6.9×10^{26}	7.6±0.2

Table 4.13: Comparison of Leading Edge Analysis Results for υ and E_{des}
(*Fractional Order Kinetics is molecules$^{0.82}$ cm$^{-1.64}$ s$^{-0.82}$)

are in good agreement with each other. The only main difference between the two experiments was the choice of underlying surface which in this study affected the desorption behaviour and units for *v*.

The observation of non-zeroth order multilayer desorption is unusual as it is inconsistent with the observations of other similar multilayer desorbing molecules from amorphous silica surfaces; for example: H_2O (see **Section 4.2**); CH_3OH [24]; and C_6H_6 [20]. One possible explanation is that some of the O_2 molecules were forming either the square planar $(O_2)_2$ dimer clusters or the linear O_4 species. Neither of these species would be detected in the gas-phase as both would dissociate back into two O_2 molecules upon leaving the surface. However, the dissociation of these species could alter the shape of the O_2 desorption peak. To determine if this could be the case, TPD experiments were performed with N_2 from bare silica and CO from bare silica as neither of these species can form clusters or react together to form larger species. The results from these experiments are discussed in **Chapter 5**. If these two TPD experiments revealed that N_2 and CO both followed zeroth order kinetics then further O_2 TPD experiments would be performed with RAIRS analysis to determine if the $(O_2)_2$ and O_4 species were present in the multilayer film. The results obtained from these proposed experiments could reveal if these species were responsible for the observed fractional order desorption behaviour of O_2.

Recent transmission IR studies have indeed detected $(O_2)_2$ species in O_2 multilayer films below 20 K [25]. By including an $(O_2)_2$ dissociation step into the reaction mechanism previously shown in **Figure 4.10** (see **Figure 4.15**), a simple two population CKS model was constructed. The values of *n* and *v* for the first step were assumed as 1 and 1×10^{13} s^{-1} respectively. The corresponding value of E_a was taken as the binding energy of the $(O_2)_2$ species in the ground state which was calculated as 1.8 kJ mol^{-1} from the average results obtained by Dayou *et al.* [26], Bussery and Wormer [27], and Aquilanti *et al*. [28]. The kinetic parameters for the second step were taken as those obtained previously using leading edge analysis under zeroth order kinetics whilst the third step remained the same. Calculations of the initial surface concentrations of $(O_2)_2$ and O_2 were assumed as 5 and 95 % of the total surface concentration of N_{tot} respectively.

$$(O_2)_2(ads) \rightarrow 2O_2(ads)$$

$$O_2(ads) \rightarrow O_2(g)$$

$$O_2(g) \rightarrow O_2(pump)$$

Figure 4.15: O_2 and $(O_2)_2$ Reaction Mechanism

The results obtained from the two population CKS model are displayed in **Figure 4.16** and revealed that all the $(O_2)_2$ dimer species dissociated immediately on the surface when the base temperature was set at 20 K. As this base temperature is considerably lower than the surface temperature where O_2 molecules are known to desorb then this suggests that the dissociation of $(O_2)_2$ would be unlikely to be the cause for the non-zeroth order desorption kinetics of O_2 multilayers.

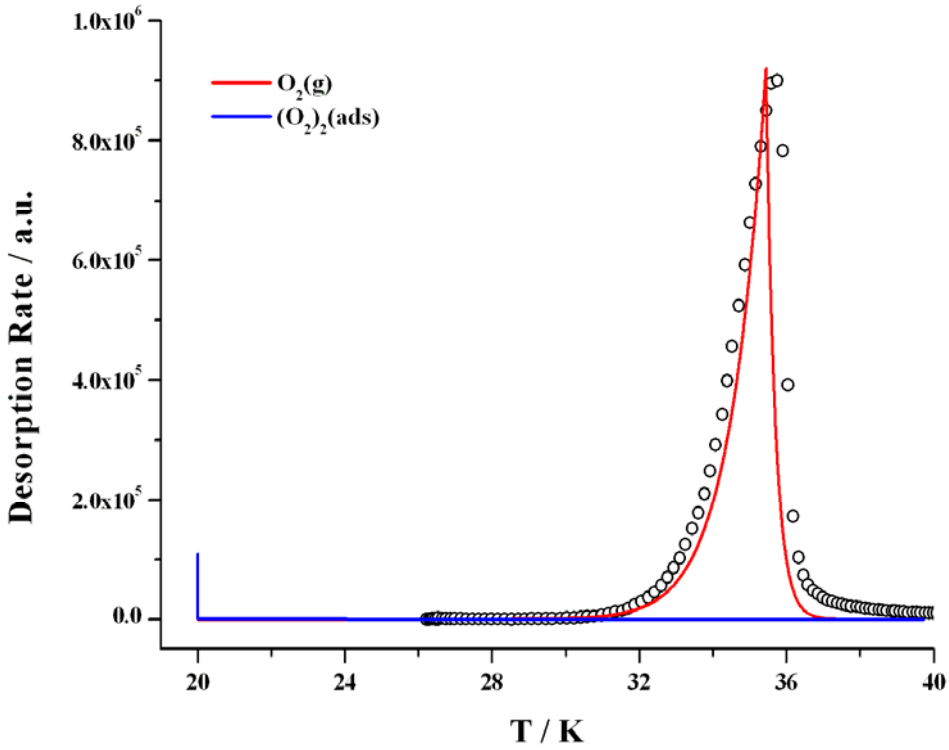

Figure 4.16: $(O_2)_2$ Dimer CKS Fit on the 200 L Dose O_2 TPD Curve

Another possible explanation was that the underlying porous and amorphous silica surface was the cause of the observed non-zeroth order desorption kinetics. If the N_2 and CO TPD experiments discussed in **Chapter 5** followed zeroth order desorption

kinetics for multilayer coverages then the silica surface would not be responsible for the fractional order observed with O_2.

Overall, the desorption of multilayer O_2 (either as O_2 molecules, $(O_2)_2$ dimer clusters or O_4 molecules) would not be directly relevant to the ISM as the abundance of O_2 is too low. These results are unlikely to be applied to the desorption of O_2 from the icy mantle coating comets as O_2 has yet to be detected in Solar comets [29]. However, O_2 and O_3 has been detected in outer Solar System icy bodies, for example: the moons of Jupiter (Ganymede, Europa and Callisto) [30-32]; and Saturn (Rhea and Dione) [33], so the multilayer O_2 desorption results obtained in this study could be applied in these environments.

4.3.5 An Interpretation of the Low O_2 Sticking Coefficient

The next set of O_2 TPD data to be analyzed in this study is that reflecting the sub-monolayer coverages. The TPD results discussed in **Section 4.3.3** revealed that the desorption peaks which exhibited sub-monolayer desorption behaviour were the 0.3 to 10 L background deposition and the 5 to 60 minute molecular beam dose desorption peaks. However, before these results could be analyzed the corresponding value of N_{tot} for each dose was required.

The values of N_{tot} for the background deposition experiments were calculated using the same procedure as for the multilayer data and are displayed in **Table 4.14**. This table also included the values for the 20, 30 and 40 L background deposition doses for comparison. The calculation of N_{tot} for the molecular dose could not be achieved by simply multiplying the O_2 molecular beam flux, F_{beam}, (as determined in **Chapter 3** from the pump-down experiments) by the irradiation time, t_{irr}, as this would provide the maximum value of the surface concentration $N_{tot\ max}$ (**Equation 4.10)**. The actual value of N_{tot} would be considerably smaller as a proportion of the O_2 molecules would have been reflected upon impact or have desorbed from the surface before the TPD part of the experiment began (as previously discussed in **Chapter 3**). To obtain the actual value of N_{tot} adsorbed onto the surface, α is required (see **Equation 4.11**) which was assumed to be 3×10^{-3}. This value for α was obtained for S in **Chapter 3** by comparing the values of F_{beam} derived from the QCM and pump-down experiments. However, this value of S (now α) was for O_2 molecules adsorbing onto the quartz crystal at a surface temperature estimated as roughly 23 and 28 K. In the future, the values of α for O_2 on

quartz and on silica will be determined by performing experiments based on the Kings and Wells method over a range of surface temperatures (see **Chapter 3** for more details). From these results, the corresponding surface, temperature and species dependent value of S will be obtained using **Equation 4.12** where $k_{des}(T)$ is the rate coefficient for the desorption species based on the surface temperature, T, (**Equation 4.13**) and J_{in} the incoming flux. The values of N_{tot} and $N_{tot\ max}$ are displayed in **Table 4.14** and reveal a difference of approximately two orders of magnitude between the two sets of values.

$$N_{totmaz} = F_{beam} \times t_{irr} \tag{4.10}$$

$$N_{tot} = F_{beam} \times t_{irr} \times \alpha \tag{4.11}$$

$$\alpha(T) = S(T) - \frac{k_{des}(T)}{J_{in}} \tag{4.12}$$

$$k_{des}(T) = \nu \exp\left(\frac{-E_{des}}{RT}\right) \tag{4.13}$$

Background Deposition		**Molecular Beam**		
Dose / L	N_{tot} **/ molecules cm^{-2} s^{-1}**	**Dose / Minutes**	$N_{tot\ max}$ **/ molecules cm^{-2} s^{-1}**	N_{tot} **/ molecules cm^{-2} s^{-1}**
0.3	3.12×10^{14}	5	$6.9\times10^{16\pm2}$	$2.1\times10^{14\pm2}$
1	9.72×10^{14}	10	$1.4\times10^{17\pm2}$	$4.2\times10^{14\pm2}$
4	1.60×10^{15}	15	$2.1\times10^{17\pm2}$	$6.3\times10^{14\pm2}$
6	2.86×10^{15}	30	$4.1\times10^{17\pm2}$	$1.2\times10^{15\pm2}$
10	2.89×10^{15}	45	$6.2\times10^{17\pm2}$	$1.9\times10^{15\pm2}$
20	5.62×10^{15}	60	$8.3\times10^{17\pm2}$	$2.5\times10^{15\pm2}$
30	8.65×10^{15}	90	$1.2\times10^{18\pm2}$	$3.6\times10^{15\pm2}$
40	1.06×10^{16}	120	$1.7\times10^{18\pm2}$	$5.1\times10^{15\pm2}$

Table 4.14: Values of N_{tot} for the Background Deposited (left) and the Maximum and Actual Value of N_{tot} for the Molecular Beam Dose Experiments (right)

To interpret if the estimated value of 3×10^{-3} for α is sensible, plots of α against T were constructed. This was achieved by assuming S to be equal to 1. However, k_{des} is also dependent on the kinetic order as this affects which value of ν, E_{des} and J_{in} is chosen. For multilayer coverages of O_2, the values derived for O_2 multilayers desorbing from bare silica in the previous sub-section (assuming zeroth order kinetics) were taken as the values for ν and E_{des} ($10^{27.2\pm2.0}$ molecules cm^{-2} s^{-1} and 9.8±2.0 kJ mol^{-1} respectively). The value for J_{in} was taken as F_{beam} (calculated from the pump-down experiments in **Chapter 3**) resulting in α becoming unitless. The relationship obtained between α and T under zeroth order, multilayer conditions is displayed in **Figure 4.17**. Error analysis was performed using the errors for ν, E_{des} and J_{in} calculated previously in this thesis. However, these were not shown on **Figure 4.17** as these were larger than the defined range for α between 0 (where no species remain adsorbed on the surface) and 1 (all species remain adsorbed).

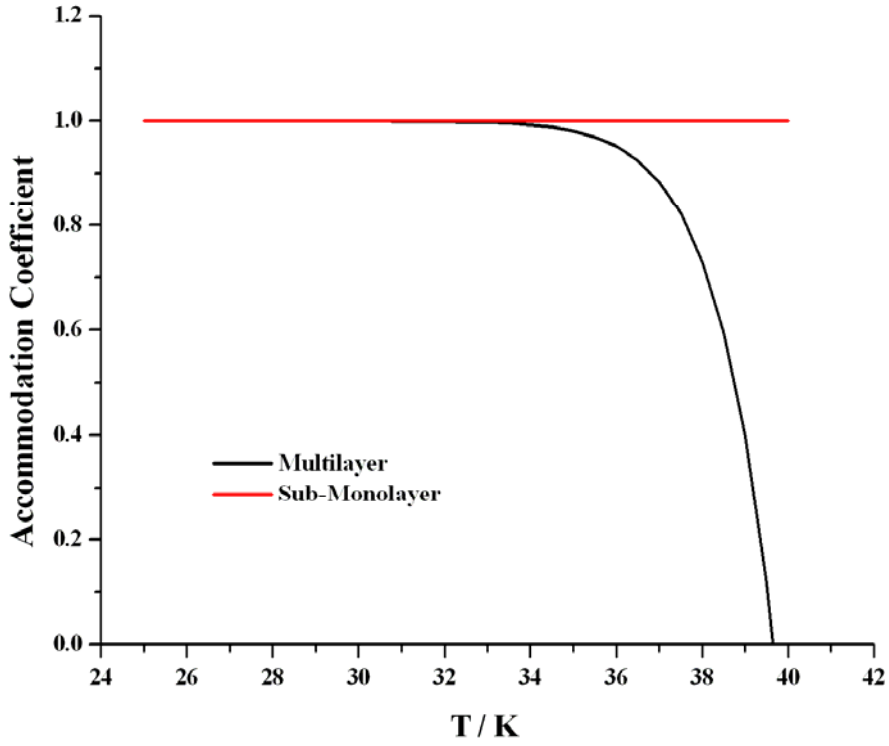

Figure 4.17: Plot of α against T under Multilayer and Sub-Monolayer Conditions

Figure 4.17 also displays the plot of α against T under sub-monolayer conditions. This was achieved by assuming S to be equal to 1 and ν as 1×10^{12} s^{-1} (which is a typical first

order value). The value of E_{des} was taken as the value obtained by analyzing the O_2 background deposition TPD data from bare silica. However, the initial observations of the sub-monolayer data in **Section 4.3.3** revealed that E_{des} was dependent on the surface coverage of O_2 at that moment in time. This would have resulted in the interpretation of S and α being too complex for the level of accuracy applied. As a consequence, the value of E_{des} was taken as the same value under zeroth order, multilayer conditions. The remaining value to determine was J_{in} but if F_{beam} was again taken as J_{in} then the calculated value of α would no longer be dimensionless. To prevent this from occurring, J_{in} was taken as the collision frequency which is equivalent to F_{beam} divided by the molecular beam area, A_{beam}, (in units of cm^{-2}).

The results displayed in **Figure 4.17** reveal that under sub-monolayer conditions, the value of α remained constant at 1. This implied that all the O_2 molecules were sticking to the surface resulting in an increase in the surface concentration. The relationship between α and T under multilayer conditions remained constant until the surface temperature increased above approximately 28.5 K where the value of α decreased rapidly to 0 by 39.7 K. From these results the value of T where α is 3×10^{-3} occurred at roughly 39.6 K implying that the surface temperature of the quartz crystal was higher than initially estimated in **Chapter 3**. However, the O_2 TPD results discussed in **Section 4.3.3** revealed that O_2 molecules can remain adsorbed on the surface above this temperature (see **Figure 4.8** and **Figure 4.9**). This is particularly true for the molecular beam dose TPD results as $N_{tot\ max}$ was considerably higher than the actual N_{tot} where the species remained adsorbed on the surface. The results also imply that the assumption of $S(T)$ was equal to 1 was valid. As a consequence, the estimate of α used to determine the actual values of N_{tot} for the molecular beam doses onto the bare silica sample seems sensible and will be used for modelling the molecular beam sub-monolayer TPD data in the next sub-section.

The results obtained for the range of N_{tot} in **Table 4.14** also reveal that only experiments using sub-monolayer coverages of O_2 could be performed using the current apparatus system. Ideally, the experiments required to fully understand the formation of H_2O in the interstellar medium would require both sub-monolayer and multilayer coverages to determine the kinetics of the surface and desorption processes. This could be achieved by increasing t_{irr} as this would have resulted in larger values of N_{tot} being dosed onto the surface. However, this procedure would have also lead to an increase in contamination

through surface bombardment. An alternative method of increasing N_{tot} would be to modify the apparatus in the future to improve the value of α. Possible modifications to the atomic beams have previously been considered in **Chapter 3**. One solution would be to control the temperature of the beam species by either passing the gas through an aluminium nozzle connected to a closed-cycle He cryostat [34] or direct the beam through a tube surrounded by a copper tube again connected to a closed-cycle He cryostat [35]. The control over the beam species temperature would allow for a greater range of surface concentrations of O_2 to be dosed onto the silica surface within a suitable range of irradiation dose times.

4.3.6 Modelling the TPD Data – Sub-Monolayer

In this section the background deposition and molecular beam sub-monolayer coverages were analyzed using the direct inversion of the Polyani-Wigner equation and fitted using a multiple E_{des} model. The initial observations in **Section 4.3.3** revealed that the underlying silica surface was affecting the desorption behaviour of the O_2 molecules. This resulted in a range of values of E_{des} for O_2 rather than a single value as derived for H_2O on silica (**Section 4.2**) and O_2 multilayers on silica (**Section 4.3.4**).

To determine E_{des} for the sub-monolayer doses, direct inversion of the Polyani-Wigner Equation was used. This technique was first used by Zubkov *et al.* [2] but has since been adapted to describe the desorption of other small molecules on similar porous surfaces (for example, C_6H_6 from bare silica [6, 7]). The technique was performed by rearranging the Polyani-Wigner Equation (**Equation 4.4**) in terms of E_{des} (**Equation 4.14**) and obtaining a function for E_{des} based on the surface concentration at that point in time, *N(t)*.

$$E_{des} = -k_B T \ln\left(\frac{dN/dt}{\nu N(t)^n}\right) \tag{4.14}$$

The first stage of the analysis was to obtain the values of N_{tot} for the background deposition and molecular beam dose which was achieved in the previous sub-section. These results were used to obtain the value of *dN/dt* using the same procedure as for the H_2O and O_2 multilayer TPD desorption. The value of $N(t)^n$ had to be calculated for each time setting, *t*, for each dose. This was achieved by first integrating the desorption peak of O_2 (in units of MASsoft counts) against *t* and extracting each integration *t* stage

to obtain the concentration of O_2 in the gas-phase N_{gas}. By substracting N_{gas} (for each t) from N_{tot} (for that dose) the concentration of O_2 remaining on the surface, $N(t)$, was obtained (see **Equation 4.15**). As first order kinetics was applied (n equalled 1), the value of $N(t)$ was equivalent to $N(t)^n$.

$$N(t) = N_{tot} - N_{gas} \tag{4.15}$$

One disadvantage of using the direct inversion of the Polyani-Wigner equation is that a value for v has to be assumed (unlike leading edge analysis). In this study, a typical first order value of 1×10^{12} s^{-1} was taken for v.

The plots of E_{des} against N for the background deposition and molecular beam dose data are displayed in **Figure 4.18** and the values of E_{des} for each dose in **Table 4.15**. The values of E_{des} for the background deposition data were similar to those obtained for the O_2 multilayer coverages using leading edge analysis and CKS. In comparison, the molecular beam dose curves were not as well aligned with each other and the range of E_{des} started approximately 3 kJ mol^{-1} higher than the background deposition data. Sensitivity analysis was obtained by altering the value of v between 1×10^{11} and 1×10^{13} s^{-1}. The results indicated that the range of E_{des} contained an average error of 1.0 kJ mol^{-1} for both the dosing methods. Overall, the range of E_{des} results revealed that as N increased, the O_2 molecules adsorbed on the surface were forced to occupy the weaker binding sites on the silica surface which required less energy for the molecule to desorb resulting in a lower starting range for E_{des}. By 20 L and 90 minutes doses, the relationship between E_{des} and $N(t)$ changes indicating that at these values of N_{tot} the desorption behaviour of O_2 molecules no longer followed first order (sub-monolayer) but fractional order kinetics before the multilayer region began.

The results obtained for the sub-monolayer O_2 TPD curves were used in a multiple E_{des} simulation model of the experimental data. The modelling technique used for the multilayer coverages could not be applied as CKS required a fixed value for E_{des}. The simulation model used in this study was previously constructed by Thrower to fit C_6H_6 desorption peaks using Fortran 90 [7]. The model works by taking the experimental time and temperature data as an input to calculate the desorption rate of O_2 through the

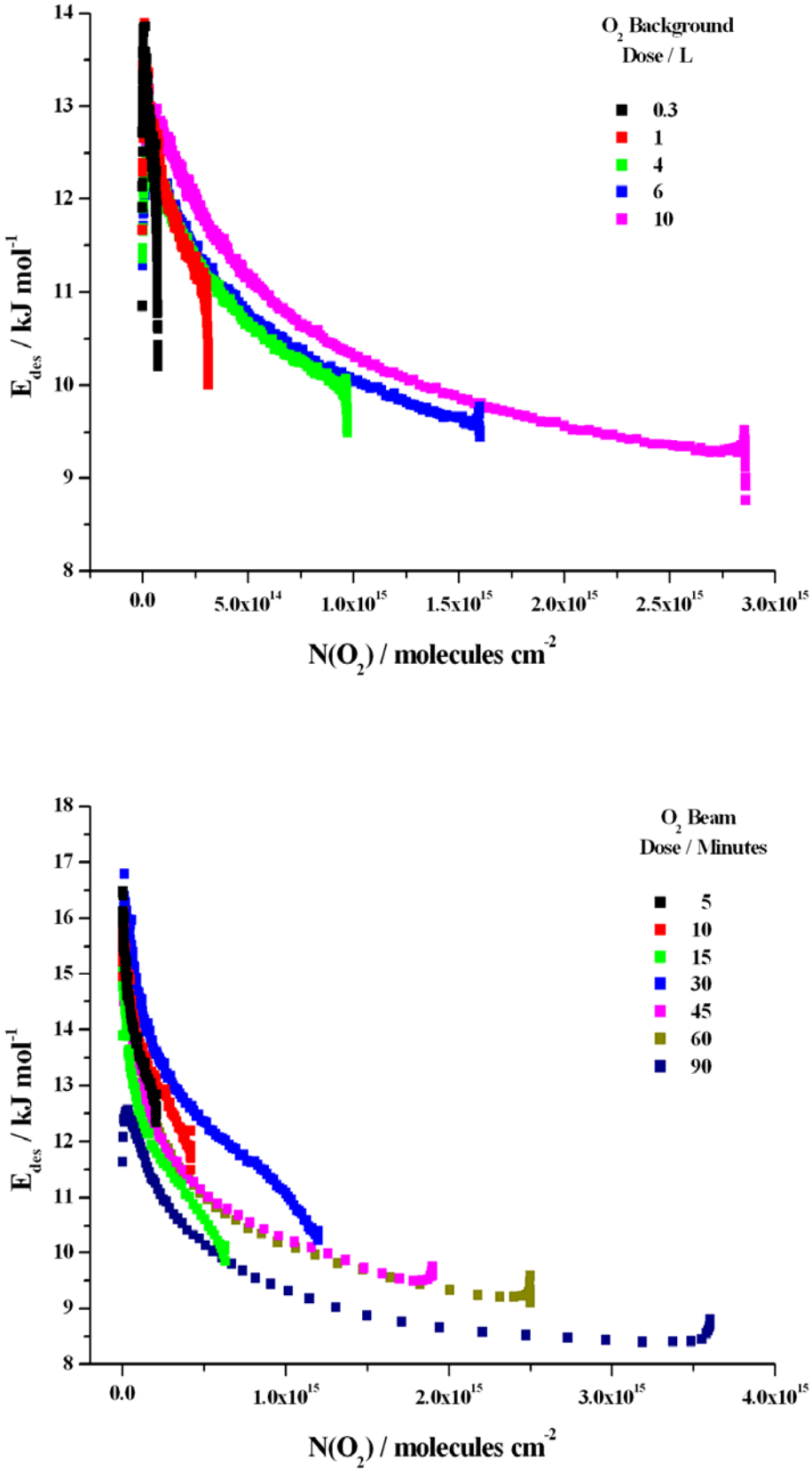

Figure 4.18: Plot of E_{des} against N for the Background Deposition (top) and Molecular Beam Dose (bottom) Data

Background Deposition		Molecular Beam Dose	
Dose / L	**E_{des} / kJ mol^{-1}**	**Dose / Minutes**	**E_{des} / kJ mol^{-1}**
0.3	12.3 – 13.4	5	12.8 - 16.5
1	11.2 – 13.1	10	11.9 - 16.1
4	10.0 – 12.3	15	10.1 - 15.7
6	9.6 – 12.4	30	10.4 - 16.4
10	9.3 – 12.9	45	9.5 - 14.8
-	-	60	9.2 - 14.7

Table 4.15: Direct Inversion of the Polyani-Wigner Equation Results for E_{des}

Polyani-Wigner equation (**Equation 4.14**). The value of E_{des} was provided as a function of $N(t)$ for each dose by fitting a polynomial curve to each of the curves displayed in **Figure 4.18** (with the exception of the 90 minute dose). An example polynomial curve fit is displayed in **Figure 4.19**. The output data calculated from the program contained the original input data along with the O_2 desorption rate and E_{des}.

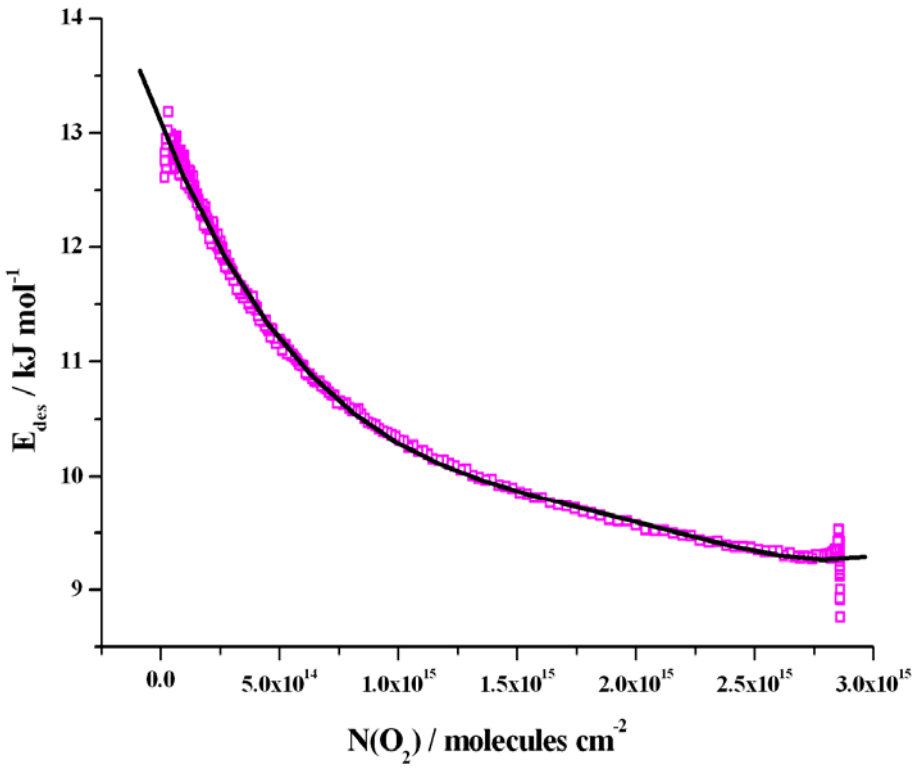

Figure 4.19: 10 L Example Polynomial Fit to Obtain the E_{des} Function

The multiple E_{des} simulation model fits to the experimental sub-monolayer TPD data are shown in **Figure 4.20**. All of the model fits agree very well with the experimental data implying that the value of E_{des} increased with decreasing *N(t)* and that sub-monolayer coverages of O_2 on silica followed first order desorption kinetics. The results obtained from this experiment will be used towards the analysis of the O_2 on cASW and O_2 on pASW TPD experiments (**Sections 4.4** and **4.5** respectively).

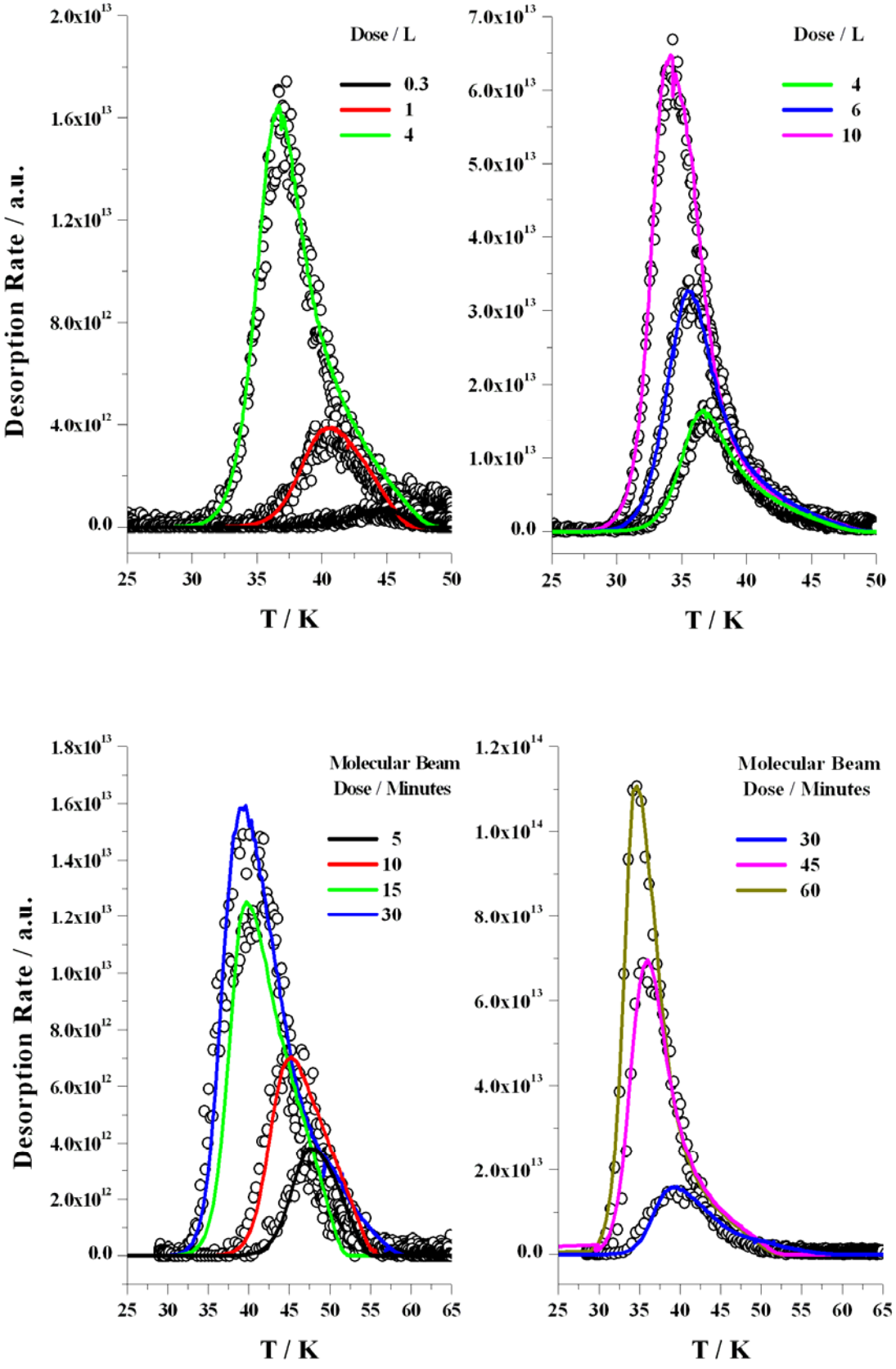

Figure 4.20: Simulation Sub-monolayer O_2 TPD Fits for Background Deposition (top) and Molecular Beam Dose (bottom)

4.3.7 Conclusions

Analysis of the O_2 TPD experiments from bare silica discussed in this section revealed that the O_2 desorption kinetics followed one of three groups: multilayer; sub-monolayer; and fractional order. Each of these regions was dependent on the initial surface concentration. The multilayer coverages were analyzed and modelled using leading edge analysis and CKS. The results concluded that the average value for E_{des} and v were 9.8±0.1 kJ mol^{-1} and $1.6\pm0.3\times10^{27}$ $molecules^{0.82}$ $cm^{-1.64}$ $s^{-0.82}$ respectively and were in good agreement with other experimental data. The results also revealed that the desorption of O_2 molecules from the bulk ice followed fractional order kinetics of 0.18±0.04 which was inconsistent with multilayer desorption of other similar molecules. Initial possible suggestions for the fractional order desorption behaviour of O_2 were due to: the underlying silica surface; O_2 desorbing as $(O_2)_2$ dimer clusters; or the O_2 molecules forming and desorbing as O_4 species. However, the simulation results obtained from a two population CKS model revealed that the dissociation of the $(O_2)_2$ dimer species occurred at surface temperatures below 20 K suggesting that the $(O_2)_2$ dimers were not responsible for the observed fractional order desorption behaviour.

Further analysis of the multilayer desorption kinetic behaviour will be explored in **Chapter 5** from the discussion of CO and N_2 TPD experiments from bare silica. If the results concluded that multilayer coverages of CO and N_2 followed non-zeroth desorption order kinetics then the observed fractional order of multilayer coverages of O_2 could be due to the underlying porous and amorphous silica surface. However, if the multilayer coverages of CO and N_2 desorb following zeroth order kinetics then the observed fractional order desorption of O_2 could be concluded as being more complex. This would be confirmed by repeating the O_2 multilayer TPD experiment from bare silica with RAIRS analysis. The results obtained from these proposed experiments could reveal whether the $(O_2)_2$ and O_4 species were responsible for the observed fractional order desorption behaviour of O_2.

Overall, the multilayer desorption of O_2 would be irrelevant under ISM conditions due to the low observed gaseous molecular abundance even though the results were required to explore the full H_2O formation mechanism on interstellar dust grains (as previously described in **Chapter 1**). However, the results obtained could be applied to the desorption of O_2 from icy objects in the outer regions of the Solar System (for example, some of the moons of Jupiter and Saturn).

Analysis and modelling of the sub-monolayer O_2 TPD data was performed using direct inversion of the Polyani-Wigner equation and a multiple E_{des} simulation model. This analytical procedure was also applied to the molecular beam dose TPD data once the values of α and S had been interpreted as 3×10^{-3} and 1 respectively. The simulations fitted the O_2 desorption peaks well implying that the underlying porous silica surface increased the value of E_{des} with decreasing $N(t)$ and that the desorption of sub-monolayer coverages of O_2 followed first order kinetics.

The final group of O_2 desorption peaks was the fractional order region which exhibited both sub-monolayer and multilayer desorption peak characteristics. The cause of this observation was concluded to be from O_2 molecules desorbing from multilayer islands which formed on the surface before a complete monolayer coverage was obtained. As a consequence, these TPD desorption peaks exhibited both 0.18 and first order desorption characteristics resulting in varying fractional order desorption kinetics depending on $N(t)$.

Overall, the kinetic parameters obtained from this experiment will be used towards analyzing the TPD results in **Sections 4.4** and **4.5**. The results from all these experiments (and those from **Section 4.2**) will be used to construct a simulation model mimicking the desorption of O_2 from the icy mantles coating interstellar dust grains. In the future, these results will also be used towards interpreting other experimental data from the dual atomic beam apparatus to determine how H_2O is formed on interstellar dust grains.

4.4 O_2 on cASW on Silica Surface

4.4.1 Introduction

This section explores the results of molecular beam dose O_2 on background deposition dose cASW TPD experiments. The results discussed in **Section 4.2.3** indicated that in a 500 L H_2O film the CSW phase change is dominant as the film thickness is sufficient to prevent the underlying silica surface from affecting the desorption of O_2. The experimental procedure for this experiment is outlined in **Section 4.4.2**. The TPD curves are discussed in **Section 4.4.3** and the results analyzed using direct inversion of

the Polyani-Wigner equation. The conclusions of these experiments are summarized in **Section 4.4.4**. The results obtained were used with those from the previous sections of this chapter to construct a larger simulation model to describe the desorption of O_2 from pASW (**Section 4.5**) and from icy mantles under ISM conditions (**Section 4.6**).

4.4.2 Experimental Procedure

The experimental procedure followed a similar method to the one for the 500 L H_2O dose TPD experiment described in **Section 4.2.2** but with the sample held at 100 K during the H_2O dose and an additional O_2 molecular beam dose performed between the H_2O background deposition dose and TPD technique. Therefore only a brief description is given here. Once UHV conditions had been achieved, the sample was positioned inline with the O_2 molecular beam and heated clean to 180 K before allowed to cool back to base temperatures. The gate valves between the atomic beam and central chambers were closed and the central chamber pressure noted. A dosing bulb was flushed and filled with water vapour previously purified using the freeze-pump-thaw technique and the sample heater used to hold the sample surface at 100 K. Once the sample temperature had stabilised at this temperature, the data acquisition was set using the same conditions as in **Sections 4.2.2** and **4.3.2**. The MASsoft program was set to monitor the intensity of H_2O, O_2, O, CO/N_2 and CH_3 species and the KP type thermocouples on the sample and cold-finger. After a short delay, 500 L of H_2O was background deposited onto the sample at a pressure of 5×10^{-7} mbar for 1000 s. With the surface held at 100 K the adsorbed H_2O molecules form the cASW ice structure. When the pressure had returned to base levels, the two programs were stopped and the sample cooled back to base temperatures.

O_2 was molecular beam dosed onto the cASW substrate following the same procedure used for this stage in **Section 4.4.2** for doses of 5, 10, 15, 30, 45, 60, 90 or 120 minutes except the MASsoft program was set to monitor the same species as those in the above H_2O dose stage. Once this stage had been completed, the TPD part of the experiment was performed following the same procedure for the TPD stage in **Section 4.2.2** but with the same MASsoft settings as for the above dosing stages. When the sample temperature reached 180 K the two programs were stopped and the heating ramp terminated. Once the sample had returned to base temperature, a second two dose TPD experiment could be performed.

After initial experiments had concluded that there was no further desorption of any species except H_2O from the sample after 60 K, the subsequent TPD experiments were performed up to a temperature of 98 K. This change to the procedure allowed any species adsorbed on the H_2O layer to desorb but without the cASW surface being destroyed or altered. Any following experiments requiring the cASW layer could start with the O_2 molecular beam dose stage providing the sample was never heated above 100 K.

A duplicate set of O_2 molecular beam doses on cASW TPD experiments were performed.

4.4.3 Results

The TPD graphs were constructed using the same method as for the previously discussed data in this chapter. **Figure 4.21** displays the O_2 and H_2O desorption traces

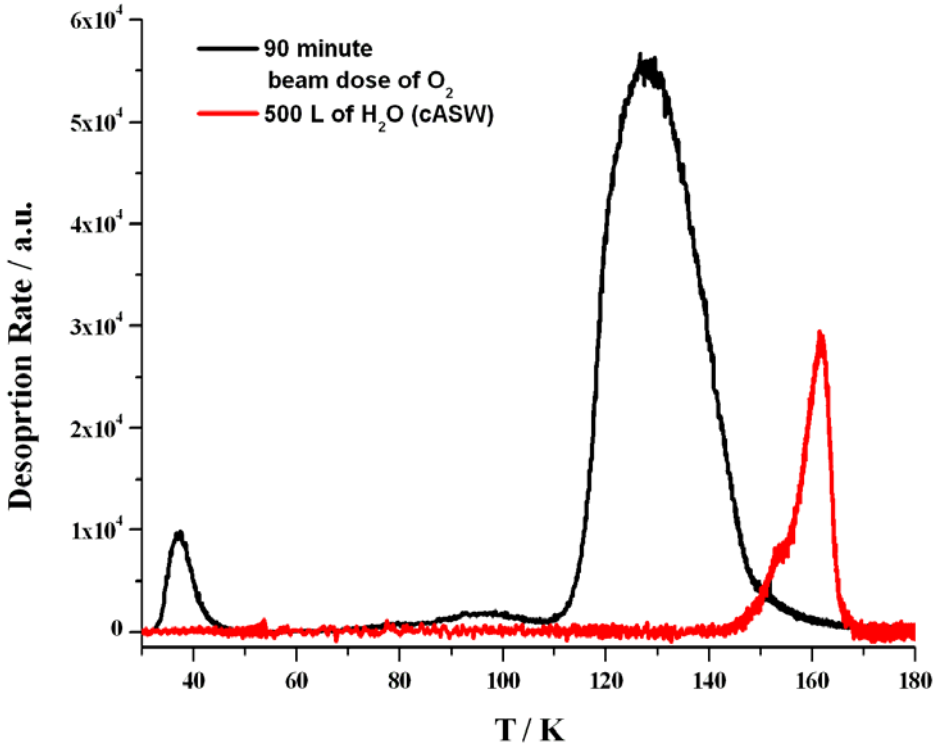

Figure 4.21: Base to 180 K TPD curves of O_2 on cASW

for a 90 minute dose from 30 to 180 K. The O_2 trace has three peaks centred at roughly 37, 97 and 127 K which represents the desorption of O_2 from the H_2O film on the silica

sample; the sample mount; and the cold-finger. The H_2O 500 L dose desorption curve followed the same double peak structure observed in **Section 4.2** for the same dose. In this experiment, the H_2O layer was removed so the film had to be re-formed before the O_2 dose was applied in the following experiment. As the desorption of O_2 from H_2O on the silica sample occurred at temperatures lower than those required to alter the structure of the H_2O film, the following TPD experiments were performed up to a surface temperature of 98 K.

The full set of O_2 TPD curves are displayed in **Figure 4.22**. Direct inversion of the Polyani-Wigner Equation was applied to these TPD curves using the same procedure as for the sub-monolayer O_2 on bare silica TPD results (see **Sections 4.3.5** and **4.3.6**). **Figure 4.23** displays the plot of E_{des} against $N(t)$ and the results of N_{tot} and E_{des} are shown in **Table 4.16**. The plot reveals that all the molecular beam dose curves align

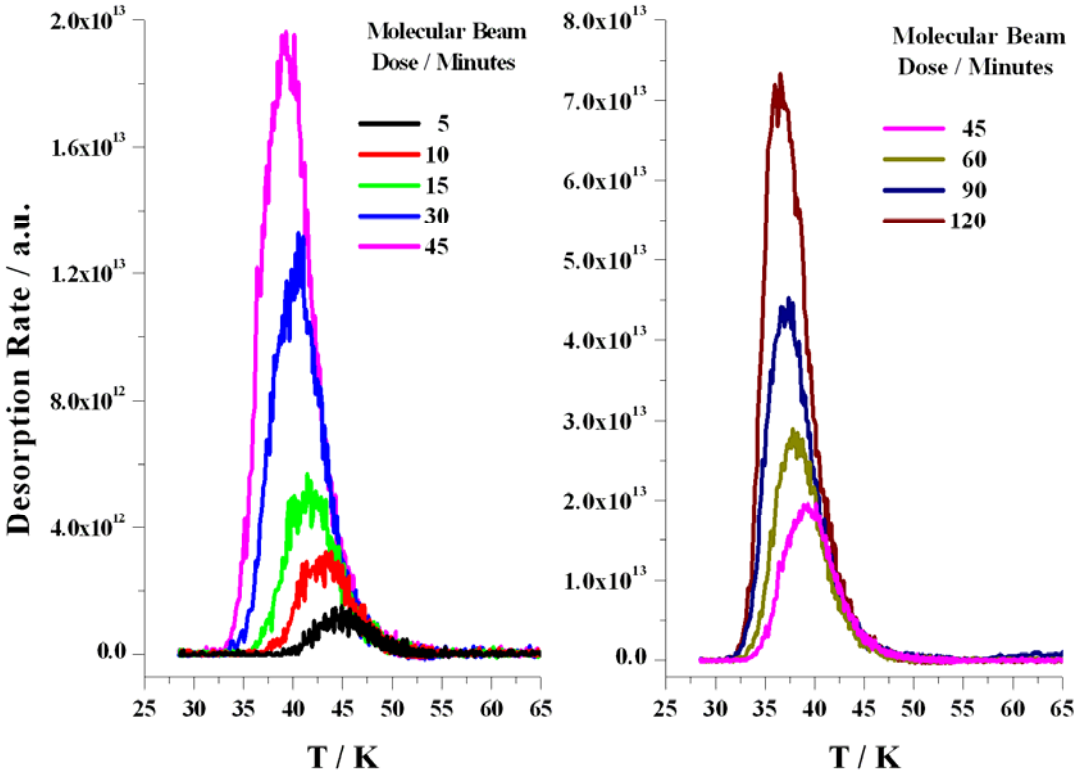

Figure 4.22: O_2 on cASW TPD Curves From Bare Silica

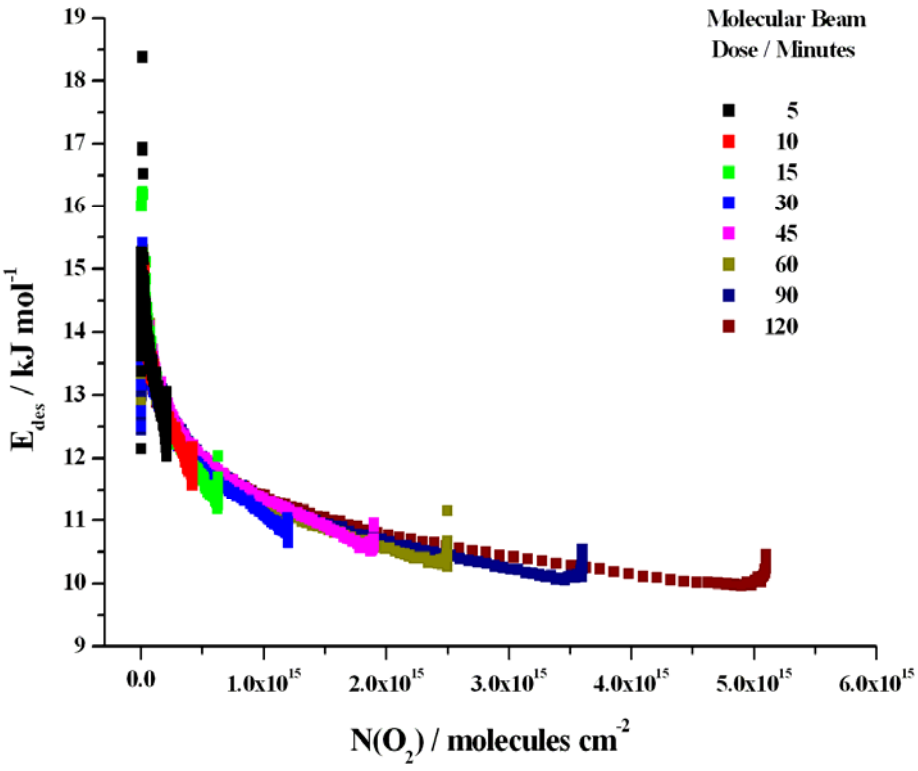

Figure 4.23: E_{des} against $N(t)$ for O_2 on cASW

Dose / Minutes	N_{tot} / molecules cm^{-2}	E_{des} / kJ mol^{-1}
5	$10^{14.4\pm2.0}$	12.4 – 18.4
10	$10^{14.6\pm2.0}$	11.8 – 15.3
15	$10^{14.8\pm2.0}$	11.3 – 16.2
30	$10^{15.1\pm2.0}$	10.8 – 15.4
45	$10^{15.3\pm2.0}$	10.6 – 15.2
60	$10^{15.4\pm2.0}$	10.3 – 15.3
90	$10^{15.6\pm2.0}$	10.1 – 13.9
120	$10^{15.7\pm2.0}$	10.0 – 14.3

Table 4.16: Values of N_{tot} and E_{des} for O_2 on cASW

well with each other unlike those from the molecular beam on bare silica in **Section 4.3.6**. As with O_2 desorbing from bare silica, the 90 and 120 minute dose curves here do not have molecules desorbing at the higher values of E_{des} observed for the shorter dose. This indicates that the cASW substrate has a surface area similar in

size to the bare silica surface resulting in the 90 and 120 minute doses no longer following first order desorption kinetics. Sensitivity analysis was carried out on the range of E_{des} by altering the value of ν between 1×10^{11} and 1×10^{13} s^{-1} (as in **Section 4.3.6**) and was deduced as 1.0 kJ mol^{-1} which is in good agreement with the error obtained for sub-monolayer coverages of O_2 desorbing from bare silica.

The O_2 desorption peaks were fitted using the same reaction mechanism with the multiple E_{des} simulation model as for the sub-monolayer O_2 TPD experiments from bare silica (see **Figure 4.24**). The results are displayed in **Figure 4.25** and the model simulation fits agree well with the experimental data. This implied that the desorption of sub-monolayer coverages of O_2 from cASW on silica followed the same desorption pattern as previously observed for the desorption of O_2 from bare silica.

$$O_2(ads) \rightarrow O_2(g)$$
$$O_2(g) \rightarrow O_2(pump)$$

Figure 4.24: Reaction Mechanism for O_2 Desorbing From cASW

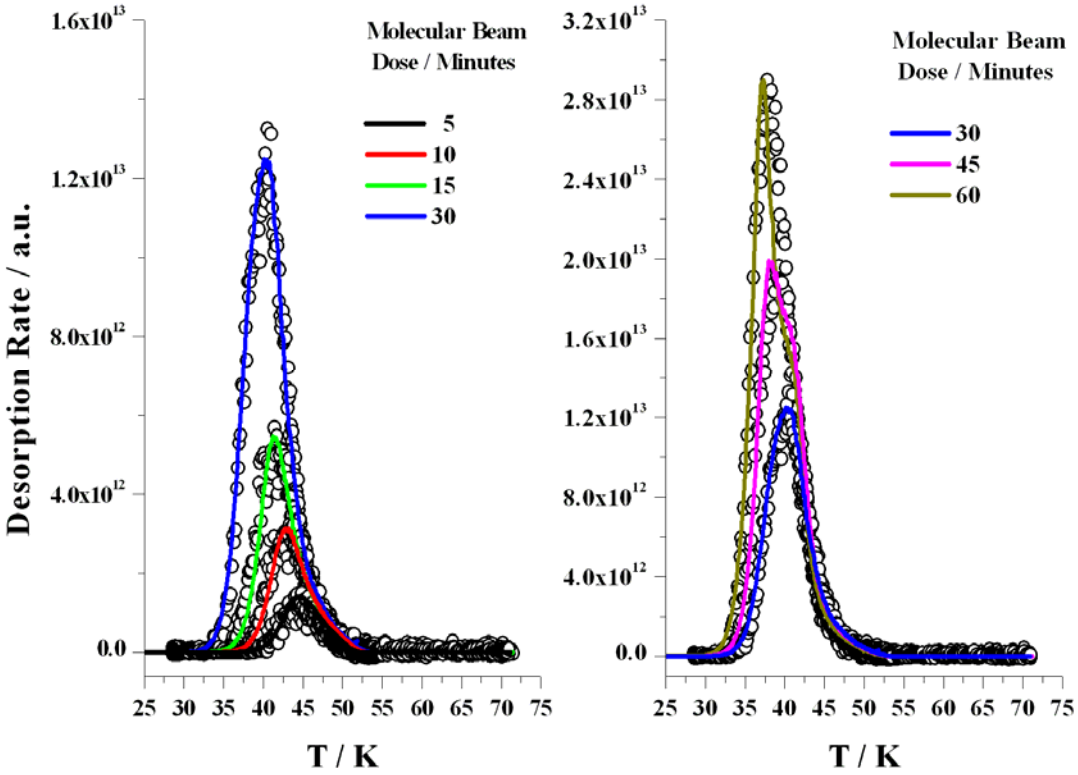

Figure 4.25: Simulated Fits of the O_2 Desoprtion Peaks from cASW on Silica

Although the experiments discussed in this section enabled the desorption kinetics of sub-monolayer coverages of O_2 to be determined, larger doses of O_2 would need to be applied to the cASW surface to explore multilayer coverages. In the future, this could be achieved by modifying the atomic beam apparatus to cool the beam species to improve the value of α and, therefore, allow larger N_{tot} to be applied. However, the results from these proposed O_2 multilayer TPD experiments from cASW on silica could not be applied to the ISM as the molecular abundance of O_2 is too small but the data would enable for a more detailed analysis of the surface and desorption processes occurring in these experiments under laboratory conditions.

Overall, the results obtained from this experiment will be used towards analyzing the O_2 from pASW on silica TPD experiments in **Section 4.5** and towards constructing a simulation model mimicking the desorption of O_2 from icy mantles under ISM conditions.

4.4.4 Conclusions

The experiments performed in this section explored the desorption behaviour of O_2 from a cASW substrate on silica. The results obtained revealed that sub-monolayer coverages of O_2 followed first order multiple E_{des} desorption kinetics similar to that of O_2 desorbing from bare silica in the previous section (see **Figure 4.26**).

The cartoon displayed in **Figure 4.27** describes the surface process occurring during this set of experiments. The first and second stages of the cartoon represent the formation of the cASW and O_2 layers respectively. As discuss in **Section 1.2.3**, the cASW layer contains a porous network but with the openings to the pores closed. The third stage of the cartoon shows the TPD part of the experiment beginning and the desorption of the O_2 molecules at approximately 30 K. By roughly 140 K, the thick cASW layer begins both to desorb and undergoes crystallisation to form CSW (fourth stage) which desorbs at a slightly higher temperature (fifth stage).

Overall, the kinetic parameters obtained from this experiment will be used towards analyzing the O_2 from pASW on silica TPD results (**Section 4.5**) and towards constructing a simulation model mimicking the desorption of O_2 from the icy mantles

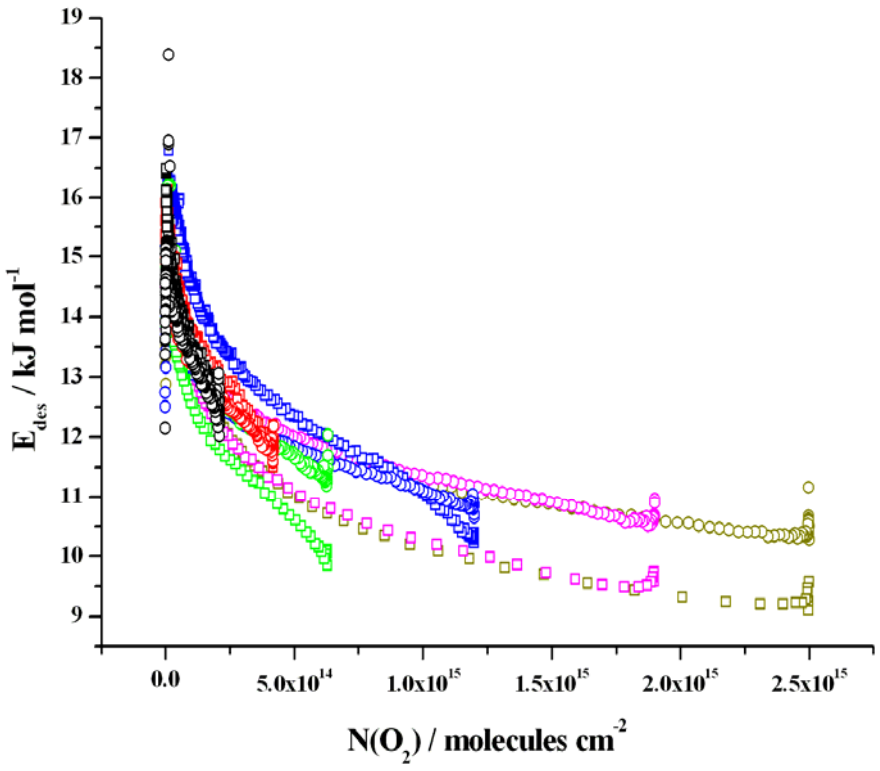

Figure 4.26: *E_{des}* against *N(t)* Comparisons of O_2 on Silica (circles) with O_2 on cASW on Silica (Squares) for Doses of 5 (black), 10 (red), 15 (green), 30 (blue), 45 (magenta) and 60 (dark yellow) Minutes

coating interstellar dust grains. The results obtained from these experiments also highlight the need for the beam apparatus to be modified to enable larger doses of O_2 to be applied to the surface. This would allow multilayer beam dose coverages of O_2 to be explored from these and similar substrates.

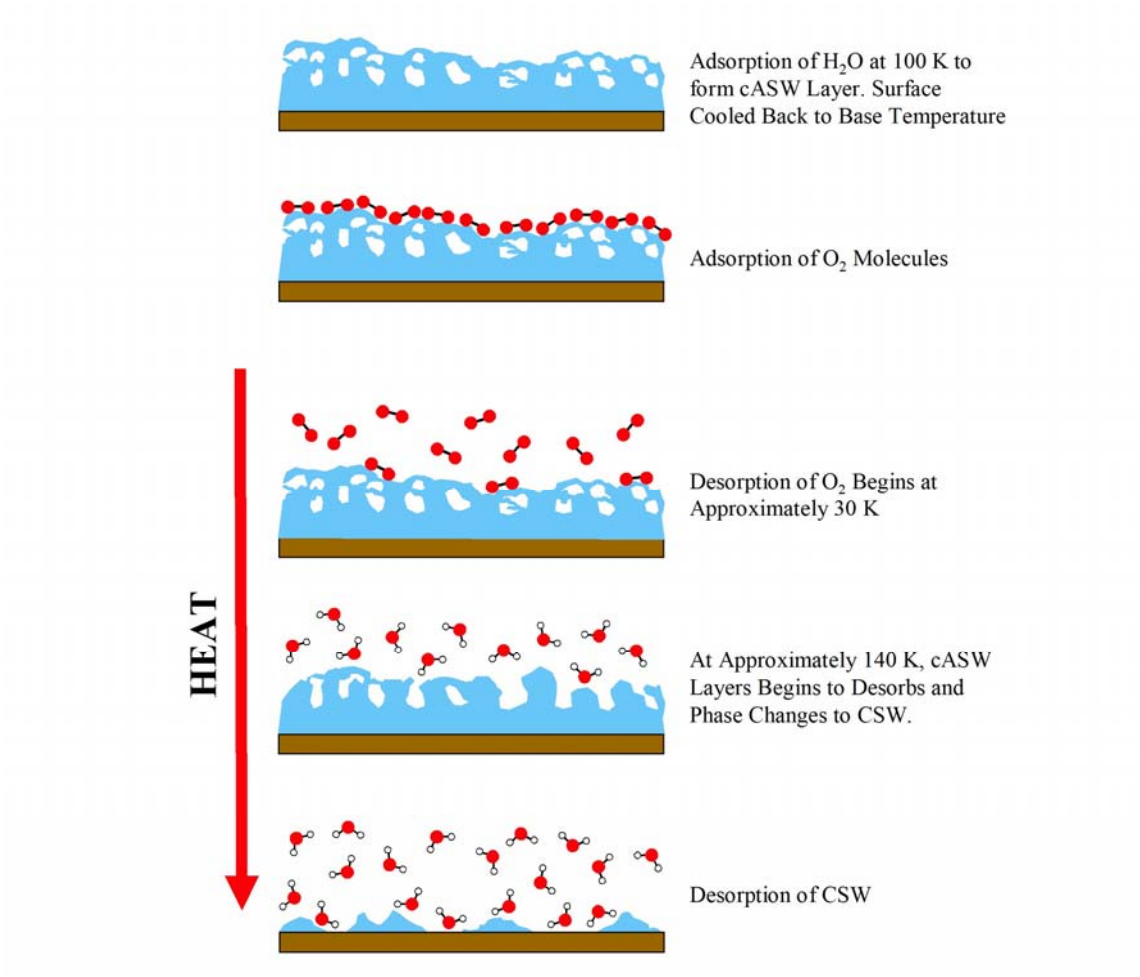

Figure 4.27: Cartoon of O_2 Desorbing From cASW

4.5 O_2 on pASW on Silica Surface

4.5.1 Introduction

This section explores the results of molecular beam dose O_2 onto a background dose pASW substrate TPD experiments on silica. The experimental procedures are outlined in **Section 4.5.2**. The TPD curves are discussed in **Section 4.5.3** and the results were initially analyzed using a direct inversion of the Polyani-Wigner equation and the multiple E_{des} model simulations. Further analysis of the TPD data was achieved by performing increasingly complex reaction mechanism simulation models using CKS. The results obtained in this section are concluded in **Section 4.5.4** and were used, along with the results in the previous sections of this chapter, towards constructing a larger simulation model to describe the desorption of O_2 from H_2O under ISM conditions (**Section 4.6**).

4.5.2 Experimental Procedure

The procedure for this experiment was similar to the initial O_2 from cASW TPD experiments on silica discussed in **Section 4.4.2**. The main difference being the sample was held at base temperature during the 500 L H_2O dose (previously held at 100 K) which prevented the adsorbed H_2O molecules from having enough energy to diffuse or rotate on the silica surface resulting in the formation of a pASW ice film. Molecular beam doses of O_2 were performed for 15, 30, 45, 60 or 90 minutes at base sample temperatures before applying TPD analysis from base surface temperatures to 180 K.

Once the sample had returned to base temperatures a second H_2O dose, O_2 dose TPD experiment could be performed.

A duplicate set of O_2 molecular beam doses on background deposition dose pASW TPD experiments were performed.

4.5.3 Results

The data from the two programs for each experiment was imported into Origin and the TPD curves constructed using the same procedure as for those previously discussed in this chapter. The O_2 and H_2O TPD traces for the 90 minute O_2 dose experiment are displayed in **Figure 4.28**. Although the H_2O curve is similar to that of the 500 L H_2O TPD curve in **Figure 4.1** and **Figure 4.21**, the O_2 curve now has two desorption peaks occurring from the sample surface. The first occurs at a similar temperature to that of O_2 desorbing from bare silica (**Figure 4.8** and **Figure 4.9**) and from cASW on silica (**Figure 4.22**). The second desorption peak roughly occurs between 140 to 150 K and is not the desorption of O_2 from other surfaces (like the cold-finger or the sample mount) but coincides with the desorption of cASW. This delayed desorption pattern has been observed for other similar molecules on pASW surfaces as previously discussed in **Chapter 1**. This observation occurred as a result of the underlying H_2O film undergoing a phase change from pASW to cASW preventing any O_2 molecules that had yet to desorb becoming trapped until the crystallisation of the H_2O film.

The O_2 TPD curves for the 15 to 90 minute O_2 molecular beam doses are displayed in **Figure 4.29**. As in **Section 4.4.3**, the TPD traces indicated that the 15 to 90 minute

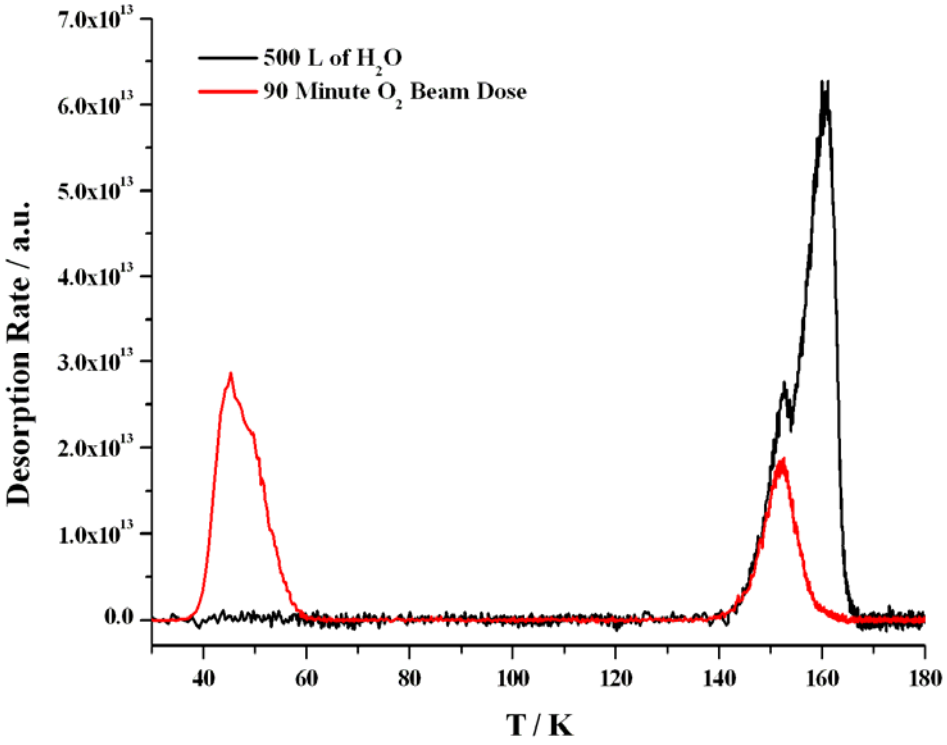

Figure 4.28: TPD curves of 90 minute O_2 Dose on 500 L of H_2O

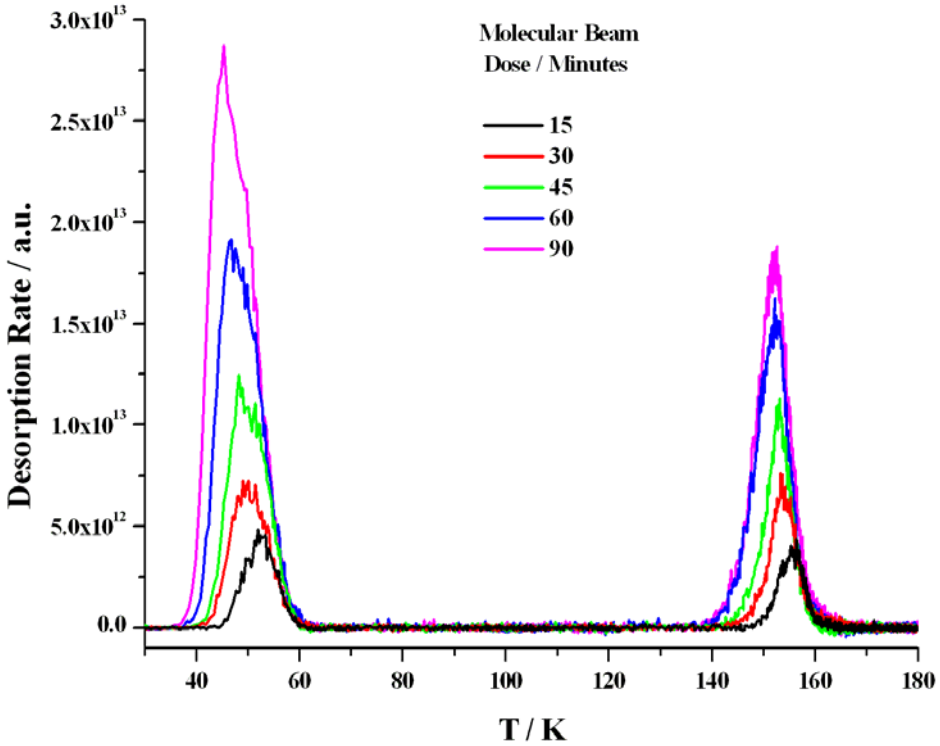

Figure 4.29: O_2 from pASW on Bare Silica TPD Data

non-trapped O_2 doses followed sub-monolayer first order multiple E_{des} desorption kinetics.

The desorption peaks of the trapped O_2 molecules all have coincident falling edges. The 90 minute dose also displays a coincident leading edge with the 60 minute dose. However, the desorption kinetics for the trapped O_2 should theoretically be the same as the non-trapped O_2 but the molecules cannot escape the H_2O ice film until the cASW to CSW phase change. As a consequence, the desorption kinetics of the trapped O_2 is controlled by the H_2O crystallisation and desorption kinetics and so cannot be analyzed using direct inversion of the Polyani-Wigner equation.

The full mechanism describing the processes occurring in this experiment is displayed in **Figure 4.30** and is based on the mechanism used by Collings *et al.* to describe their

$$O_2(s) \rightarrow O_2(g)$$
$$O_2(ads) \rightarrow O_2(pore)$$
$$H_2O(pASW) \rightarrow H_2O(cASW)$$
$$H_2O(pASW) + H_2O(cASW) \rightarrow 2H_2O(cASW)$$
$$O_2(pore) + H_2O(pASW) \rightarrow O_2(ntrap) + H_2O(pASW)$$
$$O_2(pore) + H_2O(cASW) \rightarrow O_2(trap) + H_2O(cASW)$$
$$O_2(ntrap) \rightarrow O_2(g)$$
$$O_2(ntrap) + H_2O(cASW) \rightarrow O_2(trap) + H_2O(cASW)$$
$$O_2(ntrap) \rightarrow O_2(pore)$$
$$H_2O(cASW) \rightarrow H_2O(g)$$
$$H_2O(cASW) \rightarrow H_2O(CSW)$$
$$O_2(trap) \rightarrow O_2(diff)$$
$$H_2O(CSW) \rightarrow H_2O(g)$$
$$O_2(diff) + H_2O(cASW) \rightarrow O_2(ads) + H_2O(cASW)$$
$$O_2(diff) + H_2O(CSW) \rightarrow O_2(ads) + H_2O(CSW)$$
$$O_2(ads) \rightarrow O_2(g)$$
$$O_2(g) \rightarrow O_2(pump)$$
$$H_2O(g) \rightarrow H_2O(pump)$$

Figure 4.30: The Full O_2 on pASW TPD Reaction Mechanism

CO from pASW TPD experiments [3]. The first step describes the multilayer desorption of O_2 from the H_2O film, *s*. However, O_2 multilayer desorption of O_2 was not observed in this study (**Figure 4.29**) as only sub-monolayer coverages were adsorbed. The second step describes the diffusion of O_2 molecules into the underlying porous pASW film, *pore*. The third and fourth steps describe the pASW to cASW phase change through the formation of nucleation centres and the autocatalytic process required for the phase change respectively. The kinetic parameters for these two steps were unable to be obtained from the previously discussed H_2O TPD experiments (see **Section 4.2**) so the values determined by Collings *et al*. were taken [3]. This assumption provided the same mathematical description for the pASW to cASW phase change but the actual mechanism for this process would be too complex to model using CKS.

The fifth to ninth reaction steps are used to describe the O_2 trapping and non-trapping processes in the ASW film during the pASW to cASW phase change. The fifth step reflects the probability of an O_2 molecule in a pASW pore where the molecule will become non-trapped, *ntrap*, whereas the sixth step reflects the probability of an O_2 molecule becoming trapped, *trap*, in a cASW pore. Most of the non-trapped O_2 molecules will desorb resulting in the first desorption peak observed in **Figure 4.28** and **Figure 4.29** (seventh step). However, as the desorption of these non-trapped molecules have a range of values for E_{des}, the molecules occupying those binding sites which require more energy to desorb could become trapped during the pASW to cASW phase change (eighth step). The ninth reaction step describes the probability of desorbed non-trapped O_2 molecules re-adsorbing.

The next collection of reaction steps (tenth to sixteenth) displayed in **Figure 4.30** describes the affect of the trapped O_2 molecules with the crystallisation and desorption of cASW and CSW. These steps are based on those previously used to model the H_2O TPD data in **Section 4.2.4**. As a consequence, the kinetic parameters used to model these H_2O steps were taken from the results obtained for the 500 L dose. The twelfth step describes the release of O_2 from the collapsing pores in the H_2O film during crystallisation. As a consequence, this step uses the same kinetic parameters as those determined in **Section 4.2.4** for the crystallisation of cASW. This step could have been combined with the H_2O crystallisation (eleventh step) but this would have involved re-fitting the H_2O desorption peaks due to the assumed first order kinetic behaviour on

the trapped O_2 molecules. However, as only the 500 L dose was performed in this study additional O_2 on pASW TPD experiments on silica over a range of H_2O doses were required to obtain a more accurate description of the cASW crystallisation process with respect to the trapped species. The diffusion of the O_2 molecules to the surface, *ads*, is shown in the fourteenth and fifteenth steps and is dependent on the surface concentration of cASW and CSW respectively. The desorption of O_2 from the surface (sixteenth step) theoretically follows the same desorption kinetics as the non-trapped O_2 molecules. These reaction steps vary slightly from those used by Collings *et al.* as CO was observed to crystallise which does not occur with O_2. However, the additional steps describing the diffusion of O_2 (dependent on cASW) and the desorption of cASW were required as a smaller surface concentration of H_2O was used resulting in these steps becoming more dominant with respect to those from just CSW.

The final two steps in this mechanism describe the removal of O_2 and H_2O from the system by pumping, *pump*. Both of these steps have separately been used to model the previous sets of TPD data discussed in this chapter so the kinetic parameters were initially taken as the same.

Initially fitting the O_2 from pASW TPD data with a reaction mechanism this complicated would result in too many variables. Instead, the model was first simplified to determine the desorption kinetics of the non-trapped O_2 molecules. This was achieved by only including the seventh and seventeenth reaction steps from **Figure 4.30** (**Figure 4.31**) using direct inversion of the Polyani-Wigner equation (as previously described in **Sections 4.3.6** and **4.4.3**). The values of N_{tot} for each O_2 dose (and therefore both desorption peaks) was calculated as before and separated into the initial surface concentrations for the non-trapped and trapped O_2 species, $N[O_2(ntrap)]$ and $N[O_2(trap)]$ respectively, by considering the non-trapped and trapped O_2 desorption peak areas. The results are displayed in **Table 4.17**.

$$O_2(\text{ntrap}) \rightarrow O_2(\text{g})$$
$$O_2(\text{g}) \rightarrow O_2(\text{pump})$$

Figure 4.31: Reaction Mechanism for Non-Trapped O_2 Desorbing from pASW

Dose / Minutes	$N[O_2(ntrap)]$ / molecules cm^{-2}	E_{des} / kJ mol^{-1}	$N[O_2(trap)]$ / molecules cm^{-2}
15	$10^{14.3\pm2.0}$	13.7 – 17.9	$4.4\times10^{14\pm2}$
30	$10^{14.5\pm2.0}$	13.0 – 17.8	$8.7\times10^{14\pm2}$
45	$10^{14.8\pm2.0}$	12.9 – 19.2	$1.3\times10^{15\pm2}$
60	$10^{14.9\pm2.0}$	12.2 – 14.4	$1.7\times10^{15\pm2}$
90	$10^{15.1\pm2.0}$	11.9 – 14.9	$2.4\times10^{15\pm2}$

Table 4.17: Value of $N[O_2(ntrap)]$ and E_{des} for Non-Trapped O_2 on pASW and $N[O_2(trap)]$ for Trapped O_2

The E_{des} ranges were obtained using the same procedure as previously discussed in **Sections 4.3.6** and **4.3.3** and are displayed in **Figure 4.32** and **Table 4.17** with an error of 1.0 kJ mol^{-1}. The plot reveals that for the 15 to 45 minute doses, the molecular beam curves align well with each other and provide a similar range of values of E_{des} to those

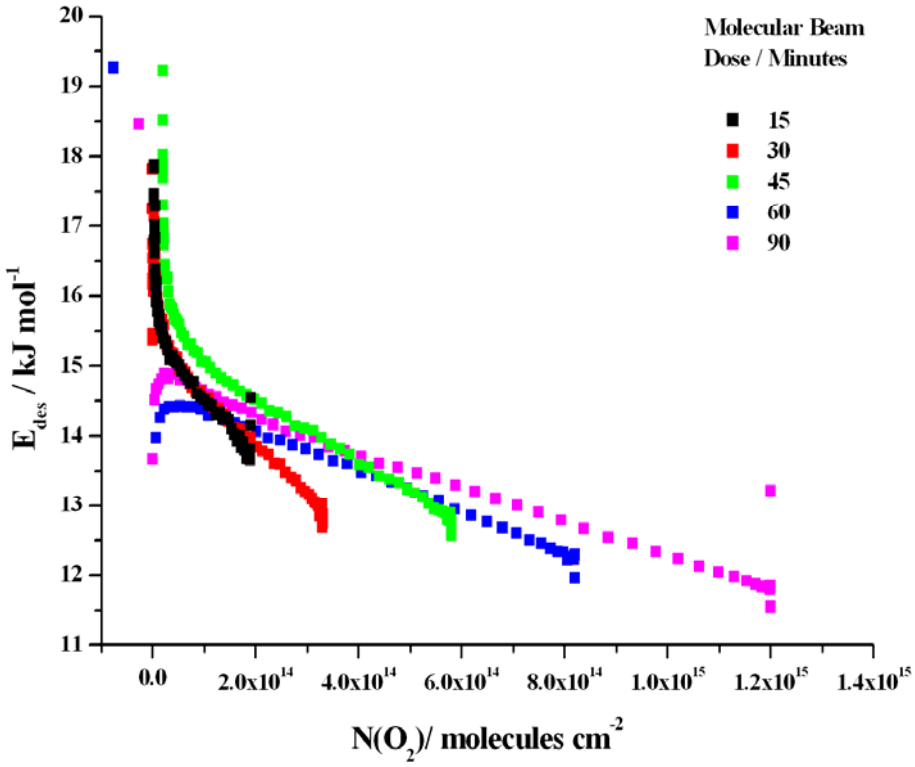

Figure 4.32: E_{des} against $N[O_2(ntrap)]$ for Non-Trapped O_2 Molecules on pASW

obtained for O_2 desorbing from cASW (**Section 4.3.3**). At longer dose times, the molecular beam curves became more linear in shape resulting in smaller ranges of E_{des} being obtained. This observation was unexpected as the molecular beam curves describing the E_{des} function for O_2 desorbing from cASW followed the same relationship at higher initial O_2 sub-monolayer surface concentrations (see **Figure 4.33**). The change in the relationship could be due to the pASW to cASW phase change. This would result in those O_2 molecules situated in the higher binding energy sites (and, therefore, those requiring a larger value of E_{des} to desorb) not being able to desorb before the pores in the pASW film closed. As a consequence the originally non-trapped O_2 molecules would become trapped (eighth step in **Figure 4.30**). Although this step is required to fully describe the desorption of non-trapped O_2 molecules, this step would initially be too complex to include and would require the multiple E_{des} model to be developed.

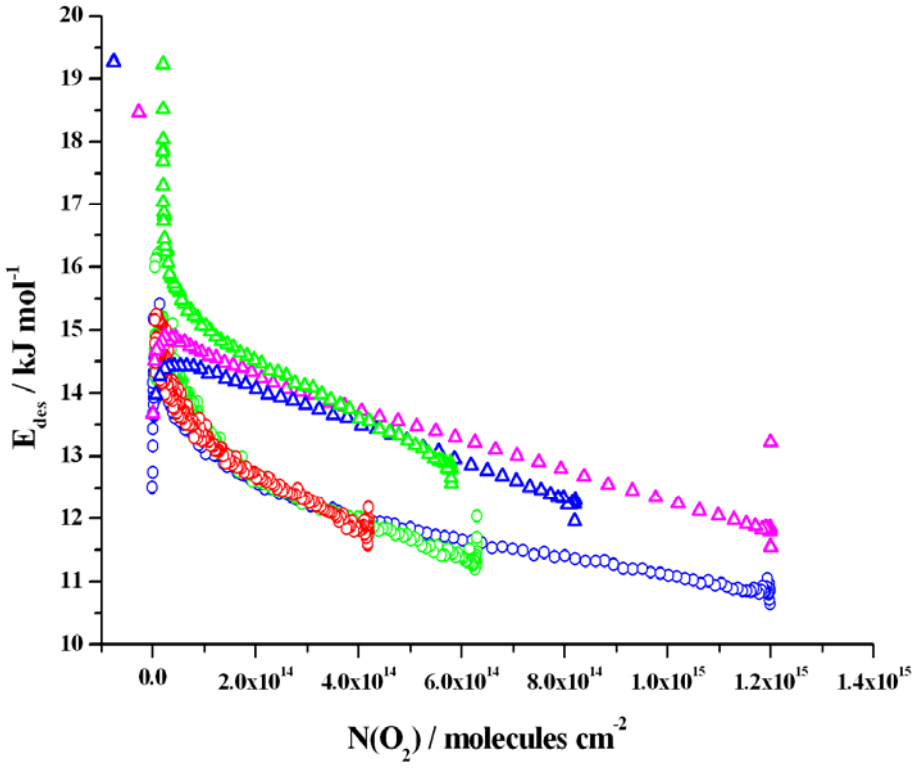

Figure 4.33: E_{des} against $N(t)$ Comparisons of O_2 on cASW (circles) for Doses of 10 (Red), 15 (Green) and 30 (Blue) Minutes with O_2 on pASW (Triangles) for Doses of 45 (Green), 60 (Blue), 90 (Magenta) Minutes

The simulation fits are displayed in **Figure 4.34** and are in very good agreement with the experimental data and with the O_2 sub-monolayer desorption kinetics obtained from bare silica (**Section 4.3.6**) and cASW (**Section 4.4.3**). To provide a more accurate description of the desorption of the non-trapped O_2 molecules the surface processes associated with the pASW to cASW phase change would need to be included. The reaction steps required for this mechanism are displayed in **Figure 4.35**. The first two

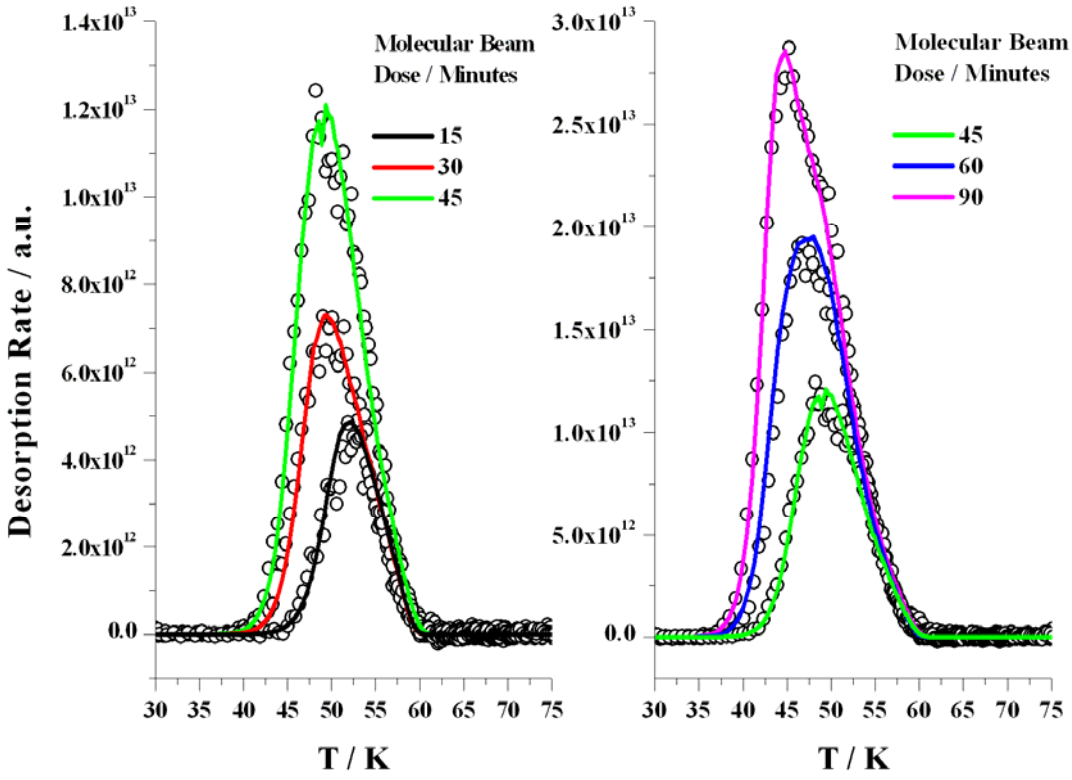

Figure 4.34: Simulated Fits of the O_2 Non-Trapped Desorption Peaks

$$H_2O(pASW) \rightarrow H_2O(cASW)$$

$$H_2O(pASW) + H_2O(cASW) \rightarrow 2H_2O(cASW)$$

$$O_2(pore) + H_2O(pASW) \rightarrow O_2(ntrap) + H_2O(pASW)$$

$$O_2(pore) + H_2O(cASW) \rightarrow O_2(trap) + H_2O(cASW)$$

$$O_2(ntrap) \rightarrow O_2(g)$$

$$O_2(ntrap) + H_2O(cASW) \rightarrow O_2(trap) + H_2O(cASW)$$

$$O_2(g) \rightarrow O_2(pump)$$

Figure 4.35: Phase Change CKS Mechanism for Non-Trapped O_2 Molecules

steps describe the pASW to cASW phase change. The third and fourth step describe the probability of an O_2 molecules becoming situated in either a non-trapped or trapped sites respectively. This enabled the total initial surface concentration of O_2 to be used. The sixth step describe those O_2 molecules initially situated in non-trapped sites to become trapped (as suggested earlier from the results of the E_{des} against $N[O_2(ntrap)]$ plot (**Figure 4.32**). The kinetic parameters for these steps were based on those deduced by Collings *et al.* for the desorption of CO from pASW [3]. However, CO is a lighter molecule so the value of E_a for the third and fourth step had to be increased in this case. A value of 11.0 kJ mol^{-1} was assumed as this lies between the values of E_{des} obtained for multilayer and sub-monolayer desorption of O_2 from bare silica. Minor adjustments were made to the values of v for the third, fourth and sixth steps until the final surface concentration of trapped O_2 molecules, $N[O_2(trap)]_f$, matched with the corresponding value calculated in **Table 4.17**. The remaining steps in the reaction mechanism describe the desorption of non-trapped O_2 (fifth) and the removal of O_2 from the system (seventh).

The current version of the multiple E_{des} model was not written to simulate a reaction mechanism this complicated. As a consequence, the simulations were performed using CKS. Ideally the desorption of O_2 (fifth step) should follow the same kinetic behaviour as used in the multiple E_{des} model. Although the value of v could remain the same, E_{des} had to be changed to a fixed value. To determine the best value of E_{des}, the reaction mechanism used to model the non-trapped O_2 molecules (**Figure 4.31**) was taken into CKS and re-modelled by adjusting the fixed value of E_{des}. The results are displayed in **Figure 4.36** where E_{des} was determined as 12.0 kJ mol^{-1}. The simulation fits are poorer than those obtained using the multiple E_{des} modelling but the desorption peaks occur at a similar surface temperature. In the future, a more accurate simulation could be made by either developing the multiple E_{des} model or by using an alternative modelling program to include the surface concentration dependence of E_{des}.

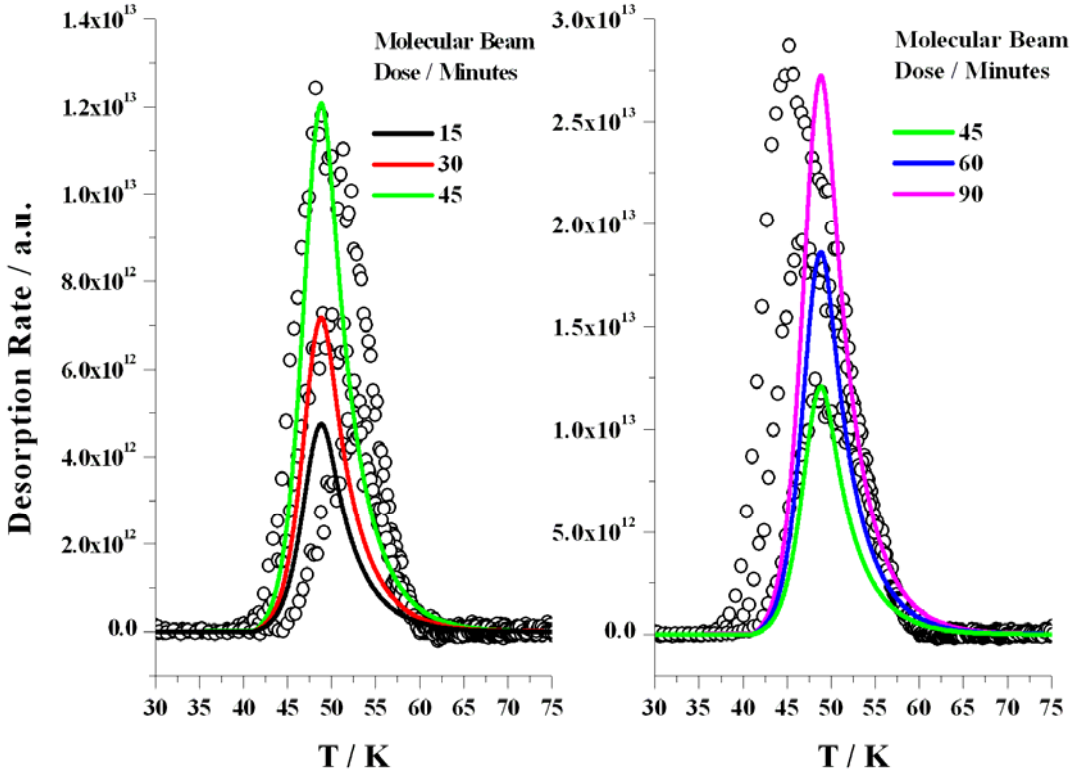

Figure 4.36: CKS Simulation of the O_2 Non-Trapped Desorption Peaks

Early simulation results using this reaction mechanism revealed that the pASW to cASW phase change was not occurring during the expected surface temperature range. The simulated result describing the *N[pASW]* with respect to surface temperature obtained by Collings *et al.* is displayed in **Figure 4.37** for *N[pASW]i* of 5.7×10^{17} molecules cm^{-2} using rate constants of 1.00×10^{-5} and 2.05×10^{-20} molecules cm^{-2} s^{-1} for the first and second phase change step respectively. Using the same rate constants, the lower value of $N[pASW]_i$ used in this study (1.8×10^{17} molecules cm^{-2}) resulted in the simulated phase change occurring at a considerably lower rate (red line in **Figure 4.37**). This observation revealed that although the mathematical interpretation was correct for the larger dose used by Collings *et al*., the current mechanism used to describe the phase change steps was dependent on $N[pASW]_i$. Adjustments to the rate constants were made until the simulated surface concentration curve (blue line) agreed by eye with the one obtained by Collings *et al*. (black line).

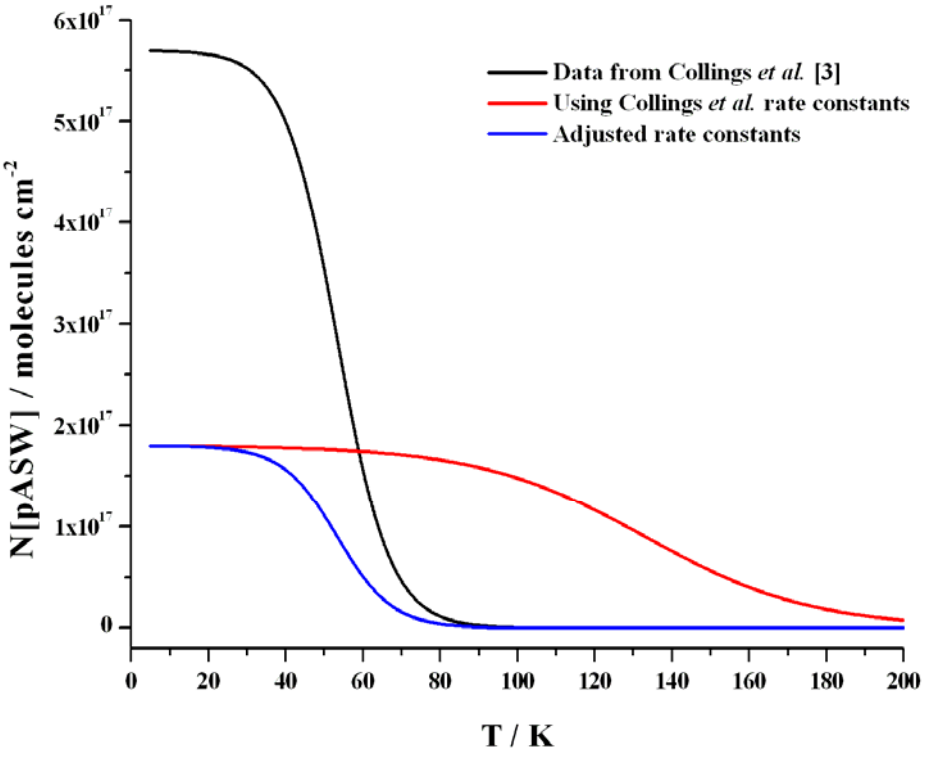

Figure 4.37: Affect of $N[pASW]_I$ and Rate Constants for the pASW to cASW Phase Change Steps. Black Line displays the Simulated Values Obtained by Collings *et al*. [3] with $N[pASW]_i$=5.7×10^{17} molecules cm^{-2} and Rate Constants 1.00×10^{-5} and 2.05×10^{-20} molecules cm^{-2} s^{-1} for the First and Second Step Respectively in **Figure 4.35**, Red Line with $N[pASW]_I$=1.8×10^{17} molecules cm^{-2} s^{-1} Using the Same Rate Constants, Blue Line with the Same Value of $N[pASW]$ but with the Rate Constants Adjusted to Match the Curve Obtained By Collings *et al*.

The simulated non-trapped O_2 desorption peaks obtained are displayed in **Figure 4.38** and **Table 4.18** (errors taken as two standard deviations). The desorption peaks are similar to those obtained using the two step fixed E_{des} CKS model (see **Figure 4.36**) suggesting that this more complex reaction mechanism provides a good description of the processes occurring in the H_2O substrate. Small adjustments to the kinetic parameters for the probability of O_2 molecules becoming situated in trapped and non-trapped sites resulted in the value of $N[O_2(trap)]_f$ being in good agreement with those calculated from the ratio desorption peak areas.

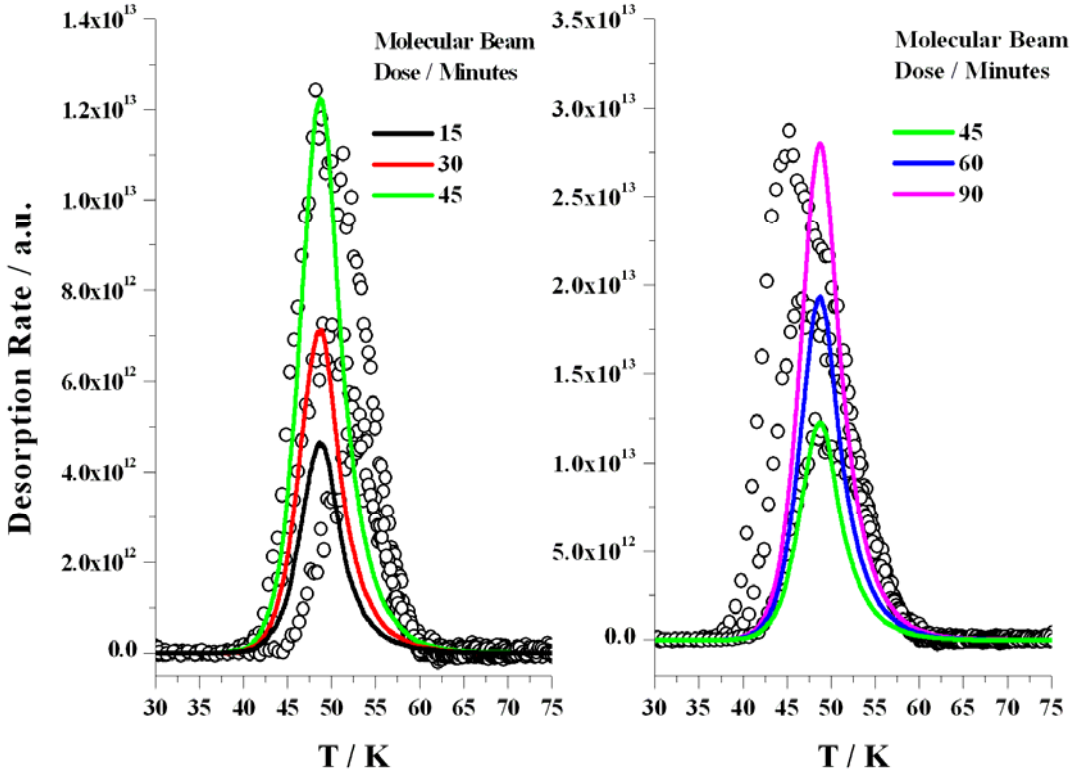

Figure 4.38: CKS Simulations of O_2 Non-Trapped Desorption Peaks

Reaction Step	v / molecules^{-1} cm^2 s^{-1}	E_a / kJ mol^{-1}	k / molecules cm^{-2} s^{-1}
H2O(pASW) → H_2O(cASW)	-	-	1.0×10^{-5}
H_2O(pASW) + H_2O(cASW) → 2 H_2O(cASW)	-	-	6.5×10^{-20}
O_2(pore) + H_2O(pASW) → O_2(ntrap) + H_2O(pASW)	$5\pm1\times10^{-3}$	11.0	-
O_2(pore) + H_2O(cASW) → O_2(trap) + H_2O(cASW)	$5\pm1\times10^{-3}$	11.0	-
O_2(ntrap) → O_2(g)	1×10^{12} *	12.0	-
O_2(ntrap) + H_2O(cASW) → O_2(trap) + H_2O(cASW)	$4.1\pm0.5\times10^{-20}$	0	-
O_2(g) → O_2(pump)	-	-	0.03±0.01

Table 4.18: Kinetic Parameters Used in the Phase Change Non-Trapped O_2 Mechanism (* First order kinetics units are s^{-1})

Overall, the results indicate that the best improvement that could be made to this mechanism would involve developing the multiple E_{des} model to allow for $N[O_2(ntrap)]$ dependent versions of E_{des} or to use an alternative simulation program. Further development of the pASW to cASW phase change step could also be made to provide a more accurate description of this process which is less sensitive to $N[pASW]_i$. However, the experiments required to determine the kinetic parameters for this phase change process can not presently be obtained using the current apparatus.

Further developments to the current reaction mechanism were made to include the desorption of the trapped O_2 molecules. Initial modelling of the desorption of the trapped O_2 molecules could not be performed accurately using a simple two step reaction mechanism as for the non-trapped species. This is due to the desorption of trapped O_2 being controlled by the crystallisation and desorption of cASW and CSW. The additional steps required to simulate the trapped O_2 and H_2O desorption peaks are displayed in **Figure 4.39**. The kinetic parameters for the H_2O reaction steps were obtained from the 500 L dose using the phase change CKS model in **Section 4.2.4** and are re-displayed in **Table 4.19**. The release of O_2 molecules from the trap pores (third step in **Figure 4.39**) occurs during the crystallisation of cASW into CSW (second step) so the kinetic parameters were taken as the same. The O_2 diffusion steps (fifth and sixth steps) were assumed to follow second order kinetics. Although the kinetics parameters for both these steps were taken as being the same, the values could be varied whilst

$$H_2O(cASW) \rightarrow H_2O(g)$$
$$H_2O(cASW) \rightarrow H_2O(CSW)$$
$$O_2(trap) \rightarrow O_2(diff)$$
$$H_2O(CSW) \rightarrow H_2O(g)$$
$$O_2(diff) + H_2O(cASW) \rightarrow O_2(ads) + H_2O(cASW)$$
$$O_2(diff) + H_2O(CSW) \rightarrow O_2(ads) + H_2O(CSW)$$
$$O_2(ads) \rightarrow O_2(g)$$
$$O_2(g) \rightarrow O_2(pump)$$
$$H_2O(g) \rightarrow H_2O(pump)$$

Figure 4.39: Additional Reaction Steps Required to Model the Desorption of Trapped O_2 and H_2O

Reaction Step	E / kJ mol^{-1}	v / molecules cm^{-2} s^{-1}	k / molecules cm^{-2} s^{1}
$H_2O(cASW) \rightarrow H_2O(g)$	48.2	1.7×10^{31}	-
$H_2O(cASW) \rightarrow H_2O(CSW)$	70.0	8.0×10^{23} *	-
$O_2(trap) \rightarrow O_2(diff)$	70.0	8.0×10^{22} *	
$H_2O(CSW) \rightarrow H_2O(g)$	49.6	5.0×10^{31}	-
$O_2(diff) + H2O(cASW) \rightarrow O_2(ads) + H2O(cASW)$	60.0	$10^{5\pm1}$ **	-
$O_2(diff) + H_2O(CSW) \rightarrow O_2(ads) + H_2O(CSW)$	60.0	$10^{5\pm1}$ **	-
$O_2(ads) \rightarrow O_2(g)$	12.0	10^{12} *	
$O_2(g) \rightarrow O_2(pump)$	-	-	0.03±0.01
$H_2O(g) \rightarrow H_2O(pump)$	-	-	0.05±0.01

Table 4.19: Kinetic Parameters Used in the Trapped O_2 Desorption Model (* units for first order reaction in s^{-1}; ** units for second order reaction in molecules^{-1} cm^2 s^{-1})

holding the remaining steps fixed. The kinetic parameters for the desorption of trapped O_2 molecules were taken from the earlier phase change CKS reaction mechanism used to describe the desorption of non-trapped O_2 molecules.

Initial simulations fits of the O_2 desorption peaks revealed that the trapped O_2 desorption peak was too large in respect to the non-trapped peak (see **Figure 4.40**). The kinetic parameters for the O_2 diffusion steps were altered but the only significant improvement in the trapped desorption peak height resulted in not all the O_2 molecules desorbing. This suggested that the earlier calculations of $N[O_2(trap)]$ and $N[O_2(ntrap)]$ were slightly under and overestimated respectively. To improve the desorption peak height ratios, the kinetic parameters describing the probability of the non-trap O_2 molecules becoming situated in trapped sites (sixth step in **Figure 4.35**) were adjusted. The final O_2 desorption simulations are displayed in **Figure 4.41** with the new kinetic parameters for the adjusted probability step shown in **Table 4.20**.

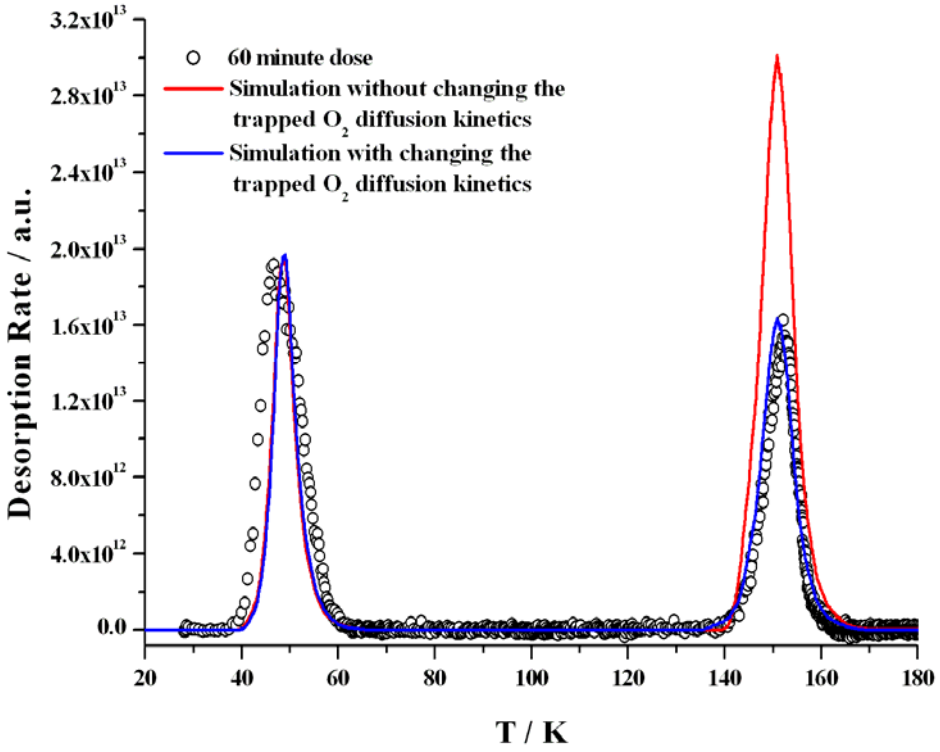

Figure 4.40: Initial and Improved Simulation Fits of the O_2 Desorption Peaks

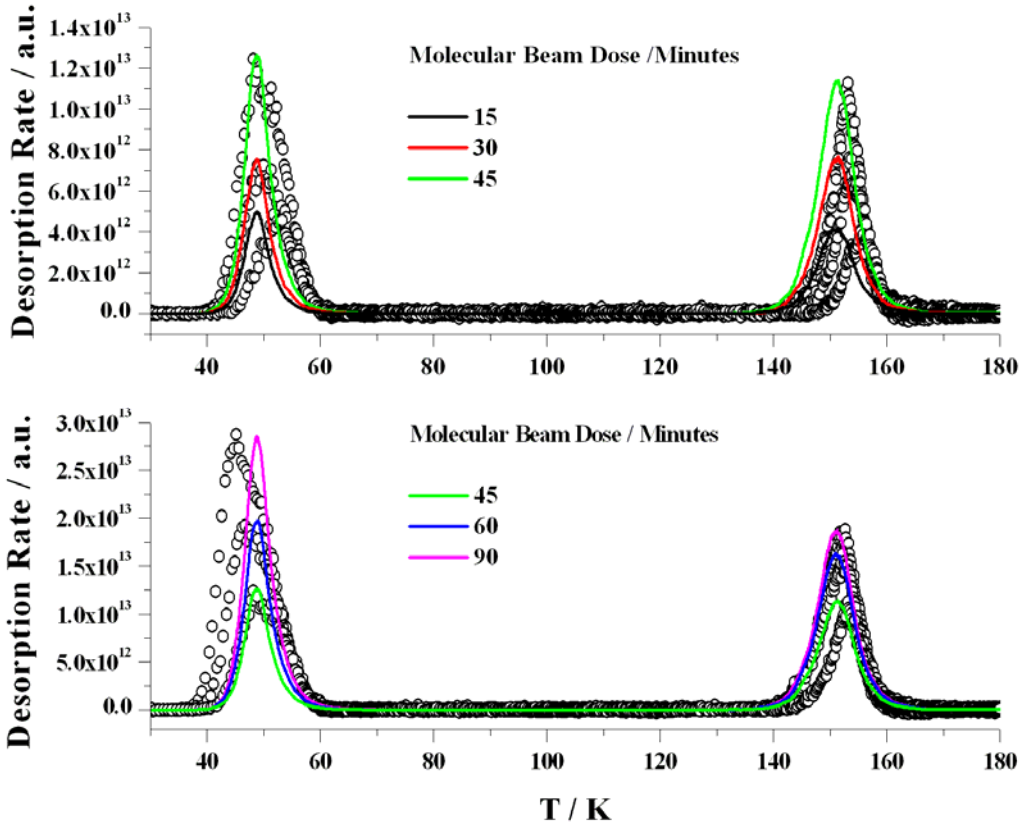

Figure 4.41: Simulated Fits of the O_2 on pASW TPD Experiment

Dose / minutes	ν / molecules^{-1} cm^2 s^{-1}
15	2.2×10^{-20}
30	2.6×10^{-20}
45	2.7×10^{-20}
60	3.0×10^{-20}
90	2.7×10^{-20}
Average	$2.6\pm0.6\times10^{-20}$

Table 4.20: New Kinetic Parameters Used for the
O_2(ntrap) + H_2O(cASW) → O_2(trap) + H_2O(cASW) Step

Overall the simulated desorption peaks are in agreement with the experimental data. The small difference in the shape and position of the desorption peaks with respect to surface coverage appeared to be a direct result of applying a fixed value for E_{des} which was required for the CKS software. In comparison to the earlier results obtained when modelling the non-trapped O_2 molecules using the multiple E_{des} program (**Figure 4.34**), the CKS desorption peaks fits are poorer. This observation indicates that a more accurate simulation of O_2 desorbing from pASW needs to include the $N[O_2(ntrap])]$ dependent of E_{des} for both the trapped and non-trapped desorption peaks. In the future, another modelling software program would have to be used which allows for the surface coverage dependent functions of E_{des} to improve the simulated desorption peak fits of O_2. The simulation results also suggest that the assumptions made to describe the H_2O crystallisation and corresponding release of O_2 from the trapped pore as two separate steps holds. Plus, as the crystallisation kinetics were obtained from a range of surface coverages (see **Section 4.2**) then these two steps are predicted to hold for other values of $N[pASW]_i$ unlike the pASW to cASW phase change. To test this theory, additional O_2 from pASW TPD experiments on silica could be performed and simulated for a range of $N[pASW]_i$ values where crystallisation is known to occur (approximately 2.5×10^{16} molecules cm^{-2}). The results from these proposed experiments would also enable these steps to be developed and combined to provide a more accurate description of the processes occurring in the H_2O film. Additionally, the results from even higher values of $N[pASW]_i$ with larger doses of O_2 than those performed in this study may also enable the kinetic parameters to be determined for the co-desorption of O_2 and CSW (which was not observed in these experiments) and improved for the diffusion of O_2

through the H_2O (fifth and sixth steps in **Figure 4.39**). However, larger doses of H_2O could not be performed using the current apparatus without the risk of the pumping system failing to return to base pressure (see **Section 4.2.3**). In the future, the apparatus could be modified to include a glass dosing tube where the gas from background dosing could be directed onto the sample (shown in red **Figure 4.42**).

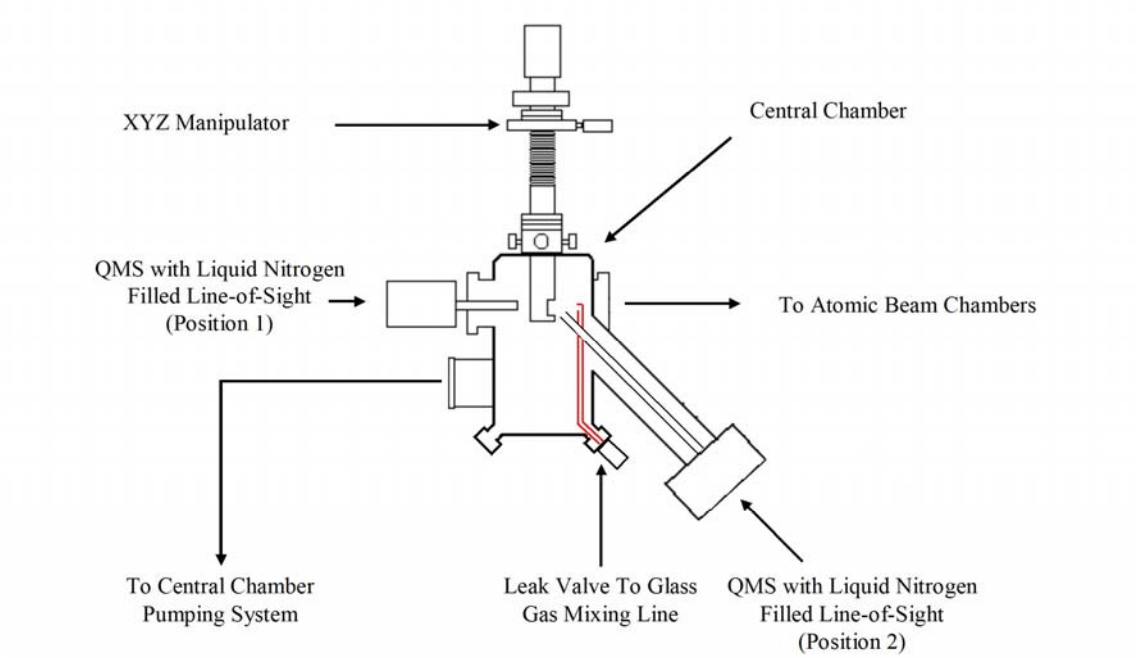

Figure 4.42: Proposed Modifications to the Apparatus to Improve Background Dosing

Other developments that could be made to provide a more accurate description of the processes occurring in this experiment could include the pASW to cASW phase change steps and the probability steps for O_2 molecules becoming situated in non-trapped and trapped sites in the H_2O film.

Another observation from these results is that all the O_2 desorption peaks are from sub-monolayers coverages of O_2. This again highlights the need for the beam apparatus to be modified to enable larger surface coverages of O_2 to be applied to the substrate but within a time constraint that would limit the amount of contamination from surface bombardment of other species. This would enable multilayer coverages of O_2 to form on the pASW substrate providing the additional data to determine the O_2 multilayer desorption kinetics. The results from this future experiment would enable the first two

steps in the full reaction mechanism (**Figure 4.30**) to be included providing a more detailed description of the desorption of O_2 from pASW.

Overall, the kinetic parameters obtained from this experiment will be used towards constructing a simulation model mimicking the desorption of O_2 from the icy mantles coating interstellar dust grains (**Section 4.6**).

4.5.4 Conclusions

The experiments discussed in this section explore the desorption kinetics of O_2 from pASW on silica. Unlike O_2 desorbing from cASW (**Section 4.4**), a proportion of the O_2 molecules become trapped in the underlying porous H_2O film. As a consequence, the desorption of these trapped molecules was not observed until the crystallisation and desorption of the H_2O film. Both the trapped and non-trapped O_2 desorption peaks contained coincident falling edges implying the sub-monolayer coverages of these molecules followed first order multiple E_{des} desorption kinetics.

Modelling of the surface and desorption processes was performed in several stages using CKS. The kinetic parameters for most of the steps in the mechanism were taken from the experiments previously discussed in this chapter. The simulation fits obtained were in good agreement with the experimental data suggesting that the reaction mechanism describe the processes occurring well. Further improvements to the fitting of the O_2 desorption peaks could be made by including surface coverage dependent versions of E_{des} rather than the fixed valued required by the CKS software. However, this would involve either using or writing another simulation program. Further improvements could be made by performing additional O_2 from pASW TPD experiments on silica for a range of $N[pASW]_i$ values above 2.5×10^{16} molecules cm^{-2} where crystallisation was calculated to begin (see **Section 4.2.4**). This would enable the kinetic for the H_2O crystallisation step and corresponding surface processes relating to trapped species step to be developed and combined providing a more accurate description of this process. If larger doses of H_2O and O_2 could be applied to the surface, then the co-desorption kinetics for O_2 and CSW along with the O_2 diffusion steps from trapped sites to be developed. However, this would require the current apparatus to be modified to reduce the risk of the pumping system failing to return to base pressures and to improve the value of α. Another development that could be made to the current reaction mechanism would be to include the pASW to cASW phase

change and the O_2 probability site steps. However, the experimental data required to determine the kinetic parameters for these processes can not presently be obtained using the dual atomic beam system.

The overall surface and desorption processes occurring in this experiment are described in the cartoon displayed in **Figure 4.43**. The first stage of the cartoon displays the layered system after the final dosing stage. As heat is applied in the TPD experiment,

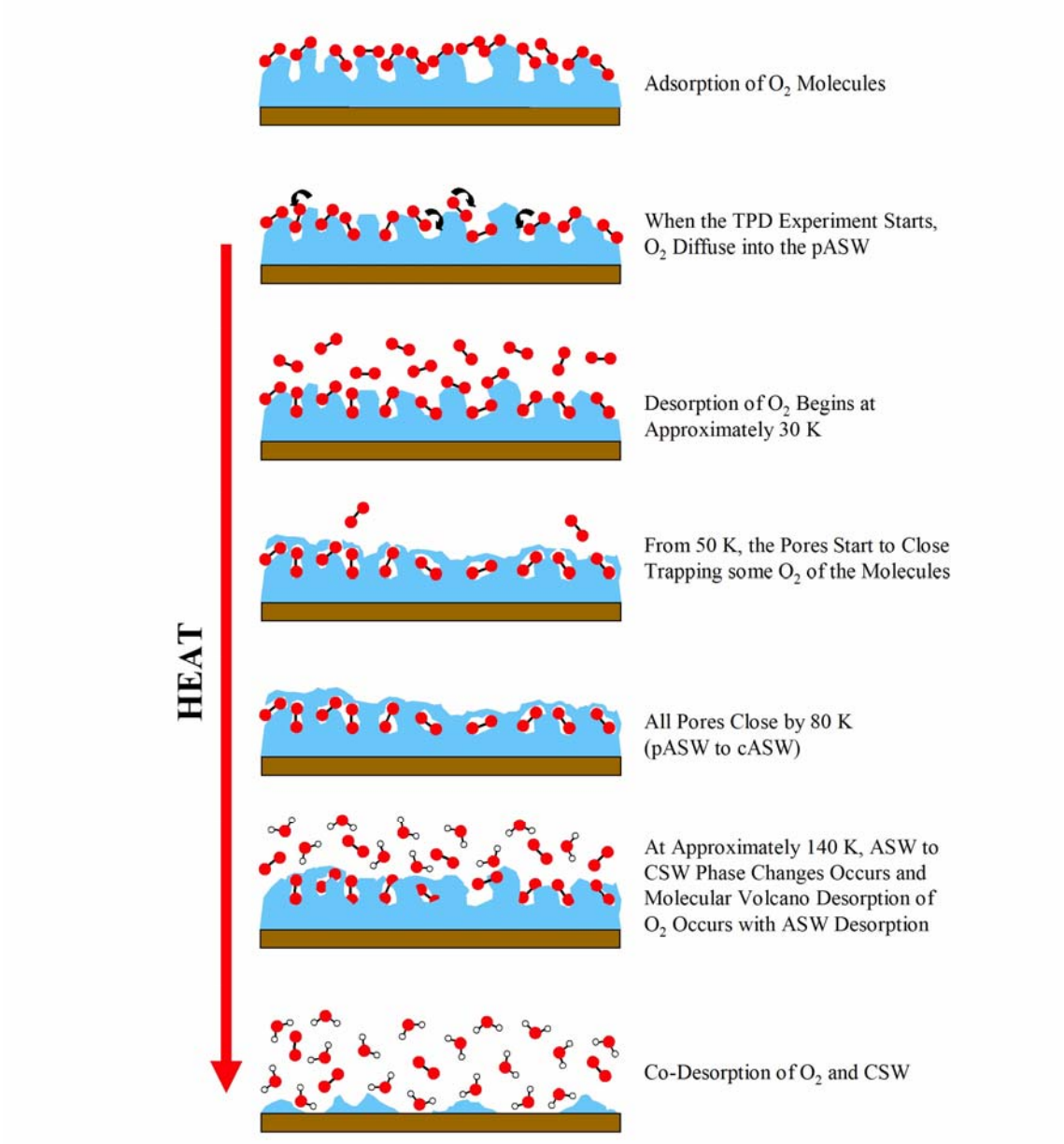

Figure 4.43: Cartoon of O_2 TPD from pASW on Bare Silica

the O_2 molecules diffuse across the surface and into the pores within the pASW layer (second stage). At roughly 30 K, the desorption of O_2 molecules, initially from low energy binding sites, is observed (third stage). As the surface temperature increases the pASW molecules start to diffuse to a more energetically favourable cASW ice (fourth stage) which has a higher density and is non reversible (as previously discussed in **Chapter 1**). By 80 K, the openings to the pores have closed resulting in any non-desorbed O_2 molecules becoming trapped (fifth stage). The delayed desorption of these molecules is not observed until the ASW to CSW phase change at roughly 140 K (sixth stage) and occurs as a molecular volcano. The final stage is the co-desorption of CSW with any remaining O_2 molecules which was not observed in this study but is expected to occur for larger doses of H_2O and O_2.

The kinetic parameters obtained from all the experiments discussed in this chapter will be used towards constructing a simulation model mimicking the desorption of O_2 from the icy mantles coating interstellar dust grains (**Section 4.6**).

4.6 The O_2 Desorption Model from an Icy Mantle in the ISM

4.6.1 Introduction

This section combines the experimental TPD results discussed in the above sections by constructing a CKS model mimicking the desorption of O_2 from icy mantles under dense molecular cloud environments in the ISM. **Section 4.6.2** describes the simulation model and results. The summary and astronomical implications are discussed in **Section 4.6.3**.

4.6.2 ISM Simulation Model

The simulation model used to mimic the desorption of O_2 from icy mantles under dense molecular cloud environments is based on the final CKS reaction mechanism used in **Section 4.5.3** (see **Figure 4.44**). This reaction mechanism was previously used to simulate the sub-monolayer O_2 coverages from pASW TPD experiments on silica and was concluded to produce simulations which were in agreement with the experimental data (for more details, see **Sections 4.5.3** and **4.5.4**). If multilayer coverages were to be

$$H_2O(pASW) \rightarrow H_2O(cASW)$$
$$H_2O(pASW) + H_2O(cASW) \rightarrow 2H_2O(cASW)$$
$$O_2(pore) + H_2O(pASW) \rightarrow O_2(ntrap) + H_2O(pASW)$$
$$O_2(pore) + H_2O(cASW) \rightarrow O_2(trap) + H_2O(cASW)$$
$$O_2(ntrap) \rightarrow O_2(g)$$
$$O_2(ntrap) + H_2O(cASW) \rightarrow O_2(trap) + H_2O(cASW)$$
$$H_2O(cASW) \rightarrow H_2O(g)$$
$$H_2O(cASW) \rightarrow H_2O(CSW)$$
$$O_2(trap) \rightarrow O_2(diff)$$
$$H_2O(CSW) \rightarrow H_2O(g)$$
$$O_2(diff) + H_2O(cASW) \rightarrow O_2(ads) + H_2O(cASW)$$
$$O_2(diff) + H_2O(CSW) \rightarrow O_2(ads) + H_2O(CSW)$$
$$O_2(ads) \rightarrow O_2(g)$$

Figure 4.44: CKS Reaction Mechanism Used to Describe the Desorption of O_2 from Icy Mantles Under Dense Molecular Cloud Environments in the ISM

included then two additional steps would be required at the start of the reaction mechanism to describe the multilayer desorption of O_2 and the diffusion of O_2 from the multilayer film into the underlying pASW film. However, due to the observed low molecular abundance of O_2 in the gas-phase, multilayer coverages of O_2 are not expected to occur in the ISM.

Before this CKS model could be applied to dense molecular cloud environments, a few changes had to be made from the original reaction mechanism. The first change was to remove the O_2 and H_2O pumping steps. This enabled the simulated $O_2(g)$ and $H_2O(g)$ species to be proportional to the predicted gas-phase concentrations of O_2 and H_2O in the dense molecular cloud environments of the ISM. The second change involved altering the heating rate from laboratory to ISM time scales (see **Table 4.21**). However, this resulted in the pASW to cASW phase change occurring at a very fast rate over a lower and narrower surface temperature range than previously observed under experimental conditions (**Figure 4.45**). As discussed in **Section 4.5.3**, the actual pASW to cASW phase change mechanism was too complicated to model using CKS so a mathematical fit using autocatalytic reactions was taken based on the results obtained by

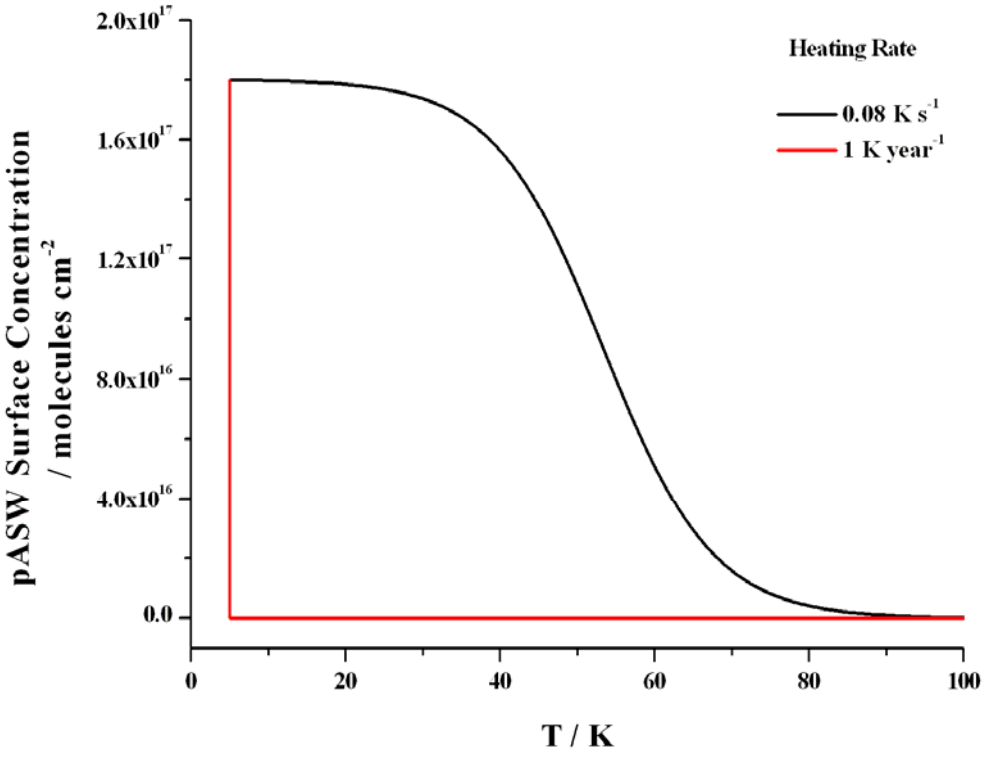

Figure 4.45: Affect on pASW Phase Change Rate with Heating Rate
(the other astronomical heating rates would be situated under the 1 K year^{-1} plot)

Collings *et al*. [3]. When the slower heating rates were applied to the model, the mathematical fit of the phase change no longer held so the kinetic parameters for the two steps were re-evaluated to provide the same mathematical fit using the same procedure applied by Collings *et al*. The new kinetic values obtained for a range of heating rates are displayed in **Table 4.21**.

Heating Rate	**Heating Rate / K s^{-1}**	**k_1 /molecules cm^{-2} s^{-1}**	**k_2 / molecules cm^{-2} s^{-1}**
Experimental	0.08	1.0×10^{-5}	6.5×10^{-20}
1K year^{-1}	3.2×10^{-8}	5.0×10^{-12}	7.5×10^{-26}
1K decade^{-1}	3.2×10^{-9}	5.0×10^{-13}	7.5×10^{-27}
1K century^{-1}	3.2×10^{-10}	5.0×10^{-14}	7.5×10^{-28}
1K millennium^{-1}	3.2×10^{-11}	5.0×10^{-15}	7.5×10^{-29}

Table 4.21: Heating Rates and pASW to cASW Phase Change Kinetic Parameters

The simulated results predicting the gas-phase concentrations of O_2 and H_2O in dense molecular cloud environments are shown in **Figure 4.46**. Simulated fits of the normalized gas-phase concentrations for these species under experimental time scales were included for comparison. The results obtained for H_2O are in good agreement with those determined by Collings *et al*. [3] revealing that the H_2O molecules desorb from the icy mantles coating interstellar dust grains at lower surface temperatures under astronomically relevant heating rates. The simulation under experimental conditions contains a small shoulder in the curve at approximately 153 K. This shoulder corresponds to the change in H_2O desorbing as dominantly cASW to CSW as a consequence of the H_2O film crystallising. The simulation curves for the slower heating rates do not contain this shoulder. Further analysis of the data revealed that no cASW molecules crystallised into CSW implying that the crystallisation step (and therefore, the desorption of CSW step) no longer occurred under these heating rates. However, this finding could be due to the modelling procedure employed as the actual crystallising process is known to be more complicated [36-41]. Plus, the kinetic results obtained in **Section 4.2** concluded that the single reaction step used did not accurately describe the crystallisation. In the future, a more complicated mechanism step or steps could be used to determine if any of the H_2O molecules in icy mantles in the dense molecular cloud undergo crystallisation.

The simulated results for O_2 are not similar to the CO normalised gas-phase concentrations obtained by Collings *et al.* which this CKS model is based on [3]. The experimental heating rate reveals that all the O_2 molecules desorb either from pores in the pASW ice (first step in simulated curve) or co-desorbing with cASW and CSW (second step). When the heating rate was slowed, the desorption of O_2 from the pASW ice no longer occurred. One possible explanation for this finding was that the slower heating rates resulted in the O_2 molecules having a longer time to diffuse across and into the underlying porous pASW film. As a consequence, the majority of the O_2 molecules became trapped as the ice underwent the pASW to cASW phase change. However, this observation could also be due to the probability steps describing an O_2 molecule becoming situated in a trapped or non-trapped site breaking down when changing to the slower heating rates.

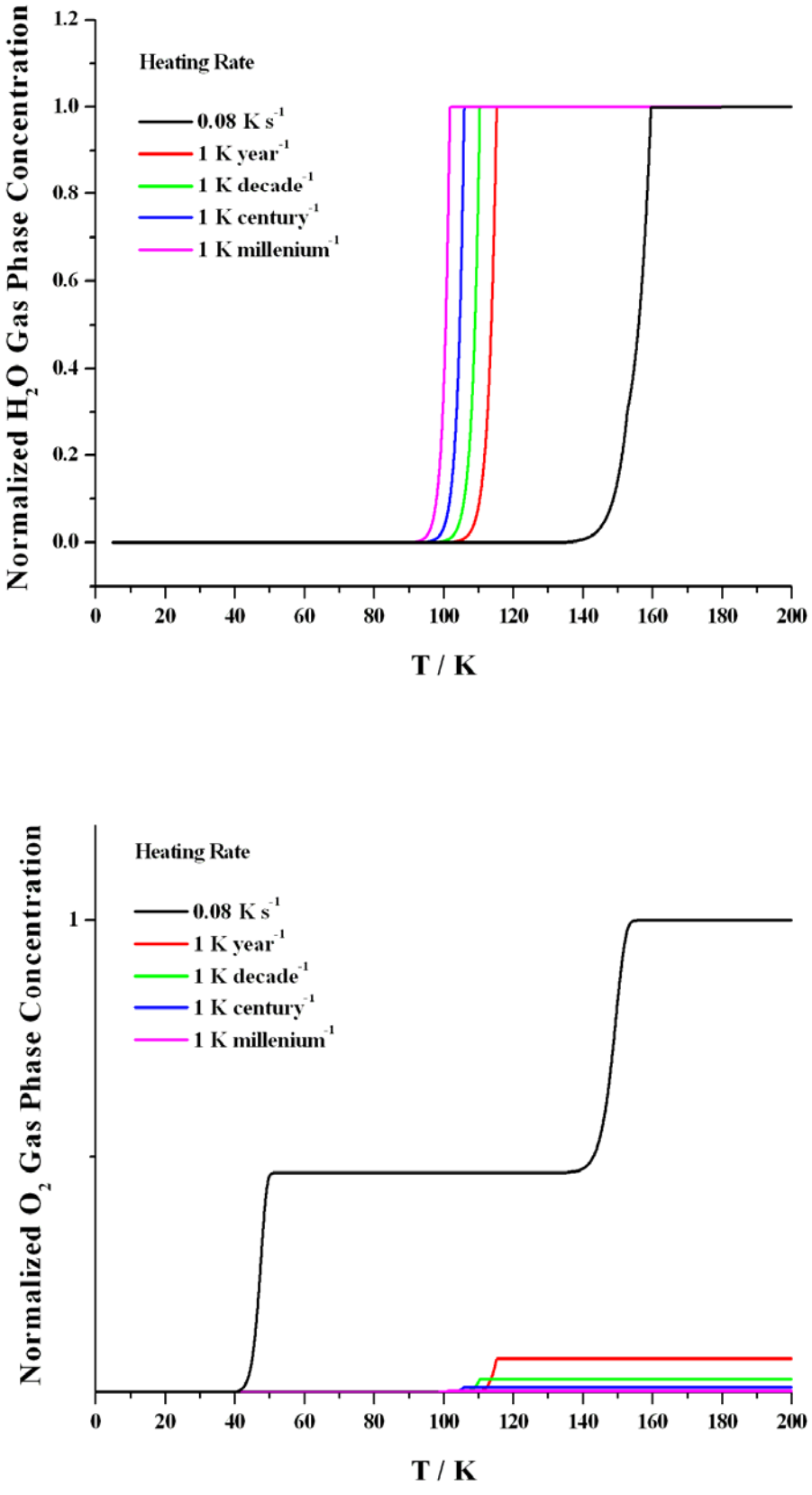

Figure 4.46: Normalized Gas Phase Concentration for Different Heating Rates for H_2O (top) and O_2 (bottom)

Another observation made with the normalized gas-phase concentrations of O_2 is that the predicted gas-phase concentration decreases with slower heating rates. Further analysis of the CKS simulation data revealed that an increasing proportion of the O_2 molecules were becoming trapped in the O_2(diff) state. Initial conclusions believed this to be due to the O_2 diffusion steps no longer holding under these slower heating rates. However, these diffusion steps are also dependent on the surface concentration of H_2O (both as cASW and CSW). The absence of the H_2O crystallisation stage prevented the O_2 molecules from diffusing from the closed pores to the surface and desorbing. This affectively removed the ninth, eleventh, twelfth and thirteenth steps in the CKS reaction mechanism (**Figure 4.44**). If this was the case then the only possible method the O_2 molecules could desorb from the pores would be when the surrounding cASW molecules desorbed resulting in the pores re-opening. In the future, additional step or steps describing this process would need to be included in the reaction mechanism along with the proposed developments for the crystallisation step (previously discussed in **Section 4.5.3**).

Despite this, some of the O_2 molecules in the plot in **Figure 4.46** were observed to desorb (thirteenth step) through the current mechanism. This desorption began to occur at around 100 K for each of the slower heating rates and does not correspond with the desorption pattern observed in the normalized gas-phase concentration plot for H_2O as expected. The reason why some O_2 molecules were observed to desorb was because there were still enough cASW molecules on the surface in the simulated model to allow for a relatively few O_2 molecules to diffuse through the eleventh step when the molecules were released from the trapped sites. This observation would have been unlikely to have occurred if the reaction steps describing the release of O_2 from trapped sites had been combined with the cASW crystallisation step (ninth and eighth steps respectively).

Overall, the results from both the H_2O and O_2 normalized gas-phase concentration plots imply that the current reaction mechanism used in CKS was too simple to produce accurate results under astronomical heating rates. The model could initially be improved in the future by developing the cASW to CSW crystallisation step to include the release of O_2 from the trapped pores. This could be achieved by replacing the current two separate crystallisation and O_2 release from trapped pores steps with the

proposed step shown in **Figure 4.47**. The kinetic parameters for this step could be determined by performing additional O_2 from pASW TPD experiments from silica data for a range of H_2O doses. Although the crystallisation process would actually be more complicated, the results obtained could improve the mathematical description of this surface process under experimental heating rates. However, to achieve this the apparatus will first have to be modified to reduce the risk of the pumping system failing to return to base pressures after a large H_2O background dose and to improve the value of α to increase the range of $N[O_2]_i$ values without the surface becoming heavily contaminated by surface bombardment. The modifications required have previously been discussed in more detail in **Sections 4.5.3** and **4.3.5** respectively. Further analysis using the results from these proposed experiments by applying astronomical relevant heating rates may also provide more detailed information as to whether any of the H_2O molecules undergo crystallisation under ISM conditions. The results obtained from this future improvement to the reaction mechanism may also reveal whether the trapped O_2 desorbed either by the change in the H_2O film structure (crystallisation) or by the desorption of cASW re-opening the closed pores. The information obtained from this could determine how the reaction mechanism could be further developed to provide a more accurate mimic of O_2 molecules desorbing from icy mantles under ISM conditions.

$$H_2O(cASW) + O_2(trap) \rightarrow H_2O(CSW) + O_2(diff)$$

Figure 4.47: Proposed Initial Replacement Step for the cASW Crystallisation and Release of Trapped O_2 Molecules

4.6.3 Conclusions

The CKS results discussed in this section attempted to mimick the desorption of O_2 from the icy mantles coating interstellar dust grains in dense molecular cloud environments under astronomically relevant heating rates. The predicted normalized gas-phase concentration results with respect to grain temperature obtained for H_2O were in good agreement with those published in the literature. Further analysis of the simulation data revealed that the H_2O molecules no longer underwent crystallisation resulting in all the H_2O molecules desorbing as cASW. However, this finding greatly affected the normalized gas-phase concentration results for O_2 as the vast majority of the molecules became stuck in the O_2(diff) state in the simulation. If no crystallisation

of H_2O occurred under ISM conditions, the trapped O_2 molecules could only be desorbed by the surrounding cASW molecules desorbing and re-opening the closed pores in the H_2O film. This surface and desorption process was not included in the current reaction mechanism so the reaction steps describing this would need to be added in the future.

Further improvements to the reaction mechanism could be made in the future by exploring the crystallisation of cASW and desorption of trapped O_2 molecules in more detail. The results obtained from these proposed experiments would provide a more accurate kinetic description of the crystallisation and desorption behaviour under experimental heating rates before being applied to astronomically relevant heating rates. The information obtained from this future experiment and simulation modelling would allow for a more detailed understanding of the desorption and surface processes occurring in the icy mantles in dense molecular cloud environments.

4.7 Summary and Conclusions

This chapter focuses on the desorption kinetics of H_2O and O_2 from a range of astrophysically relevant surfaces using temperature programmed desorption (TPD). The data collected was used to build an increasingly complex kinetic simulation model which was then applied to mimic the desorption of O_2 from the icy mantles coating interstellar dust grains in dense molecular cloud environments.

The first set of experiments explored in this chapter was the H_2O TPD experiments from bare silica (**Section 4.2**). The results revealed that the H_2O molecules always desorbed following zeroth order kinetics without any observable transition between sub-monolayer and multilayer coverages. This observation was caused by the interaction between the H_2O molecules being greater than between the H_2O molecules and silica surface resulting in the formation of three-dimensional H_2O clusters or islands. As a consequence, the desorption of H_2O from these multilayer islands followed zeroth order kinetics even at low surface coverages. At doses below 80 L, the H_2O molecules desorbed as one single cASW peak. As the surface coverage increased, a second desorption peak was observed corresponding to the desorption of CSW indicating that the cASW desorption rate was competing with the cASW crystallisation

rate. The kinetic parameters for the desorption and crystallisation steps were determined using leading edge analysis and CKS. The kinetic parameters obtained are summarized in **Table 4.22** and the desorption steps are in good agreement with those in the literature. The crystallisation step was assumed to be first order but the value of v obtained was sufficiently outside the expected range for first order kinetic steps. This implied that the one step crystallisation process used in this study could mathematically fit the experimental data well but could not describe the actual crystallisation accurately. In the future, the reaction mechanism used could be developed to improve the kinetic results for the crystallisation step. However, this could only be achieved based on the results obtained from other research groups as the current apparatus is not designed to perform the required experiments.

Step	v **/ molecules cm^{-2} s^{-1}**	E_a **/ kJ mol^{-1}**
H_2O(cASW) → H_2O(g)	$1.7\pm0.6\times10^{31}$	48.5±0.4
H_2O(cASW) → H_2O(CSW)	$6.0\pm2.6\times10^{22}$ *	70.0±2.0
H_2O(CSW) → H_2O(g)	$3.6\pm3.4\times10^{31}$	49.6±0.2

Table 4.22: Kinetic Parameters for H_2O TPD Experiment from Bare Silica (*First Order Units are s^{-1})

The experiments discussed in **Section 4.3** explored the desorption kinetics of O_2 from bare silica. Unlike the H_2O desorption peaks from bare silica, the sub-monolayer to multilayer transition was observed. The multilayer coverages were analyzed using leading edge analysis and CKS. The kinetic parameters for the desorption step are displayed in **Table 4.23**. The results also revealed that the O_2 molecules desorbed from the bulk ice following fractional order kinetics of 0.18±0.04 which was inconsistent with the multilayer desorption of other similar species. Initial possible suggestions for

Coverage	v	E_{des} **/ kJ mol^{-1}**
Multilayer	$1.6\pm0.3\times10^{27}$ molecules$^{0.82}$ cm$^{-1.64}$ s$^{-0.82}$	9.8±0.1
Sub-monolayer	1.0×10^{12} s^{-1}	9.3-13.4 (background) 9.2-16.5 (O_2 beam)

Table 4.23: Desorption Kinetics of O_2 from Bare Silica

this observation were due to: the underlying silica surface; O_2 desorbing as $(O_2)_2$ clusters; or O_2 desorbing as O_4 species. However, the simulation results obtained from a two population CKS model revealed that the dissociation of the $(O_2)_2$ dimer species occurred at surface temperatures below 20 K suggesting that the $(O_2)_2$ dimers were not responsible for the observed fractional order desorption behaviour.

Further analysis of multilayer desorption kinetics from bare silica will be explored in **Chapter 5** for CO and N_2. If these species also desorbed following fractional order kinetics then the underlying silica surface could be concluded as the cause for the unexpected multilayer desorption behaviour. Alternatively, if these species followed typical zeroth order kinetics then the desorption behaviour of O_2 could be concluded as being more complex.

Overall the multilayer desorption kinetics obtained for O_2 are irrelevant under ISM conditions due to the low observed molecular abundance. However, these findings could be applied to the desorption of O_2 from icy objects in the outer regions of the Solar System where this species has been detected.

Analysis and modelling of the sub-monolayer O_2 TPD data using background and molecular beam dosing was achieved using direct inversion of the Polyani-Wigner equation and a multiple E_{des} simulation model. The simulations obtained fitted the desorption peaks well implying that the underlying silica surface increased the value of E_{des} with decreasing O_2 surface concentration resulting in the desorption peaks containing coincident falling edges despite following first order kinetics. The largest range of E_{des} for both desorption methods are displayed in **Table 4.23** for a fixed value of v. However, only sub-monolayer coverages of O_2 were obtained using molecular beam dosing due to the small value of α. To obtain multilayer coverages using the O_2 molecular beam the apparatus will have to be modified so that the temperature of the beam species could be controlled which would improve the value of α (**Chapter 3** and **Section 4.3.5**). This could be achieved by either passing the gas through an aluminium nozzle connected to a closed-cycle He cryostat or by directing the beam through a tube surrounded by a copper tube again connected to a closed-cycle He cryostat. The control over the beam species temperature would allow for a greater range of surface concentrations of O_2 to be dosed onto the silica surface within a suitable range of

irradiation dose times. The same modifications are likely to have to be applied to the hydrogen atomic and molecular beam too. Although multilayer coverages of O_2 are unlikely to occur in the ISM, due to the observed low molecular abundance, the kinetic data obtained from the multilayer coverages will provide a more detailed understanding of the surface and desorption processes occurring on the silica surface which could lead to future improvements being made to the simulated reaction mechanism.

Section 4.4 discussed the O_2 from cASW TPD experiment on silica. The results concluded that the O_2 molecules followed first order multiple E_{des} desorption kinetics similar to those obtained for sub-monolayer coverages of O_2 desorbing from bare silica. These findings implied that the underlying cASW had no affect on the desorption of the above O_2 layer. However, the O_2 TPD experiment discussed in **Section 4.5** revealed that by dosing H_2O using a cooler surface temperature to form pASW did greatly affect the desorption behaviour of O_2. The most noticeable difference was there were two O_2 desorption peaks. Analysis of the data revealed that a proportion of the O_2 molecules became trapped in the H_2O film during the pASW to cASW phase change. The desorption of both the trapped and non-trapped species followed the same desorption kinetic parameters as O_2 from cASW (within experimental error). The delay in the desorption of the trapped species was controlled by the crystallisation of cASW to form a molecular volcano.

Further analysis of the data was performed by constructing CKS models based on the kinetic parameters obtained in **Sections 4.2** and **4.4**. The simulation fits were in agreement with the experimental data. Further improvements to the reaction mechanism in the future could include: O_2 surface coverage dependent values of E_{des} (similar to those used in the multiple E_{des} model); development of the pASW to cASW phase change steps; combining the trapped O_2 release step with the cASW crystallisation step; and improving the trapped O_2 diffusion step. However, these proposed changes to the reaction mechanism would involve either using or constructing another more complex simulation program.

Additionally, only sub-monolayer coverages of O_2 from both cASW and pASW TPD experiments on silica were explored in this study. In the future, larger molecular beam doses could be applied enabling the desorption kinetics of multilayered O_2 from both these substrates to be determined once the modifications suggested above have been

made. This would provide a more detailed understanding of the processes occurring in these experiments.

The final section of this chapter (**Section 4.6**) discussed the CKS modelling results attempted to mimic the desorption of O_2 from the icy mantles coating dust grains in dense molecular cloud environments of the ISM. The CKS model used was based on the one constructed and developed in **Section 4.5** and enabled the simulated $H_2O(g)$ and $O_2(g)$ species to be proportional to the predicted gas-phase concentrations of H_2O and O_2 in these environments. The results obtained for H_2O were similar to those in the literature and revealed that these molecules entered the gas-phase at lower grain temperatures with slower heating rates. Further analysis of the simulation results concluded that all the species desorbed as cASW and that no molecules crystallised to form CSW. However, this one step crystallisation reaction had previously been concluded not to describe the kinetics of the crystallisation process well (**Section 4.2**). This observation again highlights the proposal for developing this part of the reaction mechanism in the future to improve the kinetic description.

The lack of cASW molecules undergoing crystallisation under astronomical heating rates directly affected the normalized gas-phase concentration of O_2. Theoretically, if there was no crystallisation of H_2O in the icy mantles then the trapped O_2 molecules would not be able to desorb as a molecular volcano. Instead, the O_2 molecules would desorb when the surrounding cASW molecules desorbed re-opening the closed pores. This process was not described in the current reaction mechanism so no trapped O_2 molecules should have been observed entering the gas-phase. However, O_2 was observed to desorb as the current mechanism described the release of O_2 from the pores in the H_2O film as a separate reaction step from the crystallisation of cASW allowing the crystallisation kinetic parameters determined in **Section 4.2** to be directly applied to both steps. In the future, both of these steps will need to be developed and combined. This could be achieved by modelling the proposed additional O_2 from pASW TPD experiments on silica for a range of H_2O doses. However, the apparatus would first need to be modified before these experiments could be performed to improve the value of α for the O_2 molecular beam doses and to reduce the risk of the pumping system failing to return to base pressures after a large H_2O dose (as previously described above and in **Section 4.5.3** respectively).

Another observation of the O_2 normalized gas-phase concentration results revealed that all of the O_2 molecules became trapped. This observation could have been due to the molecules being able to diffuse deeper into the pASW film and becoming trapped or that the probability steps determining whether O_2 molecules would become situated in a trapped or non-trapped site no longer held when applied to astronomically relevant heating rates. In the future these steps would also need to be develop to provide a more accurate description of the desorption of O_2 from icy mantles in dense molecular clouds.

Overall, if this model could be developed further from the results obtained in this chapter and those proposed in the future then not only could this provide a more accurate model mimicking the desorption of O_2, but this model could also be used toward constructing a model describing the processes associated with O in icy mantles in dense molecular cloud environments.

4.8 References

[1] D. A. King, *Surf. Sci.*, 1975, **47**, 384.

[2] T. Zubkov, R. S. Smith, T. R. Engstrom and B. D. Kay, *J. Chem. Phys.*, 2007, **127**, 184707.

[3] M. P. Collings, J. W. Dever, H. J. Fraser and M. R. S. McCoustra, *Astrophys. Space Sci.*, 2003, **285**, 633.

[4] V. Pirronello, O. Biham, C. Liu, L. Shen and G. Vidali, *Ap. J.*, 1997, **483**, L131.

[5] S. D. Green, A. S. Bolina, R. Chen, M. P. Collings, W. A. Brown and M. R. S. McCoustra, *Mon. Not. R. Astron. Soc.*, 2009, **398**, 357.

[6] J. D. Thrower, M. P. Collings, F. J. M. Rutten and M. R. S. McCoustra, *J. Chem. Phys.*, 2009, **131**, 244711.

[7] J. D. Thrower, Heriot-Watt University, 2009.

[8] S. Kaya, J. Weissenrieder, D. Stacchiola, S. Shaikhutdinov and H.-J. Freund, *J. Phys. Chem. C*, 2007, **111**, 759.

[9] S. Wendt, M. Frerichs, T. Wei, M. S. Chen, V. Kempter and D. W. Goodman, *Surf. Sci.*, 2004, **565**, 107.

[10] M. Klaua and T. Madey, *Surf. Sci.*, 1984, **136**, L42.

[11] K. J. Wu, L. D. Peterson, G. S. Elliott and S. D. Kevan, *J. Chem. Phys.*, 1989, **91**, 7964.

[12] B. J. Hinch and L. H. Dubois, *J. Chem. Phys.*, 1992, **96**, 3262.

[13] A. S. Bolina, A. J. Wolff and W. A. Brown, *J. Phys. Chem. B*, 2005, **109**, 16836.

[14] J. L. Daschbach, B. M. Peden, R. S. Smith and B. D. Kay, *J. Chem. Phys.*, 2004, **120**, 1516.

[15] S. Haq, J. Harnett and A. Hodgson, *Surf. Sci.*, 2002, **505**, 171.

[16] H. J. Fraser, M. P. Collings, M. R. S. McCoustra and D. A. Williams, *Mon. Not. R. Astron. Soc.*, 2001, **327**, 1165.

[17] R. J. Speedy, P. G. Debenedetti, R. S. Smith, C. Huang and B. D. Kay, *J. Chem. Phys.*, 1996, **105**, 240.

[18] D. R. Haynes, N. J. Tro and S. M. George, *J. Phys. Chem.*, 1992, **96**, 8502.

[19] R. S. Smith, T. Zubkov and B. D. Kay, *J. Chem. Phys.*, 2006, **124**, 114710.

[20] J. D. Thrower, M. P. Collings, F. J. M. Rutten and M. R. S. McCoustra, *Mon. Not. R. Astron. Soc.*, 2009, **394**, 1510.

[21] D. J. Burke, A. J. Wolff, J. L. Edridge and W. A. Brown, *J. Chem. Phys.*, 2008, **128**, 104702.

[22] A. S. Bolina, A. J. Wolff and W. A. Brown, *J. Chem. Phys.*, 2005, **122**, 044713.

[23] K. Acharyya, G. W. Fuchs, H. J. Fraser, E. F. van Dishoeck and H. Linnartz, *Astron. Astrophys.*, 2007, **466**, 1005.

[24] S. D. Green, A. S. Bolin, R. Chen, M. P. Collings, W. A. Brown and M. R. S. McCoustra, *Mon. Not. R. Astron. Soc.*, 2009, **398**, 357.

[25] N. J. Mason, *private communication*.

[26] F. Dayou, M. I. Hernandez, J. Campos-Martinez and R. Hernandez-Lamoneda, *J. Chem. Phys.*, 2005, **123**, 074311.

[27] B. Bussery and P. E. S. Wormer, *J. Chem. Phys.*, 1993, **99**, 1230.

[28] V. Aquilanti, D. Ascenzi, M. Bartolomei, D. Cappelletti, S. Cavalli, M. de Castro Vitores and F. Pirani, *J. Am. Chem. Soc.*, 1999, **121**, 10794.

[29] K. Altwegg, H. Balsiger, J. Geiss, R. Goldstein, W. H. Ip, A. Meier, M. Neugebauer, H. Rosenbauer and E. Shelley, *Astron. Astrophys.*, 1993, **279**, 260.

[30] J. R. Spencer, W. M. Calvin and M. J. Person, *J. Geophys. Res.*, 1995, **100**, 19049.

[31] J. R. Spencer and W. M. Calvin, *Astron. J.*, 2002, **124**, 3400.

[32] K. S. Noll, R. E. Johnson, A. L. Lane, H. A. Domingue and H. A. Weaver, *Science*, 1996, **273**, 341.

[33] K. S. Noll, D. P. Roush, D. P. Cruikshank, R. E. Johnson and Y. J. Pendleton, *Nature*, 1997, **388**, 45.

[34] E. Matar, H. Bergeron, F. Dulieu, H. Chaabouni, M. Accolla and J. L. Lemaire, *J. Chem. Phys.*, 2010, **133**, 104507.

[35] N. Watanabe and A. Kouchi, *Ap. J.*, 2002, **571**, L173.

[36] Z. Dohnalek, G. A. Kimmel, R. L. Ciolli, K. P. Stevenson and R. S. Smith, *J. Chem. Phys.*, 2000, **112**, 5932.

[37] R. S. Smith, C. Huang and B. D. Kay, *J. Phys. Chem. B*, 1997, **101**, 6123.

[38] T. Kondo, H. S. Kato, M. Bonn and M. Kawai, *J. Chem. Phys.*, 2007, **127**, 094703.

[39] D. J. Safarik, R. J. Meyer and C. B. Mullins, *J. Chem. Phys.*, 2003, **118**, 4660.

[40] D. J. Safarik and C. B. Mullins, *J. Chem. Phys.*, 2004, **121**, 6003.

[41] G. Zimbitas, S. Haq and A. Hodgson, *J. Chem. Phys.*, 2005, **123**, 174701.

Chapter 5 - CO and N_2 Temperature Programmed Desorption

Contents

5.1 Introduction

This chapter focuses on the desorption kinetics of background dosing CO and N_2 TPD experiments from bare silica. Particular attention was paid to the multilayer coverages as in **Chapter 4** multilayer coverages of O_2 were found to follow fractional order desorption kinetics. This finding was inconsistent with the observation of other similar species desorbing from amorphous silica surfaces as these followed zeroth order kinetics [1, 2]. One suggestion to the source of this unusual behaviour was the desorption kinetics were affected by the dissociation of $(O_2)_2$ dimer clusters or O_4 which formed in the O_2 film. However, the results from a preliminary two population CKS model previously discussed in **Chapter 4** revealed that the $(O_2)_2$ dimer dissociated at surface temperatures below 20 K. This is considerably cooler than when O_2 molecules were observed to desorb from the bare silica substrate suggesting that, although $(O_2)_2$ dimers could be present in the O_2 film at low surface temperatures, the dimer clusters were unlikely to effect the desorption behaviour of O_2 multilayer coverages.

Another possible suggestion was the known porous and amorphous silica surface used in these experiments was affecting the desorption kinetics. To explore this suggestion further, TPD experiments were performed investigating the multilayer desorption kinetics of CO and N_2 from bare silica. Both of these species are similar in size and mass to O_2 but neither of them can form dimer clusters as these molecules contain a full outer electron shell. If the desorption behaviour of these species followed fractional order desorption kinetics then the silica surface could be concluded as being the cause. Alternatively, if these species followed zeroth order then this would imply the desorption mechanism of O_2 was more complex than previously assumed.

The experimental procedures for the CO and N_2 TPD experiments from bare silica are outline in **Section 5.2**. The TPD results and modelling is discussed for each experiment in **Section 5.3**. The kinetic parameters were obtained using leading edge analysis and fitted with a CKS model. The overall summary and conclusions to these experiments and comparison to the O_2 multilayer TPD results are discussed in **Section 5.4** along with the astronomical implications.

5.2 Experimental Procedures

The CO and N_2 background dosing TPD experiments from bare silica both follow a similar procedure to the O_2 background dosing TPD experiments previously discussed in **Chapter 4** (**Section 4.3.2**). As a consequence, only a brief description for both the experiments is given here.

Once UHV conditions have been obtained, the sample was heated clean at 180 K and cooled back to base temperature. The sample was positioned inline with the atomic beams, with the gate valves between the central chamber and the atomic beam chambers closed, and the central chamber pressure noted. A dosing bulb was flushed and filled with the required gas. The data acquisition program in both cases was set to monitor the central chamber pressure and the thermocouple voltages. The MASsoft software was programmed to monitor the intensity of H_2O, CO/N_2, O_2 and CH_3 (contaminate) species and the KP-type thermocouple voltages of the silica sample and cold finger over time.

After the two programs were started, the required gas was leaked into the central chamber *via* a leak valve from the gas lines for a range of doses. Once the dose was complete and the pressure had returned to back to base levels, the MASsoft and data acquisition program were stopped. The sample was re-positioned in front of the QMS (in position 1) and the central chamber pressure noted. The two programs, using the same settings as in the above dosing stage, were started. After a few minutes delay, a linear heating ramp was applied to the sample heater from base temperatures up to 70 K. After the sample had reached this temperature, the two programs were stopped and the heating ramp terminated.

Once the sample had returned to base temperatures, a second dose TPD experiment could be performed. A duplicate set of experiments for each dose was obtained for both species.

5.3 Results

5.3.1 Introduction

The TPD results and modelling of the two experiments discussed in this chapter are discussed separately. **Sections 5.3.2** and **5.3.3** describe the desorption kinetics obtained from CO and N_2 on bare silica respectively. In both cases, only the multilayer coverages were analyzed using leading edge analysis and fitted with CKS using the same procedures as previously described in **Chapter 4**. The kinetic parameters obtained from these two experiments will be compared with those for multilayer coverages of O_2 in **Section 5.4**.

5.3.2 CO TPD on Bare Silica Results and Modelling

The TPD graphs were constructed as in the previous chapter but with the sample temperature calibration shown in **Equation 5.1** as a result of a new heater being used. The results are displayed in **Figure 5.1** and are similar to those obtained in **Chapter 4** for O_2. The 10 and 15 L doses exhibit coincident falling edges implying first order multiple E_{des} desorption typical of sub-monolayer coverages. As the surface coverage increases, the desorption peaks contain both coincident leading and falling edges indicating that the CO molecules were desorbing from three-dimensional islands before a complete monolayer was formed. Above 30 L, the desorption peaks appear to roughly have coincident leading edges suggesting the CO molecules were desorbing from the bulk ice. However, these multilayer desorption peaks are considerably less well aligned than those observed for multilayer coverages of O_2 from bare silica. Closer examination of the apparatus revealed that this observation was a consequence of a non-constant current leak occurring in the heater circuit. In the future, the heater circuit will need to be checked and repaired to remove this leakage and the experiment repeated.

$$T_{sample} = -0.10028V^5 + 1.25499V^4 - 4.45497V^3 - 2.42677V^2 + 89.17129V - 30.46953 \quad (5.1)$$

To determine if the 50, 100 and 200 L doses were in the expected multilayer surface coverage region, the values of the initial surface concentration, $N[CO]_i$ were calculated. The results are displayed in **Table 5.1** along with those obtained for O_2 in **Chapter 4**. Although the apparatus system had changed slightly between performing the O_2 and CO experiments, the values of N are of similar size. This was expected as the mass and size

of the CO molecules are similar to those for O_2 and both the species had been adsorbed onto the same sample surface at similar base temperatures. As a consequence, the values of N_i for the 50, 100 and 200 L CO doses indicate that these surface coverages are within the multilayer region and, therefore, should exhibit coincident leading edges.

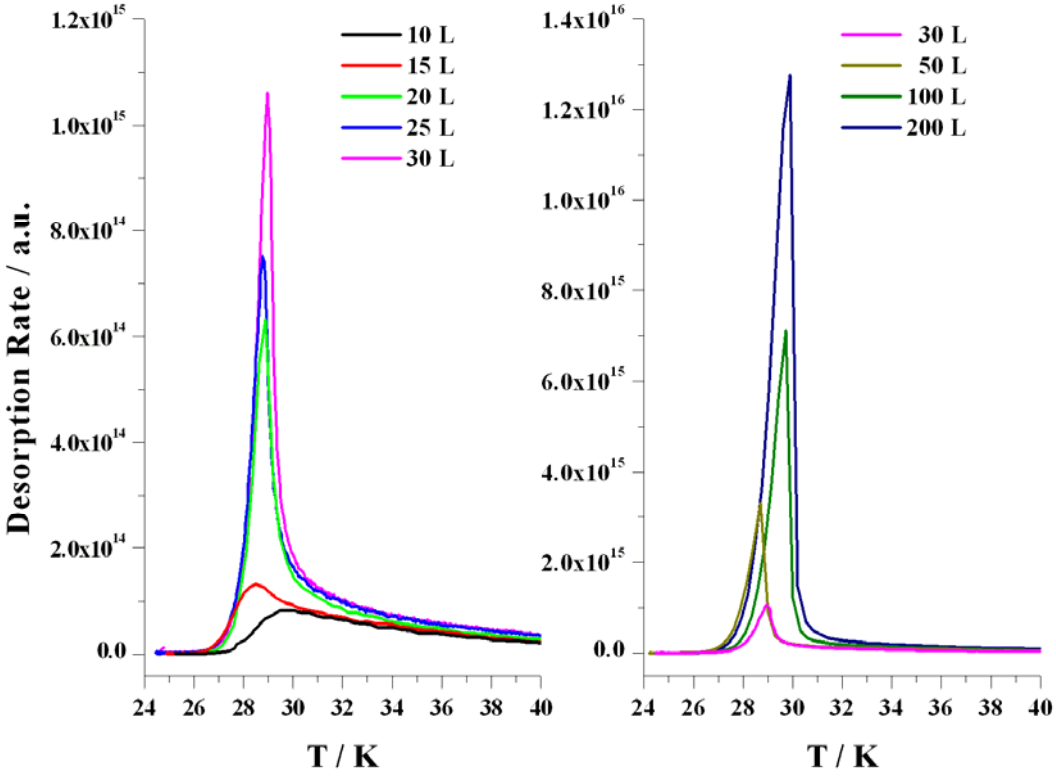

Figure 5.1: CO TPD Results from Bare Silica

The 30 L O_2 dose was previously observed to also follow multilayer desorption kinetics. However, this surface coverage was concluded to be close to the fractional order region where the O_2 desorption peaks exhibit a combination of multilayer and sub-monolayer characteristics. As the corresponding value of N for the CO 30 L dose is smaller than for O_2, it is unclear whether this CO surface coverage would lie in the multilayer or fractional order region. Usually, the kinetic behaviour boundaries are determined from the desorption peak characteristics but due to the poor surface temperature alignment of the leading and falling edges this could not be achieved. As a consequence, the 30 L CO dose was excluded from the CO multilayer analysis.

Dose / L	$N[CO]_i$ / molecules cm^{-2}	$N[O_2]_i$ / molecules cm^{-2}
10	$3.10\times10^{15\pm1}$	$2.89\times10^{15\pm1}$
15	$4.05\times10^{15\pm1}$	-
20	$6.52\times10^{15\pm1}$	$5.62\times10^{15\pm1}$
25	$7.00\times10^{15\pm1}$	-
30	$8.11\times10^{15\pm1}$	$8.65\times10^{15\pm1}$
50	$1.61\times10^{16\pm1}$	$1.35\times10^{16\pm1}$
100	$3.19\times10^{16\pm1}$	$2.72\times10^{16\pm1}$
200	$6.29\times10^{16\pm1}$	$5.20\times10^{16\pm1}$

Table 5.1: Calculated Values of $N[CO]_i$ and $N[O_2]_i$

To enable the kinetic desorption parameters for CO multilayer coverages to be obtained, the corresponding desorption peaks were shifted with respect to surface temperature until the leading edges all aligned with the 200 L dose (see **Figure 5.2**).

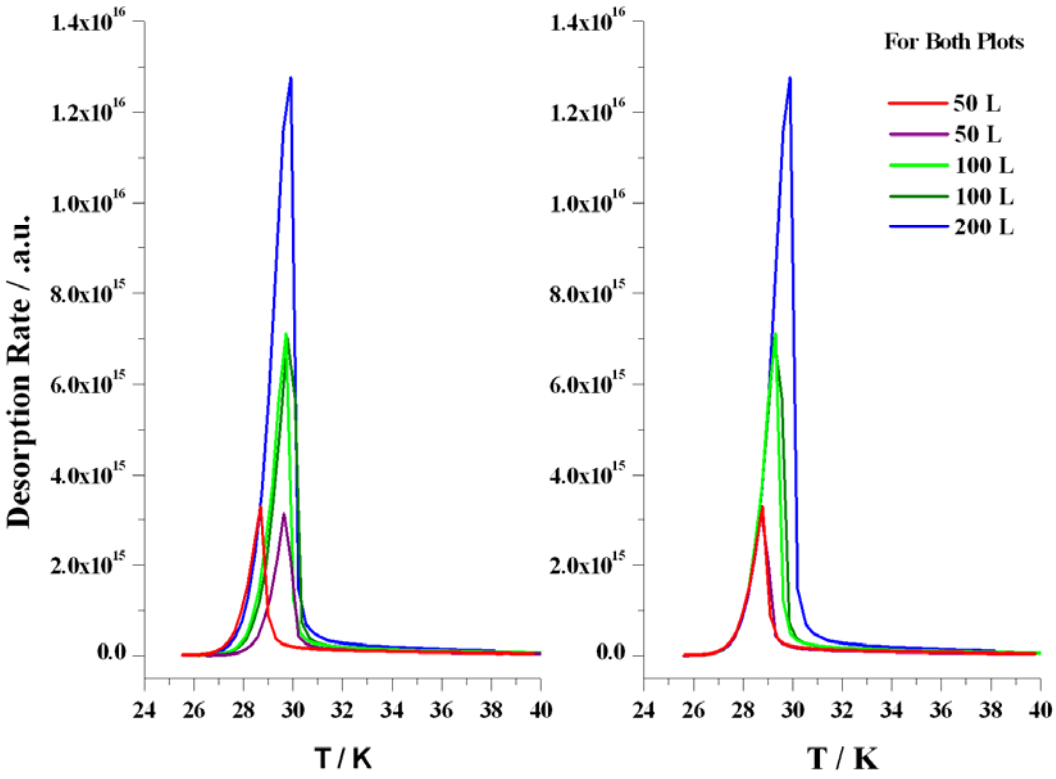

Figure 5.2 Non-shifted (left) and Shifted (right) Multilayer CO Desorption Peaks

Before leading edge analysis could be applied, the value of *n* had to be calculated to deduce whether the silica substrate might be affecting the desorption kinetics of CO. This was achieved using the same procedure as previously described for the O_2 multilayer coverages on bare silica TPD experiments in **Chapter 4**. The results are displayed in **Figure 5.3** and **Table 5.2** with the average mean value calculated as 0.09±0.11. This indicated that the multilayer coverages of CO also did not truly follow zeroth order desorption kinetics, like O_2, and that the desorption kinetics were weakly

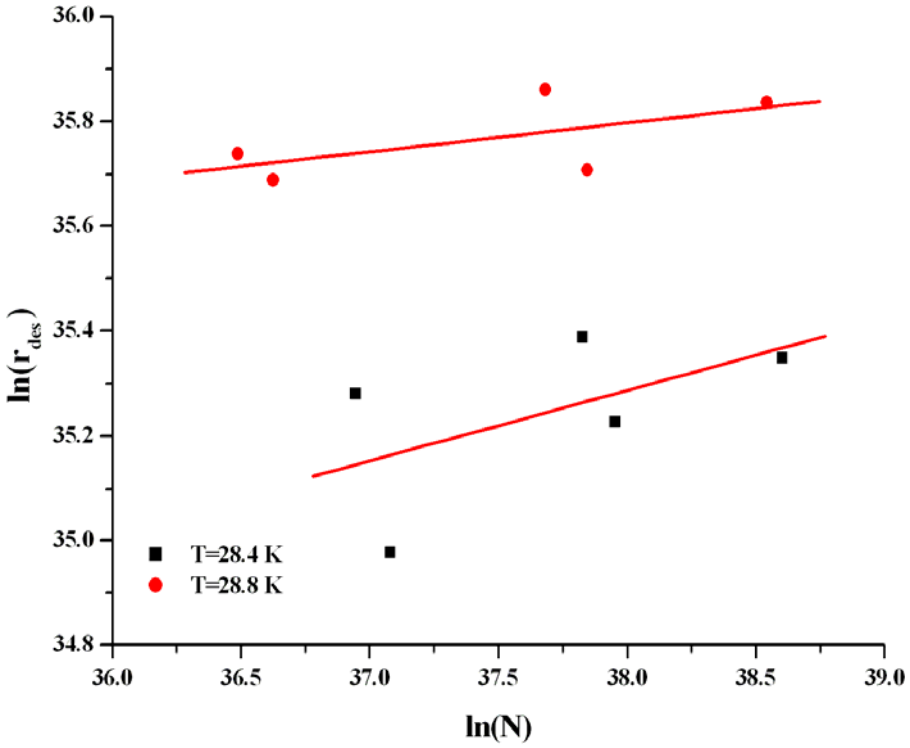

Figure 5.3: Kinetic Order Determination Plot of $\ln(r_{des})$ against ln(N)

T / K	*n*
28.4	0.13±0.11
28.8	0.05±0.11
Average	0.09±0.11

Table 5.2: Kinetic Order Values from **Figure 5.3**

affected by the underlying silica surface. However, unlike O_2, this multilayer fractional order desorption could not be caused by the dissociation of dimer clusters as the CO molecules are unable to form these species due to the molecules containing a full outer shell of electrons. Additionally, the value of *n* obtained for CO is roughly half that for O_2. This difference could be a consequence of the molecular interaction between two CO molecules being weaker than between two O_2 molecules suggesting that the desorption kinetics of O_2 were affected by more than just the underlying silica surface.

The kinetic parameters for CO were obtained by applying leading edge analysis using the same procedure as previously described in **Chapter 4**. The results are displayed in **Table 5.3** along with the calculated mean average values and errors taken as the second standard deviation. As with the H_2O and O_2 TPD analysis, *v* is quoted in the format of powers and lies in the upper end of the expected range for typical zeroth order kinetics. The multilayer desorption kinetics of CO from a range of surfaces has been explored by other research groups [3, 4] and theirs results are shown in **Table 5.4**. In comparison, both of the kinetic parameters obtained in this study are relatively higher and outside the experimental error range. A small proportion of this difference could have arisen from the different values obtained for *n*. However, as the experiment performed in this study was affected by the non-constant current leakage, then the experimental errors quoted could be underestimated.

Dose / L	***v* / molecules$^{0.91}$ cm$^{-1.82}$ s$^{-0.91}$**	***E_{des}* / kJ mol^{-1}**
50	$10^{33.89}$	10.9
100	$10^{33.5}$	10.7
200	$10^{31.1}$	9.4
Average	$10^{33.0\pm2.5}$	10.4±1.4

Table 5.3: Leading Edge Analysis Results for CO Desorbing from Bare Silica

Surface	***v* / molecules$^{0.91}$ cm$^{-1.82}$ s$^{-0.91}$**	***E_{des}* / kJ mol^{-1}**
Polycrystalline Gold Coated Copper [3]	7×10^{26}	7.10
pASW [4]	7×10^{26}	6.8

Table 5.4: Comparison Kinetic Parameters of CO Desorption

To improve the accuracy of the kinetic parameters obtained in this study, the experimental data was fitted using a CKS model. The reaction mechanism used is shown in **Figure 5.4** where *ads* describes those CO species adsorbed on the silica surface; *g* those in the gas phase; and *pump* those removed from the central chamber by the pumping system. The kinetic parameters for the first step were based on those obtained through leading edge analysis. The last step was temperature independent and the value of *k* was deduced by comparing the simulated falling edge with the experiment data for each dose.

$$CO(ads) \rightarrow CO(g)$$
$$CO(g) \rightarrow CO(pump)$$

Figure 5.4: Reaction Mechanism for CO Desorbing from Bare Silica

The CKS results are displayed in **Figure 5.5**. Overall, the CKS fits describe the experimental data well indicating that the desorption kinetics of multilayer coverages of CO follow fractional order desorption kinetics. This observation provides further evidence that the underlying porous and amorphous silica surface is affecting the multilayer desorption kinetics for specific species. The kinetic parameters used for each dose along with the average values are shown in **Table 5.5** and are similar to those obtained through leading edge analysis. Error analysis was applied by taking the second standard deviations. Although this has improved the accuracy of the kinetic parameters, the values obtained are still higher than those in the literature.

In the future, the apparatus will be modified to remove the observed current leakage. When this has been achieved, the CO TPD experiment could be repeated with additional doses to determine the values of v and E_{des} more accurately. However, the results obtained from this proposed experiment could not be used towards understanding the formation of H_2O on interstellar dust grains and, therefore, would be unlikely to be repeated in the near future.

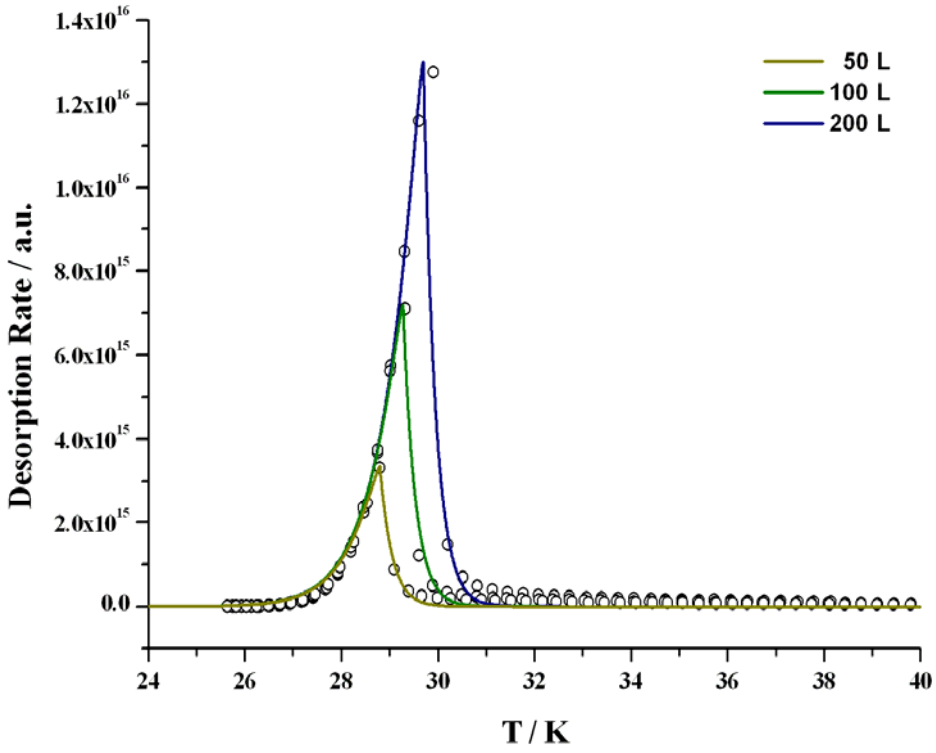

Figure 5.5: CKS Fits of Multilayer CO TPD from Silica

Dose / L	ν / molecules$^{0.91}$ cm$^{-1.82}$ s$^{-0.91}$	E_{des} / kJ mol^{-1}
50	8.5×10^{32}	10.4
100	7.5×10^{32}	10.5
200	6.0×10^{32}	10.4
Average	$7.3\pm2.5\times10^{32}$	10.4±0.1

Table 5.5: Kinetic Parameters Required to Fit the CKS Model

5.3.3 N_2 TPD on Bare Silica Results and Modelling

The TPD graphs were constructed using the same procedure as for the CO data in the above section and are shown in **Figure 5.6**. The 10 and 15 L doses again both exhibit coincident falling edges indicating that the desorption kinetics of sub-monolayer coverages of N_2 followed first order multiple E_{des} desorption behaviour. At 30 L and higher, the desorption peaks all roughly have coincident leading edges. As with CO, these surface coverages suggest that the N_2 molecules were desorbing from the bulk ice but the alignment of the desorption peaks were affected by the current leakage. The

remaining 20 dose exhibits both a coincident falling and leading edge indicating that at this surface coverage the molecules were desorbing from multilayer islands of N_2 before a complete monolayer was formed.

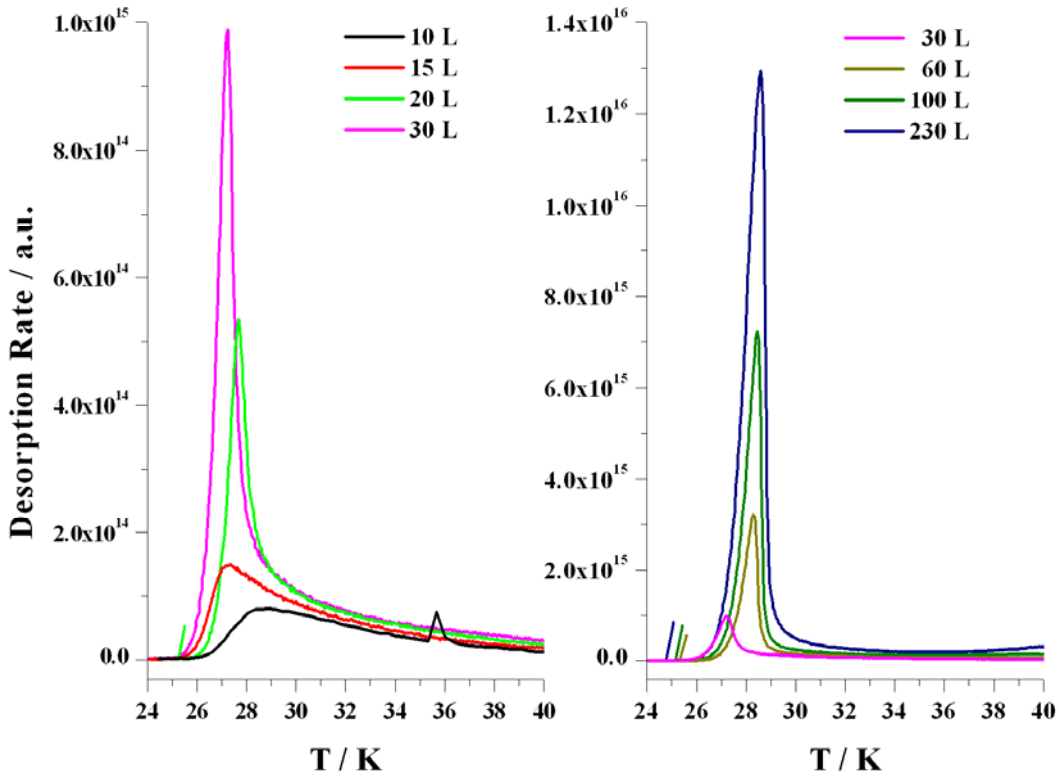

Figure 5.6: N_2 TPD Results from Bare Silica

Overall, the TPD results reveal that the N_2 desorption pattern is similar to the CO TPD results from bare silica (as previously discussed in the above sub-section). This was expected as the two species are relatively the same in terms of size and mass. Further evidence to support this observation was obtained by calculating the initial surface concentration values of N_2, $N[N_2]_i$. The results are shown in **Table 5.6** and are in good agreement with CO and O_2 (**Table 5.1**). The 30 L dose for N_2 almost has the same value of N as the corresponding dose for O_2 suggesting that this N_2 dose lies just within the multilayer region unlike the corresponding 30 L dose for CO. These differences in N_i are a consequence of the background dosing technique highlighting the need to determine the exact dose from the experimental data (for more details see **Chapter 4**).

Dose / L	$N[N_2]_i$ / molecules cm^{-2}
10	$10^{15.44\pm2.00}$
15	$10^{15.63\pm2.00}$
20	$10^{15.81\pm2.00}$
30	$10^{15.93\pm2.00}$
60	$10^{16.25\pm2.00}$
100	$10^{16.52\pm2.00}$
230	$10^{16.83\pm2.00}$

Table 5.6: Calculated Values of $N[N_2]_i$

To enable the N_2 multilayer desorption kinetics to be determine, the desorption peaks were shifted with respect to surface temperature until the leading edges all aligned with the 200 L dose (see **Figure 5.7**).

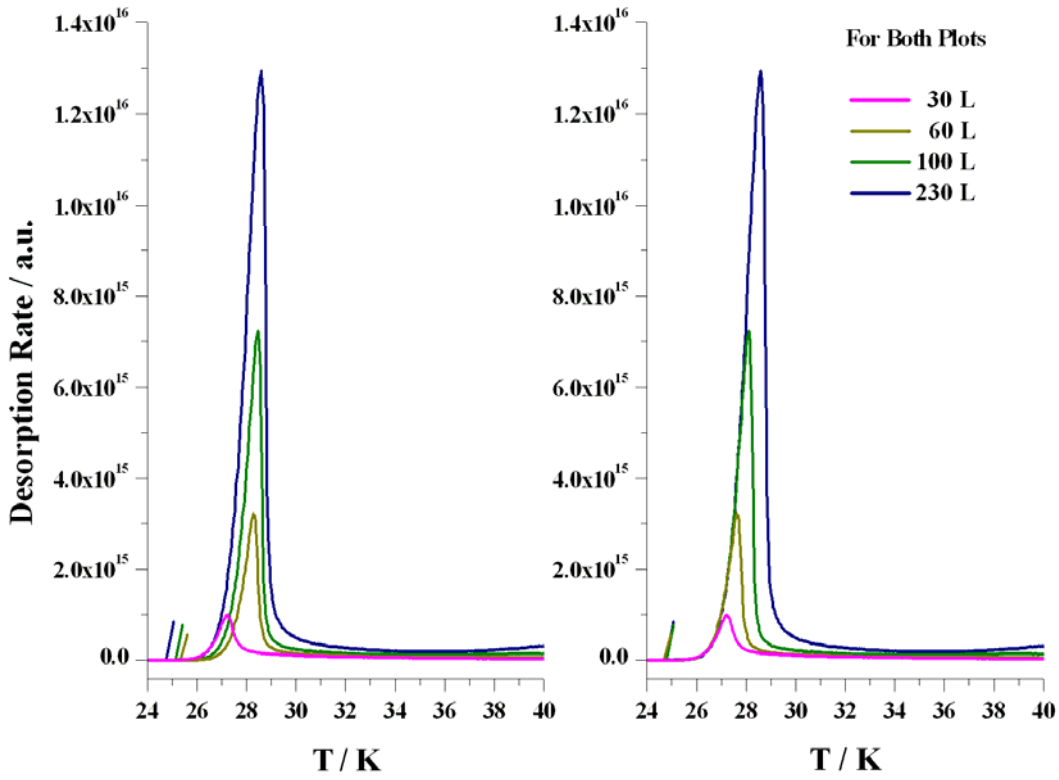

Figure 5.7: Non-shifted (left) and Shift (right) Multilayer N_2 Desorption Peaks

The first part of the kinetic analysis was to determine if the underlying silica surface was affecting the desorption kinetics. This was achieved by calculating *n* using the same procedure as above. The results are displayed in **Figure 5.8** and **Table 5.7** and reveal that the multilayer N_2 followed approximately zeroth order implying that the underlying surface had negligible affect on the desorption kinetics unlike with CO and O_2.

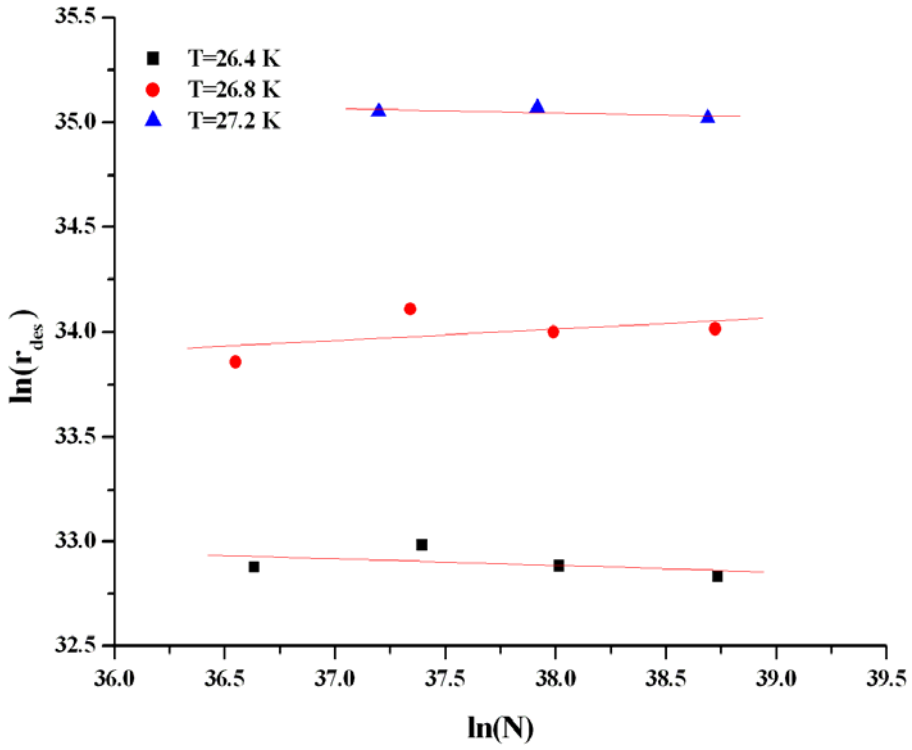

Figure 5.8: Kinetic Order Determination Plot of $\ln(r_{des})$ against ln(N)

T / K	*n*
26.4	-0.03±0.04
26.8	0.05±0.07
27.2	-0.02±0.03
Average	0.00±0.08

Table 5.7: Kinetic Order Values from **Figure 5.8**

Leading edge analysis was applied to the data with *n* set to 0 and the results for each dose are displayed in **Table 5.8**. This table also includes the average value and errors determined from the second standard deviation. As before, *v* is quoted in the format of powers. However, the value of *v* obtained for N_2 is approximately three orders of magnitude higher than for CO and lies outside the expected range for typical zeroth order kinetics. The value of E_{des} obtained in this study was approximately 4.6 kJ mol^{-1} higher than the multilayer desorption value obtained by Fuchs *et al*. [5] from a polycrystalline gold surface which is outside the experimental error. The errors obtained for both the kinetic parameters in this study are also considerably higher than those previously calculated for O_2 and CO suggesting that the problems arising from the current leak were more pronounced in this experiment. To improve the accuracy of the kinetic parameters, a CKS model was constructed and fitted to the experimental data.

Dose / L	***v* / molecules cm^{-2} s^{-1}**	**E_{des} / kJ mol^{-1}**
30	$10^{37.9}$	11.9
60	$10^{38.3}$	12.0
100	$10^{34.8}$	10.1
200	$10^{34.1}$	9.8
Average	$10^{36.3\pm4.2}$	11.0±2.3

Table 5.8: Leading Edge Analysis Results for N_2 Desorbing from Bare Silica

The reaction mechanism used to describe the desorption of N_2 from bare silica is shown in **Figure 5.9** and is based on the reaction mechanism used for CO (see **Figure 5.5**). The kinetic parameters for the first step were taken from the leading edge analysis results. The last step was temperature independent and the values of *k* were deduced as in the previous sub-section.

$$N_2(ads) \rightarrow N_2(g)$$
$$N_2(g) \rightarrow N_2(pump)$$

Figure 5.9: Reaction Mechanism for N_2 Desorbing from Bare Silica

The CKS results are displayed in **Figure 5.10** and **Table 5.9**. Overall the simulation results were in fairly good agreement with the experimental data with only slight

variations observed at the very top and bottom of the desorption peak's leading edge. This observation suggests that the value of *n* could have been slightly higher than zeroth but still within the error range calculated. If this was the case, then the underlying silica surface would have had a minor affect on the multilayer desorption kinetics of N_2 although this would be expected to be of a lesser extent than observed for CO and N_2 as the $N_2 - N_2$ molecular interaction is weaker than that of CO – CO and $O_2 - O_2$.

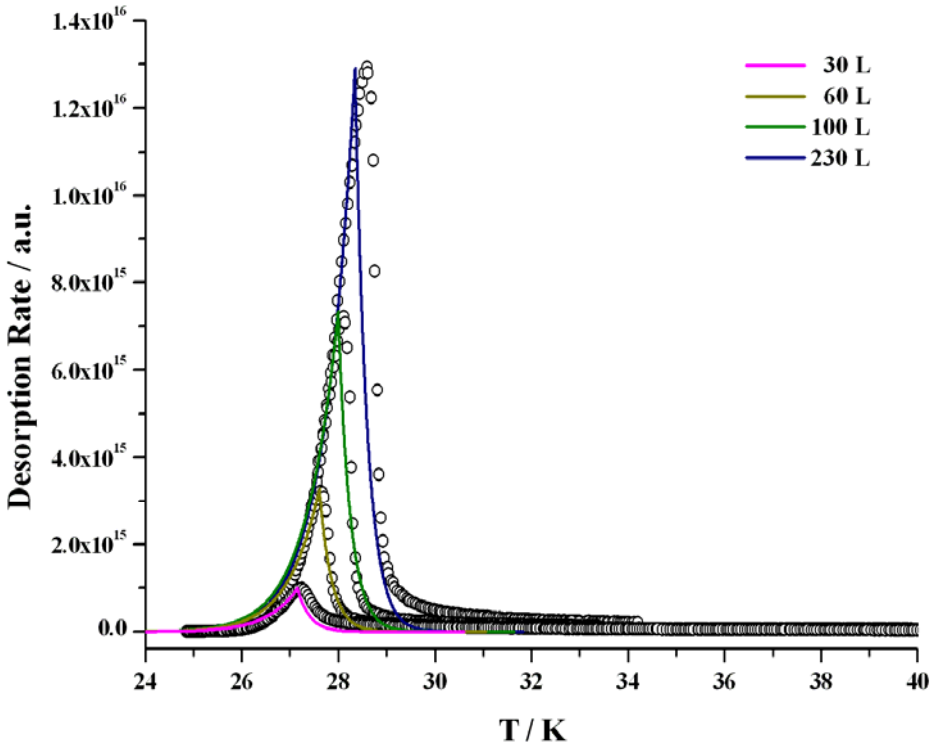

Figure 5.10: CKS Fits of Multilayer N_2 TPD from Silica

Dose / L	*v* / molecules cm^{-2} s^{-1}	E_{des} / kJ mol^{-1}
30	5.0×10^{33}	9.6
60	5.0×10^{33}	9.7
100	5.0×10^{33}	9.6
200	1.0×10^{35}	10.3
Average	$10^{34.0\pm1.3}$	9.8±0.6

Table 5.9: Kinetic Parameters Required to Fit the CKS Model

Another observation with the simulated results was that all of the values of v and E_{des} used to obtain the best fit (except one) were lower than those derived through leading edge analysis. Again, this could have been associated with the value of n used. However, both of these observations could have been a consequence of the non-constant current leakage being more pronounced in these experiments. For the case of this study, the experimental errors applied to the kinetic results are underestimated resulting in the parameters obtained lying just outside the experimental range of those obtained by Fuchs *et al.* [5]. In the future, the apparatus will be modified to remove this current leak before performing any other TPD experiments. However, the results obtained by repeating this N_2 TPD experiment from bare silica could not be used towards understanding the formation of H_2O on interstellar dust grains and. Therefore, are unlikely to be repeated in the near future.

5.4 Summary and Conclusions

This chapter focused on the multilayer coverage results obtained from TPD experiments of CO and N_2 on bare silica (**Sections 5.3.2** and **5.3.3** respectively) to determine if the underlying silica surface was affecting the multilayer desorption kinetics of O_2. Values of n, v and E_{des} for each species were calculated and the average values with errors are shown in **Table 5.10**. The results revealed that n decreased roughly by half as the species changed from O_2 to CO to N_2 indicating that the molecular interaction decreased with the different species. Overall, these results suggest that the underlying surface was responsible for the fractional order multilayer desorption kinetics observed for CO and O_2.

Multilayer Species	***n***	***v* / molecules cm^{-2} s^{-1} ***	***E_{des}* / kJ mol^{-1}**
O_2	0.18±0.04	$10^{27.2\pm0.1}$	9.8±0.1
CO	0.09±0.11	$10^{32.9\pm0.2}$	10.4±0.1
N_2	0.00±0.08	$10^{34.0\pm1.3}$	9.8±0.6

Table 5.10: Kinetic Order Values for O_2, CO and N_2 Multilayer Coverages Desorbing from Bare Silica
(* Assumed Zeroth Order Units)

For N_2, the value of *n* obtained indicated that the underlying silica surface had negligible affect. However, the errors obtained for both CO and N_2 were considerably larger than for O_2 due to the observation of the non-constant current leak from the heater circuit. As a consequence, the value of *n* could have been slightly higher than the results suggested. Evidence supporting this came from the slightly poorer CKS fits obtained for N_2 in comparison to CO and O_2 suggesting that the underlying silica surface may have had a minor affect on the desorption kinetics. To prove if this was the case, the apparatus will need to be modified to remove the source of the current leak and the experiment repeated.

Overall, the kinetic parameters obtained for CO and N_2 were just outside the experimental error range to those in the literature. However, the observed current leakage in the sample heater circuit resulted in the desorption peaks being shifted in surface temperature by a non-constant value. Although attempts were made to shift the desorption peaks to obtained coincident leading edges, the error involved would be larger than the experimental error quoted. This conclusion could also be used to explain why the values of E_{des} for CO and N_2 were considerably larger than those found in the literature [3-5]. In the future, the apparatus will be modified to remove this current leakage before any other TPD experiments are performed. Once this has been achieved, the experiments discussed in this chapter could be repeated. However, these experiments were performed to determine if the underlying silica surface was affecting the desorption kinetics rather than obtaining the desorption kinetics. As a consequence, these experiments are unlikely to be repeated in the near future as the results obtained would not provide any additional information which could be used towards understanding the formation of H_2O on interstellar dust grains.

5.5 References

[1] S. D. Green, A. S. Bolina, R. Chen, M. P. Collings, W. A. Brown and M. R. S. McCoustra, *Mon. Not. R. Astron. Soc.*, 2009, **398**, 357.

[2] J. D. Thrower, M. P. Collings, F. J. M. Rutten and M. R. S. McCoustra, *Mon. Not. R. Astron. Soc.*, 2009, **394**, 1510.

[3] S. E. Bisschop, G. W. Fuchs, E. F. van Dishoeck and H. Linnartz, *Astron. Astrophys.*, 2007, **474**, 1061.

[4] M. P. Collings, J. W. Dever, H. J. Fraser and M. R. S. McCoustra, *Astrophys. Space Sci.*, 2003, **285**, 633.

[5] G. W. Fuchs, K. Acharyya, S. E. Bisschop, K. I. Oberg, F. A. van Brocekhuizen, H. J. Fraser, S. Schlemmer, E. F. van Dishoeck and H. Linnartz, *Faraday Discussion*, 2006, **133**, 331.

Chapter 6 - Preliminary Atomic O Beam TPD Experiments

Contents

6.1 Introduction

This chapter focuses on the results obtained from preliminary atomic O beam post-irradiation TPD experiments. Consideration to cracking reactions in the QMS source was applied to the TPD data before the desorption features were assigned based on the conclusions obtained in **Chapters 4** and **5** and from the literature. **Section 6.2** outlines the experimental procedure and **Section 6.3** discusses the results for each experiment separately. The first experiment explored the TPD results of a 30 minute atomic O beam dose on bare silica in comparison to the 30 minute O_2 molecular beam TPD previously discussed in **Chapter 4**. The findings observed from this experiment along with the corresponding O_2 molecular beam dose on pASW TPD experiment were used towards analyzing the results obtained for a 4 hour atomic O beam dose on 200 L of pASW on silica TPD experiments. The third and fourth experiments explored the atomic O beam dose TPD observations on 100 L of O_2 on 200 L of pASW on silica and on 100 L of ^{13}CO on 200 L of pASW on silica respectively. The summary and conclusions of this chapter are discussed in **Section 6.4** along with the astronomical implications and suggestions for future experiments.

6.2 Experimental Procedure

All the TPD experiments discussed in this chapter follow similar procedures to those previously discussed in this thesis. As a consequence, only a brief description applicable to all the experiments is given here.

Once UHV conditions have been obtained, the sample was heated clean at 180 K before being allowed to cool back to base temperature. The sample was positioned in-line with the atomic beam sources, with the gate valves between the atomic beam and central chambers closed, and the central chamber pressure noted. The data acquisition program was set to monitor the central chamber pressure and the thermocouple voltages. The MASsoft software was programmed to monitor the intensity of the species of interest and the KP-type thermocouple voltages of the silica sample and cold finger over time.

In the first experiment, an atomic beam dose was applied directly onto the silica surface. However, in the other experiments the atomic O beam dose was applied onto a substrate

which had been previously background dosed onto the silica. This was achieved by flushing and filling a dosing bulb with the required gas for the substrate. After the two programs were started, the gas was leaked into the central chamber *via* a leak valve from the gas lines for a set dose. Once the pressure had returned back to base levels, the two programs were stopped. If a second background dose was required (as in the third and fourth experiment) then this procedure was repeated.

Once the substrate had been formed (if required), the atomic O beam dose was performed. The atomic O beam was formed by leaking O_2 into the oxygen plasma chamber at the ideal plasma chamber pressure of 1.0×10^{-4} mbar (previously determined in **Chapter 3**) and a RF power of 140 W. Once the atomic beam was stable, the two programs were started using the same conditions as before. After a short time delay, the gate valve between the central and oxygen plasma chambers was opened for a set dose time. When the dose was completed and the pressures returned back to base levels, the two programs were stopped and the atomic beam terminated.

The final stage for all the experiments was the TPD analysis. In each case, the sample was positioned in front of the QMS (located in position 1, see **Figure 2.3** in **Chapter 2**) and the central chamber pressure noted. The two programs were started using the same settings as for the dosing stage or stages. After a few minutes delay, a linear heating ramp was applied to the sample heater from base temperatures up to 180 K. After the sample had reached this temperature, the two programs were stopped and the heating ramp terminated.

6.3 TPD Results

6.3.1 Introduction

This section focuses on the TPD results obtained from the preliminary atomic O beam irradiation experiments. Comparisons with this data were made with the desorption observations previously discussed in this thesis and with those in the literature. **Section 6.3.2** explores the findings from a 30 minute atomic O beam dose on bare silica TPD experiment whilst **Section 6.3.3** discusses the observations from a 4 hour atomic O beam dose on 200 L of pASW on silica TPD experiments. **Sections 6.3.4** and **6.3.5** explore the findings obtained from a 4 hour atomic O beam dose on 100 L of O_2 on

200 L of pASW on silica TPD experiment and from a 4 hour atomic O beam dose on 100 L of ^{13}CO on 200 L of pASW on silica TPD experiment respectively.

6.3.2 Atomic O Beam Dose on Bare Silica

The experiment discussed in this sub-section explores the initial findings for a 30 minute atomic O beam irradiation TPD experiment on bare silica. The TPD graph was constructed using the same procedure as for those previously described in **Chapter 4** and is displayed in **Figure 6.1**. The initial observations revealed that O_2 formed the most intense desorption peaks. However, from this plot alone, the origin of the O_2 species is unclear as a proportion of the molecules could have been formed by atomic O surface reactions, adsorbed as non-dissociated beam species and as a product of O_3 cracking in the QMS source. Another observation of the TPD graph suggested that the base surface temperature was around 6 K which is too low to be achieved using the current apparatus system (see **Chapter 2**). This observation occurred as the base

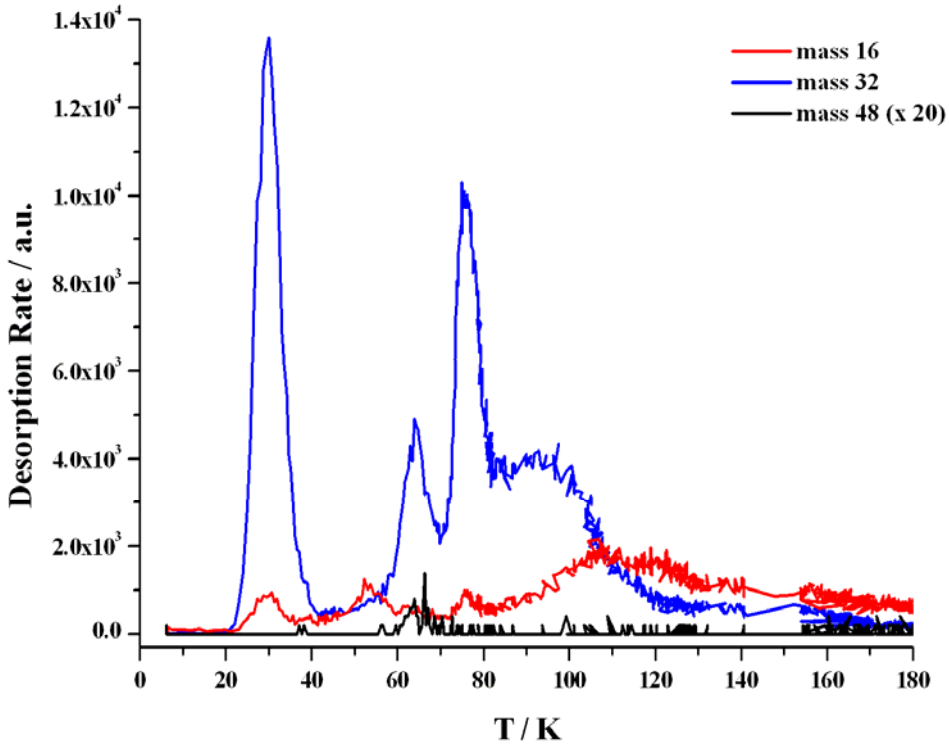

Figure 6.1: Raw TPD Curves for Masses 16, 32 and 48

temperature was outside the previously calibrated surface temperature range (approximately 16 to 300 K) but was expected to be roughly 15 K. At this surface temperature, the O atoms were believed to be able to diffuse across the surface but not the O_2 molecules [1].

The initial surface concentrations of O and O_2 adsorbed onto the surface, $N[O]_i$ and $N[O_2]_i$, were estimated using **Equations 6.1** and **6.2** respectively where F_{beam} is the O_2 molecular beam flux, t_{irr} the irradiation time, α the accommodation coefficient and $[O:O_2]$ the O:O_2 dissociation fraction. This calculation was based on the procedure used to estimate $N[O_2]_i$ for the O_2 molecular beam dose experiments in **Chapter 4**. However, the results from the cracking fraction experiments performed in **Chapter 3** were unable to provide the value of $[O:O_2]$ without further modifications to the apparatus.

$$N[O]_i = F_{beam} t_{irr} \alpha [O:O_2] \tag{6.1}$$

$$N[O_2]_i = F_{beam} t_{irr} \alpha (1 - [O:O_2]) \tag{6.2}$$

An estimate of $[O:O_2]$ was achieved by monitoring the mass 16 and 32 signals using the SRS mass spectrometer off-axis from the atomic and molecular oxygen beams. With the central chamber under UHV conditions and the sample and QCM raised out-of-line of the beams, an atomic O plasma was formed at a plasma chamber pressure, P, of 5.0×10^{-5} mbar. Once the plasma was stable, the program monitoring the SRS mass spectrometer was started and a baseline of the background gases in the central chamber obtained. After a short delay, the gate valve between the central and oxygen plasma chambers was opened. When the mass signals were stable for a few minutes, the RF power was turned off changing the atomic O beam into the O_2 molecular beam. Once the mass signals had again become stable for a few minutes, the gate valve was closed and the program monitoring the SRS mass spectrometer terminated. This procedure was repeated with P held at 7.5×10^{-5}, 1.0×10^{-4} and 2.0×10^{-4} mbar.

The data obtained revealed that the mass 32 signal (O_2) increased noticeably when the RF power was turned off. The fraction of O atoms in the atomic beam in comparison to O_2 was obtained and the results are shown in **Table 6.1** along with the average value.

***P* / mbar**	***[O:O$_2$]***
5.0×10^{-5}	0.37
7.5×10^{-5}	0.32
1.0×10^{-4}	0.32
2.0×10^{-4}	0.26
Average	0.32±0.09

Table 6.1: Estimated Dissociation Fraction Results for the Atomic O Beam

Error analysis was applied by taking the second standard deviation. The average value obtained for *[O:O$_2$]* is in good agreement with those determined for atomic O beams using a RF powered plasma source [2] (as in this study) or MW powered plasma source [3]. Using this result and those values obtained in **Chapter 3**, the values of N_i for this experiment were estimated and are displayed in **Table 6.2** along with the corresponding value of $N[O_2]_i$ calculated for the 30 minute O_2 molecular beam dose TPD experiment on silica (previously discussed in **Chapter 4**). Although this procedure provide an estimate of *[O:O$_2$]*, the small contribution to the mass 16 signal from CO or CO_2 formed by the reaction of O with C or the recombination of O_2 on the chamber walls was not considered. As a consequence, the dissociation fraction experiments will still need to be performed to provide a more accurate value. Additionally, these estimates of N_i assume that α remained the same for both the atomic and molecular oxygen beams. In the future, experiments based on the Kings and Wells method will be performed to determine if this is the case (for more details, see **Chapter 3**). The results from these experiments, along with the experiments to calculate *[O:O$_2$]*, will enable more accurate values of N_i to be obtained. The separate

Beam Dose TPD Experiment	**N_i / species cm^{-2}**
Atomic O Beam	[O] = 3.5×10^{14} [O_2] = 7.3×10^{14}
O_2 Molecular Beam	1.2×10^{15}

Table 6.2: Calculated Values of N_i for the Atomic O Beam TPD and Corresponding O_2 Molecular Beam TPD Experiment (**Section 4.3.5**)

initial surface concentrations of O and O_2, $N[O]_i$ and $N[O_2]_i$ respectively, could then be deduced allowing the proportion of O_2 molecules adsorbed as non-dissociated beam species onto the surface to be removed from the TPD data.

The analysis of the TPD data was further developed by considering the cracking fractions of O_2 and O_3. Usually a species is observed by the impact of 70 eV electrons from the QMS source ionising the gas (as shown in the first three reactions in **Figure 6.2**) and the resulting ion being detected. In some cases, the internal energy deposited into the ionised molecules by the electron impact is sufficient to crack the parent ions (fourth and fifth reaction) allowing the daughter ions to also be detected. In this TPD experiment, the daughter ions observed have the same mass to charge ratio as some of the other parent ions. For example, the presence of O_2 is observed by the mass to charge signals corresponding to the O_2^+ and O^+ ions (second and fifth reaction). Similarly, O_3 is detected by the O_3^+, O_2^+ and O^+ parent and daughter ions. As a consequence, the observed mass 16 signal is a mixture of O atoms from the surface and from cracked O_2 and O_3 species and the observed mass 32 signal is a mixture of O_2 molecules and cracked O_3 species.

$$O(g) \rightarrow O^+(g) + e^-$$

$$O_2(g) \rightarrow O_2^+(g) + e^-$$

$$O_3(g) \rightarrow O_3^+(g) + e^-$$

$$O_3^+(g) \rightarrow O_2^+(g) + O(g)$$

$$O_2^+(g) \rightarrow O^+(g) + O(g)$$

Figure 6.2: Cracking Reactions in the QMS Source

To determine the proportion of the signal from the species desorbing from the surface the proportion of the detected ions needs to be related to the total ion intensity observed. These are expressed mathematically in **Equations 6.3**, **6.4** and **6.5** where O_{tot}^+, $O_{2_{tot}}^+$ and $O_{3_{tot}}^+$ are the total ion intensities detected for masses 16, 32 and 48 respectively, [O], [O_2] and [O_3] the actual species concentrations of O, O_2 and O_3 respectively desorbing from the surface and *sf* the scaling factor of the ion (shown first in the bracket) originating from the species (shown second).

$$O^+_{tot} = [O_3]sf\left(O^+, O_3\right) + [O_2]sf\left(O^+, O_2\right) + [O]sf\left(O^+, O\right) \tag{6.3}$$

$$O^+_{2_{tot}} = [O_3]sf\left(O^+_2, O_3\right) + [O_2]sf\left(O^+_2, O_2\right) \tag{6.4}$$

$$O^+_{3_{tot}} = [O_3]sf\left(O^+_3, O_3\right) \tag{6.5}$$

The actual value of [O_3] was calculated by rearranging **Equation 6.5** to give **Equation 6.6**. This equation was then substituted into **Equation 6.4** and rearranged to provide a formula relating the value of [O_2] in terms of $O^+_{2_{tot}}$, $O^+_{3_{tot}}$ and the relevant values of *sf* (see **Equation 6.7**). The same procedure was applied to **Equation 6.3** by substituting in **Equations 6.6** and **6.7** to provide a formula for [O] (**Equation 6.8**).

$$[O_3] = \frac{O^+_{3_{tot}}}{sf\left(O^+_3, O_3\right)} \tag{6.6}$$

$$[O_2] = \frac{\left(O^+_{2_{tot}} - \frac{O^+_{3_{tot}} sf\left(O^+_2, O_3\right)}{sf\left(O^+_3, O_3\right)}\right)}{sf\left(O^+_2, O_2\right)} \tag{6.7}$$

$$[O] = \frac{O^+_{tot} - \left(\frac{O^+_{3_{tot}} sf\left(O^+, O_3\right)}{sf\left(O^+_3, O_3\right)}\right) - \left(\frac{\left(O^+_{2_{tot}} - \frac{O^+_{3_{tot}} sf\left(O^+_2, O_3\right)}{sf\left(O^+_3, O_3\right)}\right) sf\left(O^+, O_2\right)}{sf\left(O^+_2, O_2\right)}\right)}{sf\left(O^+, O\right)} \tag{6.8}$$

The values of *sf* were derived from a combination of the cracking fraction for the ion from the species shown in the bracket, c_{frac}, and the sensitivity factor, s_{factor}, which links the QMS count rate to the partial pressure of the species. The value of c_{frac} regarding $sf\left(O^+, O_2\right)$ was calculated from the O_2 and O mass signal data obtained in the background dosing part of the O_2 TPD experiments on bare silica from **Chapter 4**. By assuming the value of O^+_2 from O_2 was equal to 1, the O mass signal was divided by a range of values for c_{frac} until the O mass signal matched the O_2 mass signal for each of

the dose files (see **Equation 6.9**). The average result is displayed in **Table 6.3** with the errors determined from the second standard derivation. In the future, the same procedure could be used to calculate the values of c_{frac} for $sf\left(O^+, O_3\right)$ and $sf\left(O_2^+, O_3\right)$ once the construction of the O_3 synthesis apparatus has been completed (see **Chapter 2** for more details). However, for this study estimates for both values of c_{frac} were obtained from the literature [4] (**Table 6.3**).

$$Ion_{parent} = \frac{Ion_{daughter}}{c_{frac}} \tag{6.9}$$

Cracking Ions	c_{frac}
O^+ from O_2	0.07±0.01
O_2^+ from O_3 [4]	0.50±0.20
O^+ from O_3 [4]	0.06±0.02

Table 6.3: c_{frac} Values for Different Cracking Reactions

The value of s_{factor} was taken as a proportionality constant between the central chamber pressure (in mbar) and the total ion count (in QMS counts). To determine s_{factor} for O_2, a calibration set of background dosing experiments were performed over a range of set pressures whilst monitoring the QMS counts through MASsoft for the parent and daughter ions. The data obtained has been previously analyzed to construct a calibration graph to convert the units of QMS counts into mbar in **Chapter 3**. A plot of central chamber pressure against total ion counts is shown in **Figure 6.3** where s_{factor} is equivalent to the gradient. In the case of O_2, s_{factor} was found to be $6.69\pm0.02\times10^{-13}$ mbar counts^{-1}. In the future, similar experiments will be performed for O and O_3 to determine the values of s_{factor} but for this study, the value of s_{factor} was assumed to remain the same for each species.

Values of *sf* were obtained by multiplying the relevant values of c_{frac} and s_{factor} together for each ion (see **Table 6.4**). These values were then applied to the TPD data using

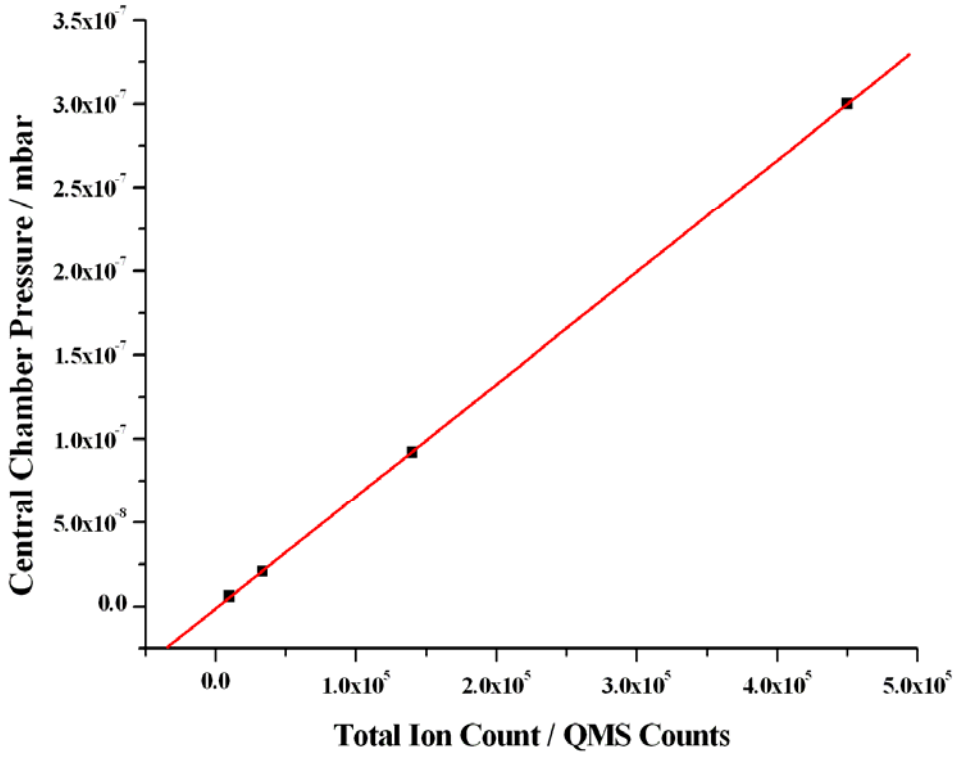

Figure 6.3: Total Ion Counts against Central Chamber Pressure Plot

Cracking Ion	*sf* / mbar counts^{-1}
O^+ from O	6.69×10^{-13}
O^+ from O_2	4.68×10^{-14}
O^+ from O_3	4.01×10^{-14}
O_2^+ from O_2	6.69×10^{-13}
O_2^+ from O_3	3.35×10^{-13}
O_3^+ from O_3	6.69×10^{-13}

Table 6.4: Calculated Values of *sf*

Equations 6.8, **6.7** and **6.6** to obtain the TPD traces corresponding only to the desorption of [O], [O_2] and [O_3] from the silica surface (see **Figure 6.4a**, **b** and **c** respectively). Overall, the results reveal the majority of the desorption species is [O_2]

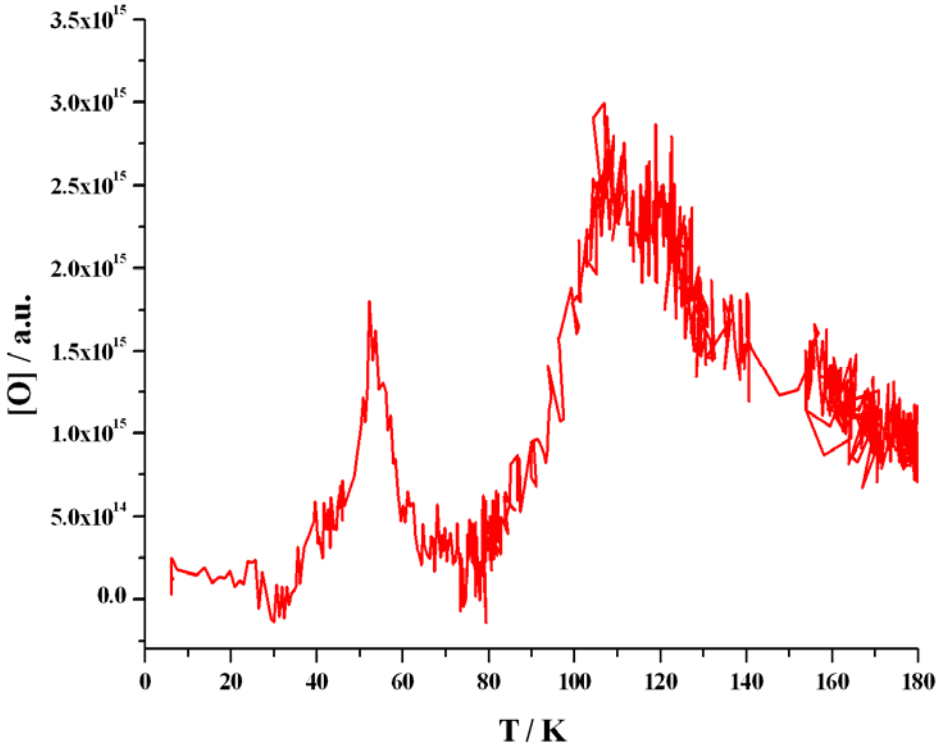

Figure 6.4a: [O] Estimate from the TPD Data Modified Using **Equation 6.8**

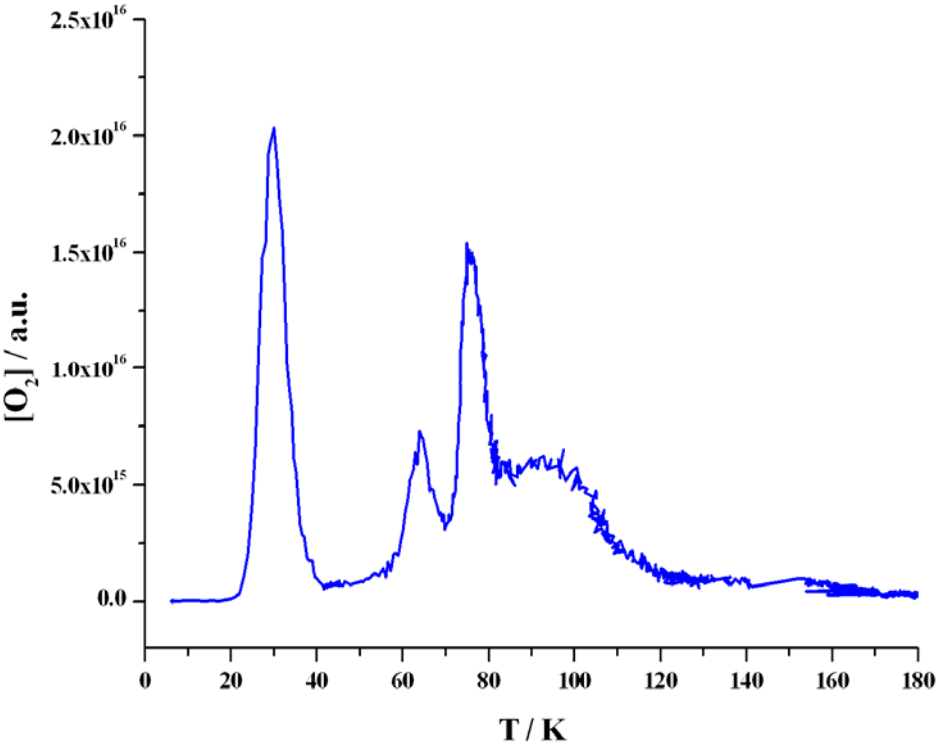

Figure 6.4b: [O_2] Estimated from the TPD Data Modified Using **Equation 6.7**

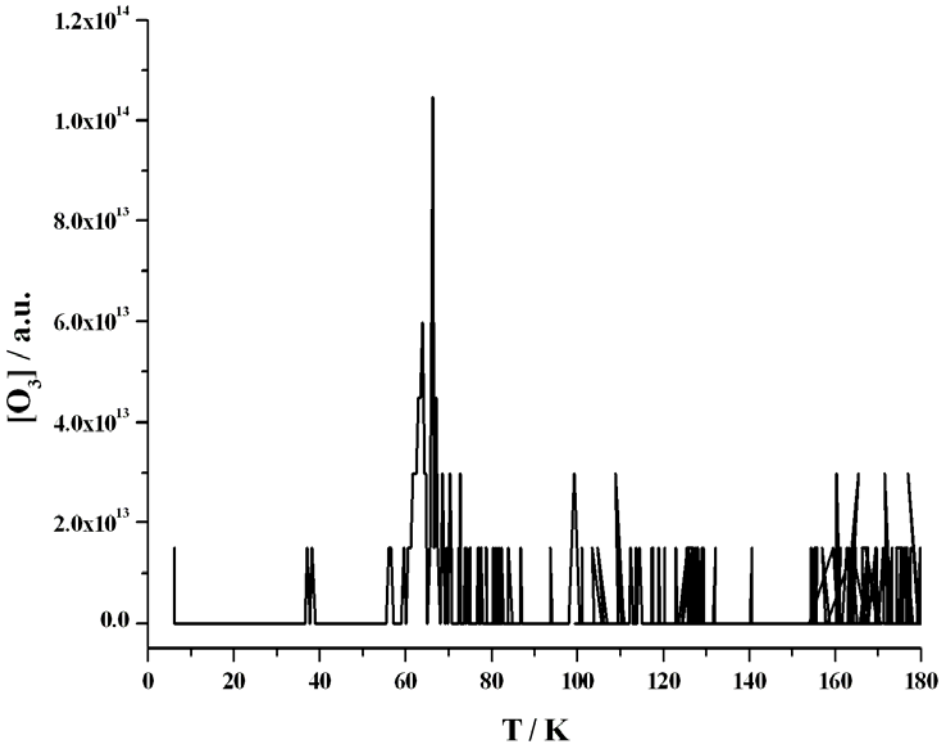

Figure 6.4c: [O_3] Estimated from the TPD Data Modified Using **Equation 6.6**

with [O_3] having the smallest concentration. From these observations, the formation of O_3 and O_2 molecules was concluded to have occurred on the surface. A simple reaction mechanism describing the formation of these species is displayed in **Figure 6.5** through a mixture of Langmuir-Hinshelwood and Eley-Rideal reactions. This reaction mechanism also includes the beam dosing reaction steps. However, studies performed by other research groups concluded that the actual surface formation mechanism for O_2

$$O(beam) \rightarrow O(ads)$$
$$O_2(beam) \rightarrow O_2(ads)$$
$$O(ads) + O(ads) \rightarrow O_2(ads)$$
$$O(g) + O_2(ads) \rightarrow O_3(ads)$$
$$O(ads) + O_2(ads) \rightarrow O_3(ads)$$

Figure 6.5: Simple Reaction Mechanism for the Formation of O_2 and O_3

and O_3 is more complicated, particularly when the change in the silica surface temperature is taken into account. For example, solid multilayer coverages of O_2 can exist in three different crystalline phases: α-O_2 (monoclinic) below around 23.9 K [5]; β-O_2 (rhombohedral) between approximately 23.9 and 43.6 K [6]; and γ-O_2 between approximately 43.6 and 54.4 K [6]. These different crystalline phases were not considered as a possibility for the non-zeroth desorption kinetics observed in the multilayer O_2 TPD experiments on silica discussed in **Chapter 4** (and further explored in **Chapter 5**) as the adsorption and desorption of the O_2 molecules occurred in the β-O_2 temperature range. However, as the base surface temperature in this preliminary experiment was lower then the change from α- to β-O_2 would need to be considered in the reaction mechanism for multilayer coverages.

From this single experiment the kinetic behaviour and parameters cannot be determined accurately. However, an attempt was made to assign the desorption peaks for [O], [O_2] and [O_3].

The initial comparison of the TPD data was made with the corresponding 30 minute O_2 molecular beam dose TPD experiment from bare silica previously shown in **Chapter 4** (see **Figure 6.6**). The desorption of O_2 from silica using the molecular beam occurred at a surface temperature approximately 10 to 15 K higher than the first O_2 desorption peak observed using the atomic beam (overlaid on **Figure 6.6**). This difference is too high to be considered to be due to the difference in the temperature calibration when the sample heater was replaced. The lower base surface temperature of approximately 15 K could suggest that the observed O_2 desorption peak was from α-O_2 instead of β-O_2 previously observed in **Chapter 4**. However, the intensity of this peak implies that O_2 molecules must have formed on the surface. The work performed by Sivaraman *et al*. concluded that O atoms can diffuse at surface temperatures as low as 15 K [1]. As a consequence, the first [O_2] desorption feature in **Figure 6.4** could be the desorption of O_2 formed on the surface by the reaction of two O atoms (**Figure 6.7**). The amount of energy released from this reaction would be equivalent to the corresponding O_2 dissociation energy. As previously discussed in **Chapter 3**, the lowest spin allowed dissociation of O_2 to form two O(^{3}P) atoms requires roughly 580 kJ mol^{-1} and occurs through the $c^1\Sigma_u^-$, $A'^3\Delta_u$ and $A^3\Sigma_u^+$ molecular excited states. The release of this amount of energy upon the formation of an O_2 molecule may have resulted in the early

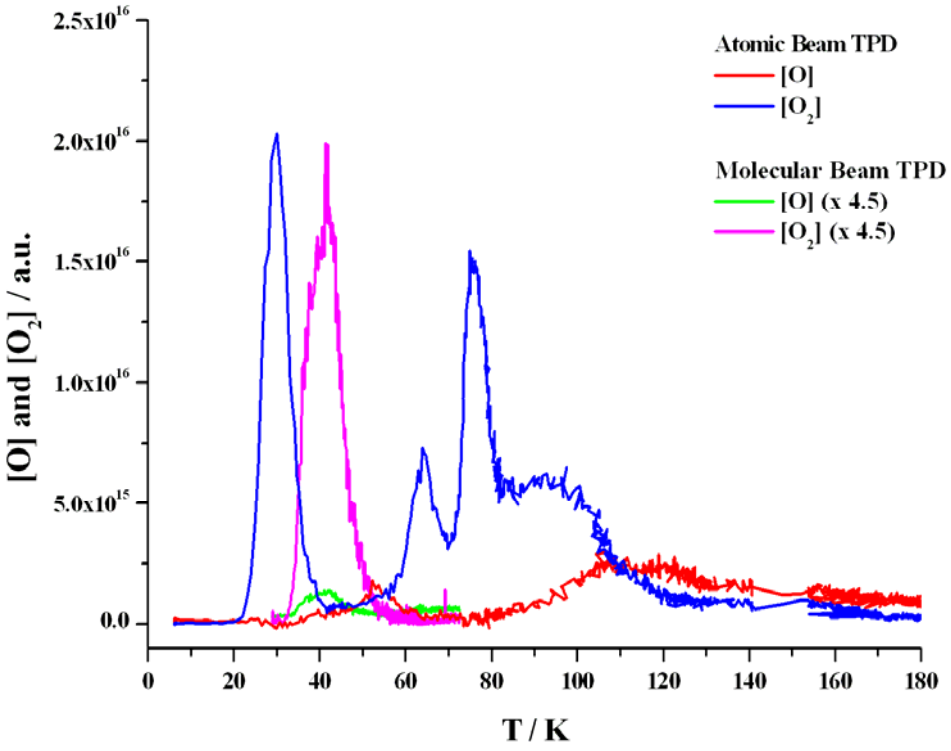

Figure 6.6: [O] and [O_2] Estimated from the Atomic Beam TPD Data Plotted with the Corresponding Values Obtained from the Molecular Beam TPD Experiment (see **Section 4.3**)

$$O(ads) + O(ads) \rightarrow O_2^*(ads)$$

$$O_2^*(ads) \rightarrow O_2^*(g)$$

Figure 6.7: Possible Surface Formation and Desorption Mechanism for the First Mass 32 Desorption Feature in **Figure 6.4**

desorption of the species. However, if the O atoms were diffusing at 15 K, then the resulting O_2 desorption peak would be expected to start at a similar temperature. The results from this preliminary TPD experiment reveals that this O_2 desorption peak does not occur until approximately 20 K suggesting that the diffusion of the O atoms is delayed. To deduce if this is the case, further O beam dose TPD experiments from bare silica would be required for a range of atomic beam irradiation times.

Additionally, this first [O_2] desorption peak also has a very small accompanying [O] desorption peak which suggests that some of the O atoms desorbed before the atoms could react to form O_2 or O_3.

An extremely small peak in the [O_2] signal is observed in **Figure 6.4** which occurs at roughly the same desorption peak temperature found for O_2 desorbing from silica (**Figure 6.6**) suggesting that this peak could be the desorption of O_2 from the silica sample. However, this feature is only just visible above the background level preventing any accurate assignment being made. In the future, additional atomic O beam irradiated silica TPD experiments could be performed for a range of irradiation times and the results compared with atomic O beam irradiated O_2 on silica TPD experiments to explore this desorption pattern in more detail.

The remaining desorption peaks were assigned based on those results in the literature. The next desorption peak to be considered occurred at approximately 52 K and was only observed for [O]. The origin of this peak was unclear as all the O and O_2 species were expected to have desorbed from the silica surface before this temperature. One possible suggestion is that these O atoms became trapped during the formation of amorphous O_3 and were release as a volcano when the O_3 molecules crystallised at around 47 K [1]. However, if this was the case then the [O] desorption peak would have been expected to occur at a slightly lower surface temperature.

The next collection of desorption peaks to be assigned were the [O_2] and [O_3] features occurring at approximately 65 K. The [O_3] peak corresponds to the desorption of O_3 from the silica surface and is in good agreement with those observations made by Sivaraman *et al*. [1] and Mokrane *et al*. [7] for O_3 desorbing from 5 keV electron irradiated O_2 films and from ASW films respectively. The origin of the O_3 species suggests that the adsorbed O atoms diffused and reacted efficiently with O_2 molecules to form O_3. Initially these species could resulted in the formation of [O_3…O] complexes, as observed in the combined RAIRS and TPD experiments performed by Sivaraman *et al*., from which the O atoms in the complex could react with neighbouring O_2 molecules to form [O_3…O_3] dimer complexes, O_3 monomers or lead to the formation of $(O_3)_n$ clusters [1]. Additionally, the formation mechanism of O_3 becomes more complicated if the amorphous to crystalline phase change is included at around 47 K. However, the formation mechanism of O_3 cannot be determined in this much

detail from TPD analysis alone. In the future, additional atomic O beam dose TPD RAIRS experiments could be performed to deduce the O_3 formation mechanism on silica in detail. Further information could be obtained by simulating the data under experimental heating rates before applying the model to the conditions found in dense molecular cloud environments. The results obtained from these simulations may also reveal why O_3 has yet to be detected in the ISM [8].

The origin of the accompanying intense [O_2] peak at 65 K was initially unexpected as all the O_2 molecules were expected to have desorbed from the silica at a lower surface at temperature. This desorption peak was unlikely to be caused from trapped O_2 in the O_3 ice as the intensity of the [O_2] peak was considerably larger than the corresponding [O_3] peak. The peak may have occurred through an O_3 destruction reaction step on the silica surface equivalent to that in the gas phase Chapman Mechanism (see **Figure 6.8**) [9] suggesting that more O_3 molecules were formed on the silica surface then implied in **Figure 6.4c**. Additionally, the large [O_2] desorption peak could include a proportion of desorbing O_3 molecules from the silica surface as the O_2^+ from O_3 cracking fraction could be underestimated which would also suggesting that more O_3 molecules were formed on the surface than the current results reveal. In the future, the O_2^+ from O_3 cracking fraction could be calculated using the same procedure as for O^+ from O_2.

$$O(ads) + O_3(ads) \rightarrow 2O_2(ads)$$

Figure 6.8: Possible O_3 Surface Destruction Reaction

The next set of desorption features occurs at approximately 75 K and was only observed for [O_2]. However, the following [O_2] feature is broad in shape implying the desorption of O_2 from the cold finger. Previous observations using the dual atomic beam apparatus revealed that between the desorption peaks of the species desorbing from the silica sample and the cold finger lies the desorption peak corresponding to the desorption from the sample mount. As a consequence, the [O_2] desorption peak at 75 K was assigned to the desorption of O_2 from this nearby surface. However, the broad desorption feature for O occurs as the surface temperature increases further and peaks at approximately the same temperature where the shoulder on the broad [O_2] peak was observed. This suggests the first peak in the broad [O_2] signal could be assigned to the desorption of surface formed O_2 molecules from the cold finger and the shoulder (with

the accompanying [O] peak) the desorption of adsorbed O_2 molecules. Desorption of O and O_2 from these surfaces at higher temperatures with respect to the silica sample was observed as the heating rate for these surrounding surfaces was slower. Additionally, if the heating ramp had not been terminated at a silica sample temperature of 180 K then a similar desorption features for [O_3] would have been observed when the sample mount and cold finger had reached approximately 65 K.

The assignment for the possible origins of the desorption peaks discussed above is displayed in **Figure 6.9**. However, further atomic O beam dose TPD experiments on silica, ideally combined with RAIRS analysis, are required along with the proposed experiments to determine α, $[O:O_2]$ and the remaining cracking fractions to provide a more detailed analysis. In the future, O_3 on silica TPD, O_2 on O_3 on silica TPD and

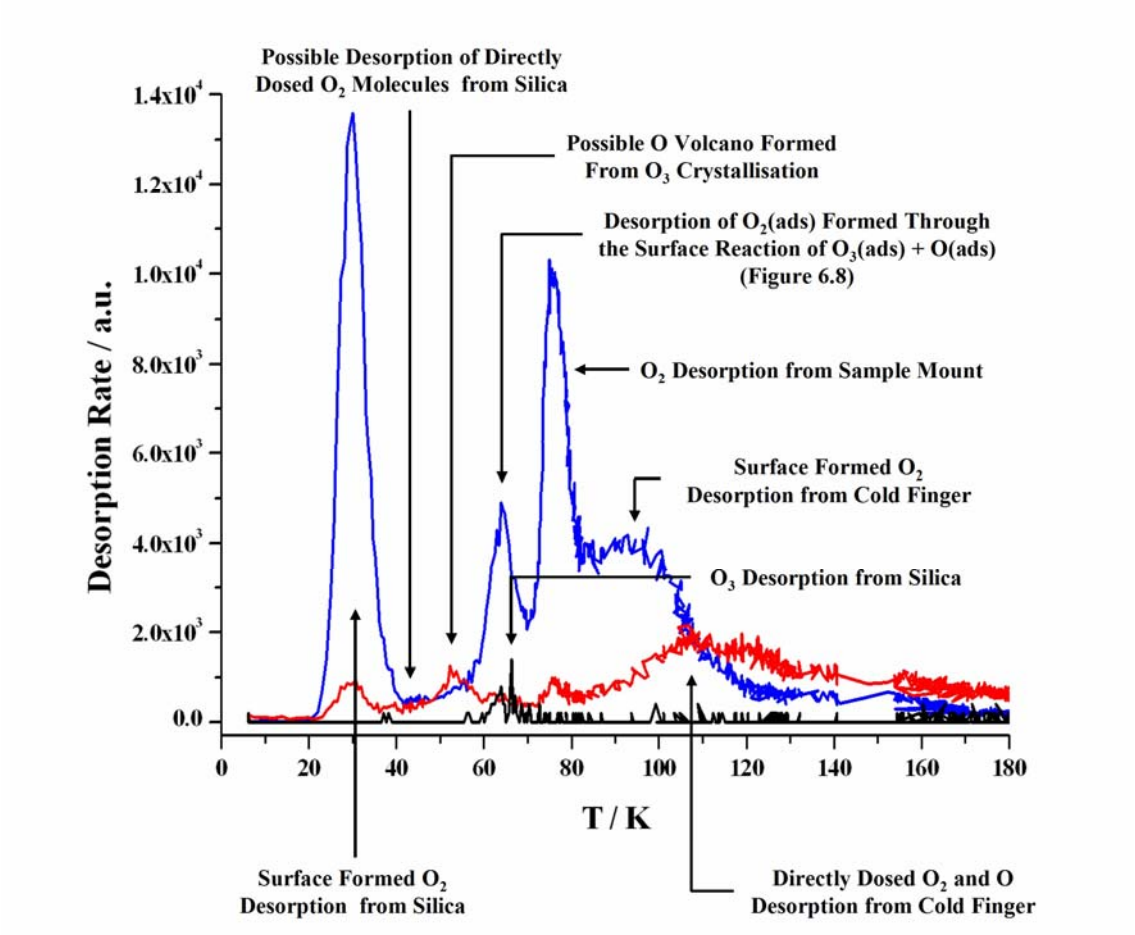

Figure 6.9: Assignment of the Masses 16 (red), 32 (blue) and 48 (× 20) (black) Desorption Peaks

atomic O beam dose on O_3 on silica TPD experiments (again ideally combined with RAIRS analysis) could be performed to understand and simulate the surface and desorption processes occurring in these experiments. Further developments could be made by applying the obtained simulation model to astronomically relevant heating rates (using the same procedure as in **Chapter 4**). The results of which may reveal why O_3 has yet to detected in the ISM.

6.3.3 Atomic O Beam Dose on 200 L of pASW on Silica

This sub-section explores the TPD results obtained from a 4 hour atomic O beam dose on 200 L of pASW on silica. The raw desorption peaks for masses 16, 18, 32, 34 and 48 (scaled by a factor of 100) are displayed in **Figure 6.10**. The base temperature for this experiment was higher than in the previous sub-section at approximately 32 K. At this base temperature, the silica surface is warm enough for both O and O_2 species to diffuse into the underlying pASW film. Analysis of the O_2 on pASW TPD experiments

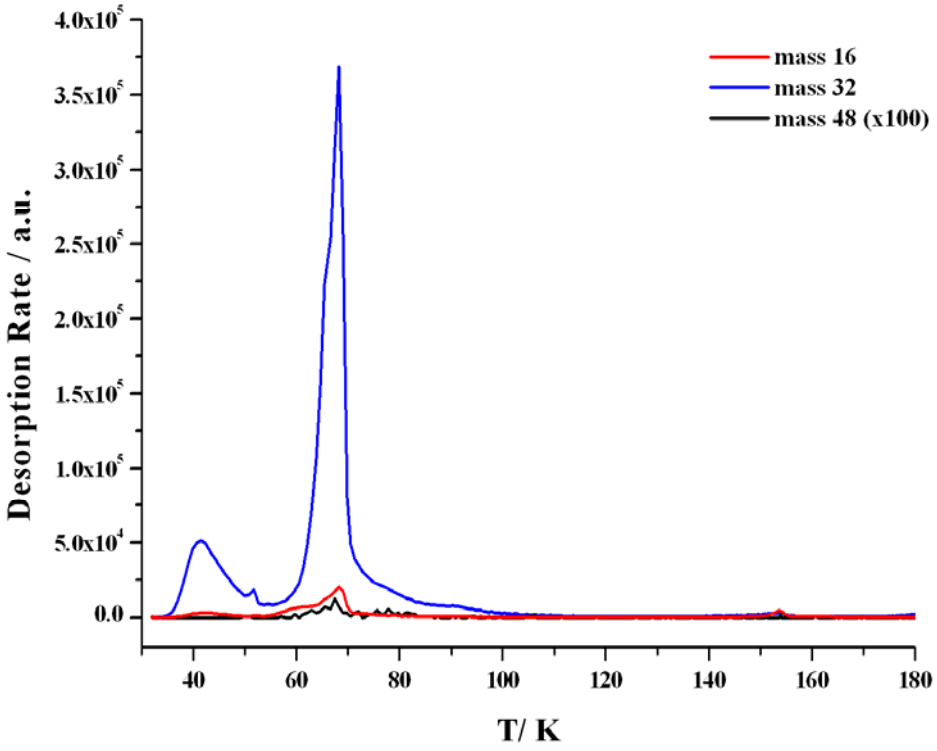

Figure 6.10a: Raw TPD Curves for Masses 16, 32 and 48 (×100)

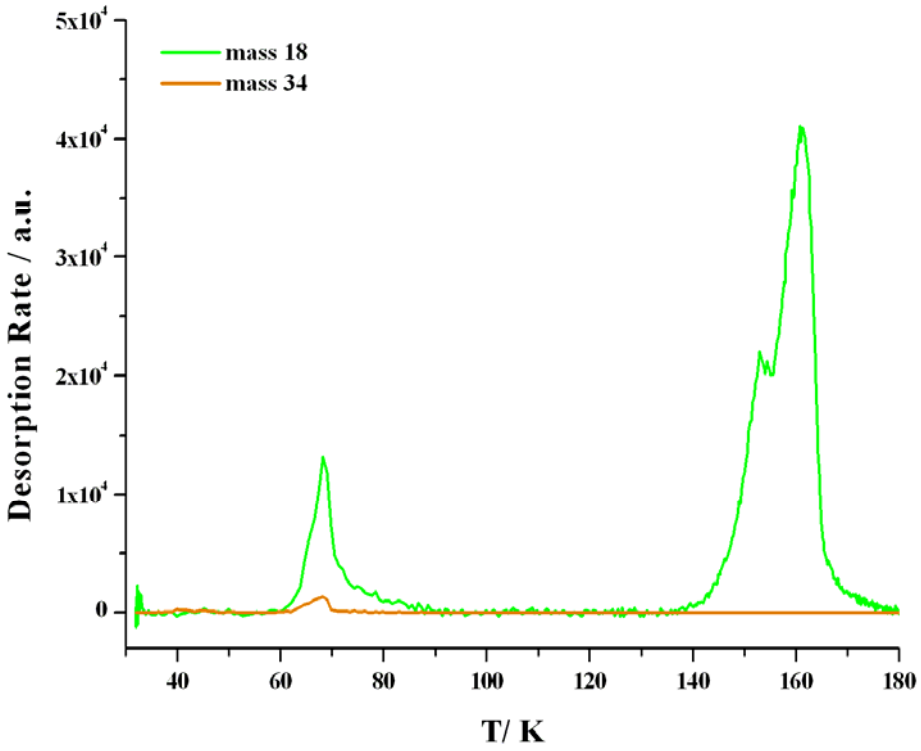

Figure 6.10b: Raw TPD Curves for Masses 18 and 34

previously discussed in **Chapter 4** also suggests that at this base temperature, the pASW to cASW phase change had started allowing for the possibility of species becoming trapped in the H_2O film.

Before the desorption peaks could be assigned, the data was analyzed to obtain an estimate of $N[O]_i$, $N[O_2]_i$ and the cracking reactions taken into consideration. $N[O]_i$ and $N[O_2]_i$ were calculated using the same procedure as described in **Section 6.3.2** and were estimated as 2.8×10^{15} atoms cm^{-2} and 5.9×10^{15} molecules cm^{-2} respectively. The cracking reactions of interest were the same as those above with additional reactions for H_2O and H_2O_2 (see **Figure 6.11**). As in the previously sub-section, the proportion of the signal intensity originating from the species desorbing from the surface, $[H_2O]$ and $[H_2O_2]$ respectively, were required. The mathematical equations for these were derived from the total ion intensities for masses 18 and 34, $H_2O^+_{tot}$ and $H_2O^+_{2_{tot}}$ respectively, (**Equations 6.10** and **6.11**) and rearranged (**Equations 6.12** and **6.13**).

$$H_2O_{tot}^+ = [H_2O] \times sf(H_2O^+, H_2O) \tag{6.10}$$

$$H_2O_{2_{tot}}^+ = [H_2O_2^+] \times sf(H_2O_2^+, H_2O_2) \tag{6.11}$$

$$[H_2O] = \frac{H_2O_{tot}^+}{sf(H_2O^+, H_2O)} \tag{6.12}$$

$$[H_2O_{2_{tot}}^+] = \frac{H_2O_2^+}{sf(H_2O_2^+, H_2O_2)} \tag{6.13}$$

$$H_2O(g) \rightarrow H_2O^+(g) + e^-$$
$$H_2O_2(g) \rightarrow H_2O_2^+(g) + e^-$$
$$H_2O_2^+(g) \rightarrow HO^+(g) + OH(g)$$
$$H_2O^+(g) \rightarrow HO^+(g) + H(g)$$
$$HO^+(g) \rightarrow H^+(g) + O(g)$$
$$HO^+(g) \rightarrow O^+(g) + H(g)$$
$$H_2O^+(g) \rightarrow O^+(g) + H_2(g)$$
$$H_2O^+(g) \rightarrow H_2^+(g) + O(g)$$
$$H_2^+(g) \rightarrow H^+(g) + H(g)$$

Figure 6.11: Additional Cracking Reaction Required for this Experiment

The cracking reactions of H_2O contribute to the value of O_{tot}^+. As a consequence, **Equation 6.3** (and, therefore, **Equation 6.8**) had to be modified to take this into account (**Equation 6.14**). Substituting in **Equations 6.6**, **6.7** and **6.12** and rearranging provided a formula for [*O*] in terms of the relevant total ion intensities and *sf* (see **Equation 6.15**). Additionally, the cracking reactions of H_2O_2, through HO^+, would also contribute to the value of O_{tot}^+. However, this was not included in the calculation of [*O*] as the equation would have required the total ion concentration of HO, HO_{tot}^+, which was not monitored in this experiment.

The value of c_{frac} for H_2O was calculated from the background dosing data obtained during the H_2O TPD experiments from bare silica (previously discussed in **Chapter 4**)

$$O^+_{tot} = [O_3]sf(O^+, O_3) + [O_2]sf(O^+, O_2) + [O]sf(O^+, O) \\ [H_2O]sf(O^+, H_2O) \tag{6.14}$$

$$[O] = \frac{\left(O^+_{tot} - \frac{O^+_{3_{tot}} sf(O^+, O_3)}{sf(O^+_3, O_3)} - \frac{sf(O^+, O_2)\left(O^+_{2_{tot}} - \frac{O^+_{3_{tot}} sf(O^+_2, O_3)}{sf(O^+_3, O_3)} \right)}{sf(O^+_2, O_2)} - \frac{H_2O^+_{tot} sf(O^+, H_2O)}{sf(H_2O^+, H_2O)} \right)}{sf(O^+, O)} \tag{6.15}$$

and was estimated as 0.010±0.003 (**Table 6.5**). Assuming the same value of s_{factor} previously calculated in **Section 6.3.2** for O_2, the additional values of *sf* were obtained using the same procedure as before (**Table 6.6**). These values were then applied to the TPD data using **Equations 6.15**, **6.7**, **6.6**, **6.12** and **6.13** to obtain the TPD traces corresponding only to the desorption of [O_3], [O_2], [H_2O], [H_2O_2] and [O] from the silica surface respectively. **Figure 6.12** displays the resulting *sf* applied TPD traces.

Cracking Ions	c_{frac}
O^+ from H_2O	0.010±0.003

Table 6.5: Additional c_{frac} Values for Different Cracking Reactions

Cracking Ions	***sf* / mbar counts^{-1}**
H_2O^+ from H_2O	6.69×10^{-13}
$H_2O_2^+$ from H_2O_2	6.69×10^{-13}
O^+ from H_2O	6.69×10^{-15}

Table 6.6: Addition Required Values of *sf*

Unlike in the previous sub-section, this TPD experiment could not be compared directly with the corresponding O_2 molecular beam dose on pASW TPD experiment on silica as the longest molecular beam dose performed was 90 minutes. However, the TPD results

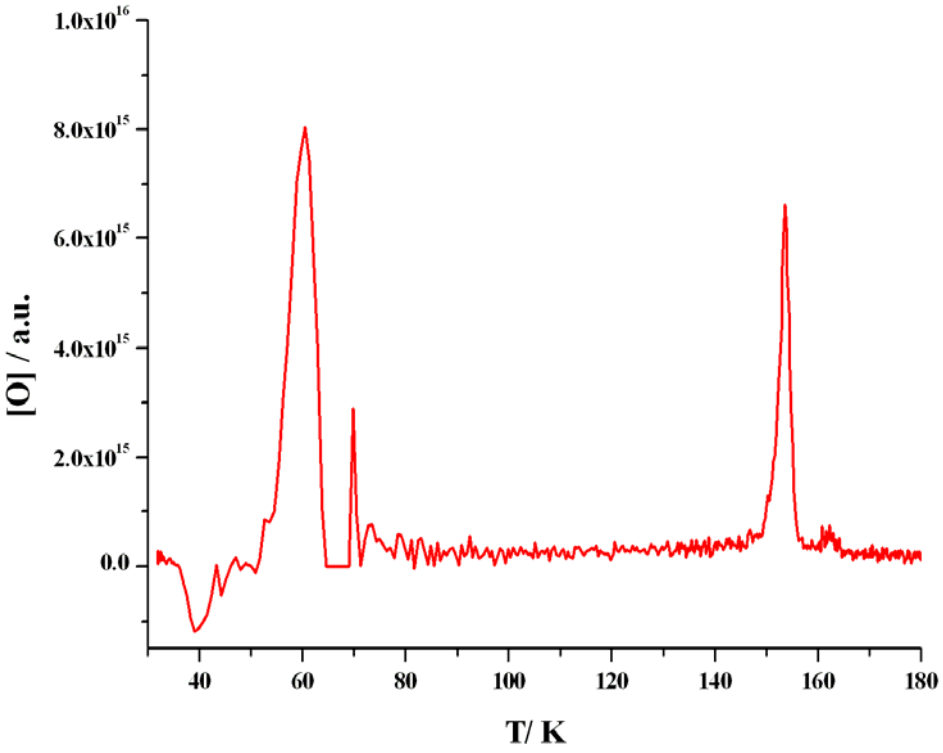

Figure 6.12a: [O] Estimated from the TPD Data Modified Using **Equation 6.15**

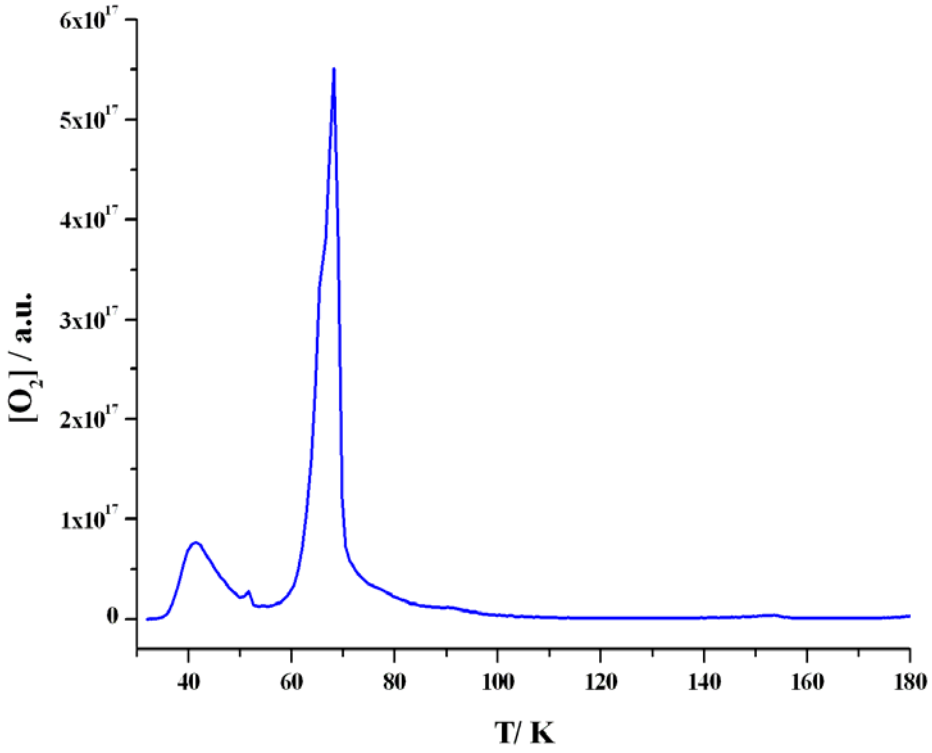

Figure 6.12b: [O_2] Estimated from the TPD Data Modified Using **Equation 6.7**

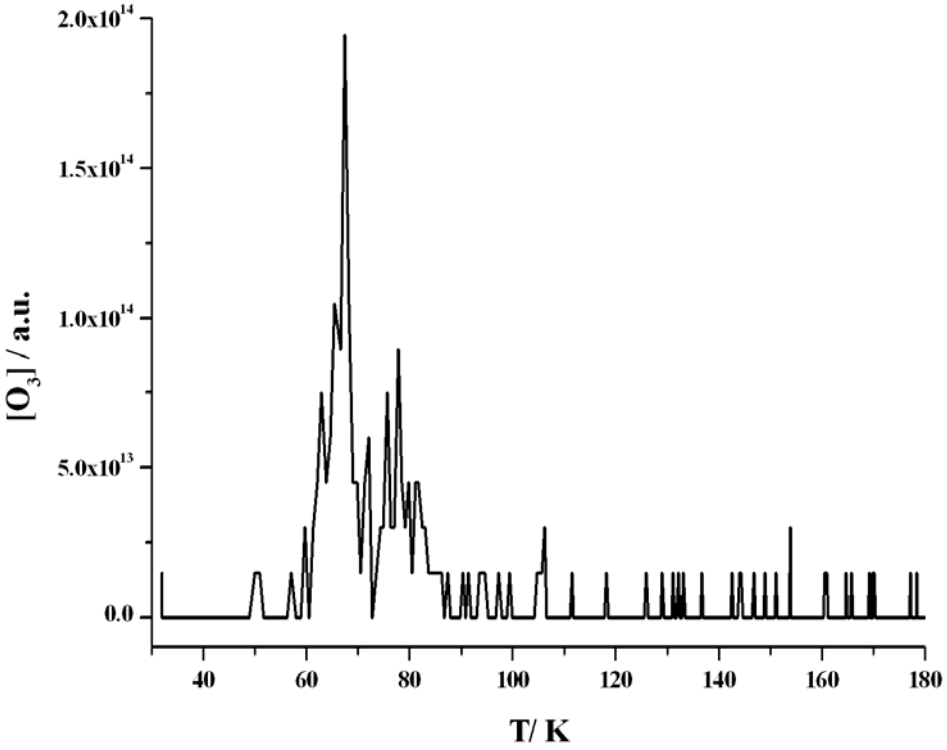

Figure 6.12c: [O_3] Estimated from the TPD Data Modified Using **Equation 6.6**

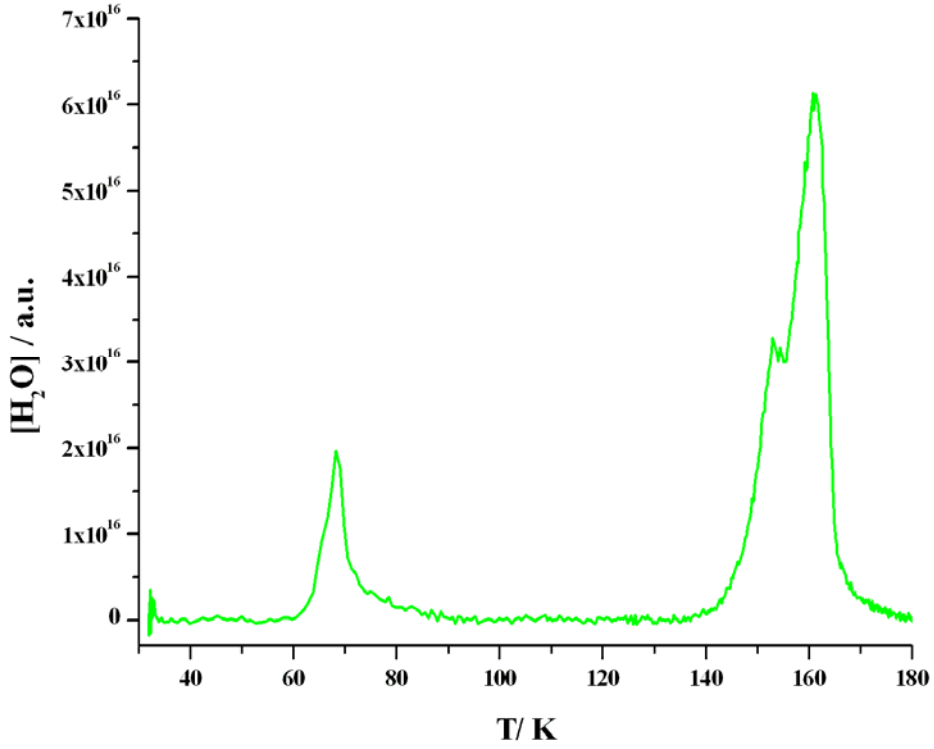

Figure 6.12d: [H_2O] Estimated from the TPD Data Modified Using **Equation 6.12**

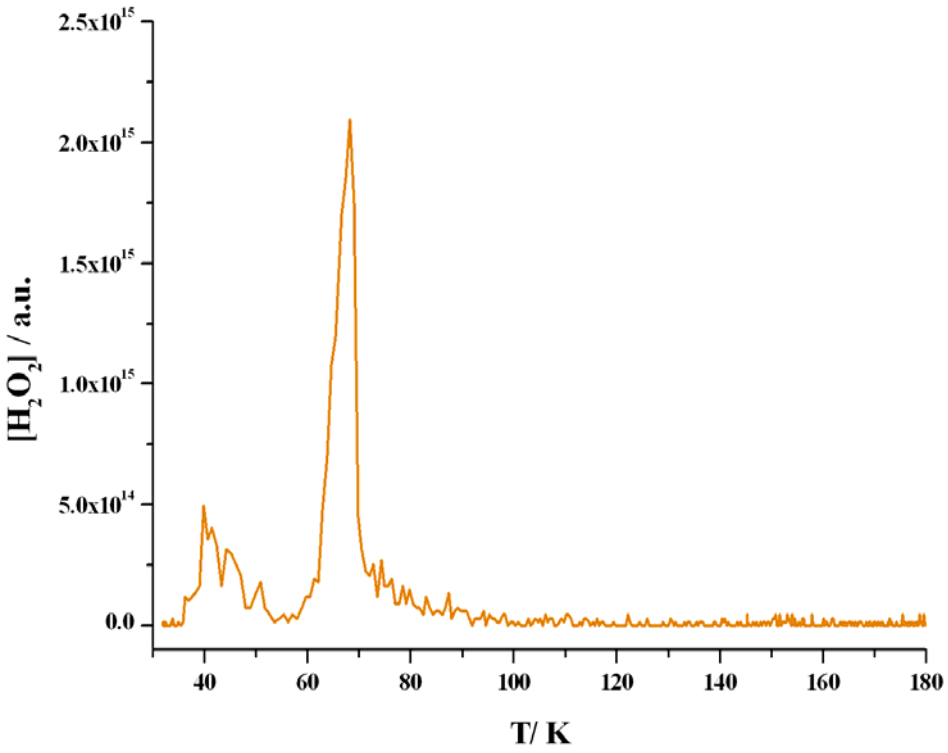

Figure 6.12e: [H_2O_2] Estimated from the TPD Data Modified Using **Equation 6.13**

from the molecular beam version of this experiment are overlaid in **Figure 6.13** over the estimated values of [O] and [O_2] (previously shown in **Figure 6.12a** and **Figure 6.12b**) as general comparisons between the two experiments could still be made towards assigning some of the desorption features. The lowest temperature desorption peak in **Figure 6.12** was for [O_2] and is in agreement with the first [O_2] desorption peak shown in **Figure 6.13** suggesting that this desorption peak corresponds to the desorption of non-trapped O_2 species from pASW. However, as the initial surface temperature was higher than in the previous experiment, it is unclear whether this desorption feature occurred only from directly dosed or as a mixture of surface formed and directly dosed O_2 molecules. In the future, additional atomic O beam irradiation of pASW on silica TPD experiments could be performed using a base surface temperature similar to the one obtained during the atomic O beam irradiation of bare silica TPD experiment (**Section 6.3.2**). The results from these proposed experiments could reveal a separate [O_2] desorption peak corresponding to the desorption of O_2 formed through surface reactions.

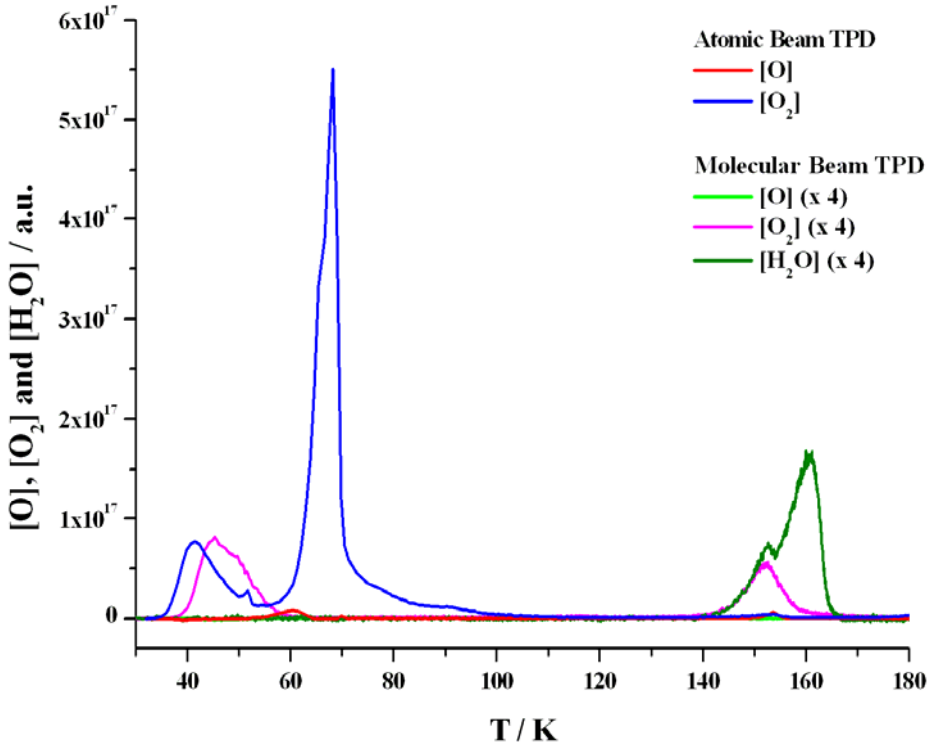

Figure 6.13: [O] and [O_2] Estimated from the Atomic Beam TPD Data Plotted with the Corresponding Values Obtained from the 90 Minute Molecular Beam TPD Experiments (see **Section 4.5**)

A relatively small [H_2O_2] desorption peak was observed just above the baseline in **Figure 6.12e** at approximately the same surface temperature as the [O_2] feature. Overall, this desorption feature implies that H_2O_2 molecules were formed on the surface. Although the exact formation mechanism cannot be determined from this experiment alone, a possible formation mechanism is shown in **Figure 6.14**. However, the first step of this mechanism can only proceed if the O atoms are in the first excited state. If the O atoms remain in their more desirable ground state (see **Chapter 3** for more details) then the formation of H_2O_2 on the surface must be formed through another mechanism. Alternatively, the appearance of this peak could suggest the atomic O beam contains a small concentration of $O(^1D)$ atoms from which the H_2O_2 molecules were formed. The co-desorption of this species with O_2 at approximately 41 K was unexpected as the formation of this species was predicted to occur in the H_2O pores and desorb during the crystallisation of the H_2O film which does not occur. Alternatively,

$$H_2O(ads) + O(^1D)(g) \rightarrow 2OH(ads)$$
$$2OH(ads) \rightarrow H_2O_2(ads)$$
$$H_2O_2(ads) \rightarrow H_2O_2(g)$$

Figure 6.14: Possible H_2O_2 Formation and Desorption Mechanism

the energy released from the surface reaction to form H_2O_2 could have been large enough to promote the species to desorb. In the future, additional atomic O beam dose on pASW on silica TPD RAIRS experiments could be performed to further explore the formation and desorption mechanism of H_2O_2. Simulations of this data and applying this model to the icy mantles coating interstellar dust grains in dense molecular cloud environments could reveal why this species has only recently been detected in the ISM [10].

The double peak structure for [H_2O] starting at approximately 140 K is in good agreement with the cASW and CSW desorption peaks determined in the TPD experiments performed in **Chapter 4** (see **Figure 6.12d** and **Figure 6.13**). However, the accompanying [O_2] molecular volcano peak with the cASW desorption peak is considerably smaller in the atomic beam experiment, especially since the irradiation dose was 4 hours rather than 90 minutes (**Figure 6.12b** and **Figure 6.13**). This observation could be a result of fewer O_2 molecules becoming trapped in the H_2O film or because the background dosing technique in this experiment used a glass tube to direct the gas onto the surface resulting in a larger initial surface concentration of H_2O. Additionally, a molecular volcano peak for [O] was also observed (**Figure 6.12a** and **Figure 6.13**). This observation could suggest that a proportion of the O atoms did not react and had become trapped in the H_2O film during the pASW to cASW phase change or this peak may have occurred due to the assumptions made in the calculation of [*O*]. In the future, additional atomic O beam dose on pASW TPD experiments using a range of atomic beam irradiation times could be performed to explore the trapping processes of O in the H_2O film in more detail.

Further assignment of the TPD data could have been made by determining the desorption peaks occurring from the cold finger as these occur at higher silica surface temperatures and are broad in shape. However, in this experiment no broad desorption features were observed suggesting that the heating rate of the cold finger was slower

than in the previous experiment discussed in **Section 6.3.2** as a results of the sample heater being replaced. If the heating ramp had been applied to a higher silica surface temperature then these peaks would have appeared. This would also have enabled those desorption peaks origination from the sample mount to be assigned as these occur shortly before those from the cold finger. However, if any desorption peaks from the sample mount did occur before the heating ramp was terminated then these would be expected to occur in the later temperature regions of the TPD plots.

The desorption peak for [O_3] occurring at approximately 67 K (**Figure 6.12c**) is in good agreement to the desorption of O_3 made in the above sub-section from silica and with those experiments performed by Mokrane *et al*. [7] from ASW films. This observation again implies that O_3 was formed through O and O_2 surface reactions. Comparisons between the desorption peak intensities can not be accurately made to deduce if a larger surface concentration of O_3 was formed as the apparatus system had been altered between this experiment and the one discussed in **Section 6.3.2**. An additional O_3 desorption peak was observed at approximately 78 K which was not observed in the previous TPD experiment. This peak was unexpected as all the formed O_3 molecules were expected to desorb around 66 K. Experiments performed by Hanson and Mauersberger exploring the vapour pressure of solid O_3 revealed that below 70 K O_3 existed only in the crystalline phase [11]. When the temperature was increased to approximately 77 K the O_3 phase corresponded to either a supercooled liquid or a metastable state along with the crystalline phase. This observation was concluded to be because the O_3 triple point occurred at 79.6±0.3 K. As previously observed for the H_2O TPD experiments on silica (see **Chapter 4**), different phases of a species results in more complex desorption peak structures being observed. The double peak structure for O_3 observed in this preliminary experiment suggests that this was caused by the two different phase structures of O_3. However, further atomic O beam on pASW on silica TPD experiments are required to explore this suggestion in more detail. The additional atomic O beam dose TPD experiments on bare silica could also reveal if this double O_3 desorption peak structure appears when longer atomic beam doses were performed. Alternatively, if the results from these proposed experiments revealed that the second desorption peak was only observed when the underlying pASW film was applied then the double peak structure for O_3 could have occurred as a result of the pASW film increases the adsorption strength of the other species. As a consequence, the addition of

the pASW film could have resulted in a proportion of the O_3 molecules undergoing this phase change before desorbing.

Intense desorption features were observed accompanying the first O_3 desorption peak for all the species of interest in this experiment (**Figure 6.12**). In **Section 6.3.2**, the appearance of the [O_2] peak was suggested to have occurred through the destructive reaction step on the surface in **Figure 6.8**. Further evidence supporting this theory comes from the observation of the [O] feature which acts as a reactant in the O_3 destruction reaction shown. A proportion of the [O_2] peak could also be O_3 as the O_2^+ from O_3 cracking fraction may be underestimated. The appearance of the [H_2O] feature (**Figure 6.12d**) was unexpected as previously no desorption peaks were observed for H_2O originating from the silica sample occurring before the desorption of cASW which starts at approximately 140 K (see **Chapter 4**). Similar, the considerably smaller [H_2O_2] feature was also unexpected as the energy released from the H_2O_2 surface formation reaction was suggested to promote the desorption of this species at approximately 41 K (**Figure 6.12e**). One possible cause for the observation of the [H_2O] and [H_2O_2] peaks may have been due to an experimental artefact. Another possible cause of these desorption peaks may have been due to the approximately 580 kJ mol^{-1} of energy released in the formation reaction of O_2 from two O atoms (see **Figure 6.7**) leading to a local disruption of the H-bonding in the bulk ice. This could have resulted in some of the H_2O species only interacting through one H-bond with neighbouring molecules instead of two.

To initially deduce if the observed H_2O desorption peak was the result of disrupted H-bonding in the bulk ice, a simple CKS model was constructed. The reaction mechanism used is shown in **Figure 6.15** where *ads* represents those molecules adsorbed on the surface, *g* those in the gas-phase and *pump* those removed from the apparatus through the pumping system. The initial concentration of the H-bonded disrupted H_2O molecules was estimated as 10^{14} molecules cm^{-2} and the activation energy of desorption, E_{des}, was assumed as 24 kJ mol^{-1} which is half the value obtained for the desorption of ASW in **Chapter 4** (due to the reduction from two to one H-bonds). The kinetic order of these H-bonded disrupted H_2O molecules was unclear. Most sub-monolayer coverages generally follow first order kinetics (as observed for O_2 in **Section 4.3**). However, H_2O desorbing from silica was found to be following zeroth

$$H_2O(ads) \rightarrow H_2O(g)$$
$$H_2O(g) \rightarrow H_2O(pump)$$

Figure 6.15: Simple H_2O H-bonded Disrupted Simulation Mechanism

order kinetics even at sub-monolayer coverages (**Section 4.2**). As a consequence, the CKS model was run under zeroth and first order kinetics with the pre-exponential factor, *v*, taken as 10^{31} molecules cm^{-2} s^{-1} and 10^{12} s^{-1} respectively. The pumping rate and heating ramp were assumed to be the same as those used for the previously CKS modelled H_2O from bare silica TPD experiments.

The simulation results are displayed in **Figure 6.16** along with the estimated [H_2O] data previously shown in **Figure 6.12d**. The first order simulation occurred at a considerably higher temperature than the observed H_2O peak in the TPD experiment

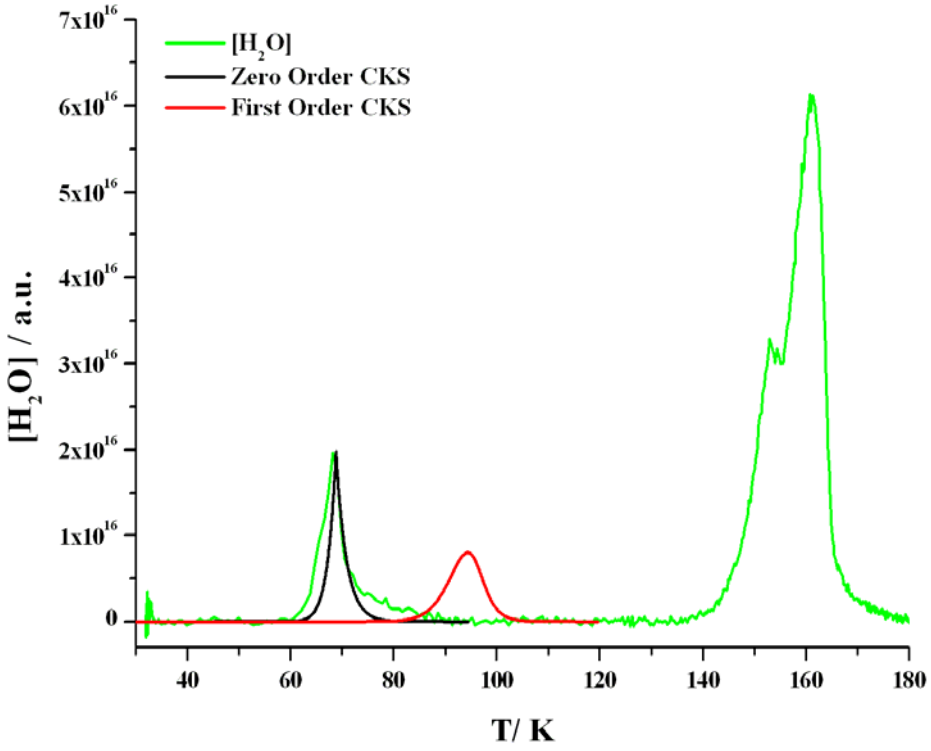

Figure 6.16: Preliminary Predicted Simple Zeroth (black) and First Order (red) Kinetic Desorption Simulations of H-bonded Distruped H_2O Compared with the Estimated Values of [H_2O] in **Figure 6.12d**

indicating that if this peak was caused by H-bonded disrupted H_2O molecules then the kinetics was unlikely to be following first order kinetics. The zeroth order simulation is in good agreement with this H_2O desorption peak. If this is the case, the corresponding observed desorption peak for H_2O_2 may have been caused from H-bonding entrapment in the H_2O film. However, although this theory simulation does provide an explanation for this unexpected desorption peak, the apparatus will need to be checked for possible artefacts and the experiment repeated for a range of atomic O beam irradiation times before a conclusion can be made.

The two remaining unassigned desorption features observed were at approximately 52 and 60 K for [O_2] and [O] respectively. The first of these occurred as a shoulder on the falling edge of the O_2 from pASW desorption peak. A similar desorption peak at this surface temperature had been observed in the previously discussed TPD experiment in **Section 6.3.2** for [O] and was suggested as an O volcano when the O_3 molecules crystallised at around 47 K. In this experiment, this desorption feature was only observed for [O_2]. However, as a longer atomic O beam irradiation time had been applied to the substrate, the larger initial surface concentration of O would have resulted in an increased probability of O atoms reacting together and desorb as O_2 during the crystallisation of O_3.

The second unassigned desorption feature for [O] is unclear as all the O atoms were expected to have desorbed or react together or with the O_2 and H_2O molecules. Interestingly, this broad feature appears to start at roughly the same silica surface temperature as the above [O_2] shoulder peak and could be the desorption of O atoms which were trapped as [O_3…O] complexes until the O_3 crystallisation. However, the proportion of [O_3…O] complexes at this surface temperature was expected to be relatively small as additional reactions to form [O_3…O_3] dimer complexes, O_3 monomers and $(O_3)_n$ clusters would have occurred. In the future, additional atomic O beam dose on pASW on silica TPD experiments could be performed (ideally combined with RAIRS analysis) to further explored the surface and desorption processes occurring in these experiments.

The assignment for the possible desorption peaks observed for the experiment discussed in this sub-section is displayed in **Figure 6.17**. The preliminary findings indicate that

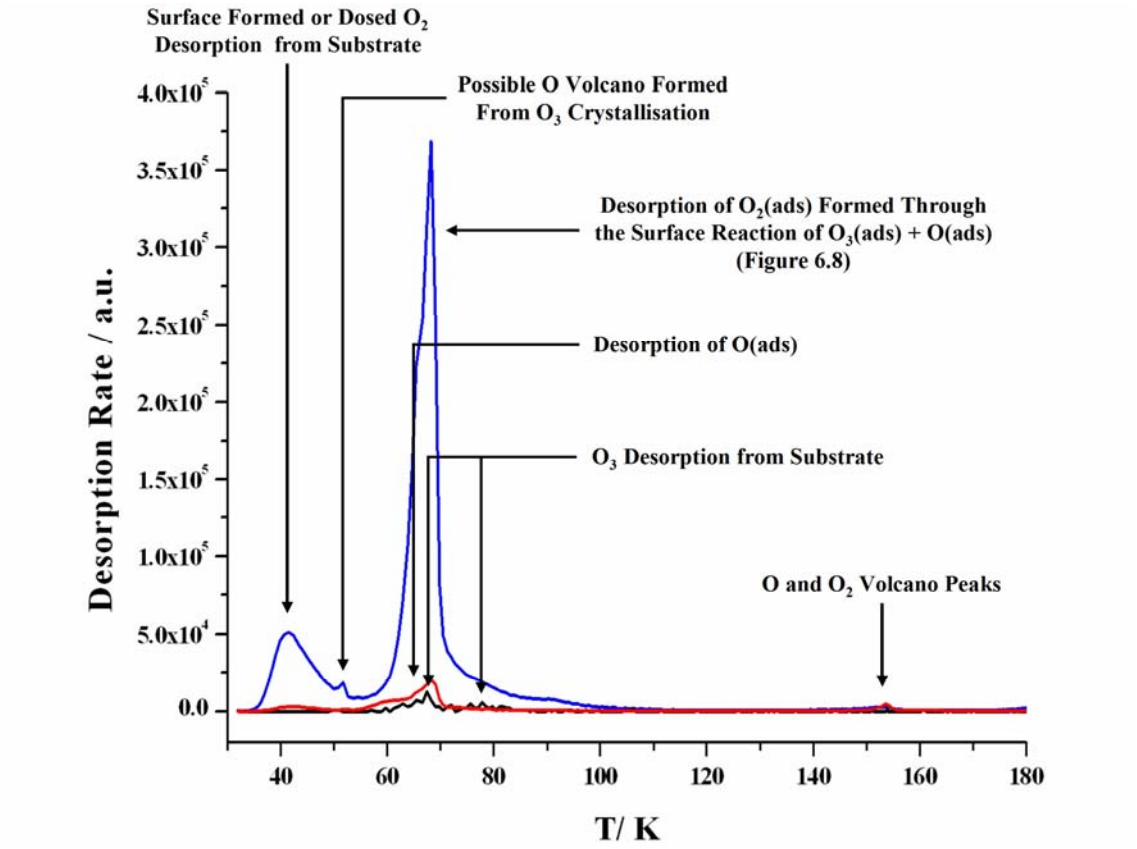

Figure 6.17a: Assignment of the Masses 16 (red), 32 (blue) and 48 (×100) (black)

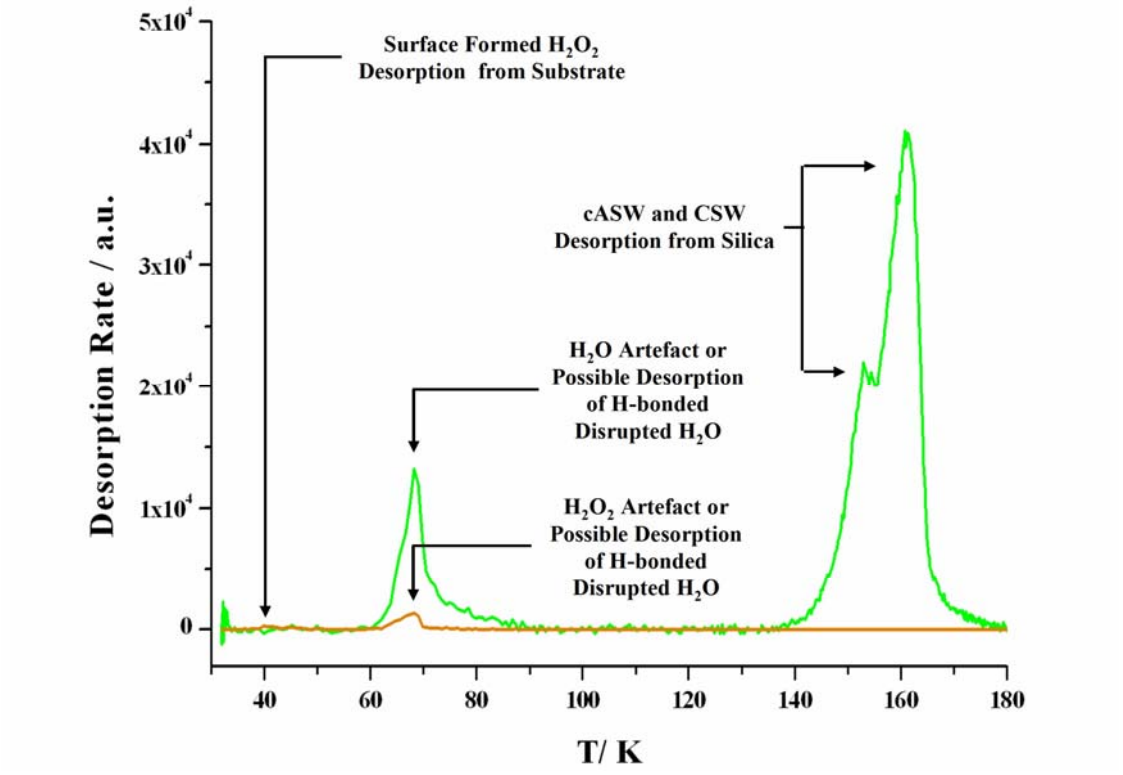

Figure 6.17: Assignment of the Masses 18 (green) and 34 (orange) Desorption Peaks

further atomic O beam dose TPD RAIRS experiments are required to provide a more detailed understanding of the surface, formation, phase change and desorption processes occurring along with the required experiments to determine α, $[O:O_2]$ and the remaining cracking fractions. In the future, the results from the planned O_3 on silica TPD, O_2 on O_3 on silica and atomic O beam dose on O_3 on silica TPD experiments would provide essential kinetic desorption and parameters to further analyze the surface processes occurring in this and future atomic O beam on pASW on silica TPD experiment.

6.3.4 Atomic O Beam Dose on 100 L of O_2 on 200 L of pASW on Silica

This sub-section describes the preliminary results for a 4 hour atomic O beam dose on 100 L of O_2 on 200 L of pASW on silica TPD experiment. The TPD plots for masses 16, 18, 32, 34 and 48 were constructed using the same procedure as in **Section 6.3.3** and are shown in **Figure 6.18**. The values of $N[O]_i$ and $N[O_2]_i$ were estimated using the same procedure as in the previous sub-sections as $2.8\times10^{+15}$ atoms cm^{-2} and $5.9\times10^{+15}$ molecules cm^{-2} respectively.

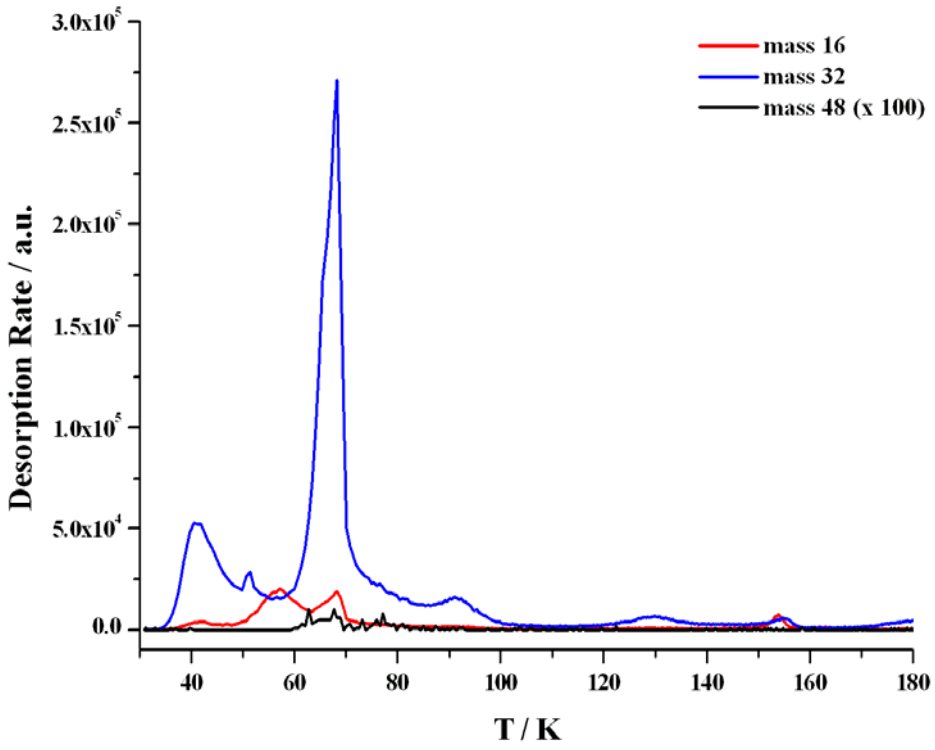

Figure 6.18a: Raw TPD Curves for Masses 16, 32 and 48 (× 100)

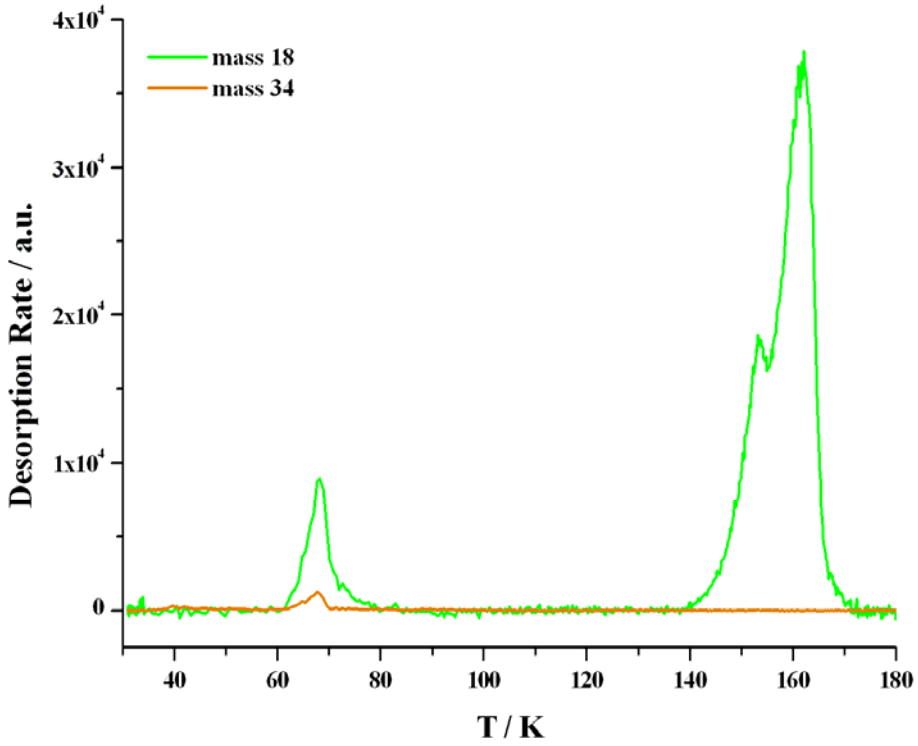

Figure 6.18b: Raw TPD Curves for Masses 18 and 34

The cracking reactions occurring in this experiment were the same as those discussed in **Section 6.3.3**. As a consequence, the same nine values of *sf* used in the above sub-section were applied to the TPD data to estimate the values of [O], [O_2], [O_3], [H_2O] and [H_2O_2] (see **Figure 6.19**). Overall, the *sf* applied TPD curves are similar to those obtained in **Section 6.3.3** allowing the desorption peaks to be assigned using the same conclusions. This was expected as the only difference between these two experiments was the addition of a 100 L background dose film of O_2 on the pASW substrate.

The lowest surface temperature desorption peaks observed were for [O_2] and [H_2O_2] at approximately 41 K which were in good agreement with those observed in the TPD experiment discussed in the previous sub-section. As a consequence, these two features were assigned as the desorption of non-trapped O_2 from the pASW substrate and the possible promoted desorption of surface formed H_2O_2 molecules respectively.

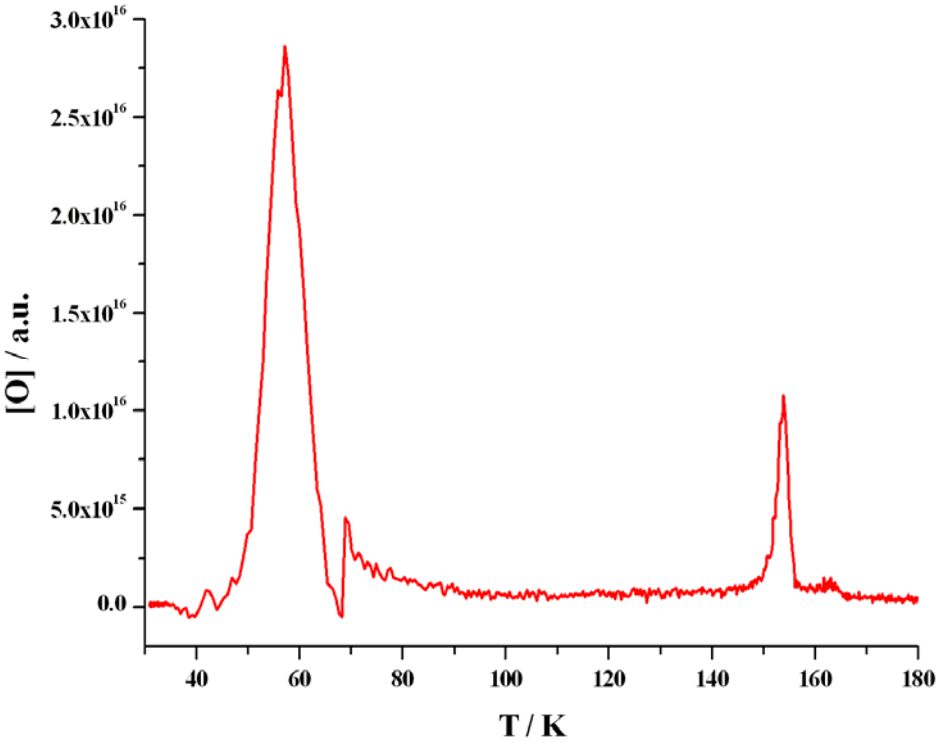

Figure 6.19a: [O] Estimated from the TPD Data Modified Using **Equation 6.15**

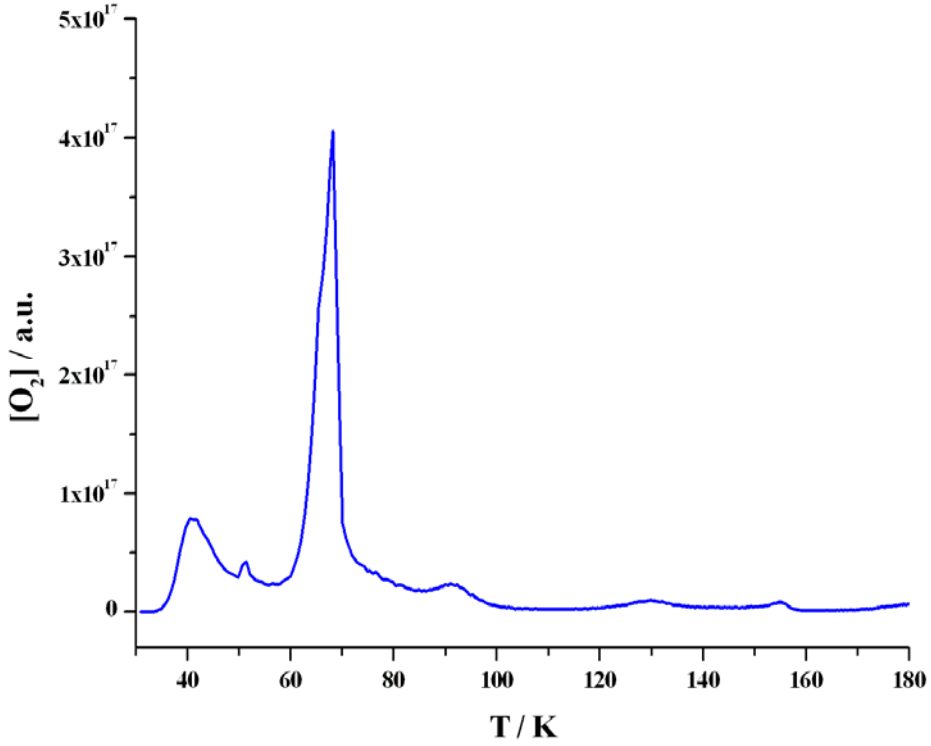

Figure 6.19b: [O_2] Estimated from the TPD Data Modified Using **Equation 6.7**

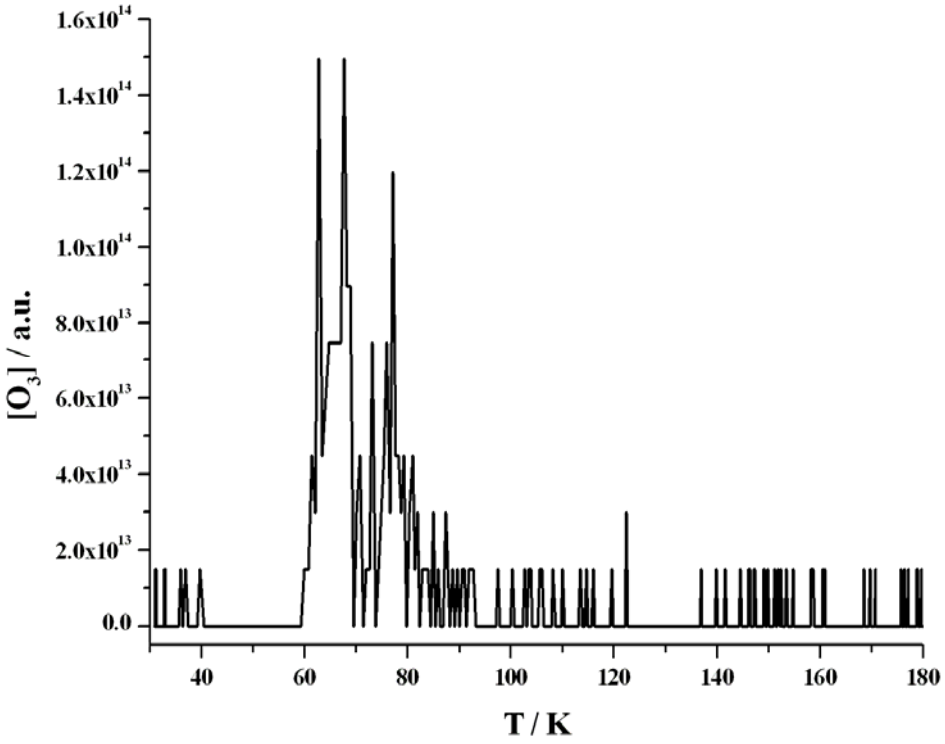

Figure 6.19c: [O_3] Estimated from the TPD Data Modified Using **Equation 6.6**

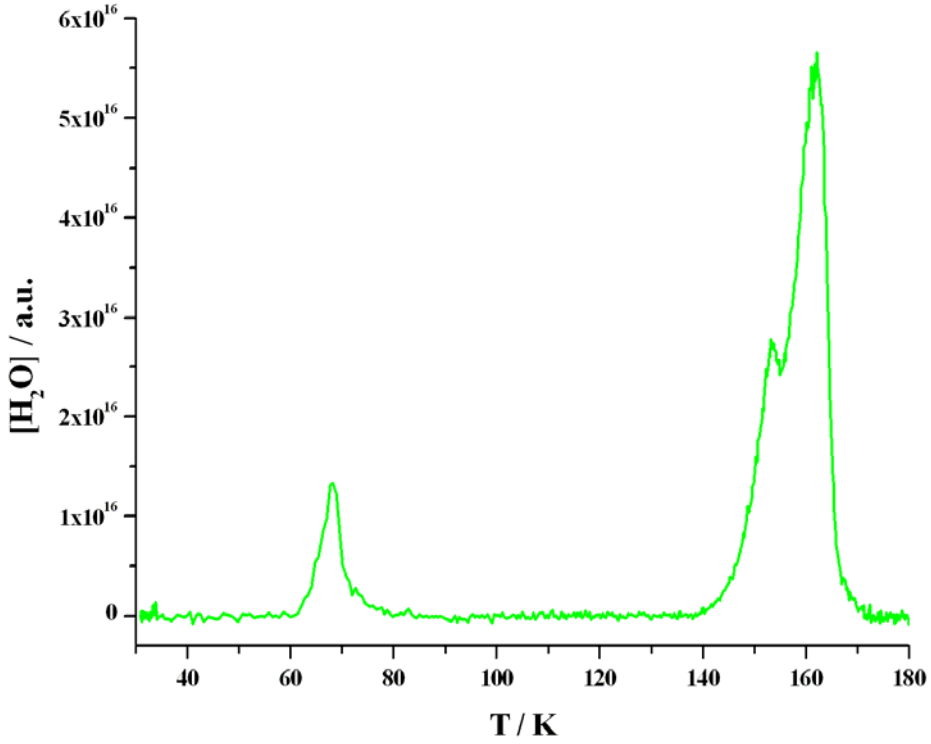

Figure 6.19d: [H_2O] Estimated from the TPD Data Modified Using **Equation 6.12**

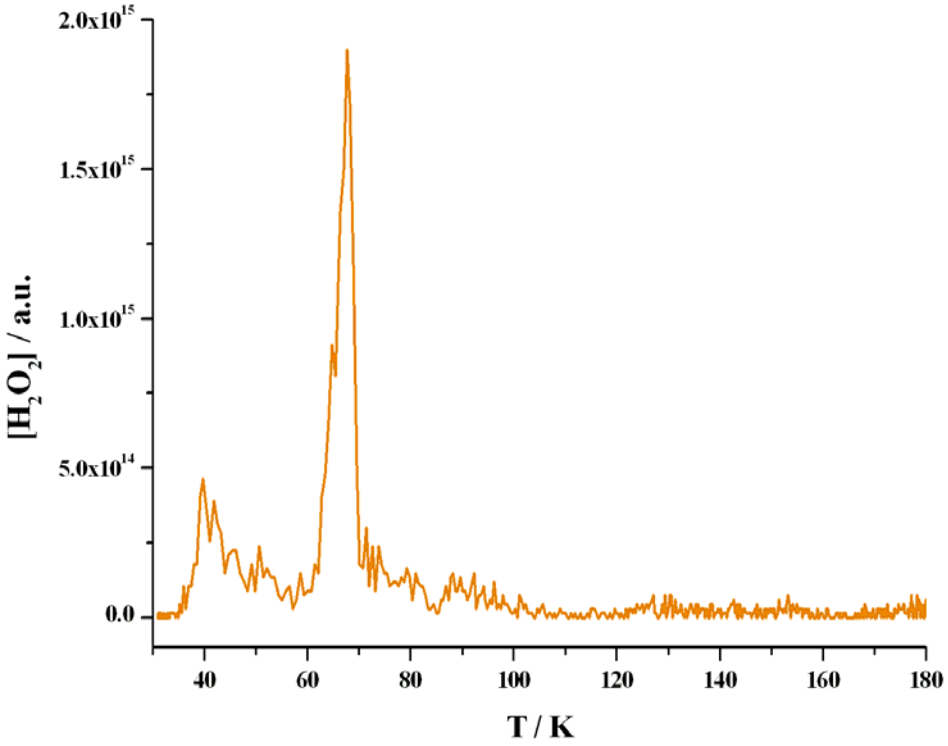

Figure 6.19e: $[H_2O_2]$ Estimated from the TPD Data Modified Using **Equation 6.13**

The next desorption peak was again observed for $[O_2]$ at approximately 52 K. This small desorption feature was observed in **Section 6.3.3** and was suggested to be a possible O_2 molecular volcano caused by the crystallisation of the formed O_3 molecules (known to occur around 47 K [1]). An additional broad mass 16 desorption peak was observed starting at approximately the same surface temperature but peaking later at around 57 K. The origin of this peak was unclear and was not observed in the experiment discussed in **Section 6.3.3**. One possible suggestion was this peak was an O volcano caused by the crystallisation of O_3 where the O atoms were initially trapped in $[O_3…O]$ complexes. However, the proportion of $[O_3…O]$ was believed to be relatively small at this surface temperature as a consequence of further O_3 surface formation reactions. An alterative suggestion was the O volcano peak could have been caused by the release of trapped O atoms during the phase change from crystalline β-O_2 (23.9 to 43.6 K) to crystalline γ-O_2 (43.6 to 54.4 K). In the future, additional atomic O beam dose on O_2 on pASW TPD (ideally combined RAIRS analysis) on silica could be performed to explore the O_3 formation and O surface processes part of the reaction mechanism in more detail.

The next collection of desorption peaks correspond to the previously assigned O_3 desorption, O_2 surface formation from O_3 and the possible H-bonded disrupted H_2O with corresponding H_2O_2 desorption at around 66 K. The observations obtained in this experiment cannot provide any more additional information on the processes occurring on the surface or the appearance of the second O_3 desorption observed at approximately 78 K. In the future, additional TPD RAIRS experiments involving directly dosed and surface formed O_3 molecules on a range of astronomically relevant surfaces could be performed to explore these processes in more detail.

Additional small desorption peaks for [O_2] were observed at approximately 91, 129 and 155 K. The origin of the first two peaks is unclear but the latter of these could be an O_2 molecular volcano as this coincides with the desorption of cASW at approximately 153 K. This molecular volcano would have been formed by the O_2 molecules (either formed by O atom reactions or adsorbed as non-dissociated beam species) which had diffused into the underlying pASW film and become trapped during the pASW to cASW phase change. As previous discussed in **Section 6.3.3**, the O_2 molecular volcano peak in this study was considerably smaller with respect to the cASW and CSW desorption peaks even though a longer beam irradiation time had been used. This was due to the background dose being directed onto the silica sample through a glass dosing tube which was not installed when the experiments described **Chapter 4** were performed. Another volcano peak approximately a tenth of the intensity of the [O_2] molecular volcano was observed for [O]. This desorption feature could suggest that not all the O atoms reacted with each other or other species either before the pASW to cASW phase change or whilst trapped inside the pores in the cASW film. However, this small peak may have occurred from the assumptions applied in calculating [O]. In the future, additional atomic O beam dose on O_2 on pASW on silica TPD experiments (ideally combined with RAIRS analysis) could be performed to explore these volcano peaks in more detail.

The start of another [O_2] desorption peak was also observed as the heating ramp was terminated. This peak may have been the start of the desorption of O_2 from the sample mount but without increasing the heating ramp the origin of this peak could not be proved.

The assignment of all the desorption peaks discussed above is displayed **Figure 6.20**. Overall, the TPD results agree well with those obtained in the previous sub-section. However, further atomic O beam dose on O_2 on pASW on silica TPD experiments (ideally combined with RAIRS analyze) are required along with all the proposed O_3 TPD RAIRS experiments and calibration experiments to determine both the O_3 and H_2O_2 formation mechanism and other surface and desorption processes occurring in these experiments in more detail.

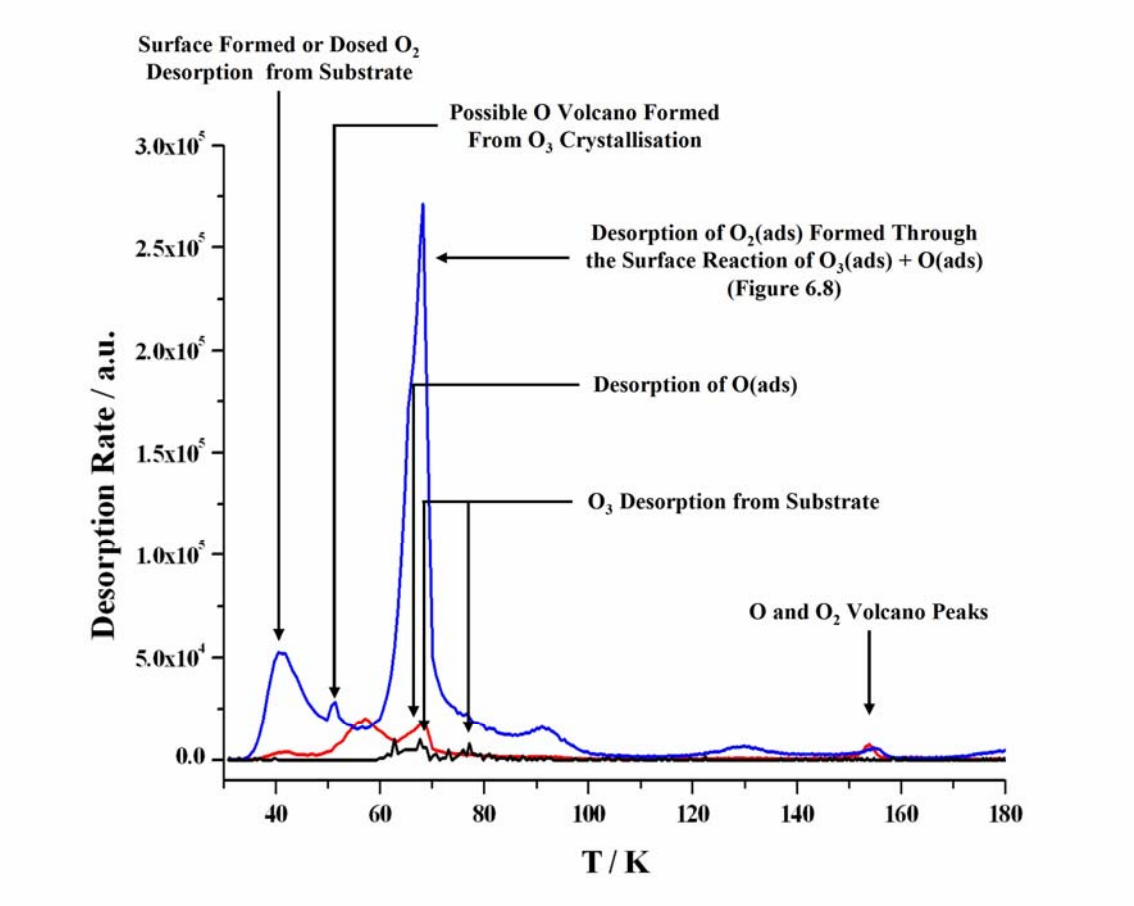

Figure 6.20a: Assignment of the Masses 16 (red), 32 (blue) and 48 (×100) (black) Desorption Peaks

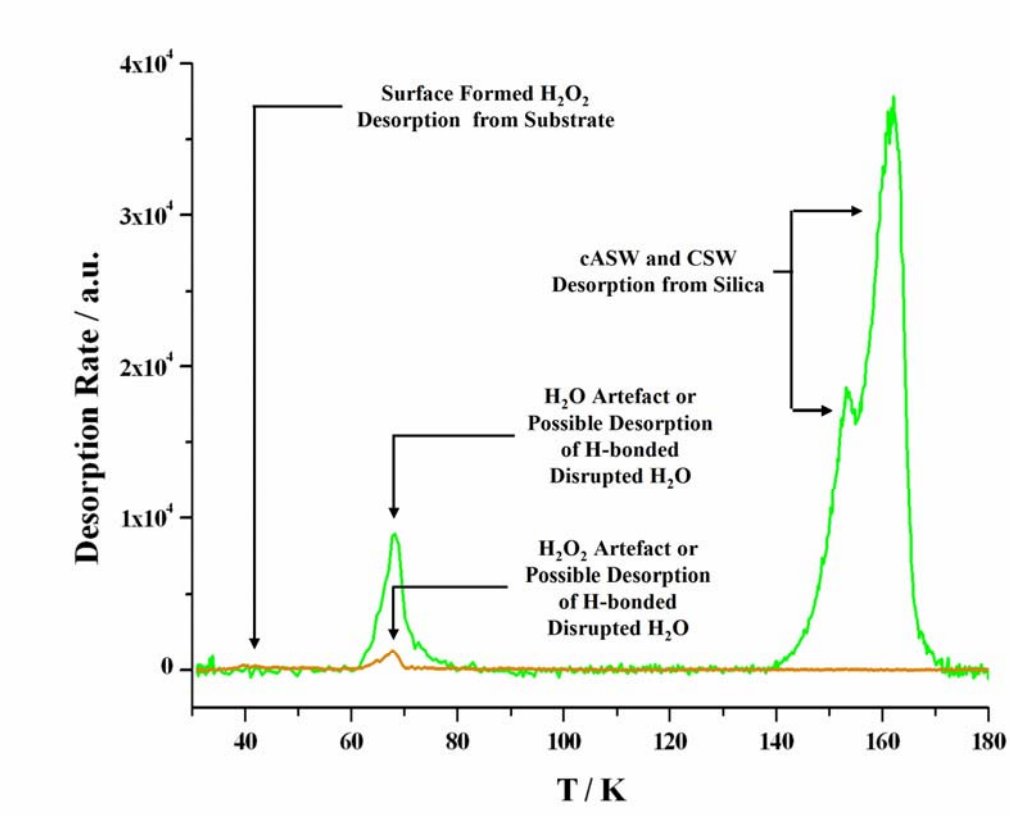

Figure 6.20b: Assignment of the Masses 18 (green) and 34 (orange) Desorption Peaks

6.3.5 Atomic O Beam Dose on 100 L of ^{13}CO on 200 L of pASW on Silica

The results of a 4 hour atomic O beam dose on 100 L of ^{13}CO on 200 L of pASW on silica TPD experiment are discussed in this sub-section. The TPD plots for masses 16, 18, 29, 32, 34, 45 and 48 were constructed using the same procedure as in **Section 6.3.3** and are shown in **Figure 6.21**. The values of $N[O]_i$ and $N[O_2]_i$ dosed onto the substrate from the atomic beam were estimated as $2.8\times10^{+15}$ atoms cm^{-2} and $5.9\times10^{+15}$ molecules cm^{-2} using the same procedure as in the previously sub-sections of this chapter.

The cracking reactions of interested were the same as those used in the TPD experiments discussed in **Sections 6.3.3** and **6.3.4** but with additional reactions for ^{13}CO and $^{13}CO_2$ (see **Figure 6.22** and **Table 6.7**). For ^{13}CO, the value of c_{frac} was calculated from the background dosing data obtained during the CO on bare silica TPD experiments (previously discussed in **Chapter 5**) and was calculated as 0.004±0.001.

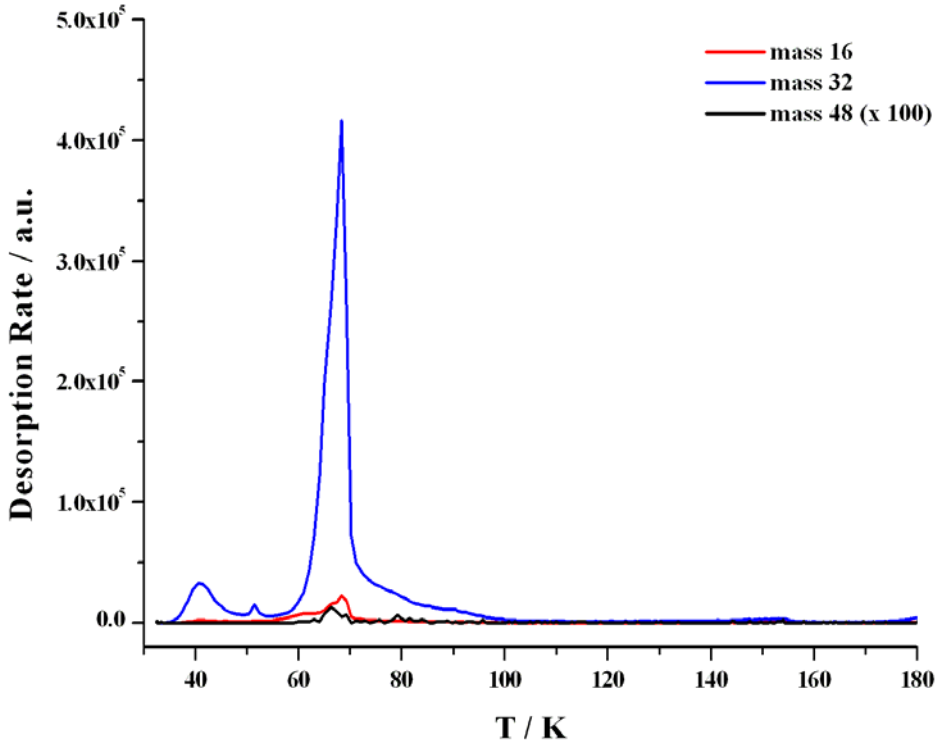

Figure 6.21a: Raw TPD Curves for Masses 16, 32 and 48 (×100)

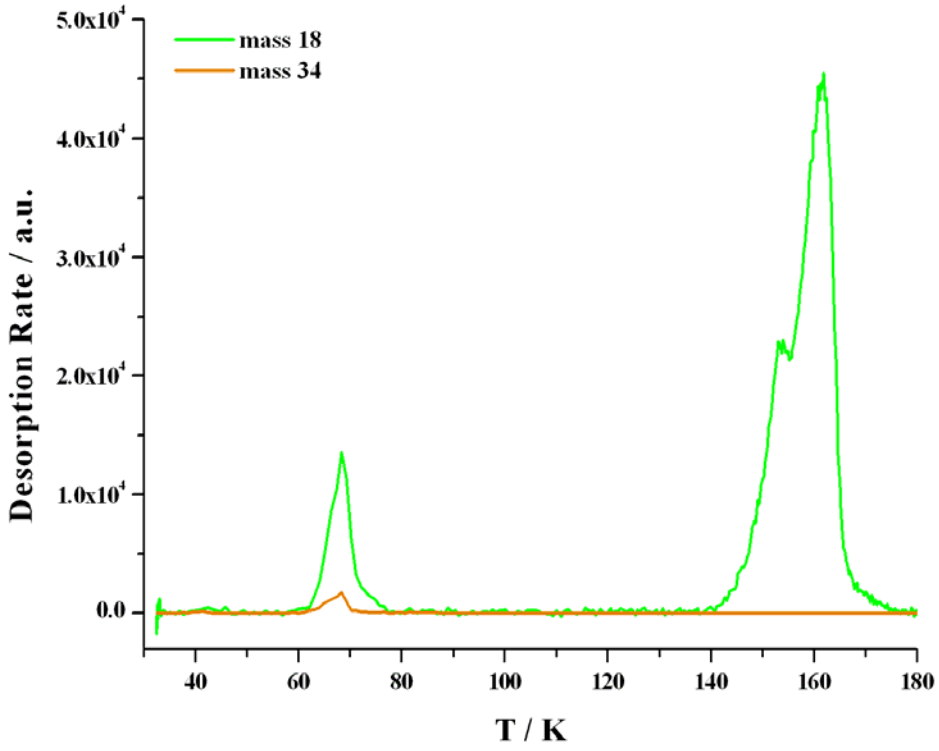

Figure 6.21b: Raw TPD Curves for Masses 18 and 34

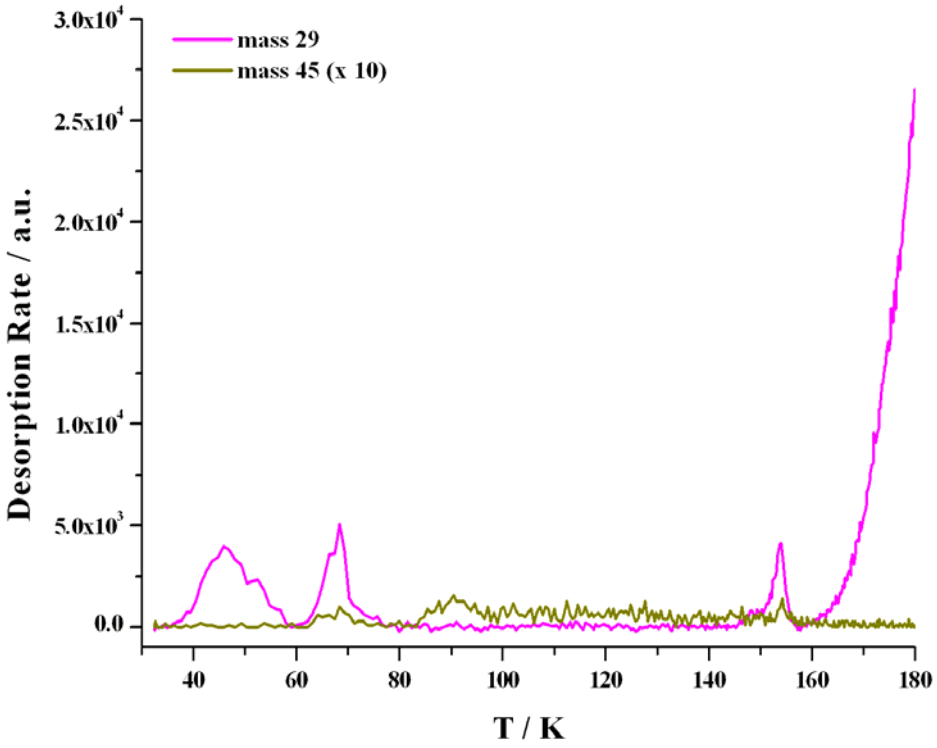

Figure 6.21c: Raw TPD Curves for Masses 29 and 45 (×10)

$$^{13}CO(g) \rightarrow {}^{13}CO^{+}(g) + e^{-}$$

$$^{13}CO_2(g) \rightarrow {}^{13}CO_2^{+}(g) + e^{-}$$

$$^{13}CO_2^{+}(g) \rightarrow {}^{13}CO^{+}(g) + O(g)$$

$$^{13}CO_2^{+}(g) \rightarrow O^{+}(g) + {}^{13}CO(g)$$

$$^{13}CO^{+}(g) \rightarrow {}^{13}C^{+}(g) + O(g)$$

$$^{13}CO^{+}(g) \rightarrow O^{+}(g) + {}^{13}C(g)$$

Figure 6.22: Additional Cracking Reaction

Cracking Ions	c_{frac}
O^{+} from ^{13}CO	0.004±0.001
$^{13}CO^{+}$ from $^{13}CO_2$ [12]	0.009±0.002
O^{+} from $^{13}CO_2$ [12]	0.009±0.002

Table 6.7: Additional Estimated Values of c_{frac}

For $^{13}CO_2$, the values of c_{frac} were both estimated from the literature as 0.009±0.002 [12]. In the future, the values of c_{frac} for $^{13}CO_2$ could be calculated from $^{13}CO_2$ background dosing experiments using the same procedure as for O_2, H_2O and ^{13}CO described in this chapter. Assuming the same value of s_{factor} for all the species (previously calculated in **Section 6.3.2** for O_2) the additional values of *sf* were determined using the same procedure as before and are shown in **Table 6.8**.

Cracking Ions	***sf***
O^+ from ^{13}CO	2.68×10^{-15}
$^{13}CO^+$ from ^{13}CO	6.69×10^{-13}
O^+ from $^{13}CO_2$	6.02×10^{-15}
$^{13}CO^+$ from $^{13}CO_2$	6.02×10^{-15}
$^{13}CO_2^+$ from $^{13}CO_2$	6.69×10^{-13}

Table 6.8: Additional Calculated Values of *sf*

As discussed previously in this chapter, the proportion of the signal intensity originating from the species desorbing from the surface were required. For $^{13}CO_2$ and ^{13}CO, the mathematical equations describing the total ion intensities of masses 29 and 45, $^{13}CO_{2_{tot}}^+$ and $^{13}CO_{tot}^+$ respectively, are displayed in **Equations 6.16** and **6.17**. The concentration of the CO_2 desorbing from the substrate, $[^{13}CO_2]$, was obtained by rearranging **Equation 6.16** to give **Equation 6.18**. For ^{13}CO, **Equation 6.18** was substituted into **Equation 6.17** and rearranged to give **Equation 6.19**. However, as the cracking reactions for ^{13}CO and $^{13}CO_2$ also contribute to the total ion signal for O then the previously derived equations in **Section 6.3.3** (**Equations 6.14** and **6.15**) no longer holds. The total ion concentration of O_{tot}^+ in this experiment is shown in **Equation 6.20**. Rearranging this equation and substituting in **Equations 6.6**, **6.7**, **6.12**, **6.18** and **6.19** provides the concentration of O desorbing from the substrate, [*O*] (**Equation 6.21**).

$$^{13}CO_{2_{tot}}^{+} = \left[^{13}CO_2\right] sf\left(^{13}CO_2^{+}, ^{13}CO_2\right) \tag{6.16}$$

$$^{13}CO_{tot}^{+} = \left[^{13}CO\right] sf\left(^{13}CO^{+}, ^{13}CO\right) + \left[^{13}CO_2\right] sf\left(^{13}CO^{+}, ^{13}CO_2\right) \tag{6.17}$$

$$\left[^{13}CO_2\right] = \frac{^{13}CO_{2_{tot}}^{+}}{sf\left(^{13}CO_2^{+}, ^{13}CO_2\right)} \tag{6.18}$$

$$\left[^{13}CO\right] = \frac{\left(^{13}CO_{tot}^{+} - \frac{^{13}CO_{2_{tot}}^{+} sf\left(^{13}CO^{+}, ^{13}CO_2\right)}{sf\left(^{13}CO_2^{+}, ^{13}CO_2\right)}\right)}{sf\left(^{13}CO^{+}, ^{13}CO\right)} \tag{6.19}$$

$$\begin{aligned} O_{tot}^{+} = {} & \left[O_3\right] sf\left(O^{+}, O_3\right) + \left[O_2\right] sf\left(O^{+}, O_2\right) + \left[O\right] sf\left(O^{+}, O\right) + \left[H_2O\right] sf\left(O^{+}, H_2O\right) \\ & + \left[^{13}CO_2\right] sf\left(O^{+}, ^{13}CO_2\right) + \left[^{13}CO\right] sf\left(O^{+}, ^{13}CO\right) \end{aligned} \tag{6.20}$$

$$\left[O\right] = \frac{\left(\begin{array}{l} O_{tot}^{+} - \frac{O_{3_{tot}}^{+} sf\left(O^{+}, O_3\right)}{sf\left(O_3^{+}, O_3\right)} \\ - \frac{sf\left(O^{+}, O_2\right)\left(O_{2_{tot}}^{+} - \frac{O_{3_{tot}}^{+} sf\left(O_2^{+}, O_3\right)}{sf\left(O_3^{+}, O_3\right)}\right)}{sf\left(O_2^{+}, O_2\right)} \\ - \frac{H_2O_{tot}^{+} sf\left(O^{+}, H_2O\right)}{sf\left(H_2O^{+}, H_2O\right)} - \frac{^{13}CO_{2_{tot}}^{+} sf\left(O^{+}, ^{13}CO_2\right)}{sf\left(^{13}CO_2^{+}, ^{13}CO_2\right)} \\ - \frac{sf\left(O^{+}, ^{13}CO\right)\left(^{13}CO_{tot}^{+} - \frac{^{13}CO_{2_{tot}}^{+} sf\left(^{13}CO^{+}, ^{13}CO_2\right)}{sf\left(^{13}CO_2^{+}, ^{13}CO_2\right)}\right)}{sf\left(^{13}CO^{+}, ^{13}CO\right)} \end{array}\right)}{sf\left(O^{+}, O\right)} \tag{6.21}$$

The TPD graphs were constructed as those previously discussed in this chapter with **Equations 6.21**, **6.7**, **6.6**, **6.12**, **6.13**, **6.18**, **6.19** and **6.21** applied (see **Figure 6.23**). This enabled the TPD traces shown to correspond to the desorption of the species of interest from the substrate.

As with the other atomic O beam TPD experiments discussed in this chapter, O_3 desorption peaks were observed indicating that this molecule was again formed on the

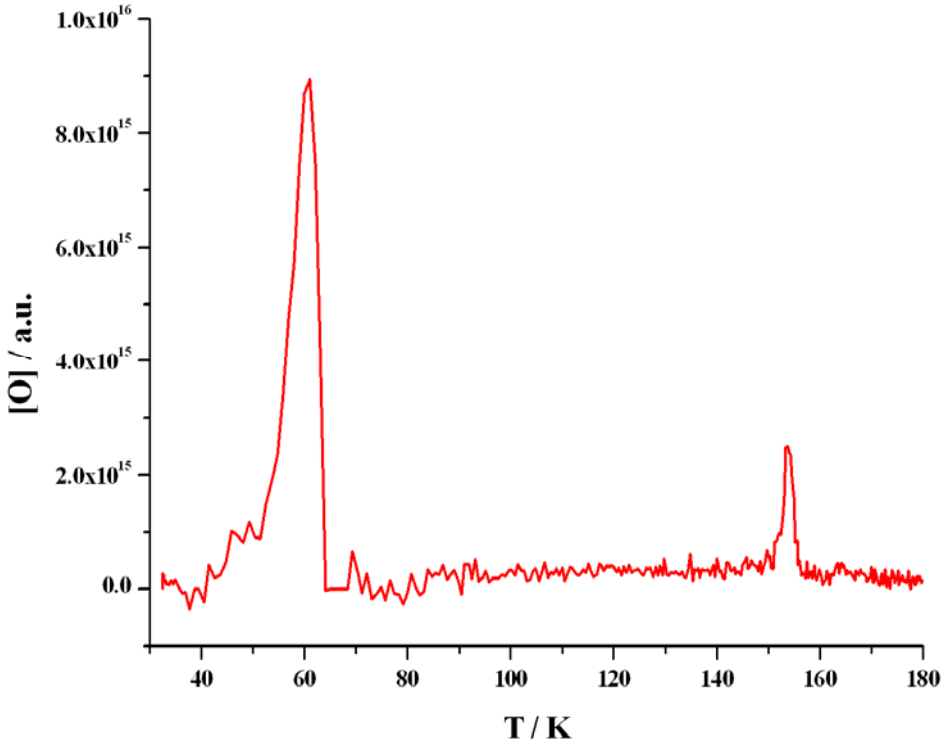

Figure 6.23a: [O] Estimated from the TPD Data Modified Using **Equation 6.21**

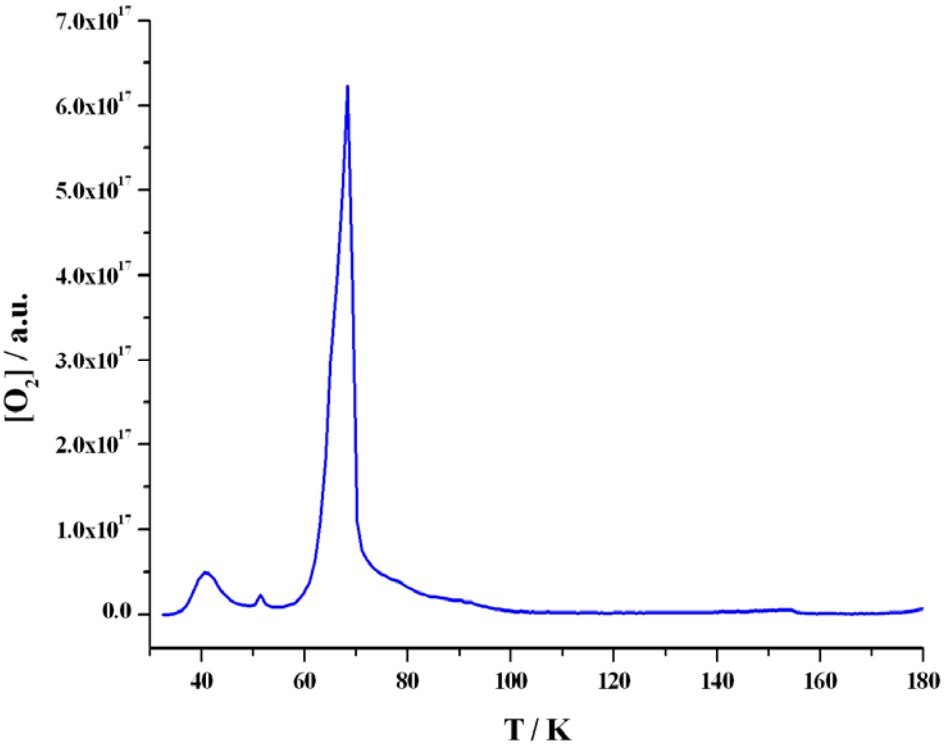

Figure 6.23b: [O_2] Estimated from the TPD Data Modified Using **Equation 6.7**

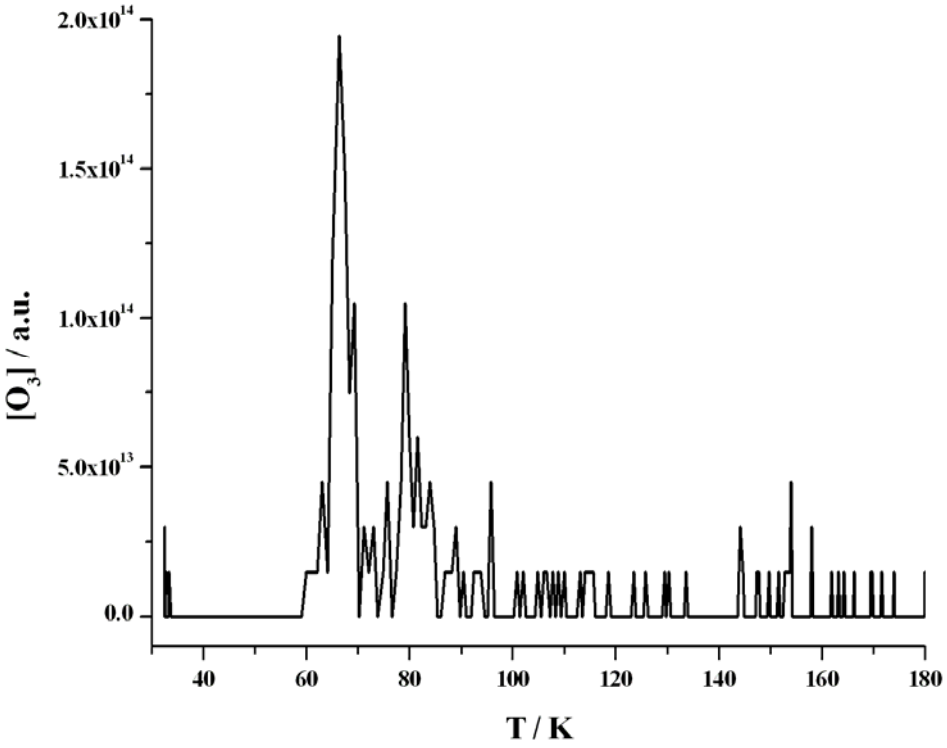

Figure 6.23c: [O_3] Estimated from the TPD Data Modified Using **Equation 6.6**

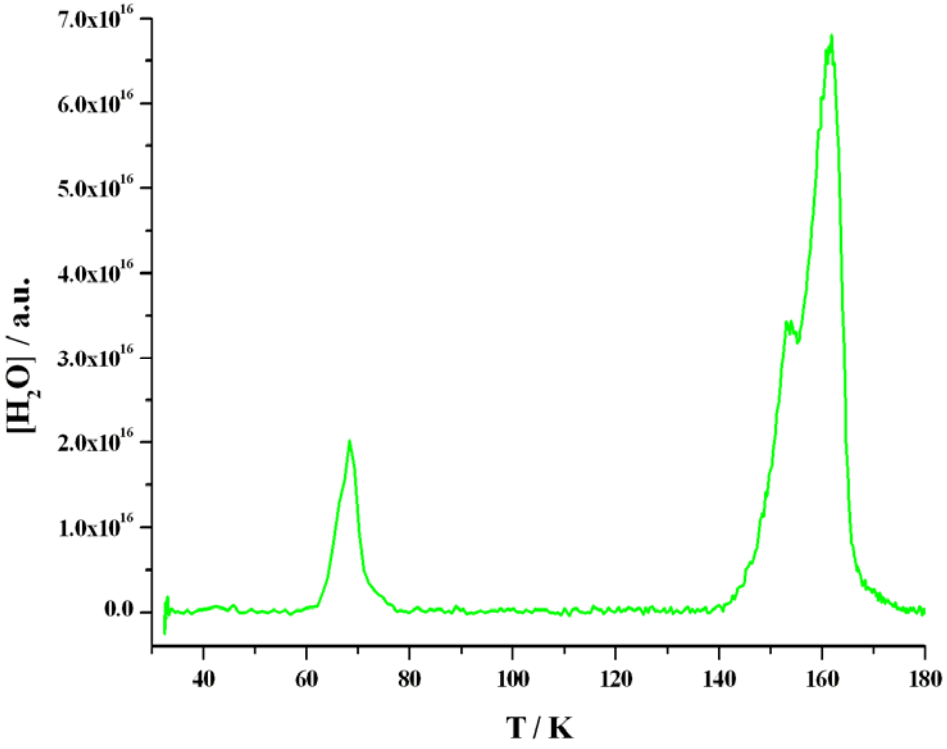

Figure 6.23d: [H_2O] Estimated from the TPD Data Modified Using **Equation 6.12**

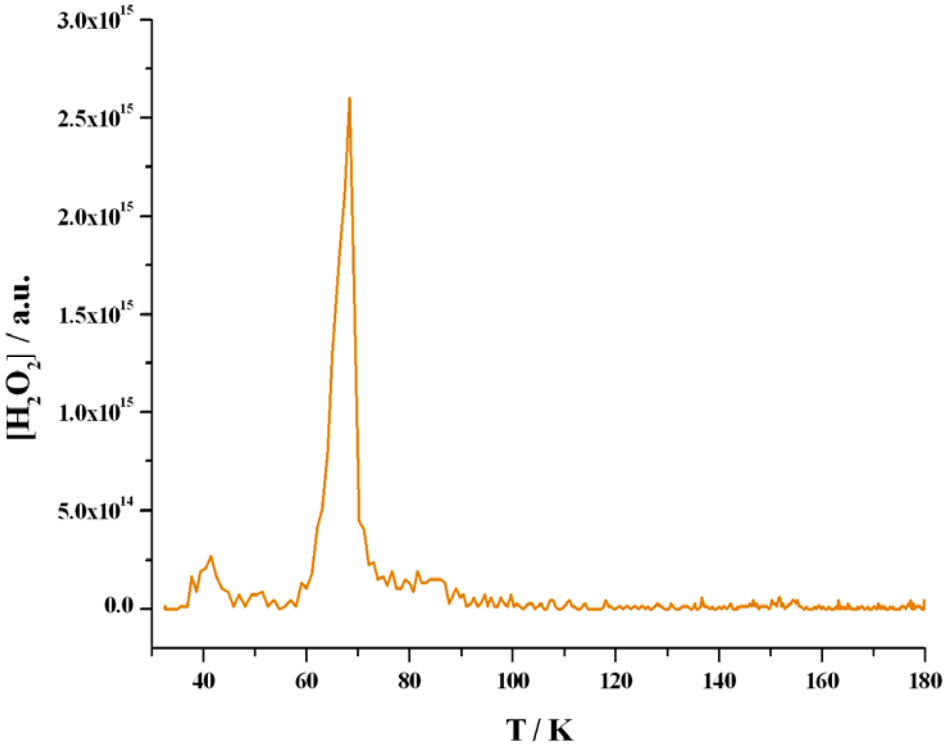

Figure 6.23e: [H_2O_2] Estimated from the TPD Data Modified Using **Equation 6.13**

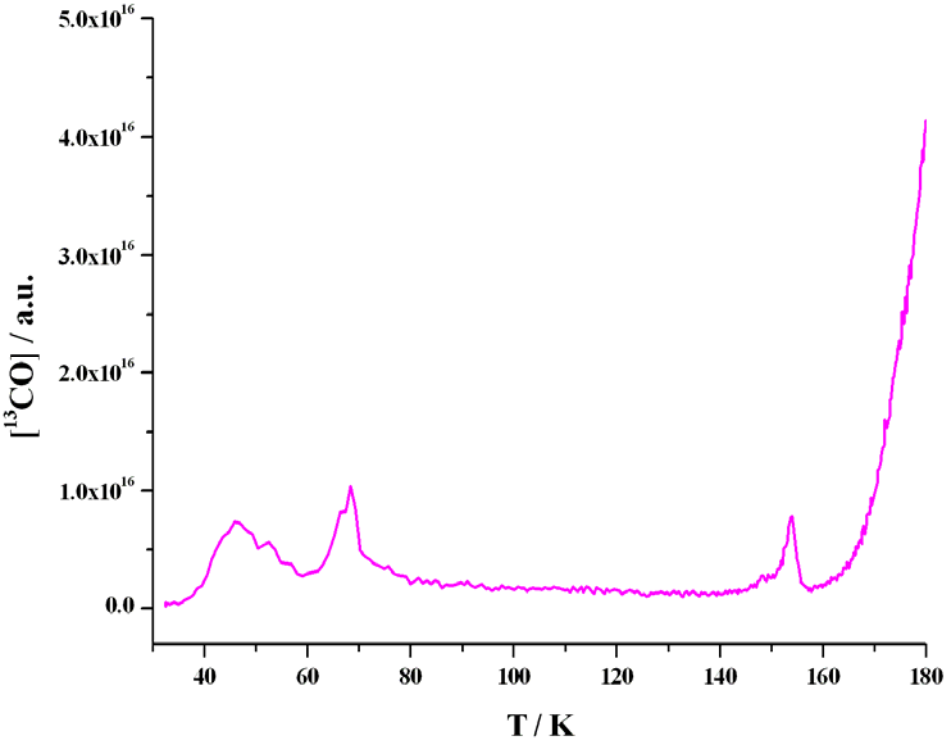

Figure 6.23f: [^{13}CO] Estimated from the TPD Data Modified Using **Equation 6.19**

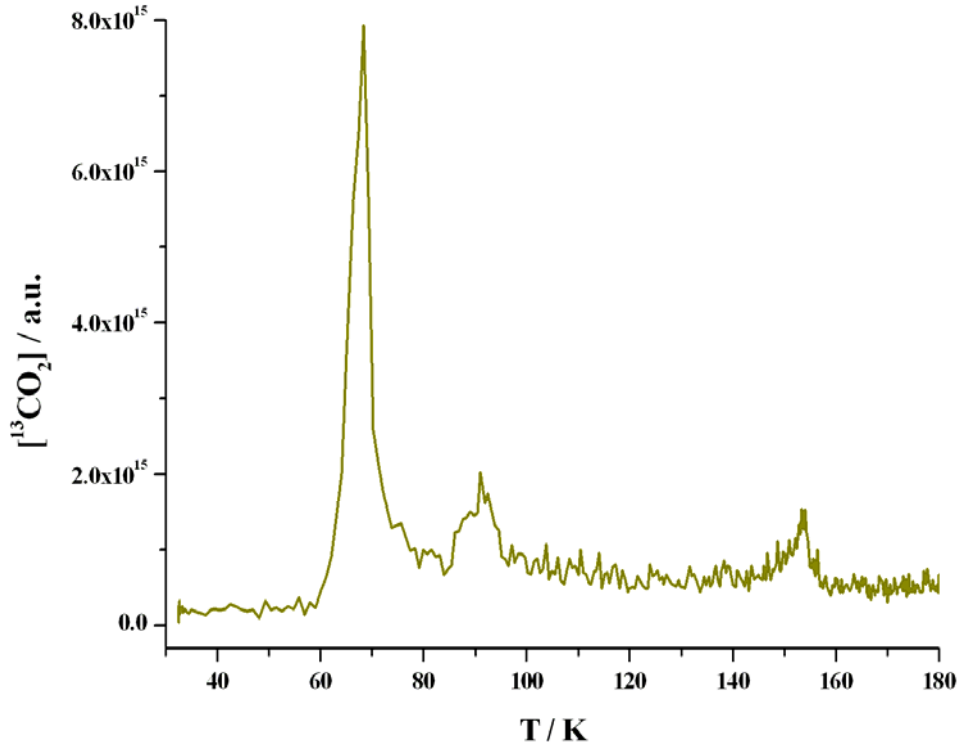

Figure 6.23g: [$^{13}CO_2$] Estimated from the TPD Data Modified Using **Equation 6.18**

surface despite the addition of the ^{13}CO film. Desorption peaks for $^{13}CO_2$ were also observed suggesting that this species too was formed on the surface. This is in good agreement with the ^{18}O beam irradiated CO on H_2O on copper TPD experiments performed by Vidali *et al*. who were able to detected $CO^{18}O$ molecules at 160 K [2]. However, without the H_2O film, no $CO^{18}O$ molecules were detected either during the dosing or in the TPD analysis. The results obtained by Vidali *et al*. concluded that the CO_2 formation mechanism contained an activation energy barrier which the O and CO could only overcome if the species became trapped and reacted together in the H_2O ice. However, the CO_2 formation reaction shown in **Figure 6.24** is spin forbidden [2] suggesting that the CO_2 molecules could have been formed by an alternative mechanism which depends on the presence of H_2O.

$$CO(X^1\Sigma^+)(ads) + O(^3P)(ads) \rightarrow CO_2(^3B_2)(ads) \rightarrow CO_2(X^1\Sigma_g^+)(ads)$$

Figure 6.24: Spin Forbidden CO_2 Formation Reaction [2]

The initial assignment of the desorption peaks was applied based on the TPD results obtained in the previous sub-sections. The lowest temperature [O_2] desorption peak occurred at approximately 41 K and was in good agreement with the observations made in **Sections 6.3.3** and **6.3.4** (**Figure 6.23b**). As before this O_2 desorption was accompanied by a small [H_2O_2] desorption peak suggesting the formation of H_2O_2. This was surprising as the addition of the 100 L multilayer ^{13}CO film situated between the O and H_2O doses was expected to considerably restrict this formation reaction. In **Section 6.3.3**, a possible surface formation mechanism for H_2O_2 was discussed (see **Figure 6.14**). However, this mechanism required the presence of O(^{1}D) atoms whereas the atomic O plasma had been characterized to restrict the concentration of O atoms in the excited state suggesting that the formation of H_2O_2 occurred through another mechanism. Additionally, the observations obtained from the atomic O beam TPD experiment discussed in this sub-section provides further evidence to this conclusion otherwise the O atoms would have to diffuse through the ^{13}CO film before reacting with the underlying H_2O molecules. This would have been unlikely to occur as the excited atoms would have deactivated (mainly through collisions) before the atoms reached the H_2O film (**Chapter 3**). To further explore this formation and desorption mechanism, additional atomic O beam dose on pASW and layered ices (which include a pASW film) on silica TPD experiments (ideally compared with RAIRS analysis) could be performed over a range of film thicknesses.

The double desorption peak structure for [O_3] at approximately 66 and 79 K was assignment to the two solid phase desorption of O_3 as before (**Figure 6.23c**). As in the previous experiments discussed in this chapter, the O_3 desorption peak at approximately 66 K was accompanied by [O_2], [H_2O], [H_2O_2] features. In **Section 6.3.2**, the appearance of the [O_2] was concluded to occur through one of the O_3 destruction reaction steps in the Chapman mechanism on the surface. The origin of the [H_2O] desorption feature was suggested in **Section 6.3.3** to originate from H-bonded disrupted H_2O molecules due to the energy released from the surface formation of O_2. The relatively small [H_2O_2] peak was believed to be caused from disrupted H-bonding entrapment resulting in the H_2O_2 molecules desorbing with the corresponding H-bonded disrupted H_2O molecules. Desorption features for [^{13}CO] and [$^{13}CO_2$] were also observed accompanying the [O_3] desorption peak at approximately 66 K. However, the origins of these features could not be assigned without consideration to the other [^{13}CO] and [$^{13}CO_2$] peaks.

The desorption peaks occurring between 140 and 170 K were initially assigned based on those results previous discussed in this thesis. The double desorption peak structure for [H_2O] (**Figure 6.23d**) was assigned to the desorption of cASW and CSW from silica. Molecular volcanoes with the desorption of cASW were observed for [O_2], [^{13}CO] and [$^{13}CO_2$] implying that a proportion of these species had become trapped in the H_2O film during the pASW to cASW phase change and were released when the H_2O film underwent crystallisation (**Figure 6.23b**, **f** and **g** respectively). The preliminary results from this TPD experiment were in good agreement for O_2 with the O_2 TPD experiments on bare silica discussed in **Chapter 4** and for CO and CO_2 with those in the literature [13, 14].

Another [^{13}CO] desorption peak occurred at approximately 46 K and was broad in shape. This finding agrees well with the CO TPD experiments on pASW performed by Collings *et al*. [15] and, therefore, was assigned to the desorption of ^{13}CO from pASW. A [^{13}CO] feature was observed at around 52 K but the origin of this peak is unclear. One possible suggestion, based on the desorption features observed at similar surface temperatures in the previous sub-sections, was that these ^{13}CO molecules were released as a molecular volcano during the O_3 crystallisation. In the future, additional atomic O beam dose and O_3 TPD experiments (ideally combined with RAIRS analysis) could be performed on a range of astronomically relevant surfaces to explore the origin of these features in more detail.

The assignment of the broad [$^{13}CO_2$] desorption feature occurring at roughly 90 K was unclear (**Figure 6.23g**). The experiments performed by Collings *et al.* observed the desorption of directly dosed $^{12}CO_2$ from H_2O at approximately 78 K [14] but this peak was not observed in this experiment. One possible explanation is that this delayed desorption arises from the formation mechanism of $^{13}CO_2$ suggesting that the species does not dominantly form through the spin forbidden reaction previously shown in **Figure 6.24**. An alternative H_2O dependent surface formation mechanism is displayed in **Figure 6.25** where the reaction route occurs through the HOCO intermediate species. If this is the case, then the surface formation of $^{13}CO_2$ would be dependent on the OH mobility and the dissociation of the intermediate species resulting in the desorption peak occurring at a higher surface temperature than expected. However, the first step of this

$$H_2O(ads) + O(^1D)(ads) \rightarrow 2OH(ads)$$
$$OH(ads) + {}^{13}CO(ads) \rightarrow HO^{13}CO(ads)$$
$$HO^{13}CO(ads) \rightarrow {}^{13}CO_2(ads) + H(ads)$$

Figure 6.25: Possible H_2O Dependent $^{13}CO_2$ Surface Formation Mechanism

mechanism is the same as the first step in the possible H_2O_2 formation mechanism previously discussed in **Section 6.3.3** (see **Figure 6.14**). As a consequence, the formation of $^{13}CO_2$ through this mechanism will only proceed if the O atoms are in the excited state and not in the preferred ground state. Additionally, the presence of the multilayer ^{13}CO film would prevented the excited atoms from reaching the underlying H_2O film without the atoms deactivating to the ground state through collisions suggesting that the surface formation of $^{13}CO_2$ would have occurred through another mechanism. In the future, further atomic O beam dose on ^{13}CO on silica and on ^{13}CO on pASW on silica TPD experiment (ideally combined with RAIRS) could be preformed to explore the surface formation of $^{13}CO_2$.

Overall, the assignment of the other [^{13}CO] and [$^{13}CO_2$] desorption peaks imply that the peaks observed at approximately 66 K were unlikely to be formed from the species desorbing from the substrate or as molecular volcanoes. As a consequence, these preliminary findings suggest that other surface processes and reactions could be responsible. In the future, the formation of these features could be determined by performing additional atomic O beam dose TPD experiments on ^{13}CO pure and ^{13}CO on H_2O layered films on silica for a range of irradiation times. Further information could be obtained by combining these proposed experiments with RAIRS analysis.

From the information discussed above, a plot of the assigned TPD data was constructed (see **Figure 6.26**). Overall, these desorption peaks agreed well with those previously assigned from the preliminary experiments discussed in the above sub-sections. However, further atomic O beam dose on ^{13}CO on pASW TPD experiments on silica (ideally combined with RAIRS analysis) are required along with all the proposed O_3 TPD RAIRS experiments and other atomic O beam dose TPD RAIRS experiments to determine both the O_3 and $^{13}CO_2$ formation mechanisms and the other surface and desorption processes occurring in these experiments in more detail.

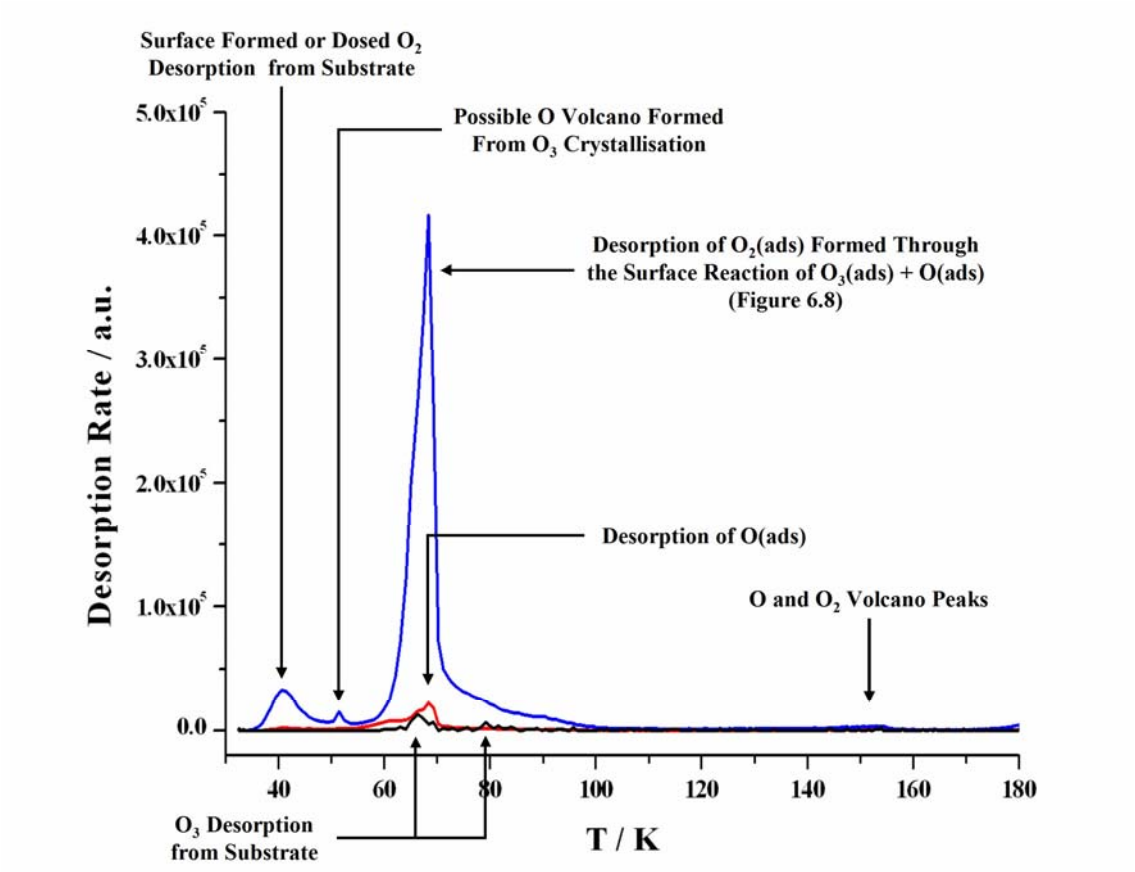

Figure 6.26a: Assigned of the Masses 16 (red), 32 (blue) and 48 (×100) (black)

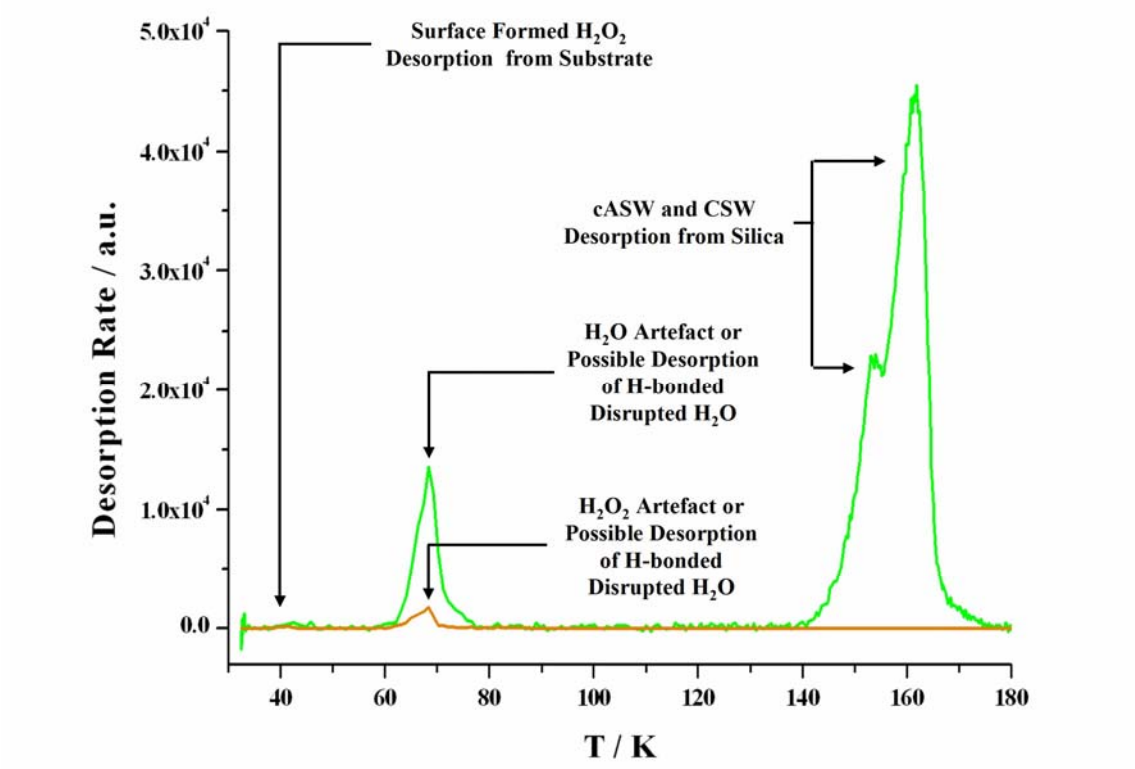

Figure 6.26b: Assignment of the Masses 18 (green) and 34 (orange) Desorption Peaks

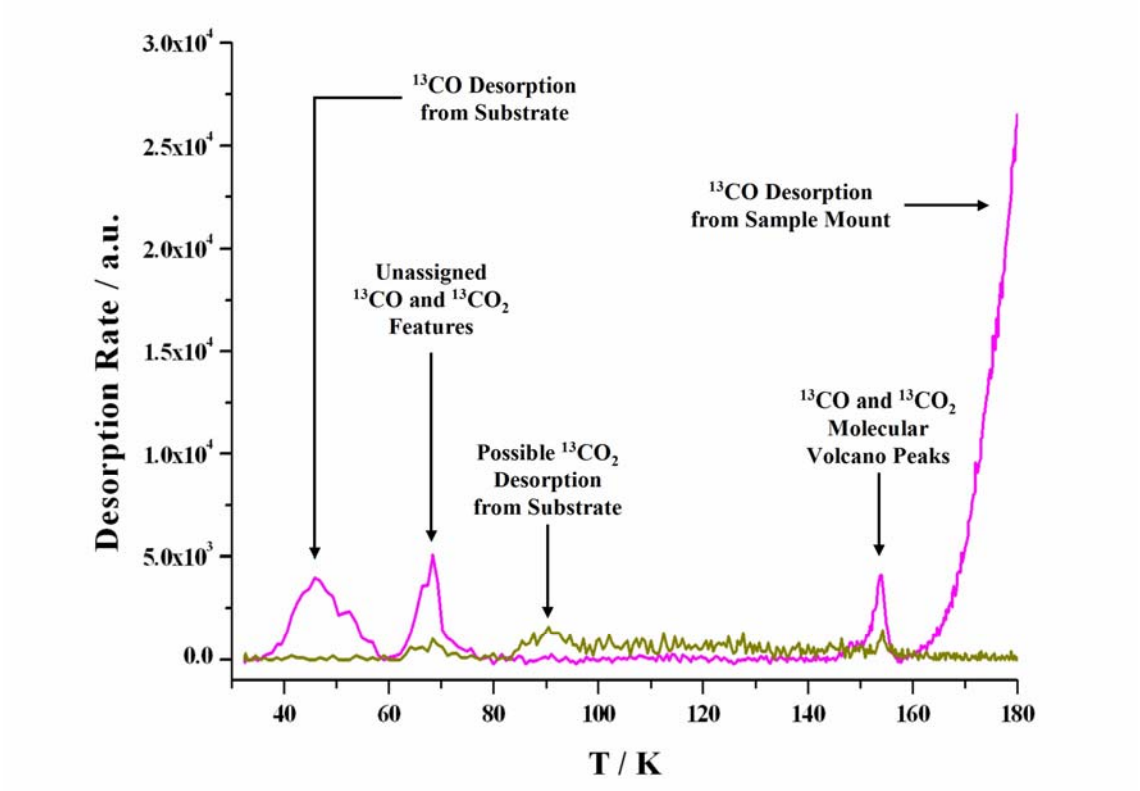

Figure 6.26c: Assignment of the Masses 29 (magenta) and 45 (× 10) (dark yellow) Desorption Peaks

6.4 Summary and Conclusions

This chapter focused on the results obtained from four preliminary atomic O beam dose TPD experiments on a range of astronomically relevant surfaces. The application of the experimentally determined and the literature values of c_{frac} enabled the TPD plots to be constructed without the desorption peaks being considerably affected through cracking reaction products. For each experiment, the desorption peaks in the raw TPD data were assigned based on the analysis of those experiments previously discussed in this thesis and from the literature.

The first experiment enabled the desorption peaks from O, O_2 and O_3 from bare silica to be assigned. The observation of small O desorption peaks suggested that the majority of the O atoms reacted with each other and other species on the surface. An unexpected result was found when the O_2 TPD curve was compared to the corresponding molecular

beam dose TPD experiment previously discussed in **Chapter 4**. In the atomic beam study, the first O_2 desorption peak occurred at a surface temperature approximately 10 to 15 K lower indicating that the origin of this feature was not from directly dosed O_2 molecules. As a consequence, the first O_2 desorption peak was assigned to the possible desorption of O_2 molecules formed on the surface by two O atoms which desorb upon formation due to the roughly 580 kJ mol^{-1} of energy released. The initial findings also reveal that the O atoms in this study do not appear to diffuse across the surface until approximately 20 K suggesting that the O atom diffusing is delayed. However, further atomic O beam dose TPD experiments from bare silica would be required to explore these observations in more detail. Additionally, the values of $N[O]_i$ and $N[O_2]_i$ calculated were based on estimated values of α and $[O{:}O_2]$. To determine these initial concentrations more accurately, experiments based on the Kings and Wells method and cracking fraction calibration will need to be performed in the future enabling a more accurate assignment and analysis of the O_2 and O_3 surface formation mechanism to be made (for more details on these proposed experiments see **Chapter 3**).

The presence of the O_3 desorption peak at 66 K was in good agreement with those in the literature and indicated that this species was formed on the surface through the reaction of O with O_2. Detailed information regarding the O_3 formation, crystallisation and desorption mechanism could not be obtained from these experiments alone without additional atomic O beam dose and O_3 TPD experiments from a range of astronomical relevant surfaces being performed. Additional information of this known complex mechanism could be achieved by combining the TPD experiments with RAIRS analysis as this would provide further temperature dependent information on the formation of O_3 complexes, monomers and clusters.

In the following TPD experiments, background doses were applied to the silica before the atomic O beam dose. The addition of these substrates resulted in a double O_3 desorption peak structure being observed with the first agreeing with the single peak in the first experiment. The second desorption peak corresponded to molecules in the crystalline phase combined with those from either a supercooled liquid or a metastable state of O_3 and was in good agreement with the conclusions made by Hanson and Mauersberger. The appearance of this second O_3 desorption peak with the presence of the underlying pASW film could have occurred as the film increased the adsorption strength of the O_3 molecules allowing enough molecules to undergo this phase change

before desorbing. Alternatively, this peak could have been observed in the atomic O beam dose on bare silica TPD experiments if longer irradiation times had been applied. In the future, further atomic O beam dose TPD experiments on substrates on silica could be performed to explore the behaviour of the second O_3 desorption peak in more detail.

In all of the atomic O beam TPD experiments which included a substrate, a 200 L film of H_2O was background dosed onto the silica. This resulted in the observation of the double H_2O desorption peak structures similar to those discussed in **Chapter 4** being obtained. Molecular volcano peaks were also observed with the desorption of H_2O which were in good agreement with those findings in this study and in the literature.

A surprising result was the observation of a H_2O desorption peak at approximately 66 K as in the previous H_2O on bare silica TPD experiments discussed in **Chapter 4**, this peak was not seen. Additionally, this desorption peak was also accompanied by a small H_2O_2 feature. Although the appearance of these peaks were unclear, a possible suggestion was the H_2O peak corresponded to the desorption of H-bonded disrupted H_2O molecules caused by the energy released in the formation of O_2 on the surface. The accompanying H_2O_2 feature could have been formed by entrapped molecules in the H-bonded disrupted H_2O molecules. Preliminary CKS simulations were performed to explore this theory with the initial findings suggesting that this could be possible under zeroth order desorption kinetics. However, additional atomic O beam dose on H_2O on silica TPD experiments over a range of O beam irradiation times would be required to explore the origins of these peaks in more detail.

Another small H_2O_2 desorption peak was also observed in the last three TPD experiment discussed in this chapter indicating that this species, like O_3, was formed on the surface. However, the H_2O_2 formation mechanism could not be determined from these experiments alone. In the future, H_2O_2 TPD experiments from bare silica and from H_2O on silica could be performed to determine the desorption kinetics of this species. The results obtained could then be used towards exploring the formation mechanism of this species both experimentally and through simulation models. This additional H_2O_2 formation route could be added to the H_2O surface formation mechanism previously shown in **Chapter 1** (redisplayed in **Figure 6.27**). The results obtained from these proposed experiments could be applied into a simulation model

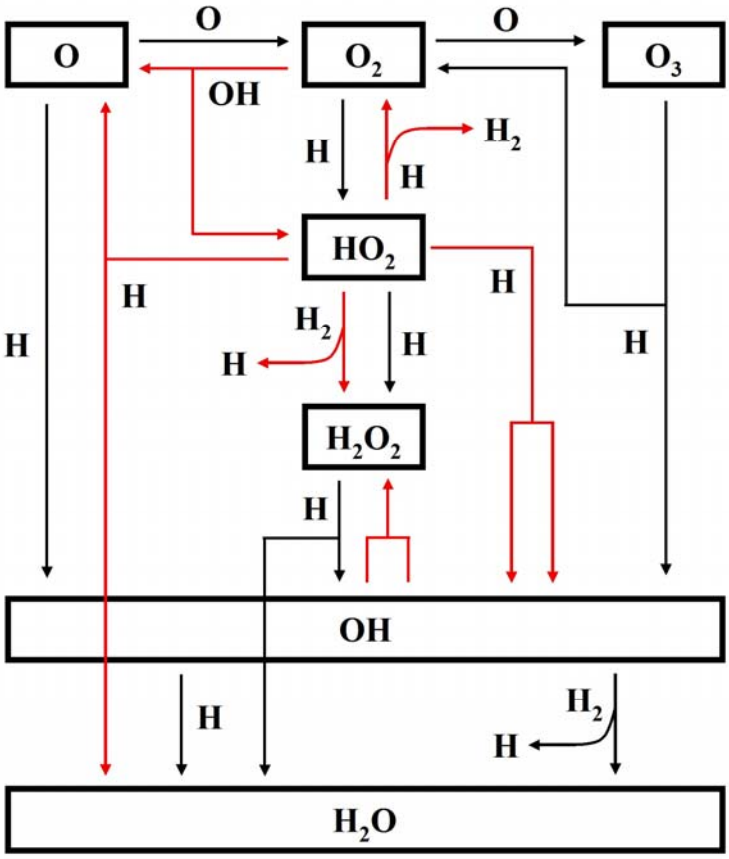

Figure 6.27: Full Formation Mechanism of H_2O

which may reveal why H_2O_2 has only recently been detected in the ISM [10]. Although the data obtained would not be relevant for diffuse cloud environments, this extra formation route could result in an overall increased formation rate of H_2O in the icy mantles coating dust grains in dense molecular cloud environments of the ISM.

The final TPD experiment discussed in this chapter explored the affect of an additional ^{13}CO film dosed on top of the H_2O film. Desorption peaks were assigned to $^{13}CO_2$ desorbing from H_2O and as a molecular volcano. The first of these two desorption peaks occurred at a surface temperature approximately 12 K higher than the directly dosed CO_2 on pASW TPD experiments performed by Collings *et al*. [14] suggesting that the surface formation mechanism was dependent on the presence of a pASW film resulting in the delayed desorption of CO_2. The exact formation mechanism could not be determined from this single experiment. In the future, additional atomic O beam dose on ^{13}CO on silica and on ^{13}CO on pASW on silica TPD and RAIRS experiments could be performed to explore the CO_2 formation mechanism in more detail. Further

developments of the data could include simulating the results under experimental and astronomical heating rates using a similar procedure to the one used in **Chapter 4** for O_2. The results obtained could be used towards explaining the observation of CO_2 in the icy mantles in dense molecular cloud environments. However, as these proposed experiments are not related towards understanding the formation of H_2O on interstellar dust grains then these experiments are unlikely to be performed in the near future.

Overall, the preliminary results from the atomic O beam dose TPD experiments discussed in this chapter suggest that O atoms could be trapped within the icy mantle matrix coating interstellar dust grains in dense molecular cloud environments. However, the results also indicate that the O atoms react on the surface to form more complex species. In the future, the results obtained for these preliminary experiments and from those proposed could be used towards constructing a simulation model mimicking the formation, crystallisation and desorption of O_3 in the laboratory before applying the model to the dust grains in the dense molecular cloud environment of the ISM. The conclusions obtained could be used towards explaining why O_2 has not been detected in the icy mantles or why O_3 has yet to be observed in the ISM [8, 16]. Further application of these results could be used towards determining the kinetics of the forward reactions in the top line of the full H_2O surface formation reaction mechanism (**Figure 6.27**) on interstellar dust grains.

6.5 References

[1] B. Sivaraman, C. S. Jamieson, N. J. Mason and R. I. Kaiser, *Ap. J.*, 2007, **669**, 1414.

[2] G. Vidali, J. Roser, G. Manico and V. Pirronello, *Adv. Spa. Res.*, 2004, **33**, 6.

[3] F. Dulieu, L. Amiaud, E. Congiu, J. H. Fillion, E. Matar, A. Momeni, V. Pirronello and J. L. Lemaire, *Astron. Astrophys.*, 2010, **512**, A30.

[4] S. Anderson and K. Mauersberger, *Rev. Sci. Instrum.*, 1981, **52**, 1025.

[5] C. S. Barrett, L. Meyer and J. Wasserma, *J. Chem. Phys.*, 1967, **47**, 592.

[6] E. M. Horl, *Acta Crystallographic*, 1992, **15**, 845.

[7] H. Mokrane, H. Chaabouni, M. Accolla, E. Congiu, F. Dulieu, M. Chehrouri and J. L. Lemaire, *Ap. J.*, 2009, **705**, L195.

[8] C. J. Bennett and R. I. Kaiser, *Ap. J.*, 2005, **635**, 1362.

[9] M. J. Pilling and P. W. Seakins, *Reaction Kinetics*, Oxford University Press, Oxford, 2005.

[10] P. Bergman, B. Parise, R. Liseau, B. Larsson, H. Olofsson, K. M. Menten and R. Gusten, *Astron. Astrophys.*, 2011, **531**, L8.

[11] D. Hanson and K. Mauersberger, *J. Chem. Phys.*, 1986, **85**, 4669.

[12] *NIST Chemistry Webbook*, Accessed 02 April 2011.

[13] A. Bar-Nun, G. Herman, D. Laufer and M. L. Rappaport, *Icarus*, 1985, **63**, 317.

[14] M. P. Collings, M. A. Anderson, R. Chen, J. W. Dever, S. Viti, D. A. Williams and M. R. S. McCoustra, *Mon. Not. R. Astron. Soc.*, 2004, **354**, 1133.

[15] M. P. Collings, J. W. Dever, H. J. Fraser, M. R. S. McCoustra and D. A. Williams, *Ap. J.*, 2003, **583**, 1058.

[16] B. Vandenbussche, P. Ehrenfreund, A. C. A. Boogert, E. F. van Dishoeck, W. A. Schutte, P. A. Gerakines, J. Chiar, A. G. G. M. Tielens, J. Keane, D. C. B. Breitfellner and M. Burgdorf, *Astron. Astrophys.*, 1999, **346**, L57.

Chapter 7 - Conclusions and Future Work

Contents

The ultimate aim of this ongoing research was to determine if the formation of water molecules on interstellar dust grains would provide an additional more efficient mechanism to match the observed molecular abundance which can not be achieved through gas phase chemistry alone. To enable this question to be answered, the new dual atomic beam ultrahigh vacuum system was constructed and calibrated in this study. Unlike the current versions of other single and dual atomic beam systems, this apparatus has been designed to explore the full surface formation mechanism using a larger combination of analytical techniques and without having to pre-dose a water ice substrate. The overall conclusions and astronomical implications obtained from the work presented in this thesis are briefly summarized in this chapter along with possible suggestions for future work and modifications to the apparatus for this on-going research.

7.1 Key Points

The key points obtained in this study are listed below with the corresponding section reference.

- **Section 2:** The majority of the new dual atomic beam system was constructed and tested for this on-going project.
- **Section 3.3** and **3.4**: The ultimate position of the silica sample with respect to the atomic O beam was determined as x = -5.0 mm, y = 0.0 mm, z = 50.0 mm, and θ = -0.5˚ from the QCM calibrations. An estimate of the O_2 F_{beam} was obtained as $5\times10^{11\pm1}$ molecules cm^{-2} s^{-1} but this was considered to be too small in comparison to other similar effusive beams. A more accurate measurement was calculated from the O_2 pump-down experiments as $2\times10^{14\pm1}$ molecules cm^{-2} s^{-1}. However, this considerably large difference between the two values of F_{beam} resulted in the sticking coefficient, S, equalling $3\times10^{-3\pm2}$ implying that the original assumption of the vast majority of the molecules remaining adsorbed on the surface after collision was invalid.
- **Section 4.2**: The results obtained from the H_2O on bare silica TPD experiment revealed that the molecules follows zeroth order desorption kinetics even under sub-monolayer coverages. Analysis using leading edge analysis and CKS

modelling revealed the desorption activation energies, E_{des}, for cASW and CSW were 48.5±0.4 and 49.6±0.2 kJ mol^{-1} respectively which were in good agreement with those in the literature [1-3].

- **Section 4.3:** Unlike the desorption of similar species from silica, multilayers of O_2 molecules followed fractional order desorption kinetics of 0.18±0.04. Possible causes for this fractional order were considered and explored in **Chapter 5**. Analysis of the TPD data concluded the value of E_{des} to be 9.8±0.1 kJ mol^{-1} and was in good agreement with the literature [4]. Overall, the results obtained for the multilayer coverages were not relevant under ISM conditions due to the low observed molecular abundance. Also, the results obtained do not appear to provide any additional information regarding the missing oxygen between diffuse and dense molecular cloud environments (see **Section 1.2.2**). The desorption of sub-monolayer coverages of O_2 followed first order kinetics, analysis of the data using direct inversion of the Polyani-Wigner equation yielded a coverage dependent range of values for E_{des} due to the underlying amorphous silica surface.
- **Section 4.4:** Desorption of sub-monolayer quantities of O_2 from cASW on silica TPD experiments concluded that the O_2 molecules followed first order with varying E_{des} desorption kinetics as in **Section 4.3**.
- **Section 4.5:** The results obtained from the desorption of sub-monolayer quantities of O_2 on pASW on silica TPD experiments revealed the presence of two O_2 desorption peaks. The desorption of the non-trapped species (lower surface temperature peak) followed the same desorption kinetics as those from cASW. The desorption of the trapped species (higher surface temperature peak) was controlled by the crystallisation of cASW. From these results, a CKS model was constructed mimicking the TPD data.
- **Section 4.6:** Attempts were made to simulate the desorption of O_2 from icy mantles coating interstellar dust grains under dense molecular cloud environments. The simulation model used was based on the CKS model constructed in **Section 4.5** and on an earlier CKS model developed by Collings *et al*. [5]. However, analysis of the simulation results revealed that the model used was too simple. Key parts of the model that could be developed in the future are the H_2O crystallisation step (as this is no longer held under astronomical heating rates) and the O_2 diffusion probability steps (as all the O_2 molecules become trapped).

- **Section 5.3:** The results obtained from multilayer CO on bare silica and multilayer N_2 on bare silica TPD experiments revealed that the underlying silica surface appeared to be affecting the desorption kinetics of some multilayer species including the previously discussed O_2. The results revealed that the desorption kinetic order values decreased roughly by half as the species changed from O_2 to CO to N_2 (0.18±0.04, 0.09±0.11, 0.00±0.08 respectively). Leading edge analysis and CKS models were applied to the data. However, the observation of a non-constant current leak in the heater circuit shifted the desorption peaks to higher surface temperatures resulting in the calculated values of E_{des} (10.4±0.1 and 9.8±0.6 kJ mol^{-1} respectively) being slightly higher than those found in the literature [5-7].
- **Section 6.3:** The preliminary atomic O beam TPD experiments from a range of astronomically relevant surfaces revealed that the formation of O_2, O_3, H_2O_2, and $^{13}CO_2$ occurred on the surface. Interestingly, the desorption of O_2 from bare silica was observed to occur at a silica surface temperature roughly 10 to 15 K lower than the corresponding O_2 directly dosed TPD experiment discussed in **Chapter 4**. The most likely cause for this observation was the O_2 molecules desorbed upon formation due to the roughly 580 kJ mol^{-1} of energy released in the O=O bond formation. The astronomical implications of this observation suggest that O exists as atoms up to a surface temperature of approximately 20 K when the atoms begin to diffuse and react together to form O_2 which desorbs upon formation. The exact surface formation mechanisms for O_3, H_2O_2 and $^{13}CO_2$ could not be determined from these experiments alone or why the $^{13}CO_2$ desorption peak occurred at approximately 12 K higher than directly dosed CO_2. Another unexpected observation was the presence of a H_2O desorption peak situated at approximately 66 K. This peak was not observed in the background dosed H_2O on silica TPD experiments discussed in **Chapter 4** and may have been caused by an experimental artefact or from the desorption of H_2O from a disrupted H-bonded network. Additionally, this lower surface temperature H_2O peak was accompanied by a considerably smaller H_2O_2 desorption peak.

7.2 Suggested Future Work and Apparatus Modifications

This section provides a list of possible suggestions for future work and modifications to the apparatus based on the key points obtained in this thesis.

- **Section 2.2**: When the testing and installation of the new chopper apparatus has been completed and added to each of the beam chambers, further single and dual atomic and molecular beam experiments could be performed using a mixture of continuous, pulsed and relative phase (0 to 180^{o}) beams. This could enable more detailed analysis of the surface process occurring to be obtained using molecular beam modulation techniques.
- **Section 2.5:** Once the O_3 apparatus has been completed, a range of TPD experiments (ideally combined with RAIRS analysis) on a range of astronomical relevant surfaces could be performed. This would enable the desorption kinetics of O_3 to be determined. The kinetic parameters could then be used towards constructing a simulation model under laboratory conditions before applying the model under astronomical heating rates. The results obtained may explain why O_3 has yet to be observed in the ISM [8].
- **Section 3.2:** To produce an atomic H plasma the secondary gas technique was required using N_2. Currently, there is no permanent equipment arrangement on the apparatus system for the second gas. In the future, the atom beam gas lines could be modified to include an additional N_2 gas cylinder. This would enable the ultimate silica sample position, F_{beam} (for both the molecular and atomic beam) and the H:H_2 dissociation fraction to be determined.
- **Section 3.2**: The results from the plasma analysis revealed that the intensity of the emission peaks varied considerably and appeared to be related to how long and how frequent the plasma source had been used previously. The current solution would be to run the atomic beams as frequently as possible in the weeks leading up to an atomic beam experiment. This procedure is made more complicated as the RF powered plasma sources causes interference with the thermocouples. In the future, the apparatus could be modified to shield the thermocouples enabling the atomic beams to run whilst other experiments were being performed in the central chamber. Another possible modification to further improve the beams' sensitivity would be to add a pressure gauge between the plasma source and the

leak value. This would enable the beam pressure to be monitored rather than the plasma chamber pressure.

- **Section 3.3** and **3.4:** From the analysis of the O_2 F_{beam} values and *S,* the actual value of the accommodation coefficient, α, is required. This could be achieved by performing experiments based on the Kings and Wells method for the O, O_2, H and H_2 beam on silica over a range of silica surface temperatures. Further modifications to the apparatus system may be required if the value of α is too small to allow for multilayer coverages to be dosed without the surface becoming contaminated. This could be achieved using similar beam cooling techniques to those currently used on the FORMOLISM and ASURA apparatus [9, 10]. Additionally, the application of this technique may reduce the beam concentration of excited species enabling the surface formation mechanisms of species like H_2O_2 and $^{13}CO_2$ to be determined in the atomic O beam TPD experiments (see **Section 6.3**) as the current suggestions depend on the presence of $O(^1D)$ atoms.
- **Section 3.4:** To determine the values of F_{beam} for the atomic O and H beams, the $O:O_2$ and $H:H_2$ dissociation fractions are required by performing cracking fraction experiments. For this to be achieved, the adaptor flange would need to be replaced with a xyz manipulator and port alignment capability to allow for a more accurate positing of the QMS in-line with the beams.
- **Section 4.2:** The CKS model used to fit the H_2O TPD data assumed a single crystallisation step which followed first order kinetics. Although the model fitted the data well, the pre-exponential value, *ν*, was considerably outside the expected first order kinetic range. This problem with the crystallisation step was further emphasised when this reaction mechanism was used towards constructing a simulation model mimicking the desorption of O_2 from icy mantles under astronomical heating rates (**Section 4.6**) as none of the H_2O molecules crystallised. In the future, the reaction mechanism could be developed to improve the kinetic description of the H_2O crystallisation.
- **Section 4.6:** The simulation results mimicking the desorption of O_2 from icy mantles under astronomical heating rates revealed that the model used was too simple. In the future, the model could be developed to include: O_2 surface coverage dependent values of E_{des}; improved description of the pASW to cASW phase change; combining the trapped O_2 release step with the cASW crystallisation step or steps (depending on the results from the suggestion made in the previous bullet point) and developing the trapped O_2 diffusion step.

- **Section 5.3:** Observations of the multilayer TPD experiments for CO on bare silica and N_2 on bare silica revealed that the data was affected by a non-constant current leakage in the sample heater circuit. Although the data was still analyzed, the values obtained for E_{des} were outside the experimental range of those found in the literature. In the future, the apparatus will need to be modified to remove this current leakage before any other TPD experiments can be performed.
- **Section 6.3:** To calculate the values of $N[O]_i$ and $N[O_2]_i$ dosed onto the surface more accurately, the experiments to determine α and $[O{:}O_2]$ are required (for more details see **Section 3.3**). Once this has been achieved, additional atomic O beam dose TPD RAIRS experiments on several astronomically relevant surfaces over a range of irradiation times could be performed. The TPD data could than be modified to obtain the surface concentrations of the species of interest using a similar procedure base on the cracking reactions occurring in the QMS source. The accuracy of this procedure could further be improved by performing the required experiments to determine the remaining cracking fractions and sensitivity factors. For each of the species of interest, the desorption kinetics could be obtained by applying either leading edge analysis for multilayer coverages or direct inversion of the Polyani-Wigner equation. The parameters obtained could then be used to construct a simulation model to explore the surface formation, destruction, desorption and other surface processes occurring in these experiments before applying the model to dense molecular cloud environments. The results obtained may contribute towards explaining why O_2 has yet to be observed in the icy mantles [11] and why O_3 have yet to be observed in the ISM [8].

Further, longer term work currently planned for the new dual atomic beam apparatus would be to perform atomic H and dual atomic H and O beam experiments on a range of astronomically relevant surfaces. The results obtained could be used towards explaining the full H_2O surface formation mechanism on interstellar dust grains under different ISM environments which is the ultimate aim of this on-going research. In the more distant future, the RF plasma source used to form the atomic O beam could be modified or replaced enabling other interstellar systems to be explored. Possible suggestions could include the H and C (fourth most abundant element in the ISM after H, He and O) and H and N (fifth most abundant element) dust grain surface chemistry systems.

7.3 References

[1] H. J. Fraser, M. P. Collings, M. R. S. McCoustra and D. A. Williams, *Mon. Not. R. Astron. Soc.*, 2001, **327**, 1165.

[2] R. J. Speedy, P. G. Debenedetti, R. S. Smith, C. Huang and B. D. Kay, *J. Chem. Phys.*, 1996, **105**, 240.

[3] D. R. Haynes, N. J. Tro and S. M. George, *J. Phys. Chem.*, 1992, **96**, 8502.

[4] K. Acharyya, G. W. Fuchs, H. J. Fraser, E. F. van Dishoeck and H. Linnartz, *Astron. Astrophys.*, 2007, **466**, 1005.

[5] M. P. Collings, J. W. Dever, H. J. Fraser and M. R. S. McCoustra, *Astrophys. Space Sci.*, 2003, **285**, 633.

[6] S. E. Bisschop, G. W. Fuchs, E. F. van Dishoeck and H. Linnartz, *Astron. Astrophys.*, 2007, **474**, 1061.

[7] G. W. Fuchs, K. Acharyya, S. E. Bisschop, K. I. Oberg, F. A. van Brocekhuizen, H. J. Fraser, S. Schlemmer, E. F. van Dishoeck and H. Linnartz, *Faraday Discussion*, 2006, **133**, 331.

[8] C. J. Bennett and R. I. Kaiser, *Ap. J.*, 2005, **635**, 1362.

[9] E. Matar, H. Bergeron, F. Dulieu, H. Chaabouni, M. Accolla and J. L. Lemaire, *J. Chem. Phys.*, 2010, **133**, 104507.

[10] N. Watanabe and A. Kouchi, *Ap. J.*, 2002, **571**, L173.

[11] B. Vandenbussche, P. Ehrenfreund, A. C. A. Boogert, E. F. van Dishoeck, W. A. Schutte, P. A. Gerakines, J. Chiar, A. G. G. M. Tielens, J. Keane, D. C. B. Breitfellner and M. Burgdorf, *Astron. Astrophys.*, 1999, **346**, L57.